



Table of Contents:

- ❖ **Effects of Ratio of Dynamic Circulation to Evaporation Rates on Exergy and ...** 99-110
Behzad Omid Kashani
- ❖ **Numerical Investigation of Convective Heat Transfer from a Horizontal Plate ...** 111-120
Mostafa Rahimi , Behnaz Parsajoua, Mohammad Vajdia
- ❖ **Intensification of CO₂ Capture by Monoethanolamine Solution in a Rotating ...** 121-128
Mahdi Hefzi Lotfabadi , Masoud Shirzadi Ahoudashti , Mahdiah Abolhasani
- ❖ **Unsteady Magneto hydrodynamic Mixed Convection Flow over a Rotating ...** 129-140
A. Sahaya Jenifer , Saikrishnan Ponnaiah , Natarajan
- ❖ **Investigation of particle resuspension from a garment using different turbulence ...** 141-154
Hamidreza Kharinezhad Arani, Ali Jafarian , Jamal Darand
- ❖ **Effects of Radiation Absorption, Soret and Dufour on Unsteady MHD Mixed ...** 155-168
Temjennaro Jamir , Hemanta Konwar
- ❖ **Magneto hydrodynamics and Aspect Ratio Effects on Double Diffusive Mixed ...** 169-188
Shivananda Moolya, Satheesh Anbalagan , Neelamegam Rajan Devic , Rekha Moolyad
- ❖ **Fluid Analysis of Double-Layered Blood Flow through a Tapered Overlapping ...** 189-196
Moses Sunday Dadaa, Abiodun Joseph Babatunde , Mohammed Muritala Tundeb
- ❖ **A New Approach for the Heat and Moisture Transfer in Desiccant Wheels ...** 197-208
Seyed Amir Hossein Zamzamin , Hassan Pahlavanzadeh, Mohamad Reza Omidkhan Nasrin
- ❖ **Computational Analysis of Automobile Radiator Roughened with Rib Roughness ...** 209-218
Robin Kumar Thapa , Vijay Singh Bisht , Kamal Rawat , Prabhakar Bhandari
- ❖ **Parameter Estimation in Mass Balance Model Applied in Fixed Bed Adsorption ...** 219-232
Rhaisa Sousa Tavares , Camila Santana Dias, Carlos Henrique Rodrigues Moura, Emerson Cardoso Rodrigues , Bruno Marques Viegas , Emanuel Negrão Macêdo , Diego Cardoso Estumano
- ❖ **Monte Carlo Optimization of a Solar Combisystem Using Photovoltaic-Thermal ...** 233-244
Maryam Karami , Kiavash Akbari, Mohammad Jalalizadeh
- ❖ **Monte Carlo Optimization of a Solar Combisystem Using Photovoltaic-Thermal ...** 245-254
Maryam Karami , Kiavash Akbari, Mohammad Jalalizadeh
- ❖ **Fabrication of Solar Desalination System and Experimental Investigation of its ...** 255-268
Reza Bahoosh, Ashkan Nazari , Mazyar Changizian , Mojtaba Moravej
- ❖ **Spectral Quasi-Linearization Approach for Unsteady MHD Boundary Layer ...** 269-278
Adeyemi Isaiah Fagbade
- ❖ **The Synthesis of Lanthanum Oxide/Ni Catalyst on the CMK-3 for the CO₂ ...** 279-288
Abbas Kakoo, Mardali Yousefpour



Journal of **HEAT AND MASS** TRANSFER RESEARCH





Semnan University



Effects of Ratio of Dynamic Circulation to Evaporation Rates on Exergy and Cooling Efficiencies an Evaporative Cooler

Behzad Omid Kashani *

Department of Mechanical Engineering, Faculty of Engineering, University of Birjand, Birjand, Iran.

PAPER INFO

Paper history:

Received: 2021-06-01

Revised: 2022-11-15

Accepted: 2022-11-20

Keywords:

Dynamic water circulation rate;
Exergy efficiency;
Cooling efficiency;
The ratio of circulation to evaporation rates.

ABSTRACT

The expected performance characteristics of a wet media in an evaporative cooler with the specified geometric and material aspects are reducing the dry-bulb temperature and increasing the moisture content of the air outlet. Inlet air conditions are not under the control of the designer or the operator, but the choice of media geometry and fabric, the external factors such as the water circulation rate, and the velocity of air passing through the media could be controlled by the designer. Based on cooling performance for the excelsior of aspen wood pad, the minimum amount of ratio of the static circulation to evaporation rates is about 8 to 12, which has been mentioned in the literature. In this work, for the cellulosic pad by considering the exergy and cooling efficiencies, the optimal ratios of circulation to evaporation rates are presented for different air velocities. It can be seen that under the constant inlet air conditions, by increasing the air velocity as: 0.5, 1.0 and 1.5 m/s, the maximum exergy efficiency values are 0.10, 0.13 and 0.18 respectively and there are some specified values (minimum) for the ratios of water circulation to evaporation rates between 2 and 2.8 for the typical cellulose pad. However, for the same air velocities, maximum cooling efficiencies occur at lower exergy efficiencies, such as 0.03, 0.04, and 0.045, respectively.

DOI: [10.22075/jhmtr.2022.23572.1346](https://doi.org/10.22075/jhmtr.2022.23572.1346)

© 2022 Published by Semnan University Press. All rights reserved.

1. Introduction

In hot, dry and desert areas, controlling the temperatures of enclosed spaces with residential and industrial uses, including those related to agricultural and livestock activities has always been considered. Evaporative Cooling Pad (ECP) is one of the most effective and cheapest technologies available to create favorable conditions inside the enclosed spaces due to low energy consumption. The basis of ECP is that the hot and dry outdoor air passes through a wet media and as the water evaporates on the surface of this wet media, the temperature of the passing air decreases [1].

In all researches on ECP performance, the operation of the circulation pump can be divided into two different types:

- 1- Circulation pump is always working continuously and the performance of the pad is always stable and in the current research, this type of circulation is called static. Most research is of this type.
- 2- The circulation pump is switched on only in a part of a certain working period and the rest of the period is off, so pad performance does not always remain stable and in this research the pad performance is called dynamic. Very little research has been done on this type.

Many studies and researches have investigated the effect of material and their geometry in wet media (pad), different air velocities passing through the pad and different atmospheric conditions on ECP performance along with static circulation in the literature [2-7].

*Corresponding Author: Behzad Omid Kashani
Email: B.KASHANI@BIRJAND.AC.IR

Paschold et al. [6] investigated the effect of two different environments such as aspen wood excelsior pad and cellulose (rigid media) pad as well as the effect of air velocity passing through the pad on the physical properties of the flow including characteristic length and Reynolds number and residential time. They reported that for aspen and cellulose pads, the Reynolds number was in the range of 492 to 730 and in the range of 1841 to 2829, respectively [6].

Martinez et al. [5] investigated the effect of wet plastic material compared to other wet materials such as cellulose and the effect of different air velocities on the static pad performance and observed that with increasing air velocity from 0.5 to 2.5 m/s, cooling efficiency decreased from 81 to 70%, but exergy efficiency did not change significantly and remained constant. Matrtinez et al. [5] also investigated the effect of different rates of static circulation on cooling and exergy efficiencies. However, they have not investigated the ratio of circulation rates to evaporation and the effect of this ratio on cooling and exergy efficiencies.

Abohorlu et al. [2] investigated the effect of wet pad of eucalyptus fibers at different air velocities on the cooling efficiency of the pad and reported that by increasing the air velocity from 0.1 to 0.6 m/s, the cooling efficiency of 71% decreased to 49%.

There are other studies to investigate the effect of different rates of static circulation, different air velocities passing through different types of pad and different atmospheric conditions on the performance of ECP in the literature [1, 4, 8-11].

According to standards for aspen wood excelsior pads with a thickness of 0.05 m, the range for the ratio of static circulation to evaporation rates was suggested between 9.5 and 10.5 [1, 11]. So far, for cellulose pads no scientific or practical standard or recommendation for the ratio has been reported.

Franco et al. investigated the effect of different static circulation rates along with the effect of passing air velocities through the cellulose pads on the air pressure drop, mass and heat transfer coefficients and cooling efficiency [8]. They report that by increasing the static circulation rate from 0.1 to 0.25 kg/s-m², the cooling efficiency does not change much (less than 1%). Also, with increasing air velocity from 0.5 to 4 m/s, due to the reduction of residential time, cooling efficiency decreased from 70 to 60%, and at the same time, the mass and heat transfer coefficients increased from 50 to 300 kg/h and from 20 to 120 W/m²-K (6 times), respectively [8].

Hu et al. [10] investigated the effect of different rates of static circulation on air pressure drop across the pad and cooling efficiency. They report that with increasing circulation rate from 0 to 39 l/min-m² and for air velocities from 0.5 to 3.5 m/s, the air pressure drop increases by 2 to 5 Pa for PVC media pads [10]. Also, for the same air velocities, by doubling the

circulation rate from 19.5 to 39 l/min-m², the cooling efficiency has increased between 2 to 3% [10].

Karaca et al. investigated the effect of 3 different values of static circulation rate of 2, 4 and 6 l/min-m² on the cooling efficiency of cellulose pad [4]. They have reported that the highest and lowest cooling efficiencies (reduction of passing air temperature) are in the circulation circuits of 4 and 6 l/min-m², respectively, and finally stated that no clear result from the effect of changing the static circulation rate on the cooling performance of the pad [4].

Franco et al. Investigated the effect of static circulation rate on the amount of water retained in 4 different cellulose pads with different geometric characteristics and reported that by increasing the circulation rate from 0.12 to 0.26 l/s-m², the amount of water retained by the pads (with identical thicknesses) can be increased from 17 to 44% [9].

According to the mentioned researches, about the effect of static circulation rate, it is observed that no standard reference has been provided to the researchers by the pads manufacturers, so the researchers have chosen the circulation rate according to individual choices and experiences, and sometimes they increased the circulation rate 3 times or even more [4, 8, 10, 12].

On the other hand, very little researches have been done by researchers to investigate the effect of dynamic circulation rate on pad performance [13-15]. Omid Kashani [15] by using dynamic performance was able to increase the energy efficiency ratio (EER) of a direct type evaporator between 10 to 15%. In a study by Sreeram, he first examined the effect of different static circulation rates of on the performance of a cellulose pad and then turned off the pump and found that until about 5 minutes later, the pad could function without any change in its cooling performance. During this period, due to the shutdown of the circulation pump, the pressure drop of the passing air has decreased by 12 Pa (which means an increase in the air passing rate, and of course, an increase in the cooling load was happened) [14].

In other words, it can be predicted that by increasing the cooling load on the one hand and reducing the electrical energy consumption (due to the shutdown of the circulation pump) on the other hand, the energy efficiency ratio (EER) of the pad with dynamic performance can be increased than its static performance [15].

In a study conducted by Rong et al., They studied the performance of cellulose pads with dynamic circulation rate and calculated the cooling efficiency the heat and mass transfer coefficients [13]. Rong et al. are one of the few researchers to investigate the effects of dynamic circulation rate variations and different air velocities on cooling performance in a cellulosic pad, to regulate the dry-bulb temperature and relative humidity of the outlet air [13]. They varied the pump-

on time (p.o.t.) duration between 3 and 120 seconds in different time control cycles (which include the durations of pump-on and pump-off). The control time cycles (c.t.c.) are chosen as 3, 4, and 5 minutes [13].

They examined the effect of 21 different dynamic circulation rates from 5.6 to 300 l/h at 3 different air velocities from 0.5 to 1.5 m/s on pad performance (cooling efficiency and mass transfer coefficients). They observed that with increasing dynamic circulation rate, the cooling efficiency of the pad for all passing air tracks increases from 45 to 60% and with the increase of the passing air speed, the cooling efficiency decreases by 20 to 25%.

According to these researches, it can be seen that the simultaneous effects of important parameters such as dynamic circulation rate and air velocity on energy and exergy efficiencies and evaporation rate have not been studied at all. The circulation rates selected by previous researchers were based on personal taste and experience and is not based on any scientific and standard principles based on the geometry and material of the pad.

The purposes of the present study are: a) to determine the maximum amount of evaporation rate (nominal evaporation capacity) for a type of cellulose pad and b) to determine the allowable range of circulation rate (or ratio of circulation rate to evaporation rate) according to the conditions of maximum cooling and exergy efficiencies of the pad. In the present work, for a typical cellulosic pad, the evaporation rate, the cooling and exergy efficiencies are investigated for different dynamic water circulation rates and different air velocities based on result of Rong et al. [13].

2. Materials and methodologies

2.1. Extracted experimental data

Due to limited laboratory and experimental facilities, the calculations in the present work are based on the extraction of experimental data from Rong et al. research [13]. As mentioned in the introduction, for a pad with dynamic performance, a suitable range of circulation rate (or the ratio of circulation to evaporation rates) for different air velocities has not been proposed so far. The selected ECP made by impregnated and corrugated cellulose paper sheets with various flute angles available from Munters AB, Kista, Sweden based on Rong et al. research [13]. The primary experimental results of Rong et al. include:

- Instantaneous values of dry bulb temperature and relative humidity of the inlet and outlet air of the wet pad for each air velocity,
- Instantaneous cooling efficiency,
- Instantaneous mass transfer coefficient in each of the 63 different operating conditions

(according to Table 1, there are 21 cases for each air velocity, then for three different passing air velocities, there are total $21 \times 3 = 63$ cases).

Then the data was extracted from the resulting curves of Rong et al [13] by Plot Digitizer software [16]]. The different amounts of dynamic water circulation rates are found by different amounts of control time cycle (c.t.c.) and pump on-time (p.o.t.). 3 different values of c.t.c. are 3, 4 and 5 minutes and 7 different p.o.t. values as 3, 5, 10, 20, 30, 60 and 120 seconds are chosen by Rong et al [13]. The static water circulation rate is 7.5 l/min. For example, if the amounts of c.t.c. and p.o.t. values are chosen as 4 minutes and 3 seconds, respectively, the dynamic circulation rate is $7.5 \times 3 / 4 / 60 = 0.125$ l/min, which is about 1:80 smaller than static circulation rate. Certainly, there was the possibility of hot spots occurrence on the pad for this amount of circulation rate as static kind, but not for dynamic one. As mentioned before, in the present work, the experimental values of the outlet air dry-bulb temperature of the cellulose pad used from Rong's results [13] values for c.t.c. and seven different p.o.t. values, so totally, there are 21 different dynamic water circulation rates, according to Table 1 for each air velocity.

By ascend arranging the different states in Table 1 according to the values of the dynamic water circulation rate as shown in Table 2, it can be seen that the dynamic water circulation rate could be varied from 4.5 l/h to 300 l/h and also the ratio of dynamic to static circulation rates could vary from 0.01 to 0.667. It can be seen that the reduction of the circulation rate to about 0.01 compared to the static circulation rate is only possible with the dynamic method.

During this periodic dynamic performance of the pad, the dry-bulb outlet temperature and the cooling efficiency are instantly measured in different air velocities, and a relationship between the dynamic circulation rate, and air passing rate, and cooling efficiency was provided for the typical pad [13]. For each amount of air velocity and all different dynamics circulation rates (21 cases), the conditions of inlet air (including dry-bulb air temperature and relative humidity) were kept constant at specified amounts, as mentioned in Table 3.

So, in the present work, only the effects of external factors (such as the circulation rate and the air velocity that can be controlled by the operator of the cooler) on pad performance (such as evaporative rate, thermal performance, energy and exergy efficiencies) have been investigated.

Here, it is assumed that the cooling evaporation process is carried out as the adiabatic process. Therefore, the wet-bulb temperature of the air remains constant through passing the pad.

2.2. Mathematical Equations

In the present work, the cooling and exergy efficiencies and the exergy values of inlet and outlet air and water through the pad are calculated.

Table 1. Dynamic and static circulation rates and their ratios for different amounts of c.t.c. and p.o.t [13]

case	c.t.c. (min)	p.o.t (sec)	dynamic water circulation rate (lit/h)	static water circulation rate (lit/h)	the ratio of dynamic to static water circulation rates
1	3	3	7.5	450	0.017
2	3	5	12.5	450	0.028
3	3	10	25	450	0.056
4	3	20	50	450	0.111
5	3	30	75	450	0.167
6	3	60	150	450	0.333
7	3	120	300	450	0.667
8	4	3	5.625	450	0.0125
9	4	5	9.375	450	0.021
10	4	10	18.75	450	0.042
11	4	20	37.5	450	0.083
12	4	30	56.25	450	0.125
13	4	60	112.5	450	0.25
14	4	120	225	450	0.5
15	5	3	4.5	450	0.01
16	5	5	7.5	450	0.017
17	5	10	15	450	0.033
18	5	20	30	450	0.067
19	5	30	45	450	0.1
20	5	60	90	450	0.2
21	5	120	180	450	0.4

The evaporative cooling process is modeled under insulation conditions, so the wet-bulb air temperature is assumed to be constant during the passage of air. The temperature of the inlet water is assumed to be the same as the wet-bulb temperature of the entering air. The following relation can find cooling efficiency ($\eta_{cooling}$):

$$\eta_{cooling} = \frac{(T_{in} - T_{out})}{(T_{in} - T_{in,wb})} \tag{1}$$

where T_{in} , T_{out} , and $T_{in,wb}$ are the inlet air dry-bulb, the outlet air dry-bulb, and the inlet air wet-bulb temperatures, °C, respectively. In the present work, T_{wb} represents the wet-bulb temperature, (°C), and is calculated based on the values of dry-bulb temperature, T (°C), and relative humidity, φ (%), by following equation [17].

$$T_{wb} = T \cdot tg^{-1} [0.151977(\varphi \times 100 + 8.31659)^{0.5}] + tg^{-1}(T + \varphi \times 100) - tg^{-1}(\varphi \times 100 - 1.676331) + 0.00391838(\varphi \times 100)^{1.5} \times tg^{-1}(0.023101 \times \varphi \times 100) - 4.686035 \tag{2}$$

Table 2. Dynamic water circulation rates for the 21 cases in ascending order [13]

case	dynamic water circulation rate (lit/h)	the ratio of dynamic to static circulation rates of water
15	4.5	0.01
8	5.625	0.0125
1	7.5	0.017
16	7.5	0.017
9	9.375	0.021
2	12.5	0.028
17	15	0.033
10	18.75	0.042
3	25	0.056
18	30	0.067
11	37.5	0.083
19	45	0.1
4	50	0.111
12	56.25	0.125
5	75	0.167
20	90	0.2
13	112.5	0.25
6	150	0.333
21	180	0.4
14	225	0.5
7	300	0.667

Table 3. Conditions of inlet air to the pad at different inlet air velocities [13]

Air velocity (m/sec)	Inlet air dry-bulb temperature (°C) (average)	Inlet air relative humidity - RH (%) (average)
0.5	45.8 – 46.5 (46.15)	3.6 – 4.0 (3.8)
1.0	44.5 – 45.0 (44.75)	4.1 – 4.9 (4.5)
1.5	40 – 45.3 (42.65)	5.4 – 8.3 (6.85)

The values of dry-bulb temperature and relative humidity for inlet air are known, so the inlet air wet-bulb temperature is explicitly obtained from equation (2). But for the outlet air, based on the adiabatic assumption of the process, the outlet air wet-bulb temperature is assumed to be equal to the inlet air wet-bulb temperature, and it is known (as mentioned

before). In each case, by applying the known values of wet-bulb temperature, T_{wb} , and outlet air dry-bulb temperature, T , from the experimental work of Rong et al. [13] (Rong et al., 2017), the relative humidity of the outlet air from equation (2) is implicitly found in terms of T_{wb} and T . The amount of evaporative water rate can be found from the following relation:

$$\dot{m}_v = \dot{m}_{a2} \cdot \omega_2 - \dot{m}_{a1} \cdot \omega_1 \quad (3)$$

where \dot{m}_{a1} and \dot{m}_{a2} are the inlet and outlet dry air mass rates, respectively, and ω_1 and ω_2 are the kg of water vapor/kg dry air, respectively. \dot{m}_a and ω are also found from the following relation:

$$\dot{m}_a = \frac{(P - \phi \cdot P_s) \cdot V}{287 \cdot T} \quad (4)$$

$$\omega = 0.622 \frac{\phi \cdot P_s}{(P - \phi \cdot P_s)} \quad (5)$$

where P , ϕ , P_s , V , and T are atmospheric pressure equal to 101325 Pa, relative humidity, water vapor saturation pressure (Pa), the volume rate of passing air, and air dry-bulb temperature in sections 1 and 2, respectively for inlet and outlet sections. The water vapor saturation pressure, P_s , is expressed in terms of Pascal (Pa) from the following relation [18]:

$$P_s = 610.8 \cdot \exp\left(\frac{T}{T + 238.2} \times 17.2694\right) \quad (6)$$

T is the dry-bulb air temperature of °C, V is the volume rate of air that is equal to the product of the velocity of air passing through the front surface area (air passage), and the front surface area ($0.6 \times 1.8 = 1.08 \text{ m}^2$).

2.2.1. Exergy Analysis

According to the Figure 1, the inlet air has index 1 and the outlet air has index 2, and the inlet circulation water is entered into the pad has index 3 and part of this water is evaporated (\dot{m}_v) and the surplus of this water is just exited at the bottom of the pad with index 4 and this water discharged into the water collection container. The water circulation rate is always higher than the rate of evaporation water. The water circulation rate can be calculated as follows:

$$\dot{m}_{w,3} = \text{dynamic circulation rate} = \frac{\dot{m}_v}{\dot{m}_v + \dot{m}_{w,A}} \quad (7)$$

Exergy is the ability to convert energy into work. Exergy can be transmitted in three ways: work, heat transfer, and mass transfer through the control surface. All processes are irreversible essentially, and some exergy is destroyed during these processes.

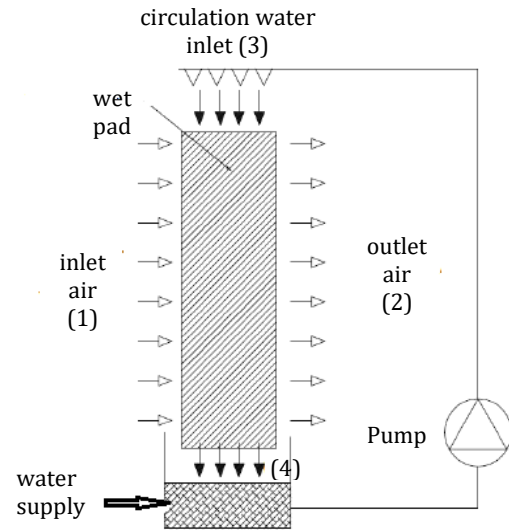


Figure 1. Overview of the control volume of a wet pad in of a direct evaporative water cooler

The exergy balance for a wet pad as a control volume, in steady-state conditions where there is no work exchange with its environment, could be written as [19-20]:

$$\sum_{in} \dot{E}x_Q + \sum_{in} \dot{m} \cdot \psi - \sum_{out} \dot{E}x_Q - \sum_{out} \dot{m} \cdot \psi - \dot{E}x_{dest} = 0 \quad (8)$$

where $\dot{E}x_Q$ and $\dot{E}x_{dest}$ are the amount of exergy exchanged due to heat transfer and the amount of exergy destruction (is always positive) during this process, respectively. Also, ψ is the specific amount of fluid exergy at each inlet and outlet flows.

2.2.1.1 Exergy of inlet and outlet air through the pad

The exergy values of air are expressed as the equation (9) as follows [20]:

$$\psi_a = \psi_{phy} + \psi_{chem} \quad (9)$$

The amount of specific physical exergy (ψ_{phy}) according to equation (9-1) can be divided into two parts: thermal and mechanical, as follows:

$$\psi_{phy} = \psi_{phys-thermal} + \psi_{phys-mechanical} \quad (9-1)$$

The contributions of physical-thermal and physical-mechanical exergies are calculated by the equations (9-2) and (9-3), respectively as below:

$$\psi_{phy-thermal} = (Cp_a + \omega Cp_v)T_0 \left(\frac{T}{T_0} - 1 - \ln\left(\frac{T}{T_0}\right) \right) \quad (9-2)$$

$$\psi_{phys-mechanical} = (1 + 1.608\omega)R_a T_0 \cdot \ln\left(\frac{P}{P_0}\right) \quad (9-3)$$

Since the wet pad is at ambient pressure and except for the slight pressure drop during air passage, it can always be considered at ambient pressure ($P = P_0$), so the physical-mechanical exergy contribution of the air is always zero.

The chemical exergy value of air is also given by equation (9-4) as follows:

$$\psi_{chem} = R_a T_0 \left[(1 + 1.608\omega) \ln \left(\frac{1 + 1.608\omega_0}{1 + 1.608\omega} \right) + 1.608\omega \ln \left(\frac{\omega}{\omega_0} \right) \right] \quad (9-4)$$

in the above equations, Cp_a , Cp_v , ω , ω_0 , T_0 and R_a are the heat capacity of the air, the heat capacity of the water vapor, the ratio of humidity, the ratio of humidity at dead state (which the system is in equilibrium with temperature, pressure, and chemical equilibrium), dry-bulb air temperature, base temperature (the same as the ambient dry-bulb temperature or inlet air dry-bulb temperature to the pad or at dead state), K, and the gas constant for air, respectively.

Dead conditions for chemical exergy are T_0 as atmosphere dry-bulb temperature (inlet air dry-bulb temperature), P_0 atmospheric pressure (constant and equal to 101325 Pa), and ω_0 as the ratio of humidity at inlet air wet-bulb temperature.

The contribution of the physical-thermal exergy of inlet air to the pad according to equation (9-2) depends on air dry-bulb temperature and air humidity ratio. As the dry-bulb air temperature and the dry-bulb temperature of the base point are the same, the above term is always zero for inlet air. By eliminating the physical-mechanical exergy term of the air, the only exergy component for the inlet air is the chemical exergy contribution which is found from equation (9-4).

2.2.1.2. Specific exergy for inflow and outflow of water through the pad

Inlet and outlet water temperatures are equal to the inlet air wet-bulb temperature to the pad, the water flow exergy is calculated according to the following simplified equation [21];

$$\psi_\omega = -R_v T_0 \ln(\phi_0) \quad (10)$$

here, R_v is gas constant for vapor, and ϕ_0 is the ratio of the water vapor pressure of the unsaturated atmospheric air to the saturated water vapor pressure at the dead state temperature. According to Figure 1 and the presence of two inlet mass flows (sections 1 and 3) and two output mass flows (sections 2 and 4), exergy efficiency is found by two different ways as below:

- (a) The general definition of exergy efficiency can be as follow:

$$\eta_{II} = \frac{\sum_{out} \dot{m} \cdot \psi}{\sum_{in} \dot{m} \cdot \psi} = \frac{\dot{m}_2 \psi_2 + \dot{m}_4 \cdot \psi_4}{\dot{m}_1 \cdot \psi_1 + \dot{m}_3 \cdot \psi_3} \quad (11)$$

$$= \frac{\dot{m}_2 \cdot \psi_2 + \dot{m}_{add} \cdot \psi_4}{\dot{m}_1 \cdot \psi_1 + (\dot{m}_v \cdot \psi_3 + \dot{m}_{add} \cdot \psi_3)}$$

And since the specific exergies are equal in sections 3 and 4, the above relation can be written as follow:

$$\eta_{II} = \frac{\dot{m}_2 \psi_2 + \dot{m}_{add} \cdot \psi_3}{\dot{m}_1 \cdot \psi_1 + (\dot{m}_v \cdot \psi_3 + \dot{m}_{add} \cdot \psi_3)} \quad (12)$$

- (b) According to the target term in equation (12), which is the output exergy term in section 2, the target exergy efficiency can be defined by the following equation (13):

$$\eta_{II,*} = \frac{\sum_{out,*} \dot{m} \cdot \psi}{\sum_{in} \dot{m} \cdot \psi} \quad (13)$$

$$= \frac{\dot{m}_2 \psi_2}{\dot{m}_1 \psi_1 + (\dot{m}_v \cdot \psi_3 + \dot{m}_{add} \cdot \psi_3)}$$

where the sign (*) relates to the target exergy flow, by comparing the equations (12) and (13), it was seen, that there is always a relationship between these two exergy efficiencies as below:

$$\eta_{II,*} < \eta_{II} \quad (14)$$

Term $\dot{E}x_{dest}$ can be rewritten from the exergy balance, equation (8) as follows:

$$\dot{E}x_{dest} = \sum_{in} \dot{E}x_Q + \sum_{in} \dot{m} \cdot \psi - \sum_{out} \dot{E}x_Q - \sum_{out} \dot{m} \cdot \psi = \sum_{in} \dot{m} \cdot \psi - \sum_{out} \dot{m} \cdot \psi \quad (15)$$

The Overall exergy efficiency can be defined as equation (16):

$$\eta_{II} = 1 - \frac{\dot{E}x_{dest}}{\sum_{in} \dot{m} \cdot \psi} \quad (16)$$

there is no similar result, such as the last equation for $\eta_{II,*}$. Here, in terms of the purpose of evaporative cooling, which is to reduce the dry-bulb temperature and to increase the humidity of the outlet air through the pad (section 2), equation (13) is used to define the targeted exergy efficiency (from now as the preferred exergy efficiency).

A review of some previous works has shown that for calculating the exergy efficiency, the exergy of water which introduced in section 3, Figure 1, referred to the exergy of water consumed (evaporated) and the exergy associated with excess water flows over evaporation in that section was not considered, so there was not any outlet water flow at section 4 [21-22]. But in the results of some other researchers, the effect of exergy related to surplus water on evaporation in sections 3 and 4 has been considered in calculating the exergy efficiency [23].

When examining the effect of the circulation rate as a variable parameter on the pad exergy efficiency, it is

necessary to consider the exergy of the surplus water flow rate (Section 4) in both numerator and denominator of the exergy efficiency fraction according to equation (13). In the present work, however, in terms of more considerable attention to outlet air conditions in the targeted exergy efficiency (equation (13)), the exergy associated with excess water flow to the evaporated is considered only at the denominator of this equation (as part of exergy in section 3).

2.3. Series of calculation steps

All necessary thermodynamic variables, including absolute humidity at the inlet and outlet, the rate of evaporated mass, the mass of excess water leaving the pad, enthalpy, entropy and heat capacity of liquid water and steam were calculated by a computer program which was written in engineering equation solver (EES) software and series of calculation steps are summarized as below:

- A. With the experimental values of dry-bulb temperature and relative humidity of the inlet air and applying equation (2), the wet-bulb temperature of inlet air to the pad is found and then based on the assumption of an adiabatic process for the control volume around the pad according to Figure 1, the wet-bulb temperature of outlet air is the same as the wet-bulb temperature of inlet air to the pad. Then, with the known variables of wet-bulb temperature and dry-bulb temperature of the output and inlet air of the pad (sections 1 and 2 at Figure 1), the absolute humidity of the inlet and outlet air of the pad are found by the EES code.
- B. With the differential amount of the absolute humidity of the outlet and inlet air and mass rate of passing air (based on the velocity of passing air through the pad), the evaporation rate (rate of water supply rate) is found.
- C. By subtracting the evaporation rate from the dynamic circulation rate, the excess water output rate from the bottom of the pad is found (section 4 of Figure 1).
- D. The inlet and outlet water temperatures at sections 3 and 4 of Figure 1 are assumed to be equal. Based on the values of air and water inlet and outlet rates to the control volume, both of the cooling and exergy efficiencies are calculated for each case by the EES code [24]. The process of calculating the rate of evaporation rate and energy and exergy efficiencies is given in the flowchart in Figure 2.

3. Results and discussion

The least expensive and safest tool to evaluate the performance of the pad is to calculate the efficiency of the first law (cooling efficiency) and the efficiency of

the second law of thermodynamics (exergy efficiency) based on the known properties of parameters in sections 1 to 4 of Figure 1.

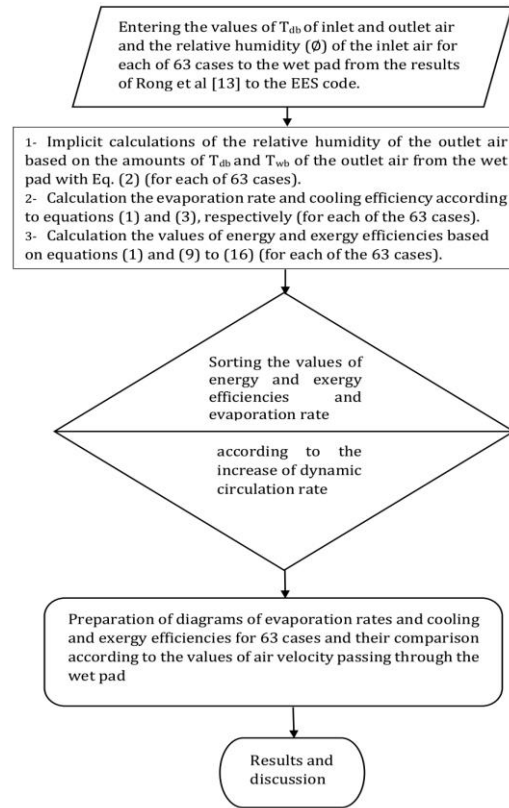


Figure 2. Flowchart of procedure of calculations performed by the EES code in the current study

Here, the pad is considered as a control volume or a black box that does not need to be examined in detail the interactions of its internal phenomena (related to the mass and heat transfer processes, capillary, and water absorption capacity of the pad and the effect of air velocity on the transmission surface). As previously mentioned in the introduction, for the pad with dynamic condition, the exergy efficiency has not been investigated so far.

For calculating the cooling efficiency, only the effect of sensible heat transfer to the passing air is considered. But in exergy efficiency, in the chemical term of exergy, the degree of chemical effectiveness (increasing the humidity of the passing air - mass transfer) and in the thermo-mechanical term, the sensible heat transfer (due to the change in dry air temperature-heat transfer) in the exergy of the passing air are considered, simultaneously. So, the simultaneous occurrence of the maximum of the energy and exergy efficiencies of pad performance is impossible. Here, the ranges of the new parameter (ratio of circulation to evaporation rates) have been investigated for the occurrence of maximum values of cooling and exergy efficiencies (first and second laws of thermodynamics) according to the air velocity passing through the pad.

The effect of dynamic water circulation rate on cooling efficiency and evaporated water rate for air velocity of 0.5 m/sec are shown in Figure 3.

In Figure 3, the similarity of the behavior of these two curves is well seen. It is also understood that by increasing the dynamic water circulation rate to a certain limit, about 50 kg/h, the cooling efficiency and evaporation rate increase dramatically, and from there on, the initial slopes of the curves decrease simultaneously and visibly. So, with increasing circulation rates up to 240 kg/h (about five times the limit value), only about 14 and 16% increment in average evaporation rate and cooling efficiency were happened, respectively. Point P and B, represent the circulation rates for occurrence states of the maximum exergy and cooling efficiencies, respectively. The circulation range C from P to B is suggested as an acceptable range for the typical pad with 0.5 m/s air velocity.

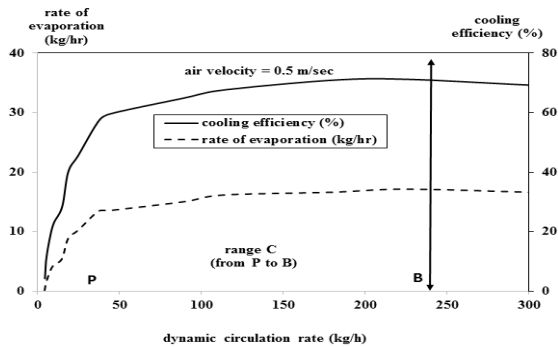


Figure 3. Evaporation rate and cooling efficiency in terms of dynamic circulation rate for 0.5 m/sec air velocity

The curves of cooling efficiency and evaporated water rate in terms of the dynamic circulation rate for all air velocities as 0.5, 1.0, and 1.5 m/sec, are given in Figures 4 and 5, respectively. In Figure 4, it is seen: first (same as Figure 3) there are an initial slope of the curves up to a specific circulation rate (point P, about 37.5 to 45 kg/h), and second cooling efficiency was reduced by increasing the air velocity which was due to the reduction of residential time of the passing air in near the surface of the wet pad, which is consistent with the literature.

And third, up to point B (range 240 to 300 kg/h, respect to all air velocities) the cooling efficiency (or evaporation rate) increased about 14 to 16% than point P. The circulation rate at point B is the nominal circulation rate (maximum evaporation rate happens in this circulation rate).

Figure 5 shows the effect of the dynamic circulation rate on the evaporation rate for different velocities of air passing through the pad. The same behavior as in Figures 3. and 4 is again observed for the curves of water evaporation rates at a specified circulation rate of (point P, with 37.5 to 45 kg/h circulation rate), but with increasing the air velocity the evaporation rate increases as a result of higher mass rate of passing dry

air and the evaporation intensification is happened due to the increased mass transfer coefficient due to the increasing Reynolds number and this behavior is expected as in the relevant literature.

Based on Figure 5, the nominal capacity (maximum evaporation rate) which happened at maximum cooling efficiency, is 35.48 kg/h at 300 kg/h circulation rate at 1.5 m/s air velocity for a typical pad. So, the nominal ratio of circulation to evaporation rates is 8.45. The evaporation rate between the occurrence position of maximum of exergy efficiency (point P as seen in Figure 8) and the nominal capacity of the pad (point B) changes only about 14% to 20%.

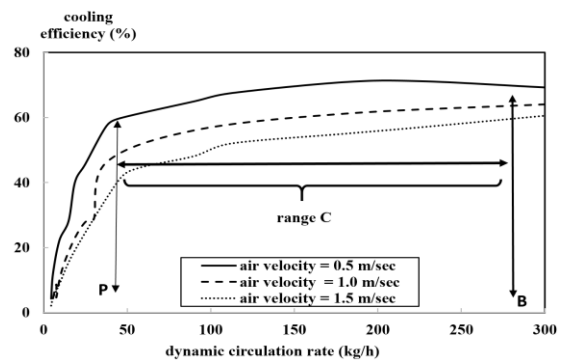


Figure 4. Cooling efficiency in terms of dynamic water circulation rate for different air velocities through the pad.

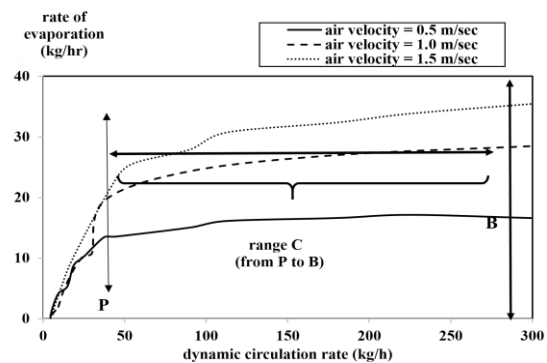


Figure 5. Evaporated water rate in terms of dynamic water circulation rate at different air velocities through the pad.

It can be seen from Table 3, dry temperature and relative humidity of the inlet air to the wet pad are kept almost the same and constant for different air velocities.

Under these conditions, the changes in dry air temperature and relative humidity of the outlet air from the wet pad in terms of dynamic circulation rate are shown in Figures 6 and 7, respectively. In these figures, it can be seen that by increasing the speed of the air passing through the wet pad, the residential time of passing air decreases near the pad and the outlet air does not have enough opportunity to reduce its temperature and gain more moisture. Therefore, with increasing the velocity of the passing air, the dry temperature of the outlet air increases and the relative humidity of the exhaust air also decreases.

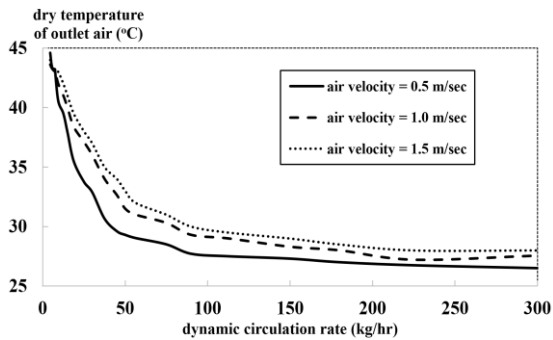


Figure 6. Outlet air dry temperature at different dynamic circulation rates

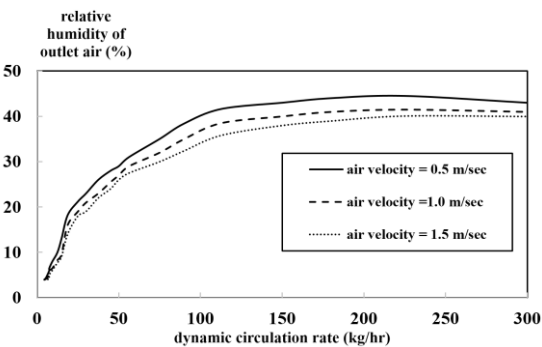


Figure 7. Relative humidity of outlet air at different dynamic circulation rates

Figure 8 shows the targeted exergy efficiency in terms of the dynamic water circulating rate for different velocities of air through the pad. As mentioned earlier, in Figures 3 to 5, the maximum of exergy efficiency occurred at the point P (with 37.6 to 45 kg/h circulation rate). For larger amounts of dynamic water circulation rate (such as point B, the circulation rate for the maximum cooling efficiency), the exergy efficiency drops. Range C is formed from the least circulation rate at point P to the highest circulation rate at point B. The exergy efficiency drop can be due to factors such as:

- (i). Decrease of the practical evaporation level due to the thickening of the layer of water coated on the wet pad surfaces or
- (ii). Different interact of heat and mass transfer phenomena from the pad to the passing air (depending on the velocity of the passage of air), as it was seen before in Figure 8, the exergy efficiency increases as the air velocity increases.

The exciting thing about the behavior of the typical pad (depending on its geometry and material) is that for this range of air velocities between 0.5 m/sec and 1.5 m/sec, maximum exergy efficiency always occurs at the specified circulation rate (37.5 to 45 kg/h). Similar investigations on the pad performance with different geometry, material, and air velocities could be useful for the industrial designers and customers of the wet pad.

In Figure 9, the curves of the ratio of circulation to evaporation rates are shown in terms of the dynamic

circulation rate for different air velocities. It is seen that the minimum amount of the ratio is about 2.8, 2, and 2 for different air velocities as 0.5, 1.0, and 1.5 m/sec, respectively, occurred at the same amount of circulation rate (37.5 to 45 kg/h where the maximum exergy efficiency has happened). In other words, this specific behavior of the pad indicates that at this amount of circulation rate, an optimal and relevance interacts happened between the evaporation and the cooling phenomena of the passing air for all different air velocities. At this special condition (position P), the maximum of exergy efficiency is happened.

For this pad, a minimum circulation rate of 50 kg/h is suggested and it is recommended that the circulation rate can be higher than this specified value (for working conditions). Figures 5. and 9. show that by a 6-fold increment of the circulation rate from point P to point B (50 kg/h to 300 kg/h), the ratio of the circulation to the evaporation rates increased simultaneously, but the evaporated rate only increased approximately 14% to 42% (from point P to B) for all passing air velocities. The rectangle abcd is the optimal domain for working condition of the pad. There are two horizontal lines at P and B, which represent the ratio of circulation to evaporation rates for occurrence the maximum exergy and energy efficiencies, respectively. And also, there are two vertical lines at P' and B', which are representative the rate of circulation for the maximum exergy and cooling efficiencies, respectively.

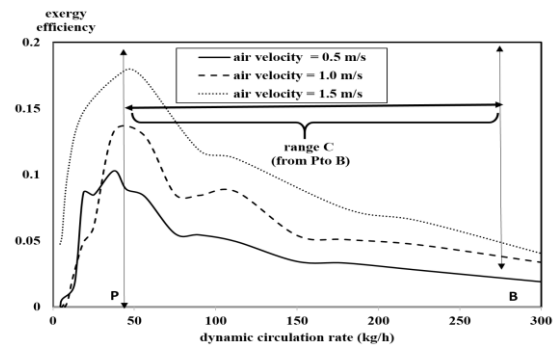


Figure 8. Exergy efficiency (Targeted) in terms of dynamic water circulation rate for different air velocities through the pad.

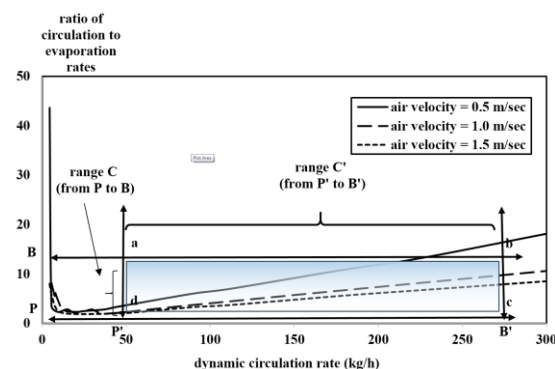


Figure 9. The ratio of the dynamic water circulation to water evaporated rates for different amounts of water circulation rate

In Figure 10, the cooling efficiency is presented in terms of the ratio of circulation to evaporation rates for different air velocities. The ranges **P** and **B**, represent the relevant ratios of circulation to evaporation rates for occurrence of maximum exergy efficiency (from 1.93 to 2.80) and cooling efficiency (from 8.50 to 13.15) for all air velocities, respectively.

Therefore, for the optimal operation of a typical pad (with specific material and geometric characteristics) in the intermediate conditions of maximum cooling and exergy efficiencies, a certain range (**C**) of the new parameter is recommended.

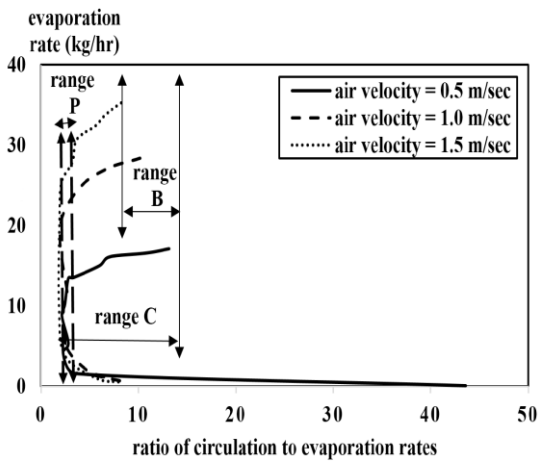


Figure 10. Cooling efficiency in terms of the ratio of the circulation to the evaporated rates

This range (**C**) is obtained by joining the two ranges **P** and **B** (related to maximum cooling and exergy efficiencies, respectively). The range **C** is formed from 1.93 to 13.15 (from the lowest amount of range **P** to highest amount of the range **B**). The pad performance conditions are somehow between the two conditions associated with the maximum exergy and cooling efficiencies. The nominal capacity (maximum evaporation rate) of the typical pad can be determined by the pad manufacturers in the most challenging working conditions (according to the climatic conditions and working days during the year and the passing air velocities).

The curves in Figure 11 have a non-functional behavior same as Figure 10, but similar to Figure 5, the evaporation rate increases with higher air velocity. Also the maximum evaporation rate occurs at maximum of the cooling efficiency conditions, not at the maximum exergy efficiency condition. Range **P** and **B**, again represent the conditions for occurrence the maximum of exergy and cooling efficiencies, respectively. And the range **C** is formed by joining of the two ranges **P** and **B**.

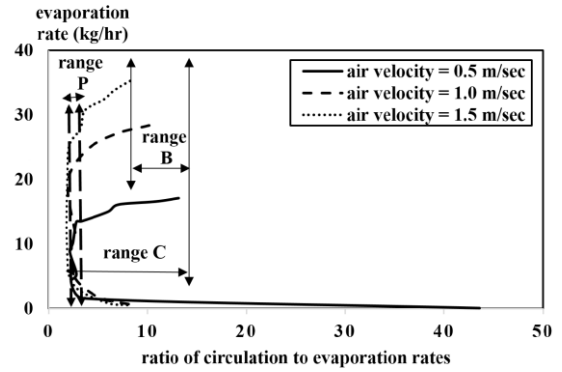


Figure 11. Water evaporation rate in terms of the ratio of circulation to evaporation rates

Figure 12 shows the variation of exergy efficiency in terms of the ratio of the circulation rate to the evaporation rate for different velocities of passage air, as well as the position and values of the maximum exergy efficiency. It can be seen that the maximum exergy efficiency in the ratio of circulation rate to evaporation rate was in the range of 1.93 to 2.80. Also with increasing the air velocity, the maximum exergy efficiency value increases as 0.10, 0.13 and 0.18 for 0.5, 1.0, and 1.5 m/sec, respectively. It seen, there are a unique non-functional behavior of the curves, so for reaching the minimum amount of the ratio of circulation to evaporation rates, by decreasing the ratio through both the lower and upper paths, the maximum of exergy efficiency is achieved.

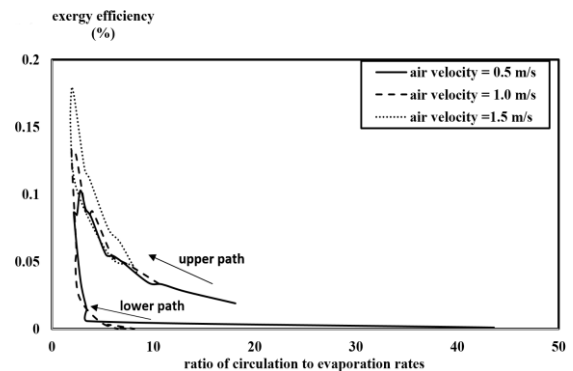


Figure 12. Exergy efficiency in terms of the ratio of circulation to evaporation rates for different air velocities

Finally, in Figure 13, the exergy efficiency is plotted in terms of cooling efficiency, and it seen that the maximum of exergy efficiency occurs when the cooling efficiency is not at its maximum value, and vice versa. By increasing air velocities, the maximum exergy and cooling efficiencies increase and decrease, respectively. The maximum cooling efficiency occurs where exergy efficiency occurs at far below their maximum values. The maximum of exergy efficiency is 0.10, 0.13, and 0.18 in these conditions, where the cooling efficiencies are 57.3%, 46.3%, and 40.8% for the air velocities of 0.5, 1.0, and 1.5 m/s, respectively.

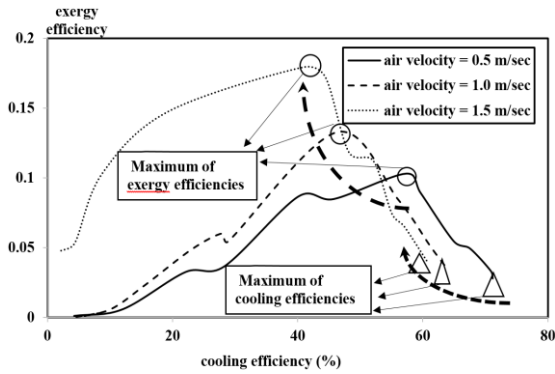


Figure 13. Exergy efficiency in terms of cooling efficiency for different velocities of air passing through the pad.

The maximum feasible of cooling efficiencies were 71.2%, 65.2%, and 60.6% for air velocities of 0.5, 1.0 and, 1.5 m/s, respectively, where the exergy efficiencies as 0.03, 0.034, and 0.04. Increasing the air velocity has three different effects on the pad performance: First it reduces the residential time of the air (reducing cooling efficiency and increasing evaporation rate), second the air velocity, the geometry and the kind of pad material, and circulation rate have complicate effects on effective contact surface area of the pad (for heat and mass transfer phenomena) and third, by changing the air velocity (and changing the Reynolds number) both the mass transfer coefficients (evaporation) and the heat transfer coefficient (cooling phenomenon) would be changed. Exergy efficiency can also be interpreted as affecting the air passing through the pad by lowering its temperature and absorbing water vapor. For cellulose and aspen wood-based pads, no minimum amount of static or dynamic water circulation rate based on the exergy approach has been recommended yet.

4. Conclusion

1. Comparing Figures 3 to 5 with Figure 8 shows that at point P, which is at the end of the steep slope of the cooling efficiency curves, it is exactly where the exergy efficiency of pad performance is maximized.
2. According to Figures 10 and 12, the simultaneous effect of the ratio of circulation to evaporation rates and the velocity of the passing air on the energy and exergy efficiencies of the pad were observed, respectively. These curves have not been achieved in previous researches on the ECP. Similar curves can be obtained for any other type of pad depending on its material and geometry, which can be applicable for pad designer and end users
3. For the typical pad was investigated here, the nominal capacity (maximum evaporation rate), the nominal ratio of dynamic circulation to evaporation rates, the recommended range of the

dynamic circulation rate, and the range of exergy and cooling efficiencies are 37.5 kg/h, 13.15 and from 37.5 to 300 kg/h, from 0.027 to 0.18, and 41% to 71%, respectively.

4. The velocity of air, effects on residential time of passing air through the pad, and also on the interaction between the mass transfer (evaporation) and heat transfer phenomena. The change of the dynamic circulation rate also impacts on the creation of an appropriate surface for the evaporation phenomenon, it is clear that in substantial amounts of the circulation rate, the flood phenomenon occurs, such as residential time and surface area for evaporation approach to zero.
5. According to Figures 9 to 11, the ranges P and B were shown from the values of the ratio of circulation to evaporation rates are related to the maximum exergy and cooling efficiencies, respectively, and their values are between 1.93 and 2.80 and between 8.50 and 13.15, respectively. So, the optimum range for the above ratio is from 1.93 to 13.15 (from the minimum of range of P to the maximum of range B). On the other hand, based on the only energy (thermal) perspective for the aspen wood-based pad, the ratio of circulation to evaporation rates with a range from 9.5 to 10.5 was suggested [1].
6. Figure 13 is a unique result that shows the exergy efficiency in terms of cooling efficiency for different air velocities passing through the pad. The positions of maximum exergy efficiency are different from the maximum cooling efficiency and with increasing air velocity, the maximum exergy efficiency increases and the maximum cooling efficiency decreases. It should be noted that this curve is the result of dynamic circulation, which is inherently different from static circulation and requires further research for static circulation, which has more uses.

Nomenclature

c.t.c.	Control time cycle
Ex	Exergy (kJ)
m	Mass (kg)
P	Pressure (Pa)
p.o.t.	Pump on-time
Q	Heat transfer (kW)
T	Temperature (°C)
y	Mole fraction
Greek Symbol	
φ	Relative humidity (%)
ω	Absolute humidity (kg vapor/kg dry air)
ϕ_0	The ratio of the water vapor pressure of the unsaturated atmospheric air to the saturated

	water vapor pressure at the dead state temperature
	The ratio of the water vapor pressure of the unsaturated atmospheric air to the saturated water vapor pressure at the dead state temperature
ψ	specific exergy (kJ/kg)
Subscripts	
a	Air
chem	Chemical
dest	Destroyed
g	Water vapor saturation
in	Inlet
o	Base
out	Outlet
phy	Physical
Q	Heat transfer
s	Saturated
thermal	Thermal
v	Water vapor in ambient condition (dead state)
w	Water
wb	Wet bulb

Acknowledgements

This research did not receive any specific grant from funding agencies in the public, commercial, or not-for-profit sectors.

References

- [1] John, R.W., 1996. *Evaporative Air Conditioning Handbook*, second ed., Chapman & Hall, New York.
- [2] Abohorlu Doğramacı, P., Riffat, S., Gan, G. and Aydin, G., 2019. Experimental study of the potential of eucalyptus fibres for evaporative cooling, *Renewable Energy*, 131, pp.250-260.
- [3] Dowdy, J.A., Handy, E.T., 1986. Heat- and Mass-Transfer Coefficients, *ASHRAE Transactions*, 92(2), pp.60-70.
- [4] Karaca, C., Yıldız, Y., Dağtekin, M. and Gümüş, Z., 2016. Effect of water flow rate on cooling effectiveness and air temperature change in evaporative cooling pad systems, *Environmental Engineering and Management Journal*, 15(4), pp.827-833.
- [5] Martínez, P., Ruiz, J., Martínez, P.J., Kaiser, A.S., and Lucas, M., 2018. Experimental study of the energy and exergy performance of a plastic mesh evaporative pad used in air conditioning applications, *Applied Thermal Engineering*, 138, pp.675-685.
- [6] Paschold, H., Li, W.W., Morales, H., and Walton, J., 2003. Laboratory study of the impact of evaporative coolers on indoor PM concentrations, *Atmospheric Environment*, 37(8), pp.1075-1086.
- [7] Sohani, A., Zabihigivi, M., Moradi, M.H., Sayyaadi, H., and Balyani, H.H., 2017. A comprehensive performance investigation of cellulose evaporative cooling pad systems using predictive approaches, 110, pp.1589-1608.
- [8] Franco, A., Valera, D.L., Madueño, A., and Peña, A., 2010. Influence of water and air flow on the performance of cellulose evaporative cooling pads used in mediterranean greenhouses, *Transactions of the ASABE*, 53(2), pp.565-576.
- [9] Franco, A., Valera, D.L., Peña, A., and Pérez, A.M., 2011. Aerodynamic analysis and CFD simulation of several cellulose evaporative cooling pads used in Mediterranean greenhouses, *Computers and Electronics in Agriculture*, 76(2), pp.218-230.
- [10] He, S., 2015. Performance Improvement of Natural Draft Dry Cooling Towers Using, *School of Mechanical & Mining Engineering*, 53(10), pp.122-130.
- [11] Takakura, T., 1982. Heating, Ventilating and Cooling Greenhouses, *Journal of Agricultural Meteorology*, 38(1), pp.65-70.
- [12] Tejero-González, A., and Franco-Salas, A., 2021. Optimal operation of evaporative cooling pads: A review, *Renewable and Sustainable Energy Reviews*, 151, 111632.
- [13] Rong, L., Pedersen, P., Jensen, T.L., Morsing, S., and Zhang, G., 2017. Dynamic performance of an evaporative cooling pad investigated in a wind tunnel for application in hot and arid climate, *Biosystems Engineering*, 156, pp.173-182.
- [14] Vishnu, S., 2014. Factors affecting the performance characteristics of wet cooling pads for cooling pads for data center applications, (M. Sc Thesis, The University of Texas at Arlington).
- [15] Omid Kashani, B., 2022. Increase of energy efficiency ratio of a direct evaporative cooler by dynamic behavior with energy and exergy analysis, *Proceedings of the Institution of Mechanical Engineers, Part C: Journal of Mechanical Engineering Science*, 236(7), pp.3818-3830.
- [16] Plot Digitizer, Department of Physics at the University of South Alabama in Mobile, AL.
- [17] Stull, R., 2011. Wet-bulb temperature from relative humidity and air temperature, *Journal of Applied Meteorology and Climatology*, 50(11), pp.2267-2269.
- [18] Tetens, O., 1930. About some meteorological terms, *Zeitschrift Geophysic*, 6, pp.297-309.
- [19] Dincer, I., and Rosen, M.A., 2015. *Exergy Analysis of Heating, Refrigerating and Air Conditioning: Methods and Applications*, Elsevier.
- [20] Kenneth, W., 1994. *Advanced Thermodynamics for Engineers*, McGraw-Hill, New York.
- [21] Farmahini-Farahani, M., Delfani, S., and Esmaeelian, J., 2012. Exergy analysis of evaporative cooling to select the optimum system in diverse climates, *Energy*, 40(1), pp.250-257.
- [22] Nada, S.A., Fouda, A., Mahmoud, M.A., and Elattar, H.F., 2019. Experimental investigation of energy and exergy performance of a direct evaporative cooler using a new pad type, *Energy and Buildings*, 203, pp.109449-109449.
- [23] Santos, J.C., Barros, G.D.T., Gurgel, J.M., and Marcondes, F., 2013. Energy and exergy analysis applied to the evaporative cooling process in air washers, *International Journal of Refrigeration*, 36(3), pp.1154-1161.
- [24] EES: Engineering Equation Solver, F-Chart Software: Engineering Software.



Semnan University



Numerical Investigation of Convective Heat Transfer from a Horizontal Plate Due to the Oscillation of a Vertically Oriented Blade

Mostafa Rahimi ^{*,a}, Behnaz Parsajou^a, Mohammad Vajdi^a

^aMechanical engineering department, University of Mohaghegh Ardabili, Ardabil P.O. Box 179, Iran.

PAPER INFO

Paper history:

Received: 2021-04-13

Revised: 2023-01-08

Accepted: 2023-01-10

Keywords:

Convective heat transfer;
Convection enhancement;
Flat plate;
Oscillating blade.

ABSTRACT

Convective heat transfer from a flat plate, which is enhanced by an oscillating blade, was numerically investigated at the present study. It was assumed that the blade is made of a rigid and thin plate and it is vertically oriented at the top of the target plate. Numerical analysis was performed using commercial software ANSYS Fluent 6.3 and the periodic oscillation of the blade was modeled by the moving mesh method. Conservation equations of mass, momentum and energy was solved in 2-D and transient form for the laminar airflow with constant physical properties. Constant temperature was considered for the plate and the details of both the flow and thermal fields were determined. The distribution of convective heat transfer coefficient was then calculated for the target plate. The effect of various parameters including the amplitude and frequency of the blade oscillation as well as the geometrical parameters was investigated on the convective heat transfer from the target plate. The results indicated that a wider area of the plate was affected by increasing the oscillation amplitude of the blade. Convective heat transfer was also enhanced over the entire target plate as the rotational Reynolds number was increased.

DOI: [10.22075/jhmtr.2023.23136.1341](https://doi.org/10.22075/jhmtr.2023.23136.1341)

© 2022 Published by Semnan University Press. All rights reserved.

1. Introduction

Temperature difference potential transfers heat between solid surfaces and adjacent fluid in many engineering applications and industrial equipments. In most of the applications such as electronic cooling and heat exchangers, convective heat transfer enhancement is desirable. Effort is made to perform heat transfer enhancement with less energy consumption also in a simple and efficient manner. The enhancement techniques are categorized as passive and active methods where the former one consumes no external energy. Due to the variety both in applications and in the improvement techniques, convective heat transfer enhancement is still an open and important research area in the field of heat transfer research.

Passive techniques in heat transfer augmentation have been employed in various manners. Both extended surfaces and surfaces with artificial

roughness have generally been used to enhance convective heat transfer in many investigations, based on which several review papers have also been published [1, 2]. Sheikholeslami et al. [3] provided another review of heat transfer enhancement in passive methods focusing on swirl flow devices. The effect of various turbulators including; coiled and corrugated tubes, twisted tape, conical ring and coiled wire on heat transfer augmentation has briefly been discussed in that review paper. Shi et al. [4] numerically investigated the effect of vortex-induced vibration in disrupting thermal boundary layer and hence increasing heat transfer rate. A cylinder with a flexible plate at the back was used as the vortex-generating device inside a plane duct in their research.

Moving a cylinder within a two-dimensional channel has been used as an active method to increase convective heat transfer from the channel walls in

*Corresponding Author: Mostafa Rahimi

Email: rahimi@uma.ac.ir

several studies. Oscillatory flows are known to cause higher heat and mass transfer. Oscillating movement is achieved either by the fluid vibration around a fixed object or by vibration of a solid body within a fluid. Although fluid vibration around a fixed object requires more energy, the same goal is achieved in both approaches. Oscillating flows are widely used in compact high-performance heat exchangers, piston engines, chemical reactors, pulsating burners, high-performance Stirling engines, cryogenic refrigeration, and in various applications in the aerospace industry and military fields [5–9]

Celik et al. [10] numerically investigated heat transfer enhancement in a plane duct by vortices shed from a transversely oscillating circular cylinder. They found that the placement of a transversely oscillating cylinder enhances convective heat transfer within thermally developing flow region considerably. In a similar study, Fu and Tong [11] numerically examined the influence of a transversely oscillating cylinder on the heat transfer from heated blocks in a plane duct flow. Beskok et al. [12] numerically investigated convective heat transfer from heated walls of a plane duct in presence of a rotationally oscillating cylinder. Pourgholam et al. [13] conducted a numerical research to investigate the effect of a rotating and oscillating blade on heat transfer enhancement from the channel walls. Jahangiri and Delbari [14] numerically studied the details of the flow and heat transfer in a mixing tank equipped with a helical single-blade mixer. They suggested a heat transfer correlation for two-phase flow developed within the mixing tank.

Convective heat transfer enhancement by the movement of a solid body as a heat source is another branch of the active methods, which has been considered in several studies. Rahman and Tafti [15] numerically investigated convection heat transfer augmentation in a system composed of an infinitesimally thin plate-fin with forced oscillation in the presence of an approaching flow. They found that combined effect of the oscillation frequency and amplitude on heat transfer augmentation could be represented by a single parameter called 'plunge velocity'. Rahimi and Soran [16] numerically investigated the effect of a plate movement on the heat transfer distribution over the plate impinging by an air jet. Sarhan [17] experimentally investigated the vibration effect of a rectangular flat plate on convective heat transfer from the plate in both horizontal and inclined positions. Goma and Al Taweel [18] analytically investigated the effect of oscillatory motion on heat transfer from a vertical surface. They concluded that higher temperature gradient in the axial direction causes to much higher heat transfer in the presence of an oscillatory motion. Akcay et al. [19] experimentally investigated the convection heat transfer from an oscillating vertical plate. They found

that the heat transfer performance increases with the increase of both oscillation frequency and amplitude.

Piezoelectric fan has also been used in convective heat transfer augmentation from solid surfaces. Chen et al. [20] experimented the flapping dynamics of a piezoelectric fan and heat transfer enhancement from the wall in a turbulent channel flow. In a similar study, Li et al. [21] studied the channel flow structure and heat transfer enhancement by a vertically oriented piezoelectric fan. They concluded that the presence of larger channel flow velocities has significant influence on the fan vibration amplitude and hence on heat transfer augmentation. Ebrahimi et al. [22] conducted an experimental and modeling study to investigate power dissipation when using piezoelectric fan. Li et al. [23] experimentally investigated the effect of blade shape and geometry on convective heat transfer induced by a piezoelectric vibrating fan. More studies concerning the flow structure and heat transfer enhancement induced by piezoelectric fans are found in several review papers [24, 25].

Convective heat transfer enhancement from large horizontal surfaces to the surrounding air is another challenging problem. This phenomenon is encountered in several practical applications such as; textiles, glass and paper production and tempering of metallic plates. Heat transfer by impinging jets as an effective approach has widely been used in such applications. Augmentation of heat transfer by a vertically oriented vibrating plate over the target surface could be an efficient and alternative method. While this approach has been employed traditionally as a hand fan, but no published study was found in the literature concerning the specifications of this approach. It is worth noting that this heat transfer mechanism is geometrically quite similar to the piezoelectric fan. However, it can be employed in larger scales and with lower frequencies. Therefore, the details of the developed flow field and heat transfer augmentation from a flat plate caused by a vertically oriented oscillating blade are investigated at the present study.

2. Problem description and the numerical approach

In order to investigate convective heat transfer from a flat plate due to the oscillation of a vertical blade, a solid surface with 0.084 m length was considered horizontally. Stagnant air at 100 kPa and 300 K was assumed as the surrounding fluid. Assuming 0.084 m height over the solid surface, a square computational domain was formed for the numerical analysis. A thin rigid blade having 0.038 m length and 1 mm thickness was supposed to be vertically pivoted at the center of the domain, so that the lower end of the blade was 4 mm away from the horizontal plate. The period and amplitude of the oscillating blade represented by τ and

θ_{max} , respectively. Schematic from the considered domain is shown in Fig. 1.

The flat plate with no slip velocity components and constant temperature of 320 K was the lower boundary condition. Boundary condition for the three remaining boundaries was zero gauge pressure at the outlet of the boundaries. The boundary conditions for the blade surfaces were no-slip velocity components with adiabatic boundary condition. In order to model the oscillation of the blade, a concentric circular section with 0.04 m radius was specified within the computational domain. This subdomain including the blade geometry was defined as the moving (oscillating) section in the numerical analysis. The circle connecting two subdomains was the interface boundary condition in the computations. Specified boundary conditions were presented in equation form at the end of the governing equations.

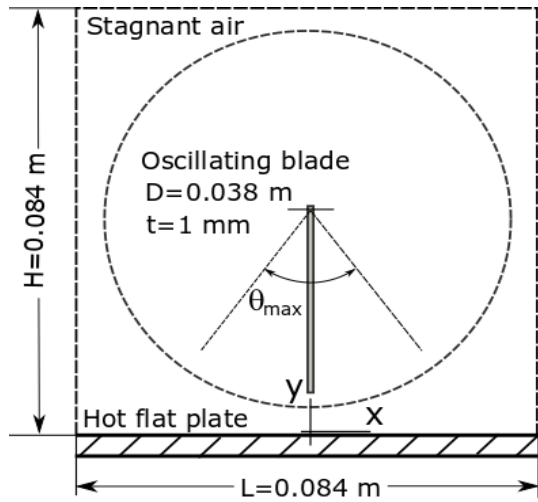


Figure 1. Schematic of the computational domain

Conservation equations of mass, momentum and energy in two dimensional and transient form were solved numerically. For a fluid with constant physical properties and in the case of laminar flow, these equations can be written as:

$$\frac{\partial u}{\partial x} + \frac{\partial v}{\partial y} = 0 \tag{1}$$

$$\frac{\partial u}{\partial t} + u \frac{\partial u}{\partial x} + v \frac{\partial u}{\partial y} = -\frac{1}{\rho} \frac{\partial p}{\partial x} + \nu \left(\frac{\partial^2 u}{\partial x^2} + \frac{\partial^2 u}{\partial y^2} \right) \tag{2}$$

$$\frac{\partial v}{\partial t} + u \frac{\partial v}{\partial x} + v \frac{\partial v}{\partial y} = -\frac{1}{\rho} \frac{\partial p}{\partial y} + \nu \left(\frac{\partial^2 v}{\partial x^2} + \frac{\partial^2 v}{\partial y^2} \right) \tag{3}$$

$$\frac{\partial T}{\partial t} + u \frac{\partial T}{\partial x} + v \frac{\partial T}{\partial y} = \alpha \left(\frac{\partial^2 T}{\partial x^2} + \frac{\partial^2 T}{\partial y^2} \right) \tag{4}$$

$$x = \pm \frac{L}{2} \rightarrow \frac{\partial p}{\partial x} = 0, \\ T = T_{\infty} \text{ (for the backflow air)}$$

$$y = H \rightarrow \frac{\partial p}{\partial y} = 0, \quad y = 0 \rightarrow u = v = 0, \\ T = T_w \tag{5}$$

$$\text{at the blade surface: } u = v = 0, \quad \frac{\partial T}{\partial n_1} = 0$$

$$\text{at the interface: } \frac{\partial u}{\partial n_2} = \frac{\partial v}{\partial n_2} = \frac{\partial T}{\partial n_2} = \frac{\partial p}{\partial n_2} = 0$$

where n_1 and n_2 are unit vectors perpendicular to the blade and the interface surface, respectively.

Numerical analysis was performed using ANSYS Fluent 6.3 commercial software. Velocity and temperature gradients were evaluated using Green-Gauss cell-based procedure. Pressure-based solver with second-order implicit formulation were used in the analysis. Pressure-velocity coupling was accomplished based on SIMPLE algorithm and the residuals were less than 10^{-3} in the conversation equations as the convergence criteria.

The oscillating motion of the blade was represented by the following sinusoidal equation:

$$\theta(t) = \theta_{max} \sin\left(\frac{2\pi}{\tau} t\right) \tag{6}$$

Based on which, the angular velocity of the blade was:

$$\omega(t) = \frac{2\pi}{\tau} \theta_{max} \cos\left(\frac{2\pi}{\tau} t\right) \tag{7}$$

The blade velocity and its angular position are shown in Fig. 2 for a period with periodicity and amplitude of $\tau = 0.1$ Sec and $\theta_{max} = 30^\circ$, respectively. Discretized values of the angular velocity are also shown in the figure that is required in the numerical calculations. Time increment value is 0.05τ at this sample representation. Discretized angular velocity values were sequentially applied in the transient numerical analysis as the blade rotational velocity over the specified time interval.

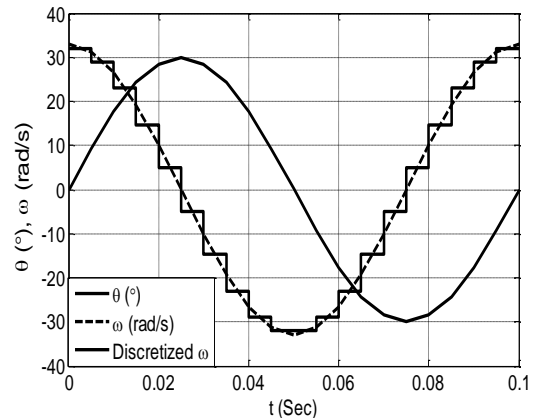


Figure 2. Variations of the angular velocity and position of the oscillating blade

3. Grid independency, time step sufficiency and the result validation

In order to use a reasonable mesh size in the numerical analysis, a systematic grid independency procedure was accomplished. While the first mesh line was 0.25 mm away from the plate surface, the mesh size was increased in the normal direction by a factor of 1.2. After several layers with increasing dimensions, mesh with constant size of almost equal to that of the last layer was generated in the remaining part of the domain. Fig. 3 indicates general characteristics of the generated mesh, with quite fewer points for the sake of simplicity.

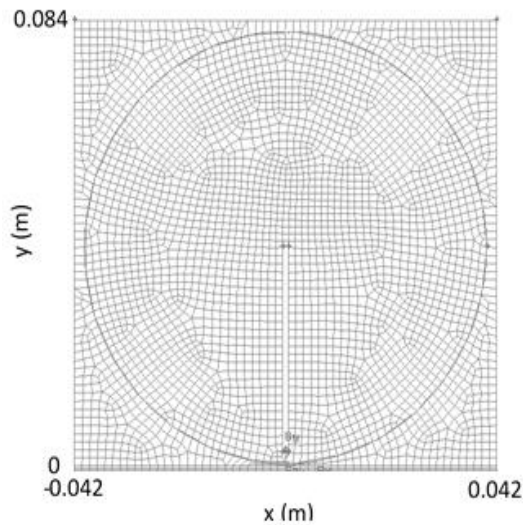


Figure 3. Schematic of generated grid with a fewer grid points

Several values were examined for the interior mesh size and each time computational analysis was conducted to obtain the flow field and the temperature distribution. Convective heat transfer coefficient over the flat plate was calculated using the temperature distribution. These results which are shown in Fig. 4 are related to the end of the fourth cycle of oscillation and when the blade is moving to the right from its upright position.

Based on the results, mesh size of 1.5 mm for the interior section of the domain predicts smaller average heat transfer coefficient. It slightly increases when using mesh size of 1 mm for the main part of the domain. However, very close values are obtained when using the mesh sizes of 0.5 mm and 0.25 mm for the main section of the computational domain. This is while, the number of grid points are approximately four times greater in the latter case.

Therefore, boundary layer mesh with 0.25 mm size at the vicinity of the plate and mesh size of 0.5 mm for the interior section of the domain were used in the main analysis. It should be mentioned that no significant change observed in the results by further reduction in the boundary layer mesh size.

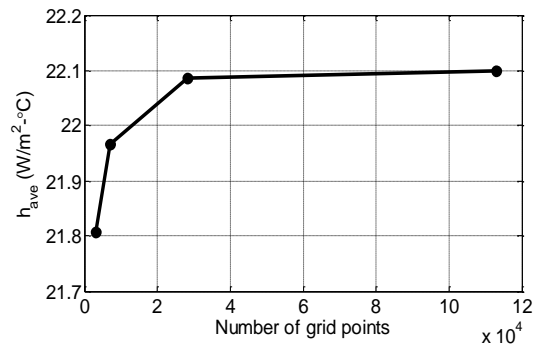


Figure 4. Average convective heat transfer coefficient over the plate for different grids, $\theta_{max} = \pi/6$, $Re_D = 6240$, $d/D = 0.105$

As indicated in Fig. 2 and based on the selected time interval, discretized angular velocity values were employed in the analysis. To specify a suitable size for the time step, the numerical analysis was conducted for several values such as; 0.1τ , 0.05τ , 0.025τ and 0.0125τ . The variation of the convective heat transfer coefficient over the plate was obtained for each time step size as shown in Fig. 5. This figure indicates that the results are significantly affected by the selected time step size. The largest time step size being 0.1τ , predicts a very different heat transfer distribution over the plate. Time step size being equal to five percent of the periodicity, which was also used in the evaluation of the appropriate mesh size, predicts a different result compared to the previous one. However, consistent results are obtained for the two smaller time step sizes so that very negligible differences exist between these two heat transfer distributions. Therefore, time step size of two and half percent of the time-period was suitable to be used in the main numerical analysis.

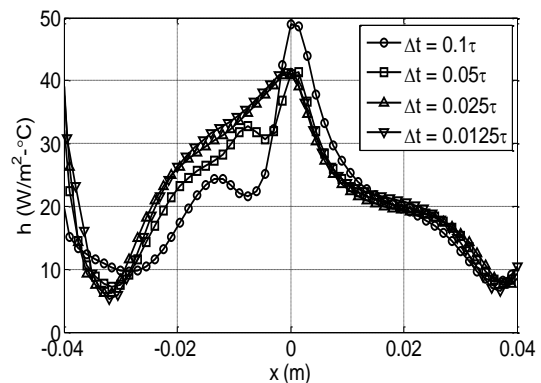


Figure 5. Convective heat transfer coefficient distributions using different time steps, $\theta_{max} = \pi/6$, $Re_D = 6240$, $d/D = 0.105$, $\tau = 0.1$ Sec.

At the present transient analysis, the initial condition was zero velocity at all grid points and the flow field was gradually developed by the blade oscillation. Based on the results and due to the depreciation of the initial conditions, a periodic flow field was established within the domain after about four periods of the blade oscillation. Also, no significant

change was detected in convective heat transfer distribution over the plate when its length was further increased. Except that the sharp rise in the convective heat transfer coefficient occurring at the left end of the plate was shifted again to a similar position. This rise was essentially the direct effect of the backflow entering into the domain from the left boundary. Also, by increasing the plate length, the number of oscillation periods required for the depreciation of the initial condition was slightly increased.

In order to evaluate the accuracy of the numerical analysis employed at the present study, no similar study was found in the published literature. Therefore, some of the results from the study of Pourgholam et al. [13] were selected for comparison. That study concerns to a laminar and steady flow between two parallel plates in which the effect of a rotating blade positioned at the center of the channel on the convective heat transfer from the walls is examined. Reynolds number of the undisturbed flow was 50 based on the hydraulic diameter of the channel. The length of the thin blade was one-sixth of the channel hydraulic diameter and its rotational velocity was 300 rpm. Assuming thermal conductivity of air constant and equal to 0.024 W/m-K and based on the channel hydraulic diameter, Nusselt number was defined using convective heat transfer coefficient. The present numerical method was employed to obtain similar results under quite the same circumstances. The results obtained from both the studies are presented in Fig. 6, which shows a reasonable consistency between these results. Therefore, the accuracy of the present numerical method could be reliable.

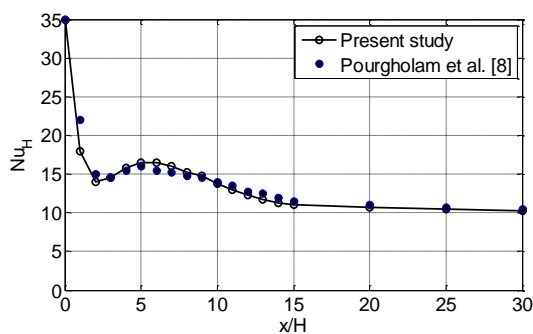


Figure 6. Comparison of the Nusselt number distributions.

4. Results and discussion

Convective heat transfer from the plate under the effect of the oscillating blade has various distributions at different instances of the blade oscillation period. In order to have a sense of the transient heat transfer distribution, the details of the flow field could also be useful. Therefore, the flow field and convective heat transfer over the plate is considered in details at the present section. Then, the effect of different parameters on the average heat transfer distribution is discussed.

4.1. Transient flow field and heat transfer distribution

As mentioned in the preceding section, the effect of the initial conditions depreciates after a few periods of oscillation and a periodic flow field is established within the computational domain. The velocity vectors at a very limited number of points from the domain and at different time instants of a half period of the blade oscillation are shown in Fig. 7. According to this figure, the time instant in which the blade crosses the upright position in its counter-clockwise rotation is considered as the starting point of the period and it is denoted by $t = 0$. At this time instant, a large amount of fluid moves behind of the blade meanwhile, a high-speed stream forms in the opposite direction at the vicinity of the plate. As a result of these two streams with opposite directions a large circulating region is formed at the left and lower corner of the domain. At the other side and in front of the blade a moderate flow moves parallel to the plate and exits from the right outlet boundary. Angular velocity of the blade decreases as it rotates in counter-clockwise direction.

As a result, the flow moving behind of the blade tends to pass through the gap formed between the tip of the blade and the target plate. The flow passing through this gap intensifies as the blade decelerates and finally stops at the end of its counter-clockwise rotation. At time instant of 0.4τ when the blade rotates in clockwise direction, consistent flows develop both at the back and front of the blade. Meanwhile, the opposite flow passing through the gap intensifies progressively as the gap size is decreased. Finally, at time instant of 0.5τ the blade is again at upright position but in its clockwise rotation and the established flow field is inversely the same with that of the starting point.

Consistent with the described flow field, convective heat transfer from the plate at different time instants is also shown in Fig. 7. This figure indicates that the convection is initially higher over the central region especially at the backside of the blade at time instant of $t = 0$. A sharp rise is also seen in the heat transfer distribution at the left end of the plate. This rise is due to the circulating flow pattern existing at that region and hence the entering flow into the domain. Convection intensity over the central region decreases rapidly as the blade rotates in counterclockwise direction and keeps out from this region. A relatively uniform distribution is seen for the convection over the central area when the blade is far from its upright position. At time instant of $t = 0.4\tau$ when the blade approaches to the central position in its clockwise rotation, convection rate intensifies again over the central region of the plate and at the backside of the blade. Finally, heat transfer distribution which is inversely the same with that of $t = 0$ is obtained for time instant of 0.5τ .

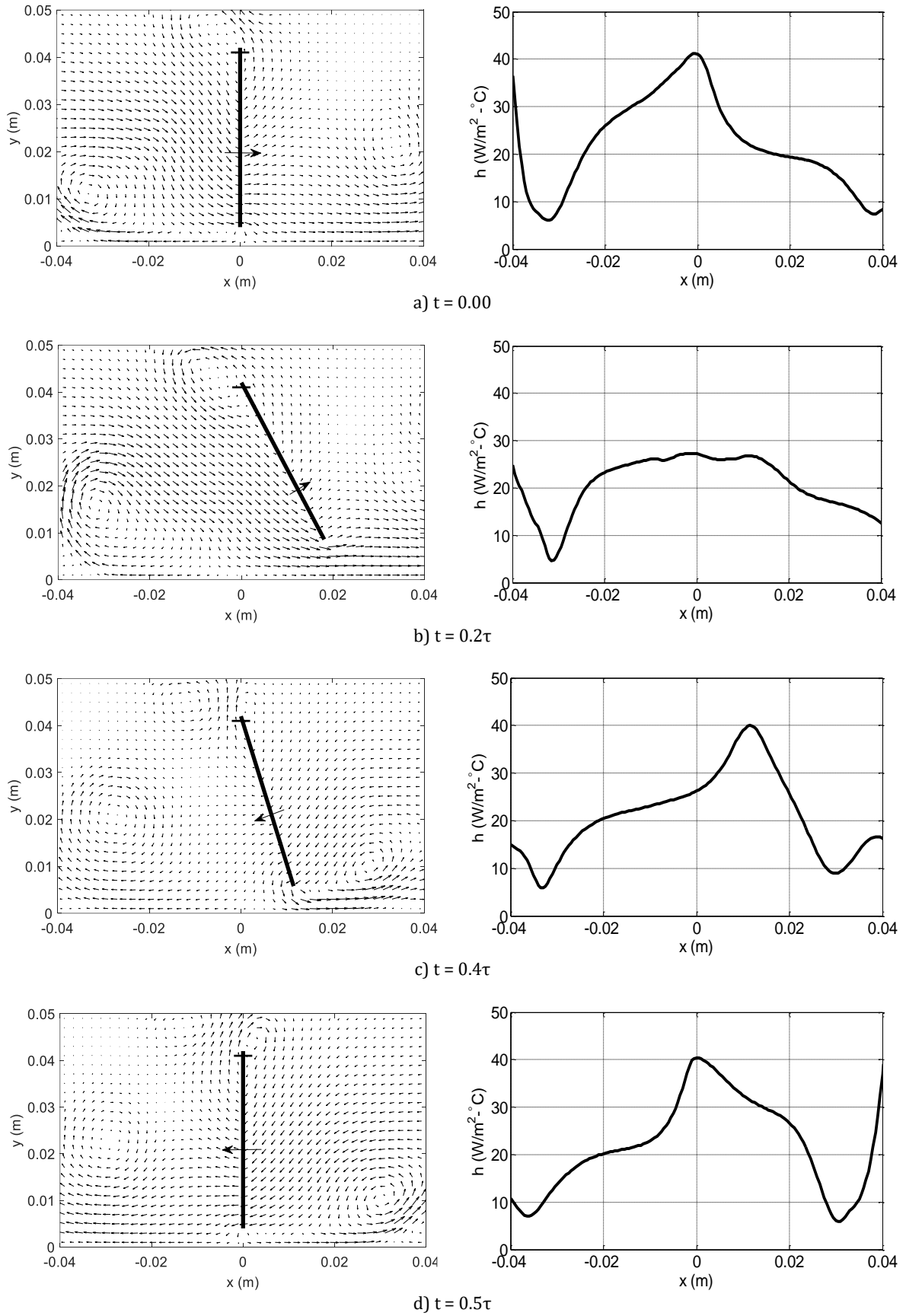


Figure 7. Velocity vectors and convective heat transfer coefficient at some points and different time instants of a half period of oscillation, $\theta_{max} = \pi/6$, $Re_D = 6240$, $d/D = 0.105$, $\tau = 0.1$ Sec.

4.2. Effect of different parameters on convective heat transfer distribution

Convective heat transfer distribution induced by an oscillating vertical blade depends on various parameters. Heat transfer coefficient can be regarded as a function of several important parameters such as;

$$h = f(v, k, D, d, x, \theta_{max}, \omega) \tag{8}$$

This expression may be rewritten using dimensional analysis in the following form

$$Nu_D = f' \left(Re_D, \frac{d}{D}, \frac{x}{D}, \theta_{max} \right) \tag{9}$$

where Nu_D and Re_D is the dimensionless Nusselt and Reynolds numbers which are defined by the following expressions:

$$Nu_D = \frac{hD}{k}, Re_D = \frac{D^2 \omega}{\nu} \tag{10}$$

As seen from Fig. 7, convective heat transfer coefficient has various distributions at different time instants. Average convection rate over a full cycle of oscillation in addition to the transient distribution could be practically meaningful and reflects heat transfer augmentation from the target plate. Therefore, average convective heat transfer coefficient was calculated and used in the presenting of the main results.

Nusselt number calculated based on the average heat transfer coefficient had generally a bell-shaped distribution over the target plate. Due to the recirculating flow pattern and also incoming flow from both the right and left boundaries of the domain, the minimum of the bell-shaped distribution is followed by an increase in the Nusselt number distribution. This rising effect which was also symmetrical at both ends, moved away from the central bell-shaped distribution when the length of the plate was further increased.

Fig. 8 indicates the effect of oscillation amplitude on the Nusselt number distribution. Based on this figure, Nusselt number is higher only over a limited section of the central part of the plate for the smallest oscillation amplitude. Average Nusselt number is significantly increased at both sides of the centerline by increasing the oscillation amplitude, while it rises slightly over the central section. Further increase in the oscillation amplitude gives rise to a uniform distribution of the Nusselt number over a large central area of the plate.

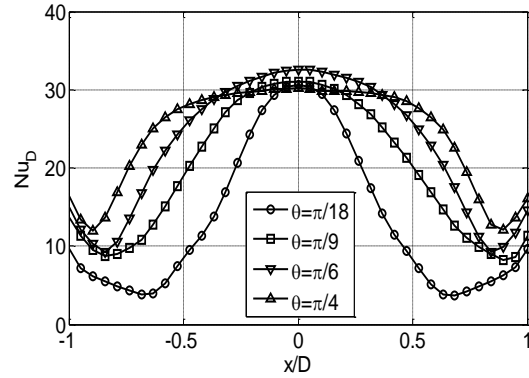


Figure 8. Average Nusselt number distribution, $d/D = 0.105, Re_D = 3120$

The effect of the rotational Reynolds number on the Nusselt number distribution is shown in Fig. 9. This figure indicates that the Nusselt number increases continuously over the entire plate as the Reynolds number is increased where, the increment is more pronounced over the central region. For air as the surrounding fluid with constant physical properties, rotational Reynolds number is evaluated based on the length and the rotational velocity of the oscillating blade according to Eq. 10. Increasing each of these two parameters results in a higher rotational Reynolds number. Existence of a higher rotational Reynolds number means that a strong flow field is being developed within the domain which results in a higher convective coefficient and hence Nusselt number distribution over the target plate.

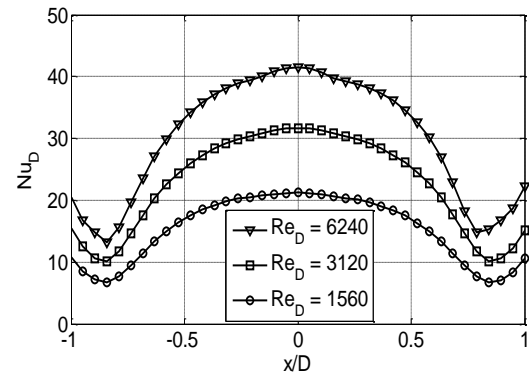


Figure 9. Average Nusselt number distribution, $d/D = 0.105, \theta_{max} = \pi/6$

Finally, the effect of the basic geometrical parameters on the Nusselt number distribution is presented in Fig. 10. Unlike to the previous parameters, it is seen from this figure that the effect of d/D is not very significant on the Nusselt number distribution. For a constant length of the oscillating blade, Nusselt number decreases slightly over the entire plate as the blade tip-to-plate is increased.

This is because the flow intensity passing through tip-to-plate gap decreases in this case and hence convective heat transfer is slightly reduced. In a similar way, when the distance between the blade tip and the plate is constant, convective heat transfer rate is slightly intensified as the length of the blade is increased.

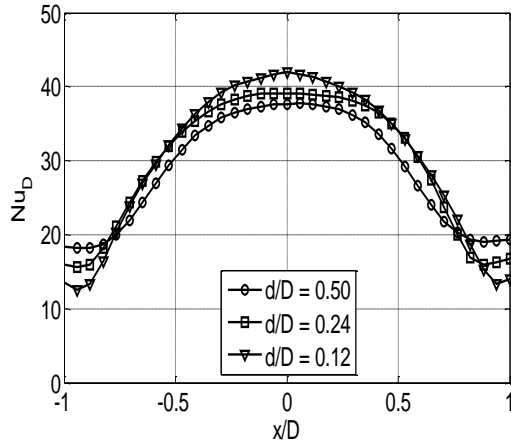


Figure 10. Average Nusselt number distribution, $Re_D = 5000$, $\theta_{max} = \pi/6$

Conclusion

Convective heat transfer from a flat plate under the effect of an oscillating vertical blade has been investigated numerically. Based on the results, convective heat transfer has various distributions over the plate at different time instants of an oscillation period. Heat transfer rate intensifies over the central region of the plate when the oscillating blade passes from its upright position in both directions. Average Nusselt number distribution over a full cycle of oscillation has a bell shape distribution whose maximum is placed at the center of the plate. More surface area of the plate is affected when the amplitude of the oscillation is increased. Meanwhile, the convection rate remains almost constant over the central region. Average Nusselt number distribution over the plate increases almost linearly as the rotational Reynolds number is increased. The effect of the dimensionless geometrical parameter denoted by d/D is not very significant on the heat transfer rate from the plate and hence on the average Nusselt number distribution.

Nomenclature

d	Blade tip-to-plate separation [m]
D	Oscillating blade length [m]
h	Convective heat transfer coefficient [W m ⁻² K ⁻¹]

H	Hydraulic diameter of the channel [m]
k	Thermal conductivity of air [0.0242 W m ⁻¹ K ⁻¹]
Nu _D	Nusselt number [h D k ⁻¹]
p	Pressure [N m ⁻²]
Re _D	Oscillation Reynolds number [D ² ω ν ⁻¹]
T	Temperature [K]
t	Time [s]
u	X-velocity component [m s ⁻¹]
v	Y-velocity component [m s ⁻¹]
x	Cartesian coordinate [m]
y	Cartesian coordinate [m]

Greek Symbols

ρ	Air density [1.225 kg m ⁻³]
τ	Oscillation period [s]
θ	Oscillation amplitude [Degree Or Rad]
ω	Angular velocity [Rad s ⁻¹]
ν	Air kinematic viscosity [1.455 × 10 ⁻⁵ m ² s ⁻¹]

References

- [1] Nagarani, N., Mayilsamy, K., Murugesan, A., and Kumar, G.S., 2014. Review of utilization of extended surfaces in heat transfer problems. *Renewable and Sustainable Energy Reviews*, 29, pp.604–613.
- [2] Gawande, V.B., Dhoble, A.S., and Zodpe, D.B., 2014. Effect of roughness geometries on heat transfer enhancement in solar thermal systems. *Renewable and Sustainable Energy Reviews*, 32, pp.347–378.
- [3] Sheikholeslami, M., Gorji, B.M. and Ganji, D.D., 2015. Review of heat transfer enhancement methods: Focus on passive methods using swirl flow devices. *Renewable Sustainable Energy Reviews*, 49, pp.444– 469.
- [4] Shi, J., Hu, J., Schafer, S.R. and Chen, C.L., 2014. Numerical study of heat transfer enhancement of channel via vortex-induced vibration. *Applied Thermal Engineering*, 70(1), p.838–845.

- [5] Khalid, A., Khan, I. and Shafie, S., 2017. Free convection flow of micropolar fluids over an Oscillating vertical plate. *Malaysian Journal of Fundamental Applied Science*, 13(4), pp.654–658.
- [6] Pradhan, B., Das, S.S., Paul, A.K. and Dash, R.C., 2017. Unsteady free convection flow of a viscous incompressible polar fluid past a semi-infinite vertical porous moving plate. *International Journal of Applied Engineering Research*, 12(21), pp.10958–10963.
- [7] Koffi, M., Andreopoulos, Y. and Jiji, L., 2017. Heat transfer enhancement by induced vortices in the vicinity of a rotationally oscillating heated plate. *International Journal of Heat and Mass Transfer*, 112, pp.862–875.
- [8] Ashafa, S., Ahmed, A.A. and Sakir, A.A., 2017. Analytical solution of the effect of MHD inclination and unsteady heat transfer in a laminar, transition and turbulent flow of a basic gaseous micro-flow past a vertically moving oscillating plate. *American Journal of Engineering & National Science* 1(2), pp.30–35.
- [9] Ellahi, R., Alamri, S.Z., Basit, A. and Majeed, A., 2018. Effects of MHD and slip on heat transfer boundary layer flow over a moving plate based on specific entropy generation. *Journal of Taibah University for Science*, 12(4), pp.476–482.
- [10] Celik, B., Raisee, M. and Beskok, A., 2010. Heat transfer enhancement in a slot channel via a transversely oscillating adiabatic circular cylinder. *International Journal of Heat and Mass Transfer*, 53(4), pp.626–634.
- [11] Fu, W.S. and Tong, B.H., 2002. Numerical investigation of heat transfer from a heated oscillating cylinder in a cross flow. *International Journal of Heat and Mass Transfer*, 45(14), pp.3033–3043.
- [12] Beskok, A., Raisee, M., Celik, B., Yagiz, B. and Cheraghi, M., 2012. Heat transfer enhancement in a straight channel via a rotationally oscillating adiabatic cylinder. *International Journal of Thermal Science*, 58, pp.61–69.
- [13] Pourgholam, M., Izadpanah, E., Motamedi, R. and Habibi, S.E., 2015. Convective heat transfer enhancement in a parallel plate channel by means of rotating or oscillating blade in the angular direction. *Applied Thermal Engineering*, 78(5), pp.248–257.
- [14] Jahangiri, M. and Delbari, O., 2020. Heat transfer correlation for two phase flow in a mixing tank. *Journal of Heat and Mass Transfer research*, 7(1), pp.1-10.
- [15] Rahman, A. and Tafti, D., 2020. Characterization of heat transfer enhancement for an oscillating flat plate-fin. *International Journal of Heat and Mass Transfer*, 147, 119001.
- [16] Rahimi, M. and Soran, R.A., 2016. Slot jet impingement heat transfer for the cases of moving plate and moving nozzle. *Journal of Brazilian Society of Mechanical Science and Engineering*, 38, pp.2651–2659.
- [17] Sarhan, A.R., Karim, M.R., Kadhim, Z.K. and Naser, J., 2019. Experimental investigation on the effect of vertical vibration on thermal performances of rectangular flat plate. *Experimental Thermal and Fluid Science*, 101, pp.231–240.
- [18] Goma, H., Al Taweel, A.M., 2005. Effect of oscillatory motion on heat transfer at vertical flat surfaces. *International Journal of Heat and Mass Transfer*, 48(8), pp.1494–1504.
- [19] Akcay, S., Akdag, U. and Palancioglu, H., 2020. Experimental investigation of mixed convection on an oscillating vertical flat plate. *International Communications in Heat and Mass Transfer*, 113, 104528.
- [20] Chen, Y., Peng, D. and Liu, Y., 2020. Heat transfer enhancement of turbulent channel flow using a piezoelectric fan. *International Journal of Heat and Mass Transfer*, 147, 118964.
- [21] Li, X.J., Zhang, J.Z. and Tana, X.M., 2018. An investigation on convective heat transfer performance around piezoelectric fan vibration envelope in a forced channel flow. *International Journal of Heat and Mass Transfer*, 126(8), pp.48–65.
- [22] Ebrahimi, N.D., Wang, Y. and Sungtaek, J., 2018. Mechanisms of power dissipation in piezoelectric fans and their correlation with convective heat transfer performance. *Sensors and actuators A: Physical* 272, pp.242–252.
- [23] Li, X.J., Zhang, J.Z. and Tana, X.M., 2018. Effects of blade shape on convective heat transfer induced by a piezoelectrically actuated vibrating fan. *International Journal of Thermal Science*, 132, pp.597–609.
- [24] Izadpanah, E., Babaie, R.M., Sadeghi, H. and Talebi, S., 2017. Effect of rotating and oscillating blade on the heat transfer enhancement of non-Newtonian fluid flow in a channel. *Applied Thermal Engineering*, 113, pp.1277–1282.

- [25] Maaspuro, M., 2016. Piezoelectric oscillating cantilever fan for thermal management of electronics and LEDs-A review. *Microelectronics Reliability*, 63, pp. 342-353.



Semnan University



Intensification of CO₂ Capture by Monoethanolamine Solution in a Rotating Packed Bed Reactor Equipped with High Frequency Ultrasonic Transducers

Mahdi Hefzi Lotfabadi ^a, Masoud Shirzadi Ahoudashti ^a, Mahdieh Abolhasani ^{*,a}

^a Faculty of Chemical, Petroleum and Gas Engineering, Semnan University, Semnan, Iran

PAPER INFO

Paper history:

Received: 2022-05-08

Revised: 2023-01-08

Accepted: 2023-01-09

Keywords:

RPB reactor;
Blade packings;
High frequency ultrasonic waves;
CO₂ absorption;
Gas-side mass transfer coefficient.

ABSTRACT

In this study, a carbon dioxide (CO₂) absorption process in a typical rotating packed bed (RPB) reactor equipped with blade packing and under a high frequency ultrasonic field has been studied. The utilized ultrasonic transducers were ultrasonic atomizer humidifiers with a frequency of 1.7 MHz. This reactor takes advantage of both controllable high gravitational force and induced effects of high frequency ultrasound, simultaneously, in a small volume. The overall volumetric gas side mass transfer coefficient (K_{Ga}) with and without ultrasound was investigated. The effects of different parameters such as rotational speed (400-1600 rpm), liquid flow rate (20- 120 L/h), monoethanolamine (MEA) concentration (1- 4 mol/L), gas flow rate (2500- 4000 L/h), and CO₂ concentration (1- 4 vol%) were investigated in the absence and presence of ultrasound. The obtained results showed that the removal efficiency increased with increasing gas and liquid flow rates, and rotational speed, as well as MEA concentration. With increasing CO₂ concentration, absorption efficiency decreased. The average arithmetic value of the relative volumetric gas-side mass transfer coefficient was enhanced 11.4% under the ultrasonic field. Moreover, the average CO₂ removal efficiency was enhanced from 27.4 % in the absence of ultrasound to 29.8% in the presence of ultrasound. Therefore, high frequency ultrasound can enhance CO₂ absorption, even in high efficiency equipment like RPBs.

DOI: [10.22075/jhmtr.2023.27119.1379](https://doi.org/10.22075/jhmtr.2023.27119.1379)

© 2022 Published by Semnan University Press. All rights reserved.

1. Introduction

Process intensification (PI) involves instruments and developing methods that leads to significant improvement in equipment and process designing and a substantial decrease in equipment size, and energy consumption, which finally results in lower cost and beneficial production, and higher production capacity [1]. PI is divided into two parts: equipment and methods. Rotating Packed Bed (RPB) reactor and ultrasonic waves are one of the most popular equipment and method of PI technologies [2]. The RPB as a high efficiency PI equipment was innovated in 1981 by Mallinson, and Ramshaw [3]. This device replaces a high centrifugal force with gravitational force and achieves high efficiency in a small volume.

The RPB technology is suitable for separation processes like absorption [4], extraction [5], distillation [6], and other processes such as polymerization [7], oxidation [8] and nanoparticle synthesis [9]. By taking advantage of both high centrifugal force and rotational speed, the RPBs can be employed in systems involving viscous liquids and in reactions with short contact time [10]. In RPBs, due to high centrifugal forces, the liquid film changes into tiny droplets which leads to the enhancement of the interfacial area and, finally increase in the mass transfer rate [11].

In comparison with conventional packed beds, the RPBs have specific advantages such as higher efficiency [12, 13], significantly smaller apparatus

*Corresponding Author: Mahdieh Abolhasani

Email: m.abolhasani@semnan.ac.ir

volumes [13, 14], and lower energy consumption. As a result, from an economic point of view, The RPBs have the lower investment and operational cost comparing the conventional packed beds [13, 14]. Although various successful applications of RPBs have been reported in the industrial scale, the technology has not yet reached its full industrial maturity [15, 16]. The number of industrial-scale applications of RPBs is very limited [17], but rapidly growing, especially in gas absorption processes. A possible reason for the limited number of industrial applications of RPBs is the low number of scale-up investigations [17]. The scale-up investigation of the RPBs has been reported in a few studies [17, 18].

As mentioned, ultrasound is among the most popular methods of PI technologies [2]. Ultrasound is a mechanical wave with a frequency above 20 kHz [19-21]. Acoustic cavitation is the significant effect of the wave propagation in the liquid medium, which induces acoustic streaming, microstreaming and heating [22, 23]. Acoustic cavitation is the process of bubble formation, growth, and collapse due to variations in the wave pressure [24]. The size of the cavitation bubbles depends on the wave frequency [25, 26]. There are two types of cavitation bubbles: stable, and transient cavitation bubbles [27, 28]. Transient cavitation bubbles exist for less than one cycle [27], which are created by low frequency waves. Transient bubbles are not very small and they can decompose to smaller bubbles.

The frequency spectrum, above 1 MHz, is named "low power ultrasound" (< 10W) which does not affect the propagation medium, and is mainly utilized for medical diagnosis [27]. These waves increase turbulence and also generate stable cavitation bubbles, acoustic streams, and acoustic fountains [28, 29]. Stable bubbles do not collapse for a long time [27, 28]. The formation of the stable bubbles creates another important effect called microstreaming. The creation of the high speed unidirectional currents of the stable bubbles causes the momentum gradients and the fluid currents, which are called the acoustic streaming [27]. These streams create the acoustic fountain (deformation) at the gas-liquid interface [26, 27, 29]. Whatever the ultrasonic frequency is higher, the liquid droplet will be smaller, and the interfacial area will increase, which causes enhancement in mass transfer rate [30] or intensification of the physical and chemical processes. Using high frequency ultrasound is an efficient way to enhance absorption processes.

Today, industrialization and the use of fossil fuels have caused the emission of greenhouse gases and global warming. Therefore, it is necessary to use alternative energy sources and reduce greenhouse gas emissions [31]. CO₂ is one of the most important emitted greenhouse gases. Therefore, CO₂ capture is an important issue, and finding new and efficient techniques to intensify it is crucial. As CO₂ absorption

is a significant factor for reducing global warming, researchers are looking for efficient methods to capture and store CO₂ [32], such as absorption [33]. As mentioned above, respect to the specific characteristics of the RPB in absorption and separation, application of RPB in CO₂ capturing attracted wide attention [34-40]. In 2011, Cheng and Tan [34], studied about removal of CO₂ from indoor air by alkanolamines in an RPB reactor for a long time to decrease the CO₂ concentration from 1000 ppm to 100 ppm. They showed that the RPB was more efficient and preferable than a conventional packed bed. In 2014, Kang et al. [35] investigated the CO₂ capturing in an RPB using diluted ammonia. They found that the height of the transfer unit (HTU) of the RPB was smaller than a conventional packed bed, which was equivalent to that and ultimately resulted in a reduction in equipment size and costs. In 2017, Wu et al. [36], studied CO₂ capture from power plants by piperazine (PZ) and diethylenetriamine (DETA) solution in an RPB. Their experiments showed that the PZ and DETA solutions compared to traditional monoethanolamine (MEA) solutions were more efficient. In 2007, Jassim et al. [37] studied about CO₂ absorption and desorption in an RPB by aqueous solution. They found that the CO₂ penetration in an MEA concentration up to 30 %w decreased.

Applications of ultrasound for increasing CO₂ absorption and saving CO₂ capture and storage (CCS) costs have been studied in recent years [2, 30, 41]. In 2017, Tay et al. [41] showed that the CO₂ absorption rate into MEA solution increases dramatically in the presence of high frequency ultrasound. In addition, they suggested that the high frequency ultrasounds lead to a high mass transfer coefficient in a compact design due to the formation of acoustic fountains and convective dynamics. In 2017, Tay et al. [30] studied the CO₂ absorption with a potassium carbonate without any promoter in the presence of high frequency ultrasound. They found that, the reaction rate assisted by ultrasonic waves was about 32 times higher than that without ultrasound. In addition, the reaction time to achieve 0.9 loadings (CO₂ mol/ K₂CO₃ mol) reduced to 400s. Finally, they showed that high frequency ultrasonic waves are an effective equipment for increasing the absorption rate in a slow kinetic reaction. In 2018, Luo et al. [2] studied the effective interfacial area and volumetric liquid-side mass transfer coefficient (K_La) using a NaOH-CO₂ mass transfer system in an RPB reactor under 20 kHz ultrasound. They reported that the $\overline{K_L a}$ under ultrasound field enhanced 5.5% compared with no ultrasound conditions.

In the above studies, the use of RPB and ultrasound in the CO₂ absorption process has been investigated separately, except in the work of Luo et al. [2]. In their study, low frequency ultrasound was used in an RPB reactor. Continuing our previous work [42] and the

work of Luo et al. [2], we decided to use high frequency ultrasonic waves in an RPB with different packing and different CO₂ absorbent. For this purpose, ultrasonic transducers with a frequency of 1.7 MHz were selected, which are known as ultrasonic atomizer humidifiers. These transducers create cold boiling [28].

In this study, we aimed to investigate the simultaneous effect of an RPB equipped with blade packing as PI equipment, and high frequency ultrasound as a PI method on the CO₂ absorption process. Therefore, measurement of CO₂ absorption percent (E), and overall volumetric gas-side mass transfer coefficient (k_Ga) under different operational conditions was performed using an MEA-CO₂ mass transfer system.

2. Material and Experimental Methods

2.1. Development of RPB Reactor

In this study, an RPB reactor with a plexiglass casing was used. The rotor is equipped with 12 stainless steel blades. Four 1.7 MHz ultrasonic transducers with a diameter of 20 mm were embedded at the bottom of the reactor. To ensure the presence of liquid on the transducers and to benefit from ultrasound effects such as cavitation, acoustic fountain, and fogging, the rotor was installed upside down. Another advantage of this structure is comfortable sealing. Two distributors with a hole diameter of 1 mm were used to distribute the liquid in the packing symmetrically. Figure 1 shows the different parts and dimensions of the RPB reactor.

2.2. Experimental Method

The schematic of the experimental setup for the CO₂ absorption process is depicted in Figure 2. The utilized absorbent was MEA with a concentration of 1-4 mol/L and a volume flow rate of 20-120 L/h. The gas mixture containing CO₂ and N₂, with a volume flow rate of 2500-4000 L/h, entered the reactor and reacted with the absorbent. The inlet CO₂ concentration was 10000-40000 ppm. The outlet gas was analyzed by CO₂ sensor

(s8 alarm 5% (senseair)). The CO₂ amount in the outlet gas was used to calculate the overall volumetric gas-side mass transfer coefficient by the following equation [42- 45]:

$$K_G a = \frac{Q_G}{\pi \times (R_o^2 - R_i^2) \times Z_b} \ln \frac{C_i}{C_o} \quad (1)$$

where Q_G is the volumetric gas flow rate, Z_b is the height of packing, and R_i and R_o are the inner and outer diameter of packing, respectively. Moreover, C_i and C_o are the CO₂ concentration in the inlet and outlet gas streams. The CO₂ removal efficiency can be determined by equation (2):

$$E (\%) = \frac{C_i - C_o}{C_i} \times 100 \quad (2)$$

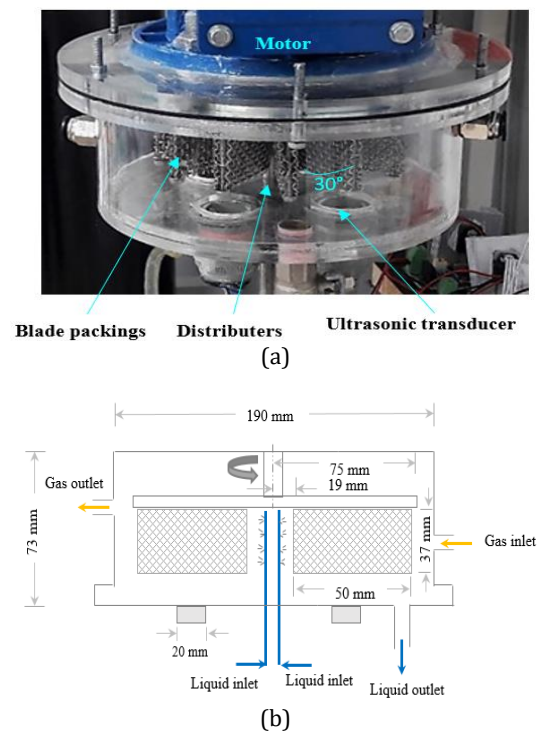
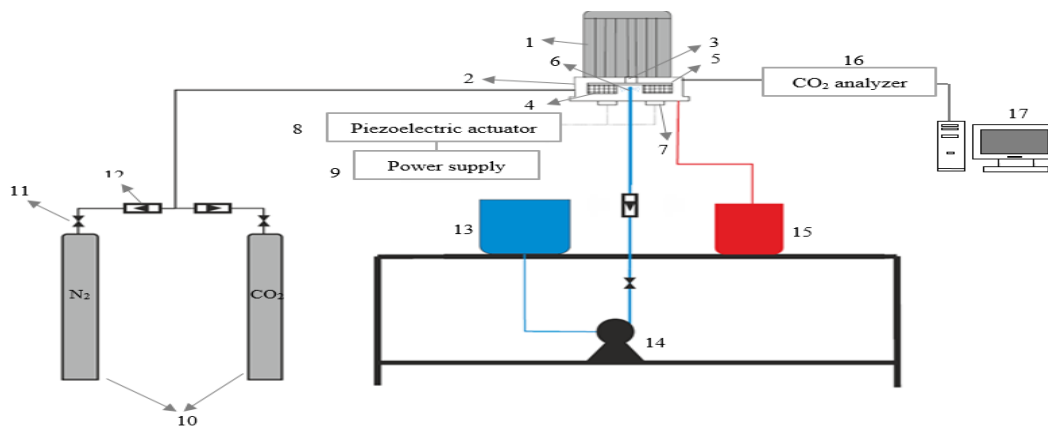


Figure 1. (a) The real view of the RPB reactor, and (b) schematic view of the reactor and dimensions (mm).



1. Motor, 2. The casing of the RPB reactor, 3. Shaft, 4. Blade packings, 5. Rotating bed, 6. Distributors, 7. Ultrasonic transducers, 8. Piezoelectric actuator, 9. Power supply, 10. CO₂ and N₂ gas cylinders, 11. Valves, 12. Rotameter, 13. MEA solution tank, 14. Pump, 15. Waste tank, 16. CO₂ analyzer, 17. Computer.

Figure 2. Schematic diagram of the CO₂ capture system

The operating pressure of the RPB reactor was 1 atm. All experiments were carried out at 25 ± 2 °C with three repetitions. The ultrasonic power was measured by a calorimetric experiment in a batch flow mode [19, 20]. The concentration of CO₂ in the outlet stream was measured with a standard deviation of less than 3 %. Effects of the rotational speed of the bed (N), liquid flow rate (Q_L), absorbent concentration (C_{MEA}), gas flow rate (Q_G), and CO₂ concentration on K_{Ga} and E were investigated.

3. Result and Discussion

3.1. Effect of Rotational Speed on K_{Ga}

Figure 3 presents the effect of N on K_{Ga}. In these experiments, Q_G, C_{MEA}, CO₂ percent, Q_L, and P_{us} were set at 3500 L/h, 1 mol/L, 2 vol%, 50 L/h, and 22.5 W, respectively. As can be seen, enhancing the rotational speed increases the volumetric gas side mass transfer coefficient. To describe this issue, we can mention that, higher rotational speed causes more collisions between rotating packed bed and absorbent solution that leads to thinner liquid films and their better distribution. These tiny droplets and the thin liquid film increase the interfacial area and improve the overall mass transfer coefficient. Moreover, the CO₂ absorption increased in ultrasonic presence. These waves cause creating tiny droplets, more interfacial area, and finally increase the removal efficiency. Also, a convergence in the diagram at high rotational speeds, it means that the centrifugal force is overcoming ultrasonic effects. For a better evaluation of the effects of high frequency ultrasound on CO₂ absorption, the relative volumetric gas-side mass transfer coefficient, $\sigma_{K_{Ga}}$, is defined as follows [2]:

$$\sigma_{K_{Ga}}(\%) = \frac{K_{Ga}a_{us} - K_{Ga}a_0}{K_{Ga}a_0} \times 100 \quad (3)$$

where 0 and us are referred to as no ultrasound and ultrasound conditions. In these experiments, for N of 400–1600 rpm, the values of $\sigma_{K_{Ga}}$ change from 32.3 % to 3.3 %, while E varies from 14.8 % to 28.9% for non-ultrasonic assisted RPB reactor (NUAR) to 19.1%-29.7% for ultrasonic assisted RPB reactor (UAR).

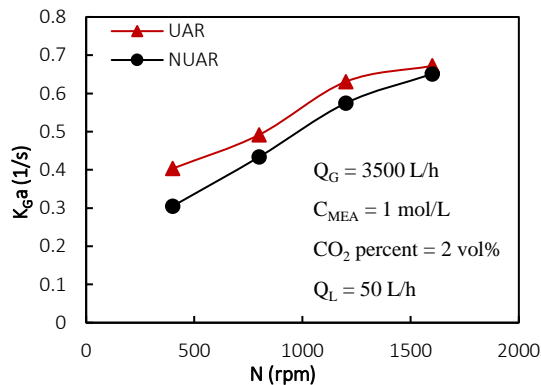


Figure 3. Effect of rotational speed on K_{Ga}.

3.2. Effect of Liquid Flow Rate on K_{Ga}

Figure 4 showed the effect of Q_L on K_{Ga}, while Q_G, C_{MEA}, CO₂ percent, N, and P_{us} were set at 3500 L/h, 1 mol/L, 2 vol%, 1200 rpm, and 22.5 W, respectively. K_{Ga} and the removal efficiency are enhanced by increasing the liquid flow rate due to decreasing liquid-side mass transfer resistance. In addition, the wetting of each unit of packing increases which is favorable for CO₂ absorption. On the other hand, increasing the liquid flow rate also has a negative aspect that reduces the residence time, but it's negligible. Also, the acoustic fountain formed by ultrasonic waves can return the absorbent solution from the bottom of the reactor to the packing zone and increases each unit of wetted packing, that is desirable for capturing process. In these experiments, for Q_L of 20–120 L/h, the values of $\sigma_{K_{Ga}}$ change from 16.9 % to 5.0 %, while E varies from 24.1 %–33.2 % for NUAR to 27.6%-34.6% for UAR.

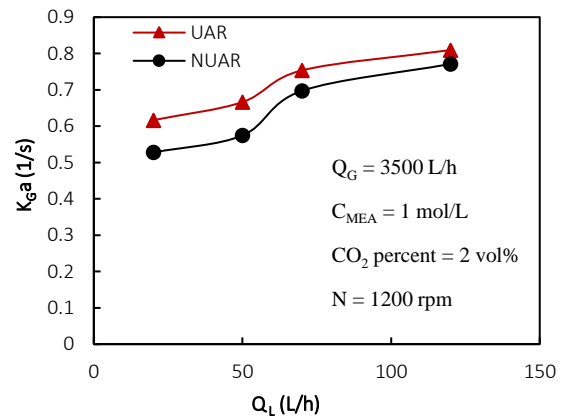


Figure 4. Effect of liquid flow rate on K_{Ga}.

3.3. Effect of MEA Concentration on K_{Ga}

Figure 5 summarizes the effect of MEA concentration on K_{Ga}, while Q_G, Q_L, CO₂ percent, N, and P_{us} were set at 3500 L/h, 50 L/h, 2 vol%, 1200 rpm, and 22.5 W, respectively.

The results show that by increasing the C_{MEA}, the K_{Ga} and removal efficiency enhance. For the constant amount of CO₂, there is more amount of MEA that causes enhancement in mass transfer driving force and finally a significant increase in removal efficiency.

On the other hand, ultrasound can spread the MEA droplets, which still didn't react completely with CO₂, to the packing zone by the acoustic fountain and fogging phenomena, and finally assist in improving the removal efficiency and K_{Ga}.

In these experiments, for C_{MEA} of 1- 4 mol/L, the values of $\sigma_{K_{Ga}}$ change from 9.8 % to 6.7 %, while E varies from 26.0 %–37.7 % for NUAR to 28.1%-39.6% for UAR.

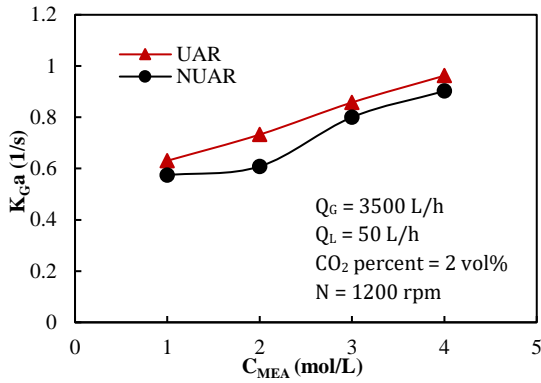


Figure 5. Effect of MEA concentration on K_{Ga} .

3.4. Effect of Gas Flow Rate on K_{Ga}

Figure 6 shows the effect of Q_G on K_{Ga} . In this section, CO_2 percent, Q_L , C_{MEA} , N , and P_{us} were 2 vol%, 50 L/h, 1 mol/L, 1200 rpm, and 22.5 W, respectively. The gas flow rate enhancement has both positive and negative effects. Decreasing the gas-side mass transfer resistance is the positive effect and decreasing the residence time is the negative effect, but it's negligible. Moreover, ultrasound can enhance the K_{Ga} . Ultrasonic waves return some of the MEA solution to the packing zone, which reduces the negative effect of gas flow rate enhancement (residence time) by increasing the volume of liquid in the packing zone, in the time interval between gas entering and exiting the reactor. In these experiments, for Q_G of 2500 -4000 L/h, the values of $\sigma_{K_{Ga}}$ change from 9.3 % to 13.4 %, while E varies from 31.3 % - 23.9 % for NUAR to 33.6%- 26.6% for UAR.

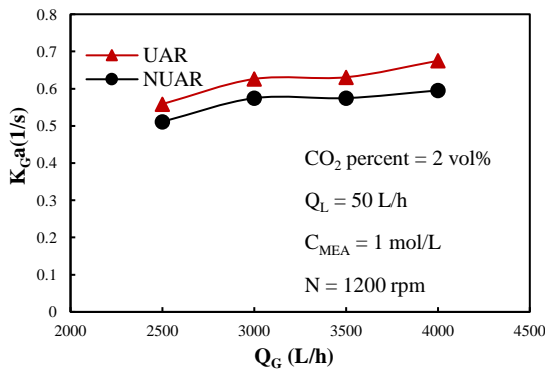


Figure 6. Effect of gas flow rate on K_{Ga} .

3.5. Effect of CO_2 Concentration on K_{Ga}

Figure 7 illustrates the effect of CO_2 concentration on K_{Ga} , while Q_G , Q_L , C_{MEA} , N , and P_{us} were set at 3500 L/h, 50 L/h, 1 mol/L, 1200 rpm, and 22.5 W, respectively. The effect of increasing this parameter on CO_2 absorption is the opposite of increasing MEA concentration. It means that for a specific amount of MEA, there are more CO_2 molecules that should be

captured. In this case (high CO_2 concentration), thermodynamics (solubility) would govern the removal efficiency instead of kinetics which finally caused a decrease in removal efficiency [46]. Furthermore, ultrasonic effects on process efficiency are similar to other parameters. In these experiments, for CO_2 concentration of 10000 - 40000 ppm (1%-4%), the values of $\sigma_{K_{Ga}}$ change from 7.4 % to 16.3 %, while E varies from 36.4 % to 22.0 % for NUAR to 38.5%- 25.0 % for UAR.

According to the above evidence, despite the very low residence time of the liquid droplets in the RPB reactor, 1.7 MHz ultrasound can significantly enhance CO_2 absorption and K_{Ga} . Using the above results, $\bar{\sigma}_{K_{Ga}}$ (the average arithmetic value of $\sigma_{K_{Ga}}$) was obtained 11.4%, respectively.

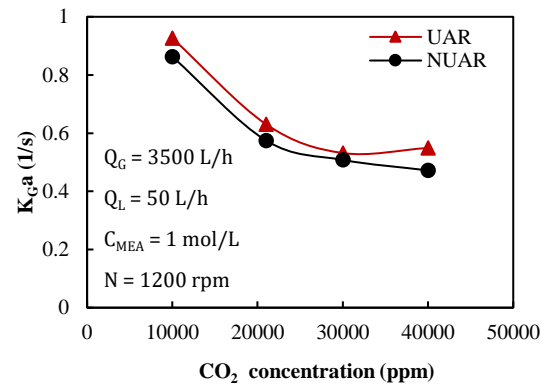


Figure 7. Effect of CO_2 concentration on K_{Ga} .

3.6. Comparison of the RPB Performance in This Study with Other Works

The comparison of the performance of the present reactor with other existing reactors with almost similar structures and conditions is done in Table 1. Although the comparison is very difficult due to the different structures of the reactors and their internal components and different operating conditions. As it was mentioned, for the first time, Luo et al [2] studied the effect of ultrasound on mass transfer coefficient using a NaOH- CO_2 system in an RPB reactor. As they reported K_{La} , it was not possible to compare our study with them. From Table 1, it can be seen that in almost similar conditions, relatively more K_{Ga} was obtained in the present work. For example, the maximum K_{Ga} of the present study is 20% more than the K_{Ga} in the work of Lin et al. [48], which is a significant increase considering as the percentage of carbon dioxide in the present study is twice. In addition, in terms of comparison with the work [42], in the same conditions, the reactor equipped with ultrasonic waves has achieved higher coefficients. Also, in the almost similar conditions, the maximum K_{Ga} of the present study is 4.17 times the K_{Ga} reported in the work of Mohammadi and Heidari [45].

Table 1. Comparison of the RPB performance in this study with other works

Type of packing	RPB rotational speed (rpm)	Liquid flow rate (L/h)	Gas flow rate (L/h)	Absorbent concentration (mol/L)	CO ₂ (%Vol)	K _{Ga} (1/s)	Efficiency (%)		Ref.	
Structured Packing	[375- 1735]	2.52	[264- 786]	NaOH [0.2- 1]	1	[0.1- 0.75]	—		[47]	
Blade Packing	[600- 1800]	[12- 30]	[540- 3960]	MEA [1]	1	[0.12- 0.8]	—		[48]	
Blade Packing	[400- 1600]	[20- 120]	[2500- 4000]	MEA [1- 4]	2	[0.3- 0.9]	[14.8- 37.7]		[42]	
Arc Blade	[400- 1600]	[18- 36]	3360	MEA [3- 12]	2	[0.13- 0.23]	[49- 78]		[45]	
Blade packing	[400- 1600]	[20- 120]	[2500- 4000]	MEA [1- 4]	2	Without US	With US	Without US	With US	This work
						[0.3- 0.9]	[0.4- 0.96]	[14.8- 37.7]	[19.1- 39.6]	

4. Conclusions

In this study, the investigation of the effect of high frequency ultrasonic waves on CO₂ absorption in the RPB reactor with twelve blade packings was done. Four 1.7 MHz ultrasonic transducers were embedded in the bottom of the reactor. All experiments were repeated in the absence and presence of ultrasound. The CO₂ absorption percent (E), and the volumetric gas-side mass transfer coefficient (k_{Ga}) were investigated by using an MEA-CO₂ mass transfer system. The effects of different parameters such as rotational speed (400–1600 rpm), liquid flow rate (20–120 L/h), MEA concentration (1- 4 mol/L), gas flow rate (2500- 4000 L/h), and CO₂ concentration (1- 4 vol%) have been investigated. According to the evidence, despite the very low residence time of the liquid droplets in the RPB reactor, 1.7 MHz ultrasound can significantly enhance CO₂ absorption. The following results have been obtained:

- The removal efficiency increased with increasing gas and liquid flow rate, and rotational speed, as well as MEA concentration.
- With increasing CO₂ concentration, absorption efficiency decreased.
- $\overline{\sigma_{K_{Ga}}}$ (The average arithmetic value of $\sigma_{K_{Ga}}$) was obtained 11.4% under the ultrasound field.
- The average CO₂ removal efficiency was enhanced from 27.4 % in the absence of ultrasound to 29.8% in the presence of ultrasound.
- High frequency ultrasound can enhance CO₂ absorption, even in high efficiency equipment like RPBs.

Nomenclature

C _i , C _o	CO ₂ mole fraction in the inlet and outlet gas [mol/mol]
C _{MEA}	MEA concentration [mol/L]
E	CO ₂ absorption efficiency, %

K _{Ga}	Overall volumetric gas-side mass transfer coefficient [1/s]
N	Rotational speed [rpm]
P	power [W]
Q	Flow rate [L/h]
R _i	The inner radius of the RPB [m]
R _o	The outer radius of the RPB [m]
Z _b	The axial height of the packings [m]

Greek Symbols

$\sigma_{K_{Ga}}$	Relative volumetric gas-side mass transfer coefficient (dimensionless)
-------------------	--

Subscripts

0	Without ultrasound
G	Gas stream
i	inlet
L	Liquid stream
o	Outlet
us	With ultrasound

Abbreviations

NUAR	Non-ultrasonic assisted RPB reactor
UAR	Ultrasonic assisted RPB reactor

References

- [1] Stankiewicz, A.I. and Moulijn, J.A., 2000. Process intensification: Transforming chemical engineering, *Chemical Engineering Progress*, 96, pp.22-34
- [2] Luo, Y., Luo, J.Z., Yue, X.J., Song, Y.J., Chu, G.W., Liu, Y., Le, Y. and Chen, J.-F., 2018. Feasibility studies of micromixing and mass-transfer in an ultrasonic assisted rotating packed bed reactor. *Chemical Engineering Journal*, 331, pp.510–516.
- [3] Ramshaw, C. and Mallinson, R.H., US 4,283,255, Mass transfer process, United States Pat 1981:12.

- [4] Zhang, L.L., Wang, J.X., Xiang, Y., Zeng, X.F. and Chen, J.F., 2011. Absorption of carbon dioxide with ionic liquid in a rotating packed bed contactor: Mass transfer study. *Industrial & Engineering Chemistry Research*, 50, pp.6957-6964.
- [5] Liu, H.S., Lin, C.C., Wu, S.C. and Hsu, H.W., 1996. Characteristics of a rotating packed bed. *Industrial & Engineering Chemistry Research*, 35(10), pp.3590-3596.
- [6] Kelleher, T. and Fair, J.R., 1996. Distillation Studies in a High-Gravity Contactor. *Industrial & Engineering Chemistry Research*, 35(12), pp.4646-4655.
- [7] Chen, J.F., Gao, H., Zou, H.K., Chu, G.W., Zhang, L., Shao, L., Xiang, Y. and Wu, Y.-X., 2010. Cationic polymerization in rotating packed bed reactor: Experimental and modeling. *AIChE Journal*, 56(4), pp.1053-1062.
- [8] Lin, C.C. and Liu, W.T., 2003. Ozone oxidation in a rotating packed bed, *Journal of Chemical Technology & Biotechnology*, 78, pp.138-141.
- [9] Kang, F., Wang, D., Pu, Y., Zeng, X.F., Wang, J.X. and Chen, J.F., 2018. Efficient preparation of monodisperse CaCO₃ nanoparticles as overbased nanodetergents in a high-gravity rotating packed bed reactor. *Powder Technology*, 325, pp.405-411.
- [10] Neumann, K., Gladyszewski, K., Groß, K., Qammar, H., Wenzel, D., Górak, A. and Skiborowski, M., 2018. A guide on the industrial application of rotating packed beds. *Chemical Engineering Research and Design*, 134, pp.443-462.
- [11] Thiels, M., Wong, D.S.H., Yu, C.H., Kang, J.L., Jang, S.S. and Tan, C.S., 2016. Modelling and Design of Carbon Dioxide Absorption in Rotating Packed Bed and Packed Column. *IFAC-PapersOnLine*, 49, pp.895-900.
- [12] Sheng, M., Xie, C., Zeng, X., Sun, B., Zhang, L., Chu, G., Luo, Y., Chen, J.-F. and Zou, H., 2018. Intensification of CO₂ capture using aqueous diethylenetriamine (DETA) solution from simulated flue gas in a rotating packed bed. *Fuel*, 234, pp.1518-1527.
- [13] Liu, Z., Esmaeili, A., Zhang, H., Xiao, H., Yun, J. and Shao, L., 2021. Carbon dioxide absorption with aqueous amine solutions promoted by piperazine and 1-methylpiperazine in a rotating zigzag bed, *Fuel*, 302, 121165.
- [14] Borhani, T.N., Oko, E. and Wang, M., 2018. Process modelling and analysis of intensified CO₂ capture using monoethanolamine (MEA) in rotating packed bed absorber. *Journal of Cleaner Production*, 204, pp.1124-1142.
- [15] Lukin, I., Pietzka, L., Groß, K., Górak, A. and Schembecker, G., 2020. Economic evaluation of rotating packed bed use for aroma absorption from bioreactor off-gas. *Chemical Engineering and Processing- Process Intensification*, 154, 108011.
- [16] Neumann, K., Gladyszewski, K., Groß, K., Qammar, H., Wenzel, D., Górak and A., Skiborowski, M., 2018. A guide on the industrial application of rotatingpacked beds. *Chemical Engineering Research and Design*, 134, pp.443-462.
- [17] Groß, K., de Beer, M., Dohrn, S. and Skiborowski, M., 2020. Scale-Up of the Radial Packing Length in Rotating Packed Beds for Deaeration Processes. *Industrial & Engineering Chemistry Research*, 59(23), pp.11042-11053.
- [18] Zhao, R.-H., Li, C.-P., Guo, F. and Chen, J.-F., 2007. Scale-up Preparation of Organized Mesoporous Alumina in a Rotating Packed Bed. *Industrial & Engineering Chemistry Research*, 46(10), pp.3317-3320.
- [19] Abolhasani, M., Karami, A. and Rahimi, M., 2015. Numerical Modeling and Optimization of the Enhancement of the Cooling Rate in Concentric Tubes under Ultrasound Field. *Numerical Heat Transfer, Part A: Applications*, 67, pp.1282-1309.
- [20] Dehbani, M., Rahimi, M., Abolhasani, M., Maghsoodi, A., Afshar, P.G., Dodmantipi, A.R. and Alsairafi, A.A., 2014. CFD modeling of convection heat transfer using 1.7 MHz and 24 kHz ultrasonic waves: A comparative study. *Heat and Mass Transfer*, 50, pp.1319-1333.
- [21] Abolhasani, M., Rahimi, M., Dehbani, M. and Shabani, S.R., 2012. CFD Modeling of Low, Medium and High Frequency Ultrasound Waves Propagation Inside a Liquid Medium. The 4rd National Conference on CFD Applications in Chemical & Petroleum Industries.
- [22] Aghapour Aktij, S., Taghipour, A., Rahimpour, A., Mollahosseini, A. and Tiraferri, A., 2020. A critical review on ultrasonic-assisted fouling control and cleaning of fouled membranes. *Ultrasonics*, 108, 106228.
- [23] Zheng, J., Guo, Y., Zhu, L., Deng, H. and Shang, Y., 2021. Cavitation effect in two-dimensional ultrasonic rolling process. *Ultrasonics*, 115, 106456.
- [24] Viriyananon, K., Mingbunjerdsuk, J., Thungthong, T. and Chaiworapuek, W., 2021. Characterization of heat transfer and friction loss of water turbulent flow in a narrow rectangular duct under 25-40 kHz ultrasonic waves, *Ultrasonics*, 114, 106366.
- [25] Parvizian, F., Rahimi, M., Hosseini, S.M., Madaeni, S.S. and Alsairafi, A.A., 2012. The Effect of High Frequency Ultrasound on Diffusion Boundary Layer Resistance in Ion-Exchange Membrane Transport, *Desalination*, 286, pp.155-165.
- [26] Abolhasani, M., Rahimi, M., Dehbani, M. and Alsairafi, A.A., 2012. CFD Modeling of Heat Transfer by 1.7 MHz Ultrasound Waves, *Numerical. Heat Transfer. part A-Application*. 62, pp. 822-841.
- [27] Legay, M., Gondrexon, N., Le Person, S., Boldo, P. and Bontemps, A., 2011. Enhancement of heat transfer by ultrasound: Review and recent advances. *International Journal of Chemical Engineering*, 2011.
- [28] Rahimi, M., Abolhasani, M. and Azimi, N., 2015. High frequency ultrasound penetration through concentric tubes: Illustrating cooling effects and cavitation intensity. *Heat and Mass Transfer*, 51, pp.587-599.
- [29] Abolhasani, M., Rahimi, M., Dehbani, M. and Alsairafi, A.A., 2012. CFD modeling of heat transfer by 1.7 MHz ultrasound waves, *Numerical Heat Transfer, Part A: Applications*, 62, pp.822-841.

- [30] Tay, W.H., Lau, K.K. and Shariff, A.M., 2017. High performance promoter-free CO₂ absorption using potassium carbonate solution in an ultrasonic irradiation system. *Journal of CO₂ Utilization*, 21, pp.383-394.
- [31] Bahoosh, R., Sedeh Ghahfarokhi, M. and Saffarian, M.R., 2018. Energy and Exergy Analyses of a Diesel Engine Running on Biodiesel Fuel. *Journal of Heat and Mass Transfer Research*, 5, pp. 95-104.
- [32] Lee, S.Y. and Park, S.J., 2015. A review on solid adsorbents for carbon dioxide capture. *Journal of Industrial and Engineering Chemistry*, 23, pp.1 - 11.
- [33] Hu, G., Smith, K.H., Wu, Y., Mumford, K.A., Kentish, S.E., and Stevens, G.W., 2018. Carbon dioxide capture by solvent absorption using amino acids: A review. *Chinese Journal of Chemical Engineering*, 26(11), pp. 2229-2237.
- [34] Cheng, H.H. and Tan, C.S., 2011. Removal of CO₂ from indoor air by alkanolamine in a rotating packed bed. *Separation and Purification Technology*, 82, pp.156-166.
- [35] Kang, J.L., Luo, Z.J., Liu, J.L., Sun, K., Wong, D.S.H., Jang, S.S., Tan, C.-S. and Shen, J.-F., 2014. Experiment and modeling studies on absorption of CO₂ by dilute ammonia in rotating packed bed. *Energy Procedia*, 63, pp.1308-1313.
- [36] Wu, T.W., Hung, Y.T., Chen, M.T. and Tan, C.S., 2017. CO₂ capture from natural gas power plants by aqueous PZ/DETA in rotating packed bed. *Separation and Purification Technology*, 186, pp.309-317.
- [37] Jassim, M.S., Rochelle, G., Eimer, D. and Ramshaw, C., 2007. Carbon dioxide absorption and desorption in aqueous monoethanolamine solutions in a rotating packed bed. *Industrial & Engineering Chemistry Research*, 46, pp. 2823-2833.
- [38] Lin, C.C. and Chu, C.R., 2015. Feasibility of carbon dioxide absorption by NaOH solution in a rotating packed bed with blade packings. *International Journal of Greenhouse Gas Control*, 42, pp.117-123.
- [39] Yu, C.H., Wu, T.W. and Tan, C.S., 2013. CO₂ capture by piperazine mixed with non-aqueous solvent diethylene glycol in a rotating packed bed, *International Journal of Greenhouse Gas Control*, 19, pp.503-509.
- [40] Lin, C.C. and Chen, Y.W., 2011. Performance of a cross-flow rotating packed bed in removing carbon dioxide from gaseous streams by chemical absorption. *International Journal of Greenhouse Gas Control*, 5, pp.668-675.
- [41] Tay, W.H., Lau, K.K. and Shariff, A.M., 2017. High frequency ultrasonic-assisted chemical absorption of CO₂ using monoethanolamine (MEA). *Separation and Purification Technology*, 183, pp.136-144.
- [42] Shirzadi Ahou Dashti, M. and Abolhasani, M., 2020. Intensification of CO₂ capture by monoethanolamine solution containing TiO₂ nanoparticles in a rotating packed bed, *International Journal of Greenhouse Gas Control*, 94, 102933.
- [43] Jassim, M.S., 2002. Process Intensification: Absorption and Desorption of Carbon Dioxide from Monoethanolamine Solutions Using Higeer Technology, (PhD Thesis, Newcastle University).
- [44] Lin, C.C. and Chu, C.R., 2015. Mass transfer performance of rotating packed beds with blade packings in carbon dioxide absorption into sodium hydroxide solution. *Separation and Purification Technology*, 150, pp.196-203.
- [45] Mohammadi Nouroddin, V. and Heidari, A., 2021. Experimental study of absorption with MEA solution in a novel Arc-RPB. *Chemical Engineering and Processing- Process Intensification*, 165, 108450.
- [46] Aroonwilas, A. and Veawab, A., 2004. Characterization and comparison of the CO₂ absorption performance into single and blended alkanolamines in a packed column. *Industrial & Engineering Chemistry Research*, 43, 9, pp.2228-2237.
- [47] Lin, C.C., Liu, W.T., and Tan, C.S., 2003. Removal of carbon dioxide by absorption in a rotating packed bed. *Industrial & Engineering Chemistry Research*, 42, pp.2381-2386.
- [48] Lin, C.C. and Kuo, Y.W., 2016. Mass transfer performance of rotating packed beds with blade packings in absorption of CO₂ into MEA solution. *International Journal of Heat and Mass Transfer*, 97, pp.712-718.



Semnan University



Unsteady Magnetohydrodynamic Mixed Convection Flow over a Rotating Sphere with Sinusoidal Mass Transfer

A. Sahaya Jenifer ^a, Saikrishnan Ponnaiah ^{*,a} , E. Natarajan ^b

^a Department of Mathematics, National Institute of Technology, Tiruchirappalli, India.

^b Department of Mathematics, Indian Institute of Space Science and Technology, Thiruvananthapuram, India.

PAPER INFO

Paper history:

Received: 2021-03-16

Received: 2023-01-04

Accepted: 2023-01-10

Keywords:

Boundary layer;
Heat transfer;
Variable properties;
Mixed convection;
MHD;
Non-uniform mass transfer;
Non-similar solution;
Rotating sphere.

ABSTRACT

This paper investigates the unsteady magnetohydrodynamic (MHD) mixed convective fluid flow over a rotating sphere. An implicit finite difference scheme, together with quasi-linearization, is used to find non-similar solutions for the governing equations. The impact of variable physical properties and viscous dissipation are included. It is observed that the skin friction coefficient in the axial direction and the heat transfer coefficient are increasing with an increase in MHD, mixed convection and rotation parameters and with time, whereas the effect is just the opposite for the skin friction coefficient in the rotational direction. The non-uniform slot suction(injection) and the slot movement influence the point of vanishing skin friction to move in the axial direction downstream (upstream).

DOI: [10.22075/jhmt.2023.22926.1339](https://doi.org/10.22075/jhmt.2023.22926.1339)

© 2022 Published by Semnan University Press. All rights reserved.

1. Introduction

The investigation of boundary layer flow and heat transfer over rotating bodies of revolution has several technical applications, including fiber coating, re-entry missile design, and rotary machine design [1]. The sphere being a well-renowned geometry used in engineering devices, many times the motion of spherical models endure rotation and suction/blowing. As a result, understanding the influence of rotation as well as mass transfer on flow over a spinning sphere is critical. Kreith et al. [2] have investigated convection heat transport and flow phenomena and Lee et al. [3] have incorporated forced flow over rotating spheres. The effects of surface blowing on the above-described geometry were investigated by Niazmand and Renksizbulut [4]. Recently, Safarzadeh and Brahimy [5] have established the flow phenomena over the rotating sphere in porous media. Many researchers have worked on flows over rotating bodies such as cylinders, disks, and cones, under different circumstances [6-8].

There is a substantial variation in fluid properties owing to the presence of a temperature gradient across a fluid medium. This temperature variation may be due to heat transfer when the fluid and the surface have dissimilarity in temperature or when there is a loss of heat present in the form of latent energy upon its liberation [9]. Together with these varying physical properties, the process of heat transfer for a variety of objects has already been thoughtfully analyzed by a significant number of researchers [10-16].

The mass transfer through a wall slot holds several tremendous practical implications in thermal protection, fuel injecting system of ramjets, drying theory, galvanizing the innermost section of the boundary layer in adverse pressure gradients, and reducing skin friction on high-speed aircraft [17]. Uniform suction (injection) creates discontinuities at the ends of the slot. An ultimate solution to overcome this is by implementing a non-uniform suction(injection), as discussed by Roy and Nath in [18]. Since then, several researchers have carried out the work on the impact of the non-uniform mass

*Corresponding Author: Saikrishnan Ponnaiah

Email: psai@nitt.edu

transfer over various two-dimensional axisymmetric bodies [12,13,15-17,19] and that over rotating bodies [11,14,21].

The boundary-layer flows are found to be both unsteady and non-similar in nature. The unsteadiness and non-similarity that occur may be due to the body's curvature or the velocity profiles at the boundary or the surface mass transfer, or perhaps an amalgamation of all the factors mentioned above. A vast majority of the researchers restrained their works to unsteady self-similar flows or steady non-similar flows due to mathematical complexities. A brief review of methods to find a non-similar solution for steady flows and the references of apposite works done up till 1967 has been stated in [21]. In the past two decades, many researchers worked on a non-similar solution for steady/unsteady flows over various shapes of non-spinning bodies [12,13,15,17,22-24]. In the case of rotating bodies, authors in [25-27] presented self-similar solutions for steady/unsteady flow over a rotating sphere, whereas in [10,11,28] have given non-similar solutions.

The inclusion of the effect of MHD and mixed convection has received keen attention recently. An enormous number of researchers have analyzed the effect of mixed convection on steady or unsteady fluid flow over various non-spinning bodies [17,29-32] and over rotating bodies [1,33-39]. On the other hand, the effect of MHD on steady or unsteady fluid flow over two-dimensional axisymmetric bodies has been observed by Sathyakrishna et al. [40], and over a rotating sphere has been studied in [10,27,41,42]. The above studies were focused on analyzing the flow problem with either mixed convection or magnetic field. The combined effect of MHD and mixed convection on a steady fluid flow over a sphere, rotating sphere, wedge, and the vertical elastic sheet has been studied in [11,12,19,43], respectively. Recently, Ghani and Rumite [44] have worked on the MHD mixed convection flow over a solid sphere by using the Keller-box method.

Further taking unsteadiness into account, Chamkha et al. [22,45] showed the combined effect of MHD and mixed convection of fluid flow at the forward stagnation region of a rotating sphere in the presence of chemical reaction and heat source and at different wall conditions. Mahdy et al. [26] have investigated the same with an analysis of entropy generation due to non-Newtonian Casson nanofluid. Recently, Jenifer et al. [46] obtained non-similar solutions for an unsteady MHD mixed convective flow over a stationary sphere with mass transfer. Gul et al. [47] have worked on the stagnation point flow of blood-based hybrid nanofluid over a rotating sphere with the inclusion of mixed convection and a time-dependent magnetic field. Considering an impulsively rotating sphere, Calabretto et al. [48] have explored the effects of unsteadiness and Mahdy et al. [49] have further extended the study to

homogeneous - heterogeneous reactions in MHD mixed nanofluid flow. Numerous writers have recently researched flow through spinning spheres while taking into account phenomena like double diffusive convection, magnetophoresis and joule heating. [50-52].

From the literature review, the sinusoidal mass transfer in the case of unsteady rotating sphere is not studied so far. The novelty of this work lies in finding non-similar solutions under the combined effects of the following circumstances.

- Temperature-dependent viscosity and Prandtl number
- MHD mixed convective flow over a rotating sphere
- Unsteady (accelerating) flow model
- Sinusoidal suction/injection through a slot
- Viscous dissipation and Joule heating

This study finds its applications in flows over rotating axisymmetric bodies where the flow is time dependent and the boundary layer can be controlled by implementing the above-mentioned factors. The governing equations are transformed with the help of nonsimilar transformations and the corresponding nonsimilar solutions are obtained by using implicit finite difference method along with quasilinearization technique. Important flow parameters such as skin friction and heat transfer coefficients are analyzed for various values of the effects taken into account. The fluid considered here is water due to its extreme practical applications in engineering.

2. Mathematical Formulation

The coordinate system and flow model over a heated sphere is presented in Figure 1. It is assumed that the sphere rotates with angular velocity $\Omega(t)$ (a time-dependent function) with its rotation axis parallel to $u_e(x, t)$. A constant magnetic field B_0 is enforced perpendicular to the sphere's surface. The mixed convective flow is supposed to be in the upward direction, and the sphere rotates in y -direction.

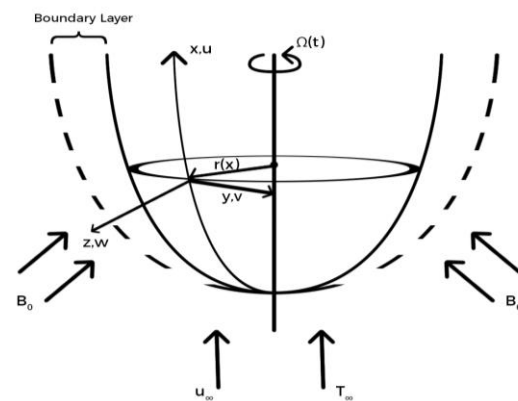


Figure 1. Flow model

The variation of temperature between the free stream and the sphere’s surface is assumed to be less than 40°C. Within this temperature limit considered, the properties of water, such as density (ρ) and specific heat (c_p) vary up to a maximum of 1%, and this minute variation allows the use of ρ and c_p as constants. On the other hand, properties such as viscosity (μ) and thermal conductivity (k) vary significantly with temperature, and so does the Prandtl number (Pr). Both μ and Pr have an inverse linear relationship with temperature as specified in [23].

$$\mu = \frac{1}{(a + bT)} \text{ and } Pr = \frac{1}{(c + dT)} \tag{1}$$

with $a = 53.41, b = 2.43, c = 0.068, d = 0.004$. (2)

The boundary layer flow is governed by the following equations:

$$(ru)_x + (rw)_z = 0 \tag{3}$$

$$u_t + uu_x + wu_z - \frac{v^2}{r}r_x = (u_e)_t + u_e(u_e)_x + \frac{1}{\rho}(\mu u_z)_z + g\beta(T - T_\infty) \sin\left(\frac{x}{R}\right) - \frac{\sigma B_0^2}{\rho}(u - u_e) \tag{4}$$

$$v_t + uv_x + wv_z + \frac{uv}{r}r_x = \frac{1}{\rho}(\mu v_z)_z - \frac{\sigma B_0^2}{\rho}v \tag{5}$$

$$T_t + uT_x + wT_z = \frac{1}{\rho} \left(\frac{\mu}{Pr} T_z \right)_z + \frac{\mu}{\rho c_p} (u_z^2 + v_z^2) + \frac{\sigma B_0^2}{\rho c_p} (u^2 + v^2 - u_e u) \tag{6}$$

Initial conditions:

$$u(x, z, 0) = u_i(x, z), \quad v(x, z, 0) = v_i(x, z), \tag{7}$$

$$w(x, z, 0) = w_i(x, z), \quad T(x, z, 0) = T_i(x, z).$$

Boundary conditions:

$$u(x, 0, t) = 0, u(x, \infty, t) = u_e(x, t), \tag{8}$$

$$v(x, 0, t) = \Omega(t)r(x), w(x, 0, t) = w_w(x, t),$$

$$T(x, 0, t) = T_w = \text{constant},$$

$$T(x, \infty, t) = T_\infty = \text{constant}.$$

The transformations to convert the equations (4)-(6) and the conditions (7) and (8) into a non-dimensional form are as follows:

$$\xi = \int_0^x \frac{U}{u_\infty} \left(\frac{x}{R}\right)^2 d\left(\frac{x}{R}\right), \bar{t} = \frac{3}{2} Re \left(\frac{\mu_e}{\rho R^2}\right) t, \tag{9}$$

$$\eta = \left(\frac{U}{u_\infty}\right) \left(\frac{Re}{2\xi}\right)^{1/2} \left(\frac{r}{R}\right) \left(\frac{z}{R}\right), Re = \frac{u_\infty R}{\nu},$$

$$\phi(\bar{t}) = 1 + \epsilon \bar{t}^2, \epsilon = 0.25, G = \frac{T - T_w}{T_\infty - T_w},$$

$$\psi(x, z, t) = u_\infty R \phi(\bar{t}) \left(\frac{2\xi}{Re}\right)^{1/2} f(\xi, \eta, \bar{t}),$$

$$\Omega = \Omega_0 \phi(\bar{t}), u = \left(\frac{R}{r}\right) \psi_z,$$

$$v = \Omega_0 r(x) \phi(\bar{t}) S(\xi, \eta, \bar{t}), w = -\left(\frac{R}{r}\right) \psi_x.$$

The above transformations satisfy (3) identically, and the non-dimensional forms of (4)-(6) are given below

$$(NF_\eta)_\eta + \phi[fF_\eta + \chi(1 - F^2)] - P[F_\bar{t} - \phi^{-1}\phi_{\bar{t}}(1 - F)] + \alpha(\xi)\phi S^2 + \phi^{-1}\lambda S_1(\xi)(1 - G) + MP(1 - F) = 2\xi\phi(F F_\xi - f_\xi F_\eta) \tag{10}$$

$$(NS_\eta)_\eta + \phi f S_\eta - P[S_\bar{t} + \phi^{-1}\phi_{\bar{t}}S] - \alpha_1(\xi)\phi FS - MPS = 2\xi\phi(F S_\xi - f_\xi S_\eta) \tag{11}$$

$$\left(\frac{1}{Pr} NG_\eta\right)_\eta + \phi f G_\eta - PG_\bar{t} + N\left(\frac{u_e}{u_\infty}\right)^2 Ec[F_\eta^2 + BS_\eta^2] + PECM\left(\frac{u_e}{u_\infty}\right)^2 \tag{12}$$

$$(F^2 + BS^2 - F) = 2\xi\phi(F G_\xi - f_\xi G_\eta)$$

with the boundary conditions

$$F(\xi, 0, \bar{t}) = 0, \quad F(\xi, \infty, \bar{t}) = 1, \tag{13}$$

$$S(\xi, 0, \bar{t}) = 1, \quad S(\xi, \infty, \bar{t}) = 0,$$

$$G(\xi, 0, \bar{t}) = 0, \quad G(\xi, \infty, \bar{t}) = 1$$

where

$$N = \frac{\mu}{\mu_\infty} = \frac{a + bT_\infty}{a + bT} = \frac{1}{E_1 + E_2 G'},$$

$$E_1 = \frac{a + bT_w}{a + bT_\infty}, E_2 = \frac{(T_\infty - T_w)b}{a + bT_\infty},$$

$$Pr = \frac{1}{c + dT} = \frac{1}{E_3 + E_4 G'},$$

$$E_3 = c + dT_w, E_4 = (T_\infty - T_w)d,$$

$$\frac{u}{u_e} = f_\eta = F, u_e = U\phi(\bar{t}),$$

$$Ec = \frac{u_\infty^2}{c_p(T_\infty - T_w)}, f = \int_0^\eta F d\eta + f_w,$$

$$\chi = \frac{2\xi dU}{U d\xi}, P = 3\xi \left(\frac{R}{r}\right)^2 \left(\frac{u_\infty}{U}\right)^2, \tag{14}$$

$$\alpha_1 = \frac{4\xi dr}{r d\xi}, M = \frac{2\sigma B_0^2 R}{3\rho\mu_\infty},$$

$$S_1(\xi) = 2\xi \left(\frac{u_\infty}{U}\right)^3 \left(\frac{R}{r}\right), \lambda = \frac{Gr}{Re^2},$$

$$Gr = \frac{g\beta\Delta T_w R^3}{\nu_\infty^2}, \nu_\infty = \frac{\mu_\infty}{\rho}, B = \left(\frac{\Omega_0 r}{U}\right)^2,$$

$$w = -\left(\frac{r}{R}\right) (2\xi Re)^{-1/2} U \phi \left[f + 2\xi f_\xi + \left(\chi + \frac{\alpha_1}{2} - 1\right) \eta F \right],$$

$$f_w = -\left(\frac{Re}{2\xi}\right)^{1/2} \phi^{-1} \int_0^x \frac{w_w(x, \bar{t})}{u_\infty} \left(\frac{r}{R}\right) d\left(\frac{x}{R}\right)$$

The velocity distribution at the boundary layer’s edge is written as,

$$\begin{aligned} \frac{u_e}{u_\infty} &= \frac{3}{2} \phi(\bar{t}) \sin \bar{x}, \quad \frac{U}{u_\infty} = \frac{3}{2} \sin \bar{x}, \\ \frac{r}{R} &= \sin \bar{x}, \quad \bar{x} = \frac{x}{R}. \end{aligned} \tag{15}$$

Hence $\xi, \beta(\xi), P(\xi), \alpha(\xi), \alpha_1(\xi), B$ and $S_1(\xi)$ can be written as expressions in \bar{x} as follows.

$$\begin{aligned} \xi &= \frac{K_1^2 K_3}{2}, \quad \chi = \frac{2K_3 K_2^{-2}}{3} \cos \bar{x}, \\ P &= \frac{2K_2^{-2} K_3}{3}, \quad \alpha = B\chi, \quad \alpha_1 = 2\chi, \\ B &= \frac{4}{9} \left(\frac{\Omega_0 R}{u_\infty} \right)^2, \quad S_1 = \frac{8K_2^{-2} K_3}{27} \end{aligned} \tag{16}$$

where

$$\begin{aligned} K_1 &= 1 - \cos \bar{x}, \quad K_2 = 1 + \cos \bar{x}, \\ K_3 &= 2 + \cos \bar{x}. \end{aligned} \tag{17}$$

The following suction/injection distribution at the wall is taken as a sinusoidal function. It exhibits a nonuniform mass transfer only in the interval $[\bar{x}_0, \bar{x}_0^*]$ which can endure a slow mass transfer at the slot's ends without breaking its continuity. Here, A is the mass transfer parameter with $A > 0$ indicating suction and $A < 0$ indicating injection through the slot. The parameter ω^* determines the slot length which is fixed at 2π whenever mass transfer is applied in this paper.

$$w_w = \begin{cases} \frac{-2Au_\infty}{(Re)^{1/2}} \sin[C(\bar{x}, \bar{x}_0)], & \bar{x} \in [\bar{x}_0, \bar{x}_0^*] \\ 0, & \text{otherwise} \end{cases} \tag{18}$$

$$C(\bar{x}, \bar{x}_0) = \omega^*(\bar{x} - \bar{x}_0).$$

The value of surface mass transfer f_w is given by

$$f_w = \begin{cases} 0, & \bar{x} \leq \bar{x}_0 \\ \frac{A}{\phi K_1} (K_3)^{-1/2} \zeta(\bar{x}, \bar{x}_0), & \bar{x} \in [\bar{x}_0, \bar{x}_0^*] \\ \frac{A}{\phi K_1} (K_3)^{-1/2} \zeta(\bar{x}_0^*, \bar{x}_0), & \text{otherwise} \end{cases} \tag{19}$$

$$\begin{aligned} \zeta(\bar{x}, \bar{x}_0) &= \frac{\sin[C(\bar{x}, \bar{x}_0) - \bar{x}] + \sin \bar{x}_0}{(\omega^* - 1)} \\ &\quad - \frac{\sin[C(\bar{x}, \bar{x}_0) - \bar{x}] - \sin \bar{x}_0}{(\omega^* + 1)}. \end{aligned}$$

It is convenient to write the equations in \bar{x} instead of ξ . \bar{x} and ξ are related by

$$\xi \frac{\partial}{\partial \xi} = Q(\bar{x}) \frac{\partial}{\partial \bar{x}} \tag{20}$$

where

$$Q(\bar{x}) = \frac{K_3 K_2^{-1}}{3} \tan \frac{\bar{x}}{2} \tag{21}$$

Substituting equations (20) and (21) in the equations (10), (11) and (12), we obtain the dimensionless equations,

$$\begin{aligned} (NF_\eta)_\eta &+ \phi[fF_\eta + \chi(1 - F^2)] \\ -P[F_\xi - \phi^{-1}\phi_\xi(1 - F)] &+ \alpha\phi S^2 \\ +\phi^{-1}\lambda S_1(\bar{x})(1 - G) &+ MP(1 - F) \\ = 2Q\phi(F F_{\bar{x}} - f_{\bar{x}} F_\eta) \end{aligned} \tag{22}$$

$$\begin{aligned} (NS_\eta)_\eta &+ \phi f S_\eta - P[S_\xi + \phi^{-1}\phi_\xi S] \\ -\alpha_1 \phi F S - MPS &= 2Q\phi(F S_{\bar{x}} - f_{\bar{x}} S_\eta) \end{aligned} \tag{23}$$

$$\begin{aligned} \left(\frac{1}{Pr} NG_\eta\right)_\eta &+ \phi f G_\eta - P G_\xi \\ +N\left(\frac{u_e}{u_\infty}\right)^2 Ec[F_\eta^2 + BS_\eta^2] \\ +PEcM\left(\frac{u_e}{u_\infty}\right)^2 (F^2 + BS^2 - F) \\ = 2Q\phi(F G_{\bar{x}} - f_{\bar{x}} G_\eta) \end{aligned} \tag{24}$$

The boundary conditions become

$$\begin{aligned} F(\bar{x}, 0, \bar{t}) &= 0, \quad F(\bar{x}, \infty, \bar{t}) = 1 \\ S(\bar{x}, 0, \bar{t}) &= 1, \quad S(\bar{x}, \infty, \bar{t}) = 0 \\ G(\bar{x}, 0, \bar{t}) &= 0, \quad G(\bar{x}, \infty, \bar{t}) = 1. \end{aligned} \tag{25}$$

The skin friction coefficients in the x - and y -directions and the heat transfer coefficient can be written as

$$\begin{aligned} C_f(Re)^{1/2} &= \frac{9K_2 K_3^{-1/2} \phi(\bar{t})}{2} \sin \bar{x} N_w(F_\eta)_w \\ \overline{C_f}(Re)^{1/2} &= \frac{9K_2 K_3^{-1/2} \phi(\bar{t})}{2} B^{1/2} \sin \bar{x} N_w(S_\eta)_w \\ Nu(Re)^{-1/2} &= \frac{3K_2 K_3^{-1/2}}{2} (G_\eta)_w \end{aligned} \tag{26}$$

where,

$$\begin{aligned} C_f &= \frac{2 \left[\mu \left(\frac{\partial u}{\partial z} \right) \right]_w}{\rho u_\infty^2}, \quad \overline{C_f} = \frac{2 \left[\mu \left(\frac{\partial v}{\partial z} \right) \right]_w}{\rho u_\infty^2}, \\ Nu &= \frac{R \left(\frac{\partial T}{\partial z} \right)_w}{(T_\infty - T_w)}, \\ N_w &= \frac{1}{a_1 + a_2 G_w} = \text{constant} \end{aligned} \tag{27}$$

3. Method of Solution

Quasilinearization is a technique introduced by Bellman and Kalaba [53], that can linearize nonlinear initial boundary value issues and is considered an extension of the Newton Raphson approach in functional space. This approach not only linearizes the original nonlinear equation, but it also gives a series of functions that converge to the nonlinear problem's solution. After quasilinearizing the highly nonlinear equations (22)-(24), the following set of linear partial differential equations are obtained.

$$\begin{aligned} A_1^m F_{\eta\eta}^{m+1} + A_2^m F_\eta^{m+1} + A_3^m F^{m+1} + A_4^m F_{\bar{x}}^{m+1} \\ + A_5^m G_\eta^{m+1} + A_6^m G^{m+1} + A_7^m S^{m+1} + A_8^m F_\xi^{m+1} \\ = A_9^m \\ B_1^m S_{\eta\eta}^{m+1} + B_2^m S_\eta^{m+1} + B_3^m S^{m+1} + B_4^m S_{\bar{x}}^{m+1} \\ + B_5^m G_\eta^{m+1} + B_6^m G^{m+1} + B_7^m F^{m+1} + B_8^m S_\xi^{m+1} \\ = B_9^m \\ C_1^m G_{\eta\eta}^{m+1} + C_2^m G_\eta^{m+1} + C_3^m G^{m+1} + C_4^m G_{\bar{x}}^{m+1} \\ + C_5^m F_\eta^{m+1} + C_6^m F^{m+1} + C_7^m S_\eta^{m+1} + C_8^m S^{m+1} \\ + C_9^m G_\xi^{m+1} = C_{10}^m \end{aligned} \tag{28}$$

Here, the superscript m and $m + 1$ denote the previous and current iterations and the coefficients are as follows

$$\begin{aligned} A_1 &= N \\ A_2 &= \phi f + 2Q\phi f_{\bar{x}} - E_2 N^2 G_\eta \\ A_3 &= -2\phi\chi F - P\phi^{-1}\phi_{\bar{t}} - MP - 2Q\phi F_{\bar{x}} \\ A_4 &= -2Q\phi F \\ A_5 &= -E_2 N^2 F_\eta \\ A_6 &= -\phi^{-1}\lambda S_1 + 2E_2^2 N^3 F_\eta G_\eta - E_2 N^2 F_{\eta\eta} \\ A_7 &= 2\alpha\phi S \\ A_8 &= -P \\ A_9 &= -\phi\chi(1 + F^2) - P\phi^{-1}\phi_{\bar{t}} + \alpha\phi S^2 - MP \\ &\quad - 2Q\phi F F_{\bar{x}} - E_2 N^2 F_\eta G_\eta + 2E_2^2 N^3 F_\eta G_\eta G \\ &\quad - E_2 N^2 F_{\eta\eta} G - \phi^{-1}\lambda S_1 \end{aligned}$$

$$\begin{aligned} B_1 &= N \\ B_2 &= \phi f + 2Q\phi f_{\bar{x}} - E_2 N^2 G_\eta \\ B_3 &= -P\phi^{-1}\phi_{\bar{t}} - \alpha_1\phi F - MP \\ B_4 &= -2Q\phi F \\ B_5 &= -E_2 N^2 S_\eta \\ B_6 &= 2E_2^2 N^3 S_\eta G_\eta - E_2 N^2 S_{\eta\eta} \\ B_7 &= -\alpha_1\phi S - 2Q\phi S_{\bar{x}} \\ B_8 &= -P \\ B_9 &= -\alpha_1\phi S F - 2Q\phi F S_{\bar{x}} - E_2 N^2 S_\eta G_\eta \\ &\quad + 2E_2^2 N^3 S_\eta G_\eta G - E_2 N^2 S_{\eta\eta} G \end{aligned}$$

$$\begin{aligned} C_1 &= \frac{N}{Pr} \\ C_2 &= \phi f + 2Q\phi f_{\bar{x}} + 2\left(E_4 N - \frac{E_2 N^2}{Pr}\right) G_\eta \\ C_3 &= -E_2 N^2 Ec \left(\frac{u_e}{u_\infty}\right)^2 (F_\eta^2 + BS_\eta^2) \\ &\quad + 2\left(-E_2 E_4 N^2 + \frac{E_2^2 N^3}{Pr}\right) G_\eta^2 + \left(E_4 N - \frac{E_2 N^2}{Pr}\right) G_{\eta\eta} \\ C_4 &= -2Q\phi F \\ C_5 &= 2NEc \left(\frac{u_e}{u_\infty}\right)^2 F_\eta \\ C_6 &= PEcM \left(\frac{u_e}{u_\infty}\right)^2 (2F - 1) - 2Q\phi G_{\bar{x}} \\ C_7 &= 2NEc \left(\frac{u_e}{u_\infty}\right)^2 BS_\eta \\ C_8 &= 2PEcM \left(\frac{u_e}{u_\infty}\right)^2 BS \\ C_9 &= -P \\ C_{10} &= G_\eta^2 \left(E_4 N - \frac{E_2 N^2}{Pr}\right) + C_3 G - 2Q\phi F G_{\bar{x}} \\ &\quad + NEc \left(\frac{u_e}{u_\infty}\right)^2 (F_\eta^2 + BS_\eta^2) + PEcM \left(\frac{u_e}{u_\infty}\right)^2 (F^2 + BS^2) \end{aligned}$$

All the coefficients above are known values from m -th iteration. With step sizes $\Delta\eta, \Delta\bar{x}, \Delta\bar{t}$ in their respective directions, the linearized partial differential equations in (28) are discretized using central difference scheme in η direction and backward difference scheme in \bar{x}, \bar{t} directions and the linear difference equations are written in the following matrix form [54]

$$X_{i,j,k}\zeta_{i,j-1,k} + Y_{i,j,k}\zeta_{i,j,k} + Z_{i,j,k}\zeta_{i,j+1,k} = W_{i,j,k}, \quad (29)$$

$$2 \leq j \leq \bar{J}$$

where the coefficient matrices are as follows

$$X_j = \begin{bmatrix} A_1 - A_2 \frac{\Delta\eta}{2} & 0 & -A_5 \frac{\Delta\eta}{2} \\ 0 & B_1 - B_2 \frac{\Delta\eta}{2} & -B_5 \frac{\Delta\eta}{2} \\ -C_5 \frac{\Delta\eta}{2} & -C_7 \frac{\Delta\eta}{2} & C_1 - C_2 \frac{\Delta\eta}{2} \end{bmatrix}$$

$$Y_j = \begin{bmatrix} -2A_1 + H_1\Delta\eta^2 & A_7\Delta\eta^2 & A_6\Delta\eta^2 \\ B_7\Delta\eta^2 & -2B_1 + H_2\Delta\eta^2 & B_6\Delta\eta^2 \\ C_6\Delta\eta^2 & C_8\Delta\eta^2 & -2C_1 + H_3\Delta\eta^2 \end{bmatrix}$$

$$Z_j = \begin{bmatrix} A_1 + A_2 \frac{\Delta\eta}{2} & 0 & A_5 \frac{\Delta\eta}{2} \\ 0 & B_1 + B_2 \frac{\Delta\eta}{2} & B_5 \frac{\Delta\eta}{2} \\ C_5 \frac{\Delta\eta}{2} & C_7 \frac{\Delta\eta}{2} & C_1 + C_2 \frac{\Delta\eta}{2} \end{bmatrix}$$

$$W_j = \begin{bmatrix} \left(A_9 + \frac{A_4}{\Delta\bar{x}} F_{i-1,j,k} + \frac{A_8}{\Delta\bar{t}} F_{i,j,k-1}\right) \Delta\eta^2 \\ \left(B_9 + \frac{B_4}{\Delta\bar{x}} S_{i-1,j,k} + \frac{B_8}{\Delta\bar{t}} S_{i,j,k-1}\right) \Delta\eta^2 \\ \left(C_{10} + \frac{C_4}{\Delta\bar{x}} G_{i-1,j,k} + \frac{C_9}{\Delta\bar{t}} G_{i,j,k-1}\right) \Delta\eta^2 \end{bmatrix}$$

$$\zeta_{i,j,k} = \begin{bmatrix} F_{i,j,k} \\ S_{i,j,k} \\ G_{i,j,k} \end{bmatrix}$$

where

$$H_1 = A_3 + \frac{A_4}{\Delta\bar{x}} + \frac{A_8}{\Delta\bar{t}}, H_2 = B_3 + \frac{B_4}{\Delta\bar{x}} + \frac{B_8}{\Delta\bar{t}}$$

$$H_3 = C_3 + \frac{C_4}{\Delta\bar{x}} + \frac{C_9}{\Delta\bar{t}}.$$

The system of tridiagonal blocks (29) is then solved by using Varga's algorithm [55] for ζ in η direction, which is discretized into \bar{J} subintervals, with fixed \bar{x}, \bar{t} and the forward marching continues in \bar{x} direction. The above-mentioned process repeats for the subsequent steps in \bar{t} direction.

The convergence of the solution at each step is assumed to be achieved when the maximum absolute difference between the current and previous iterations is less than the tolerance value, which is set at 10^{-4} . Here, the step sizes are taken as $\Delta\eta = 10^{-2}, \Delta\bar{x} = 5 \times 10^{-4}$ and $\Delta\bar{t} = 10^{-2}$. η_∞ is considered to be 6.

4. Results and Discussion

The precision of our study is ensured by comparing the obtained solutions with those available in the literature in both steady and unsteady cases.

In the case of steady flow, the effect of rotation B on the skin friction parameters $[(F_\eta)_w, -(S_\eta)_w]$ and the heat transfer parameter, $[(G_\eta)_w]$ are presented in Figure 2, and the effect of mixed convection parameter λ on skin friction coefficient in x -direction $[C_f(Re)^{1/2}]$ is shown in Figure 3.

The results are compared with those of Roy and Saikrishnan [14] and Chen et al. [29], respectively.

Also, in the case of unsteady flow, the impact of MHD parameter M on $C_f(Re)^{1/2}$ at times $\bar{t} = 0, 2$ are presented in Figure 4 and are compared with those of Sathyakrishna et al. [40]. All the above-mentioned studies agree with our results.

The variations in the skin friction coefficients in the x, y -directions and the heat transfer coefficient $[C_f(Re)^{1/2}, \bar{C}_f(Re)^{1/2}, Nu(Re)^{-1/2}]$ at various streamwise locations due to the MHD parameter M with $T_\infty = 18.7^\circ\text{C}, \Delta T_w = 10^\circ\text{C}, B = 1, \lambda = 20, A = 0, Ec = 0$ are presented in Figure 5 and Figure 6 for both steady and unsteady cases. From the figures, $C_f(Re)^{1/2}$ enhances from zero, hits maximum value and then declines as \bar{x} increases. With an increase in M and \bar{t} , both $C_f(Re)^{1/2}$ and $Nu(Re)^{-1/2}$ increase, whereas the effect is just the opposite on $\bar{C}_f(Re)^{1/2}$. The reason for this is the magnetic field B_0 induces a magnetic force which in turn creates a supporting force in the meridian direction and an opposing force in the rotational direction. Hence, increasing M accelerates the flow in x -direction and decelerates the flow in y -direction and thus resulting in the enhancement of $C_f(Re)^{1/2}, Nu(Re)^{-1/2}$ and reduction in $\bar{C}_f(Re)^{1/2}$. For fixed M , $Nu(Re)^{-1/2}$ decreases monotonically as \bar{x} increases. In the case of steady flow, the significance of the MHD parameter is not pronounced on $C_f(Re)^{1/2}$ and $Nu(Re)^{-1/2}$. However, the effect becomes significant with time \bar{t} .

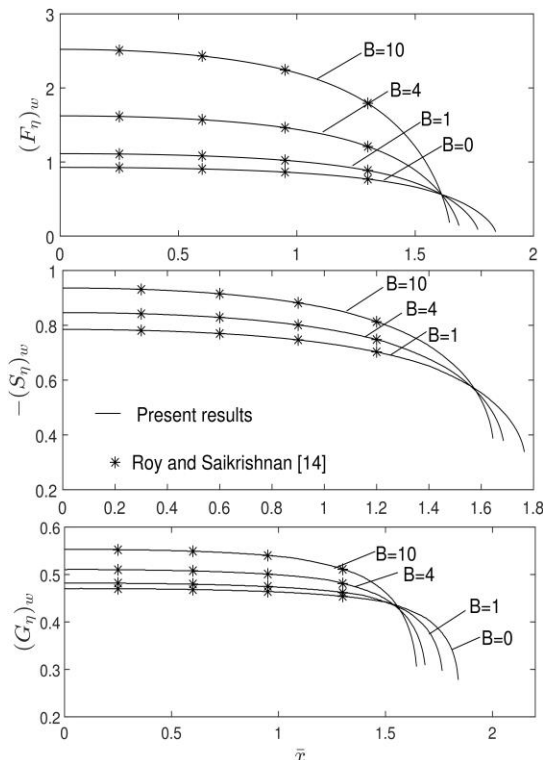


Figure 2. Comparison of the velocity profiles in x, y -directions and temperature profile for a steady flow with those of Roy and Saikrishnan [14] where $T_\infty = 18.7^\circ\text{C}, \Delta T_w = 20^\circ\text{C}$, constant viscosity and Prandtl number

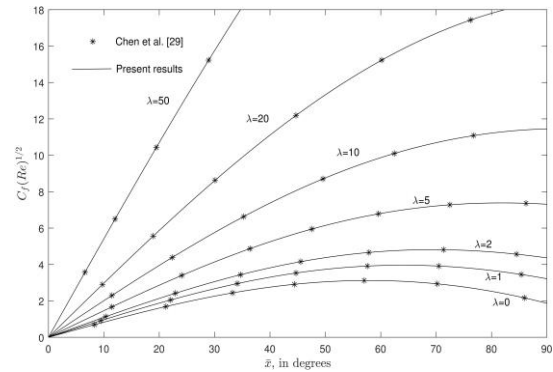


Figure 3. Comparison of the skin friction parameter in the x -direction with those of Chen et al. [29] where $T_\infty = 18.7^\circ\text{C}, \Delta T_w = 10^\circ\text{C}$, constant viscosity and Prandtl number

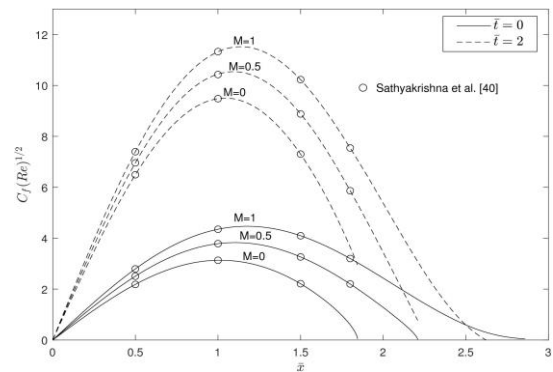


Figure 4. Comparison of the skin friction parameter in the x -direction for an unsteady flow with those of Sathyakrishna et al. [40] where $T_\infty = 18.7^\circ\text{C}, \Delta T_w = 10^\circ\text{C}$

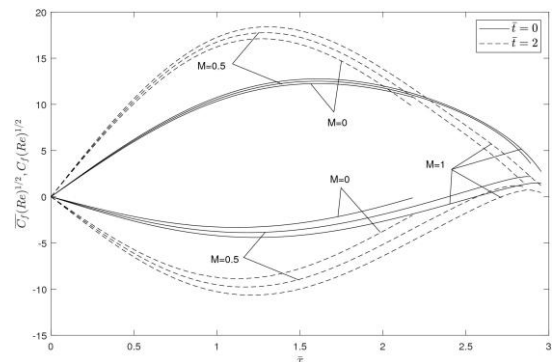


Figure 5. Effect of the MHD parameter M on the skin friction coefficients in x, y -directions for $\lambda = 20, B = 1$

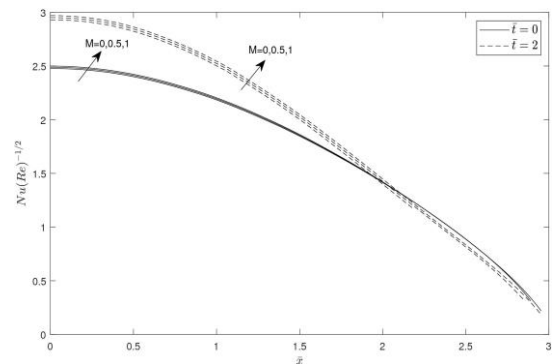


Figure 6. Effect of the MHD parameter M on the heat transfer coefficient for $\lambda = 20, B = 1$

Figure 7 and Figure 8 depict the influence of the mixed convection parameter λ on $C_f(Re)^{1/2}$, $\overline{C_f}(Re)^{1/2}$ and $Nu(Re)^{-1/2}$ over time for $T_\infty = 18.7^\circ\text{C}$, $\Delta T_w = 10^\circ\text{C}$, $B = 1, M = 1, A = 0, Ec = 0$. The presence of mixed convection parameter $\lambda \neq 0$ signifies favorable pressure gradient. This results in thinning of momentum and temperature boundary layers. As a consequence, both $C_f(Re)^{1/2}$ and $Nu(Re)^{-1/2}$ increase and $\overline{C_f}(Re)^{1/2}$ decreases as λ increases at both times $\bar{t} = 0, 2$. It is to be noted that the significance of λ is more prominent on $C_f(Re)^{1/2}$ than on $\overline{C_f}(Re)^{1/2}$ because there is no explicit dependence of the mixed convection parameter λ in equation (23).

Figure 9 and Figure 10 show the impact of rotation parameter B on $C_f(Re)^{1/2}$, $\overline{C_f}(Re)^{1/2}$ and $Nu(Re)^{-1/2}$ for $T_\infty = 18.7^\circ\text{C}$, $\Delta T_w = 10^\circ\text{C}$, $M = 1, \lambda = 10, A = 0, Ec = 0$. It is found that increasing rotation parameter B results in an increase of $C_f(Re)^{1/2}$ and $Nu(Re)^{-1/2}$ and decrease of $\overline{C_f}(Re)^{1/2}$ at both $\bar{t} = 0$ and 2. This is because the fluid entering in the axial direction has been forced outward in the rotational direction due to the centrifugal force and has been replaced by the cooler fluid from the normal direction. This results in accelerating the fluid flow in the axial direction and contracting the thickness of momentum boundary layer in that direction as well as the thickness of the thermal boundary layer. Meanwhile, in the rotational direction, the momentum boundary layer thickens. Also, the effect of B on $Nu(Re)^{-1/2}$ is found to be small since B affects it indirectly.

For the steady flow, $\overline{C_f}(Re)^{1/2}$ vanishes while $C_f(Re)^{1/2}$ does not. As B increases, the point of vanishing skin friction coefficient in y -direction moves slightly downwards, indicating an ordinary separation. It is also observed that $C_f(Re)^{1/2}$ vanishes for $B > 0, \bar{t} > 0$, and the point of vanishing skin friction in that direction moves upstream as B increases. However, this does not imply separation since it is unsteady.

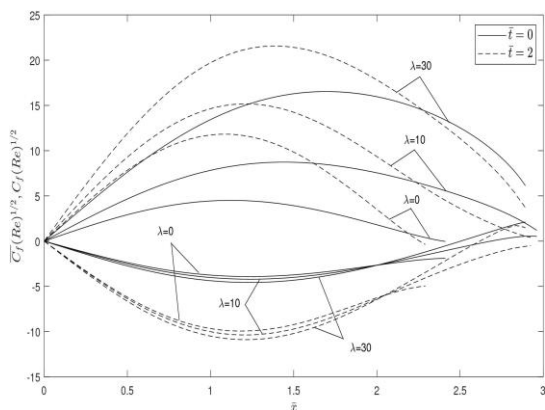


Figure 7. Effect of the mixed convection parameter λ on the skin friction coefficients in x, y -directions for $M = 1, B = 1$

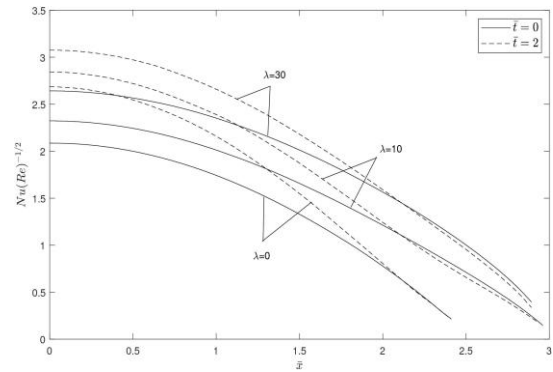


Figure 8. Effect of the mixed convection parameter λ on the heat transfer coefficient for $M = 1, B = 1$

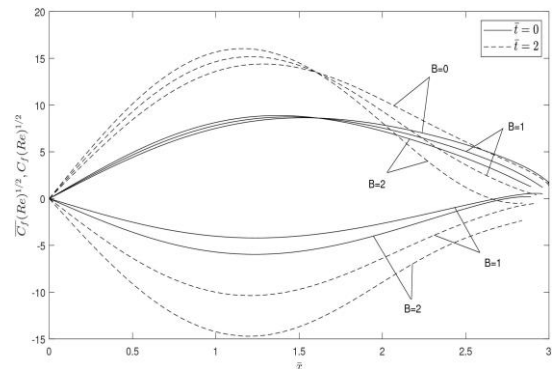


Figure 9. Effect of the rotation parameter B on the skin friction coefficients in x, y -directions for $M = 1, \lambda = 10$

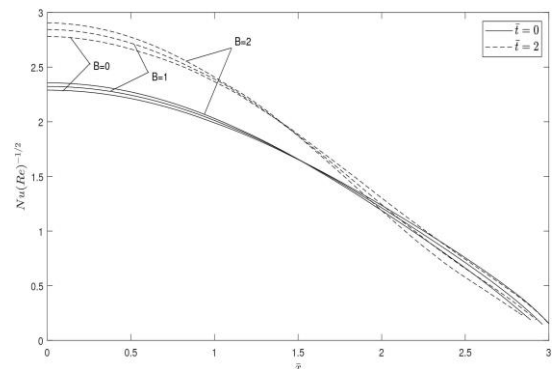


Figure 10. Effect of the rotation parameter B on the heat transfer coefficient for $M = 1, \lambda = 10$

The impact of the viscous dissipation parameter Ec on $Nu(Re)^{-1/2}$ for $A = 0, M = 1, \lambda = 2, B = 1$ has been shown in Figure 11. The heat transfer coefficient $Nu(Re)^{-1/2}$ decreases for the change of values of Ec from 0 to -0.1 in both steady and unsteady cases. At $\bar{x} = 1.5$, the percentage decrease of $Nu(Re)^{-1/2}$ is 129% when $\bar{t} = 0$ and 413% at $\bar{t} = 2$ as Ec changes from 0 to -0.1 . Also, the occurrence of negative $Nu(Re)^{-1/2}$ is physically simulated by the reversal of heat transfer direction.

The reason for this can be seen from the temperature profile G at $\bar{x} = 1.5$ depicted in Figure 12. For $Ec \neq 0$ and $\bar{t} = 2$, the temperature G gets below zero near the wall. This is because nonzero Ec emphasizes the presence of the viscous dissipation and M too being nonzero brings on joule heating in the

energy equation. Due to the impact of these two heating, the fluid near the wall heats up and its temperature becomes more than T_w , although originally T_w was higher. This results in the wall being heated up instead of being cooled and hence the heat transfer reversal observed in Figure 11. However, such a phenomenon is not observed in the steady case. Ec does not show much of a difference in the skin friction coefficients in x, y –directions as well as the velocity profiles. Hence, the corresponding figures are omitted in this paper.

Figures 13-16 show the influence of non-uniform mass transfer on $C_f(Re)^{1/2}$, $\overline{C_f}(Re)^{1/2}$ and $Nu(Re)^{-1/2}$ for $\lambda = 0.5, B = 1$ and $M = 0.5$, at $\bar{t} = 0$ and $\bar{t} = 2$. The effect of suction/injection is examined through two slots $[\bar{x}_0, \bar{x}_0^*]$, one at $[0.5, 1]$ and the other at $[1.25, 1.75]$, but not simultaneously. In the case of slot suction ($A > 0$), as the slot starts, $C_f(Re)^{1/2}$ and $Nu(Re)^{-1/2}$ increase and hit their maximum before the slot's end. Contrastingly, $\overline{C_f}(Re)^{1/2}$ decreases as the slot starts and hits its minimum before the slot's end. As the suction parameter increases, the fluid at the sphere's surface, which has low velocity, is sucked through the slot $[\bar{x}_0, \bar{x}_0^*]$ and is replaced by the fluid in the subsequent layers with comparatively higher velocity. This augments the velocity gradients in both x and y –directions at the wall ($F_\eta, -S_\eta$)_w and thus resulting in increasing $C_f(Re)^{1/2}$ and decreasing $\overline{C_f}(Re)^{1/2}$.

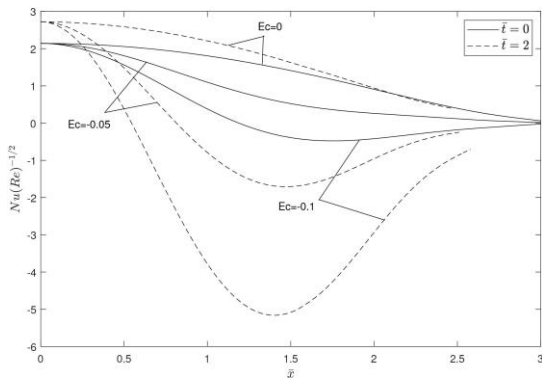


Figure 11. Effect of the viscous dissipation parameter Ec on the heat transfer coefficient for $\lambda = 2, M = 1, B = 1$

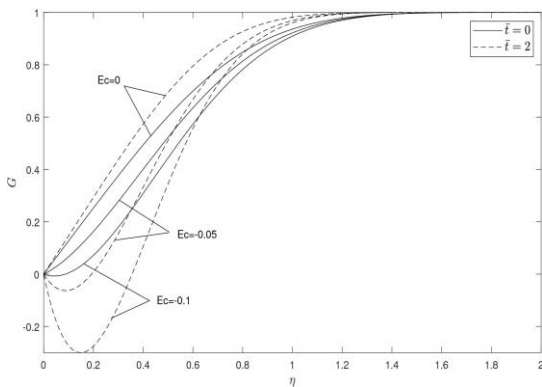


Figure 12. Effect of the viscous dissipation parameter Ec on the temperature profile at $\bar{x} = 1.5$ for $\lambda = 2, M = 1, B = 1$

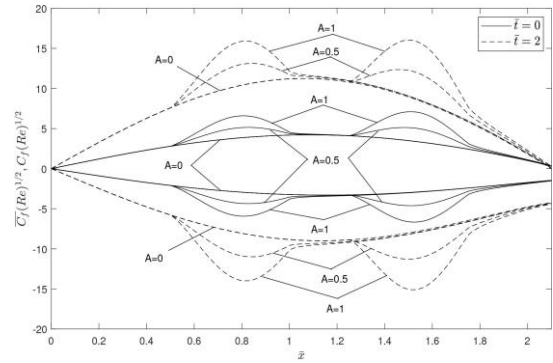


Figure 13. Effect of the non-uniform slot suction A on the skin friction coefficients in x, y –directions for $\lambda = 0.5, M = 0.5, B = 1$, slots at $\bar{x}_0 = 0.5, 1.25$

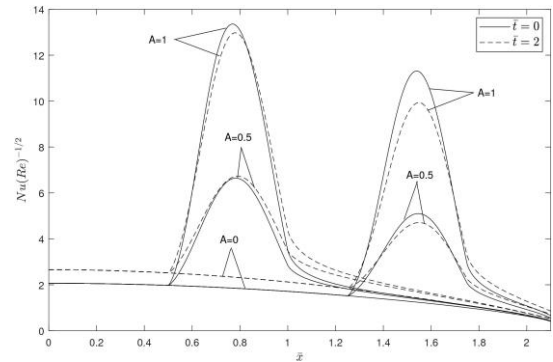


Figure 14. Effect of the non-uniform slot suction A on the heat transfer coefficient for $\lambda = 0.5, M = 0.5, B = 1$, slots at $\bar{x}_0 = 0.5, 1.25$

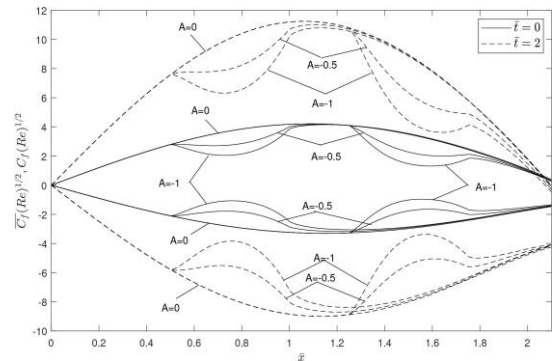


Figure 15. Effect of the non-uniform slot injection A on the skin friction coefficients in x, y –directions for $\lambda = 0.5, M = 0.5, B = 1$, slots at $\bar{x}_0 = 0.5, 1.25$

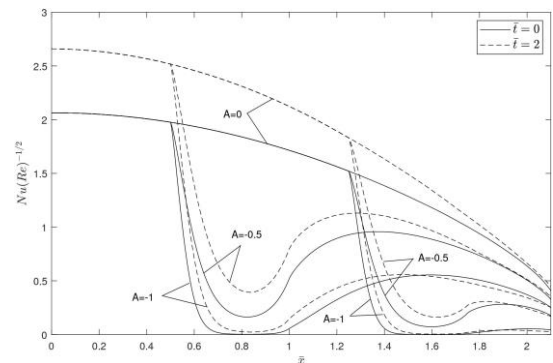


Figure 16. Effect of the non-uniform slot injection A on the heat transfer coefficient for $\lambda = 0.5, M = 0.5, B = 1$, slots at $\bar{x}_0 = 0.5, 1.25$

Moreover, since the fluid being sucked is warmer than the adjacent layers, the more the suction, the steeper the temperature gradient at the wall and hence $Nu(Re)^{-1/2}$ is enhanced.

The slot injection's ($A < 0$) effect on skin friction and heat transfer coefficients is qualitatively opposite to that of suction in the slot region. In all the above cases, regardless of A , the coefficients $[C_f(Re)^{1/2}, -\overline{C_f}(Re)^{1/2}, Nu(Re)^{-1/2}]$ are enhanced as \bar{t} increases and the impact is more pronounced in the unsteady case, since the flow is accelerating with \bar{t} . For the steady case ($\bar{t} = 0$), the suction/injection doesn't impact the zero skin frictions in both directions. However, when $\bar{t} > 0$, the point of zero skin friction in x -direction moves downstream with an increase in suction parameter ($A > 0$). The slot movement in the downstream direction from $[0.5,1]$ to $[1.25,1.75]$ helps the vanishing point of $C_f(Re)^{1/2}$ move further downstream. Meanwhile, the opposite effect is seen with an enhancement in the injection parameter. It should be emphasized here that zero skin friction in only one direction/both directions does not imply the ordinary/singular separation as the flow considered here is unsteady.

Conclusion

An unsteady MHD mixed convection boundary layer flow problem over a geometry of rotating sphere has been solved numerically, and the observations are as follows.

- The MHD parameter (M) affects the skin friction coefficient in x -direction and heat transfer coefficient noticeably in the unsteady case than it does in the steady case for fixed non-zero values of rotation and mixed convection parameters.
- The mixed convection parameter (λ) is found to have a prominent effect on the skin friction coefficient in the x -direction and the heat transfer coefficient in the y -direction, in both steady and unsteady cases.
- For non-zero values of rotation parameter B , an ordinary separation is noted in the steady case as $\overline{C_f}(Re)^{1/2}$ vanishes while $C_f(Re)^{1/2}$ does not. It is observed that $C_f(Re)^{1/2}$ vanishes for $B > 0$, $\bar{t} > 0$, and that point of vanishing moves upstream as the rotation parameter increases.
- At both times $\bar{t} = 0$ and 2 , the more the magnitude of viscous dissipation parameter (Ec) the less the heat transfer coefficient as a result of heating due to viscous and joule heating effects. Moreover, the unsteadiness results in drastic decrement in the heat transfer coefficient as dissipation increases.
- The temperature drops below zero in the vicinity of the sphere's surface in the unsteady case, indicating the fluid near the surface of the sphere getting warmer instead of colder.

- For fixed non-zero values of B, M, λ and $\bar{t} > 0$, non-uniform slot suction or slot movement helps the vanishing skin friction in x -direction to move slightly downstream, whereas the injection shows the opposite effect.

Nomenclature

A	Dimensionless mass transfer parameter
B_0	Magnetic field strength (T)
B	Dimensionless rotation parameter
c_p	Specific heat at constant pressure ($kJ \cdot kg^{-1} \cdot K^{-1}$)
C_f	Skin friction coefficient in the x -direction
$\overline{C_f}$	Skin friction coefficient in the y -direction
Ec	Eckert number (viscous dissipation parameter)
f	Dimensionless stream function
f_w	Surface mass transfer distribution
F	Dimensionless velocity component in the x -direction
g	Gravity ($m \cdot s^{-2}$)
G	Dimensionless temperature
Gr	Grashof number
k	Thermal conductivity ($W \cdot m^{-1} \cdot K^{-1}$)
M	MHD parameter
N	μ/μ_∞ Viscosity ratio
Nu	Nusselt number
Pr	Prandtl number
r	Radius of the section normal to the axis of the sphere (m)
R	Radius of the sphere (m)
Re	Reynolds number
S	Dimensionless velocity component in the y -direction
t	Dimensional time (s)
\bar{t}	Dimensionless time
T	Temperature (K)
u, v, w	Dimensional velocity components in x, y, z -directions, respectively ($m \cdot s^{-1}$)
U	Steady state velocity at the boundary layer's edge ($m \cdot s^{-1}$)
x, y, z	Dimensional meridional, azimuthal and normal distances, respectively (m)
\bar{x}	Dimensionless meridional distance
\bar{x}_0, \bar{x}_0^*	Ends of slot
Greek Symbols	
χ	Dimensionless pressure gradient
β	Volumetric coefficient of thermal expansion (K^{-1})
$\Delta\eta, \Delta\bar{x}, \Delta\bar{t}$	Step sizes in η, \bar{x} - and \bar{t} -directions, respectively
η, ξ	Transformed coordinates
ϵ	Constant used in the continuous function of time
λ	Mixed convection parameter
μ	Dynamic viscosity ($kg \cdot m^{-1} \cdot s^{-1}$)

ν	Kinematic viscosity ($m^2 \cdot s^{-1}$)
ρ	Density ($kg \cdot m^{-3}$)
σ	Electrical conduction ($\Omega^{-1} \cdot m^{-1}$)
ψ	Dimensional stream function ($m^2 \cdot s^{-1}$)
$\phi(\bar{t})$	Continuous function of time
Ω	Angular velocity ($rad \cdot s^{-1}$)
ω^*	Slot length parameter

Subscripts

e	Conditions at the edge of boundary layer
w	Conditions at the surface of the sphere
∞	Conditions in the free stream
x, z, \bar{x}	Partial derivatives with respect to these variables
\bar{t}, ξ, η	

Acknowledgements

The authors are thankful to the reviewers for their valuable comments. The first author would like to thank National Institute of Technology Tiruchirappalli for supporting through an institute fellowship.

References

- [1] Lien, F.S., Chen, C.K. and Cleaver, J.W., 1986. Mixed and Free Convection Over a Rotating Sphere with Blowing and Suction. *Journal of Heat Transfer*, 108(2), pp.398–404.
- [2] Kreith, F., Roberts, L.G., Sullivan, J.A. and Sinha, S.N., 1963. Convection Heat Transfer and Flow Phenomena of Rotating Spheres. *International Journal of Heat and Mass Transfer*, 6(10), pp.881–895.
- [3] Lee, M.H., Jeng, D.R. and De Witt, K.J., 1978. Laminar Boundary Layer Transfer Over Rotating Bodies in Forced Flow. *Transactions of the ASME*, 100, pp.496–502.
- [4] Niazmand, H. and Renksizbulut, M., 2005. Flow Past a Spinning Sphere with Surface Blowing and Heat Transfer. *Journal of Fluids Engineering*, 127(1), pp.163–171.
- [5] Safarzadeh, S. and Brahimi, A., 2022. Convection Heat Transfer and Flow Phenomena from a Rotating Sphere in Porous Media. *Scientia Iranica*, 29(2), pp.588–596.
- [6] Attia, H.A., 2009. Steady Flow Over a Rotating Disk in Porous Medium with Heat Transfer. *Nonlinear Analysis: Modelling and Control*, 14(1), pp.21–26.
- [7] Al-Maliky, R.F., 2013. Numerical Investigation of Laminar Flow Over a Rotating Circular Cylinder. *International Journal of Mechanical & Mechatronics Engineering*, 13(3), pp.32–44.
- [8] Towers, P.D. and Garrett, S.J., 2016. Similarity Solutions of Compressible Flow Over a Rotating Cone with Surface Suction. *Thermal Science*, 20(2), pp.517–528.
- [9] Schlichting, H. and Gersten, K., 2016. *Boundary-Layer Theory*, Springer.
- [10] Mahdy, A., 2018. Simultaneous Impacts of MHD and Variable Wall Temperature on Transient Mixed Casson Nanofluid Flow in the Stagnation Point of Rotating Sphere. *Applied Mathematics and Mechanics*, 39(9), pp.1327–1340.
- [11] Rajakumar, J., Saikrishnan, P. and Chamkha, A., 2016. Non-similar Solution of Steady MHD Mixed Convection Flow Over a Rotating Sphere. *Computational Thermal Sciences*, 8(6), pp.509–523.
- [12] Rajakumar, J., Saikrishnan, P. and Chamkha, A., 2016. Non-uniform Mass Transfer in MHD Mixed Convection Flow of Water Over a Sphere with Variable Viscosity and Prandtl Number. *International Journal of Numerical Methods for Heat & Fluid Flow*, 26(7), pp.2235–2251.
- [13] Revathi, G., Saikrishnan, P. and Chamkha, A., 2013. Non-similar Solution for Unsteady Water Boundary Layer Flows Over a Sphere with Non-uniform Mass Transfer. *International Journal of Numerical Methods for Heat & Fluid Flow*, 23(6), pp.1104–1116.
- [14] Roy, S. and Saikrishnan, P., 2003. Non-Uniform Slot Injection (Suction) Into Steady Laminar Water Boundary Layer Flow Over a Rotating Sphere. *International Journal of Heat and Mass Transfer*, 46(18), pp.3389–3396.
- [15] Saikrishnan, P. and Roy, S., 2002. Steady Nonsimilar Axisymmetric Water Boundary Layers with Variable Viscosity and Prandtl Number. *Acta Mechanica*, 157(1–4), pp.187–199.
- [16] Saikrishnan, P. and Roy, S., 2003. Non-uniform Slot Injection (Suction) Into Water Boundary Layers Over (i) a Cylinder and (ii) a Sphere. *International Journal of Engineering Science*, 41(12), pp.1351–1365.
- [17] Ganapathirao, M., Ravindran, R. and Pop, I., 2013. Non-uniform Slot Suction (Injection) on an Unsteady Mixed Convection Flow Over a Wedge with Chemical Reaction and Heat Generation or Absorption. *International Journal of Heat and Mass Transfer*, 67, pp.1054–1061.
- [18] Roy, S. and Nath, G., 1994. Non-uniform Slot Injection (Suction) or Wall Enthalpy into a Steady Nonsimilar Compressible Laminar Boundary Layer. *Acta Mechanica*, 103, pp.45–61.
- [19] Ganapathirao, M. and Ravindran, R., 2015. Non-uniform Slot Suction/Injection Into Mixed Convective MHD Flow Over a Vertical Wedge with Chemical Reaction. *Procedia Engineering*, 127, pp.1102–1109.
- [20] Subhashini, S.V., Takhar, H.S. and Nath, G., 2007. Non-uniform Mass Transfer or Wall Enthalpy Into a Compressible Flow Over a Rotating Sphere. *Heat and Mass Transfer*, 43(11), pp.1133–1141.
- [21] Dewey, C.F. and Gross, J.F., 1967. Exact Similar Solutions of the Laminar Boundary-Layer

- Equations, *Advances in Heat Transfer*, Elsevier, 4, pp.317–446.
- [22] Chamkha, A.J. and Ahmed, S.E., 2012. Unsteady MHD Heat and Mass Transfer by Mixed Convection Flow in the Forward Stagnation Region of a Rotating Sphere at Different Wall Conditions. *Chemical Engineering Communications*, 199(1), pp.122–141.
- [23] Eswara, A.T. and Nath, G., 1994. Unsteady Nonsimilar Two-Dimensional and Axisymmetric Water Boundary Layers with Variable Viscosity and Prandtl Number. *International Journal of Engineering Science*, 32(2), pp.267–279.
- [24] Roy, S., Takhar, H.S. and Nath, G., 2004. Unsteady MHD Flow on a Rotating Cone in a Rotating Fluid. *Meccanica*, 39(3), pp.271–283.
- [25] Anilkumar, D. and Roy, S., 2004. Self-Similar Solution of the Unsteady Mixed Convection Flow in the Stagnation Point Region of a Rotating Sphere. *Heat and Mass Transfer*, 40(6), pp.487–493.
- [26] Mahdy, A., Chamkha, A.J. and Nabwey, H.A., 2020. Entropy Analysis and Unsteady MHD Mixed Convection Stagnation-Point Flow of Casson Nanofluid Around a Rotating Sphere. *Alexandria Engineering Journal*, 59(3), pp.1693–1703.
- [27] Takhar, H.S. and Nath, G., 2000. Self-Similar Solution of the Unsteady Flow in the Stagnation Point Region of a Rotating Sphere with a Magnetic Field. *Heat and Mass Transfer*, 36(2), pp.89–96.
- [28] Sau, A., 1994. Unsteady Non-similar Compressible Boundary Layer Flow over a Rotating Sphere. *Acta Mechanica*, 106(3–4), pp.207–213.
- [29] Chen, T.S. and Mucoglu, A., 1977. Analysis of Mixed Forced and Free Convection About a Sphere. *International Journal of Heat and Mass Transfer*, 20(8), pp.867–875.
- [30] Devi, C.D.S. and Nath, G., 1988. Unsteady Mixed Convection Over Two-Dimensional and Axisymmetric Bodies. *Wärme- Und Stoffübertragung*, 22(1–2), pp.83–90.
- [31] Natarajan, E., Basak, T. and Roy, S., 2008. Natural Convection Flows in a Trapezoidal Enclosure With Uniform and Non-Uniform Heating of Bottom Wall. *International Journal of Heat and Mass Transfer*, 51(3–4), pp.747–756.
- [32] Natarajan, E., Basak, T. and Roy, S., 2007. Natural Convection in a Trapezoidal Cavity With Linearly Heated Side Wall (s). In *Heat Transfer Summer Conference*, 42746 pp. 1021–1030.
- [33] Hatem, N., Philippe, C., Mbow, C., Kabdi, Z., Najoua, S. and Daguene, M., 1996. Numerical Study of Mixed Convection Around a Sphere Rotating About Its Vertical Axis in a Newtonian Fluid at Rest and Subject to a Heat Flux. *Numerical Heat Transfer, Part A: Applications*, 29(4), pp.397–415.
- [34] Hatzikonstantinou, P., 1990. Effects of Mixed Convection and Viscous Dissipation on Heat Transfer about a Porous Rotating Sphere. *ZAMM - Journal of Applied Mathematics and Mechanics*, 70(10), pp.457–463.
- [35] Le Palec, G. and Daguene, M., 1987. Laminar Three-Dimensional Mixed Convection About a Rotating Sphere in a Stream. *International Journal of Heat and Mass Transfer*, 30(7), pp.1511–1523.
- [36] Rajasekaran, R. and Palekar, M.G., 1985. Mixed Convection About a Rotating Sphere. *International Journal of Heat and Mass Transfer*, 28(5), pp.959–968.
- [37] Rajasekaran, R. and Palekar, M.G., 1985. Viscous Dissipation Effects on Mixed Convection About a Rotating Sphere. *International Journal of Engineering Science*, 23(8), pp.789–795.
- [38] Tieng, S.M. and Yan, A.C., 1992. Investigation of Mixed Convection About a Rotating Sphere by Holographic Interferometry. *Journal of Thermophysics and Heat Transfer*, 6(4), pp.727–732.
- [39] Patil, P.M., Benawadi, S. and Shanker, B., 2022. Influence of Mixed Convection Nanofluid Flow over a Rotating Sphere in the Presence of Diffusion of Liquid Hydrogen and Ammonia. *Mathematics and Computers in Simulation*, 194, pp.764–781.
- [40] Sathyakrishna, M., Roy, S. and Nath, G., 2001. Unsteady Two-Dimensional and Axisymmetric MHD Boundary-Layer Flows. *Acta Mechanica*, 150(1–2), pp.67–77.
- [41] Turkyilmazoglu, M., 2011. Numerical and Analytical Solutions for the Flow and Heat Transfer near the Equator of an MHD Boundary Layer over a Porous Rotating Sphere. *International Journal of Thermal Sciences*, 50(5), pp.831–842.
- [42] Kazem, S., Tameh, M.S. and Rashidi, M.M., 2019. An Improvement To The Unsteady MHD Rotating Flow Over a Rotating Sphere Near the Equator via Two Radial Basis Function Schemes. *The European Physical Journal Plus*, 134(12), p.611.
- [43] Vajravelu, K., Li, R., Dewasurendra, M. and Prasad, K.V., 2017. Mixed Convective Boundary Layer MHD Flow Along a Vertical Elastic Sheet. *International Journal of Applied and Computational Mathematics*, 3(3), pp.2501–2518.
- [44] Ghani, M. and Rumite, W., 2021. Keller-Box Scheme to Mixed Convection Flow over a Solid Sphere with the Effect of MHD. *MUST: Journal of Mathematics Education, Science and Technology*, 6(1), pp.97–120.
- [45] Chamkha, A.J. and Ahmed, S.E., 2011. Unsteady MHD Heat and Mass Transfer by Mixed Convection Flow in the Forward Stagnation Region of a Rotating Sphere in the Presence of Chemical Reaction and Heat Source. In

- Proceedings of the World Congress on Engineering, 1 pp.133–138.
- [46] Sahaya Jenifer, A., Saikrishnan, P. and Lewis, R.W., 2021. Unsteady MHD Mixed Convection Flow of Water over a Sphere with Mass Transfer. *Journal of Applied and Computational Mechanics*, 7(2), pp.935–942.
- [47] Gul, T., Ali, B., Alghamdi, W., Nasir, S., Saeed, A., Kumam, P., Mukhtar, S., Kumam, W. and Jawad, M., 2021. Mixed Convection Stagnation Point Flow of the Blood Based Hybrid Nanofluid around a Rotating Sphere. *Scientific Reports*, 11(1), pp.1–15.
- [48] Calabretto, S.A., Levy, B., Denier, J.P. and Mattner, T.W., 2015. The Unsteady Flow Due to an Impulsively Rotated Sphere, *Proceedings of the Royal Society A: Mathematical, Physical and Engineering Sciences*, 471(2181), p.20150299.
- [49] Mahdy, A.E.N., Hady, F.M. and Nabwey, H.A., 2021. Unsteady Homogeneous-Heterogeneous Reactions in MHD Nanofluid Mixed Convection Flow Past a Stagnation Point of an Impulsively Rotating Sphere. *Thermal Science*, 25(1 Part A), pp.243–256.
- [50] Almakki, M., Mondal, H., Mburu, Z. and Sibanda, P., 2022. Entropy Generation in Double Diffusive Convective Magnetic Nanofluid Flow in Rotating Sphere with Viscous Dissipation. *Journal of Nanofluids*, 11(3), pp.360–372.
- [51] Das, K., Kundu, P.K. and Sk, M.T., 2022. Magnetophoretic Effect on the Nanofluid Flow Over Decelerating Spinning Sphere with the Presence of induced Magnetic Field. *Journal of Nanofluids*, 11(1), pp.135–141.
- [52] Mahmood, Z., Alhazmi, S.E., Khan, U., Bani-Fwaz, M.Z. and Galal, A.M., 2022. Unsteady MHD Stagnation Point Flow of Ternary Hybrid Nanofluid over a Spinning Sphere with Joule Heating. *International Journal of Modern Physics B*, 36(32), p.2250230.
- [53] Bellman, R.E. and Kalaba, R.E., 1965. *Quasilinearization and Nonlinear Boundary Value Problems*, The RAND Corporation, American Elsevier Publishing Company, Inc., New York.
- [54] Inouye, K. and Tate, A., 1974. Finite-Difference Version of Quasi-Linearization Applied to Boundary-Layer Equations. *AIAA Journal*, 12(4), pp.558–560.
- [55] Varga, S., 2000. *Matrix Iterative Analysis*, Springer-Verlag Berlin Heidelberg.



Semnan University



Investigation of particle resuspension from a garment using different turbulence dispersion models

Hamidreza Kharinezhad Arani, Ali Jafarian *, Jamal Darand

Faculty of Mechanical Engineering, Tarbiat Modares University, P.O. Box 14115-143, Tehran, Iran.

PAPER INFO

Paper history:

Received: 2021-11-04

Received: 2022-08-19

Accepted: 2022-08-25

Keywords:

Particle turbulence dispersion model;
Particulate matter;
Resuspension;
Controlled space;
Eulerian-Lagrangian approach;
Resuspension probability.

ABSTRACT

One of the most important sources of aerosol production in a controlled space is the human. The flow around the individual and the particles on the garment play an essential role in aerosol distribution in the environment. Such spaces are simulated from a Lagrangian or Eulerian point of view. In this research, particle resuspension from a user's garment under horizontal and vertical unidirectional systems was studied. For this purpose, a computer program was developed and used for examination of the impacts of different particle turbulence dispersion models, such as Discrete Random Walk, in a controlled space. Moreover, the effects of flow direction, velocity, and particle density on the probability of resuspension of particles with different diameters were investigated. The results demonstrated that the vertical *unidirectional* system had advantages over its horizontal variant, and that increased flow velocity provided positive feedback in the vertical system but negative feedback in the horizontal one. In the horizontal system, the resuspension probability for the sizes of 5 and 0.5 microns has increased by 177 and 355 percent, respectively, compared to the vertical system. It is worth noting that the results of the isotropic and non-isotropic models for particles size below 5 microns were quite the same. For the particles size over 5 microns, the maximum percentage discrepancy of 138 in resuspension probability between the non-isotropic and isotropic models is obtained.

DOI: [10.22075/jhmtr.2022.25113.1359](https://doi.org/10.22075/jhmtr.2022.25113.1359)

© 2022 Published by Semnan University Press. All rights reserved.

1. Introduction

Interior air quality is a very important issue, which is of even greater significance in a controlled space such as a clean room, a space with controlled pollutant and aerosol levels much lower than in common interior spaces. The main purpose of designing a clean space is to control the amount of pollutant particles in the area. For categorization and specification of the application of a controlled space, the number of aerosols in the room volume is used as criterion. This demonstrates the significance of air quality and accuracy in the calculations made for these spaces. The number of aerosols that are there depends on different factors such as resuspension of particles from surfaces or particle-producing sources [1,2]. One of the most important sources of particles is the user of the controlled space, producing most of the aerosols. To

simulate the space, an Eulerian or a Lagrangian approach needs to be adopted. In a Lagrangian approach, several models of particle turbulence dispersion are presented, each with its own accuracy, advantages, and disadvantages.

The literature involves two areas. One includes cases where particle turbulence dispersion models are used. Over the years, several studies have been carried out on the effects of different such models in particle deposition in channels and similar conditions. Some notable examples from the above area of research follow. Tian and Ahmadi [3] studied the effects of different boundary conditions beside the wall on particle deposition rate. The impacts of turbulence on particle dispersion and deposition were examined using Discrete Random Walk (DRW) and Continuous Filtered White-Noise (CFWN), and the accuracy and validity of simulation of the two turbulence models in

*Corresponding Author: Ali Jafarian
Email: jafarian@modares.ac.ir

the current field was discussed. They showed that the DRW and CFWN turbulent dispersion models are both capable methods for modeling particle velocity fluctuations in the turbulent flow of the channel. Gao et al. [4] also conducted a study of the effects of turbulent flow models on duct deposition results, and provided a correction factor for the DRW model. They found that the RSM model can successfully predict the transition from the diffusion region to the inertia-moderated region. Mito and Hanratty [5] used the Langevin equation to describe turbulent dispersion of fluid particles in a channel flow. The difference between these models in simulation of controlled environments has not yet been studied, as they have been used commonly to inspect deposition in very small ducts. Kang and et al. [6] studied the influence of temperature and vertical location of inlet supply air in a displacement ventilation room. In their study, discrete random walk (DRW) model was utilized to simulate the stochastic velocity fluctuations in the airflow. The results showed that the inlet location would slightly influence the ventilation efficiency.

Detachment and resuspension of particles is an important source of aerosol concentration in interior spaces [2]. Understanding air current and, subsequently, aerosol suspension due to human factors, such as movement, provides some insight on mechanisms of concentration variation in interior spaces. Research in this area includes studies on simulation of the human walk model and its effects on concentration. Due to the complexity of this movement, some researchers have considered it as a falling-disc or footstep motion [2, 7-9]. Kubota and et al [6] experimentally investigated the human foot movement and particle resuspension from the floor. Zhao, & Zhang [9] simulated the movement of foot walking. The movement of foot can cause the resuspension of ground particles. Indoor human activities can cause resuspension of particulate matter in space. Boulbair et al. [10] studied CFD (using DRW model) of the unsteady airflow field around and under the shoe. They showed that Particle resuspension fractions increased with particle size and walking speed. Sun et al. [11] performed a series of experiments to study the coupling effects between human walking and ventilation condition on indoor particle resuspension.

Qian, & Ferro [13] reviewed the particle resuspension due to human walking in indoor environments. They concluded that particles resuspension is an important source for indoor particulate matter compared to other indoor sources. In addition, they showed that resuspension increases with particle size in the range of 0.7-10 μm . Sajadi et al. [12] used Fluent and DRW to simulate resuspension of particles and examine the particle surface resuspension rate resulting from the fall of a disc. One of the most notable studies on resuspension of

particles in the room is the experimental research conducted by Qian [13], where Arizona Test Dust (ATD) was used for examination of the rate of surface particle resuspension (PR) resulting from an individual's walking and movement on three different surface materials. Previous studies have hardly considered the effects of the current around an individual, movement of the entire body, and type of ventilation. Tsai [14] investigated the variations in concentration due to particle resuspension from the garment in a clean room. A piece of fabric was placed in a container with a class-100 clean room. Although better, improved Lagrangian turbulence models have been provided, numerical research on particle movement in controlled spaces is conducted mostly using the Discrete Random Walk model. Aracena and et al. [15] performed experiments to determine the critical angular velocities of a particle on a rotating rough surface. Their experiments showed that the adhesion forces must be considered in forces balance of particle detachment. Benabed and et al. [16] experimentally studied human walking-induced particle resuspension in a full-scale chamber with two flooring types. This work revealed that the resuspension of PM1 and PM2.5 is many orders of magnitude lower than PM10. Habchi et al. [17] investigated resuspension under the effect of transient flow using the DRW model. Kazzaz et al. [18] studied resuspension as influenced by oscillatory flow in a simple geometry.

Recently, Al Assaad et al. [19] studied developed a new empirically validated CFD modeling methodology for particle release from human skin and clothing in specific office settings. Ren [20] and et al. investigated experimentally the deposition of particles onto clothing and the resuspension of particles from clothing using a fluorescent-tracking technology.

As stated before, in previous studies of particle motion in controlled spaces, the importance of the turbulence dispersion models has not been addressed. Also, these studies mainly focused on the effect of the human walking on particulate matter sources in conventional ventilation systems, and less attention has been paid to the particles resuspension from the individual's body in unidirectional ventilation systems. In addition, the effect of isotropic and non-isotropic turbulence models on the resuspension and detachment of particles from surfaces has not been investigated.

So, the present paper attempts to fill the research gaps mentioned above. In this regard, the present research investigates the probability of particle resuspension from a garment in a controlled environment under vertical and horizontal unidirectional ventilation on an individual's body for different particle diameters to demonstrate the influence of flow direction and particle size. In addition, parameters such as particle density and

ventilation flow velocity are considered. For evaluation of the validity of different discrete-phase turbulence models with respect to particle size, isotropic and non-isotropic turbulence is studied, along with different particle turbulence dispersion models.

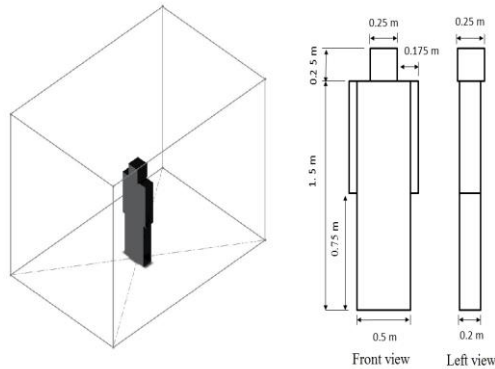


Figure 1. Left and front view of the user individual used in the simulation, along with schematics of the physical model (user in the room)

2. Physical model

The unidirectional ventilation room is the most common types of room, which can in turn be of the vertical or horizontal type. A unidirectional flow with a velocity of 0.3 to 0.45 m/s (the Reynolds number of 13000 to 20000) passes along the room in the controlled space simulated in this study [21]. This class-5 ISO clean room is 4 meters long, 2.7 meters wide, and 3 meters high. The intake and exhaust are considered here in two different arrangements: vertical unidirectional ventilation with a flow from the ceiling to the floor and horizontal unidirectional ventilation with a flow between two parallel walls.

Before entering the controlled space, the air passes through H13-class filters. The room is considered empty with no equipment present except the individual. The garment is assumed to be in compliance with the ISO-5 standard. The user's geometry and dimensions, as well as coordinates, are provided in detail in Figure 1. According to the figure, vertical unidirectional ventilation utilizes the entire ceiling as the flow air intake with exhausts on the floor, and horizontal unidirectional ventilation has its flow air intake facing the user, with the wall on the opposite side functioning as the air exhaust.

3. Mathematical description of the problem

In the analysis made in this research, air in standard conditions is used as the carrying fluid. According to the model geometry and flow characteristics in the present work, Reynolds number will be above 3750 which is resulted in passing turbulent flow through the user garment. It means that fluid velocity would be the

sum of a mean and a fluctuating value at each point inside the field.

Several studies have been conducted so far to solve the problem of turbulent flow fields containing particles. Zhang and Chen [22] used the standard k- ϵ model in their investigation, which provided acceptable accuracy, but the results were far from those of experiments in some cases. As for deposition, Gao et al. [4] used three models, including k- ϵ RNG, k- ω SST, and Reynolds Stress Model (RSM), and concluded that k- ω SST and RSM provided better results. RSM calculates the amount of fluctuation in different directions, and is regarded as a non-isotropic model. Therefore, the present study uses RSM. Arizona Test Dust is used widely in investigation of aerosol distribution in clean spaces, so much so that standard high-efficiency filter tests are also conducted using the particles [13]. Over 70% of the ATD mass is silicon dioxide. In the present study, this material is used along with aluminum oxide to inspect particle resuspension from the garment surface. The characteristics of these materials are provided in Table 1, which are used for calculation of critical tension, required to resuspend the above particles.

Table 1. Characteristics of the Arizona Test Dust ingredients [2]

Material	ρ (10^3 kg/ m^3)	K (10^{10} N/ m^2)	W_A (10^{-3} N/ m^2)	Mass percentage
SiO ₂	2.20	7.3	10.7	68-76
Al ₂ O ₃	3.96	36	15.3	10-15

In the current study, particle density is assumed to be 2000 kg/m³, in accordance with previous studies [13].

3.1. Particle movement modeling

In the Lagrangian approach, particle behavior is regarded as a discrete phase, so the relevant equations should be analyzed separately in the reference coordinate system. The particle movement equation is Newton's second law, which is defined as Equation 1.

$$m_p \frac{du_p}{dt} = F_{fr} + F_g + F_b + F_s + F_{br} \quad (1)$$

The right side of the equation represents the sum of the forces applied to the particle, including friction, gravity, buoyancy, Saffman lift, and Brownian. Friction is the main cause of the particles driving in and out of the room [23]. The friction force applied to the particle is similar to the drag force induced to a spherical particle in a laminar flow, which is calculated as Equation 2.

$$F_{fr} = \frac{1}{2C_c} C_d A_f \rho_f |u_r|^2 \quad (2)$$

This force is in the same direction as particle and fluid relative velocity. The equation used for calculation of the drag coefficient is defined as Equation 3 [3].

$$C_d = \begin{cases} \frac{Re}{24} & Re_r \leq 1 \\ \frac{Re}{24} \left[1 + \frac{Re^{0.687}}{0.15^{-1}} \right] & 1 < Re_r \leq 1000 \\ 0.44 & 1000 < Re_r \end{cases} \quad (3)$$

C_c is Cunningham correction factor, and is obtained by Equation 4 [23]:

$$C_c = 1 + Kn \left(1.257 + 0.4 \exp\left(\frac{-0.55}{Kn}\right) \right) \quad (4)$$

where Kn is Knudsen number.

The gravity force induced to the particle is calculated by Equation 5.

$$F_g = \frac{\pi \rho_p d_p^3}{6} g \quad (5)$$

The buoyant force functions in the opposite direction of gravity, and is proportional to the volume of the object, carrying fluid density, obtainable from Equation 6.

$$F_b = -\frac{\pi \rho_f d_p^3}{6} g \quad (6)$$

F_{br} is the Brownian force. It is possible to demonstrate that the Brownian force can be modeled as white noise, a random even parameter with Gaussian distribution and zero average. White-noise spectrum intensity is described by Equation 7 [25]:

$$S_{nn} = \frac{2k_B T \beta}{\pi m_p} \quad (7)$$

where β is the particle velocity factor in the Lagrangian equation ($du/dt + \beta u = n(t)$), T is temperature (in Kelvin), and k is Boltzmann constant. The amount of the Brownian force can be obtained from Equation 8 [26].

$$n(t_i) = G_i \sqrt{\frac{\pi S_{nn}}{\Delta t}} \quad (8)$$

The presence of velocity gradient in the continuous phase induces a lift force to the particle, which is known as the Saffman lift, defined by Equation 9 [27].

$$F_s = 1.61 \rho_f v_f^{\frac{1}{2}} d_p^2 |\nabla \times \vec{u}_f|^{-\frac{1}{2}} [(\vec{u}_f - \vec{u}_p)] (\nabla \times \vec{u}_f) \quad (9)$$

Some parameters need to be defined for studying and solving the movement of particles, one of the most important being particle relaxation time, obtained in Stokes regime by Equation 10.

$$\tau_r = \frac{\rho_p d_p^2 C_c}{18 \mu_f} \quad (10)$$

Another noteworthy parameter, also used in Lagrangian turbulent section equations, is particle terminal velocity, i.e., velocity of freefalling under the influence of gravity, obtained in Stokes regime, which is calculated by Equation 11.

$$V_{ter} = \frac{g d_p^2 C_c}{18 \mu_f} (\rho_p - \rho_f) \quad (11)$$

3.2. Evaluation of discrete phase turbulence

Turbulent fluid flow and velocity fluctuations directly affect particle movement, where the instantaneous velocity felt by the particle changes due to the changes in the forces applied to it. Velocity fluctuates randomly in a turbulent flow, where each particle experiences different velocities at the same spot at different times. Several methods have been proposed for indicating the effect of turbulence in the particle movement equation. The five methods used in this study are introduced below.

3.2.1. Discrete Random Walk

The best-known method of modeling continuous phase velocity fluctuations is the Discrete Random Walk method. Its greatest feature is that it samples particle velocity fluctuations with Gaussian distribution, zero average, and mean variance equal to the root mean square of the turbulent velocity fluctuation, which are calculated by Equation 12 and 13. In this sampling method, the fluctuating velocity is kept constant in a time interval corresponding to the time scale of vortices. In non-isotropic conditions, Reynolds stress components (u'^2, v'^2, w'^2) are directly used [28].

$$\sqrt{u'^2} = \sqrt{v'^2} = \sqrt{w'^2} = V_{rms} = \sqrt{\frac{2k}{3}} \quad (12)$$

$$u_f = (\bar{u} + \xi \sqrt{u'^2}) \hat{i} + (\bar{v} + \xi \sqrt{v'^2}) \hat{j} + (\bar{w} + \xi \sqrt{w'^2}) \hat{k} \quad (13)$$

where ξ represents a random number with Gaussian distribution. A Gaussian distribution is defined with an average value and a standard deviation, which are 0 and 1 here, respectively. Thus, fluid velocity in the movement equation is as shown in Equation 13.

In the analysis procedure, the above random number changes in accordance with the turbulence field. The change is specified given the length scale of the eddy and the time it takes the particle to cross it. The lifetime of the eddy is determined by Equation 14:

$$\tau_e = 2T^L \quad (14)$$

where T^L is the Lagrangian integral time scale of the particle, calculated by Equation 15.

$$T^L = C_L \frac{k}{\varepsilon} \tag{15}$$

C_L is assumed to be 0.3, and particle crossing time is obtained by Equation 16:

$$t_{cross} = -\tau_r \ln \left[1 - \left(\frac{l_e}{\tau_r |\bar{u} - \bar{u}_p|} \right) \right] \tag{16}$$

where τ_r is particle relaxation time, and l_e is eddy length scale, calculated by Equation 17 [29].

$$l_e = 0.165 \frac{k^{3/2}}{\varepsilon} \tag{17}$$

In the discrete random walk method, the particle interacts with the turbulent field either while it crosses the eddy, or until the eddy dies out; therefore, the time of interaction of the particle with the turbulent field is the smaller duration.

3.2.2. Fourier-Kraichnan method [30]

Kraichnan presented a simple method that creates a random field similar to pseudo-isotropic turbulence. Having studied turbulence simulation using the fluid energy spectrum function, he suggested an idea for fluid velocity fluctuations, and measured the fluid energy spectrum. In this method, fluid velocity fluctuations are calculated using Equations 18, 19, and 20 [30, 31], applicable in incompressible conditions.

$$\begin{aligned} \bar{W}_f(\vec{X}_p, t) &= \sqrt{\frac{2}{N}} \left[\sum_{n=1}^N \bar{u}_1(\vec{k}_n) \cdot \cos(\vec{k}_n \cdot \vec{X}_p + \omega_n t) \right. \\ &\quad \left. + \bar{u}_2(\vec{k}_n) \cdot \sin(\vec{k}_n \cdot \vec{X}_p + \omega_n t) \right] \end{aligned} \tag{18}$$

$$\bar{u}_1(\vec{k}_n) = \vec{\xi}_n \times \vec{k}_n, \bar{u}_2(\vec{k}_n) = \vec{\zeta}_n \times \vec{k}_n \tag{19}$$

$$\vec{k}_n \cdot \bar{u}_2(\vec{k}_n) = \vec{k}_n \cdot \bar{u}_1(\vec{k}_n) = 0 \tag{20}$$

in these equations, $\xi_n, \zeta_n,$ and ω_n (frequency value) are acquired independently from Gaussian distribution. Each of the k_n parameters is a random Gaussian value with a standard deviation of 0.5, which is considered as a function of the energy spectrum, and n is the number of utilized series, which is usually 100.

Nondimensional values are described by Equation 21.

$$\vec{X} = \frac{\vec{x}}{l_0}, t^* = \frac{t}{t_0}, \bar{W}_f = \frac{\bar{u}'}{\sqrt{\bar{u}'^2}} \tag{21}$$

where l_0 and t_0 are factors of flow and geometry, and W_f represents nondimensional fluid phase velocity fluctuations.

3.2.3. Model based on Langevin equation

In this model, benefitting from Langevin equation, the relation and correlation between the fluid and the

particle (Eulerian) is recognized by Frenkiel family of exponential functions, and the correlation between particle velocity and its history is acquired by the Langevin equation (Equation 22).

$$du = u(t + dt) - u(t) = -\frac{u}{T_L} + \sigma_f \sqrt{\frac{2}{T_L}} dW \tag{22}$$

Here, dW is Wiener Process (white noise) which averages zero ($\langle dW \rangle = 0$), and time interval equals variance ($\langle (dW)^2 \rangle = dt$). The advantage of using this formula is that it provides better physical compatibility. Berlemont et al. [32] proposed an innovative extension of discrete Langevin formula, utilized below. It is not simply a proposed discretization derived for a correlation function but rather a continuous model found on a random differential equation, resulting in the real form of correlation. The discretization of the equation is formulated as Equation 23:

$$u^{n+1} = au^n + b\xi^n \tag{23}$$

where ξ is a random number obtained from normal Gaussian distribution.

The equation is valuable in that it focuses on the main physical idea of the model, and materializes it. Fluid velocity is given in a certain t^n time frame, and is determined in the next time frame $t^{n+1} = t^n + \Delta t$ by the sum of the predefined values of a phrase containing the memory of the previous velocity and a random phrase for acceleration fluctuations.

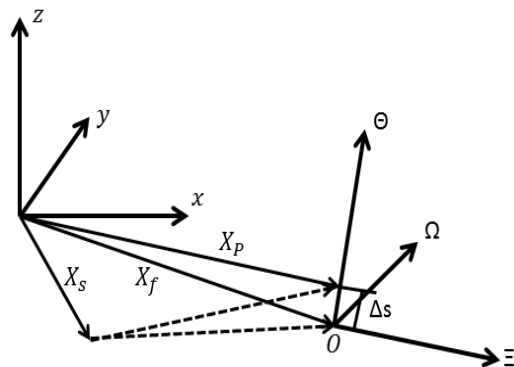


Figure 2. Particle and fluid point position at moments t and $t + \Delta t$

To obtain the values of the a and b coefficients, the above equation is multiplied by u^n and u^{n+1} , and the mean result is calculated from Equations 24 and 25.

$$a = \frac{\langle u^n u^{n+1} \rangle}{\langle (u^n)^2 \rangle} = R_L(\Delta t) = \exp\left(-\frac{\Delta t}{T_L}\right) \tag{24}$$

$$b = [\langle u^{n+1} u^{n+1} \rangle - a^2 \langle (u^n)^2 \rangle] = (1 - a^2) \sigma_f^2 \tag{25}$$

Subsequent use of the exponential correlation in steady state results in Equation 26.

$$\langle (u^n)^2 \rangle = \sigma_f^2 \tag{26}$$

3.2.4. Lagrangian Temporal Construction Model (LTCM)

Lu et al. [33] presented a new model with better compatibility with experimental results. This method is based on Lagrangian correlation of random particle movement from X_s to X_f .

The fluid point and the particle are assumed to be at the same position (X_s) at moment t , and reach positions X_f and X_p , respectively, after a time step (Δt). The distance between these two is shown in Figure 2 as Δs . The local coordinates $0 - \Theta \Xi \Omega$ are defined by particle movements. X_f , X_s , and X_p are located at the original coordinates. In the first step of LTCM, particle position and velocity at moment zero are given, and the initial fluid fluctuations are then obtained through the Discrete Random Walk model. In the second step, the fluid point position at X_f is calculated by the velocity differential equation.

The particle position X_p is acquired through momentary velocity and the particle movement equation. All the values required for formation of a local system of coordinates are thus obtained. once that step is taken, a return is made to the second step, where the acquired location data are set, and the fluctuation velocities in the local system of coordinates are calculated. Afterwards, the local coordinates need to be converted to the original ones, and the new value of velocity is used to set initial velocity.

According to Equations 27 and 28 the relations between particle velocity fluctuations in the initial and secondary positions are calculated in LTCM model.

$$W_i(X_p) = a_i b_i W_i(X_s) + \psi \quad (i = 1,2,3) \quad (27)$$

$$\psi_i = \sqrt{1 - (\alpha_i b_i)^2} \quad (28)$$

Frenkiel proposed the following forms (Equations 29 and 30) of temporal and local correlation functions for α_i and b_i .

$$\alpha_i = \exp\left(\frac{-\Delta t}{T_i^L}\right) \quad (29)$$

$$b_i = \exp\left(\frac{-\Delta s}{2\Lambda_i}\right) \cos\left(\frac{\Delta s}{2\Lambda_i}\right) \quad (30)$$

These functions use length scales, where Λ_1 is the longitudinal scale, and Λ_2 and Λ_3 are the transverse ones, as estimated Equations 31 and 32 [33].

$$\Lambda_1 = 2.502 T_i^L \sqrt{\overline{u_i^2}} \quad (31)$$

$$\Lambda_2 = \Lambda_3 = 0.5 \Lambda_1 \quad (32)$$

3.2.5. Langevin-Lagrangian Temporal Construction Model (L-LTCM)

This method is a mixture of Langevin and Lagrangian Time Construction Models. The definition of this method is similar to that of Lagrangian Time Construction Model, different in that Langevin equation is used here instead of Eulerian correlations. As in the coefficient acquired in the Langevin Equation 25 is used in Equation 28 and Equation 33 [34].

$$\psi = (1 - a^2) \sigma_f^2 \xi^n \quad (33)$$

4. Resuspension

A physical process through which a particle is detached from the surface. It usually occurs due to aerodynamic forces created by the shear flow. In this study, an improved version of the Johnson-Kendell-Roberts model [35] is used to simulate particle resuspension under an applied shear tension.

Furthermore, Soltani and Ahmadi [36] extracted an analytical model to predict particle surface detachment, and referred to rolling as the most probable mechanism of spherical particle resuspension from real surfaces. Therefore, the shear tension velocity required for particle detachment is as follows (Equation 34).

$$u_c^* = \left[\frac{a^2 C_c f_{po} \exp\left(-\frac{0.6}{A_c^2}\right)}{2.52 \rho d_p^3} \right]^{1/2} \quad (34)$$

If shear velocity is higher than the above value, the particle qualifies for detachment. However, it should be observed whether the particle enters the main flow, or is deposited. For evaluation of the effects of the air flow around an individual over the particle surface, resuspension rate and resuspension probability are defined as Equations 36 and 37, respectively [12, 37].

$$PR = \frac{N_R}{N_L} \quad (35)$$

$$RR = \frac{R}{L} = \frac{PR}{T_r} \quad (36)$$

$$C = \frac{N_R}{V} = PR \times \frac{L \times A}{V} \quad (37)$$

In Equation 35, particle resuspension probability is the proportion of the number of particles resuspended from the surface (N_R) to the number of particles present on the surface (N_L), and resuspension rate (RR) is the proportion of resuspension flux (in particles per second per cubic meter) to particle load (L) on the surface (in particles per cubic meter), according to Equation 36. Particle resuspension rate can be obtained based on the probability of particle resuspension, which is the proportion of resuspension probability to resuspension time. rate is the significant parameter for distribution of particles with different diameters, as also explored in the present research.

4.1. Lagrangian analysis of particle resuspension

There are particles on the surface, which are detached given the appropriate circumstances. Focused on previously in the section on detachment, the circumstances provide the critical shear velocity on the surface. The flow around the surface determines the value of shear velocity thereon, and the particle is detached from the surface if it rises to a value higher than critical shear velocity. It then moves, either returning to the surface and resettling, or entering the main flow and being removed from the calculation zone. In this method, particles are observed from the source, i.e., the surface, and the computational cost of the procedure is thus significantly lower than when the particle is followed in the entire room space.

4.2. Mesh and number-of-particles independence studies

4.2.1. Mesh independence study

After evaluation of the model, a mesh of appropriate density needs to be chosen to prevent the results from dependence on the one selected for the studied case. In this regard, according to Figure 3, a three-dimensional

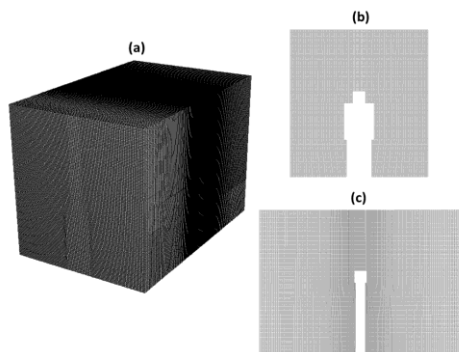


Figure 3. A typical structured grid of the physical model geometry: (a) three-dimensional view, (b) front view, and (c) side view

structured grid of the physical model geometry has been generated in Gambit software. For investigation of the mesh independence of the results, meshes with 590920, 980000, 1892000, and 2860000 cells are examined. Figure 4 shows vertical velocity over the line created on Figure 1 for different numbers of cells. Clearly, no significant changes are observed in the simulation results as the number of cells is increased from 1892000 to 2860000. Therefore, the 1892000-cell mesh is selected for the simulation.

4.2.2. Number-of-particles independence study

The computational cost of Lagrangian analysis is directly proportional to the number of particles used in the analysis. Therefore, it is highly desirable to reduce the number of particles as far as possible to save up run time. However, the number of particles should not be

lower than the minimum number of particles required for accurate results.

Presence of a random number in the DRW algorithm and other models changes PR. After mesh independence is studied, therefore, independence from the number of particles present on the unit of area that are tracked for rising should be studied.

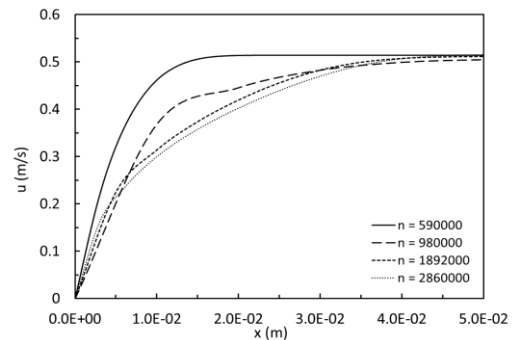


Figure 4. Vertical velocity mesh independence study

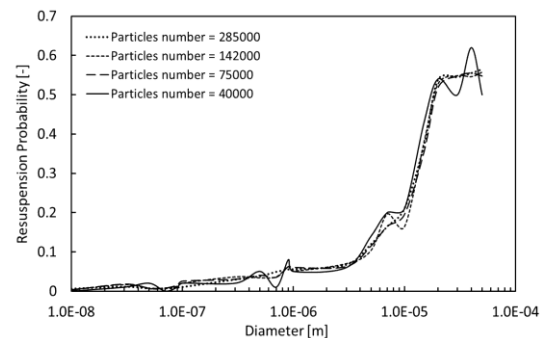


Figure 5. Study of independence from the number of particles for the probability of particle resuspension from the garment

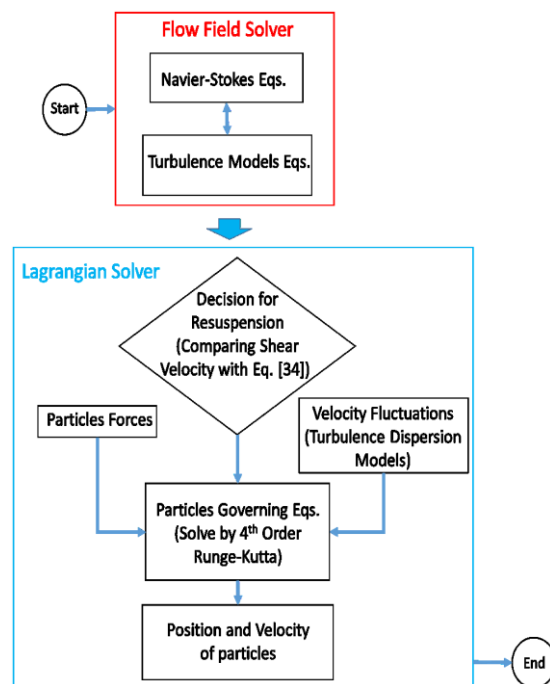
Figure 5 shows independence from the number of released particles for calculation of the probability of particle resuspension from the user's garment in a vertical unidirectional system with an entrance velocity of 0.5 m/s (Langevin model). 142000 is found to be the appropriate number of particles on the garment to be exposed to the incoming flow.

4.3. Boundary conditions

In the fluid phase, the inlet boundary condition of the room is the velocity inlet, where the velocity varies from 0.3 to 0.45 m/s. The outlet boundary condition is the outflow, and no-slip boundary conditions are adopted at the room walls and garment. In the discrete phase, the escape type boundary condition is assumed at the inlet and outlet of the room. The reflect boundary condition is imposed for particles collide with the walls and garment. At the walls, the reflect boundary with a restitution coefficient of 1 is used. As stated before, the resuspension boundary condition is applied through comparing the shear velocity with the value of relation (34). Table 2 lists the boundary conditions used in the present work.

Table 2. Boundary conditions of governing equations

	Room walls	Room inlet	Room outlet	Garment
Fluid phase				
velocity	no slip	velocity inlet	outflow	no slip
pressure	zero gradient	-	atmospheric pressure	zero gradient
Discrete phase				
	reflect	escape	escape	reflect & resuspension

**Figure 6.** Solution algorithm of the governing equations in the present work

4.4. Solution method

In this study, FLUENT software has been utilized to solve the flow field governing equations. A three-dimensional steady-state numerical simulation has been conducted by using the finite volume method. In this method, the SIMPLE algorithm was used for the velocity-pressure coupling. The second-order upwind and the central-difference discretization schemes were applied for convective and diffusive terms, respectively. The convergence criteria for the flow field were controlled by the maximum residual level of $1e-5$ for each governing equation and $1e-3$ for the maximum net mass flow rate between inlet and outlet. In this work, the effect of the particles on the fluid was ignored. Hence, first of all, the governing equations of flow field were solved and the flow information was then used in the Lagrangian solver. In the Lagrangian solver, at first, the amount of all forces applied to the particles were calculated and then the flow velocity fluctuations were modeled with the aid of the

aforementioned turbulence dispersion models. Finally, Lagrangian equations were directly solved by the fourth order Runge-Kutta method and then the position and velocity of the particles in the flow field were calculated. The detail of the solution algorithm is presented in Figure 6.

5. Results

In this section, the validity of the turbulence dispersion models is conducted against the experimental data. Then, the simulation of particle resuspension and the effect of isotropic anisotropy on this phenomenon in the horizontal unidirectional ventilation system are being investigated. In the next step of the simulation, turbulence dispersion in horizontal and vertical unidirectional systems on particle resuspension probability is studied. Finally, turbulence dispersion models' evaluation is performed in terms of the accuracy and computational speed.

5.1. Model validation

Before the analysis is made, it is vital to evaluate the developed code and selected models. For this purpose, experimental data are taken from Tsai [14], focused on particles released from a piece of polyester fabric in an ISO-5 clean room in steady-state conditions and reporting particles of 10 to 0.01 microns. The rectangular piece of fabric with dimensions of 0.147×0.179 meters was placed in a box with a volume of 1400 cm^3 . The unidirectional flow in the container passed from a side wall to another at 0.15 m/s .

In this section, Tsai's [14] experimental research is simulated numerically, and the findings are analyzed. The sources of particles in the clean room include only the piece of fabric and the unidirectional ventilation system. The concentration diagram obtained from the experimental data can thus be compared to the particle resuspension probability diagram. RSM is used to simulate fluid flow turbulence. With particle load (L) on the polyester surface assumed to be as in Equation 38, the concentration in the room is calculated using Equation 37.

$$L = 2.527 \times 10^7 D \quad (38)$$

Figure 7 depicts the numbers of particles with different diameters per unit of volume in the class-100 clean room, on which basis the concentration of particles with diameters below 0.6 microns is nearly zero, followed by a relative maximum. An important finding is that the particle distribution behavior based on particle diameter in clean rooms is a function of particle resuspension probability, an effective factor in particle concentration. Consequently, the resuspension probability parameter is useful in investigation of particle resuspension and concentration in controlled spaces.

It is clear from Figure 7 that the distribution models have an acceptable trend in specification of concentration, and that all the models predict the rise in probability similarly to the concentration diagram generated from experimental results. Due to the micron-sized particles considered in this section, the difference in prediction of resuspension probability by different models is minimal.

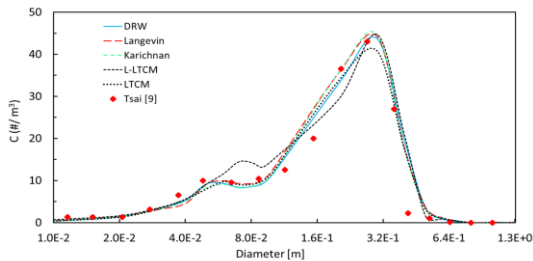


Figure 7. Concentration of particles with different diameters

In terms of computational cost and accuracy, DRW can be considered as an appropriate model for particles in a clean room with diameters in the above range. This diameter range is common for a controlled-space study, but a wider range is considered in this research for investigation of model predictions.

At the moment a particle rises from a horizontal surface, Saffman force is strongly applied to it in the opposite direction of the rise due to velocity gradient close to the surface. Saffman force is directly proportional to d_p^2 . Therefore, the larger the diameter, the greater the force opposing the rise. Simulation shows that flow hydrodynamic forces overcome the particle at 0.6 microns. The trend continues up to the maximum resuspension. The flow force is applied to the particle through the friction force (i.e., drag), and is proportional to d_p^3 . After the peak, the force decreases, and particle resuspension from the surface recedes as a result. As the trend continues, it becomes highly unlikely for particles with large diameters to be resuspended from the surface.

5.2. Particle resuspension in a vertical unidirectional ventilation system

This section explores the predictions of turbulence dispersion models on the probability of particle resuspension from a user’s body in a vertical flow from ceiling to floor. It should be noted that air flow is predicted by the RSM model. Commonly, flow velocity ranges between 0.3 and 0.5 m/s. The air velocity in the clean room is first assumed to be 0.5 m/s, and the effects of velocity, particle density, and isotropic turbulence are then studied.

According to the resuspension probability trend in Figure 8, it is possible to split the diagram to three sections. The dominant forces are drag and gravity in the first section (Section 1), drag and Brownian in the middle section (Section 2), and the Brownian force in

the final section (Section 3). The general trend of prediction suggests that particles with diameters of above 5 microns have a high probability of rising, and ones with diameters of above 20 microns have high chances of being removed from the garment. This trend has also been observed in experimental studies for particle resuspension [14, 16] which is due to the general trend of probability.

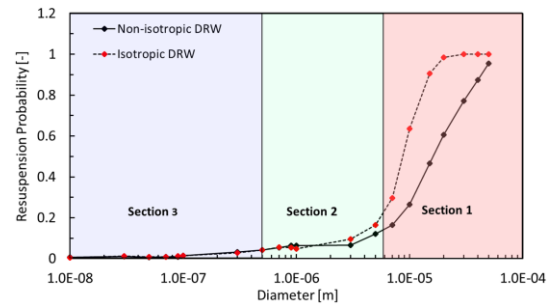


Figure 8. Probability of particle resuspension from the user’s garment in a vertical unidirectional ventilation system at a velocity of 0.5 m/s provided by two DRW models

Figure 8 shows the difference between the effects of isotropic and non-isotropic flow on the particles in the drag force dominance region for particles with perpendicular to the surface are calculated more profoundly, which helps particle rising; for sub-micron particles, however, which are influenced more severely by the Brownian force, the isotropic or non-isotropic nature of the turbulence exhibits little effect. Another reason is that the drag forces, which transfer flow turbulence effects to the particle, are significantly less effective at lower diameters. While the isotropic DRW model predicts this, the isotropic and non-isotropic DRW models provide essentially similar simulations for sub-micron particles. Kraichnan model simulates the fluctuations more acutely against DRW, and more particles in wide diameter ranges are therefore resuspended with higher resuspension probability.

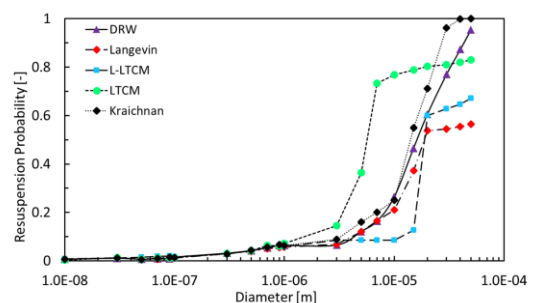


Figure 9. Probability of particle resuspension from the user’s garment in a vertical unidirectional ventilation system at a velocity of 0.5 m/s provided by different dispersion models

As a general rule, self-correlating models such as Langevin, LTCM, and L-LTCM predict similar behavior. According to the correlation coefficients, there are

variations in the simulation of these models, as evident in Figure 9. The vertical unidirectional system simulations demonstrate that the system causes particles with diameters of 5 microns or above to rise, and greatly increases their concentration in the environment. Therefore, garment and underwear designed for rooms with this type of ventilation should generate fewer particles of the above size range.

5.2.1. Effects of velocity on particle resuspension

This section explores the effects of velocity on particle resuspension in a vertical unidirectional ventilation system examined using DRW. The fluid flow around the user is simulated at three different velocities (0.3, 0.4, and 0.5 m/s), and the DRW model is then used.

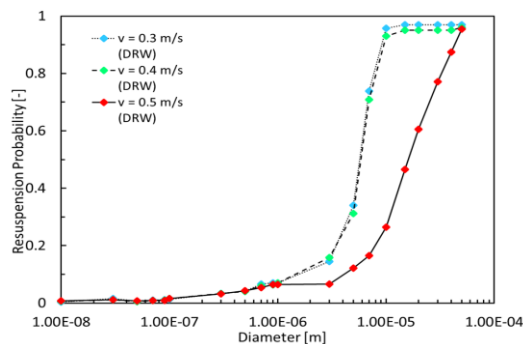


Figure 10. Probability of particle resuspension from the user's garment in a vertical unidirectional ventilation system for different velocities examined with the DRW model

As seen in Figure 10, the probability of resuspension of large particles and their concentration in the clean space increases as unidirectional ventilation velocity decreases. The above decrease exhibits little effect on the probability of resuspension of small particles. Another cause of concern is that particle concentration rises on a broader scale as velocity decreases, which requires preparations. From a physics point of view, the rise results from the lower velocity gradient on the surface and the subsequent decrease in the Saffman force opposing particle rising.

5.2.2. Effects of density on particle resuspension

For examination of the effects of density in particle rising, aluminum oxide particles are simulated, and the results are compared to those concerning silicon dioxide particles.

Possible resuspension probability is shown in Figure 11 for the two materials. Clearly, particle resuspension grows as density increases for diameters of over one micron due to the gravity force, which causes the great increase in resuspension rate for larger diameters by helping the particle to get detached from the surface. On average, a 10% increase is observed in resuspension for a growth only by 80% in density.

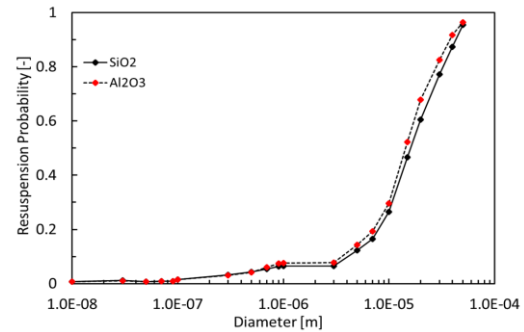


Figure 11. Probability of silicon dioxide and aluminum oxide particle resuspension from the user's garment in a vertical unidirectional ventilation system examined with the DRW model

The results demonstrate how changes in density affect particle resuspension against diameter. For particles with diameters smaller than one micron, there is a small recession in resuspension probability due to the decrease in Brownian distribution, explained by the less energy received by higher-density particles as a result of the fluid molecules.

5.3. Particle resuspension in a horizontal unidirectional ventilation system

This section reviews the predictions made by particle turbulence dispersion models on the probability of particle resuspension from a user's garment under a horizontal flow. The flow surrounding the individual is simulated by the RSM model. Ventilation intake flow velocity is assumed to be 0.25 m/s. The effects of velocity on particle resuspension are examined below.

The particle resuspension procedure in a horizontal ventilation system is similar to that in a vertical system, but eddies take shape around the user in a horizontal system, which makes them more effective on resuspension of smaller particles, so particles of a wider range of sizes enter the system. Moreover, the probability of resuspension and deposition of particle cycles is high in a horizontal ventilation system. On the other hand, a larger particle, with a higher probability of resuspension in a vertical ventilation system, has a lower chance of resuspension in a horizontal one due to the same direction of the flow and the gravitational force.

With the walking individual's leg movements neglected, his presence can be considered similar to that of a moving individual in a clean room, or to flow with different relative velocities in the direction of horizontal ventilation. Therefore, particle resuspension probability is an expression of particle resuspension for a moving individual in such a ventilation system.

Figure 12 depicts the DRW predictions for particles of different diameters resuspended from a user's garment in a horizontal ventilation system with a flow velocity of 0.25 m/s.

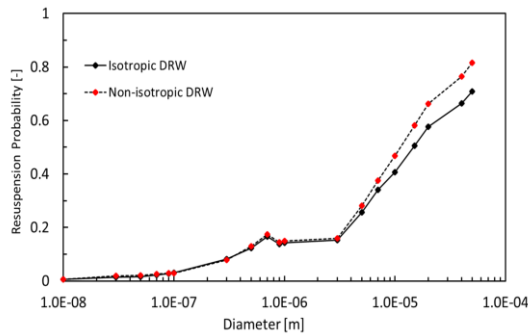


Figure 12. DRW predictions on particle resuspension from the user’s garment in a horizontal ventilation system with a current velocity of 0.25 m/s

The model anticipates a 25% chance of resuspension for particles with diameters of over 5 microns, and 15% for 0.5- to 5-micron particles, while resuspension probability for a similar velocity in a vertical system is predicted to be 97% for particles larger than 5 microns in diameter and below 8% for particles smaller than 5 microns. The isotropic DRW model exhibits similar predictions for particles with diameters smaller than 5 microns, while there is discrepancy and divergence for larger particles, resulting from the more profound effect of Brownian motion and lower influence of turbulence. The results indicate the tendency of the horizontal system to rise more particles with diameters between 0.5 and 5 microns and induct them in a clean room. This is an important range, as filters exhibit the lowest efficiency in removal of particles with diameter sizes lying therein. For example, bacteria, which are detrimental to clean rooms used in medical and pharmaceutical applications, are categorized as such particles.

5.3.1. Effects of velocity on particle resuspension

Figure 13 shows the probability of particle resuspension from a user’s garment at different velocities using the DRW model. Unlike in the vertical system, velocity is directly proportional to particle resuspension probability here. Due to the intensifying effect of the flow on the eddy surrounding the user’s body, more particles are detached from the garment surface to enter the main flow.

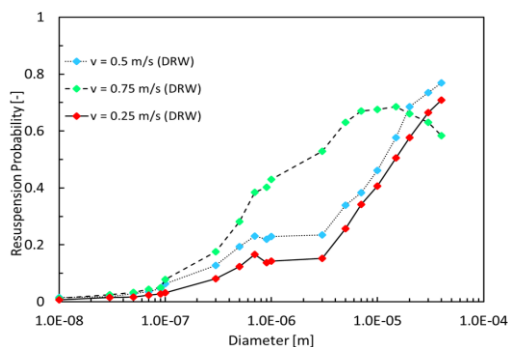


Figure 13. Probability of particle resuspension from the user’s garment for different velocities in a horizontal unidirectional ventilation system examined using the DRW model

Moreover, a horizontal system releases a wide range of particles into the controlled space, while resuspension probability is lower in a horizontal system than in a vertical one.

5.3.2. Models evaluation

According to Table 3, all implemented turbulence dispersion models in the present work were compared through three characteristics, including: 1. simulation accuracy for particles size below 0.6 microns, 2. simulation accuracy for particles size above 0.6 microns, and 3. computational speed. In general, in term of computational accuracy, Langevin and L-LTCM models have the highest and lowest accuracy in resuspension probability prediction, respectively. In term of computational speed, the highest and lowest accuracy respectively belong to DRW and Fourier-Kraichnan models. Finally, it can be claimed that Langevin model has the highest performance compared to other models. Computational speed is very important for simulation in the Lagrangian approach. According to the results, calculation speed of the Langevin model ranks second among the models; but its computational speed is acceptable in comparison with other models. Consequently, Langevin model is recommended as an appropriate turbulence dispersion model to simulate particle motion in controlled spaces.

Table 3. The comparison of the turbulence dispersion models performance implemented in the present study

Characteristic	Models				
	DRW	Fourier-Kraichnan	Langevin	LTCM	L-LTCM
Simulation accuracy for particles size below 0.6 microns	x	✓✓	✓✓✓	✓	xx
Simulation accuracy for particles size above 0.6 microns	✓✓	✓✓	✓✓	✓✓	xx
Computational speed	✓✓✓	xx	✓✓	✓✓	✓

Guide: ✓✓✓ excellent, ✓✓ very good, ✓ good, x weak, xx too weak

6. Conclusion

In this study, particle resuspension probability was introduced for controlled space ventilation systems, and it was then inspected using different particle turbulence dispersion models. Notable results obtained from the present study can be listed as below:

- Increasing flow rate and velocity in a vertical ventilation system decreases particle rising,

while converse behavior is observed in a horizontal system. At the same velocities, a horizontal unidirectional ventilation system resuspends more particles with diameter sizes between 0.1 and 10 microns, which are more difficult to remove from the system using filters.

- Rooms with horizontal ventilation systems require higher standards of user garments for the same cleanliness class.
- Due to the decreasing turbulence effects and increasing Brownian influence (close to the walls), most models offer similar performance for particles of sizes less than one micron.
- The resulting discrepancy between the self-correlating and the Kraichnan and DRW models grows as velocity or diameter size increases.
- The assumption of isotropic turbulence is not appropriate for particles with diameters of over one micron.
- Employment of non-isotropic turbulence models is quite significant in distribution of particles with diameters of 10 microns or above, so such fluid flows should be simulated by non-isotropic turbulence models.
- Langevin model has the highest performance compared to other models in term of computational speed and accuracy.

Nomenclature

a	Contact radius [m]	k_n	Gaussian numbers
A	Garment area [m ²]	l_e	Eddy length scale [m]
A_f	Particle forehead area [m ²]	l_0	Length scale of physical model [m]
C	Concentration [kgm ⁻³]	L	Particle concentration on the surface [#m ⁻²]
C_c	Cunningham slip correction factor [#m ⁻³]	m	Mass [kg]
C_d	Drag force factor	N_d	Number of deposited particles [#]
C_L	Heat driving force velocity [ms ⁻¹]	N_L	Particle number on the surface [#]
d	Diameter [m]	N_R	Number of Resuspended particles [#]
dW	White Noise function	N_0	Initial number of particles [#]
F	Particle induced force [N]	PR	Resuspension Probability
f_{po}	Separation force [N]	R	Resuspension flux [#s ⁻¹ m ⁻²]
g	Gravitational acceleration vector [ms ⁻²]	R_E	Eulerian correlation
G_1, G_2	Gaussian numbers [kgs ⁻¹]	R_L	Lagrangian correlation
J	Wall particle flux [kgs ⁻¹]	Re	Reynolds number
k	Turbulent kinetic energy, Boltzmann constant [m ² s ⁻² , JK ⁻¹]	RR	Resuspension rate [s ⁻¹]
k_B	Boltzmann constant [JK ⁻¹]	s_{nn}	White noise intensity spectrum
K	Yang complex coefficient [Nm ⁻²]	t	Time [s]
Kn	Knudsen number	t_d	Deposition Time [s]
		t_0	Time scale [s]
		t_d^+	Nondimensional time duration
		t^*	Nondimensional time
		t_{cross}	Particle crossing time [s]
		t_{int}	Particle-eddy interaction time [s]
		T	Absolute temperature [K]
		T_r	Resuspension time [s]
		T_i^L	Particle lagrangian integral time scale [s ⁻¹]
		u	X-aligned velocity [ms ⁻¹]
		\vec{u}	Velocity vector [ms ⁻¹]
		\bar{u}	Mean velocity [ms ⁻¹]
		u'	Fluctuations Velocity [ms ⁻¹]
		u^*	Shear velocity [ms ⁻¹]
		u_r	Relative particle-fluid velocity [ms ⁻¹]
		v	Y-aligned velocity [ms ⁻¹]
		V	Room volume [m ³]
		V_d	Deposition velocity [m ³ s ⁻¹]
		V_d^+	Nondimensional deposition velocity
		V_{ter}	Terminal velocity [ms ⁻¹]
		w	Z-aligned velocity [ms ⁻¹]
		W	Nondimensional velocity fluctuation
		W_A	Adhesion thermodynamic work [J]
		\vec{x}	position Vector [m]
		\vec{X}	position [m]
		\vec{X}	Nondimensional position Vector

y_0	Length of injected particle[m]
y_0^+	Nondimensional length of injected particle
β	Mobility coefficient [m^2/s]
Δ_c	Nondimensional roughness
ε	Turbulent Energy Dissipation Rate [m^2s^{-3}]
ζ	Gaussian Random Number
μ	Fluid Dynamic Viscosity [$\text{kgm}^{-1}\text{s}^{-1}$]
ν	Fluid Kinematic Viscosity [m^2s^{-1}]
ξ	Gaussian Random Number
Λ	Eulerian length scale [m]
ρ	Density [kgm^{-3}]
σ	Velocity variance [ms^{-1}]
τ_d	Nondimensional Particle Relaxation Time
τ_e	Lifetime of eddy [s]
τ_r	Particle Relaxation Time [s]
ω	Frequency velocity fluctuations in Fourier [s^{-1}]
b	Buoyancy
br	Brownian
f	Fluid
fr	Drag
g	Gravity
p	Particle
r	Relative
s	Saffman

Acknowledgements

The authors declare that they have no conflict of interest.

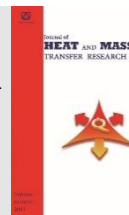
References

- [1] Mouritz, A.P., Gellert, E., Burchill, P. and Challis, K., 2001. Review of advanced composite structures for naval ships and submarines. *Composite structures*, 53(1), pp.21-42.
- [2] Zhang, X., Ahmadi, G., Qian, J., & Ferro, A. 2008. Particle detachment, resuspension and transport due to human walking in indoor environments. *Journal of Adhesion Science and Technology*, 22(5-6), pp.591-621.
- [3] Tian, L., & Ahmadi, G. 2007. Particle deposition in turbulent duct flows—comparisons of different model predictions. *Journal of Aerosol Science*, 38(4), pp.377-397.
- [4] Gao, N., Niu, J., He, Q., Zhu, T., & Wu, J. 2012. Using RANS turbulence models and Lagrangian approach to predict particle deposition in turbulent channel flows. *Building and Environment*, 48, pp.206-214.
- [5] Mito, Y., & Hanratty, T. J. 2002. Use of a modified Langevin equation to describe turbulent dispersion of fluid particles in a channel flow. *Flow, turbulence and combustion*, 68(1), pp.1-26.
- [6] Kang, Y., Wang, Y., & Zhong, K. 2011. Effects of supply air temperature and inlet location on particle dispersion in displacement ventilation rooms. *Particuology*, 9(6), pp.619-625.
- [7] Kubota, Y., Hall, J. W., & Higuchi, H. 2009. An experimental investigation of the flowfield and dust resuspension due to idealized human walking. *Journal of fluids engineering*, 131(8).
- [8] Khalifa, H. E., & Elhadidi, B. 2007. Particle levitation due to a uniformly descending flat object. *Aerosol science and technology*, 41(1), pp.33-42.
- [9] Zheng, S., Du, W., Zhao, L., & Zhang, J. 2018. Simulation of Particle Resuspension Caused by Footsteps. *Environmental Processes*, 5(4), pp.919-930.
- [10] Boulbair, A., Benabed, A., Janssens, B., Limam, K., & Bosschaerts, W. 2022. Numerical study of the human walking-induced fine particles resuspension. *Building and Environment*, 216, p.109050.
- [11] Sun, Z., Zheng, S., Fu, Y., & Chai, M. 2022. Characteristics of indoor human-induced particle resuspension under different ventilation conditions. *Indoor and Built Environment*, p.1420326X221084032.
- [12] Sajadi, B., Saidi, M. H., Ahmadi, G., Kenney, S. M., & Taylor, J. 2013. On the induced airflow and particle resuspension due to a falling disk. *Particulate Science and Technology*, 31(2), pp.190-198.
- [13] Qian, J., Peccia, J., & Ferro, A. R. 2014. Walking-induced particle resuspension in indoor environments. *Atmospheric Environment*, 89, pp.464-481.
- [14] Tsai, C. S. J. 2015. Contamination and release of nanomaterials associated with the use of personal protective clothing. *Annals of Occupational Hygiene*, 59(4), pp.491-503.
- [15] Aracena, K. D. L. Á. V., Uñac, R. O., Ippolito, I., & Vidales, A. M. 2020. Movement initiation of millimeter particles on a rotating rough surface: The role of adhesion. *Particuology*, 53, pp.92-99.
- [16] Benabed, A., Boulbair, A., & Limam, K. 2020. Experimental study of the human walking-induced fine and ultrafine particle resuspension in a test chamber. *Building and Environment*, 171, p.106655.
- [17] Habchi, C., Ghali, K., & Ghaddar, N. 2016. Coupling CFD and analytical modeling for investigation of monolayer particle resuspension by transient flows. *Building and Environment*, 105, pp.1-12.
- [18] Kazzaz, M., Habchi, C., Ghali, K., Ghaddar, N., Alotaibi, S., & Chakroun, W. 2017. Micro-particle indoor resuspension under periodic airflows: a numerical-analytical study and experimentations. *Building and Environment*, 123, pp.299-314.
- [19] Al Assaad, D., Yang, S., & Licina, D. 2021. Particle release and transport from human skin and clothing: A CFD modeling methodology. *Indoor air*, 31(5), pp.1377-1390.
- [20] Ren, J., Tang, M., & Novoselac, A. 2022. Experimental study to quantify airborne particle

- deposition onto and resuspension from clothing using a fluorescent-tracking method. *Building and environment*, 209, p.108580.
- [21] Whyte, W. 2010. *Cleanroom technology: fundamentals of design, testing and operation*. John Wiley & Sons.
- [22] Zhang, Z., & Chen, Q. 2007. Comparison of the Eulerian and Lagrangian methods for predicting particle transport in enclosed spaces. *Atmospheric environment*, 41(25), pp.5236-5248.
- [23] Pourfarzaneh, A., Jafarian, A., & Kharinezhad Arani, H. 2019. Numerical study of particulate turbulent flow to investigate recovery period in cleanrooms. *Scientia Iranica*, 26(1), pp.331-345.
- [24] Khajenoori, M., & Haghighi Asl, A. 2018. Two-dimensional Simulation of Mass Transfer and Nano-Particle Deposition of Cigarette Smoke in a Human Airway. *Journal of Heat and Mass Transfer Research*, 5(1), pp.79-85.
- [25] Ounis, H., Ahmadi, G., & McLaughlin, J. B. 1991. Dispersion and deposition of Brownian particles from point sources in a simulated turbulent channel flow. *Journal of Colloid and Interface Science*, 147(1), pp.233-250.
- [26] Kao, H. M., Chang, T. J., Hsieh, Y. F., Wang, C. H., & Hsieh, C. I. 2009. Comparison of airflow and particulate matter transport in multi-room buildings for different natural ventilation patterns. *Energy and Buildings*, 41(9), pp.966-974.
- [27] Mahdavianesh, M., Noghrehabadi, A. R., Behbahaninejad, M., Ahmadi, G., & Dehghanian, M. 2013. Lagrangian particle tracking: model development. *Life Science Journal*, 10(8s), pp.34-41.
- [28] Vahedi, S. M., Parvaz, F., Rafee, R., & Khandan Bakavoli, M. 2018. Computational fluid dynamics simulation of the flow patterns and performance of conventional and dual-cone gas-particle cyclones. *Journal of Heat and Mass Transfer Research*, 5(1), pp.27-38.
- [29] Zhang, P., Roberts, R. M., & Bénard, A. 2012. Computational guidelines and an empirical model for particle deposition in curved pipes using an Eulerian-Lagrangian approach. *Journal of Aerosol Science*, 53, pp.1-20.
- [30] Kraichnan, R. H. 1970. Diffusion by a random velocity field. *The physics of fluids*, 13(1), pp.22-31.
- [31] Sajjadi, H., Salmanzadeh, M., Ahmadi, G., & Jafari, S. 2016. Simulations of indoor airflow and particle dispersion and deposition by the lattice Boltzmann method using LES and RANS approaches. *Building and Environment*, 102, pp.1-12.
- [32] Berlemont, A., Desjonqueres, P., & Gouesbet, G. 1990. Particle Lagrangian simulation in turbulent flows. *International Journal of Multiphase Flow*, 16(1), pp.19-34.
- [33] Zhang, X., Ahmadi, G., Qian, J., & Ferro, A. 2008. Particle detachment, resuspension and transport due to human walking in indoor environments. *Journal of Adhesion Science and Technology*, 22(5-6), pp.591-621.
- [34] Pozorski, J., & Minier, J. P. 1998. On the Lagrangian turbulent dispersion models based on the Langevin equation. *International Journal of Multiphase Flow*, 24(6), pp.913-945.
- [35] Johnson, K. L., Kendall, K., & Roberts, A. 1971. Surface energy and the contact of elastic solids. *Proceedings of the royal society of London. A. mathematical and physical sciences*, 324(1558), pp.301-313.
- [36] Soltani, M., & Ahmadi, G. 1994. On particle adhesion and removal mechanisms in turbulent flows. *Journal of Adhesion Science and Technology*, 8(7), pp.763-785.
- [37] Qian, J. 2007. Particle resuspension via human activity. Ph. D. Thesis.



Semnan University



Effects of Radiation Absorption, Soret and Dufour on Unsteady MHD Mixed Convective Flow past a Vertical Permeable Plate with Slip Condition and Viscous Dissipation

Temjennaro Jamir* , Hemanta Konwar

Kohima Science College, Jotsoma, Nagaland 797002, India.

PAPER INFO

Paper history:

Received: 2022-10-18

Revised: 2023-01-28

Accepted: 2023-02-03

Keywords:

Radiation absorption;
Porous medium;
Slip flow;
Soret;
Dufour;
Viscous Dissipation.

ABSTRACT

Objective: The objective of current study is to discuss the effects of the Soret and Dufour with radiation absorption, applied heat source and viscous dissipation on an unsteady MHD mixed convective flow with velocity slip condition across a semi-infinite vertical permeable plate in porous medium. **Method:** A similarity transformation is used to turn the governing partial differential equations with proper boundary conditions into coupled, non-linear ordinary differential equations with variable coefficients. The inbuilt MATLAB solver bvp4c is used to generate numerical solutions. **Findings:** The effects on momentum, thermal and solutal boundary layers for various parametric values are graphically depicted. Skin friction, Nusselt number and Sherwood number are all tabulated and discussed in detail. An improvement in radiation absorption corresponds to enhancement of the heat transfer rate up to 59% while leading to a decline in mass transfer rate around 20%. The momentum, thermal and solutal boundary layers are all found to be boosted when the Soret effect is higher. For higher estimation of slip effect, the skin friction is found to decay around 23%. Also, as more time goes by the thermal and concentration boundary layers are enhanced. **Novelty:** Results obtained in this studied has also been compared and verified with available scientific literature and is found to be in good agreement, which establishes assurance in the numerical results reported in the study.

DOI: [10.22075/jhmt.2023.28693.1399](https://doi.org/10.22075/jhmt.2023.28693.1399)

© 2022 Published by Semnan University Press. All rights reserved.

1. Introduction

Navier explored a boundary condition of fluid slip at a solid surface such that the solid surface velocity is proportional to the shear stress at the surface in the history of fluid flow via channels, that is $u = h \partial u / \partial y$, where the slip coefficient is h and the velocity along the x -axis is u [1]. The flow regime is known as the slip flow regime, and the significance of its consequences in applications such as micro channel and mechanical device lubrication, where a little layer of lubricant is applied to the surfaces to prevent them from rubbing against one another, or when the surfaces are coated with a particular type of coating to lessen friction. Furthermore, in polymer melts, which frequently display tiny wall slip, make the insufficiency of the no-slip criterion abundantly clear. The synchronisation of

the velocities and stresses is one of the boundary requirements that must be met at the contact between a porous material and fluid layer.

Beavers and Joseph [2] analysed fluid flow at the boundary between a porous medium and fluid layer in an experimental research and established a slip boundary conditions at the porous interface.

Pal and Talukdar [3] also contributed a numerical analysis on the influence of ohmic heating and magnetic field for a mixed convective fluid flow problem taking into consideration the boundary slip effect. A numerical study of the velocity and thermal wall slip on MHD boundary layer viscous flow over a non-linearly-stretching sheet was also considered by Ramya et al. [4].

*Corresponding Author: Temjennaro Jamir
Email: temjennaro@kscj.ac.in

Numerous research has also focused on issues with heat and mass transfer in radiative convective flow. Because of its far-reaching contributions in the realm of engineering, such as its use in MHD bearings and MHD pumps. Surface heat transfer is significantly impacted by thermal radiation. Researchers' attention has recently been drawn to thermal radiation as a mode of energy transfer, and the necessity of including radiative transfer in these processes has been highlighted by recent developments in hypersonic flights, power plants for interplanetary flight, missile re-entry rocket combustion chambers, and gas cooled nuclear reactors. The radiative influence on heat transmission in a vertical porous material was investigated by Raptis [5], Hossain and Takhar [6], Manjula and Muthucumaraswamy [7]. Numerous studies on the effect of radiation on fluid flow have been conducted over the years. Because of very significant contributions to humanity, such as nuclear power plants, studies on the effect of radiation absorption have recently become a trend. Ibrahim et al. [8] conducted one of the early studies on radiation absorption on MHD mixed convective flow for a semi-infinite vertical plate. Sreedevi et al. [9] studied this effect of radiation absorption in the present of hall current for a stretching sheet. We also find the work by Aly et al. [10] who accounted unsteady convective flow with radiation effect for a vertical plate embedded in porous medium, Matta et al. [11] who stressed on the unsteady MHD flow with chemical and radiation effects for a porous plate, also fluid flow past a stretching sheet with heat source and temperature dependent fluid properties was analysed by Hemanta [12]. Khan et al. [13] considered the entropy analysis for hydromagnetic radiative flow of ternary nanofluid by an exponentially stretching surface subject to entropy generation. Some recent studies based on radiative effects are also shown in Refs. [14-18].

The rate of heat generation in the boundary influences the rate of thermal distribution in flow. This is evident in a variety of manufacturing applications, including fire modelling, the fabrication of electronic chips, etc. Surface temperature and flow velocity both affect how heatwaves spread. As a result, when thermal radiation occurs, a significant difference in temperature is present somewhere in the system.

Because of this, heat generation and absorption for many systems are not constant and rely on the environment and temperature of the system. As found in studies conducted by Nemati et al. [19] who accounted periodic magnetic field effect with heat generation/absorption for a Non-Newtonian fluid, Elsayed et al. [20] presents the effects of heat generation absorption on boundary layer flow of Nano fluid for a stretching cylinder, Khan et al. [21] who examined the variable heat source for unsteady stagnation-point flow of magnetized Oldroyd-B fluid.

The impact of ohmic heating for a double diffusive Nano fluid flow for stretching cylinder is considered in the study conducted by Yasir et al. [22]. Also as found in the investigation conducted by Sheikholeslami [23] for thermal solar system, the thermal performance was found to be incremented upon elevating heat absorption.

With the increasing need for advancement, betterment and efficient technology there arises a need for advancement in research approaches and hence making every small progress an important contribution to research and advancement. Due to the temperature and mass differences in a medium there arises a mass and heat flux which are also known as the Soret and Dufour effect respectively, which are important mechanism in the transport phenomenon; it has it varied applications in vapour deposition process for optical fibre fabrication, in fluid flow fractionation, it is used to separate distinct polymers. Okuyade et al. [24] examined the effects of Soret and Dufour for an unsteady convective flow with constant suction. The Dufour effect on unsteady MHD flow past a vertical plate embedded in porous medium with ramped temperature is addressed by Sarma and Ahmed [25]. The Soret effect for a steady MHD fluid flow through a vertical porous plate with aligned magnetic field was presented by Mopuri et al. [26]. We also find in the study of Sowmiya and Kumar [27] who considered the Dufour effect for MHD mixed convective flow with bouyancy effect. Some relevant advancements about Soret and Dufour effects are also highlighted in Refs. [28-32].

The literature review cited above confirms that no attempt has been made to consider the impact of Soret and Dufour under the influence of radiation of absorption, heat source, viscous dissipation, chemical and thermal radiation, with the velocity slip condition for a semi-infinite vertical permeable plate under the presence of pressure gradient. Few researchers even worked on unsteady flow problem with slip effect. Here our main objective is to scrutinize the combined effect of radiation absorption, Soret and Dufour effects with slip parameter for unsteady fluid flow. A comparison has been made with the work presented by Pal and Talukdar [3] and thus the results found in this study are thus verified accordingly. For the purpose of graphical and tabular data, the MATLAB's built-in solver bvp4c technique will be implemented. We prioritise the following research questions in relation to the flow problem under consideration.

What impact does the radiation absorption parameter have on the thermal and solutal boundary layers, fluid momentum, for mixed convective unsteady MHD heat-absorbing fluid flow?

When slip flow is taken into account in the mixed convective flow system for the vertical permeable plate

in presence of MHD and radiation absorption, how are the skin friction, heat, and mass transfer rates are affected?

What changes in the flow field do the Soret and Dufour effects have on the velocity, heat, and mass transfer?

What effects does the time parameter have on the fluid flow over a vertical permeable plate with MHD and slip flow in terms of velocity, heat transfer, and mass transfer?

2. Mathematical Formulation

We address the unsteady two-dimensional mixed convective flow of an incompressible, viscous, electrically conducting, and heat-absorbing fluid through a semi-infinite vertical permeable plate submerged in a uniform porous medium with a slip boundary condition at the interface of the porous and fluid layers.

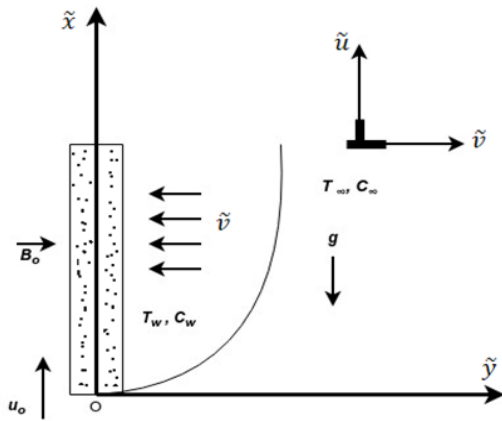


Figure 1. Geometry of the problem

In the presence of radiation and concentration buoyancy effects in the direction of the \tilde{y} -axis, a uniform transverse magnetic field of magnitude B_0 is applied. The induced magnetic field and the Hall Effect are thought to be insignificant due to the relatively low transversely applied magnetic field and magnetic Reynolds number. It is presumptively assumed that no voltage is applied, which denotes that there is no electric field. All physical variables are independent of \tilde{x} since the motion is two-dimensional and the length of the plate is sufficient. The temperature and concentration on the wall are kept constant at T_w and C_w , respectively, which are greater than T_∞ and C_∞ of the ambient fluid. Additionally, it is assumed that the diffusing species and the fluid undergo a homogenous first-order chemical reaction with rate constant $\tilde{K}r$.

The governing equations that describe the physical conditions under these hypotheses, in addition to Boussinesq's approximation, are characterized in

vector form as: (Ramya et al. [4], Kebede et al. [18], Sarma and Ahmed [25]).

Conservation of Mass

$$\nabla \cdot \mathbf{V} = 0 \tag{1}$$

Conservation of Momentum

$$\rho \left[\frac{\partial \mathbf{V}}{\partial \tilde{t}} + (\mathbf{V} \cdot \nabla) \mathbf{V} \right] = -\nabla P + \mathbf{J} \times \mathbf{B} + \rho g + \mu \nabla^2 \mathbf{V} - \frac{\mu}{\tilde{K}} \mathbf{V} \tag{2}$$

Conservation of Energy

$$\rho c_p \left[\frac{\partial \tilde{T}}{\partial \tilde{t}} + (\mathbf{V} \cdot \nabla) \tilde{T} \right] = k \nabla^2 \tilde{T} - \nabla \tilde{q}_r - Q_0 (\tilde{T} - T_\infty) + \mu (\nabla \mathbf{V} \cdot \nabla \mathbf{V}) + Q_1 (\tilde{C} - C_\infty) + \frac{\rho D_m K_T}{c_s} \nabla^2 \tilde{C} \tag{3}$$

Conservation of Species

$$\frac{\partial \tilde{C}}{\partial \tilde{t}} + (\mathbf{V} \cdot \nabla) \tilde{C} = D_m \nabla^2 \tilde{C} + \frac{D_m K_T}{T_m} \nabla^2 \tilde{T} - \tilde{K}r (\tilde{C} - C_\infty) \tag{4}$$

We now make the standard boundary-layer approximation, based on a scale analysis, and write the governing equations (Pal and Talukdar [3], Ibrahim et al. [8])

$$\frac{\partial \tilde{v}}{\partial \tilde{y}} = 0 \tag{5}$$

$$\frac{\partial \tilde{u}}{\partial \tilde{t}} + \tilde{v} \frac{\partial \tilde{u}}{\partial \tilde{y}} = -\frac{1}{\rho} \frac{\partial P}{\partial \tilde{x}} + \nu \frac{\partial^2 \tilde{u}}{\partial \tilde{y}^2} + g (\beta_T (\tilde{T} - T_\infty) + \beta_C (\tilde{C} - C_\infty)) - \left(\frac{\sigma B_0^2}{\rho} + \frac{\nu}{\tilde{K}} \right) \tilde{u} \tag{6}$$

$$\frac{\partial \tilde{T}}{\partial \tilde{t}} + \tilde{v} \frac{\partial \tilde{T}}{\partial \tilde{y}} = \alpha \frac{\partial^2 \tilde{T}}{\partial \tilde{y}^2} - \frac{1}{\rho c_p} \frac{\partial \tilde{q}_r}{\partial \tilde{y}} - \frac{Q_0}{\rho c_p} (\tilde{T} - T_\infty) + \frac{\mu}{\rho c_p} \left(\frac{\partial \tilde{u}}{\partial \tilde{y}} \right)^2 + \frac{Q_1}{\rho c_p} (\tilde{C} - C_\infty) + \frac{D_m K_T}{c_s c_p} \frac{\partial^2 \tilde{C}}{\partial \tilde{y}^2} \tag{7}$$

$$\frac{\partial \tilde{C}}{\partial \tilde{t}} + \tilde{v} \frac{\partial \tilde{C}}{\partial \tilde{y}} = D_m \frac{\partial^2 \tilde{C}}{\partial \tilde{y}^2} + \frac{D_m K_T}{T_m} \frac{\partial^2 \tilde{T}}{\partial \tilde{y}^2} - \tilde{K}r (\tilde{C} - C_\infty) \tag{8}$$

The radiative heat flux \tilde{q}_r can be represented as follows using the Roseland approximation (Raptis [5]):

$$\frac{\partial \tilde{q}_r}{\partial \tilde{y}} = -4a^* \sigma^* (T_\infty^4 - \tilde{T}^4) \tag{9}$$

It is considered that the temperature variation within the flow is thought to be minimal enough that \tilde{T}^4 can be linearized by using the Taylor's series to expand around T_∞ and disregarding terms of higher order. Hence

$$\tilde{T}^4 \cong 4T_\infty^3 \tilde{T} - 3T_\infty^4 \tag{10}$$

The appropriate boundary conditions for the said fluid problem are: (Pal and Talukdar [3])

$$\tilde{u} = \tilde{h} \frac{\partial \tilde{u}}{\partial \tilde{y}}, \quad \tilde{T} = T_w + \varepsilon(T_w - T_\infty)e^{\tilde{\omega}\tilde{t}}, \tag{11}$$

$$\tilde{C} = C_w + \varepsilon(C_w - C_\infty)e^{\tilde{\omega}\tilde{t}} \quad \text{at } \tilde{y} = 0$$

$$\tilde{u} \rightarrow \tilde{u}_\infty = u_0(1 + \varepsilon e^{\tilde{\omega}\tilde{t}}), \quad \tilde{T} \rightarrow T_\infty, \tag{12}$$

$$\tilde{C} \rightarrow C_\infty, \quad \text{as } \tilde{y} \rightarrow \infty$$

Suction velocity is either a time-dependent function or a constant, as shown by Eq. (5).

$$\tilde{v} = -v_0(1 + \varepsilon A e^{\tilde{\omega}\tilde{t}}) \tag{13}$$

Here, suction towards the plate is shown by the negative sign. Outside the boundary layer (Kim [33]) Eq. (6) gives:

$$-\frac{1}{\rho} \frac{dP}{d\tilde{x}} = \frac{d\tilde{u}_\infty}{d\tilde{t}} + \frac{\sigma B_0^2}{\rho} \tilde{u}_\infty + \frac{\vartheta}{\tilde{K}} \tilde{u}_\infty \tag{14}$$

The governing equations and their accompanying boundary conditions must now be converted. The following non-dimensional quantities are displayed in a dimensionless manner.

$$u = \frac{\tilde{u}}{u_0}, u_\infty = \frac{\tilde{u}_\infty}{u_0}, \eta = \frac{v_0}{\vartheta} \tilde{y}, t = \frac{v_0^2}{\vartheta} \tilde{t}, \omega = \frac{\vartheta}{v_0^2} \tilde{\omega}, \tag{15}$$

$$h = \frac{v_0}{\vartheta} \tilde{h}, \quad T = \frac{\tilde{T} - T_\infty}{T_w - T_\infty}, \quad C = \frac{\tilde{C} - C_\infty}{C_w - C_\infty}$$

Eq. (6) to Eq. (8) can be converted to the dimensionless version using the above dimensionless variables:

$$\frac{\partial u}{\partial t} - (1 + \varepsilon A e^{\omega t}) \frac{\partial u}{\partial \eta} = \frac{du_\infty}{dt} + \frac{\partial^2 u}{\partial \eta^2} \tag{16}$$

$$+ GrT + GmC + \left(M + \frac{1}{K}\right)(u_\infty - u)$$

$$\frac{\partial T}{\partial t} - (1 + \varepsilon A e^{\omega t}) \frac{\partial T}{\partial \eta} = \frac{1}{Pr} \frac{\partial^2 T}{\partial \eta^2} - (Rd + Q)T \tag{17}$$

$$+ Ec \left(\frac{\partial u}{\partial \eta}\right)^2 + RC + Du \frac{\partial^2 C}{\partial \eta^2}$$

$$\frac{\partial C}{\partial t} - (1 + \varepsilon A e^{\omega t}) \frac{\partial C}{\partial \eta} = \frac{1}{Sc} \frac{\partial^2 C}{\partial \eta^2} + Sr \frac{\partial^2 T}{\partial \eta^2} - KrC \tag{18}$$

The boundary conditions update as:

$$u = h \frac{\partial u}{\partial \eta}, T = 1 + \varepsilon e^{\omega t}, C = 1 + \varepsilon e^{\omega t} \text{ at } \eta = 0 \tag{19}$$

$$u \rightarrow u_\infty = 1 + \varepsilon e^{\omega t}, T \rightarrow 0, C \rightarrow 0, \text{ as } \eta \rightarrow \infty \tag{20}$$

3. Method of Solution

It is impossible to solve the partial differential Eq. (16) -Eq. (18) with boundary conditions Eq. (19) and Eq. (20) in closed form. It may, however, be solved if these equations are reduced to a set of dimensionless ordinary differential equations by modelling the u (velocity), T (temperature), and C (concentration) as:

$$u(\eta, t) = f_0(\eta) + \varepsilon e^{\omega t} f_1(\eta) + O(\varepsilon^2) \tag{21}$$

$$T(\eta, t) = T_0(\eta) + \varepsilon e^{\omega t} T_1(\eta) + O(\varepsilon^2) \tag{22}$$

$$C(\eta, t) = C_0(\eta) + \varepsilon e^{\omega t} C_1(\eta) + O(\varepsilon^2) \tag{23}$$

Substitute Eq. (21) - Eq. (23) into Eq. (16) -Eq. (20), equalize the harmonic and non-harmonic components, considering only the first order terms $O(\varepsilon)$ and simplifying to yield the following sets of equations for f_0, T_0, C_0 and f_1, T_1, C_1 .

$$f_0'' + f_0' - \left(M + \frac{1}{K}\right)f_0 = -\left(GrT_0 + GmC_0 + M + \frac{1}{K}\right) \tag{24}$$

$$f_1'' + f_1' - \left(M + \frac{1}{K} + \omega\right)f_1 = -\left(GrT_1 + GmC_1 + M + \frac{1}{K} + \omega + Af_0'\right) \tag{25}$$

$$T_0'' + PrT_0' - Pr(Rd + Q)T_0 = -Pr(RC_0 + DuC_0'' + Ec f_0'^2) \tag{26}$$

$$T_1'' + PrT_1' - Pr(Rd + Q + \omega)T_1 = -Pr(RC_1 + DuC_1'' + AT_0' + 2Ec f_0' f_1') \tag{27}$$

$$C_0'' + ScC_0' - ScKrC_0 = -ScSrT_0'' \tag{28}$$

$$C_1'' + ScC_1' - Sc(Kr + \omega)C_1 = -Sc(AC_0' + SrT_1'') \tag{29}$$

Here the prime represents regular differentiation with respect to η .

The associated boundary conditions are:

$$f_0 = hf_0', \quad f_1 = hf_1', \quad T_0 = 1, \quad T_1 = 1, \tag{30}$$

$$C_0 = 1, \quad C_1 = 1 \quad \text{at } \eta = 0$$

$$f_0 = 1, \quad f_1 = 1, \quad T_0 \rightarrow 0, \quad T_1 \rightarrow 0, \tag{31}$$

$$C_0 \rightarrow 0, \quad C_1 \rightarrow 0 \quad \text{as } \eta \rightarrow \infty$$

Now using `bvp4c`, a built-in solver in MATLAB(Shampine et al.[34]) the highly coupled non-

linear ordinary differential Eq. (24) – Eq. (29) along with the boundary condition Eq. (30) and Eq. (31) are solved by setting:

$$\begin{aligned}
 f_0 &= y_1, & f'_0 &= y_2, & f_1 &= y_3, & f'_1 &= y_4, \\
 T_0 &= y_5, & T'_0 &= y_6, & T_1 &= y_7, & T'_1 &= y_8, \\
 C_0 &= y_9, & C'_0 &= y_{10}, & C_1 &= y_{11}, & C'_1 &= y_{12}
 \end{aligned}
 \tag{32}$$

By using the equation Eq. (32) into Eq. (24) to Eq. (29) the following system of first order ordinary differential equations, Eq. (33) –Eq. (38) may be derived, along with boundary conditions equations Eq. (39) and Eq. (40):

$$\begin{aligned}
 y_2' &= \left(M + \frac{1}{K}\right)y_1 - y_2 \\
 &\quad - \left(Gry_5 + Gmy_9 + M + \frac{1}{K}\right)
 \end{aligned}
 \tag{33}$$

$$\begin{aligned}
 y_4' &= \left(M + \frac{1}{K} + \omega\right)y_3 - y_4 \\
 &\quad - \left(Gry_7 + Gmy_{11} + M + \frac{1}{K} + \omega + Ay_2\right)
 \end{aligned}
 \tag{34}$$

$$\begin{aligned}
 y_6' &= \frac{Pr}{1 - PrDuScSr} \\
 &\quad \times \{(Rd + Q)y_5 - y_6 - Ry_9 - Ecy_2^2 \\
 &\quad - ScDu(Kry_9 - y_{10})\}
 \end{aligned}
 \tag{35}$$

$$\begin{aligned}
 y_8' &= \frac{Pr}{1 - PrDuScSr} \\
 &\quad \times [(Rd + Q + \omega)y_7 - y_8 - Ry_{11} - Ay_6 \\
 &\quad - 2Ecy_2y_4 \\
 &\quad - ScDu\{(Kr + \omega)y_{11} - y_{12} \\
 &\quad - Ay_{10}\}]
 \end{aligned}
 \tag{36}$$

$$\begin{aligned}
 y_{10}' &= Sc \left[Kry_9 - y_{10} \right. \\
 &\quad - Sr \left[\frac{Pr}{1 - PrDuScSr} \{(Rd \right. \\
 &\quad + Q)y_5 - y_6 - Ry_9 - Ecy_2^2 \\
 &\quad \left. - ScDu(Kry_9 - y_{10})\} \right]
 \end{aligned}
 \tag{37}$$

$$\begin{aligned}
 y_{12}' &= Sc \left[(Kr + \omega)y_{11} - y_{12} - Ay_{10} \right. \\
 &\quad - Sr \left[\frac{Pr}{1 - PrDuScSr} \{(Rd + Q \right. \\
 &\quad + \omega)y_7 - y_8 - Ry_{11} - Ay_6 \\
 &\quad - 2Ecy_2y_4 \\
 &\quad - ScDu\{(Kr + \omega)y_{11} - y_{12} \\
 &\quad \left. \left. - Ay_{10}\}\} \right] \right]
 \end{aligned}
 \tag{38}$$

Boundary Conditions:

$$\begin{aligned}
 y_1 &= hy_2, & y_3 &= hy_4, & y_5 &= 1, \\
 y_7 &= 1, & y_9 &= 1, & y_{11} &= 1 \quad \text{at } \eta = 0
 \end{aligned}
 \tag{39}$$

$$\begin{aligned}
 y_1 &= 1, & y_3 &= 1, & y_5 &\rightarrow 0, \\
 y_7 &\rightarrow 0, & y_9 &\rightarrow 0, & y_{11} &\rightarrow 0 \quad \text{as } \eta \rightarrow \infty
 \end{aligned}
 \tag{40}$$

The most essential measures for the current condition are the skin-friction coefficient C_f , Nusselt number Nu and Sherwood number Sh . (Pal and Talukdar [3])

$$C_f = \frac{\mu \left(\frac{\partial \tilde{u}}{\partial \tilde{y}}\right)_{\tilde{y}=0}}{\rho u_0^2} = \left(\frac{\partial u}{\partial \eta}\right)_{\eta=0} = f_0'(0) + \varepsilon e^{\omega t} f_1'(0)
 \tag{41}$$

$$\begin{aligned}
 Nu &= \frac{\vartheta \left(\frac{\partial \tilde{T}}{\partial \tilde{y}}\right)_{\tilde{y}=0}}{v_0(T_w - T_\infty)} = \left(\frac{\partial T}{\partial \eta}\right)_{\eta=0} \\
 &= T_0'(0) + \varepsilon e^{\omega t} T_1'(0)
 \end{aligned}
 \tag{42}$$

$$\begin{aligned}
 Sh &= \frac{\vartheta \left(\frac{\partial \tilde{C}}{\partial \tilde{y}}\right)_{\tilde{y}=0}}{v_0(C_w - C_\infty)} = \left(\frac{\partial C}{\partial \eta}\right)_{\eta=0} \\
 &= C_0'(0) + \varepsilon e^{\omega t} C_1'(0)
 \end{aligned}
 \tag{43}$$

4. Results and Discussion

We plot velocity, temperature, and concentration profiles to determine the physical significance of the problem and display the tabular statistics for C_f, Nu, Sh for distinct values of parameters involved. For the sake of this study, we will use the following default values for computation:

$$\begin{aligned}
 Gr &= 4; & Gm &= 2; & M &= 2; & K &= 5; & Pr &= 0.71; \\
 Du &= 0.6; & Sc &= 0.6; & Rd &= 2; & Q &= 1; & R &= 2; \\
 Ec &= 0.01; & Sr &= 1; & Kr &= 1; & A &= 0.5; & \omega &= 1; \\
 h &= 0.2; & t &= 1; & \varepsilon &= 0.01;
 \end{aligned}$$

The present calculated numerical values for the skin-friction coefficient, Nusselt number, and Sherwood number that are shown in Table 1, Table 2 and Table 3 and are in excellent agreement with the computed results of Pal and Talukdar [3] which validates the results and data discussed below.

Figure 2-3 depict the actions of magnetic parameter M and permeability parameter K on velocity within the boundary layer. Because of the Lorentz force that acts as the resistive force due to magnetic field reduces the thickness of the momentum boundary layer. We find that upon incrementing K , the resistive force of the porous medium decreases that aids the fluid to move faster hence incrementing fluid velocity. The result is applicable in reservoir engineering for enhanced oil recovery. Table 4 shows a decay about 8% in C_f inside $2 \leq M \leq 4$, whereas C_f undergoes a growth upto 0.4% within the range $5 \leq K \leq 7$.

Figures 4-5 show the impact of Prandtl number Pr taken as 0.71 (air), 1.00 (electrolytic solution), 7.00 (water), 11.40 (water at 40°C) on velocity and temperature respectively. As Pr grows, the thickness of the thermal boundary layer decreases, just as a higher value of Pr makes the fluid more viscous and decreases the thickness of the momentum boundary layer; slowing the fluid velocity. Thus, as a result, average temperature and velocity are lower within the boundary layer. This is because fluids with a greater Prandtl number have higher viscosity, which reduces velocity. In addition, fluids with smaller values of Pr are highly conductive. Table 4 shows that for values of Pr within the range $0.71 \leq Pr \leq 3$, C_f undergoes negative growth about 7%, while Nu is drastically reduced about 140% whereas we see a positive growth upto 50% in Sh .

Figure 6-7 show the impact of Eckert number Ec on velocity and temperature. In fluid flow Ec is a quantity that establishes the kinetic energy of a flow's relative relevance in a heat transfer scenario. The expression is simplified to a balance of convection and conduction when $Ec \ll 1$ the terms in the energy expressions represent, making it possible to disregard the effects of pressure fluctuations, dissipation, and body forces on energy balance. As a result, a rise in Ec shows that dissipative heat or additional kinetic energy is being accumulated in the fluid particles as a result of frictional heating, which improves the fluid's total velocity and temperature. It is also evident from Table 4 that C_f and Nu is varied by a growth upto 0.1% and 2.2% respectively while Sh is effected by a decay around 1% within the range $0.01 \leq Ec \leq 0.03$.

Consequently, upon varying values of radiation absorption R , both velocity and temperature appear to be increasing, which is due to the buoyancy force generated by the absorption of radiation parameter that subsequently increases the flow rate and

temperature profile as seen in Figures 8-9. Taking in account Table 4 the influence of R on C_f, Nu is noted to differ by a positive growth upto 8% and 59% respectively while Sh to be undergoing a decay around 20% within $2 \leq R \leq 4$.

The temperature response is plotted against Du in Figure 10, and it is revealed that the thermal boundary layer is thickened upon improving Du this is due to the fact that an increase in Du denotes a general increase in the concentration gradient over temperature gradient. The temperature field therefore rises as the concentration gradient increases. Consequently, we observe from Table 4 that Nu is improved around 11%, while Sh reduces around 4% for $0.2 \leq Du \leq 0.6$. The impact of both Sr and Du , as seen in Figure 11, is to increase the fluid flow velocity throughout the boundary layer. However, a distinct velocity overshoot exists near the plate, and thereby the profile falls to attain its boundary condition. We also observe that C_f is improved upto 1.5% and 5.6% for Du and Sr respectively.

The effects of Soret Sr on temperature and concentration are seen in Figures 12-13. As seen in figure the fluid flow temperature and species concentration are found to rise as the Soret effect improves, which is due to mass transfer from lower to greater solute concentration driven by the temperature gradient hence higher Soret effect indicate stronger fluid molecule diffusivity. From Table 4 it is interesting to note that in Nu and Sh both get augmented about 5% and 45% respectively with Sr ranging within $0.5 \leq Sr \leq 1.5$.

Figures 14-15 demonstrate velocity and concentration profiles for varied Schmidt number Sc values of 0.22 (hydrogen), 0.30 (helium), 0.60 (water vapour), and 0.78 (ammonia). The velocity profile lowers because of the heavier diffusing species. It is also worth noting that with lower $Sc(0.22)$ value the peak value (at $\eta = 0.8$) is relatively more far from the plate than the highest value (at $\eta = 0.7$) for larger $Sc(0.78)$, and the concentration distribution was established to fall faster as Sc increased, resulting in the velocity and concentration boundary layers being lowered at the same time. Physically stated, a decrease in molecular diffusion results from an increase in Sc . As a result, the concentration of the species is higher for low Sc values and decrease for high Sc values. Furthermore, as presented in Table 4, as the values of Sc vary from $0.60 \leq Sc \leq 2.62$ it can be stated that C_f, Nu and Sh values undergo decay around 11%, 3% and 181% respectively.

As we increase the values of chemical reaction Kr , we see in Figures 16-18 a rise in the velocity and concentration profile, which finally leads to a simultaneous depletion in the velocity and the concentration boundary layer thickness. On the graph,

upon increasing the value of the chemical reaction Kr has a noticeable impact on the concentration boundary layer. The figure makes it abundantly obvious that the concentration of species that is slightly larger than one at the initial point that gradually falls to satisfy the boundary condition at $\eta \rightarrow \infty$. Additionally, it has been shown that incrementing the value of Kr results in a drop in the species concentration in the boundary layer. In addition, we notice a fall in the temperature profile, it is clear because when the Kr increases, the thermal boundary layer loses energy, causing the fluid temperature to drop. Furthermore, from Table 4, as the values of Kr vary from $1 \leq Kr \leq 3$ it can be concluded that C_f , Nu and Sh values are decremented about 7.1%, 7% and 64% respectively.

The effect of slip parameter h on the momentum boundary layer is seen in Figure 19. Rising h causes the velocity gradient near the surface to increase, before decrementing to its free stream value. Table 4 also shows that within the range $0.2 \leq h \leq 0.4$, the C_f experiences a decay around 23%.

It is also worth noting that when time t increases, each of these factors have opposing effects on velocity, temperature and concentration as seen in Figures 20-22. The velocity gradually approaches its greatest value near the plate, and then the profile falls till it reaches the bare minimum at $\eta \rightarrow \infty$. All times are relevant to this circumstance. It is also noticed that the peak value grows with time. In the flow area, temperature rises with passing time. This occurs as a result of the fluid capacity to store heat energy as time goes on. The solutal boundary layer species concentration rises with time, increasing the layer thickness in the process.

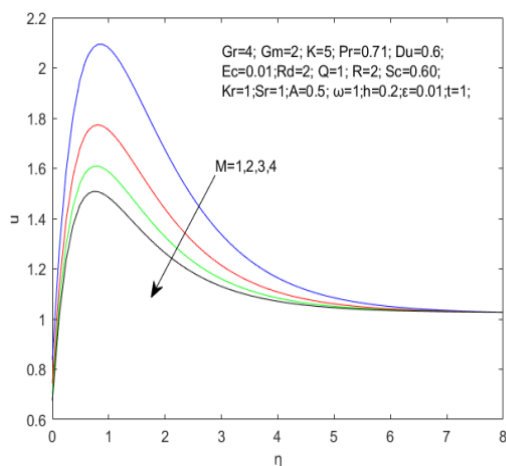


Figure 2. Velocity for varying Magnetic parameter M

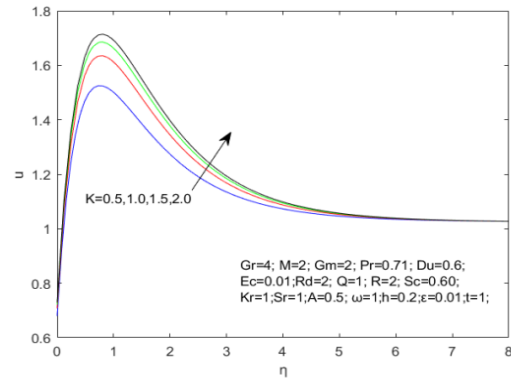


Figure 3. Velocity for varying Permeability parameter K

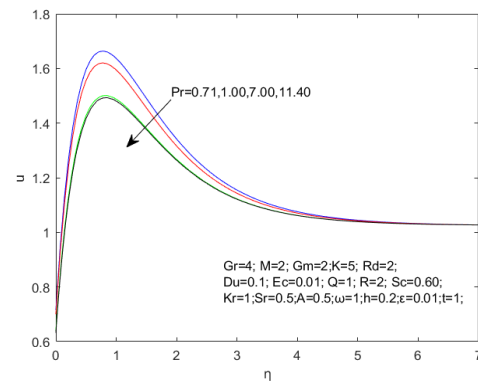


Figure 4. Velocity for varying Prandtl number Pr

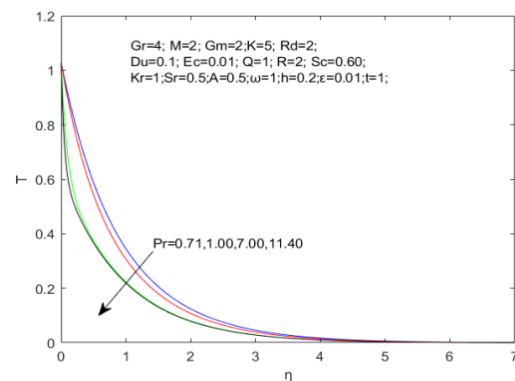


Figure 5. Temperature for varying Prandtl number Pr

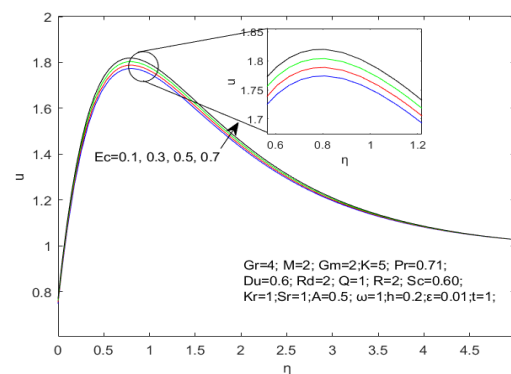


Figure 6. Velocity for varying Eckert number Ec

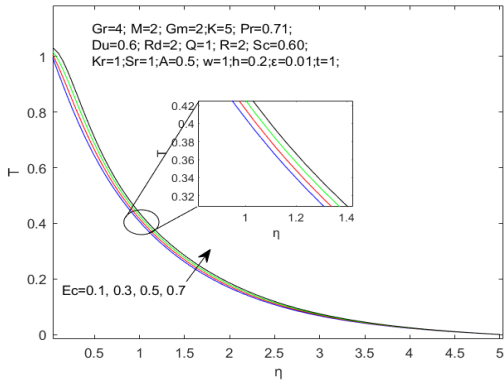


Figure 7. Temperature for varying Eckert number Ec

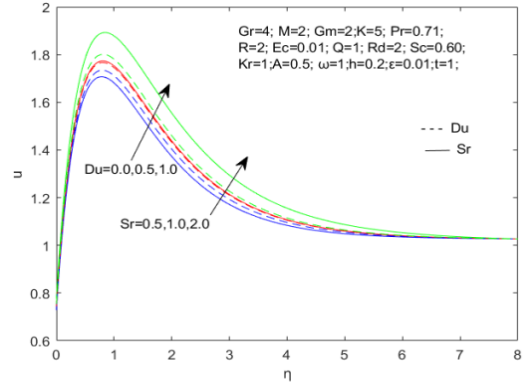


Figure 11. Velocity for varying Soret Sr and Dufour number Du

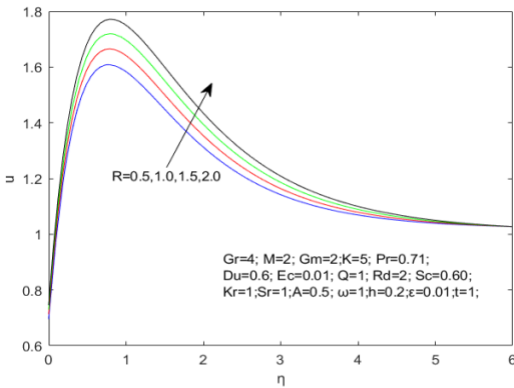


Figure 8. Velocity for varying absorption of radiation parameter R

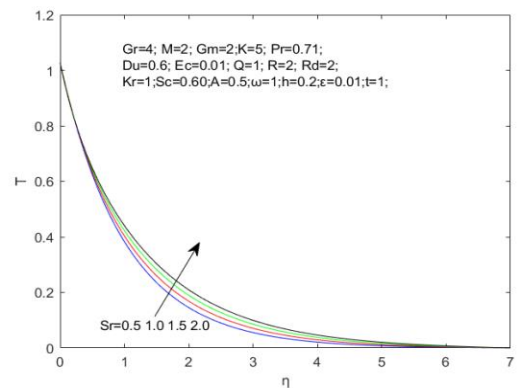


Figure 12. Temperature for varying Soret number Sr

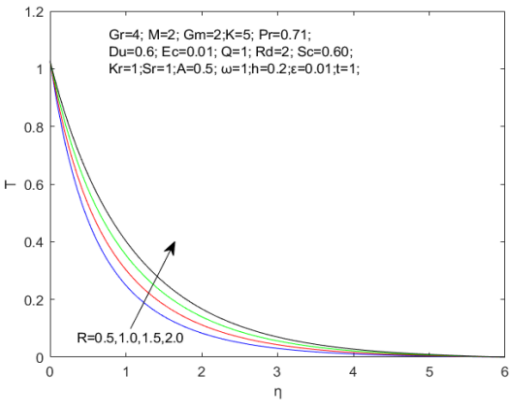


Figure 9. Temperature for varying absorption of radiation parameter R

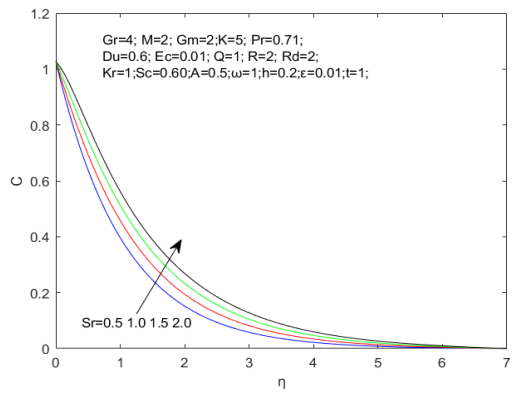


Figure 13. Concentration for varying Soret number Sr

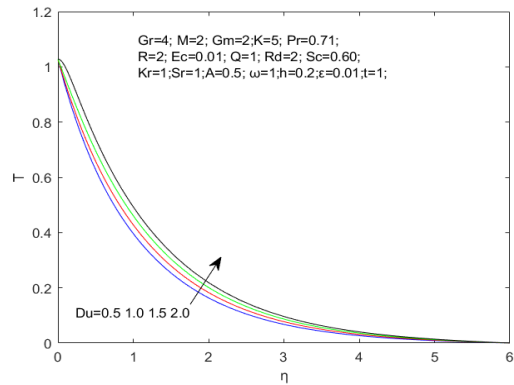


Figure 10. Temperature for varying Dufour Du

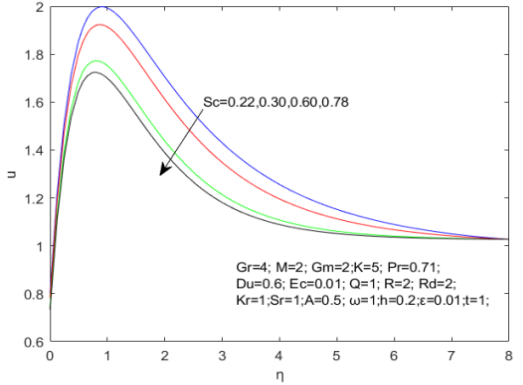


Figure 14. Velocity for varying Schmidt number Sc

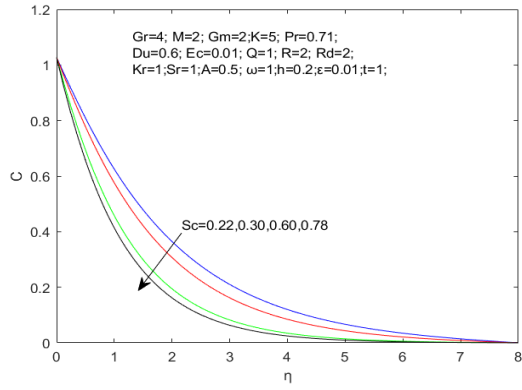


Figure 15. Concentration for varying Schmidt number Sc

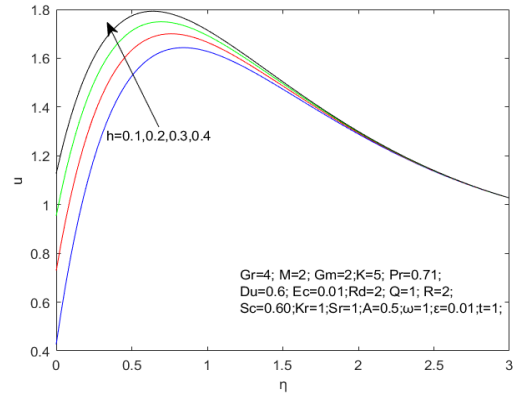


Figure 19. Velocity for varying slip parameter h

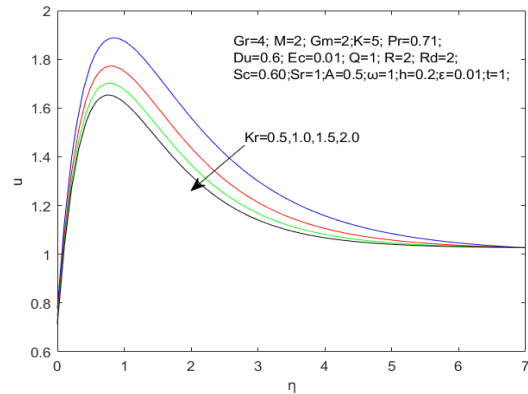


Figure 16. Velocity for varying Chemical reaction Kr

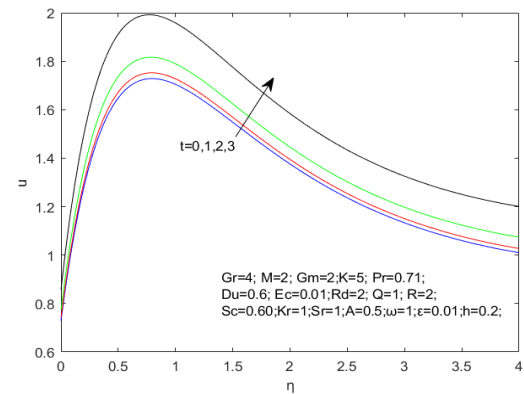


Figure 20. Velocity for varying time t

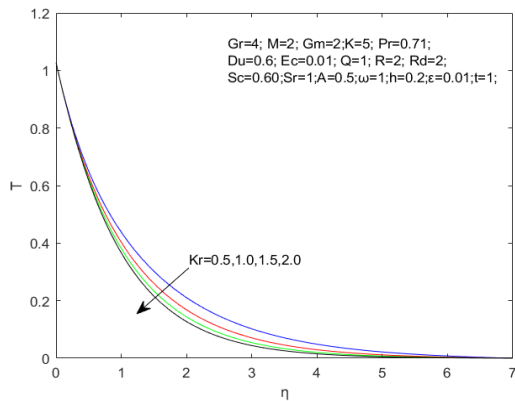


Figure 17. Temperature for varying Chemical reaction Kr

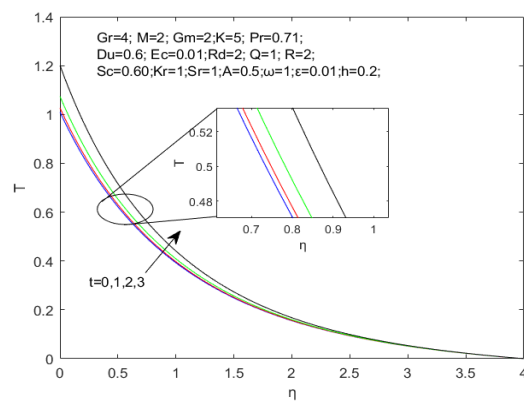


Figure 21. Temperature for varying time t

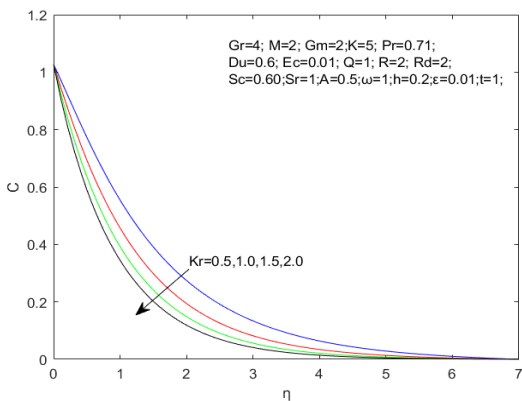


Figure 18. Concentration for varying Chemical reaction Kr

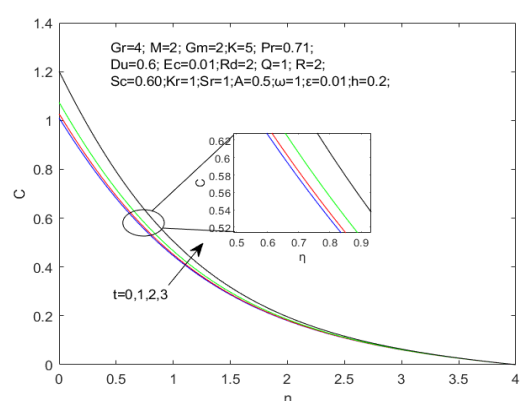


Figure 22. Concentration for varying time t

Table 1. Effects of h on C_f, Nu, Sh for reference values $Pr = 0.7, A = 0.5, \varepsilon = 0.2, \omega = 0.1, t = 1.0, Kr = 0.1, Du = 0.0, Ec = 0.0, Sr = 0.0$

h	Pal and Talukdar [3]			Present		
	C_f	Nu	Sh	C_f	Nu	Sh
0.0	6.4047	-1.3822	-0.9087	6.4047	-1.3822	-0.9088
0.1	5.3082	-1.3822	-0.9087	5.3082	-1.3822	-0.9088
0.3	3.9540	-1.3822	-0.9087	3.9540	-1.3822	-0.9088
0.5	3.1503	-1.3822	-0.9087	3.1503	-1.3822	-0.9088

Table 2. Effects of Rd on C_f, Nu, Sh for reference values $Pr = 0.7, A = 0.5, \varepsilon = 0.2, \omega = 0.1, t = 1.0, h = 0.3, Kr = 0.1, Du = 0.0, Ec = 0.0, Sr = 0.0$

Rd	Pal and Talukdar [3]			Present		
	C_f	Nu	Sh	C_f	Nu	Sh
1.0	4.1838	-0.9254	-0.9087	4.1838	-0.9255	-0.9088
2.0	3.9540	-1.3822	-0.9087	3.9540	-1.3822	-0.9088
3.0	3.8015	-1.7436	-0.9087	3.8015	-1.7437	-0.9088
4.0	3.6901	-2.0488	-0.9087	3.6901	-2.0489	-0.9088

Table 3. Effects of Kr on C_f, Nu, Sh for reference values $Pr = 0.7, A = 0.5, \varepsilon = 0.2, \omega = 0.1, t = 1.0, h = 0.3, Du = 0.0, Ec = 0.0, Sr = 0.0$

Kr	Pal and Talukdar [3]			Present		
	C_f	Nu	Sh	C_f	Nu	Sh
0.00	4.0441	-1.3400	-0.8098	4.0439	-1.3401	-0.8099
0.50	3.7512	-1.4825	-1.1864	3.7513	-1.4825	-1.1864
0.75	3.6744	-1.5226	-1.3178	3.6744	-1.5227	-1.3178
1.00	3.6149	-1.5546	-1.4325	3.6149	-1.5546	-1.4326

Table 4: Effects of $Gr, Gm, M, K, Pr, R, Q, Rd, Ec, Du, Sc, Sr, Kr, h$ on C_f, Nu, Sh for reference values $A = 0.5; \omega = 1; h = 0.2; t = 1; \varepsilon = 0.01$

Gr	Gm	M	K	Pr	R	Q	Rd	Ec	Du	Sc	Sr	Kr	h	C_f	Nu	Sh
4	2	2	5	0.71	2	1	2	0.01	0.2	0.60	0.5	1	0.2	3.5876	-1.1492	-0.9396
5														3.9266	-1.1470	-0.9402
6														4.2658	-1.1446	-0.9410
	3													3.9499	-1.1468	-0.9403
	4													4.3123	-1.1441	-0.9411
		3												3.4028	-1.1511	-0.9390

4			3.2975	-1.1523	-0.9387
	6		3.5961	-1.1492	-0.9396
		7	3.6022	-1.1491	-0.9396
			3.5158	-1.3737	-0.8760
		1	3.3234	-2.7564	-0.4704
			3.7331	-0.8057	-1.0347
		3	3.8726	-0.4742	-1.1264
			3.4746	-1.4491	-0.8557
		2	3.3902	-1.7060	-0.7830
			3.4746	-1.4491	-0.8557
		3	3.3902	-1.7060	-0.7830
			3.5891	-1.1367	-0.9433
		0.02	3.5906	-1.1241	-0.9470
			3.6139	-1.0892	-0.9651
		0.03	3.6407	-1.0246	-0.9740
			3.4272	-1.2000	-1.2911
		0.4	3.2959	-1.2194	-1.7998
			3.6922	-1.1160	-0.7195
		0.6	3.7875	-1.0870	-0.5106
			3.4277	-1.2010	-1.2773
		1	3.3332	-1.2262	-1.5412
			3.1279	-1.1526	-0.9386
		2.62	2.7726	-1.1548	-0.9380
		1			
		1.5			
		2			
		3			
		0.3			
		0.4			

Conclusion

The following interpretations of the flow field may be formed for varying values of parameters associated in the flow field:

1. Fluids with a high Prandtl number have a high viscosity and thermal conductivity, which deteriorate the skin friction about 7% and heat transfer rate about 140% but improves the mass transfer rate upto 50% when Pr changes from 0.71 to 3.0
2. As the radiation absorption parameter improves the skin friction improves about 8% and heat flow rate significantly augments around 59%, while Sherwood number reduces around 20% when R alters from 2 to 4
3. The viscous dissipation created in the fluid flow tends to increase velocity, temperature distribution and improves the heat flow rate about 2.2% for when Ec varying from 0.01 to 0.03
4. The Soret effect has been found to significantly improve the skin friction, heat and mass transfer rates by significant percentages of about 5.6%, 5% and 45% respectively when Sr changes from 0.5 to 1.5.
5. The Dufour effect can be improved to augment the heat transfer rate about 11% and cause mass transfer rate to deteriorate around 4% when Du shifts from 0.2 to 0.6.
6. The slip parameter can be improved to enhance velocity profile and to deteriorate skin friction around 2.3% as h shifts from 0.2 to 0.4.

7. The velocity, temperature, and species concentration distribution all continue growing as more time goes by.

It is intended that the physics of flow across the permeable vertical plate with velocity slip may be used as the foundation for various engineering and scientific applications using our current model. Additionally, it can serve as inspiration for next experiments, which are now lacking.

In subsequent studies, we will use the proper velocity slip notion to further generalize comparisons to various body forms.

Nomenclature

a^*	Mean absorption coefficient	P	Fluid pressure Nm^{-2}
A	Real positive constant	Pr	Prandtl number $\frac{\vartheta}{\alpha}$
B	Magnetic field flux	Q	Non-dimensional heat source parameter $\frac{Q_0 \vartheta}{\rho c_p v_0^2}$
B_0	Magnetic field strength T	Q_0	Dimensional heat absorption coefficient Wm^{-3}
\tilde{C}	Species concentration Kgm^{-3}	Q_1	Dimensional radiation of absorption
C	A scaled concentration	\tilde{q}_r	Radiative heat flux Wm^{-2}
C_f	Skin friction	R	Non-dimensional radiation of absorption $\frac{(C_w - C_\infty) \vartheta}{(T_w - T_\infty) v_0^2}$
C_∞	Ambient fluid's species concentration Kgm^{-3}	Rd	Radiation parameter $\frac{16\alpha^* \sigma^* T_\infty^3 \vartheta}{\rho c_p v_0^2}$
C_w	Wall concentration	Sc	Schmidt number $\frac{\vartheta}{D_m}$
c_p	Specific heat at constant pressure $JKg^{-1}K^{-1}$	Sh	Sherwood number
c_s	Concentration susceptibility	Sr	Soret number $\frac{D_m K_T}{\vartheta T_m} \left(\frac{T_w - T_\infty}{C_w - C_\infty} \right)$
D_m	Molecular diffusivity coefficient $m^2 s^{-1}$	\tilde{T}	Dimensional fluid temperature K
Du	Dufour number $\frac{D_m K_T}{c_s c_p \vartheta} \left(\frac{C_w - C_\infty}{T_w - T_\infty} \right)$	T	A scaled temperature
Ec	Eckert number $\frac{u_0^2}{c_p (T_w - T_\infty)}$	T_∞	Ambient fluid temperature K
Gm	Solutal Grashof number $\frac{g \beta_c (C_w - C_\infty) \vartheta}{v_0^2 u_0}$	T_m	Mean fluid temperature
Gr	Thermal Grashof number $\frac{g \beta_T (T_w - T_\infty) \vartheta}{v_0^2 u_0}$	\tilde{t}	Dimensional time s
g	Acceleration due to gravity ms^{-2}	t	Non-dimensional time
\tilde{h}	Dimensional slip parameter m	u	A scaled velocity
h	Non-dimensional slip parameter	\tilde{u}	Dimensional velocities \tilde{x} direction ms^{-1}
J	Current density	u_0	Characteristic velocity ms^{-1}
k	thermal conductivity $Jm^{-1}s^{-1}K^{-1}$	u_∞	Non- dimensional free stream
\tilde{K}	Permeability of porous medium m^2	\tilde{u}_∞	Dimensional free stream velocity ms^{-1}
K	Non-dimensional permeability $\frac{v_0^2 \tilde{K}}{\vartheta^2}$	\tilde{v}	Dimensional velocities \tilde{y} direction ms^{-1}
$\tilde{K}\tilde{r}$	Dimensional chemical reaction	v_0	Scale of suction velocity ms^{-1}
Kr	Non-dimensional chemical reaction $\frac{\tilde{K}\tilde{r} \vartheta}{v_0^2}$	V	Flow velocity vector
K_T	Thermal diffusion ratio Kgm^{-3}	\tilde{x}	Dimensional distances along the plate m
M	Magnetic parameter $\frac{\sigma B_0^2 \vartheta}{\rho v_0^2}$	\tilde{y}	Dimensional distances perpendicular to the plate m
Nu	Nusselt number	Greek symbols	
		β_c	Concentration expansion coefficients Kg^{-1}
		β_T	Thermal expansion coefficients K^{-1}
		α	Fluid thermal diffusivity $m^2 s^{-1}$
		ρ	Fluid density Kgm^{-3}
		σ	Electrical conductivity of fluid $Kg^{-1}m^{-3}s^3A^2$
		ϑ	Kinematic viscosity $m^2 s^{-1}$
		μ	Dynamic viscosity $Kgm^{-1}s^{-1}$
		η	A scaled coordinate m
		σ^*	Stefan-Boltzmann constant $Wm^{-2}K^{-4}$
		ε	A small positive constant

- $\tilde{\omega}$ Frequency of oscillation s^{-1}
 ω A scaled frequency
 ∇ Differential operator

References

- [1] S. Goldstein, 1965. *Modern developments in fluid dynamics*. New York, Dover Publications, 1965.
- [2] B. G. S and Joseph D D, 1967. Boundary conditions at a natural permeable wall, *Journal of Fluid Mechanics*, 30(1), pp. 197–207
- [3] D. Pal and B. Talukdar, 2010. Perturbation analysis of unsteady magnetohydrodynamic convective heat and mass transfer in a boundary layer slip flow past a vertical permeable plate with thermal radiation and chemical reaction, *Communications in Nonlinear Science and Numerical Simulation*, 15(7), pp. 1813–1830 doi: 10.1016/j.cnsns.2009.07.011.
- [4] D. Ramya, R. S. Raju, J. A. Rao, and A. J. Chamkha, 2018. Effects of velocity and thermal wall slip on magnetohydrodynamics (MHD) boundary layer viscous flow and heat transfer of a Nano fluid over a non-linearly-stretching sheet: a numerical study, *Propulsion and Power Research*, 7(2), pp. 182–195 doi: 10.1016/j.jppr.2018.04.003.
- [5] A. Raptis, 2011. Free convective oscillatory flow and mass transfer past a porous plate in the presence of radiation for an optically thin fluid, *Thermal Science*, 15(3), pp. 849–857 doi: 10.2298/TSC1101208032R.
- [6] M. A. Hossain and H. S. Takhar, 1996. Radiation effect on mixed convection along a vertical plate with uniform surface temperature, *Heat and Mass Transfer*, 31(4), pp. 243–248 doi: 10.1007/s002310050052.
- [7] L. Manjula and R. Muthucumaraswamy, 2021. Heat and Mass Transfer Effect on an Infinite Vertical Plate in the Presence of Hall Current and Thermal Radiation with Variable Temperature, *International Journal of Applied Mechanics and Engineering*, 26(3), pp. 131–140 doi: 10.2478/ijame-2021-0040.
- [8] F. S. Ibrahim, A. M. Elaiw, and A. A. Bakr, 2008. Effect of the chemical reaction and radiation absorption on the unsteady MHD free convection flow past a semi infinite vertical permeable moving plate with heat source and suction, *Communications in Nonlinear Science and Numerical Simulation*, 13(6), pp. 1056–1066 doi: 10.1016/j.cnsns.2006.09.007.
- [9] G. Sreedevi, R. R. Rao, D. R. V. P. Rao, and A. J. Chamkha, 2016. Combined influence of radiation absorption and Hall current effects on MHD double-diffusive free convective flow past a stretching sheet, *Ain Shams Engineering Journal*, 7(1), pp. 383–397 doi: 10.1016/j.asej.2015.11.024.
- [10] A. M. Aly, A. J. Chamkha, and Z. A. S. Raizah, 2020. Unsteady coupled heat and mass transfer by free convection from a vertical plate embedded in porous media under impacts of radiation and chemical reaction, *Journal of Heat and Mass Transfer Research*, 7(2), pp. 95–103 doi: 10.22075/JHMTR.2019.10763.1149.
- [11] S. Matta, B. S. Malga, L. Appidi, and P. P. Kumar, 2021. Radiation and chemical reaction effects on unsteady MHD free convection mass transfer fluid flow in a porous plate, *Indian Journal of Science and Technology*, 14(8), pp. 707–717 doi: 10.17485/ijst/v14i8.20.
- [12] H. Konwar, 2022. Flow, Heat and Mass Transfer past a Stretching Sheet with Temperature Dependent Fluid Properties in Porous Medium, *Journal of Heat and Mass Transfer Research*, 9, pp. 17–26 doi: 10.22075/jhmtr.2022.25036.1357.
- [13] S. A. Khan, T. Hayat, and A. Alsaedi, 2022. Thermal conductivity performance for ternary hybrid nanomaterial subject to entropy generation, *Energy Reports*, 8, pp. 9997–10005 doi: 10.1016/j.egy.2022.07.149.
- [14] S. A. Khan, T. Hayat, A. Alsaedi, and B. Ahmad, 2021. Melting heat transportation in radiative flow of nanomaterials with irreversibility analysis, *Renewable and Sustainable Energy Reviews*, 140, pp. 110739 doi: <https://doi.org/10.1016/j.rser.2021.110739>.
- [15] M. Yasir, M. Khan, and A. Ahmed, 2022. Non-linear radiative flow of unsteady Oldroyd-B nanofluid subject to Arrhenius activation energy, *Waves in Random and Complex Media*, 0(0), pp. 1–15 doi: 10.1080/17455030.2022.2135791.
- [16] S. A. Khan, T. Hayat, and A. Alsaedi, 2022. Entropy optimization for nanofluid flow with radiation subject to a porous medium, *Journal of Petroleum Science and Engineering*, 217, pp. 110864 doi: <https://doi.org/10.1016/j.petrol.2022.110864>.
- [17] S. A. Khan, T. Hayat, and A. Alsaedi, 2022. Numerical study for entropy optimized radiative unsteady flow of Prandtl liquid, *Fuel*, 319, pp. 123601 doi: <https://doi.org/10.1016/j.fuel.2022.123601>.
- [18] T. Kebede, E. Haile, G. Awgichew, and T. Walelign, 2020. Heat and Mass Transfer in Unsteady Boundary Layer Flow of Williamson Nanofluids, *Journal of Applied Mathematics*, 2020(1890972) doi: <https://doi.org/10.1155/2020/1890972>.
- [19] M. Nemati, M. Sefid, and A. R. Rahmati, 2021. Analysis of the Effect of Periodic Magnetic Field, Heat Absorption / Generation and Aspect Ratio of the Enclosure on Non-Newtonian Natural Convection, *Journal of Heat and Mass Transfer Research*, 8, pp. 187–203 doi: 10.22075/JHMTR.2021.22119.1322.
- [20] E. M. A. Elbashesy, H. G. Asker, and B. Nagy, 2022. The effects of heat generation absorption on boundary layer flow of a nanofluid containing gyrotactic microorganisms over an inclined stretching

- cylinder, *Ain Shams Engineering Journal*, 13(5), pp. 101690 doi: 10.1016/j.asej.2022.101690.
- [21] M. Khan, M. Yasir, A. Saleh, S. Sivasankaran, Y. Rajeh, and A. Ahmed, 2022. Variable heat source in stagnation-point unsteady flow of magnetized Oldroyd-B fluid with cubic autocatalysis chemical reaction, *Ain Shams Engineering Journal*, 13(3), pp. 101610 doi: 10.1016/j.asej.2021.10.005.
- [22] M. Yasir, A. Ahmed, M. Khan, Z. Iqbal, and M. Azam, 2022. Impact of ohmic heating on energy transport in double diffusive Oldroyd-B nanofluid flow induced by stretchable cylindrical surface, *Proceedings of the Institution of Mechanical Engineers, Part E: Journal of Process Mechanical Engineering*, 0(0) doi: 10.1177/09544089211064116.
- [23] M. Sheikholeslami, 2022. Numerical investigation of solar system equipped with innovative turbulator and hybrid nanofluid, *Solar Energy Materials and Solar Cells*, 243, pp. 111786
- [24] W. I. A. Okuyade, T. M. Abbey, and A. T. Gima-label, 2018. Unsteady MHD free convective chemically reacting fluid flow over a vertical plate with thermal radiation, Dufour, Soret and constant suction effects, *Alexandria Engineering Journal*, 57(4), pp. 3863–3871 doi: 10.1016/j.aej.2018.02.006.
- [25] S. Sarma and N. Ahmed, 2022. *Dufour effect on unsteady MHD flow past a vertical plate embedded in porous medium with ramped temperature*. Nature Publishing Group UK, 2022. Doi: 10.1038/s41598-022-15603-x.
- [26] O. Mopuri, R. Kodi, C. Ganteda, R. Sriakulapu, and G. Lorenzini, 2022. MHD Heat and Mass Transfer Steady Flow of a Convective Fluid Through a Porous Plate in The Presence of Diffusion Thermo and Aligned Magnetic Field, *Journal of Advanced Research in Fluid Mechanics and Thermal Sciences*, 89(1), pp. 62–76 doi: 10.37934/arfmts.89.1.6276.
- [27] C. Sowmiya and B. R. Kumar, 2022. MHD mixed convection flow in a permeable vertical plate with buoyancy and Dufour effects, *Journal of Porous Media*, 25(11), pp. 71–81 doi: 10.1615/JPorMedia.2022044034.
- [28] M. Venkateswarlu, D. V. Lakshmi, and O. D. Makinde, 2020. Thermodynamic analysis of hall current and Soret number effect on hydromagnetic Couette flow in a rotating system with a convective boundary condition, *Heat Transfer Research*, 51(1), pp. 83–102 doi: 10.1615/HeatTransRes.2019027139.
- [29] V. Meenakshi, 2021. Dufour and Soret Effect on Unsteady MHD Free Convection and Mass Transfer Flow Past an Impulsively Started Vertical Porous Plate Considering with Heat Generation, *Journal of Heat and Mass Transfer Research*, 8(2), pp. 257–266 doi: 10.22075/JHMTR.2021.21229.1301.
- [30] B. K. Taid and N. Ahmed, 2022. MHD Free Convection Flow across an Inclined Porous Plate in the Presence of Heat Source, Soret Effect, and Chemical Reaction Affected by Viscous Dissipation Ohmic Heating, *Biointerface Research in Applied Chemistry*, 12(5), pp. 6280–6296 doi: <https://doi.org/10.33263/BRIAC125.62806296>.
- [31] M. Yasir, M. Khan, and Z. U. Malik, 2023. Analysis of thermophoretic particle deposition with Soret-Dufour in a flow of fluid exhibit relaxation/retardation times effect, *International Communications in Heat and Mass Transfer*, 141, pp. 106577 doi: <https://doi.org/10.1016/j.icheatmasstransfer.2022.106577>.
- [32] S. A. Khan, T. Hayat, and A. Alsaedi, 2022. Simultaneous features of Soret and Dufour in entropy optimized flow of reiner-rivlin fluid considering thermal radiation, *International Communications in Heat and Mass Transfer*, 137, pp. 106297 doi: <https://doi.org/10.1016/j.icheatmasstransfer.2022.106297>.
- [33] Y. J. Kim, 2000. Unsteady MHD convective heat transfer past a semi-infinite vertical porous moving plate with variable suction, *International Journal of Engineering Science*, 38(8), pp. 833–845 doi: 10.1016/S0020-7225(99)00063-4.
- [34] L. Shampine, J. Kierzenka, and M. Reichelt, 2000. Solving boundary value problems for ordinary differential equations in MATLAB with bvp4c, *Tutorial Notes*, 75275, pp. 1–27 doi: https://classes.engineering.wustl.edu/che512/bvp_paper.pdf.



Semnan University



Magnetohydrodynamics and Aspect Ratio Effects on Double Diffusive Mixed Convection and Their Prediction: Linear Regression Model

Shivananda Moolya ^{a,b}, Satheesh Anbalagan ^{*a} , Neelamegam Rajan Devi^c,
Rekha Moolya^d

^aSchool of Mechanical Engineering, Vellore Institute of Technology, Vellore, Tamilnadu, INDIA-632014.

^bUniversity of Technology and Applied Sciences, PO Box 74, Al-Khuwair Postal code 133, Sultanate of Oman.

^cDepartment of Physics, Auxilium College (Autonomous), Tamilnadu, INDIA-632006.

^dGopalan College of Engineering and Management, Bangalore, Karnataka, India, 560048.

PAPER INFO

Paper history:

Received: 2022-08-07

Received: 2023-01-14

Accepted: 2023-01-26

Keywords:

Aspect ratio;
Double-diffusion;
Taguchi;
Linear regression model;
Optimization

ABSTRACT

Magnetohydrodynamic application in the biomedical field made the researcher work more on this field in recent years. The major application of this concept is in scanning using laser beams, delivering a drug to the targeted points, cancer treatment, enhancing image contrast, etc. These applications are depending on the flow and heat transfer properties of the magnetic conducting fluid and on the geometry of the flow field. An increase in the demand for the miniature in the shape and size of the clinical devices attracts the researcher to work more on design optimization. In this study optimization of magnetic field strength, geometry of domain, Prandtl number, Reynolds number for a steady, incompressible double-diffusive flow is performed using Taguchi and Analysis of variance technique. Linear regression model is used to predict the average Nusselt and Sherwood numbers. Numerical simulations were performed using finite volume method (FVM) based numerical techniques. Experiments are designed based on Taguchi orthogonal array and FVM based numerical codes were used to obtain the results. Results show that an increase in the aspect ratio from 0.5 to 2.0 improves the heat transfer rate by 62.0% and the mass transfer rate by 38.5%. As the Prandtl number increases from 0.7 to 13.0, heat transfer rate increases by 80.0% and mass transfer by 75.0%. This specific study could be applied in designing of solar ponds and to investigate heat and mass transfer effects during cancer treatments.

DOI: [10.22075/jhmtr.2023.28029.1387](https://doi.org/10.22075/jhmtr.2023.28029.1387)

© 2022 Published by Semnan University Press. All rights reserved.

1. Introduction

Double diffusive mixed convection is widely used in many industrial and medical applications like solar ponds, material processing, Drug delivery systems, cancer treatments, solar air conditioning, packaging of electronic items, food processing, etc. Considering the wide application of double-diffusive mixed convection in the industrial and medical areas, further study is required to optimize the parameter influencing heat and mass transfer for maximum performance. Several numerical studies have been performed for the optimization of heat and mass transfer of the cavity

flow. Rodrigues et al. [1] performed optimization of the geometry of the lid-driven cavity with two fins inside the cavity for mixed-type convection. They found that the asymmetric geometry of the fin plays a major role in controlling the temperature. Baag et al. [2] numerically studied the MHD effect using micropolar-type fluid flow on a vertical surface. They found that backflow is controlled by opposing buoyancy parameters. Khader and Megahed [3] used the Finite Difference Method to analyze the heat transfer on a liquid thin film over a stretching sheet using a numerical method. Li et al. [4] performed optimization

*Corresponding Author: Satheesh Anbalagan

Email: satheesh.a@vit.ac.in; egsatheesh@gmail.com

of nanoparticle size and other parameters on natural convection. They found that aspect ratio and Rayleigh number are the most significant parameters to control the thermal performance of the cavity. Iyi and Hasan [5] numerically performed the analysis on the effect of moistness using the buoyancy-driven flow of turbulence nature in a cavity. Li, et al. [6] have numerically optimized heat transfer in a microchannel using the field synergy principle. They found that internal cavity configuration plays a major role in controlling heat transfer. Mohammadi et al. [7] have optimized the heat transfer of flow of nanofluid inside a coil using Taguchi analysis. They found an optimum combination of a selected parameter for maximum performance. Srinivas, et al. [8] analyzed chemical reactions and thermal diffusion effect using MHD flow in a porous channel. The effect of different dimensional numbers has been considered in this analysis. Nath and Krishnan [9] performed an optimization analysis using Taguchi and the utility method of a double-diffusive type of flow using a channel filled with nanofluid. They compared the results of those methods and found that the utility method predicts marginally less Nu and Sh. Raei [10] used a Taguchi method for optimizing the heat exchanger operating with aluminum oxide nanofluid. Kishore, et al. [11] have done an optimization analysis of thermal electric generators using the Analysis of Variance (ANOVA) and the Taguchi method. They compared Taguchi and full factorial ANOVA results and found an 11.8% deviation. Iftikha et al. [12] performed a study on natural convective heat and mass transfer with inclined MHD effect using fractional operators. Hatami et al. [13] performed an optimization analysis of heat transfer using natural convection in a circular cavity. The results of their findings are, the Lewis number plays a major role in controlling the Nusselt number. Optimization of the cooled condenser for forced convection is performed by Kumara et al. [14]. The results of the Taguchi method show that improved performance is observed for 2-4 tubes kept at a 3-5 mm gap. Mamourian et al. [15] have optimized heat transfer by mixed convection and generation of entropy in a lid-driven cavity using the Taguchi method. They found the value of the optimum percentage of nanoparticles, wavelength, and Richardson number for better thermal performance of the cavity. Shirvan et al. [16] have numerically investigated and optimized the parameters involved in mixed convection using nanofluid flow in a cavity. The PISO algorithm is used to optimize the position of the heat sink and source in a closed enclosure Soleimani et al., [17]. An optimal combination for better thermal performance of the cavity is presented in this work. Position of multiple heat source optimization in a cavity was performed by Madadi and Balaji [18], using ANN and genetic algorithm. The result shows that a combination of ANN and GA will reduce the

computational period. Paulo et al. [19] analyzed the mixed convection laminar flow in a domain where two openings as an inlet and outlet in the vertical walls. Alinejad and Esfahani [20] used the Taguchi design approach to optimize the mixed convection in an enclosure. Taguchi's analysis shows that all the selected parameters show a significant effect on output. An optimal level of the selected parameters is also presented in the work. Gorobets et al. [21] published a numerical study on heat transfer with hydrodynamics effect in small diameter tube bundles. Hatami et al. [22] used a T-shaped cavity filled with a porous material and nanofluid to analyze and optimize heat transfer. ANN and GA are used by Mathew and Hotta [23] for optimizing IC chip arrangements on SMPS for mixed convection heat transfer. Results of the work show that the hybrid arrangement of chips is more effective than ordinary methods. Pichandi and Anbalagan [24] used a 2D enclosure to analyze the fluid flow and heat transfer analysis with the sinusoidal wave. LBM method is used for the analysis. Mirzakhani et al. [25] performed a sensitivity analysis to improve mixed convection and to reduce the coefficient of drag of fluid flow in a cavity with a rotating cylinder. The result of the analysis gives the effective values to increase the mean Nusselt number and reduce the drag coefficient. Sensitivity analysis and optimization are performed by Pordanjani et al. [26] to find the magnetic field effect on convection and entropy generation of nanofluid flow in an inclined domain. They found that Bejan and generation of entropy enhance with an increase in the thermal source length. Behbahan et al. [27] investigated the effect of aspect ratio on the melting thermal characteristics of metal foam. Investigation shows that aspect ratio plays a major role in changing the phase of copper foam. Selimefendigil and Öztop [28] Performed MHD convection optimization in a trapezoidal domain filled with nanofluid. Sudhakar et al. [29] used the ANN method to optimize the heat source configuration in a duct under mixed convection. Results show that CNN gives more accurate and fast results than computational studies. Tassone et al. [30] conducted optimization and heat transfer analysis of the cooling system using MHD flow in a WCLL blanket. Yigit and Chakraborty [31] performed a numerical analysis to find the effect of boundary condition and aspect ratio using Bingham fluids. Their investigation concludes that buoyancy forces improve flow by increasing the Rayleigh number. Hamzah et al. [32] published a research work on the effect of MHD on natural convection considering nanoparticle fluid flow in a U-Shape cavity. Yang and Yeh [33] optimized arrays of fins in a channel for mixed-type convection. A correlation of the aspect ratios for the maximum performance for different inclination angles is proposed in this study. Numerical investigation of the mixed convection effect in a square lid-driven cavity

under the combined effects of thermal and mass diffusion is numerically investigated [34]. Izadi et al. [35] performed a numerical analysis to find the effect of heat source and cavity aspect ratio using a C-shaped cavity on natural convection. They found a linear relationship between Nu and the aspect ratio of the enclosure. Béghein et al. [36] performed a numerical study on double-diffusive convection using a rectangular cavity. Alsobaai [37] used optimized petroleum residue thermal cracking using a three-level factorial design. Sathiyamoorthi and Anbalagan [38] presented their numerical study on entropy generation in double-diffusive natural convection in a square enclosure with the presence of a rectangular block at the center. They found that an increase in the Rayleigh number significantly increases entropy generation. An increase in Hartmann number decreases total entropy generation. Aljabair et al. [39] published a research article on the mixed convection of nanofluid flow in a lid-driven domain of sinusoidal nature. Teamah [40] performed numerical analysis on double diffusion using the rectangular domain. Recently, Moolya and Satheesh [41,42] performed a numerical study on the effect of an inclined magnetic field on double-diffusive mixed convection by considering different inclination angles. In the study, it is found that the magnetic field has a negative impact and the inclination angle has a positive impact on heat and mass transfer. Further, the work is extended for finding the optimum combination of the selected parameter for maximum performance. In the analysis, it is found that the Richardson number is the least significant parameter compared to all the selected parameters. Hasan et al. [43] used a mechanical chamber of triangular shape to analyze the periodic natural convection effect using CNT nanofluid. Raju et al. [44] performed a study on heat transmission and flow characteristics of nanofluid in a radiated flexible porous channel. They found that the distribution of temperature is higher in case-1, but the opposite finding is observed in a momentum boundary layer. Hossain et al [45] conducted a numerical study on the MHD convection effect using nanofluid with radiation. This analysis would help in designing thermal devices that work on nanofluids. Priyadharshini et al. [46] investigated the use of heat and mass transfer in MHD flow over a stretching sheet using a machine learning technique. They found that machine learning technology reduces the cost of simulation in the analysis of metal flow in metallurgy. Azad et al. [47] performed numerical analysis on heat and mass transfer properties in an enclosure using variable buoyancy ratio. Results show that an increase in the dimensionless time supports heat and mass transfer. Kavya et al. [48] used a stretching cylinder to study the magnetic-hybrid nanoparticle effect suspended in Cu nanoparticles. Their major finding is magnetic field reduces fluid velocity. Farahani [58] conducted an efficacy study on the magnetic field effect

on heat transfer using nanofluid in a flattened tube with nanofluid. Senejani and Baniamerian [59] performed an optimization study of shell and tube heat exchangers using genetic, particle swarm, and Jaya optimization algorithms. Based on the above literature study, it is concluded that optimization of the geometry of the cavity and other related parameters to enhance the thermal performance of the cavity is needed to study further for better accuracy in the relevant field. Above mentioned literature it is found that aspect ratio also plays a major role in the present work, the aspect ratio is also considered one of the parameters. Also, by considering the importance of the Richardson number, it cannot be neglected without further investigation which was found as an insignificant parameter in the preceding study [41]. Therefore, to find the importance of the natural and forced convection effect, Grashof and Reynolds numbers are introduced. Hence in the present study, a two-dimensional domain, double-diffusive mixed convective laminar incompressible flow with MHD effect is considered. The performance of the cavity is determined by comparing Nusselt and Sherwood numbers for a different combination of dimensionless numbers. FVM-based numerical codes are used for the analysis and optimization is carried out using the Taguchi approach. The best combination of different dimensional numbers and the aspect ratio for maximum performance is obtained from the analysis. Residual plots obtained from linear regression models are used to correlate the fitted values with the observed values to check the accuracy of the obtained results. Following are the novelties of this study

- Analysis of the effect of nonlinear MHD effect on double-diffusive mixed convection by considering different aspect ratios
- The impact of thermal and momentum diffusivity on the heat transfer property of the cavity is analyzed
- A most significant parameter which controls the heat and mass transfer rate is analyzed
- An optimum combination of the selected parameter to maximize the rate of heat and mass transfer is determined by optimization analysis.
- Prediction models are developed. template, created in Microsoft Word 2013. Margins, column widths, line spacing, and type styles are built-in throughout this document. Author can use this document as a template and simply type own text into it.

2. Problem description and governing equations

A horizontal two-dimensional cavity model selected in this study is shown in Figure 1. The aspect ratio (L/H) is varied from 0.5 to 2.0 for the analysis. A horizontal magnetic field (B_0) is induced to the cavity

in a horizontal direction. Vertical sides of the cavity are kept with zero temperature and concentration gradients. Maximum temperature and concentration are kept to the top and bottom walls of the cavity. The upper wall is made to move towards positive x-direction to give a force convection effect and all other walls are kept stationary. The Newtonian and incompressible fluid is assumed for the analysis. All the thermal and physical properties of the fluid are assumed as constant except the density term. The variation of density term in the buoyancy force is calculated using a model developed by Boussinesq as shown in equation 1.

$$\rho = \rho_0 [1 - \beta_T(T - T_c) - \beta_c(c - c_c)]. \quad (1)$$

$$\beta_T = -\frac{1}{\rho_0} \left(\frac{\partial \rho}{\partial T} \right)_{P,c}; \quad \beta_c = -\frac{1}{\rho_0} \left(\frac{\partial \rho}{\partial c} \right)_{P,T}. \quad (2)$$

where β_c is the concentration volumetric coefficient of expansion and β_T is the thermal volumetric coefficient of expansion. The equations shown below are the governing equations used for flow, heat, and mass transfer respectively.

$$\frac{\partial u}{\partial x} + \frac{\partial v}{\partial y} = 0 \quad (3)$$

$$u \frac{\partial u}{\partial x} + v \frac{\partial u}{\partial y} = -\frac{1}{\rho} \frac{\partial p}{\partial x} + \nu \left(\frac{\partial^2 u}{\partial x^2} + \frac{\partial^2 u}{\partial y^2} \right) \quad (4)$$

$$u \frac{\partial v}{\partial x} + v \frac{\partial v}{\partial y} = -\frac{1}{\rho} \frac{\partial p}{\partial y} + \nu \left(\frac{\partial^2 v}{\partial x^2} + \frac{\partial^2 v}{\partial y^2} \right) + g [\beta_T(T - T_c) + \beta_c(c - c_c)] + \frac{B_o^2 \sigma}{\rho} v \quad (5)$$

$$u \frac{\partial T}{\partial x} + v \frac{\partial T}{\partial y} = \alpha \left(\frac{\partial^2 T}{\partial x^2} + \frac{\partial^2 T}{\partial y^2} \right) \quad (6)$$

$$u \frac{\partial c}{\partial x} + v \frac{\partial c}{\partial y} = D \left(\frac{\partial^2 c}{\partial x^2} + \frac{\partial^2 c}{\partial y^2} \right). \quad (7)$$

here, ν (kinematic viscosity), ρ (density), α (thermal diffusivity), B_o (magnetic induction), σ (electrical conductivity), and D (mass diffusivity) respectively. The dimensionless form of the equations mentioned above is written as follows:

$$X = \frac{x}{L}; \quad Y = \frac{y}{L}; \quad U = \frac{u}{U_{max}};$$

$$V = \frac{v}{U_{max}}; \quad \theta = \frac{T - T_c}{T_h - T_c}; \quad C = \frac{c - c_c}{c_h - c_c};$$

$$P = \frac{p}{\rho U_{max}^2}$$

Equations from (3) to (7) are written in the dimensionless form using the above dimensionless group.

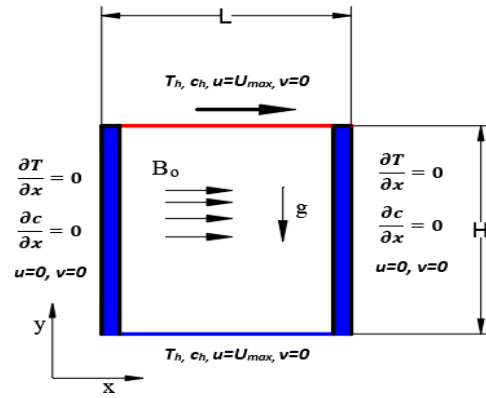


Figure 1. Schematic demonstration of the present problem

$$U \frac{\partial U}{\partial X} + V \frac{\partial U}{\partial Y} = -\frac{\partial P}{\partial X} + \frac{1}{Re} \left(\frac{\partial^2 U}{\partial X^2} + \frac{\partial^2 U}{\partial Y^2} \right) \quad (8)$$

$$U \frac{\partial U}{\partial X} + V \frac{\partial U}{\partial Y} = -\frac{\partial P}{\partial X} + \frac{1}{Re} \left(\frac{\partial^2 U}{\partial X^2} + \frac{\partial^2 U}{\partial Y^2} \right) \quad (9)$$

$$U \frac{\partial V}{\partial X} + V \frac{\partial V}{\partial Y} = -\frac{\partial P}{\partial Y} + \frac{1}{Re} \left(\frac{\partial^2 V}{\partial X^2} + \frac{\partial^2 V}{\partial Y^2} \right) + Ri(\theta + NC) + \frac{Ha^2}{Re} V \quad (10)$$

$$U \frac{\partial \theta}{\partial X} + V \frac{\partial \theta}{\partial Y} = \frac{1}{Re Pr} \left(\frac{\partial^2 \theta}{\partial X^2} + \frac{\partial^2 \theta}{\partial Y^2} \right) \quad (11)$$

$$U \frac{\partial C}{\partial X} + V \frac{\partial C}{\partial Y} = \frac{1}{Re Sc} \left(\frac{\partial^2 C}{\partial X^2} + \frac{\partial^2 C}{\partial Y^2} \right) \quad (12)$$

1. Reynolds number (Re) : $\frac{U_{max} L}{\nu}$
2. Richardson number (Ri) : $\frac{Gr_T}{Re^2}$
3. Buoyancy ratio (N) : $\frac{\beta_c(c_h - c_c)}{\beta_T(T_h - T_c)} = \frac{Gr_c}{Gr_T}$
4. Hartmann number (Ha) : $B_o L \sqrt{\frac{\sigma}{\rho U_{max}^2}}$
5. Prandtl number (Pr) : $\frac{\nu}{\alpha}$
6. Schmidt number (Sc) : $\frac{\nu}{D}$
7. Thermal Grashof number (Gr_T) : $\frac{g \beta_T (T_h - T_c) L^3}{\nu^2}$
8. solutal Grashof number (Gr_c) : $\frac{g \beta_c (c_h - c_c) L^3}{\nu^2}$

Following are the boundary condition of the problem selected,

Upper wall: $u = U_{max}; v = 0; T = T_h; c = c_h$

Lower wall: $u = v = 0; T = T_c; c = c_c$

Left and Right walls: $u = v = 0; \frac{\partial T}{\partial x} = \frac{\partial C}{\partial x} = 0$

3. Numerical Solution

The discretization of governing equations was done by FVM using uniform grid sizes. Pressure-velocity coupling equations were solved using the SIMPLE algorithm technique derived by (50). Convection-diffusion terms are solved by a central difference scheme. Equations obtained after discretization was solved iteratively using C++ code. In this selected criterion the convergence of the solution for the equations is 10^{-7} . Nusselt number and Sherwood number are used to analyze the behavior of flow and the thermal characteristics of the fluid inside the cavity. Convective heat and species transfer inside the cavity are analyzed using flow behavior. Local and average Nu and Sh of the cavity hot wall are calculated as follows:

$$Nu = -\left(\frac{\partial \theta}{\partial Y}\right)_{Y=H}; \quad Nu_{avg} = \int_0^L Nu dX. \quad (13)$$

The following equations are used to calculate Local Sh and average Sh,

$$Sh = -\left(\frac{\partial C}{\partial Y}\right)_{Y=H}; \quad Sh_{avg} = \int_0^L Sh dX. \quad (14)$$

4. Result and Discussion

4.1. Grid Independence Study and Validation of Codes

A rectangular domain is used for the grid study. Several computations for the average Nu and Sh were performed for the uniform structured grid size from 41×21 to 201×101 . The aspect ratio (L/H) selected for the grid-independent analysis is 2.0, therefore the number of grid sizes in the x-axis is two times the y-axis. Results of the simulation show an error of 0.6385 between the grid size 41×21 and 81×41 in average Nu and 10.63 in average Sh, 0.7918 in average Nu, and 2.3226 in average Sh between grid size 81×41 and 121×61 , 0.5901 in average Nu and 0.368 in average Sh between grid size 121×61 and 161×81 , 0.3551 in average Nu and 0.0736 in average Sh between grid size 161×81 and 201×101 is observed. There is a marginal variation in error is observed for both average Nu and Sh when the grid size changes from 121×61 to 161×81 . Therefore 121×61 grid size is used for further analysis. Temperature and streamline contours of the present study are compared with Ji, et al. [49] as shown in Figure 2, and found good agreement between both results. Table 1 presents the validation of codes for the average Nu and the literature results. Obtained results show an excellent match with the literature results.

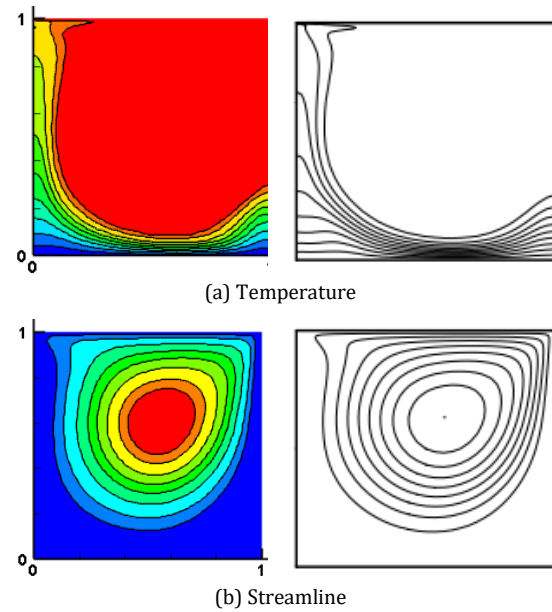


Figure 2. Comparison of (a) temperature and (b) streamline of the present study (left side) with Ji et al. [49] (right side)

Table 1. Comparison of avg. Nu of present work with the literature results for $Gr=100, Pr=0.71$ at different Re.

Literature	Re		
	100	400	1000
Present work	2.02	3.98	6.20
Hussain <i>et al.</i> [51]	2.03	4.07	6.58
Kefayati <i>et al.</i> [52]	2.09	4.08	6.54
Sheremet and Pop [53]	2.05	4.09	6.70
Sharif [54]	-	4.05	6.55
Iwatsu <i>et al.</i> [55]	1.94	3.84	6.33
Waheed [56]	2.03	4.02	6.48

4.2. Effect of the Magnetic Field, Prandtl number, and Aspect ratio

The temperature, concentration, and flow fields are shown below for different Ha, Pr, and aspect ratios. Thermal and concentration lines are orthogonal to the left and right walls since they are adiabatic walls. This ensures no heat and mass transfer through the walls. In streamline contour, a vertex is seen on the right portion of the domain due to the movement of the upper edge in the positive x-direction and the diffusion due to the buoyancy force. Figures 3(a), 3(b), and 3(c) show the variation of the contours of temperature, concentration, and streamlines for different Ha. The pattern of the contour plots indicates, the magnetic field greatly affects the temperature and concentration distribution inside the cavity. The negative effect is observed inside the cavity for both Nu and Sh as the value of Ha increases. This negative effect is mainly due to a decrease in the flow velocity due to the increase in the magnetic effect.

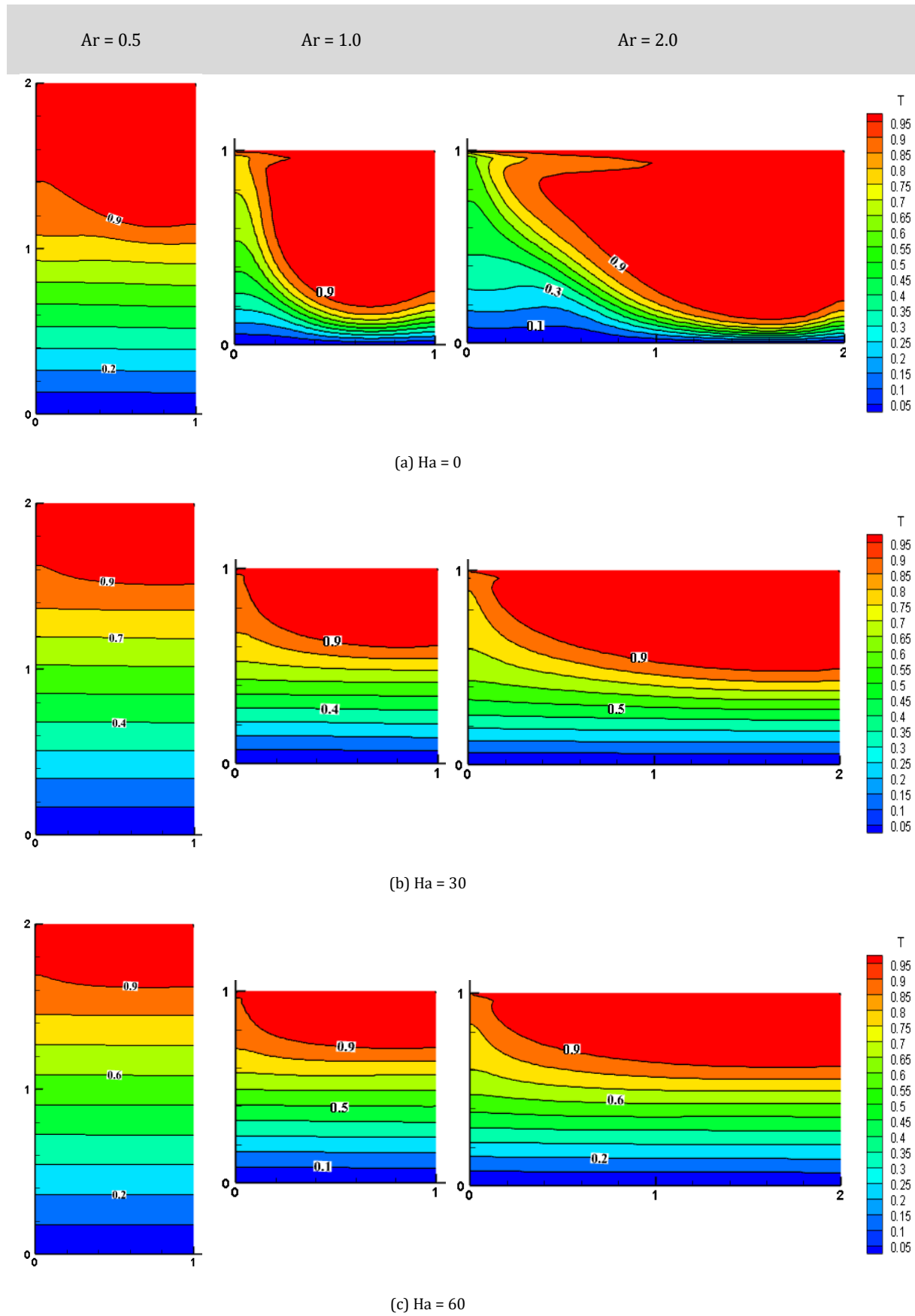


Figure 3 (a). Temperature contours at different Ha and Ar for $Re = 100$, $Pr = 7.0$, and $Grt = 1000$

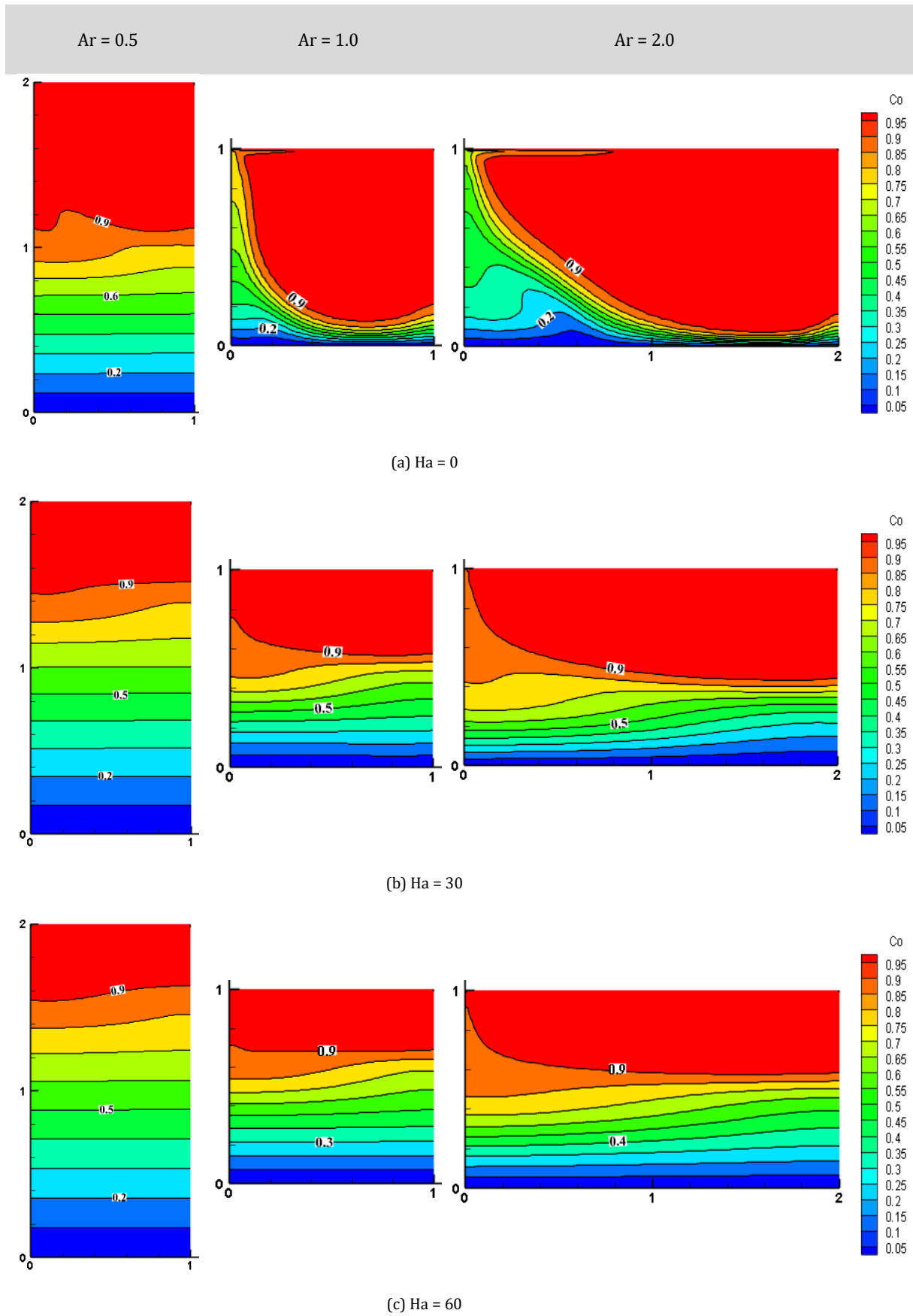


Figure 3 (b). Concentration contours at different Ha and Ar for $Re = 100$, $Pr = 7.0$, and $Grt = 1000$

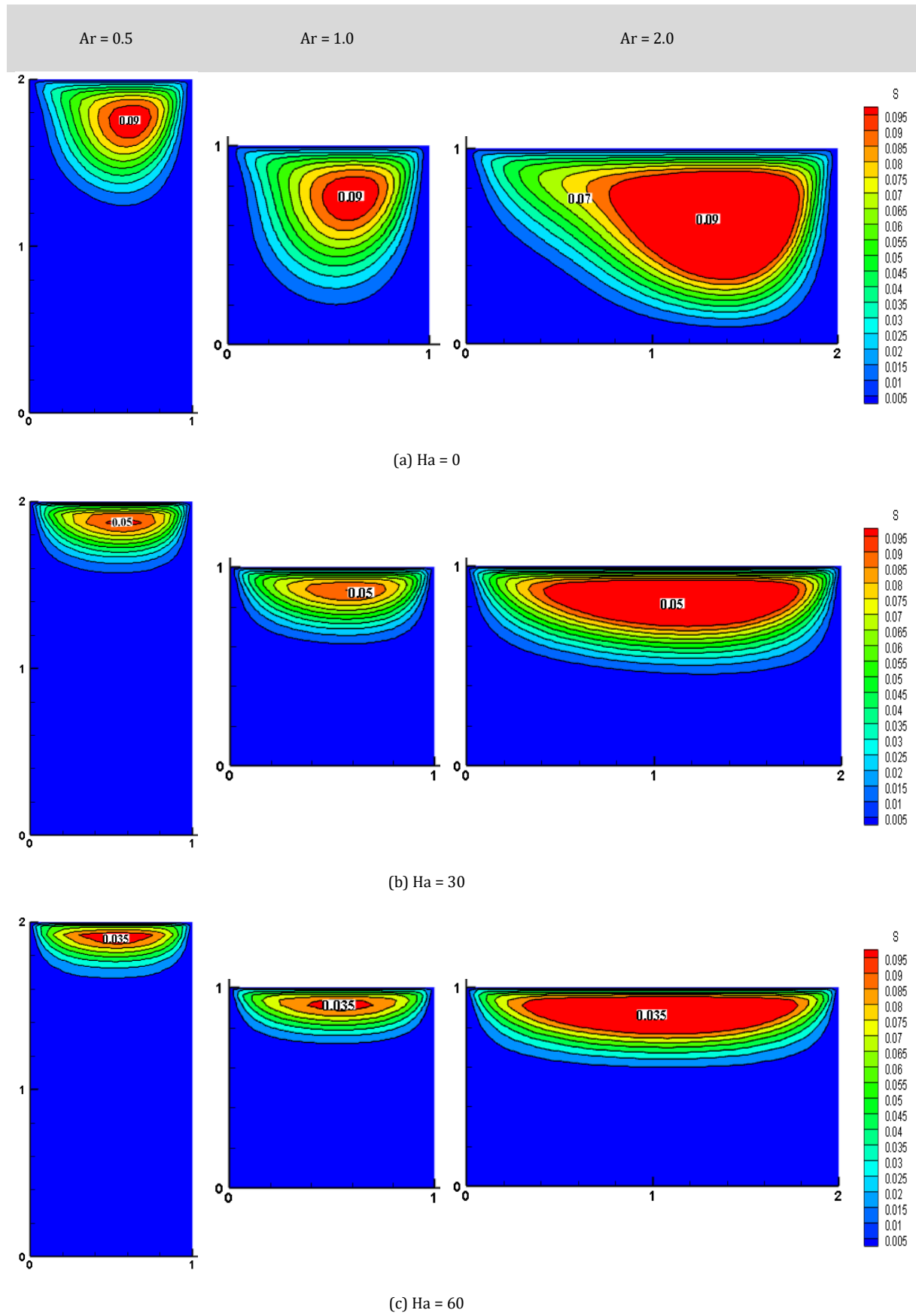


Figure 3 (c). Streamline contours at different Ha and Ar for $Re = 100$, $Pr = 7.0$, and $Grt = 1000$

Figures 4(a), 4(b), and 4(c) show the effect of Pr on the thermal performance of the cavity. More concentration and temperature distribution are observed as the value of Pr increases. An increase in the avg. Nu and Sh at the hot wall indicate improvement in the heat and mass transfer rate.

Compare to the thermal distribution, the magnitude of the concentration distribution is observed more because Le is maintained as 5. Not much change is observed in streamline contours because Ha is maintained as high and at the high magnetic field, flow velocity retards.

The effect of an aspect ratio of the cavity on heat and the species transfer rate is shown in Figure 5. Three different aspect ratios are taken for the analysis. Flow is observed as very weak for an aspect ratio less than one but increases for an aspect ratio greater than one. This is mainly due to an increase in the supply of heat at the top side of the cavity.

CFD analysis for the optimization of the performance of lid-driven cavity for heat and mass transfer has been performed by selecting the aspect ratio, thermal Grashof number, Reynolds number, Hartmann number and Prandtl number as the control parameters and average Nu and Sh are the responses.

Taguchi method of experimental design is used in this analysis for optimizing the performance of lid-driven cavities. In the following session, the method used for the present numerical analysis has been discussed.

4.3. Taguchi Method

Taguchi method is used to find the optimal combination of selected parameters for maximum performance of the domain in terms of average Nusselt and Sherwood numbers.

The parameters considered for the analysis are the cavity aspect ratio (Ar), Thermal Grashoff number (Gr), Reynold's number (Re), Hartmann number (Ha), and Prandtl number (Pr), and their level are shown in Table II.

Normally in the Taguchi method, L8, L16, L18, and L27 orthogonal arrays are used for parameter assignment. In this analysis, the L27 orthogonal array is considered which consists of 27 samples data shown in Table III.

The CFD codes were run as per Taguchi L27 combinations. The software used for the Taguchi analysis is Minitab 15.0.

The results of the Taguchi analysis and CFD simulation are shown in Table IV. Taguchi method reduces the number of experiments a researcher is

required to perform which intern reduces the cost involved. The signal to Noise Ratio (S/N ratio) plot is used to discover the dominant level of the selected parameters.

The rank for each factor is assigned depending on the delta value obtained from the S/N ratio response table. The minimum rank in the table shows the maximum influence of factors on the output response. Five active parameters at three different levels were analyzed.

An optimal combination of levels of these factors for extreme performance of the domain is found. Graphs and contour plots are also used to investigate the heat and species transfer pattern in the cavity.

The present analysis uses L27 orthogonal with DOF 26. Five parameters and each parameter at 3 levels require 35=243 experiments in a full factorial design, however, the Taguchi design requires only 27 runs which will reduce the time and cost.

Table 2. Levels of independent parameters

Independent Factors	Level-1	Level-2	Level-3
Ar	0.5	1	2
Grt	10 ³	10 ⁴	10 ⁵
Re	100	500	1000
Ha	0	30	60
Pr	0.7	7	13

The S/N ratio is used to measure the variation in the Taguchi analysis method. The choice of the S/N ratio definition is based on the property response parameter or the characteristic value. Three different types of characteristic values are NB (Normal is the Best), SB (Smaller is the Best), and LB (Larger is the Better).

The main aim of the present analysis is to maximize the heat and mass transfer rate; therefore, LB is selected for the analysis. The S/N ratio calculated for the selected characteristic values is shown in Table IV and is calculated using the following expression, Eq. (15).

$$S/N_{LB} = -10 \log \left[\frac{1}{r} \sum_{j=1}^r \frac{1}{y_j^2} \right] \quad (15)$$

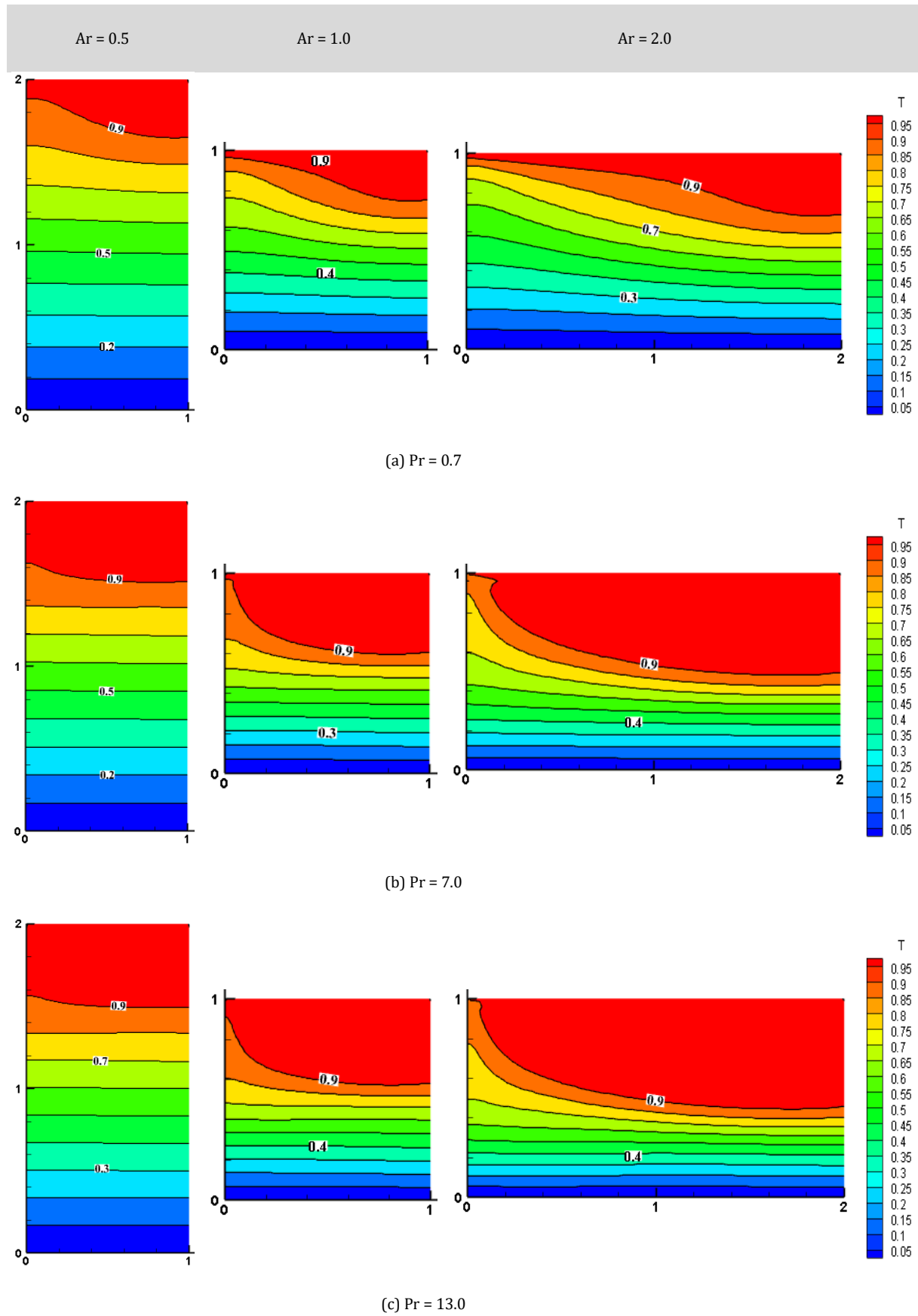


Figure 4 (a). Temperature contours at different Pr and Ar for $Re = 100$, $Ha = 0$, and $Grt = 1000$

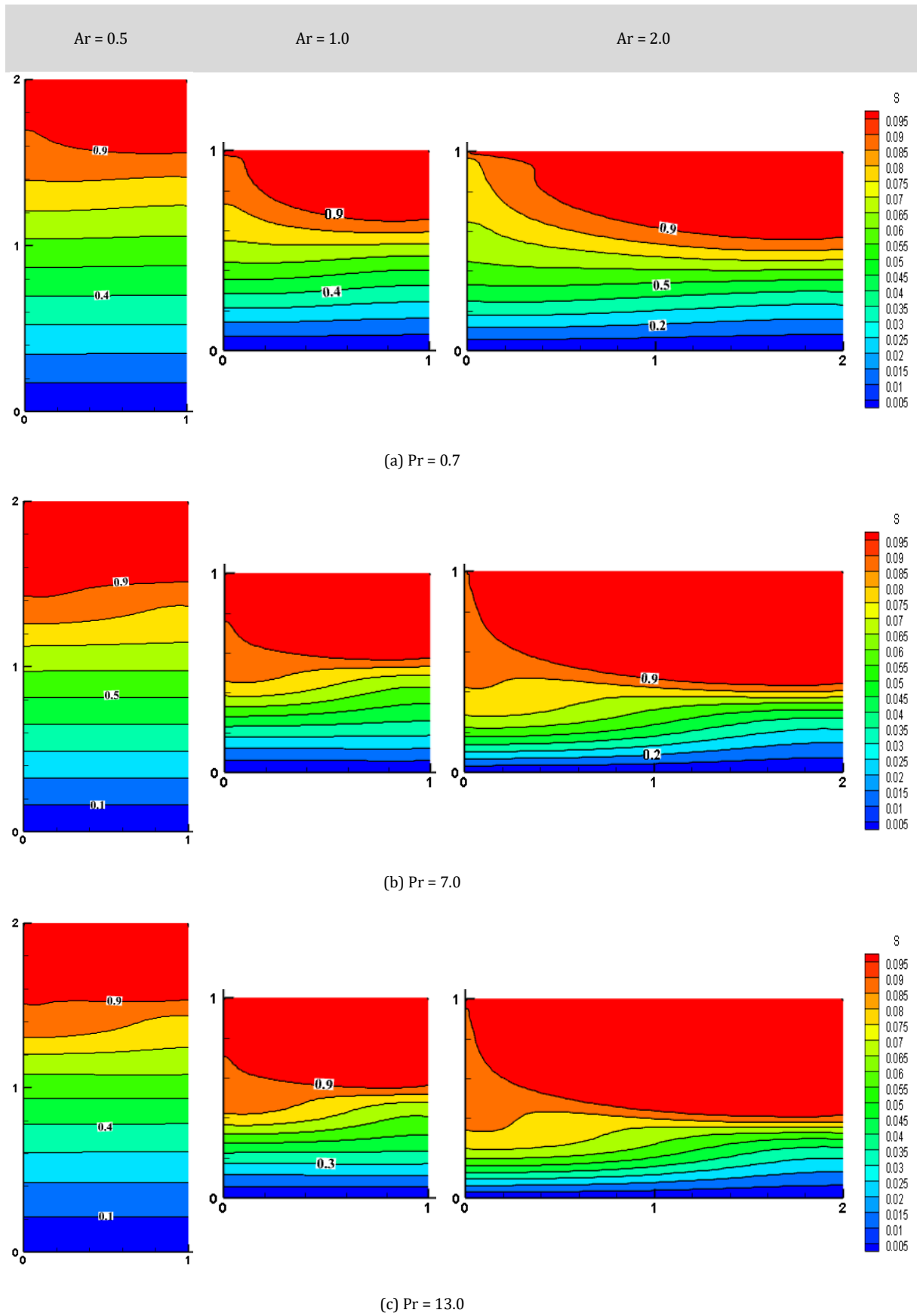


Figure 4 (b). Concentration at different Pr for $Re = 100$, $Ha = 0$, and $Grt = 1000$

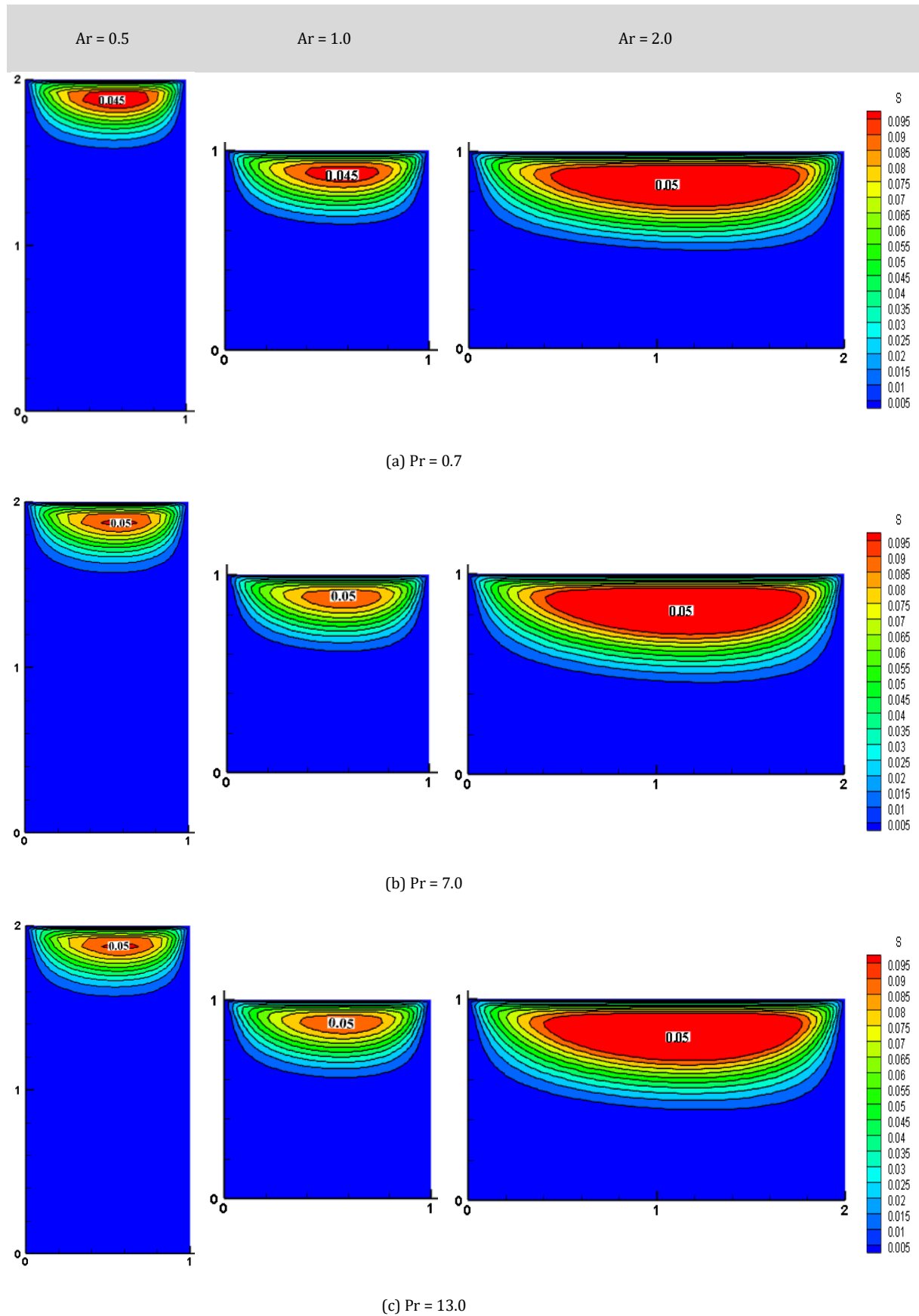


Figure 4 (c). Streamline contours at different Pr and Ar for Re = 100, Ha=0, and Grt=1000

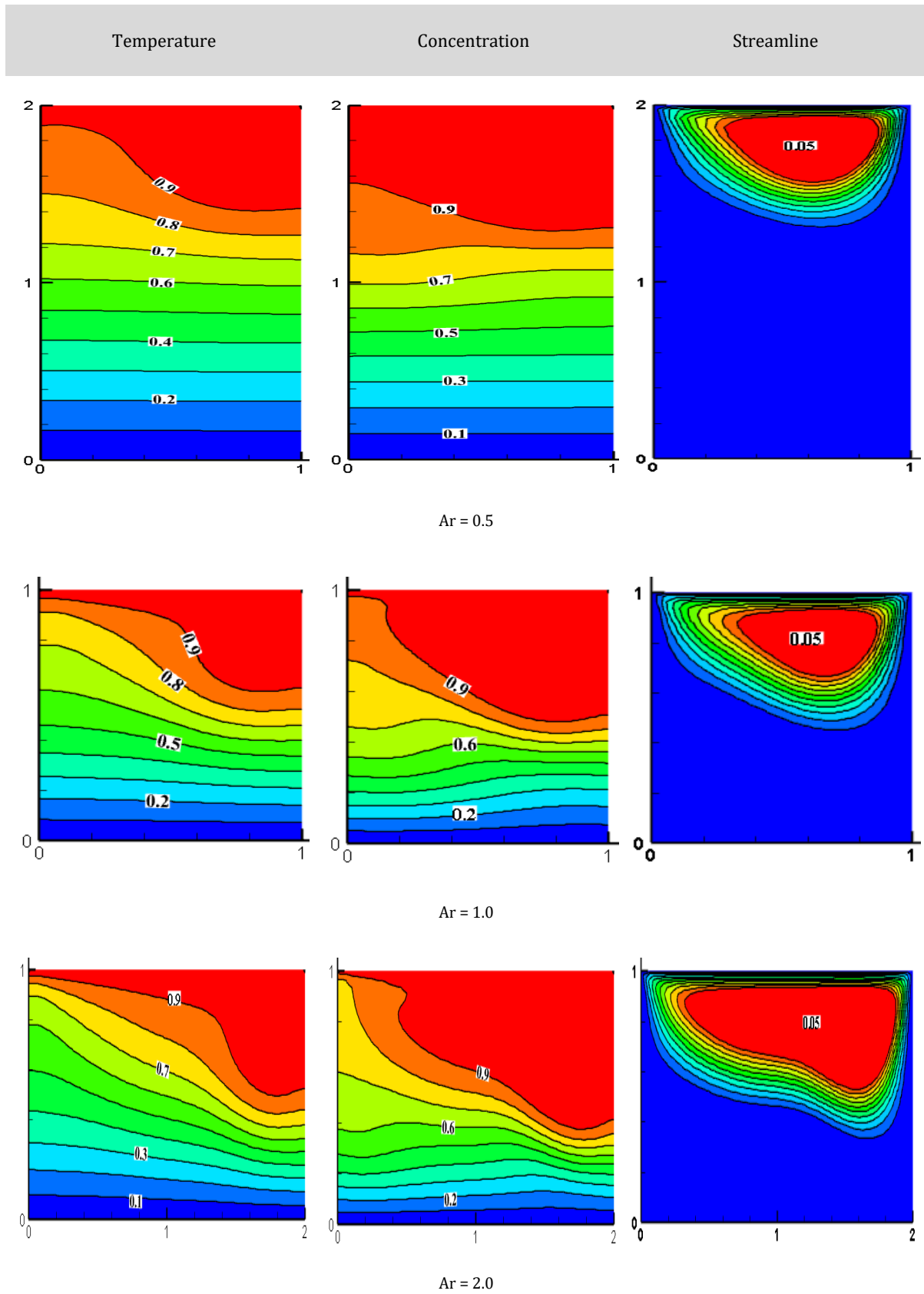


Figure 5. Temperature, Concentration and Streamline contours at different Ar for Re = 100, Pr=0.7, Grt=1000 and Ha = 0

Table 3. L27 Taguchi orthogonal array table

Iteration No.	Factors				
	Ar	Grt	Re	Ha	Pr
1	0.5	1000	100	0	0.7
2	0.5	1000	100	0	7
3	0.5	1000	100	0	13
4	0.5	10000	500	30	0.7
5	0.5	10000	500	30	7
6	0.5	10000	500	30	13
7	0.5	100000	1000	60	0.7
8	0.5	100000	1000	60	7
9	0.5	100000	1000	60	13
10	1	1000	500	60	0.7
11	1	1000	500	60	7
12	1	1000	500	60	13
13	1	10000	1000	0	0.7
14	1	10000	1000	0	7
15	1	10000	1000	0	13
16	1	100000	100	30	0.7
17	1	100000	100	30	7
18	1	100000	100	30	13
19	2	1000	1000	30	0.7
20	2	1000	1000	30	7
21	2	1000	1000	30	13
22	2	10000	100	60	0.7
23	2	10000	100	60	7
24	2	10000	100	60	13
25	2	100000	500	0	0.7
26	2	100000	500	0	7
27	2	100000	500	0	13

Where y_j is the value of j th response data and r is the iteration number. The optimization of the selected parameters has been obtained by linking the Taguchi and ANOVA method. Figures 6 and 7 show the effect of independent variables on the average Nusselt and Sherwood numbers based on the S/N ratio. Steep variations of S/N ratios for Pr and Re indicate that these factors have the maximum influence to control the heat and mass transfer rates. As the aspect ratio increases the heat transfer rate also increases, this is mainly due to an increase in the length of the edge compared to height. The maximum value of 11.164 is found at level 3 of the aspect ratio and then the sharp reduction in the S/N ratio is found in other levels of Ar. The effect of the thermal Grashof number is the least preference to control the value of Nu and Sh is observed in the same graph. No difference in the value of S/N ratios of Nu and Sh is observed by varying the value of Ha from 30 to 60. As Reynold's number increases the heat and mass transfer rate also increases this is mainly because of the increase in the

mean velocity of the fluid. The effect of Ha and Grt in controlling the heat and mass transfer is comparatively less. Tables V and VI describe the rank of each parameter in controlling the thermal efficiency of the cavity. The order of significance is Pr, Re, Ar, Ha, and Grt in controlling both heat and mass transfer rates. The same pattern is observed in the S/N graph. Level 3 of Pr, Re, and Ar, and level 1 of Grt and Ha are the more significant levels. The corresponding values of the S/N ratio of average Nu are 12.040, 11.103, 11.164, 10.333, and 7.820 and similarly, the same order and level of significance are observed in controlling the mass transfer rate. The corresponding values of the S/N ratio of average Sh are 18.522, 14.080, 14.532, 12.229, and 13.527 respectively.

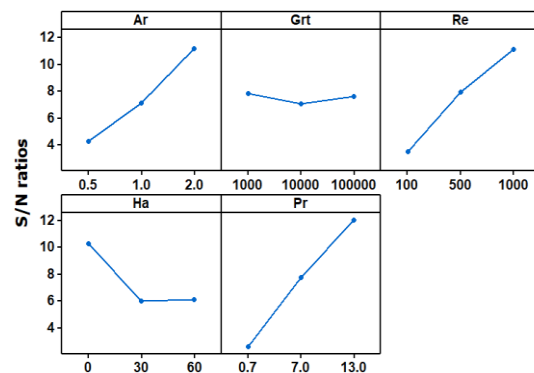


Figure 6. Graph of Independent variables effect on avg. Nu mean S/N ratios

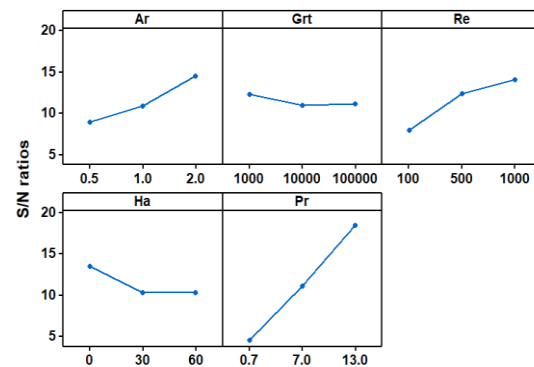


Figure 7. Graph of Independent variables effect on avg. Sh mean S/N ratios

4.4. Analysis of variance

The significance of different parameters to control heat and mass transfer in a lid-driven cavity is performed by adapting the method of analysis of variance (ANOVA). Five parameters at 3 levels have been considered for the analysis. The main purpose of this study is to find the finest arrangement of the selected factors to maximize the heat and species transfer rate. The significance of factors to control the thermal properties of the cavity is analyzed by taking a 95 % confidence level. The temperature and species transfer rates are analyzed using average Nu and Sh

values. Tables VII and VIII elucidate the significance and sum of squares of average Nu and Sh respectively. The contribution of each parameter to the total sum of squares (SS) is also seen in the same tables. This contribution percentage gives a clear idea about the importance of each factor in deciding the response. Using all those tables, a combination of parameters for optimal performance of the cavity can be easily predicted.

Table 4. S/N ratio table for average Nu and Sh

Trial No.	avg. Nu	S/N ratio	avg. Sh	S/N ratio
1	1.185	1.477	1.302	2.293
2	1.512	3.594	2.808	8.968
3	1.795	5.082	4.673	13.391
4	1.113	0.929	1.446	3.202
5	1.316	2.386	2.611	8.338
6	1.775	4.986	4.643	13.335
7	1.085	0.711	1.605	4.110
8	2.144	6.623	2.501	7.962
9	4.174	12.412	8.374	18.459
10	1.148	1.200	1.379	2.793
11	2.670	8.332	4.663	13.373
12	3.084	9.781	8.373	18.457
13	2.084	6.377	2.719	8.689
14	4.925	13.847	6.461	16.206
15	8.960	19.046	10.605	20.510
16	1.043	0.368	1.175	1.402
17	1.244	1.897	1.609	4.130
18	1.382	2.812	4.113	12.284
19	1.780	5.009	2.852	9.103
20	5.852	15.346	7.951	18.007
21	10.665	20.559	15.267	23.675
22	1.054	0.456	1.256	1.979
23	1.348	2.596	1.724	4.729
24	4.437	12.943	12.038	21.611
25	2.326	7.332	2.582	8.237
26	5.957	15.500	8.387	18.472
27	10.889	20.740	17.738	24.978

Table 5. Response table of S/N ratio on avg. Nu

Level	Ar	Grt	Re	Ha	Pr
1	4.244	7.820	3.469	10.333	2.651
2	7.073	7.063	7.910	6.032	7.791
3	11.164	7.599	11.103	6.117	12.040
Delta	6.920	0.757	7.634	4.300	9.389
Rank	3	5	2	4	1

Table 6. Response table of S/N ratio on avg. Sh

Level	Ar	Grt	Re	Ha	Pr
1	8.895	12.229	7.865	13.527	4.645
2	10.872	10.956	12.354	10.386	11.132
3	14.532	11.115	14.080	10.386	18.522
Delta	5.637	1.274	6.215	3.141	13.877
Rank	3	5	2	4	1

Table 7. ANOVA table for avg. Nu

Factors	DOF	(SS)	Variance	Value-F	Value-P	% Contribution
Ar	2	45.231	22.615	7.44	0.005	20.47
Grt	2	0.655	0.327	0.11	0.898	0.30
Re	2	39.764	19.882	6.54	0.008	18
Ha	2	20.412	10.206	3.36	0.061	9.24
Pr	2	66.228	33.114	10.90	0.001	29.98
Error	16	48.620	3.039	-	-	-
Total	26	220.910	-	-	-	100

Table 8 shows the analysis of variance for average Nu. From the P-value, it is clear that Pr, Ar, and Re are the significant factors to control the heat and mass transfer rate. The percentage contribution of Pr is more in both heat and mass transfer and which are 29.98% and 53% respectively. The contribution of Grt is comparatively very less in both cases; therefore, this parameter can be neglected for further analysis. The most optimal combination is Ar = 2.0, Grt =103, Re = 1000, Ha = 0 and Pr = 13.0. The residual plots were obtained by feeding the data obtained from the numerical studies into analytical software as shown in Figure 8 for average Nu and Figure 9 for average Sh. A normal distribution is observed in the residual plots indicating good agreement about the validity of the results (Joardar, Das, and Sutradhar, [57]). The normal probability plot shows the linear relationship which indicates error terms are distributed normally. The histogram of residuals indicates that residuals are distributed normally. From the above plots, it is clear that there is a good correlation between fitted values and the observed values.

The regression model equation for average Nu and Sh for the selected parameters is shown in equations 16 and 17. The standard error (S) of the average Nu regression model is found as 1.57 and for the average Sh regression model is obtained as 2.32. The smaller values of S indicate that the model offers better fits due to minor residuals.

$$\text{Avg Nu} = -2.12+2.07\text{Ar}+0.000002\text{Grt}+0.00326\text{Re}-0.0343\text{Ha}+0.310\text{Pr} \tag{16}$$

$$\text{Avg Sh} = -3.56+2.98\text{Ar}+0.000002 \text{ Grt}+0.00333\text{Re}-0.0284\text{Ha}+0.626\text{Pr} \tag{17}$$

From these equations, it is clear that Ar, Grt, Re, and Pr have a positive impact on average Nu and average Sh, whereas Ha has a negative impact.

Table 8. ANOVA table for avg. Sh

Factors	DOF	(SS)	Variance	Value-F	Value-P	% Contribution
Ar	2	93.846	46.923	8.53	0.003	17.78
Grt	2	2.060	1.030	0.19	0.831	0.39
Re	2	46.392	23.196	4.22	0.034	8.79
Ha	2	17.766	8.883	1.61	0.230	3.36
Pr	2	279.705	139.853	25.42	0.000	53
Error	16	88.020	5.501	-	-	-
Total	26	527.788	-	-	-	100

4.5. Confirmation Test

A confirmation test was performed for the optimum combination. The simulations are performed using the optimal combination of Ar, Grt, Re, Ha, and Pr. The obtained results from this combination are compared with the results of all the simulations used in the analysis.

It is observed that the highest value of Nu and Sh is obtained in optimum combination. This confirms that the optimum combination is the best combination for maximizing heat and mass transfer.

The thermal, concentration, and flow fields for the optimal combination obtained from Taguchi and ANOVA results are offered in the form of isotherms, isoconcentration, and streamlines in Figure10.

The nature of the contours is perfectly validated with the obtained results. Considering the wide range of applications mentioned in the introduction section about the MHD flows and diffusion effect in controlling the thermal performance in medical and biomedical, power production, furnace design, and production of glass sheets, the present numerical results help to select the best combinations to improve the performance.

The value of average Nu and Sh obtained from the confirmation test for the optimal combination is 18.176 and 34.668 which clearly shows the highest values compare to all other combinations used in the analysis.

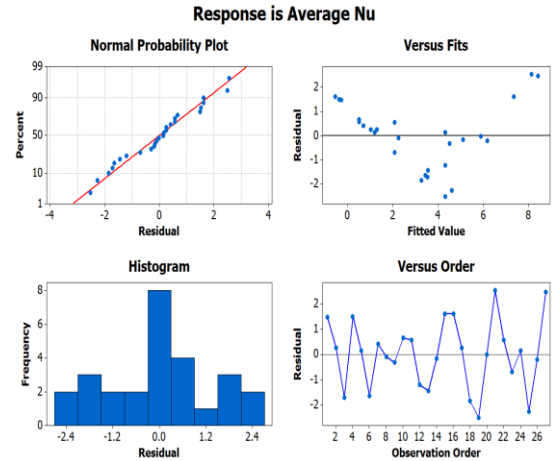


Figure 8. Average Nu residual plot

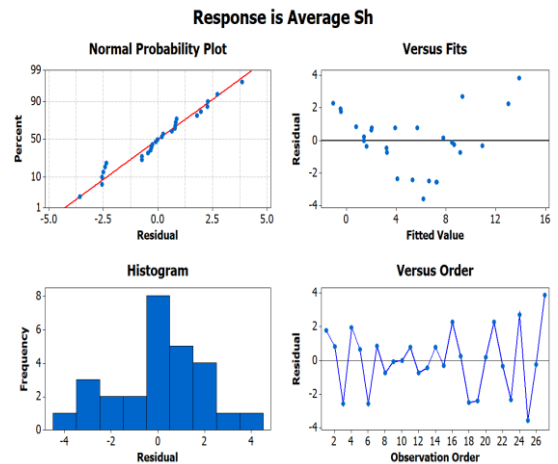


Figure 9. Average Sh residual plot

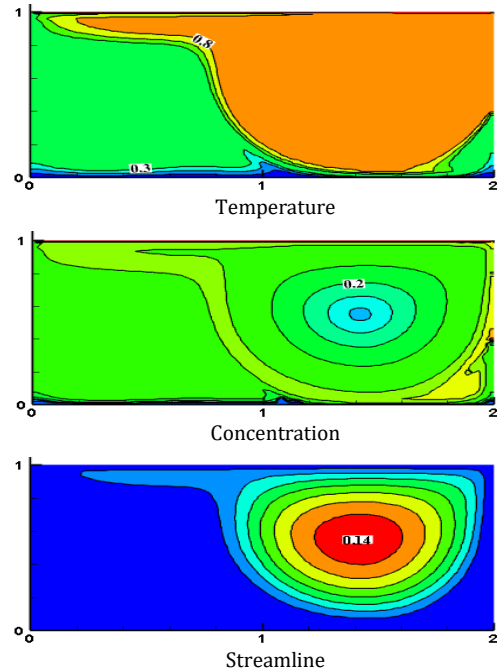


Figure 10. Temperature, concentration and streamline contours at an optimized combination

Conclusion

In this work effect of different dimensionless numbers and their optimization for the supreme performance of the selected domain is numerically performed using a lid-driven cavity. The performance of the cavity is arbitrated using avg Nu and Sh values. The results obtained from the analysis are as follows.

- With an increase in Pr value to the third level, the heat transfer rate increases by 79.98%, and mass transfer by 74.92% which is the most significant parameter.
- Similarly, an increase in Re improves the heat transfer rate by 68.76% and the mass transfer rate by 44.140%. Re is the second significant parameter for the selected range of values.
- An increase in the aspect ratio improves the heat transfer rate by 61.98% and the mass transfer rate by 38.79%.
- The optimum level for the maximum performance of the cavity is obtained as Ar = 2.0, Grt = 103, Re = 1000, Ha = 0.0 and Pr = 13.0.
- The average Nu and Sh are dependent maximum on Pr, Re, and Ar and the effect of Grt and Ha are comparatively negligible.
- The value of average Nu and Sh obtained from the confirmation test for the optimal combination is 18.176 and 34.668 which clearly shows the highest values compare to all other combinations used in the analysis.
- The regression model shows a positive impact of all selected parameters on average Nu and Sh and a negative impact with Ha.

Nomenclature

Ar	Aspect ratio
Bo	Magnetic induction (tesla)
c	Concentration
C	Dimensionless concentration
D	Mass diffusivity(m ² s ⁻¹)
g	Gravitational acceleration(ms ⁻²)
GrC	Grashof number concentration
GrT	Grashof number temperature
h	Heat transfer coefficient(Wm ⁻² K ⁻¹)
hs	Solutal transfer coefficient(ms ⁻¹)
H	Enclosure height(m)
Ha	Hartmann number
L	Enclosure length(m)
Le	Lewis number
N	Buoyancy ratio
Nu	Nusselt number
p	Pressure(Nm ⁻²)
P	Non-dimensional pressure
Pr	Prandtl number
Re	Reynolds number
Ri	Richardson number
Sc	Schmidt number
Sh	Sherwood number

T	Dimensional temperature(K)
u,v	Dimensional velocity component (ms ⁻¹)
U,V	Dimensionless velocity components
x,y	Dimensional co-ordinates
X,Y	Dimensionless Cartesian coordinates
r	Iteration number

Greek symbol

α	Thermal diffusivity(m ² s ⁻¹)
β	Fluid thermal expansion coefficient(K ⁻¹)
θ	Dimensionless temperature
ν	Effective kinematic viscosity(m ² s ⁻¹)
ρ	Density(kgm ⁻³)
σ	Fluid electrical conductivity(sm ⁻¹)

Subscripts

avg	Average
C	Cold, Concentration
h	Hot
T	Thermal
max	Maximum

References

- [1]. P.M. Rodrigues, C. Biserni, C.C. de Escobar, L.A.O. Rocha, L.A. Isoldi, E.D. dos Santos, Geometric optimization of a lid-driven cavity with two rectangular intrusions under mixed convection heat transfer: A numerical investigation motivated by constructal design, International Communications in Heat and Mass Transfer, 117, 104759, (2020)
- [2]. S. Baag, S.R. Mishra, G.C. Dash, M.R.Acharya, Numerical investigation on MHD micropolar fluid flow toward a stagnation point on a vertical surface with heat source and chemical reaction, Journal of King Saud University - Engineering Sciences, 29(1), 75-83, (2017).
- [3]. M.M. Khader, and A.M. Megahed, Numerical simulation using the finite difference method for the flow and heat transfer in a thin liquid film over an unsteady stretching sheet in a saturated porous medium in the presence of thermal radiation, Journal of King Saud University - Engineering Sciences, 25(1), 29-34, (2013).
- [4]. Z. Li, A.K. Hussein, O.Younis, S.Rostami, W. He, Effect of alumina nano-powder on the natural convection of water under the influence of a magnetic field in a cavity and optimization using RMS: Using empirical correlations for the thermal conductivity and a sensitivity analysis, International Communications in Heat and Mass Transfer, 112, 104497, (2020).
- [5]. D. Iyi, and R. Hasan, Numerical investigation of the effect of moisture on buoyancy-driven low turbulence flow in an enclosed cavity, International Journal of Heat and Mass Transfer, 136, 543-554, (2019).

- [6]. F. Li, W. Zhu, and H. He, Numerical optimization on microchannel flow and heat transfer performance based on field synergy principle, *International Journal of Heat and Mass Transfer*, 130, 375–385, (2019).
- [7]. M. Mohammadi, A. A. Reza, N. Farouji, M.P. Fard, An optimization of heat transfer of nanofluid flow in a helically coiled pipe using Taguchi method, *Journal of Thermal Analysis and Calorimetry*, 138(2), 1779–1792, (2019).
- [8]. S. Srinivas, T. Malathy, A.S. Reddy, A note on thermal-diffusion and chemical reaction effects on MHD pulsating flow in a porous channel with slip and convective boundary conditions, *Journal of King Saud University - Engineering Sciences*, 28(2), 213–221, (2016)
- [9]. R. Nath and M. Krishnan, Optimization of double diffusive mixed convection in a BFS channel filled with Alumina nanoparticle using Taguchi method and utility concept, *Scientific Reports*, Springer US, 9(1), 1–19, (2019).
- [10]. B. Raei, Statistical analysis of nanofluid heat transfer in a heat exchanger using Taguchi method, *Journal of heat and mass transfer research*, 8(1), 29–38, (2021).
- [11]. R. Kishore, A.M. Sanghadasa S. Priya, Optimization of segmented thermoelectric generator using Taguchi and ANOVA techniques, *Scientific Reports*. Springer US, 7(1), 1–15, (2017).
- [12]. N. Iftikhar, D. Baleanu, M.B. Riaz, S. M. Husnine, Heat and mass transfer of natural convective flow with slanted magnetic field via fractional operators, *Journal of Applied and Computational Mechanics*, 7(1), 189–212, (2021).
- [13]. M. Hatami, D. Song, D. Jing, Optimization of a circular-wavy cavity filled by nanofluid under the natural convection heat transfer condition, *International Journal of Heat and Mass Transfer*, 98, 758–767, (2016).
- [14]. Kumara, J.B. Joshi, A.K. Nayak, P.K. Vijayan, 3D CFD simulations of air cooled condenser-III: Thermal-hydraulic characteristics and design optimization under forced convection conditions, *International Journal of Heat and Mass Transfer*, 93, 1227–1247, (2016).
- [15]. M. Mamourian, K.M. Shirvan, R.Ellahi, A.B. Rahimia, Optimization of mixed convection heat transfer with entropy generation in a wavy surface square lid-driven cavity by means of Taguchi approach, *International Journal of Heat and Mass Transfer*, 102, 544–554, (2016).
- [16]. K.M. Shirvan, K. M, M. Mamourian, R. Ellahi, Numerical investigation and optimization of mixed convection in ventilated square cavity filled with nanofluid of different inlet and outlet port, *International Journal of Numerical Methods for Heat and Fluid Flow*, 27(9), 2053–2069, (2017).
- [17]. S. Soleimani, D.D. Ganji, M. Gorji, H.Bararnia, E.Ghasemi, Optimal location of a pair heat source-sink in an enclosed square cavity with natural convection through PSO algorithm, *International Communications in Heat and Mass Transfer*, 38(5), 652–658, (2011).
- [18]. R.R. Madadi, and C. Balaji, Optimization of the location of multiple discrete heat sources in a ventilated cavity using artificial neural networks and micro genetic algorithm, *International Journal of Heat and Mass Transfer*, 51(9–10), 2299–2312, (2008).
- [19]. M. Paulo, G. Menon, M.D. Ramos, Mixed convection study in a ventilated square cavity using nanofluids, *Journal of heat and mass transfer research*, 6(2), 143–153, (2019).
- [20]. J. Alinejad and J.A. Esfahani, Taguchi design of three dimensional simulations for optimization of turbulent mixed convection in a cavity, *Meccanica*, 52(4–5), pp. 925–938, (2017).
- [21]. V. Gorobets, V. Trokhaniak, Y. Bohdan, I. Antypov, Numerical Modeling of Heat Transfer and Hydrodynamics in Compact Shifted Arrangement Small Diameter Tube Bundles, *Journal of Applied and Computational Mechanics*, 7(1), pp. 292–301.
- [22]. M.Hatami, J. Zhou, J. Geng, D. Song, D. Jing, Optimization of a lid-driven T-shaped porous cavity to improve the nanofluids mixed convection heat transfer, *Journal of Molecular Liquids*, 231, 620–631, (2017).
- [23]. V.K. Mathew, and T.K. Hotta, Numerical investigation on optimal arrangement of IC chips mounted on a SMPS board cooled under mixed convection, *Thermal Science and Engineering Progress*, 7, 221–229, (2018).
- [24]. P. Pichandi and S. Anbalagan, Natural convection heat transfer and fluid flow analysis in a 2D square enclosure with sinusoidal wave and different convection mechanism, *International Journal of Numerical Methods for Heat and Fluid Flow*, 28(9), 2158–2188, (2018).
- [25]. S. Mirzakhani, K.M. Shirvan, M. Mamourian, Ali J.Chamkha, Increment of mixed convection heat transfer and decrement of drag coefficient in a lid-driven nanofluid-filled cavity with a conductive rotating circular cylinder at different horizontal locations: A sensitivity analysis, *Powder Technology*, 305, 495–508, (2017).
- [26]. A.H. Pordanjani, S.M. Vahedi, S. Aghakhani, M. Afrand, H.F. Öztöp, N.A. Hamdeh, Effect of magnetic field on mixed convection and entropy generation of hybrid nanofluid in an inclined enclosure: Sensitivity analysis and optimization, *European Physical Journal Plus*, 134(8), 412, (2019).

- [27]. Behbahan, A. Noghrehabadi, C.P. Wong, I. Pop, M.B. Nejad, Investigation of enclosure aspect ratio effects on melting heat transfer characteristics of metal foam/phase change material composites, *International Journal of Numerical Methods for Heat and Fluid Flow*, 29(9), 2994–3011, (2019).
- [28]. F. Selimefendigil and H.F. Öztöp, Modeling and optimization of MHD mixed convection in a lid-driven trapezoidal cavity filled with alumina-water nanofluid: Effects of electrical conductivity models, *International Journal of Mechanical Sciences*. 136, 264–278, (2018).
- [29]. T.V.V. Sudhakar, C. Balaji, S.P. Venkateshan, Optimal configuration of discrete heat sources in a vertical duct under conjugate mixed convection using artificial neural networks, *International Journal of Thermal Sciences*. 48(5), 881–890, (2009).
- [30]. Tassone, MHD mixed convection flow in the WCLL: Heat transfer analysis and cooling system optimization, *Fusion Engineering and Design*, 146, 809–813, (2019).
- [31]. S. Yigit and N. Chakraborty, Influences of aspect ratio and wall boundary condition on laminar Rayleigh-Bénard convection of Bingham fluids in rectangular enclosures, *International Journal of Numerical Methods for Heat and Fluid Flow*, 27(2), 310–333, (2017).
- [32]. H. K. Hamzah, F.H. Ali, M. Hatami, D. Jing, Effect of Two Baffles on MHD Natural Convection in U-Shape Superposed by Solid Nanoparticle having Different Shapes, *Journal of Applied and Computational Mechanics*, 6, 1200–1209, (2020).
- [33]. M.H. Yang and R.H. Yeh, Optimization of fin arrays in an inclined channel for mixed convection, *Applied Thermal Engineering*, 148(482), 963–976, (2019).
- [34]. A.M. Al-Amiri, K.M. Khanafer, Numerical simulation of double-diffusive mixed convection within a rotating horizontal annulus, *International Journal of Thermal Sciences*, 45(6), 567–578, (2006).
- [35]. M. Izadi, R. Mohebbi, A. Chamkha, I. Pop, Effects of cavity and heat source aspect ratios on natural convection of a nanofluid in a C-shaped cavity using Lattice Boltzmann method, *International Journal of Numerical Methods for Heat and Fluid Flow*, 28(8), 1930–1955, (2018).
- [36]. C. Béghein, F. Haghighat, F. Allard, Numerical study of double-diffusive natural convection in a square cavity, *International Journal of Heat and Mass Transfer*, 35(4), 833–846, (1992).
- [37]. A.M. Alsobaai, Thermal cracking of petroleum residue oil using three level factorial design, *Journal of King Saud University - Engineering Sciences*, 25(1), 21–28, (2013).
- [38]. S. Arun, A. Satheesh, Mesoscopic analysis of heatline and massline during double-diffusive MHD natural convection in an inclined cavity, *Chinese Journal of Physics*. 56(5), 2155–2172, (2018).
- [39]. S. Aljabair, A.L.Ekaid, S.H. Ibrahim, I. Alesbe, Heliyon Mixed convection in sinusoidal lid driven cavity with non-uniform temperature distribution on the wall utilizing nano fluid, *Heliyon*, 7, e06907, (2021).
- [40]. M.A. Teamah, A.F. Elsafty, E.Z. Massoud, Numerical simulation of double-diffusive natural convective flow in an inclined rectangular enclosure in the presence of magnetic field and heat source, *International Journal of Thermal Sciences*, 52(1), 161–175, (2012).
- [41]. S. Moolya, A. Satheesh, Role of magnetic field and cavity inclination on double diffusive mixed convection in rectangular enclosed domain, *International Communications in Heat and Mass Transfer*. 118, 104814, (2020).
- [42]. S. Moolya, A. Satheesh, Optimization of the effect of Prandtl number, inclination angle, magnetic field, and Richardson number on double-diffusive mixed convection flow in a rectangular domain, *International Communications in Heat and Mass Transfer*, 126, 105358, (2021).
- [43]. M. J. Hasan, A. K. Azad, Z. Islam, R. Hossain, and M. M. Rahman, “Periodic Unsteady Natural Convection on CNT Nano-powder Liquid in a Triangular Shaped Mechanical Chamber,” *Int. J. Thermofluids*. 15, 100181, (2022)
- [44]. C. S. K. Raju, N. A. Ahammad, K. Sajjan, N. A. Shah, S. J. Yook, and M. D. Kumar, “Nonlinear movements of axisymmetric ternary hybrid nanofluids in a thermally radiated expanding or contracting permeable Darcy Walls with different shapes and densities: Simple linear regression,” *Int. Commun. Heat Mass Transf.*, 135, 106110, (2022)
- [45]. R. Hossain, A. K. Azad, M. J. Hasan, and M. M. Rahman, “Radiation effect on unsteady MHD mixed convection of kerosene oil-based CNT nanofluid using finite element analysis,” *Alexandria Eng. J.* 61 (11), 8525–8543, (2022)
- [46]. P. Priyadarshini, M. V. Archana, N. A. Ahammad, C. S. K. Raju, S. jin Yook, and N. A. Shah, “Gradient descent machine learning regression for MHD flow: Metallurgy process,” *Int. Commun. Heat Mass Transf.*, 138, 106307, (2022).
- [47]. A. K. Azad et al., “Numerical study on heat and mass transfer characteristics in a confined enclosure with variable buoyancy ratio,” *Results Eng.*, 15, 100569, (2022).
- [48]. S. Kavva, V. Nagendramma, N. A. Ahammad, S. Ahmad, C. S. K. Raju, and N. A. Shah, “Magnetic-hybrid nanoparticles with stretching/shrinking cylinder in a suspension of MoS₄ and copper

- nanoparticles," *Int. Commun. Heat Mass Transf.*, 136, 106150, (2022)
- [49]. T.H. Ji, S.Y. Kim, J.M. Hyun, Transient mixed convection in an enclosure driven by a sliding lid, 629–638, (2007).
- [50]. Suhas V. Patankar, *Numerical Heat Transfer and Fluid Flow*, Series in computational methods in mechanics and thermal sciences (1980).
- [51]. S. Hussain, S.E. Ahmed, T. Akbar, Entropy generation analysis in MHD mixed convection of hybrid nanofluid in an open cavity with a horizontal channel containing an adiabatic obstacle, *International Journal of Heat and Mass Transfer*, 114, 1054–1066, (2017).
- [52]. G.H.R. Kefayati, M.G. Bandy, H. Sajjadi, D.D. Ganji, Lattice Boltzmann simulation of MHD mixed convection in a lid-driven square cavity with linearly heated wall, *Scientia Iranica*, 19(4), pp. 1053–1065, (2012).
- [53]. M.A. Sheremet, I. Pop, Mixed convection in a lid-driven square cavity filled by a nanofluid: Buongiorno's mathematical model, *Applied Mathematics and Computation*, 266, 792–808, (2015).
- [54]. M.A.R. Sharif, Laminar mixed convection in shallow inclined driven cavities with hot moving lid on top and cooled from bottom, *Applied Thermal Engineering*, 27(5–6), 1036–1042, (2007).
- [55]. R. Iwatsu, J.M. Hyun, K. Kuwahara, Mixed convection in a driven cavity with a stable vertical temperature gradient, *International Journal of Heat and Mass Transfer*, 36(6), 1601–1608, (1993).
- [56]. M. A. Waheed, Mixed convective heat transfer in rectangular enclosures driven by a continuously moving horizontal plate, *International Journal of Heat and Mass Transfer*, 52(21–22), 5055–5063, (2009).
- [57]. H. Joardar, N. Das, G. Sutradhar, An experimental study of effect of process parameters in turning of LM6/SiCP metal matrix composite and its prediction using response surface methodology, *International Journal of Engineering, Science and Technology*, 3(8), 132–141, (2012).
- [58]. S. D. Farahani, Efficacy of Magnetic Field on Heat Transfer of Nanofluid Flow in Flatten Tube with Porous Medium, *J. Heat Mass Transf. Res.*, 9, 99–106, (2022).
- [59]. A. K. Senejani and Z. Baniamerian, Multi Objective Optimization of Shell & Tube Heat Exchanger by Genetic, Particle Swarm and Jaya Optimization Algorithms: Assessment of Nanofluids as the Coolant, *J. Heat Mass Transf. Res.*, 9, (1), 1–16, (2022).



Semnan University



Fluid Analysis of Double-Layered Blood Flow through a Tapered Overlapping Stenosed Artery with a Porous Wall

Moses Sunday Dada^a, Abiodun Joseph Babatunde^{*a}, Mohammed Muritala Tunde^b

^a Department of Mathematics, University of Ilorin, Ilorin, Nigeria

^b School of Early Childhood Care and Primary Education, Federal College of Education (T) Potiskum, Yobe State, Nigeria

PAPER INFO

Paper history:

Received: 2021-10-04

Received: 2023-02-02

Accepted: 2023-02-03

Keywords:

Porous wall;
Resistance to flow;
Wall Shear Stress;
Slip parameter;
Darcy number.

ABSTRACT

In this present work, we examine the fluid of double-layered blood flow through a tapered overlapping stenosed artery with a porous wall. This two-layered blood flow problem comprises the peripheral layer as Newtonian fluid flows and the central core layer of suspension of the erythrocytes as another Newtonian fluid flows and was analytically solved which the numerical results are shown graphically and discussed. It was found that resistance to flow accelerates with rising slip parameter, blood viscosity, and artery length while a rise in Darcy number and radius of the centre core to the tube radius in the unobstructed region decreases the resistance to flow.

Also, the resistance to flow rises with increasing stenosis height whereas it increases with a rise in values of artery shape. The wall shear stress drops as the Darcy number accelerates and rises with rising viscosity of the blood and slip parameter. Furthermore, fluctuation of wall shear stress at the neck of the stenosis drops as the Darcy number increases. Moreover, it is observed that the shear stress increases with rising viscosity of the blood and slip parameter. This work is able to forecast the major attribute of the physiological flows which have played an important role in biomedical researches.

DOI: [10.22075/jhmtr.2023.24296.1352](https://doi.org/10.22075/jhmtr.2023.24296.1352)

© 2022 Published by Semnan University Press. All rights reserved.

1. Introduction

The vascular system is an organ system that allows blood to transport nutrients and circulate oxygen, hormones, blood cells, carbon-II-oxide to and fro the cells in the system of the body to provide nourishment and preventing stabilization of temperature, diseases and sustain homeostasis. Atherosclerosis is a process of continuous thickening and hardening of the walls of medium-sized and large blood vessels due to the deposition of fat on their inner lining. Stenosis growth is responsible for many coronary artery diseases such as strokes, heart attack, peripheral vascular diseases, and death in the world at large. Because of the dangers involved, it is very vital to look forward for the symptoms that cause blockage of arteries, like the Transient Ischemic Attack and stroke, so that adequate measures may be observe before the situation gets worst. The importance of the hemodynamic factors play a vital role in the beginning and the development of atherosclerosis which drew the attention of Mann et

al. [1]. Stenosis proliferation conditions under various flow situations have been addressed by a number of researchers such as Asha et al. [2] that studied the geometry of stenosis and its effects on the blood flow through an artery and Srivastava [3] said that the significance of the peripheral layer accelerates as blood vessel diameter decelerating., Arun, [4] examined the mathematical modelling on blood flow under atherosclerotic condition. Two-layered model of blood flow through composite stenosed artery was investigated by Padma et al [5] they observed that existence of peripheral layer is useful in representation of diseased arterial system.

Medhavi [6-8] examined two-phase arterial blood flow through a composite stenosis. A macroscopic two-phase blood flow through a bell-shaped stenosis in an artery with a permeable wall was studied by Srivastav et al., [9], Babatunde and Dada [10] investigated the effects of hematocrit level on wall shear stress and flow resistance in a tapered and overlapping stenosed

*Corresponding Author: Babatunde Abiodun Joseph
Email: babatundeabiodunjoseph@gmail.com

artery with porosity, they observed that the resistance to flow increases with increase in either stenosis height or artery shapes while the influence of hematocrit level has slight decrease. The two-layered (K.L-Newtonian) model of blood flow in an artery with six types of mild stenoses was examined by Ponalagusamy et al. [11]. Puskar R. Pokhrel, [12] studied the analysis of two-layered blood flow through artery with mild stenosis and observed that the pressure gradient of the blood flow increases in the ratio of thickness of stenosis with radius of artery.

Eldesoky et al. [13] studied the numerical study of unsteady MHD pulsatile flow through a porous medium in an artery using Generalized Differential Quadrature Method and several scholars. The flowing of the blood has been taken as Newtonian fluid, non-Newtonian fluid, single or two-layered fluid flows by different researchers while studying the flows through atherosclerosis. It's obvious that blood flow can be taken as a one-layered model in a big vessel. However, the flow through the small artery is double-layered. Bugliarello and Sevilla [14] examined the velocity distribution and other characteristics of steady and pulsatile blood flow in fine glass tubes and Titiloye et al. [15] studied the mathematical modelling of two-layered blood flow through a tapered artery with an overlapping stenotic condition and observed that there is a cell-free plasma layer, for blood flowing through small arteries and a core region of suspension of all the erythrocytes.

In a case of overlapping, there is a suturing of a layer of tissue above or under another in order to add more strength. Chakravarty and Mandal, [16] studied mathematical modelling of blood flow in overlapping arterial stenosis and observed that the flux decreases as the resistive impedance decreasing out of the stenotic flow in vivo, the gravity of the overlapping stenosis affects the resistive impedance seriously, also the wall shear stress accelerates as the amplitude of the pressure gradient drops. Sapna et al., [17]

examined mathematical modelling of blood flows in a three-layered stenosed artery, said that the resistance to flow and wall shear stress are significantly very low for the two-fluid non-Newtonian model than those of the two-fluid model.

The endothelial walls are said to be highly porous with ultramicroscopic pores through that filtration occurs and fat is believed to rise the porosity of the blood vessel wall. Such a rise in permeability results from damaged, dilated or inflamed vessel walls. As such Rupesh et al [18], examined double-fluid blood flows in the stenosed artery with a permeable wall.

The study, therefore, considers the combined effects of a tapered and overlapping stenosed artery with a porous wall on the double-layered blood flows. This problem considers the flowing blood as a double-layered Newtonian flow, comprises of a core region of suspension of all the erythrocytes taking to be another Newtonian fluid flows, the viscosity of which can vary depending on the flow situations and a peripheral region of Newtonian fluid flows of constant viscosity, in a vessel that the wall is porous. The problems were solved analytically.

2. Formulation of the problem

The laminar, incompressible, and Newtonian double-layered flow of blood, comprises of a central core layer of red cell suspensions in plasma of radius R_1 and a peripheral plasma layer of a thickness $(R-R_1)$, through axisymmetric one-dimensional tapered and overlapping stenosed artery is being examined. The cylindrical polar coordinate (r, θ, z) , is used for any point in the fluid, where z is measured along the axis of the artery and r and θ along the radial and circumferential directions respectively.

The mathematical representation that corresponds to the geometry of this present work is expressed after Titiloye et al., [15] as:

$$\frac{R(z)}{R_0} = \begin{cases} \left(\frac{mz}{R_0} + 1 \right) - \frac{\delta \cos \varphi}{R_0 L_0} (z-d) \left\{ 11 - \frac{94}{3L_0} (z-d) + \frac{32}{L_0^2} (z-d)^2 - \frac{32}{3L_0^3} (z-d)^3 \right\}, & d \leq z \leq d + \frac{3L_0}{2} \\ \left(\frac{z}{R_0} + 1 \right), & \text{otherwise} \end{cases} \quad (1)$$

$$\frac{R_1(z)}{R_0} = \begin{cases} \left(\frac{mz}{R_0} + 1 \right) \beta - \frac{\delta \cos \varphi}{R_0 L_0} (z-d) \left\{ 11 - \frac{94}{3L_0} (z-d) + \frac{32}{L_0^2} (z-d)^2 - \frac{32}{3L_0^3} (z-d)^3 \right\}, & d \leq z \leq d + \frac{3L_0}{2} \\ \left(\frac{mz}{R_0} + 1 \right) \beta, & \text{otherwise} \end{cases} \quad (2)$$

where $R(z)$, R_0 represent the radius of the tapered arterial segment in the constricted region and the constant radius of the normal artery in the non-stenotic region respectively, φ represents the angle of tapering, $\frac{3L_0}{2}$ is the length of overlapping stenosis, d denotes the location of the stenosis, $\delta \cos \varphi$ is taken to be the critical height of the overlapping stenosis, β is the ratio of the central core radius to the tube radius outside the stenotic region and $m = \tan \varphi$ represents the slope of the tapered vessel. In order to exploring the feasibility of the different shapes of the artery, which classified as diverging tapering ($\varphi > 0$), non-tapered artery ($\varphi = 0$), and converging tapering ($\varphi < 0$).

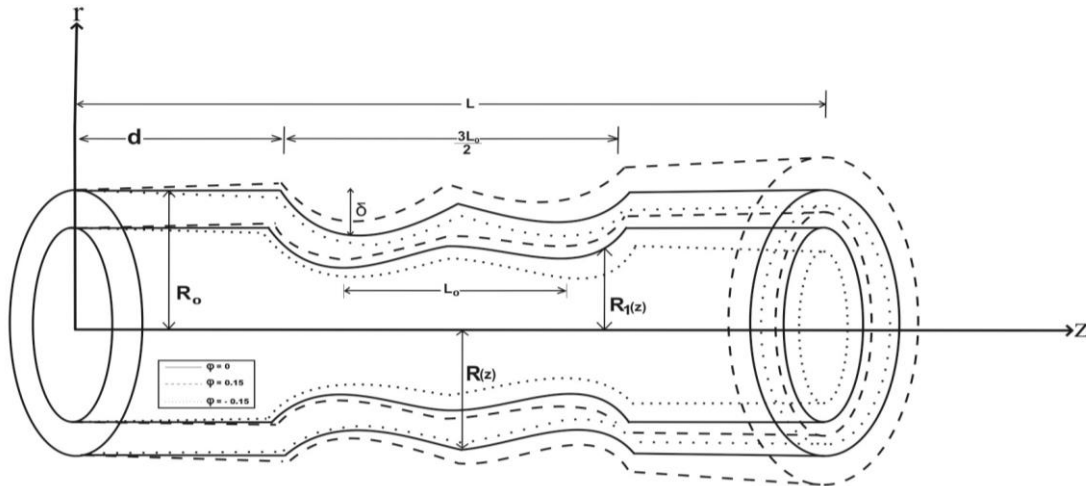


Figure 1. Geometry of a two-layered overlapping stenosed artery [15]

3. Mathematical Formulation

The equations of motion for one-dimensional fluid flow, steady, laminar in the case of stenosed artery ($\delta \ll R_0$) are described by Sharanet al. [19] as

$$\frac{dp}{dz} = \frac{\mu_p}{r} \frac{\partial}{\partial r} \left(r \frac{\partial}{\partial r} \right) w_p, \quad R_1(z) \leq r \leq R(z), \quad (3)$$

$$\frac{dp}{dz} = \frac{\mu_c}{r} \frac{\partial}{\partial r} \left(r \frac{\partial}{\partial r} \right) w_c, \quad 0 \leq r \leq R_1(z), \quad (4)$$

where (r, z) are the radial and axial coordinates in the two-dimensional cylindrical polar coordinate system and $\frac{dp}{dz}$ denotes the pressure gradient (μ_p, w_p) and (μ_c, w_c) represents the viscosity and velocity of the fluid flows in the peripheral layer ($R_1(z) \leq r \leq R(z)$) and central layer ($0 \leq r \leq R_1(z)$), respectively.

The corresponding boundary conditions given by (Beavers, [20]) for the present problem can be expressed by [18] as

$$\frac{\partial w_c}{\partial r} = 0 \quad \text{at } r = 0 \quad (5a)$$

$$w_p = w_c \quad \text{and} \quad \mu_p \frac{\partial w_p}{\partial r} = \mu_c \frac{\partial w_c}{\partial r} \quad \text{at } r = R_1(z) \quad (5b)$$

$$w_p = w_B \quad \text{and} \quad \frac{\partial w_p}{\partial r} = \frac{\alpha}{\sqrt{k}} (w_B - w_f) \quad \text{at } r = R(z) \quad (5c)$$

where $w_f = -\frac{k}{\mu_p} \frac{dp}{dz}$ represents the velocity in the porosity boundary, μ_p denotes the plasma viscosity of the fluid in a peripheral layer, α is the slip parameter, k is the Darcy number and w_B is the slip velocity, are dimensionless quantities depending on the material within the boundary region.

4. Analysis

Equation (3) is integrating with respect to r , applying the boundary condition (5a), we have

$$\frac{\partial w_p}{\partial r} = \frac{r}{2\mu_p} \frac{dp}{dz} \quad (6)$$

Also, Equation (6) is integrating with the aid of boundary condition (5b), we have

$$w_p = \frac{r^2}{4\mu_p} \frac{dp}{dz} - \frac{R^2}{4\mu_p} \frac{dp}{dz} + w_B \quad (7)$$

Using boundary condition (5c) on Equation (6), we have

$$w_B = \frac{\sqrt{k}}{2\alpha\mu_p} \frac{dp}{dz} [R - 2\alpha\sqrt{k}] \quad (8)$$

Substituting Equation (8) into Equation (7), we have

$$w_p = \frac{r^2}{4\mu_p} \frac{dp}{dz} - \frac{R^2}{4\mu_p} \frac{dp}{dz} + \frac{\sqrt{k}}{2\alpha\mu_p} \frac{dp}{dz} [R - 2\alpha\sqrt{k}]$$

Hence,

$$w_p = -\frac{R_0^2}{4\mu_p} \frac{dp}{dz} \times \left\{ \left(\frac{R}{R_0} \right)^2 - \left(\frac{r}{R_0} \right)^2 - 2 \left(\frac{R}{R_0} \right) \left(\frac{\sqrt{k}}{\alpha R_0} \right) + \frac{4k}{R_0^2} \right\} \quad (9)$$

Similarly, from Equation (4) following the same processes, we have

$$w_c = -\frac{R_0^2}{4\mu_p} \frac{dp}{dz} \times \left\{ \mu \left[\left(\frac{R_1}{R_0} \right)^2 - \left(\frac{r}{R_0} \right)^2 \right] - 2 \left(\frac{R}{R_0} \right) \left(\frac{\sqrt{k}}{\alpha R_0} \right) + \frac{4k}{R_0^2} \right\} \quad (10)$$

where $\mu = \frac{\mu_p}{\mu_c}$ and μ_c is the viscosity of the blood flows in the central core layer.

The flux flow rate is given as

$$Q = 2\pi \left\{ \int_0^{R_1} r w_c dr + \int_{R_1}^R r w_p dr \right\} \quad (11)$$

After simplifying Equation (11), it becomes

$$Q = -\frac{\pi R_0^4 dp}{8\mu_p dz} \left\{ \left(\frac{R_1(z)}{R_0}\right)^4 (1 + \mu) + \left(\frac{R(z)}{R_0}\right)^4 - 2\left(\frac{R(z)}{R_0}\right)^2 \left(\frac{R_1(z)}{R_0}\right)^2 + \frac{8k}{R_0^2} \left(\frac{R(z)}{R_0}\right)^2 - \left(\frac{R(z)}{R_0}\right)^3 \frac{\sqrt{k}}{R_0\alpha} \right\} \quad (12)$$

Therefore, the pressure gradient from Equation (12) is

$$\frac{dp}{dz} = -\frac{8\mu_p Q}{\pi R_0^4 F(z)} \quad (13)$$

where

$$F(z) = \left\{ \left(\frac{R_1(z)}{R_0}\right)^4 (1 + \mu) + \left(\frac{R(z)}{R_0}\right)^4 - 2\left(\frac{R(z)}{R_0}\right)^2 \left(\frac{R_1(z)}{R_0}\right)^2 + \frac{8k}{R_0^2} \left(\frac{R(z)}{R_0}\right)^2 - \left(\frac{R(z)}{R_0}\right)^3 \frac{\sqrt{k}}{R_0\alpha} \right\}$$

Integrating Equation (13) along the length of the artery, we have

$$\int_{p_0}^{p_1} dp = \int_0^L -\frac{8\mu_p Q}{\pi R_0^4 F(z)} dz \quad (14a)$$

where p_0 and p_1 are the pressures at $z=0$ and $z=L$ respectively.

$$p_1 - p_0 = -\frac{8\mu_p Q}{\pi R_0^4} \left\{ \int_0^d \sigma(z) dz + \int_d^{d+\frac{3L_0}{2}} \sigma(z) dz + \int_{d+\frac{3L_0}{2}}^L \sigma(z) dz \right\} \quad (14b)$$

where $\sigma(z) = \frac{1}{F(z)}$

The resistance to flow λ given by (Malek et al. [21] and Babatunde and Dada, [10]) as

$$\lambda\lambda = \frac{p_1 - p_0}{Q Q}$$

Hence,

$$\lambda = -\frac{8\mu_p}{\pi R_0^4} \left\{ \int_0^d \sigma(z) dz + \int_d^{d+\frac{3L_0}{2}} \sigma(z) dz + \int_{d+\frac{3L_0}{2}}^L \sigma(z) dz \right\} \quad (15a)$$

The stenosis is present in the region $d \leq z \leq d + \frac{3L_0}{2}$. If there is no stenosis $\frac{R(z)}{R_0} = \left(\frac{mz}{R_0} + 1\right)$ and $\frac{R_1(z)}{R_0} = \left(\frac{mz}{R_0} + 1\right)\beta$ from Equations (1) and (2) respectively. Therefore,

$$\lambda = -\frac{8\mu_p}{\pi R_0^4} \left\{ \int_0^d \zeta(z) dz + \int_d^{d+\frac{3L_0}{2}} \sigma(z) dz + \int_{d+\frac{3L_0}{2}}^L \zeta(z) dz \right\} \quad (15b)$$

where

$$\zeta(z) = \frac{1}{\left\{ \left(\frac{mz}{R_0} + 1\right)\beta \right\}^4 (1 + \mu) + \left(\frac{mz}{R_0} + 1\right)^4 - 2\left(\frac{mz}{R_0} + 1\right)^2 \left(\frac{mz}{R_0} + 1\right)\beta^2 + \frac{8k}{R_0^2} \left(\frac{mz}{R_0} + 1\right)^2 - \left(\frac{mz}{R_0} + 1\right)^3 \frac{\sqrt{k}}{R_0\alpha} \right\}}$$

The resistance to flow for Newtonian fluid flow when there is no stenosis ($\delta = 0$) is given by

$$\lambda_N = -\frac{8\mu_p}{\pi R_0^4} \int_0^L \psi(z) dz \quad (16)$$

where

$$\psi(z) = \left[\left(\frac{mz}{R_0} + 1\right)^4 + \frac{8k}{R_0^2} \left(\frac{mz}{R_0} + 1\right)^2 - \left(\frac{mz}{R_0} + 1\right)^3 \frac{\sqrt{k}}{R_0\alpha} \right]$$

Thus, the dimensionless resistance to flow may be expressed as

$$\bar{\lambda} = \frac{\lambda}{\lambda_N} \quad (17)$$

The wall shear stress may be expressed as

$$\tau_s = -\frac{R dp}{2 dz} = \frac{4\mu_p Q \left(\frac{R}{R_0}\right)}{\pi R_0^3 F(z)} \quad (18)$$

The wall shear stress for Newtonian fluid flow when there is no stenosis ($\delta = 0$) is given as

$$\tau_N = \frac{4\mu_p Q \left(\frac{mz}{R_0} + 1\right)}{\pi R_0^3 \psi(z)} \quad (19)$$

Thus, the wall shear stress in non-dimension form is expressed as

$$\bar{\tau} = \frac{\tau_s}{\tau_N} \quad (20)$$

The wall shear stress at the neck of the stenosis is define as

$$\tau_{wm} = \left[\frac{4\mu\mu_c Q \left[\left(\frac{mz}{R_0} + 1\right) - \frac{\delta}{R_0} \right]}{\pi R_0^3 \eta} \right] \quad (21)$$

where

$$\eta = \left[\left(\left(\frac{mz}{R_0} + 1\right) - \frac{\delta}{R_0} \right)^4 + \frac{8k}{R_0^2} \left(\left(\frac{mz}{R_0} + 1\right) - \frac{\delta}{R_0} \right)^2 - \left(\left(\frac{mz}{R_0} + 1\right) - \frac{\delta}{R_0} \right)^3 \frac{\sqrt{k}}{R_0\alpha} \right]$$

Thus, the dimensionless wall shear stress at the neck of the stenosis is given as

$$\bar{\tau}_m = \frac{\tau_{wm}}{\tau_N} \quad (22)$$

The analytical solution of the second integral on the right-hand side of Equation (15b) is a tedious work which can be solved by numerical method, while the solution of the first and third integrals is easier. Equations (15b) - (22) can be use to determine the resistance to flow and the wall shear stress in the stenosed artery.

5. Numerical results and discussion

In order to explore this present work, the results are displayed graphically. In this section, fluid analysis of two-layered blood flow through a tapered overlapping stenosed artery with porosity had been shown. The values of the parameters are considered with its range (Titiloye et al. [15] and Babatunde and Dada, [10]) as

$$Q=0.1, \quad L=2.5, \quad L_0 = 1.0, \quad d=0.5, \quad R_0 = 1,$$

$$\frac{\delta}{R_0} = 0.1 - 0.5, \quad k = 0.1 \text{ to } 0.2, \quad \alpha = 0.1 \text{ to } 0.2,$$

$$\beta=0.90-0.96 \text{ and } \mu=0.1-0.3, \quad \varphi= - 0.15, 0.00 \text{ and } 0.15.$$

Figure 2 shows the resistance to flow against stenosis height with artery shape for several values of slip parameter. Revealed that resistance to flow accelerates with a rise in the slip parameter.

Figure 3 represents the resistance to flow against stenosis height with artery shape for several values of Darcy number. It was observed that resistance to flow decreases with increasing the Darcy number.

Figure 4 displays the resistance to flow against stenosis height with artery shape for several values of blood viscosity. It depicts that resistance to flow rises with increasing the blood viscosity.

Figure 5 displays the resistance to flow against stenosis height for several values of artery shapes. It revealed that resistance to flow increases with a rise in the slip parameter and Its increases with a rise in values of artery shape φ .

Figure 6 represents the resistance to flow against stenosis height with artery shape for several values of β . Depicts that resistance to flow reduces with a rise in the value of β .

Figure 7 shows the resistance to flow against stenosis height with artery shape for several values of artery length. Reveals that resistance to flow increases with increases in the artery length.

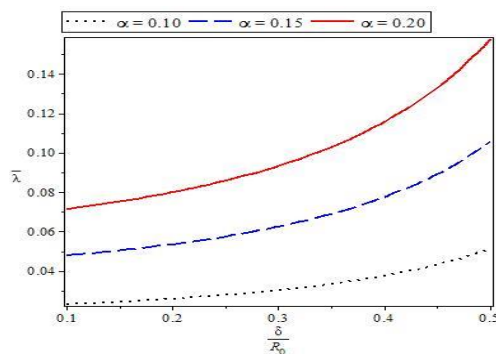


Figure 2. Resistance to flow for several values of slip parameter at an angle $\varphi=0.15$.

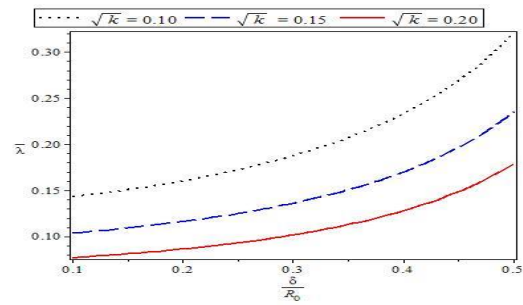


Figure 3. Resistance to flow for several values of Darcy number at an angle $\varphi=0.1$

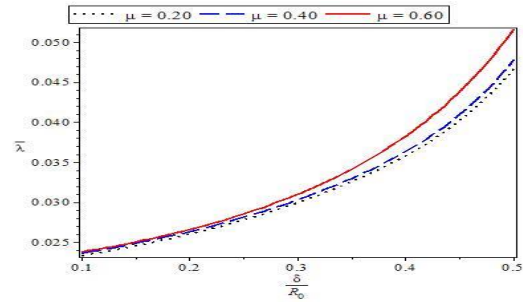


Figure 4. Resistance to flow for several values of viscosity of the blood at an angle $\varphi = 0.15$

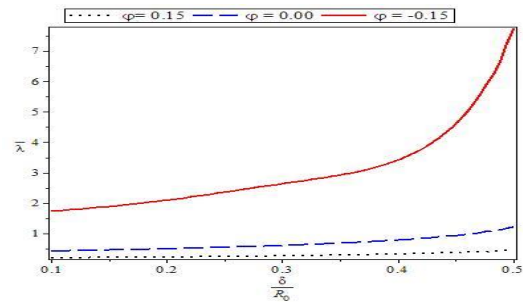


Figure 5. Resistance to flow for several values of artery shape

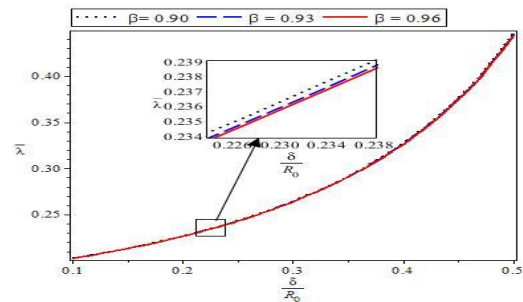


Figure 6. Resistance to flow for several values of β at an angle $\varphi=0.15$.

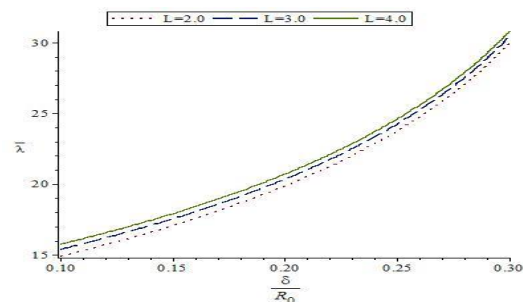


Figure 7. Resistance to flow for several values of artery length at an angle $\varphi=0.15$.

Figure 8 represents the wall shear stress for several values of slip parameters. It depicts that wall shear stress rises with a rise in the slip parameter.

Figure 9 displays the wall shear stress for several values of Darcy number. It is found that shear stress reduces with a rise in the value of Darcy number.

Figure 10 shows the wall shear stress for several values of stenosis height. It depicts that wall shear stress rises with increasing the value of stenosis height at the stenosis region while the wall shear stress drops with a rise in the value of stenosis height where there is no stenosis.

Figure 11 displays the wall shear stress for several values of blood viscosity. It depicts that shear stress rises as the value of viscosity of blood increases.

Figure 12 represents wall shear stress at the neck of the stenosis for different values of Darcy number. It depicts that increasing Darcy number reduces the fluctuation of the wall shear stress at the throat of stenosis.

Figure 13 represents the fluctuation of wall shear stress at the neck of the stenosis for several values of slip parameter. It displays that as slip parameter increases, the fluctuation of the shear stress at the neck of stenosis rises.

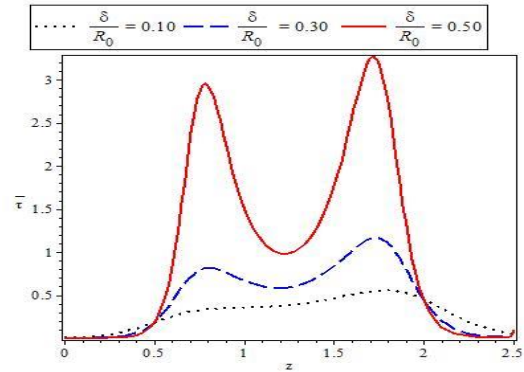


Figure 10. Wall shear stress for several values of stenosis height at an angle $\phi=0.15$.

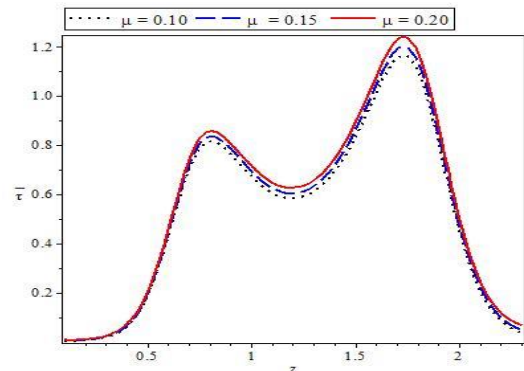


Figure 11. Wall shear stress for several values of viscosity of blood at an angle $\phi=0.15$.

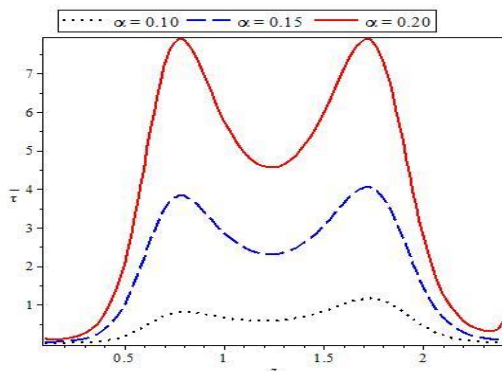


Figure 8. Wall shear stress for several values of slip parameter at an angle $\phi=0.15$.

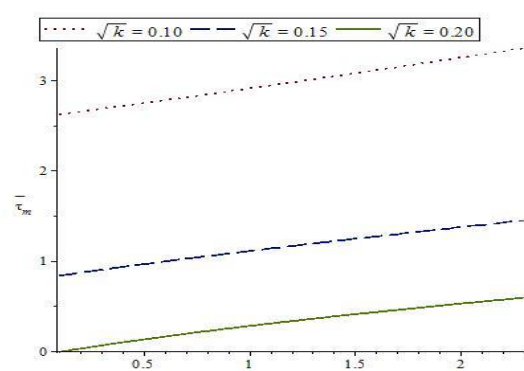


Figure 12. Wall shear stress at the neck of the stenosis for several values of Darcy number at $\phi=0.15$.

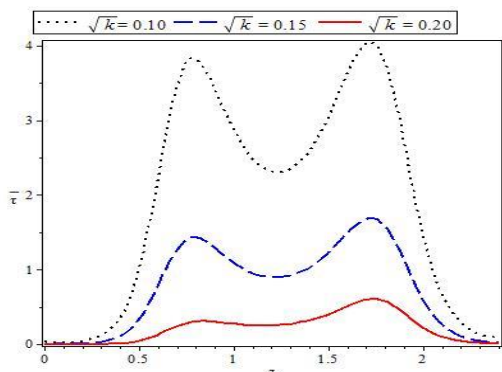


Figure 9. Wall shear stress for several values of Darcy number angle $\phi=0.15$.

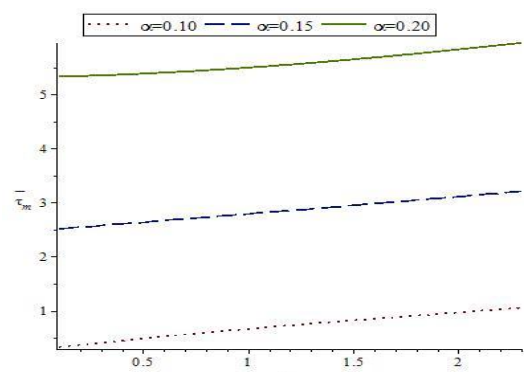


Figure 13. Fluctuation of shear stress at the neck of the stenosis for several values of slip parameter at $\phi=0.15$.

Conclusion

The fluid analysis of two-layered blood flow through a tapered overlapping stenosed artery with permeable wall was determined in this present work. This double-layered blood flow comprises the peripheral layer fluid flows and the central core layer of suspension of the erythrocytes as Newtonian fluid flows and was solved analytically. Different fluid parameters were introduced to analyse the effects of slip parameter, Darcy number, blood viscosity, artery shape and stenosis height on the resistance to the flow and the wall shear stress of the blood. The results have been studied in the case of tapered overlapping stenosed artery are shown as follow:

- i. It is found that resistance to flow increases with increasing slip parameter, blood viscosity, artery length. It occurs due to influence of slip parameter on blood flow increases the internal viscosity of the blood flow which causes rise to the Lorentz force.
- ii. The influence of β and Darcy number decreases the resistance to flow.
- iii. Fluctuation of wall shear stress at the neck of the stenosis decreases as Darcy number increases.
- iv. We found that shear stress rises as viscosity of the blood increasing and slip parameter. However, we observed that the presence of peripheral layer in a porous artery aids the functioning of the diseased artery.

Nomenclature

All variables using this manuscript, listed in nomenclature.

(r, θ, z)	Cylindrical polar coordinate system
L	Length of the arterial segment
w_f	velocity in the porosity boundary
w_B	Slip velocity
μ_c	Viscosity of the blood flows in the central core layer
μ_p	Viscosity of the blood flows in the peripheral layer
Q	Volumetric flow flux
w_c	Axial velocity of the blood flows in the central core layer
w_p	Axial velocity of the blood flows in the peripheral layer
α	Slip parameter
τ	Wall shear stress
τ_s	Wall shear stress at the maximum height of the stenosis

τ_N	Wall shear stress in the absence of stenosis
τ_{wm}	Wall shear stress at the neck of stenosis
$\bar{\tau}_m$	Wall shear stress in dimensionless form
β	Ratio of center core radius to the tube radius outside the stenotic region
m	Slope of the tapered vessel
k	Darcy number
R(z)	Radius of tapered artery in the region of stenosis
R_0	Radius of the non-tapered artery in the non-stenotic region
R_1	Radius of the plasma
L_0	Length between throat of two stenosis
φ	Tapered angle
δ	Maximum height of the stenosis at some location z
λ_N	Resistance to flow with no stenosis
r	Radius of the artery
P	Pressure
d	Location of the stenosis
λ	Resistance to flow
$\frac{dp}{dz}$	Pressure gradient
$\delta \cos \phi$	Critical height of the overlapping stenosis
z	Axial distance

Acknowledgements

The authors gratefully acknowledge the reviewers' comments that improved the quality of the article.

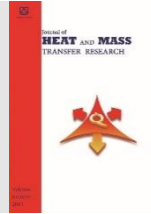
References

- [1] Mann F. C., Herrick J. F., Essex H. E., and Blades E. J., 1938. Effects on blood flow of decreasing the lumen of blood vessels, *Surgery*, 4, 249–252.
- [2] Asha K. N. and Neetu Srivastava, 2021. Geometry of Stenosis and Its Effects on the Blood Flow Through an Artery-A Theoretical Study, *AIP Conference Proceedings*, 2375, Issue 1: 10.1063/5.0066510.
- [3] Srivastava V.P., Rastogi R. and Vishnoi R., 2010. A two-layered suspension blood flow through an overlapping stenosis, *Computers and Mathematics with Applications*, 60, 432–441.
- [4] Arun Kumar Maiti, 2016. *Mathematical Modelling on Blood Flow Under-*

- Atherosclerotic condition. *Americal Journal of Applied Mathematics*, Vol. 4, No.6, 324-329.
- [5] Padma Joshi, Ashutosh Pathak and Joshi B.K, 2009. Two-layered model of blood flow through composite stenosed artery. *AAM*, vol. 4(2), 343-354.
- [6] Medhavi A., 2011. On macroscopic two-phase arterial blood flow through an overlapping stenosis, *e-Journal of Science and Technology*, 6, 19-31.
- [7] Medhavi A., Srivastav R. K., Ahmad Q. S. and Srivastava V. P., 2012. Two-phase arterial blood flow through a composite stenosis, *e-Journal of Science and Technology*, 7(4), 83-94.
- [8] Medhavi A., 2013. A macroscopic two-phase blood flow through a stenosed artery with a permeable wall, *Appl Bionics and Biomechanics*, 10(1), 11-18.
- [9] Srivastava V.P., Tandon M. and Srivastav R. K., 2012. A macroscopic two-phase blood flow through a bell-shaped stenosis in an artery with a permeable wall, *Appl. and Appl Math.*, 7(1), 37-51.
- [10] Babatunde A. J. and Dada M. S., 2021. Effects of Hematocrit level on Blood flow through a tapered and overlapping stenosed Artery with Porosity. *JHMTR*, (1-9), 2007-1293.
- [11] Ponalagusamy R and Manchi R., 2020. The two-layered (K.L-Newtonian) model of blood flow in an artery with six types of mild stenosis. *Applied Mathematics and Computation*, Elsevier, vol. 367.
- [12] Puskar R. Pokhrel, 2021, Analysis of Two-layered Blood Flow through Artery with Mild Stenosis, *Humanities and Social Sciences Journal*, 13(1), 145-154.
- [13] Eldesoky I. M., Kernel M. H. & Hussien R. M., Abumandour, 2013. Numerical study of unsteady MHD pulsatile flow through a porous medium in an artery using Generalized Differential Quadrature Method, *Intern. Jour. of Materials, Mechanics and Manufacturing*, 1(2).
- [14] Bugliarello G. and Sevilla, 1970. Velocity distribution and other characteristics of steady and pulsatile blood flow in fine glass tubes, *Biorheol*, 7, 85-107.
- [15] Titiloye E.O, Babatunde A.J. and Dada M.S., 2016. Mathematical modelling of two-layered blood flow through a tapered artery with an overlapping stenotic condition, *faculty of physical sci., University of Ilorin*. ISSN: 2408-4808. Vol.3, 208-223.
- [16] Chakravarty. S. and Mandal P. K., 1994. The Mathematical modelling of blood flow through an overlapping Arterial stenosis. *Math. & Comp. Modelling*, Vol.19, Issue 1, page 59-70.
- [17] Sapna Ratan Shah, Anuradha, and Anamika, 2017. Mathematical modelling of blood flow through three-layered stenosed artery". *International Journal for Research in Applied Science & Eng. Tech.*, Vol. 5 Issue VI, ISSN: 2321-9653.
- [18] Rupesh K. Srivastav and V.P. Srivastava, 2014. On two-fluid blood flow through the stenosed artery with a permeable wall. *Applied Bionics and Biomechanics*, 11. 39-45.
- [19] Sharan M. and Popel A. S., 2001. A two-phase model for the flow of blood in narrow tubes with increased viscosity near the wall, *Birheol*, 38, 415-428.
- [20] Beavers G. S. and Joseph D. D., 1967. Boundary conditions at a naturally permeable wall. *Journal of Fluid Mech*, 30(1), 197-207.
- [21] Malek A. and Haque A., 2017. Hematocrit level on blood flow through a stenosed artery with a permeable wall. *AAM: An international journal*, ISSN: 1932-9466.



Semnan University



A New Approach for the Heat and Moisture Transfer in Desiccant Wheels Concerning Air Stream Velocity

Seyed Amir Hossein Zamzamian ^{*,a}, Hassan Pahlavanzadeh ^b,
Mohamad Reza Omidkhah Nasrin ^b

^a Energy Department, Materials and Energy Research Center (MERC), Karaj, Iran.

^b Faculty of Chemical Engineering, Tarbiat Modares University, Tehran, Iran.

PAPER INFO

Paper history:

Received: 2022-10-04

Revised: 2023-01-28

Accepted: 2023-02-11

Keywords:

Desiccant wheel;
Explicit program;
Heat transfer;
Mathematical model;
Mass transfer.

ABSTRACT

Many investigators have presented mathematical work on desiccant wheels but there is a considerable discrepancy between published values and experimental values. A mathematical model based on the two-dimensional Navier-Stokes equation has been derived to show the dehumidification trend of desiccant dehumidifier concerning air stream velocity. In this model the effect of air stream velocity on wheel performance as a momentum equation combined with heat and mass transfer has been studied.

The current model is capable of predicting the transient and steady-state transport in a desiccant wheel. It reveals the moisture and temperature in both the airflow channels and the sorbent felt, in detail, as a function of time. The predicted results are validated against the data taken from experimental results, with reasonable accuracy. Therefore, the numerical model is a practical tool for understanding and accounting for the complicated coupled operational process inside the wheel. Consequently, it is useful for parameter studies.

DOI: [10.22075/jhmtr.2023.28610.1395](https://doi.org/10.22075/jhmtr.2023.28610.1395)

© 2022 Published by Semnan University Press. All rights reserved.

1. Introduction

In the desiccant cooling process, which is a new kind of refrigeration method, the fresh air is dehumidified and then sensibly and evaporatively cooled before being sent to the conditioned space [1]. Desiccant-enhanced air conditioning equipment has exhibited both the capability to improve humidity control and the potential to save energy costs by lowering the latent energy requirement of the supply air stream. Controlling temperature and humidity within a conditioned space is important for a wide variety of applications. Desiccant dehumidifier, running in open cycle, can be driven by low-grade heat sources, e.g. solar energy, waste heat and natural gas. A procedure for the energy and exergy analyses of open-cycle desiccant cooling systems have been developed and it has been applied to an experimental unit operating in ventilation mode with natural zeolite as the desiccant [2]. Beccali et al. has presented a simple model to

evaluate the performance of rotary desiccant wheels based on different kind of solid desiccants e.g. silica gel. The 'Model 54' has been derived from the interpolation of experimental data obtained from the industry and the correlations developed for predicting outlet temperature and absolute humidity. The 'Model 54' consists of 54 coefficients corresponding to each correlation for outlet absolute humidity and temperature and it is found that the model predicts very well the performance of silica gel desiccant rotor. Then a psychro-metric model has been presented to obtain relatively simple correlations for outlet temperature and absolute humidity. The developed psychro-metric model is based on the correlations between the relative humidity and enthalpy of supply and regeneration air streams [3]. Then the update on the desiccant wheel models developed. It is to be mentioned that the psychro-metric model is valid only for the desiccant wheel running with identical volume

*Corresponding Author: Seyed Amir Hossein Zamzamian.
Email: azamzamian@merc.ac.ir

air flows in supply and regeneration side. When system runs with volume air flow ratio between supply and regeneration side, the model needs further modification. Some correction factors in order to update the model for correct prediction of the temperature and humidity of processed air at the outlet of desiccant wheel have been developed and also incorporated [4]. Many mathematical models on the rotary desiccant dehumidifier have been proposed. Maclaine-Cross IL presented that a finite difference computer program, MOSHMX, can be developed based on a detailed numerical analysis [5]. Barlow presented that DESSIM could be written where the dehumidifier was discretized and each node was treated as a counter flow heat and mass exchanger in which both the heat and mass transfer are assumed to be uncoupled [6]. Then Collier and Cohen developed ET/DESSIM that is more accurate than DESSIM [7]. The mathematical model by finite difference method to predict the performance and to optimize the operation parameters of rotary desiccant wheels have been proposed. The effect of the rotational speed on the performance of an adiabatic rotary dehumidifier was parametrically studied, and the optimal rotational speed was determined by examining the outlet adsorption side humidity profiles and humidity wave front inside the desiccant dehumidifier [8]. The mathematical model of a rotary desiccant wheel have been used to calculate the performance of stationary or rotary bed and transient or steady state operation is founded by considering some of the key components [9]. This is helpful for predicting the performance and evaluating the benefits of rotary desiccant wheels concerning the complicated heat and mass transfer in the rotary desiccant matrix that was suggested [10-11]. The continuity and energy conservation equations for the transient coupled heat and mass transfer using a finite differential model have been established and solved, that the present study was mostly derived from this research [12-13]. A simple mathematical model for explanation of the rotary desiccant wheel, in which the optimum rotational speed for achieving the maximum performance offered have been presented [14]. On the other hand, a mathematical model for a fixed desiccant bed to show the dehumidification trend of desiccant dehumidifier concerning Ackermann correction factor with no rotation have been derived [15]. As mentioned, in all activities like the above references, the attitude, model solution and outcome analysis are much different from this research. There are various numerical modeling presented of rotary wheels and also calculation of mass and heat transfer in those models by various researchers [8-9]. In these activities the effect of conduction within the desiccant wall has been considered. Also in this model an optimized velocity for exchangers has been determined. Experimental measurements on rotary silica gel exchangers has been presented in these

researches and by using temperature distribution within wheel, an experimental statement for the optimized velocity of rotation has been suggested. They have some suggestions for analysis of exchangers or silica gel rotary wheels by using psychro-metric chart. Their focus is mainly on the understanding of the measure of mass transfer in silica gel rotary desiccant systems simply or by experimental parametric analysis, and also their experimental measurements has been done on silica gel desiccant wheel. As a general result, one can say that the type and atmosphere of these works are completely different [8-11].

Studies in recent years have been necessary to improve the system's performance and reliability and reduce their costs and also to enhance the commercial competitiveness of desiccant dehumidification systems and expand their market [16-20]. For example, the one-dimensional model by using MATLAB programing to simulate the desiccant wheel has been presented when it was combined with the direct evaporative cooling, or indirect evaporative cooling, or hybrid desiccant cooling systems then it has compared between their performances [16]. An experimental comparison between the fully and annular packed beds by Adding a new configuration that integrating each of them with oscillated helical coil heat pipes have been done [17]. Also the effect of channel geometry of the desiccant wheel on its performance has been studied and that in this case, Five types of channels have been examined (triangular, square, hexagonal, sinusoidal-1, and sinusoidal-2) [20].

In Table 1 and Table 2 some of the previously investigated solid desiccant dehumidifier packed bed configurations including targets and some approaches have been summarized. In this regard, the detailed discussion of the current designs configurations and the main differences between them may help future researchers to come up with novel, innovative designs, to overcome the system's drawbacks and make them actual viable alternative competitors in the dehumidification market [33].

Of course, it should be noted that this study was conducted with a time interval from the previous research. This is because some theoretical studies and experimental researches have been completed. Finally, the ultimate goal of this study is to develop a new mathematical explicit model to analyze desiccant performance. With the implementation of a control volume technique, difference equations have been developed which were in turn used in the derivation of the governing differential equations for momentum in the air stream and also for heat and mass transfer both within the desiccant and in the air stream. These finite difference equations were solved using a quasi-central finite difference scheme. Boundary and initial conditions, Ackermann correction factor, thickness of desiccant matrix, air stream velocity and density,

rotation speed, angle of regeneration section are examples of the parameters that have been changed throughout the analysis of each total mass, enthalpy

(energy) and momentum changes. The effects of such parameter changes have been investigated as well.

Table 1. Comparative study of some previous solid desiccant packed bed investigations.

Target	Desiccant Kind
Theoretical and experimental investigations of 5 different values of diameter ratio for a hollow cylindrical shape used as a radial flow single-stage solid desiccant dehumidifier [21].	Silica Gel
Theoretical and experimental investigations of an eight-layer silica gel single-stage packed bed system were employed to study the influence of configuration and operational parameters on efficiency [22].	Silica Gel
A single-stage single-packed bed was used to experimentally analyze the efficiency of the desiccant bed for radial flow [23].	Activated Alumina
Experimental and theoretical examinations for a hollow packed bed to simulate the transient combination heat and mass transfer [24].	Silica Gel
Theoretical and experimental investigation for two packed beds assembly to simulate the thermal swing adsorption cycle [25].	Silica Gel
Introducing an intercooler heat exchanger between two sections of a single packed bed. Theoretical and experimental investigation for the intercooler effect [26].	Silica Gel
Experimental comparison between two different configurations. The first one is a traditional axial packed bed and the second is a heat exchanger with desiccant granules inside the fin gaps [27].	Silica Gel
Experimental investigation of a fixed double bed dehumidifier using two finned tube heat exchangers with desiccant granules between its fins and actuated shutters to direct the airflow [28].	Silica Gel
Introducing a tool for accurate prediction of the thermal performance of a single-stage packed bed [29].	Silica Gel
A humidifier was used to increase the indoor humidity in typical winter conditions in Italy [19].	Silica Gel
A novel MFBDD system was designed and experimentally studied [30].	Silica Gel
Prediction of the characteristics of the transient mass and heat transfer of the desorption process of a packed bed using a CFD model [31].	Silica Gel
Adding a water heating and cooling device to Shamim's configuration [30]. Calculating numerically the transient heat and mass transfer, optimization for all parameters [18].	Silica Gel
An experimental investigation of a Z-annular packed bed with three diametrical ratios that offered radial distribution of airflow [32].	Silica Gel
An experimental comparison between the fully and annular packed beds. Adding a new configuration by integrating each of them with oscillated helical coil heat pipes [17].	Silica Gel

Table 2. Comparison of the Approaches of different solid desiccant dehumidifiers

Approaches	Regeneration Method
The adsorption period for appropriate performance was found to be about 15 min for a 7.2 diameter ratio. This period decreased with increasing the bed diameter ratio or the airflow rate [21].	Electrical heater
The inlet temperature was the main parameter that affects the desorption rates. After an hour, the accumulated water quantity between the first and last layers of the bed might range from 200 to 400 % based on the inlet condition [22].	Electrical heater
This system reached very low levels of 1.2 g/kg at inlet conditions of air humidity from 18.7 to 12.5 g/kg [23].	Electrical heater
Desorption time and temperature had a large effect on the adsorption process performance. Pre-cooling or cooling the adsorption bed enhanced the cycle performance [24].	Electrical heater
By extending the length of the bed, the humidity ratio of the outlet air decreased. The cycle performance was enhanced by raising the velocity of the inlet air [25].	Electrical heater
The optimum intercooler position was found to be within a range of 0.45 to 0.65 of the total bed lengths for a bed length range of 5 to 100 cm. For a high air flow rate desiccant bed, the intercooler had no effect [26].	Electrical heater
Using finned tube air-water heat exchanger enhanced dehumidification performance as a result of cooling the desiccant material during the adsorption process [27].	Hot water heat exchanger
This system could use low-grade heat supply temperature sources below 55° C. The Specific Cooling Power (SCP) was ranged between 30 and 180 (W kg ⁻¹ of adsorbent) [28].	Hot water heat exchanger
A small fin pitch (4 mm) had the best performance. A new semi-empirical formula is used as an accurate prediction tool of the system performance with the variation of the operating condition [29].	Hot water heat exchanger.
The regeneration bed increased the humidity ratio of the building supplied air from 1.5 g kg ⁻¹ to 5.3 - 6.1 g.kg ⁻¹ and temperature of 60° C [19].	Heating coil
This novel configuration decreased the pressure drop of the bed by approximately 98% and increased the average adsorption capacity by 36% compared to a conventional desiccant dehumidification system [30].	Dry nitrogen
The theoretical results showed an agreement with the experimental results obtained in [30-31].	Dry nitrogen
Adding heating and cooling water enhanced the system performance. Adsorption and desorption isotherms have a significant influence on the system performance [18].	Heating water
The best performance of the Z-annular configuration was achieved by lowering the temperature to around 4.22 to 5.47° C below that of the standard bed. The pressure drop in the Z-annular bed is larger than that in the standard packed bed [32].	300W heating element.
The annular bed had an adsorption rate larger than the full bed. The temperature reduction was between 20° C to 3° C due to using a heat pipe [17].	300W heating element.

2. Mathematical Model of a Two Dimensional Rotary Wheel

2.1 Basic Equations

A rotary regenerative desiccant wheel is shown in figure 1(a). It is a rotary cylindrical wheel of length L and diameter d_w and it is divided into two sections: adsorption section (angle fraction ϕ_0) and regeneration section (fraction $1-\phi_0$), where the adsorption and regeneration air streams are in a counter flow arrangement. The wheel generally consists of a matrix of numerous flow channels which have, depending on the manufacturing process, a rectangular, triangular or sinusoidal shape. The channel walls are parallel to the axis of the wheel, and are made of composite materials which have a desiccant content of 0.7 -0.8.

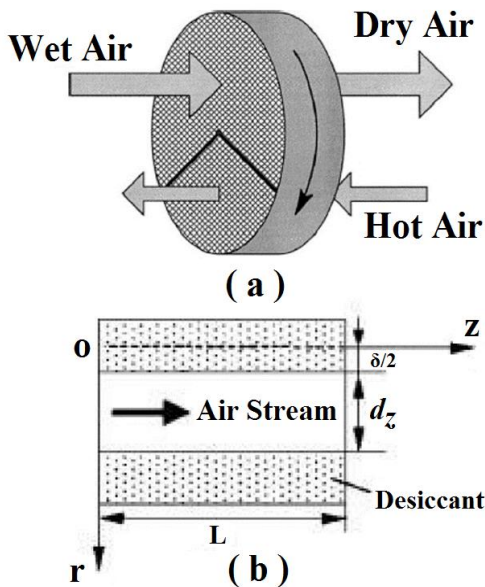


Figure 1. Schematic of the desiccant wheel showing (a) the entire wheel, (b) a side view of one of the ducts

It is assumed that the velocity of air stream and the diameter of micro channels effect on desiccant performance. The rotary wheel is a total enthalpy exchanger when it operates as a revolving exchanger circulating between two opposing air streams. Four equations concerning water content balance and energy conservation are used to describe the complicated heat and mass transfer occurring in moisture adsorption and regeneration and one equation is used to describe momentum. As already mentioned, in the previous studies the specifications of the dehumidification desiccant wheel have been completely presented [34-35]. In terms and the structure of governing equations and to solve the model, in the numerical examination of an unsteady thermo-solutal mixed convection when the extra mass and heat diffusions, there have been some similarities to work. [36].

For simplicity, some assumptions are made:

1. Two dimensional air stream flow is considered.
2. The axial heat conduction and mass diffusion in the fluid are neglected.
3. Effect of centrifugal force is neglected due to low rotation speed of the rotary dehumidifier
4. No leakage takes place between dehumidification and regeneration sections.
5. Heat and mass transfer in radial direction is not taken into consideration.
6. The thermodynamic properties in the solid are constant and uniform.
7. Shell of the rotary dehumidifier satisfies the insulated condition.
8. Velocity profile is one dimensional and considerable along z direction.

Consequently, the model used in this study is transient and two dimensional. Heat and mass conservation for the air stream

$$\frac{\partial(\rho_{da}Y)}{\partial \tau} + \omega \frac{\partial(\rho_{da}Y)}{\partial \phi} + \frac{\partial(\rho_{da}Yu)}{\partial z} = K_Y \cdot f_v (Y_w - Y) \tag{1}$$

Conservation of energy for the process air:

$$\frac{\partial(\rho_{da}C_{pe}t)}{\partial \tau} + \omega \frac{\partial(\rho_{da}C_{pe}t)}{\partial \phi} + \frac{\partial(\rho_{da}uC_{pe}t)}{\partial z} = A_f \cdot \alpha \cdot f_v (t_w - t) + K_Y \cdot f_v (Y_w - Y) C_{pv} t \tag{2}$$

Conservation of water content for the absorbent:

$$\frac{\partial W}{\partial \tau} + \omega \frac{\partial W}{\partial \phi} - D_{eff} \left[\frac{1}{r} \frac{\partial^2 W}{\partial \phi^2} + \frac{\partial^2 W}{\partial z^2} \right] = \frac{K_Y \cdot f_v}{\rho_w} (Y - Y_w) \tag{3}$$

Conservation of energy for the absorbent:

$$\frac{\partial t_w}{\partial \tau} + \omega \frac{\partial t_w}{\partial \phi} - \frac{\lambda}{\rho_w (C_{pw} + WC_{pl})} \cdot \left[\frac{1}{r} \frac{\partial^2 t_w}{\partial \phi^2} + \frac{\partial^2 t_w}{\partial z^2} \right] = \frac{1}{\rho_w (C_{pw} + WC_{pl})} [A_f \cdot \alpha \cdot f_v (t - t_w) + K_Y \cdot f_v (Y - Y_w) Q] \tag{4}$$

Momentum equation for the process air:

$$\frac{\partial(\rho_g \cdot u)}{\partial \tau} + \frac{\partial(\rho_g \cdot u^2)}{\partial z} = \frac{\Delta P}{L} \tag{5}$$

2.2 Auxiliary relations

The Ackerman heat transfer correction factor for mass transfer fluxes in phase j [37]:

$$A_f = \frac{C_f}{e^{C_f} - 1} \tag{6}$$

$$C_f = \frac{\sum_i J_{i,j} C_{p,i,j}}{h_j} \quad (j = g \text{ or } l) \tag{7}$$

For air stream process:

$$C_f = \frac{J \cdot C_{pa}}{h} \tag{8}$$

$$J = K_Y (Y_w - Y) \quad (9)$$

Mass transfer coefficient is calculated by acquiring experimental data. For air and water system, relationship between mass and heat transfer coefficient is given below:

$$K_Y = \frac{\alpha}{C_{p_e} Le} \quad (10)$$

where Le is Lewis number that for air and water system is equal to one. Heat transfer coefficient is obtained by optimization of experimental and theory data.

Table 1. Experimental condition to obtain heat and mass transfer coefficient

Variable	Environmental Condition	Input data
Relative humidity (%)	25	35.5
Temperature(C)	27.6	30.2
Velocity (m/s)	-	4.6

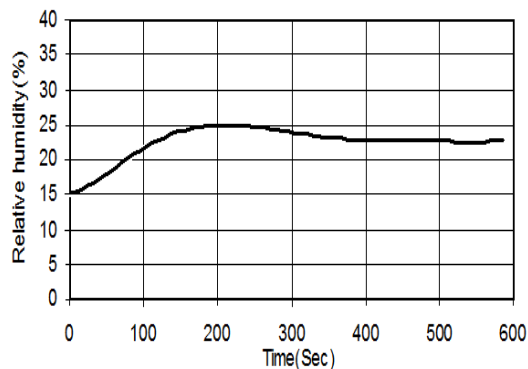


Figure 2. Relative humidity versus time at experimental condition

Mathematical correlation for the curve in figure 2 is given below:

$$RH_{EXP} = 3 \times 10^{-7} \tau^3 - 3 \times 10^{-4} \tau^2 + 0.1066 \tau + 14.072 \quad (11)$$

where RH_{EXP} is outlet relative humidity which is calculated experimentally.

By using error function and optimization between experimental and theory data, final correlations for heat and mass transfer coefficient are obtained as below:

$$\alpha = 0.671 m_i Re^{-0.51} (C_{p_a} + Y.C_v) \quad (12)$$

$$K_Y = 0.704 m_i Re^{-0.51} \quad (13)$$

For enthalpy calculations, different correlations were developed corresponding to different kinds of desiccant wheel, which are as follows for two types of Silica Gel [3]:

$$\text{Type I} \quad h = 0.312 h_{reg} + 0.8688 h_m \quad (14)$$

$$\text{Type II} \quad h = 0.1148 h_{reg} + 0.8852 h_m - 0.9474 \quad (15)$$

Enthalpy in the regeneration and inlet side of the wheel calculate by:

$$h = C_{p_a} t + C_{p_v} t Y \quad (16)$$

In the equations (12-16), the air humidity ratio near the wall of adsorbent is unknown; Therefore, three auxiliary relations are needed:

$$Y_w = 0.62198 \frac{RH}{\left(\frac{P_{atm}}{P_{ws}} + RH\right)} \quad (17)$$

Experimental value for silica gel relative humidity expression [10]:

$$RH = 0.0078 - 0.05759W + 24.1655W^2 - 124.478W^3 + 204.226W^4 \quad (18)$$

$$\ln(P_{ws}) = \frac{\lambda_1}{(t_w + 273.15)} + \lambda_2 + \lambda_3(t_w + 273.15) + \lambda_4(t_w + 273.15)^2 + \lambda_5(t_w + 273.15)^3 + \frac{\lambda_6}{\ln(t_w + 273.15)} \quad (19)$$

where the coefficients are as follows:

$$\begin{aligned} \lambda_1 &= -5800.2206 & \lambda_2 &= 1.3914933 \\ \lambda_3 &= -0.04860239 & \lambda_4 &= 0.41764768 \times 10^{-4} \\ \lambda_5 &= -0.14452093 \times 10^{-7} & \lambda_6 &= 6.5459673 \end{aligned}$$

Heat transfer coefficient is given below [11]:

$$\alpha = 0.671 m_i Re^{-0.51} (C_{p_a} + Y.C_v) \quad (20)$$

The adsorption heat of regular density silica gel is calculated by [11]:

$$Q = \begin{cases} -13400 W + 3500, & W \leq 0.05 \\ -1400 W + 2950, & W > 0.05 \end{cases} \quad (21)$$

The surface diffusivity for adsorption of silica gel is given as [11]:

$$D_{eff} = D_0 \left[-0.974 \times 10^{-3} \frac{Q}{t_w + 273.15} \right] \quad (22)$$

In this study, regular density (RD) silica gel is chosen as desiccant and several auxiliary equations are

appended meanwhile. The calculation conditions of the base case are listed.

For regeneration section, if $2\pi - \phi R \leq \phi < 2\pi$, then

$$Y_{in} = Y_2, \quad t_{in} = t_2 \quad (23)$$

For dehumidification section, $0 \leq \phi < 2\pi - \phi R$, then

$$Y_{in} = Y_1, \quad t_{in} = t_1 \quad (24)$$

In addition, the periodic boundary conditions are given as:

For air stream:

$$Y(0, z, \tau) = Y(2\pi, z, \tau) \quad (25)$$

$$t(0, z, \tau) = t(2\pi, z, \tau) \quad (26)$$

For desiccant bed:

$$W(0, z, \tau) = W(2\pi, z, \tau) \quad (27)$$

$$t_w(0, z, \tau) = t_w(2\pi, z, \tau) \quad (28)$$

If the transient problem is taken into consideration, the initial conditions are also necessary:

For desiccant,

$$W(\phi, z, 0) = W_0, \quad t_w(\phi, z, 0) = t_0 \quad (29)$$

For dehumidification air stream, $0 \leq \phi < 2\pi - \phi R$,

$$Y(\phi, z, 0) = Y_1, \quad t(\phi, z, 0) = t_1 \quad (30)$$

For regeneration air stream, $2\pi - \phi R \leq \phi < 2\pi$,

$$Y(\phi, z, 0) = Y_2, \quad t(\phi, z, 0) = t_2 \quad (31)$$

here, t_1 and t_2 denote the inlet air temperatures for dehumidification section and regeneration section, respectively, t_0 and Y_0 stand for temperature and humidity ratio at initial conditions, and Y_1, Y_2 stand for inlet air humidity for dehumidification and regeneration sections. Momentum equation boundary conditions for the process air:

Adsorption:

$$u(0, \tau) = u_0 \quad (32)$$

$$u(L, \tau) = u_a \quad (33)$$

Regeneration:

$$u(0, \tau) = u_0 \quad (34)$$

$$u(L, \tau) = u_r \quad (35)$$

2.3 Experimental Setup

In figure 3, the experimental setup of a solid adsorption cooling system with the cooling capacity of about 2 Cooling Ton and in figure 4, a schematic design of an adsorption cooling system provided with a rotary desiccant wheel is shown. Generally, the system consists of a cooling cycle and a desiccant wheel. Inlet air can be provided from point 1 or point 1'. If the air flows from point 1, it passes through a filter to lose any probable dust. In point 2, the filtered air is starting to flow through the desiccant wheel. The desiccant wheel rotates by an AC motor with a changeable rotation control system. Using this system, one can set the rotary speed according to the desired conditions to increase the quality of regeneration process. In point 3, air loses moisture by the adsorbent, and because of the condensation of moisture, temperature of the air increases. Then by passing the air through the evaporator of cooling cycle, its temperature reduces to the desired measure. The cooled air flows into the desired room and cools it which is point 4. For regeneration of the desiccant, outdoor air is consumed. At point 5, air flows into the regeneration chamber of desiccant. Air stream passes through an electric heater and its temperature rises. As a result, at point 6, there is a hot stream of air which is suitable to regenerate the desiccant. As the hot air passes through the desiccant, releases the moisture adsorbed by the desiccant and carries it out. Because of this process, at point 7, air temperature reduces a little but gains moisture. There are compressors and condenser of the cooling cycle at the end part of the system. A fan is used to cool the condenser which is cooled by the mandatory air stream made by the fan. In this research which is done to reach the above mentioned goals, only experimental test is done on the rotary desiccant wheel. Then, experimental conditions for inlet and outlet streams are like the ones in figure 5.



Figure 3. Photo of the solid adsorption cooling system equipment and wheel for doing experiments

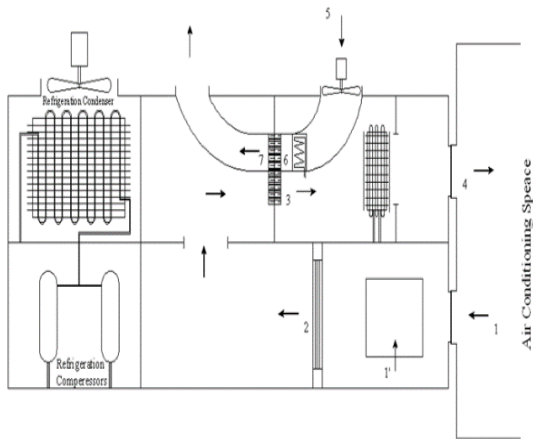


Figure 4. A schematic design of the full adsorption cooling system

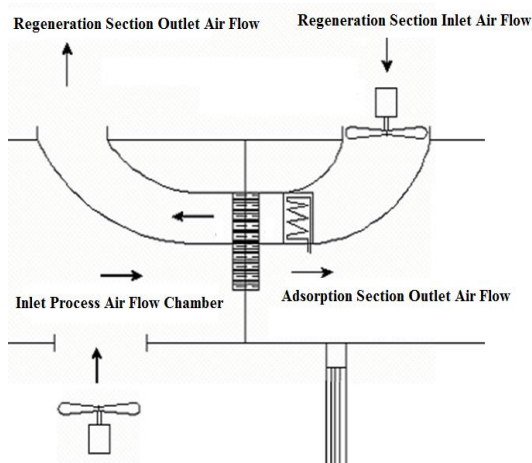


Figure 5. Schematic picture of the experimental system

3. Results and discussion

3.1 Model validation

In order to validate the current model, several comparisons are conducted in this section between measured results derived from experimental investigation and the ones predicted by the current model. The wheel used in the comparison is a commercially available desiccant dehumidification wheel. The dimensions of the wheel are listed in Table 2. The cross-area of each elementary channel is assumed to be 0.81 mm², and the number of gross elements is assumed as 14,600. In addition, the thickness of the adsorption is 0.1mm. The initial conditions in the cases are 20°C temperature and 25% relative humidity (or 3.69 g/kg-DA). The moisture content in the desiccant is in equilibrium with the ambient condition and is determined by Eq. 14 on the basis of inlet air temperature and humidity. The inlet parameters, including temperature and humidity ratio, are considered as a function of time and gradually increased from the ambient condition to the set points. The delay time is around 4 min in accordance with the experimental data. Wheel rotational speed is

10 rph, and airflow rate for both the adsorption and regeneration sections is 0.897 m³/s.

Table 2. Geometrical characteristics of desiccant wheel

Wheel dimensions	Unit	Value
Wheel depth	m	0.2
Wheel diameter	m	0.2
Wheel volume	m ³	0.178
Adsorption face area	m ²	0.593
Regeneration face area	m ²	0.593

Figures 6-7 plots the comparison of predicted and measured parameters, such as outlet air adsorption temperature and relative humidity or moisture removal capacity (MRC), in a transient process. In this case, adsorption inlet temperature is 31°C and regeneration inlet temperature is 88°C. Both inlet air humidity ratios are 12.5 g/kg-DA, which represent 45.1 and 3.1% RM, respectively. From Fig. 6 and Fig. 7, the prediction approaches the steady state a little more quickly than of the actual experiment. This is because the prediction is conducted under ideal operating conditions, while the actual system is affected by many uncertain factors, e.g. unstable heating and flow leakage

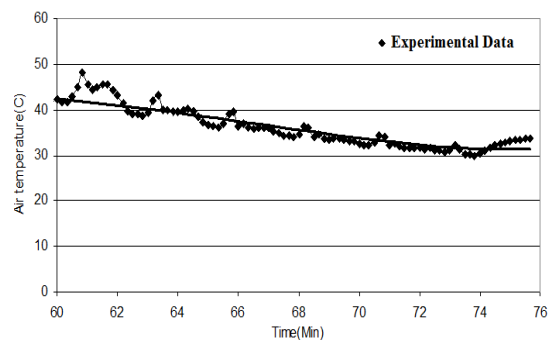


Figure 6. Outlet Air temperature versus time at experimental condition and theoretical model

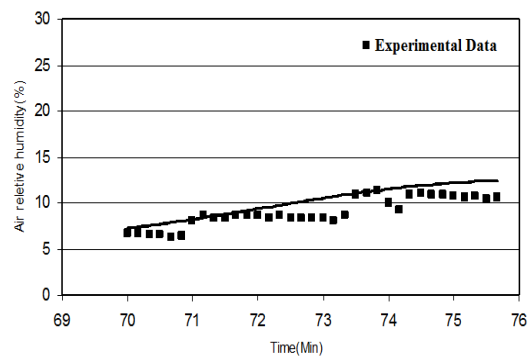


Figure 7. Outlet Relative humidity versus time at experimental condition and theoretical model

Figure 8 shows the comparison of predicted and measured air stream velocity in a steady state. In this case, regeneration inlet temperature is still 88°C, but adsorption inlet temperature is 35°C. The result illustrates that the predicted adsorption outlet air stream velocity is slightly more than the velocity in the experimental data. The difference is between 1 and 2 m/s. The moisture removal capacity is close to that of the experimental result. The regeneration outlet temperature is not compared because data were unavailable.

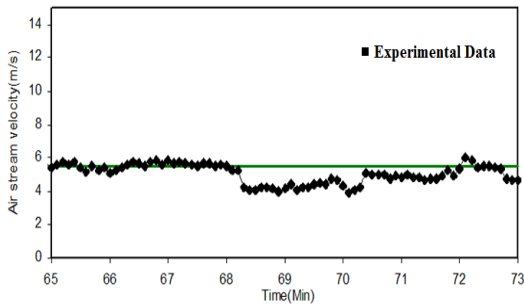


Figure 8. Air stream velocity versus time at experimental condition and theoretical model

3.2 Periodic profiles

The model can reveal the moisture and temperature morphology in both the airflow channel and the sorbent in detail. A typical periodic profile of the thermal parameters of an element in a steady state, including temperature and moisture content, is shown in Fig.9 to Fig.11. The adsorption inlet humidity ratio is 75% in the case shown. These figures show periodic performance in one and two complete rotation of the wheel. Second periods are different from the first one because of the bed temperature. When hot air stream enter the wheel from other side of the channel, bed temperature raises and consequently, the bed water content decreases. The periodic profile is formed as a result of the periodic alternation between adsorption and regeneration. The numerical model provides a strong tool for understanding and accounting for the complicated coupled processes inside the wheel.

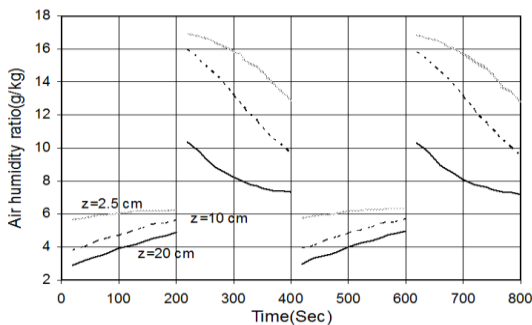


Figure 9. Periodic profile of predicted transient parameters of an element in a steady state for air humidity ratio

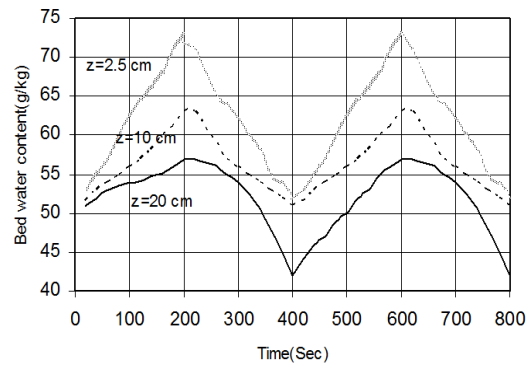


Figure 10. Periodic profile of predicted transient parameters of an element in a steady state for bed water content

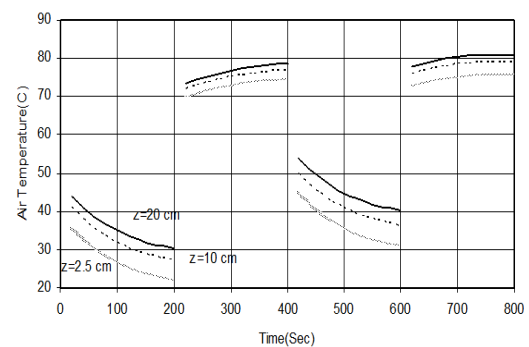


Figure 11. Periodic profile of predicted transient parameters of an element in a steady state for air temperature

3.3 Discussion on air stream velocity

Alongside the canal of desiccant wheel, since the temperature is more effective as the air temperature increases and reduces moisture, air stream velocity increases which can be proved by experimental results too. That is, with comparing the figures 12 and 13, air stream velocity increases from the initial amount of 4.6 m/s to the final amount of 6.5 m/s. But air stream velocity decreases in each section as time passes, since temperature which is the effective parameter decreases in each section as time passes (because gas is cooled)

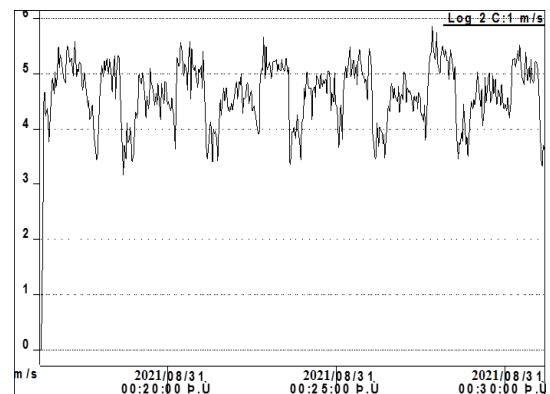


Figure 12. Velocity of inlet air stream versus time according to the experiment conditions

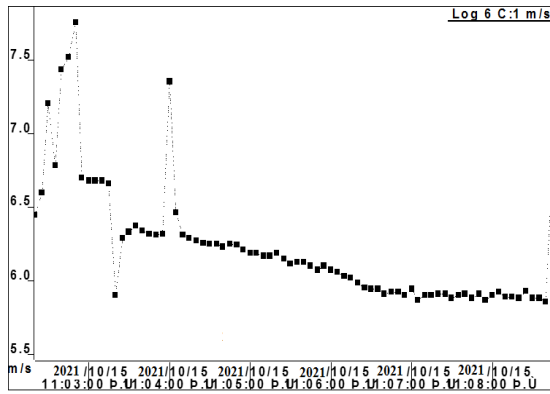


Figure 13. Experimental data for velocity of outlet air stream through wheel (m/s) versus time (s) which is recorded from 11:03 to 11:08 by the instrument

4. Conclusion

A mathematical model based on the two-dimensional Navier-Stokes equation was developed in an effort to investigate the transport phenomena occurring within the porous sorbent and the airflow channels in a desiccant wheel. These governing equations include those terms due to heat and mass transfer within the sorbent and between the sorbent and the flow channel. The model can reveal the moisture and temperature in both the airflow channel and the sorbent in detail as a function of time. The results predicted by the current model are further validated with reasonable accuracy against data taken from experimental results. Therefore, the numerical model is assumed to be a positive tool that accounts for the transport phenomena within the wheel and, consequently, is ideal for parameter studies that can lead to design optimization. As a demonstration of its utility, the model is employed to study the effect of periodic rotational of the wheel. The results illustrate that the rotational of the wheel influences both the transient and the steady-state performance of a desiccant wheel.

Acknowledgements

This study has been conducted based on a research Grant No. 528706 in the Materials and Energy Research Centre (MERC), which is hereby appreciated.

Nomenclature

A_f	Ackermann heat transfer correction factor
C_{pa}	Specific heat of air ($J \cdot kg^{-1} \cdot K^{-1}$)
C_{pl}	Specific heat of water ($J \cdot kg^{-1} \cdot K^{-1}$)
C_{pw}	Specific heat of desiccant ($J \cdot kg^{-1} \cdot K^{-1}$)
C_{pv}	Specific heat of water vapor ($J \cdot kg^{-1} \cdot K^{-1}$)
C_{fg}	Latent heat of water ($J \cdot kg^{-1}$)
C_{pz}	Specific heat of supporting materials ($J \cdot kg^{-1} \cdot K^{-1}$)

C_{pe}	Equivalent specific heat ($J \cdot kg^{-1} \cdot K^{-1}$)
D_{eff}	Effective diffusivity of desiccant ($m^2 \cdot s^{-1}$)
D_0	Effective diffusivity of desiccant at standard condition ($m^2 \cdot s^{-1}$)
f_v	Ratio of desiccant surface area to volume ($m^2 \cdot m^{-3}$)
f_s	Ratio of free flow area to section area of rotary wheel
h	Enthalpy ($J \cdot kg^{-1}$)
h_{in}	Enthalpy inlet or in the process side of the wheel ($J \cdot kg^{-1}$)
h_{reg}	Enthalpy in the regeneration side of the wheel ($J \cdot kg^{-1}$)
J	Mass flux ($kg \cdot m^{-2} \cdot s^{-1}$)
K_Y	Coefficient of mass convection ($kg \cdot m^{-2} \cdot s^{-1}$)
L	Thickness of the desiccant matrix (m)
m_i	Mass flow air per unit section area wheel ($kg \cdot m^{-2} \cdot s^{-1}$)
M_w	Desiccant mass per unit volume ($kg \cdot m^{-3}$)
M_z	Mass of supportive structure per unit volume ($kg \cdot m^{-3}$)
P_{ws}	Saturation pressure (Pa)
ΔP	Pressure drop in desiccant matrix channel (Pa)
P_{atm}	Atmospheric pressure (Pa)
Q	Adsorption heat ($J \cdot kg^{-1} \cdot water$)
r_1	Radius of the matrix axis (m)
r_2	Radius of the rotary wheel (m)
RH	Relative humidity
t	Temperature of air ($^{\circ}C$)
t_w	Temperature of desiccant ($^{\circ}C$)
T_{db}	Dry bulb temperature of the air ($^{\circ}C$)
u	Air stream velocity ($m \cdot s^{-1}$)
u_a	Velocity of dehumidification air stream ($m \cdot s^{-1}$)
u_r	Velocity of regeneration air stream ($m \cdot s^{-1}$)
W	Water content of desiccant ($kg_{water} \cdot kg^{-1}_{adsorbent}$)
Y	Humidity ratio ($kg_{moisture} \cdot kg^{-1}_{dry air}$)
Y_w	Humidity ratio near desiccant wall ($kg_{moisture} \cdot kg^{-1}_{dry air}$)

Greek symbols

α	Coefficient of heat transfer ($W \cdot m^{-2} \cdot K^{-1}$)
ρ_{da}	Dry air density ($kg \cdot m^{-3}$)
ρ_g	Wet air density ($kg \cdot m^{-3}$)
ρ_w	Water density ($kg \cdot m^{-3}$)
η	Dehumidifier performance
λ	Thermal conductivity of desiccant ($W \cdot m^{-1} \cdot K^{-1}$)
τ	Time (sec)
ω	Rotation speed (sec^{-1})
r, ϕ, z	Polar coordinates
ϕ_R	Angle of regeneration section

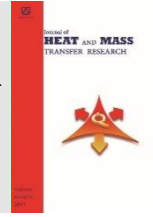
References

- [1] Staton, J.C., Scott, E.P., Kander, R.G., Thomas, J.R., 1998. Heat and mass transfer characteristics of desiccant polymers. M.S. Thesis, Virginia Polytechnic Institute and State University, Virginia, USA.
- [2] Konogula, M., Carpinlioglu, Ö.M., Yildirim, M., 2004. Energy and exergy analysis of an experimental open cycle desiccant cooling system. *Applied Thermal Engineering*, 24, pp. 919-932.
- [3] Beccali, M., Adhikari, R.S., Butera, F., Franzitta, V., 2004. Update on desiccant wheel model. *International Journal of Energy Research*, 28, pp. 1043-1049.
- [4] Beccali, M., Butera, F., Guanella, R., Adhikari, R.S., 2003. Simplified models for the performance evaluation of desiccant wheel dehumidification. *International Journal of Energy Research*, 27, pp. 17-29.
- [5] Maclaine-Cross, I.L., 1988. Proposal for a desiccant air conditioning system. *ASHRAE Transaction*, 94, pp.1997-2009.
- [6] Barlow, R.S., 1982. Analysis of Adsorption Process and of Desiccant Cooling System; a Pseudo-Steady-State Model for Coupled Heat and Mass Transfer. Solar Energy Research Institute TR, pp. 631-1330.
- [7] Collier, R.K., Cohen, B.M., 1991. An analytic investigation of methods for improving the performance of desiccant cooling system. *ASME Journal of Solar Energy Science and Engineering*, 113, pp. 157-163.
- [8] Zheng W, Worek WM, 1993. Numerical simulation of combined heat and mass transfer processes in a rotary dehumidifier. *Numerical Heat Transfer*, 23, pp. 211-232.
- [9] Zheng, W., Worek, W.M., Novosel, V., 1995. Performance optimization of rotary dehumidifiers. *ASME Journal of Solar Energy Science and Engineering*, 117, pp. 40-44.
- [10] Zhang, H.F., Yu, J.D., Liu, Z.S., 1996. The research and development of the key components for desiccant cooling system. *World Renewable Energy Congress*, pp. 653-656.
- [11] Zhang, L.Z., Niu, J.L., 2002. Performance comparisons of desiccant wheels for air dehumidification and enthalpy recovery. *Applied Thermal Engineering*, 22, pp. 1347-1367.
- [12] Dai, Y.J., Wang, R.Z., Zhang, H.F., 2001. Parameter analysis to improve rotary desiccant dehumidification using a mathematical model. *International Journal of Thermal Science*, 40, pp. 400-408.
- [13] Dai, Y.J., Wang, R.Z., Xu, Y.X., 2002. Study of solar powered solid adsorption desiccant cooling system used for grain storage. *Renewable Energy*, 25, pp. 417-430.
- [14] Pahlavanzadeh, H., Mozaffari, H., 2003. Performance optimization of rotary desiccant dehumidifiers. *Iranian Journal of science and Technology*, 27, pp.337-344.
- [15] Pahlavanzadeh, H., Zamzamin, A.H., 2006. A mathematical model for a fixed desiccant bed dehumidifier concerning Ackermann correction factor. *Iranian Journal of science and Technology*, 30, pp. 1-9.
- [16] Lee, Y., Park, S., Kang, S., 2021. Performance analysis of a solid desiccant cooling system for a residential air conditioning system. *Appl. Therm. Eng.*, 182, pp. 1-8.
- [17] Yeboah, S.K., Darkwa, J., 2021. Experimental investigation into the integration of solid desiccant packed beds with oscillating heat pipes for energy efficient isothermal adsorption processes. *Thermal Sci. Eng. Progress*, 21, pp. 100791.
- [18] Yu, L., Shamim, J.A., Hsu, W., Daiguji, H., 2021. Optimization of parameters for air dehumidification systems including multilayer fixed-bed binder-free desiccant dehumidifier. *Int. J. Heat Mass Transfer*, 172, pp. 121.
- [19] De Antonellis, S., Colombo, L., Freni, A., Joppolo, C., 2021. Feasibility study of a desiccant packed bed system for air humidification. *Energy*, 214, pp. 119002.
- [20] Bhabhor, K.K., Jani, D.B., 2021. Performance analysis of desiccant dehumidifier with different channel geometry using CFD. *J. Build. Eng.*, 44, pp. 103021.
- [21] Awad, M.M., Hamed, A.H., Bekheit, M.M., 2008. Theoretical and experimental investigation on the radial flow desiccant dehumidification bed. *Appl. Therm. Eng.* 28, pp. 75-85.
- [22] Kabeel, A.E., 2009. Adsorption-desorption operations of multilayer desiccant packed bed for dehumidification applications. *Renewable Energy*, 34, pp. 255-265.
- [23] Abd-Elrahman, W.R., Hamed, A.H., El-Emam, S.H., Awad, M.M., 2011. Experimental investigation on the performance of radial flow desiccant bed using activated alumina. *Appl. Therm. Eng.*, 31, pp.2709-2715.
- [24] Hamed, A.H., Abd-Elrahman, W.R., El-Emam, S.H., Awad, M.M., 2013. Theoretical and experimental investigation on the transient coupled heat and mass transfer in a radial flow desiccant packed bed. *Energy Convers. Manage.*, 65, pp. 262-271.
- [25] Ramzy, A.K., Kadoli, R., TP, A.B., 2013. Experimental and theoretical investigations on the cyclic operation of TSA cycle for air dehumidification using packed beds of silica gel particles. *Energy*, 56, pp. 8-24.
- [26] Ramzy, A.K., AbdelMeguid, H., Elawady, W.M., 2015. A novel approach for enhancing the utilization of solid desiccants in packed bed via intercooling. *Appl. Therm. Eng.*, 78, pp. 82-89.
- [27] Finocchiaro, P., Beccali, M., Gentile, V., 2016. Experimental results on adsorption beds for air dehumidification. *Int. J. Refrig.*, 63, pp. 100-112.
- [28] Pistocchini, L., Garone, S., Motta, M., 2016. Air dehumidification by cooled adsorption in silica gel grains. Part I: Experimental development of a prototype. *Appl. Therm. Eng.*, 107, pp. 888-897.
- [29] Pistocchini, L., Garone, S., Motta, M., 2017. Air dehumidification by cooled adsorption in silica gel grains. part ii: theoretical analysis of the

- prototype testing results. *Appl. Therm. Eng.*, 110, pp.1682–1689.
- [30] Shamim, J.A., Hsu, W.L., Kitaoka, K., Paul, S., Daiguji, H., 2018. Design and performance evaluation of a multilayer fixed-bed binder-free desiccant dehumidifier for hybrid air-conditioning systems: part i–experimental. *Int. J. Heat Mass Transfer*, 116, pp. 1361–1369.
- [31] Hsu, W.L., Paul, S., Shamim, J.A., Kitaoka, K., Daiguji, H., 2018. Design and performance evaluation of a multilayer fixed-bed binder-free desiccant dehumidifier for hybrid air-conditioning systems: part II–theoretical analysis. *Int. J. Heat Mass Transfer*, 116, pp. 1370–1378.
- [32] Yeboah, S.K., Darkwa, J., 2019. Experimental investigations into the adsorption enhancement in packed beds using Z-Annular flow configuration. *Int. J. Therm. Sci.*, 136, pp.121–134.
- [33] Abd-Elhady, M.M., Salem, M.S., Hamed, A.M., EL-Sharkawy, I.I., 2022. Solid desiccant-based dehumidification systems: A critical review on configurations, techniques, and current trends. *Int. J. of Refrigeration*, 133, pp.337–352.
- [34] Pahlavanzadeh, H., Zamzamian, S.A.H., Omidkhah Nasrin M.R., 2007. ANALYSIS OF EFFECTIVE PARAMETERS ON A ROTARY DESICCANT WHEEL PERFORMANCE. *MECHANICAL ENGINEERING SHARIF*, 23(40), pp. 155-162.
- [35] Zamzamian, S.A.H., Pahlavanzadeh, H., 2011. Theoretical and Experimental Investigation of the Key Components for a Rotary Desiccant Wheel. *Iranian Journal of Chemistry and Chemical Engineering (IJCCE)*, 30(3), pp. 25-30.
- [36] Ghaffarpasand O., 2018. Characterization of unsteady double-diffusive mixed convection flow with solet and dufour effects in a square enclosure with top moving lid. *Journal of Heat and Mass Transfer Research*, 5, pp. 51-68.
- [37] Winkelmann JGM, Sijbring H, Beenackers AACM, De Vries E.T., 1992. Modeling and simulation of industrial formaldehyde absorbers. *Chemical Engineering Science*, 47, pp.3785-3792.



Semnan University



Computational Analysis of Automobile Radiator Roughened with Rib Roughness

Robin Kumar Thapa ^a, Vijay Singh Bisht ^a, Kamal Rawat ^b, Prabhakar Bhandari ^{*c}

^a Department of Thermal Engineering, Faculty of Technology, Veer Madho Singh Bhandari Uttarakhand Technical University, Dehradun 248007, India.

^b Mechanical Engineering department, MIET, Meerut-250005, India.

^c Mechanical Engineering department, SOET, KR Mangalam University, Gurgaon -122103, India.

PAPER INFO

Paper history:

Received: 2022-06-26

Revised: 2023-02-05

Accepted: 2023-02-12

Keywords:

Heat transfer augmentation;
Nanofluid;
Pumping power;
Car radiator;
Artificial roughness.

ABSTRACT

Heat transfer enhancement in a car radiator using different nano fluids has been performed very often, but use of artificial roughness has been seldom done. In the present work, artificial roughness in the form of ribs has been incorporated in car radiator. A numerical comparative study has been performed between the ribbed automobile radiator and conventional radiator (flat tube). The nanofluid (Al₂O₃/Pure Water) has been used as a coolant in the car radiator configuration. The pitch is kept 15 mm (constant) for all the studies performed. The Reynolds number of the flow is selected in the turbulent regime i.e. ranging from 9350 to 23000 and the concentration of the nanofluid is taken from 0.1 to 1.0 %. It has been observed that the heat transfer rate improved with the ribbed roughness as compared to conventional configuration, but the pumping power has also increased. Furthermore, heat transfer rate also increased with increase in nano-particle concentration. The maximum heat transfer enhancement of 79% reported at nanofluid concentration of 1.0% and Reynolds number of 9350 for ribbed configuration.

DOI: [10.22075/jhmtr.2023.27617.1382](https://doi.org/10.22075/jhmtr.2023.27617.1382)

© 2022 Published by Semnan University Press. All rights reserved.

1. Introduction

In the automotive market, there is a huge demand for more powerful engines with aesthetic car design. The design department has to go through multiple challenges in doing so. One of the major problems is the dissipation of the waste heat produced by the engines (about one third of total heat) through cooling system. The waste heat should be rejected very effectively otherwise it may lead to various problems like increase in pollution, increase in fuel consumption and may even damage the engine components. With the increase in engine power, the radiator size also increases to dissipate extra waste heat. However, increasing the size of the radiator will lead to major design changes. This problem can be resolved by increasing the efficiency of cooling systems without changing the radiator size. The efficiency of the cooling system can be enhanced by using active and passive

methods. However, active method required external power. An efficient cooling system can decrease fuel consumption and helps to improve the engine performance [1].

The performance of the cooling system can be enhanced by using various heat transfer enhancement techniques viz. effective geometry, modified coolant, increased surface area etc. Apart from that use of fins and various designs of micro-channels are other ways to improve the performance [2]. Initially, Water was used as a working fluid to extract heat. However, due to its freezing point limitation, water has been mixed with freezing point depressants for its application. Weight fraction of freezing point depressant in the working fluid depends upon the local weather conditions.

However, use of freezing point depressant also affects the thermal conductivity of the working fluid [3]. The thermal characteristics of working fluid can be

*Corresponding Author: Prabhakar Bhandari.

Email: prabhakar.bhandari40@gmail.com

augmented by introducing nano particles. The use of nanofluids as a working fluid in engine cooling system has gain huge attention of researchers [4].

Choi and Eastman [5] were the first to show the use of nanofluids by using metal and metals oxides as suspended nanoparticles in base fluid. Afterwards, various researchers have used nanofluids to enhance the thermal performance of the car radiator. Ahmed et al. [6] investigated the thermal performance of the car radiator with TiO_2 -water nanofluids for the laminar flow regime. They concluded that the performance of the car radiator is optimal with 0.2% concentration of TiO_2 -water nanofluid. Naraki et al. [7] investigated the effect of CuO -water nanofluid on heat transfer in a car radiator and concluded that, heat transfer significantly increased with the use of nanofluid. Apart from that, they also reported heat transfer rate increased with increase in nano particle concentration and decreases with temperature. Heris et al. [8] also investigated thermal performance of CuO nanoparticles with water and ethylene glycol mixture and reported that Nusselt number increased with increase of Reynolds number and nano particle concentration. SiO_2 based nanofluid was also used in car radiator, and it was found that heat transfer enhanced by using nanofluid and significantly affected with particle concentration, flow rate and inlet temperature [9]. Various researchers have also used Al_2O_3 based nanofluids in automobile radiator to enhance the thermal performance [10-12]. Senthilraja et al. [13] compared the performance of a radiator using CuO and Al_2O_3 based nanofluids and concluded that CuO based nanofluid has performed better than Al_2O_3 based nanofluids. Furthermore, researchers also studied the effect of various types of inserts along with nanofluids on the thermal performance of radiator. Chougule et al. [14] experimentally investigated effect of wire coil insert with nanofluid in a circular tube. They observe augmented thermal performance for low volume concentration of CNT/water nanofluid. Recently, Singh et al. [15-16] had proposed dimple and protrusion in conical insert inside of heat exchanger for enhancing the performance.

In internal combustion engines, about 65% of the heat energy generated is wasted. About half of this total waste heat is dissipated through the cooling systems and the rest of the waste heat is lost through the tail pipes in exhaust gases. If cooling systems do not work effectively, then the performance of engine is strongly affected. Most of the studies have been focused on passive techniques and uses various inserts and different nanofluids. However, heat transfer augmentation in conventional car radiator using different nanofluids has been performed very often. Apart from that, use of artificial roughness has been seldom done. Therefore, in the present work computational study of roughened automobile radiator tubes with Al_2O_3 based nanofluid has been performed.

2. CFD Modelling

Fig. 1(a) shows the actual geometry of the car radiator which is considered for the present problem. It consists of the flat tubes since they offer low resistance to the surrounding air in comparison circular cross-section tubes. The horizontal fins are present between the vertical flat tubes. However, to reduce the computational cost and time, in the present work, only the single flat tube is considered and furthermore simulation has been performed for vertically halved portion to take the advantage of symmetry in the model as shown in figure.

Fig. 1(b) shows half of the single flat tube simulated in this study with specifications. The length of the flat tube is 310 mm. The width and height of the flat tube's cross-section are 3 mm and 20 mm respectively. The ribs were wrapped all around the inside wetted face of the flat tube.

Total of 20 ribs were placed in the radiator tube along its length and ribs are having a pitch of 15 mm as depicted in Fig. 2. The isometric view and specifications of the ribbed geometry is depicted in Fig. 2(a) and Fig. 2(b), respectively.

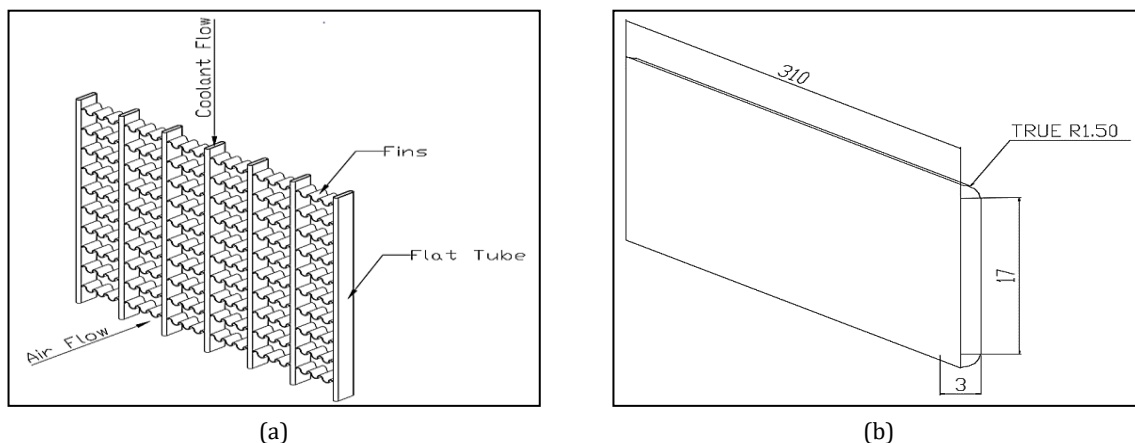


Fig. 1. (a) Actual model of the car radiator (b) Computational domain of single flat radiator tube (axis symmetric view)

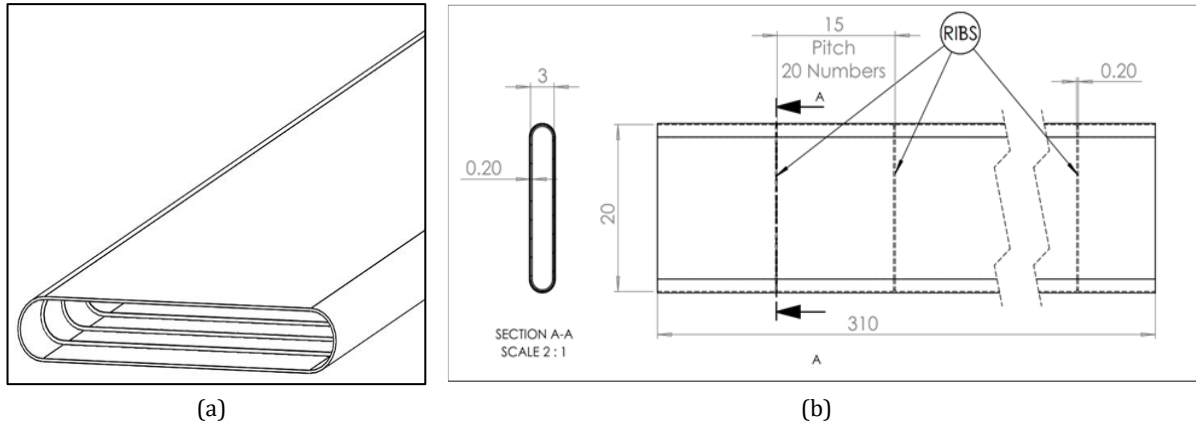


Fig. 2. Ribbed flat tube configuration (a) isometric view (b) Side and top view with specification

The continuity, momentum and energy equations for single phase flow are shown below:

Conservation of mass:

$$\nabla \cdot (\rho_{eff} \vec{u}) = 0 \tag{1}$$

Conservation of momentum:

$$\nabla \cdot (\rho_{eff} \vec{u} \vec{u}) = -\nabla P + \nabla \cdot (\mu_{eff} \nabla \vec{u}) - (\rho\beta)_{eff} (T - T_0)g \tag{2}$$

Conservation of energy:

$$\nabla \cdot ((\rho C_p)_{eff} \vec{u} T) = \nabla \cdot (k_{eff} \nabla T) \tag{3}$$

where, ρ , C_p , k , μ shows fluid density, specific heat, thermal conductivity and dynamic viscosity, respectively. While, the subscript eff is used for denoting effective value of nano fluid. \vec{u} is the velocity vector.

The heat transfer coefficient (CFD) and the corresponding Nusselt number can be calculated using the expressions shown below:

$$h_{nf}(CFD) = \frac{\rho_{nf}(A_t V_t) C_{p,nf} (T_{in} - T_{out})}{A_p (T_b - T_w)} \tag{4}$$

$$Nu_{nf}(CFD) = \frac{h_{nf}(CFD) d_h}{k_{nf}} \tag{5}$$

where, T_w is the weighted average temperature of the solid surface of tube which in interacting with the working fluid and is calculated directly from the FLUENT module of ANSYS. T_b is the bulk temperature and is calculated as

$$T_b = \frac{T_{in} + T_{out}}{2} \tag{6}$$

where, T_{in} and T_{out} is inlet and outlet temperature of the working fluid.

Nusselt number enhancement for ribbed radiator tube has also been calculated with respect to the flat or plain radiator tube for different nano particle concentrations. It has been calculated as:

Nu enhancement =

$$\frac{Nu(ribbed\ tube) - Nu(flat\ tube)}{Nu(flat\ tube)} \times 100\% \tag{7}$$

Pressure drop has been calculated as the difference of pressure values at inlet and outlet of the tube. Further, pumping power required for the fluid circulation in the flat/ribbed tube is calculated as product of mass flow rate with pressure drop.

The thermo-physical properties of nano fluid i.e. density, specific heat, thermal conductivity, and viscosity were obtained using following expressions:

Density of nano fluid has been calculated by the expression given by Pak and Cho [17]

$$\rho_{nf} = \phi \rho_p + (1 - \phi) \rho_{bf} \tag{8}$$

where, subscript p, bf and nf represents nano particles, base fluid and nano fluids. ϕ denotes the particle concentration.

Specific heat capacity of nanofluid was evaluated from the expression by Xuan and Roetzel [18]

$$C_{p,nf} = \frac{\phi \rho_p C_{p,p} + (1 - \phi) \rho_{bf} C_{p,bf}}{\rho_{nf}} \tag{9}$$

While, thermal conductivity has been calculated by Hamilton model [19]

$$k_{nf} = \frac{k_p + (\Phi - 1)k_{bf} - \phi(\Phi - 1)(k_{bf} - k_p)}{k_p + (\Phi - 1)k_{bf} + \phi(k_{bf} - k_p)} \tag{10}$$

where, Φ is empirical shape factor given by $\Phi = 3/\Psi$. Ψ is the particle sphericity of nano-particle which is measured as the ratio of surface area of a sphere that has same volume as the nano-particle to the actual surface area of the nano-particle. Since the shape of the particle considered in this study is spherical therefore the particle sphericity will come out to be 1. Hence the empirical shape factor considered in this study is 3.

The effective viscosity of nanofluid has been determined by Masoumi et al. [20]

$$\mu_{nf} = \mu_{bf} + \frac{\rho_p V_B d_p^2}{72 C \delta} \tag{11}$$

where V_B is the Brownian motion velocity

The thermo-physical properties considered for the base fluid and nano particles are tabulated in Table.1 For *turbulence* modelling, the k-epsilon turbulence model with enhanced wall treatment has been employed. SIMPLE algorithm was applied to resolve the pressure-velocity coupling while all the equations are discretized using second order formulations.

Table 1. Thermo-physical properties of base fluid (Water) and nano particles (Al_2O_3)

Properties	Base fluid (Water)	nano particles (Al_2O_3)
Density (kg/m^3)	988	3970
Dynamic Viscosity ($kg/m-s$)	0.0005468	-
Thermal Conductivity ($W/m-k$)	0.6436	40
Specific Heat ($J/kg-k$)	4179.55	765

For both the configurations, a high-quality grid was generated using the slicing technique in ANSYS

meshing application. The generated mesh for the ribbed configurations is shown in Fig. 3(a). The orthogonal quality has been maintained above 0.3 and the skewness below 0.77. Small sized elements are created in the region of high gradients i.e. near the walls and ribs.

The grid comprised of hexahedral and wedge shaped elements. Inflation layer also generated around the walls to capture the boundary layer and important feature of the flow. The cell wall distance, y is calculated as 0.0185 mm for $y+$ of 5. It is the distance of the cell centre of the first layer of elements from the wall. Therefore, the thickness of first layer of inflation layer is taken as 0.04 mm to achieve $y+$ of 5 at the wall.

Fig. 3(b) shows the variation of Nusselt number with number of elements for $Re = 9350$ for conventional radiator tube configuration. Total of five different cases has been considered in the grid independence test. It has been observed that last two grids has shown less than 1% variation in Nusselt number, so grid size having 525605 number of elements has been used in further study.

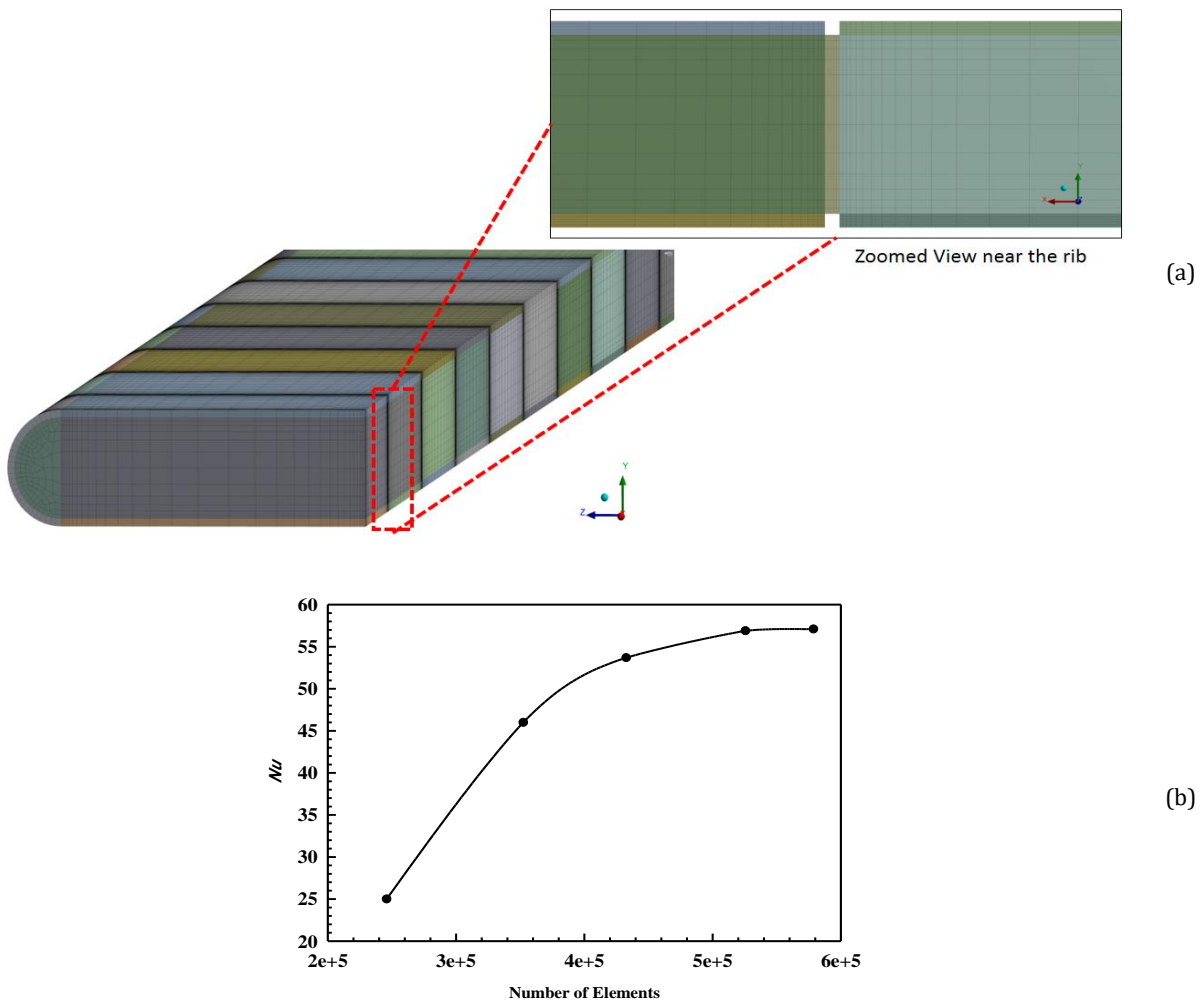


Fig. 3. (a) Grid generated for the ribbed flat tube configuration (b) Variation of Nusselt number in conventional radiator tube configuration with number of elements for $Re = 9350$

3. Validation

The present CFD model has been validated by comparing the results with published results of Delavari et al. [21] as depicted in Fig. 4(a). The validation has been performed under turbulent regime (Reynolds 9000-23000) for Al₂O₃ based nanofluid with different particle concentrations (0.1, 0.5 and 1%). From the comparison, it is found that results obtained though CFD model has good agreement with published results and the variation is not more than 8%. Furthermore, present work was also validated with the Nusselt number correlations provided by Dittus-Boelter and Gnielinski. The comparisons of Nusselt number value calculated from present study and correlations were shown in Fig. 4(b). It was observed that average percentage error between the present results and Dittus-Boelter correlations is 13.53%, while for Gnielinski correlation, the deviation of 3.1% was observed.

4. Result & Discussion

Fig. 5 (a & b) shows the velocity contours in the radiator tube with artificial roughness in the form of ribs. Fig. 5 (a) represents the results for the Reynolds number of 9350 and Fig. 5 (b) represents the results for the Reynolds number of 23000. Two extreme values of *Re* was considered for better understanding of flow physics. It can be observed that the artificial roughness has broken the laminar sub-layer region of the boundary layer at the walls and created a recirculation zone behind the ribs. This has helped to increase the heat transfer rate in the ribbed radiator tube configurations.

Fig. 6 (a & b) shows the contours of turbulent kinetic energy (TKE) in the ribbed radiator tube. Fig. 6 (a) represents the TKE contour for the Reynolds number 9350 and Fig. 6 (b) represents the TKE results for the Reynolds number 23000.

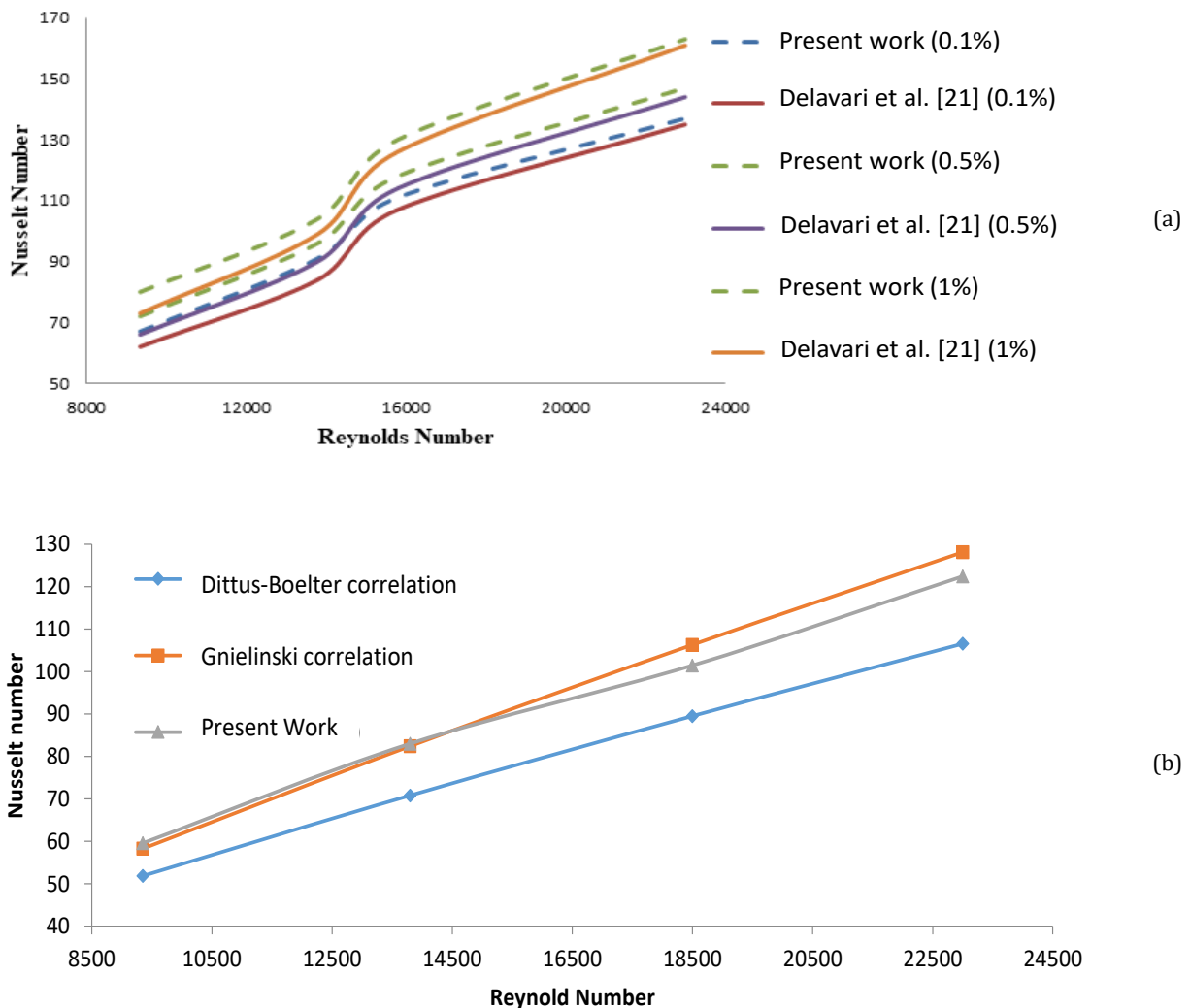


Fig. 4. (a) Comparison of present work with Delavari et al. [21] (b) Comparison of the Nusselt numbers calculated using correlations and from present work

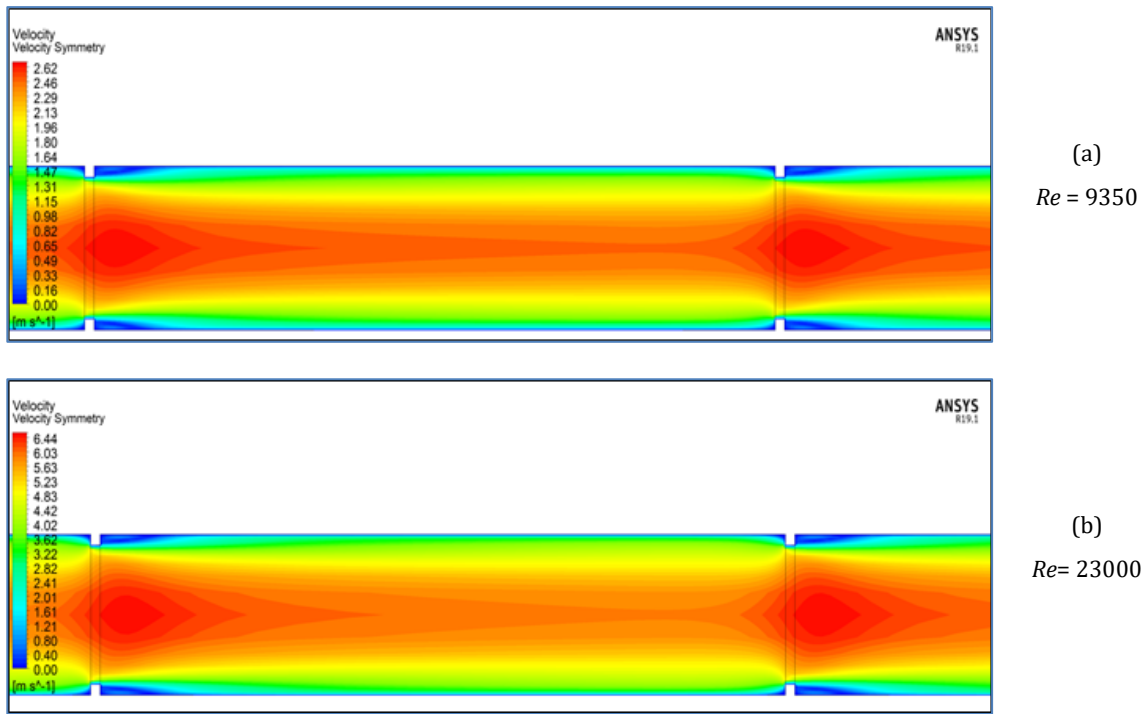


Fig. 5. Velocity contours at 1% nano-fluid concentration for (a) $Re = 9350$ (b) $Re = 23000$

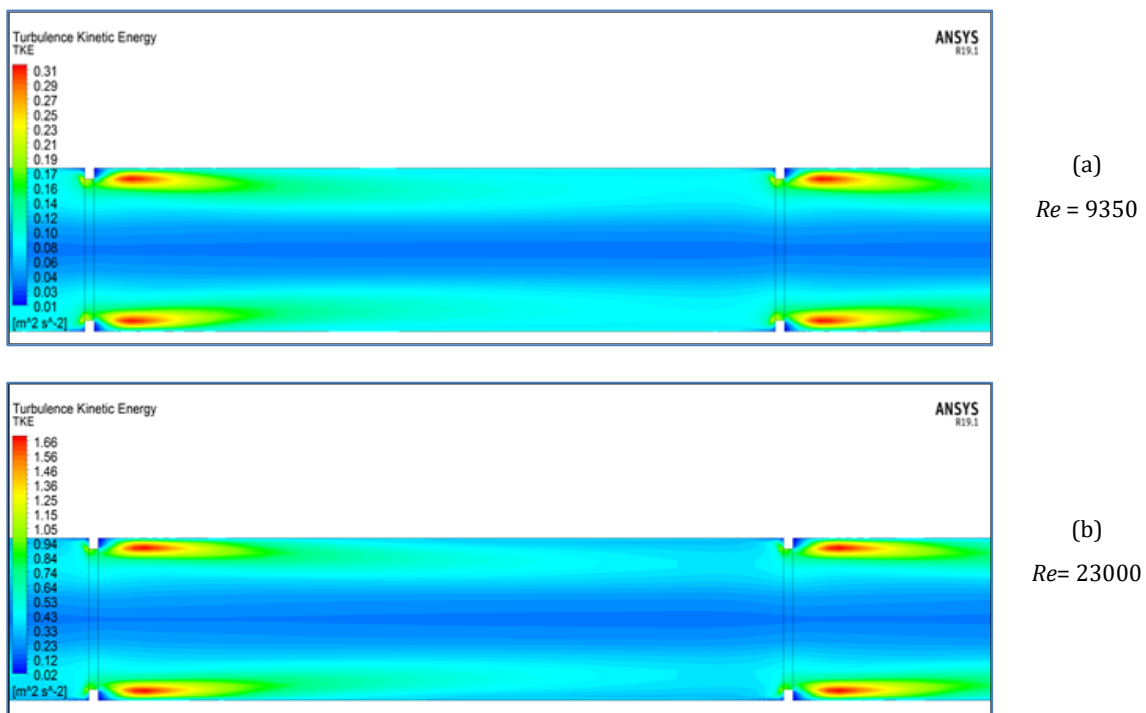


Fig. 6. Turbulent Kinetic Energy contours at 1% nano-fluid concentration for (a) $Re = 9350$ (b) $Re = 23000$

Fig. 7 shows the variation of the Nusselt number with Reynolds number in a conventional radiator tube and radiator tube with artificial roughness. The results are shown for different concentration of nanofluids (0.1 to 1%) for the turbulent flow regime (Reynolds number ranging from 9350 to 23000).

It can be observed from the figure that Nusselt no. increases with the Reynold number in both

conventional radiator tube and ribbed radiator tube configurations. It is also clear from the figure that the heat transfer significantly improved with the use of artificial roughness. Similar observation was reported by Yadav and his group [22-24] in case of solar air heaters. Apart from that, the effect of nanofluid concentration on Nusselt number can be seen.

Fig. 8 represents variation of percentage enhancement of Nusselt number with Reynolds number for ribbed radiator tube. The results are shown for different concentration of nanofluids (0.1 to 1%) for the turbulent flow regime (Reynolds number ranging from 9350 to 23000). It can be observed from figure that percentage enhancement in Nusselt number is more at lower Reynolds and then it decreases with increase in Reynolds number. For 1 % nanofluid, the heat transfer enhancement at Reynolds 9350 is about 79% and at Reynolds 23000 it is around 18 % which is lowest. At Reynolds 15500, all the three curves (0.1, 0.5 and 1.0%) intersect each other which indicates same enhancement at that location.

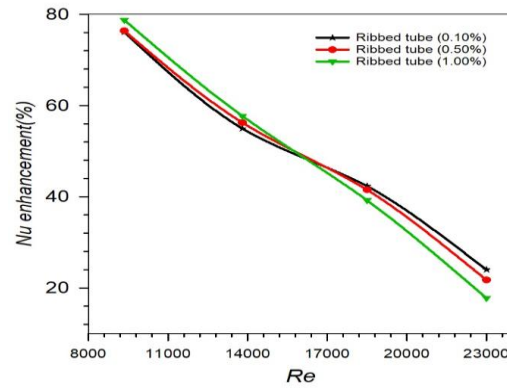


Fig. 8. Nusselt number enhancement percentage for ribbed flat tube configurations

The hydraulic performances for both radiator configurations are evaluated with the help of pressure drop and pumping power requirement. Fig. 9 shows the variation of the pressure drop with Reynolds number in a flat radiator tube with and without artificial roughness. The results are shown for different concentration of nanofluids (0.1 to 1%) for the turbulent flow regime (Reynolds number ranging from 9350 to 23000). It can be observed from the plot that ribbed tube has higher pressure drop compared to flat plat tube. This is attributed to increase in flow obstruction. Moreover, it can also be pointed that with increase in nano particle concentration, the pressure drop increases. Similar trend was observed for pumping power in Fig. 10.

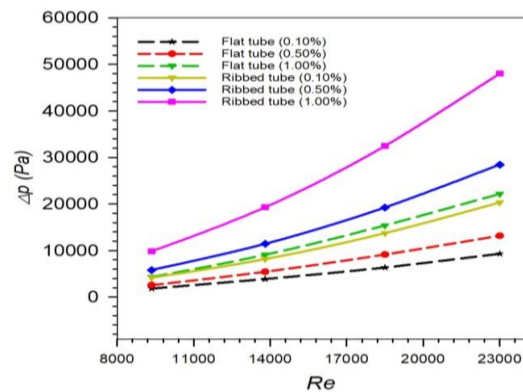


Fig. 9. Variation of pressure drop with Reynolds number

To assess the overall thermal performance of all configurations, various parameters has been used. It is commonly observed that with increase in heat transfer characteristics, pressure drop penalty also increases. Therefore, to evaluate the overall performance the parameter thermo-hydraulic performance factor (TPF) has been evaluated [25-28]. Fig. 11 shows the variation of TPF with Re for all configurations. The base case considered for evaluation of TPF is flat radiator tube with 0.1% nano fluid concentration. Among all the cases, ribbed radiator tube with 0.1% nano particle concentration has yielded best performance.

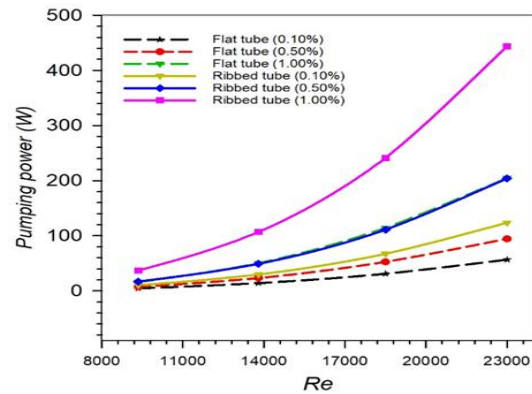


Fig. 10. Variation of pumping power with Reynolds number

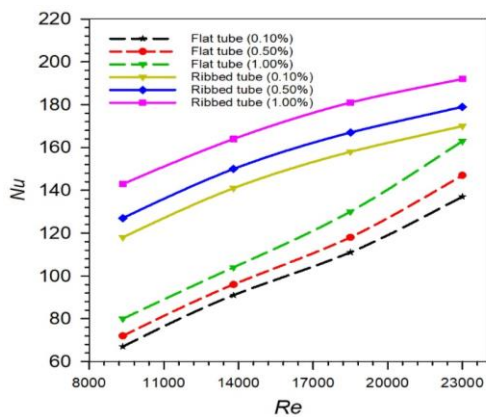


Fig. 7. Nusselt number variation for radiator tube with and without roughness

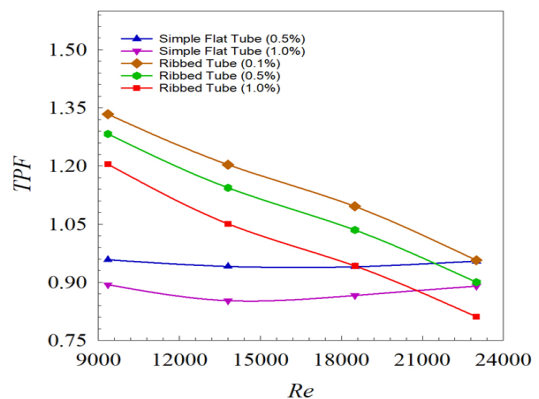


Fig. 11. Variation of TPF with Re for all configurations

Conclusion

In the present work, artificial roughness in the form of ribs has been provided in the simple flat tube of the car radiator. The water and Al_2O_3 nano-particles based nanofluid is used as a coolant for the study, with particle concentration varied between 0.1 - 1.0 %. The Reynolds number of the flow has been simulated in the range of 9350-23000. The Nusselt number and pumping power for all the configurations were studied in details. Following conclusions were drawn from the study:

1. For any configuration of the flat radiator tube (simple, or ribbed), the heat transfer coefficient increases with the increase in Reynolds number.
2. The heat transfer rate also increases with increase in nano-particle concentration from 0.1 to 1.0%.
3. On increasing the Reynolds number or nano-particle concentration the pumping power also increases significantly.
4. The application of artificial roughness in the form of ribs can increase the heat transfer coefficient as compared to that of simple flat tube for a particular Reynolds number.
5. For ribbed flat tube, the heat transfer enhancement is highest (79%) at $Re = 9350$ and lowest (18%) at $Re = 23000$ for nanofluid concentration of 1%.
6. For a constant heat flux, the required pumping power can be increased by up to 67% if ribs are employed in the conventional radiator tube at nano-fluid concentration of 1%.

Nomenclature

A_t	Cross sectional area of flat tube [mm^2]
A_p	Heat transfer area [mm^2]
C_p	Heat capacity [J/kgK]
C	Correction factor
d_h	Hydraulic diameter [mm]
d_p	Particle diameter [mm]
h_{nf}	Heat transfer coefficient [$\text{W}/\text{m}^2\text{K}$]
K	Thermal conductivity [W/mK]
Nu	Nusselt number

T_w	Average wall temperature of flat tube [K]
T_b	bulk temperature [K]
T_{in}	Inlet temperature [K]
T_{out}	Outlet temperature [K]
\vec{u}	Velocity vector [m/s]
V_t	Velocity at the inlet of flat tube [m/s]
Δp	Pressure drop [N/m^2]

Greek symbols

ρ	Density [kg/m^3]
μ	Dynamic viscosity [kg/ms]
\emptyset	Empirical shape factor
Ψ	Particle sphericity of nano-particle
δ	Distance between the nano particles [nm]

Subscript

nf	Nano fluid
bf	Base fluid
p	Nano particle

References

- [1] Goudarzi, K. and Jamali, H., 2017. Heat transfer enhancement of Al_2O_3 -EG nanofluid in a car radiator with wire coil inserts. *Applied Thermal Engineering*. 118, pp.510-517.
- [2] Arora, N. and Gupta, M., 2020. An updated review on application of nanofluids in flat tubes radiators for improving cooling performance. *Renewable and Sustainable Energy Reviews*. 134, pp.110242.
- [3] Naddaf, A., Heris, S.Z. and Pouladi, B., 2019. An experimental study on heat transfer performance and pressure drop of nanofluids using graphene and multi-walled carbon nanotubes based on diesel oil. *Powder Technology*, 352, pp.369-380.
- [4] Pak, B. C. and Cho, Y. I., 1998. Hydrodynamic and heat transfer study of dispersed fluid with sub-micron metallic oxide particles. *Experimental Heat Transfer*, 11, pp.151-170.

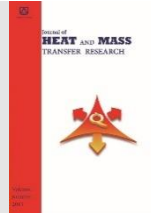
- [5] Choi, S. U. and Eastman, J. A., 1995. Enhancing thermal conductivity of fluids with nanoparticles. Argonne National Lab., IL (United States).
- [6] Ahmed, S. A., Ozkaymak, M., Sözen, A., Menlik, T. and Fahed, A., 2018. Improving car radiator performance by using TiO₂-water nanofluid. *Engineering science and technology an international journal*. 21(5), pp.996-1005.
- [7] Naraki, M., Peyghambarzadeh, S. M., Hashemabadi, S. H. and Vermahmoudi, Y., 2013. Parametric study of overall heat transfer coefficient of CuO/water nanofluids in a car radiator. *International Journal of Thermal Sciences*. 66, pp.82-90.
- [8] Heris, S. Z., Shokrgozar, M., Poorpharhang, S., Shanbedi, M. and Noie S. H., 2014. Experimental study of heat transfer of a car radiator with CuO/ethylene glycol-water as a coolant. *Journal of dispersion science and technology*, 35(5), pp.677-684.
- [9] Naraki, M., Peyghambarzadeh, S. M., Hashemabadi, S. H. and Vermahmoudi, Y., 2013. Parametric study of overall heat transfer coefficient of CuO/water nanofluids in a car radiator. *International Journal of Thermal Sciences*. 66, pp.82-90.
- [10] Bhogare, R. A. and Kothawale, B. S., 2014. Performance investigation of automobile radiator operated with Al₂O₃ based nanofluid. *IOSR Journal of Mechanical and Civil Engineering*. 11(3), pp.23-30.
- [11] Nambeesan, K. P., Parthiban, R., Kumar, K. R., Athul, U. R., Vivek, M. and Thirumalini, S., 2015. Experimental study of heat transfer enhancement in automobile radiator using Al₂O₃/water-ethylene glycol nanofluid coolants. *International Journal of Automotive & Mechanical Engineering*. 12, pp. 2857-2865.
- [12] Dhale, L. P., Wadhawe, P. B., Kanade, D. V. and Sable, Y. S., 2015. Effect of nanofluid on cooling system of engine. *International Journal of Engineering and Applied Sciences*. 2(10), pp.257815.
- [13] Senthilraja, S., Vijayakumar, K. C. and Gangadevi, R., 2015. Experimental investigation of Heat transfer performance of different nanofluids using automobile radiator. In: *Applied mechanics and materials*, vol. 787, Trans Tech Publications Ltd, pp. 212-216.
- [14] Chougule, S. S., Nirgude, V. V., Gharge, P. D., Mayank, M. and Sahu, S. K., 2016. Heat transfer enhancements of low volume concentration CNT/water nanofluid and wire coil inserts in a circular tube. *Energy Procedia*. 90, pp.552-558.
- [15] Singh, B. P., Bisht, V. S., Bhandari, P. and Rawat, K. Thermo-Fluidic Modelling of a Heat Exchanger Tube with Conical Shaped Insert having Protrusion and Dimple Roughness. *Aptisi Transactions on Technopreneurship*. 3(2), pp.13-29.
- [16] Singh, B. P., Bisht, V. S. and Bhandari, P., 2021. Numerical Study of Heat Exchanger Having Protrusion and Dimple Roughened Conical Ring Inserts In Advances in Fluid and Thermal Engineering, Lecture Notes in Mechanical Engineering. pp. 151-161.
- [17] Pak, B. C. and Cho, Y. I., 1998. Hydrodynamic and Heat Transfer Study of Dispersed Fluids with Submicron Metallic Oxide Particles. *Experimental heat transfer*. 11(2), pp. 151-170.
- [18] Xuan, Y. and Roetzel, W., 2000. Conceptions for Heat Transfer Correlation of Nanofluids. *International journal of heat and mass transfer*. 43(19), pp. 3701-3707.
- [19] Hamilton, R. L. and Crosser, O. K., 1962. Thermal conductivity of heterogeneous two-component systems. *Industrial and Engineering Chemistry Fundamentals*. 1(3), pp. 187-191.
- [20] Masoumi, N., Sohrabi, N. and Behzadmehr, A., 2009. A new model for calculating the effective viscosity of nanofluids. *Journal of Physics D: Applied Physics*, 42(5), pp.055501.
- [21] Delavari, V. and Hashemabadi, S. H., 2014. CFD simulation of heat transfer enhancement of Al₂O₃/water and Al₂O₃/ethylene glycol nanofluids in a car radiator. *Applied Thermal Engineering*. 73, pp.378-388.
- [22] Yadav, A. S., Shukla, O. P. and Bhadoria, R. S., 2022. Recent advances in modelling and simulation techniques used in analysis of solar air heater having ribs. *Materials Today: Proceedings*. 62(3), pp.1375-1382.
- [23] Yadav, A. S. and Gattani, A., 2022. Revisiting the influence of artificial roughness shapes on heat transfer enhancement, *Materials Today: Proceedings*. 62(3), pp. 1383-1391.
- [24] Yadav, A. S., Agrawal, A., Sharma, A., Sharma, S., Maithani, R. and Kumar, A., 2022. Augmented artificially roughened solar air heaters, *Materials Today: Proceedings*. 63, pp. 226-239.
- [25] Bhandari, P., 2022. Numerical investigations on the effect of multi-dimensional stepness in open micro pin fin heat sink using single phase liquid fluid flow. *International Communications in Heat and Mass Transfer*. 138, pp.106392.
- [26] Bhandari, P. and Prajapati, Y. K., 2021. Fluid flow and heat transfer behaviour in distinct array of stepped micro pin fin heat sink. *Journal of Enhanced heat transfer*. 28(4), pp. 31-61.
- [27] Bhandari, P., Prajapati, Y. K. and Uniyal, A., 2022, Influence of three dimensionality effects on thermal hydraulic performance for stepped micro pin fin heat sink. *Meccanica*. 2022.

[28] Bhandari, P. and Prajapati, Y. K., 2022. Influences of tip clearance on flow and heat transfer characteristics of open type micro pin

fin heat sink. *International Journal of Thermal Sciences*. 179, pp.107714.






Semnan University



Research Article

Parameter Estimation in Mass Balance Model Applied in Fixed Bed Adsorption Using the Markov Chain Monte Carlo Method

Rhaisa Sousa Tavares ^a, Camila Santana Dias ^b, Carlos Henrique Rodrigues Moura ^b,
Emerson Cardoso Rodrigues ^c, Bruno Marques Viegas ^d ,
Emanuel Negrão Macêdo ^c , Diego Cardoso Estumano ^{*d} 

^a Graduate Program in Process Engineering, Federal University of Pará, Pará, Brazil.

^b Graduate Program in Natural Resource in the Amazon, Federal University of Pará, Pará, Brazil.

^c Faculty of Chemical Engineering, Federal University of Pará, Pará, Brazil.

^d Faculty of Biotechnology, Federal University of Pará, Pará, Brazil.

PAPER INFO

Paper history:

Received: 2022-08-10

Revised: 2023-02-15

Accepted: 2023-02-21

Keywords:

Adsorption;
Breakthrough curve;
MCMC;
Parameter estimation;
Convergence analysis.

ABSTRACT

In this work, a mathematical model is adopted to predict the breakthrough curve in a fixed bed adsorption process, neglecting radial dispersion effects in the bed, with properties such as interstitial velocity and porosity being constant, linear adsorption kinetics and equilibrium relationship represented by the Langmuir isotherm. The resulting partial differential equation is numerically solved by the Method of Lines (MOL), while the Markov Chain Monte Carlo method is employed to estimate the model parameters, using simulated measures and a priori Gaussian probability distribution for the parameters, varying the mean and standard deviation. A convergence analysis was performed to look for numerical convergence between the number of nodes (N) used and the computational cost (CPU time) and it was observed that N = 100 obtained the lowest computational cost (less than 0.2 s). The estimated values of Peclet's number (Pe) and Langmuir's constant (KL) showed deviations of 7% and 0.01%, respectively, compared to their exact value which shows that the estimates were accurate, i.e., the parameters are close to the exact value. Also, the estimated values were within the credibility interval of 99 % established, which shows precise estimates. The information taken from these estimates has become of fundamental importance in predicting the behavior of the breakthrough curve at different points in the bed, showing that the MOL in combination with the MCMC are efficient tools in the direct and inverse analysis of models of breakthrough curves.

DOI: [10.22075/jhmtr.2023.28050.1389](https://doi.org/10.22075/jhmtr.2023.28050.1389)

© 2022 Published by Semnan University Press. All rights reserved.

1. Introduction

Pollution of water resources by the recalcitrant presence of emerging contaminants stimulates environmental concern about this topic and makes efforts aimed at remedying its negative effects on the environment relevant. In this sense, studies to develop

effective methodologies for the treatment of these contaminants have been carried out around the world [1-9]

Among the already known methods that are effective for environmental remediation purposes are photocatalysis [10], membrane ultrafiltration

*Corresponding Author: Diego Cardoso Estumano.

Email: dcestumano@ufpa.br

[11], ozonation [12], photo-Fenton reaction [13] and ion exchange [14]. In this scenario, adsorption stands out as an attractive alternative for presenting relative simplicity of execution, low implementation cost compared to other approaches, and considerable level of effectiveness [15-17].

Adsorption can be performed in batch; however, this mode of operation is inappropriate when dealing with large-scale wastewater treatment [18-20]. Thus, for its industrial application, the use of fixed bed columns is suitable since they allow the continuous passage of effluents with a high load of pollutants through a column filled with adsorbent [18;21-22].

Before the elaboration of a project of an industrial scale fixed-bed column, a mathematical model capable of successfully representing the dynamics of experimentally obtained breakthrough curves is needed [23-24]. Many analytical models have been widely used to describe the breakthrough curves in fixed bed column adsorption systems [25-29].

Despite their importance, these models fail to identify mechanisms such as axial dispersion in the bed and mass transfer between phases. In addition, they need experimental curves for their parameters to be estimated, limiting the scope of the analysis to this specific curve [30-34].

To overcome the limitations of analytical models in representing breakthrough curves, several works have used more complex approaches in relation to the topic

of adsorption in a fixed bed, some of which are highlighted in Table 1. In order to contribute to previous studies a model obtained from a mass balance for the fluid phase was used in this work, which is based on the conservation of mass in the system, kinetics, and conditions adsorption equilibrium[23].

The parameter estimation was performed from Bayesian inference perspective's to cover the effect that uncertainties intrinsic to the experimental execution would exert on the value found for the parameters. Since such effects can cause incompatibilities in the modeling by allowing physically improbable parameters to be obtained and, thus, affecting the design and operation of the process[35].

The Bayesian method of Markov Chain Monte Carlo (MCMC) was used in the estimation process. Simulated measurements were used to verify the elaborated code, and different levels of uncertainty were assigned to evaluate the effect produced on the results. The prior probability distribution, the one that contains previously available information about the analyzed system, was evaluated here by changes made to its characteristic metrics such as mean and standard deviation. The measurements that are usually obtained only at the exit of the bed were used to estimate information on the adsorptive process at other points in the column.

Table 1. Different approaches applied to the study of adsorption in a fixed bed column.

Breakthrough curve models	Equilibrium Isotherms	Kinetic	Solution Method	Parameter Estimation	Reference
Thomas Bohart-Adams Yan	-	-	Nonlinear adjustment	Origin Pro 8	[36]
Computational fluid dynamics (CFD)	Non-linear Langmuir	Linear Drive Force (LDF)	COMSOL Multiphysics	Empirical correlations	[24]
Thomas, Yoon-Nelson, Adams-Bohart and Wolbourska	-	-	Microsoft Excel's Solver Extension	Linear and Nonlinear Regression	[37]
Mass balance in fluid phase	Langmuir and BET	Linear Drive Force (LDF)	Runge-Kutta-Fehlberg Method	Minimization of an objective function using the downhill simplex optimization method	[38]
Logistic Model (Bohart-Adams, Yoon-Nelson and Thomas), Wolborska, Modified Dose-response, Clark, Gompertz and LogGompertz. Mass Transfer Model	Langmuir	Linear Drive Force (LDF)	Finite Elements	Comsol Multiphysics V5.4.	[34]
Hydrus-1D, Thomas, Yoon-Nelson and Bohart-Adams	General sorption model that, depending on the value of the parameters, may fall into the Langmuir, Freundlich or linear isotherm	-	Hydrus-1D	Levenberg-Marquardt and operational parameters by experiments	[39]

2. Direct Problem – Mass Balance

The representation of physical model is presented in Figure 1 and demonstrates in a simplified way an adsorption column with ascending feed of initial concentration C_0 and output current C .

The mass balance in a differential element of the bed was carried out assuming the following hypotheses: negligible radial dispersion, the significant variation was considered only in the axial direction, the solid/fluid interfaces establish a thermodynamic equilibrium state, porosity and interstitial velocity are constant [38].

$$\frac{\partial C(z,t)}{\partial t} + u_0 \frac{\partial C(z,t)}{\partial z} = D_{ax} \frac{\partial^2 C(z,t)}{\partial z^2} - \frac{\rho_L}{\varepsilon_L} \frac{\partial q(z,t)}{\partial t} \quad 0 < z < L, t > 0 \tag{1.a}$$

$$\frac{\partial q(z,t)}{\partial t} = k_s (q^*(z,t) - q(z,t)) \quad 0 < z < L, t > 0 \tag{1.b}$$

Langmuir Isotherm:

$$q^*(z,t) = \frac{q_{max} k_L C(z,t)}{1 + k_L C(z,t)} \tag{1.c}$$

Initial conditions:

$$C(z,0) = 0 \quad 0 < z < L, t = 0 \tag{1.d}$$

$$q(z,0) = 0 \quad 0 < z < L, t = 0 \tag{1.e}$$

Boundary conditions:

$$-D_{ax} \frac{\partial C(z,t)}{\partial z} = u_0 (C_0 - C(z,t)) \quad z = 0, t > 0 \tag{1.f}$$

$$\frac{\partial C(z,t)}{\partial z} = 0 \quad z = L, t > 0 \tag{1.g}$$

where u_0 is the fluid velocity, D_{ax} is the dispersion coefficient, ε_L is the bed void fraction, k_s is the kinetic constant, q_{max} is the maximum capacity of adsorption and k_L is the Langmuir parameter.

The dimensionless groups presented in Equation 2 were adopted; thus, the mass balance model in dimensionless form is shown in Equation 4.

$$\tau = \frac{t}{t_{ref}}; \quad \eta = \frac{z}{L}; \quad \theta = \frac{C}{C_0}; \quad Q = \frac{q}{q_r} \tag{2.a-f}$$

$$Pe = \frac{u_0 L}{D_{ax}}; \quad t_{ref} = \frac{L}{u_0}$$

$$K_s = k_s t_{ref}; \quad K_L = k_L C_e; \quad q_r = \frac{C_0}{\rho_L} \tag{2.g-k}$$

$$Q^* = \frac{q^*}{q_r}; \quad Q_{max} = \frac{q_{max}}{q_r}$$

where q_{max} , the maximum adsorption capacity in the column, is given by Equation (3):

$$q_{max} = \frac{C_0 Q}{1000W} \int_0^{t_r} \left(1 - \frac{C}{C_0}\right) dt \tag{3}$$

where Q is the volumetric flow rate (cm^3/min) and W is the adsorbent mass (g).

$$\frac{\partial \theta(\eta,\tau)}{\partial \tau} + \frac{\partial \theta(\eta,\tau)}{\partial \eta} = \frac{1}{Pe} \frac{\partial^2 \theta(\eta,\tau)}{\partial \eta^2} - \frac{1}{\varepsilon_L} \frac{\partial Q(\eta,\tau)}{\partial \tau} \quad 0 < \eta < 1, \tau > 0 \tag{4.a}$$

$$\frac{\partial Q(\eta,\tau)}{\partial \tau} = K_s (Q^*(\eta,\tau) - Q(\eta,\tau)) \quad 0 < \eta < 1, \tau > 0 \tag{4.b}$$

$$Q^*(\eta,\tau) = \frac{Q_{max} K_L \theta(\eta,\tau)}{1 + K_L \theta(\eta,\tau)} \quad 0 < \eta < 1, \tau > 0 \tag{4.c}$$

Initial conditions:

$$\theta(\eta,0) = 0 \quad 0 < \eta < 1, \tau = 0 \tag{4.d}$$

$$Q(\eta,0) = 0 \quad 0 < \eta < 1, \tau = 0 \tag{4.e}$$

Boundary conditions:

$$-\frac{\partial \theta(\eta,\tau)}{\partial \eta} = Pe (1 - \theta(\eta,\tau)) \quad \eta = 0, \tau > 0 \tag{4.f}$$

$$\frac{\partial \theta(\eta,\tau)}{\partial \eta} = 0 \quad \eta = 1, \tau > 0 \tag{4.g}$$

3. Metodology

3.1. Direct Model Solution – Methods Of Line

The numerical procedure used to solve the non-linear partial differential equation (PDE) was the method of lines. This method is used to solve the mass

balance model carried out in an adsorption column, to discretize the domain of the dependent variable $\theta(\eta, \tau)$ in space, transforming the obtained PDE into a system of time-continuous ordinary differential equations (ODEs) $\theta_i(\tau)$ [40].

The schematic representation shown in Figure 1 summarizes the discretization of the dimensionless domain in the range of $\eta = [0, 1]$. In the method of lines, the domain $0 < \eta < 1$ is discretized into $\Delta\eta$ equal lengths, where $\Delta\eta = 1/N - 1$ and N is the number of nodes in the spatial domain. Therefore, N ODEs are developed by discretizing the governing PDE and boundary conditions [40].

Equations 4.a-c describe the dynamics that occur in the bed and correspond to the internal points of mesh in the domain interval. Equations 5.a-c show the discretized PDE.

$$\frac{d\theta_i}{d\tau} = -\frac{\theta_i - \theta_{i-1}}{\Delta\eta} + \frac{1}{Pe} \frac{\theta_{i+1} - 2\theta_i + \theta_{i-1}}{\Delta\eta^2} - \frac{1}{\varepsilon_L} \frac{dQ_i}{d\tau} \quad (5.a)$$

$$\frac{dQ_i}{d\tau} = K_i (Q_i^* - Q_i) \quad (5.b)$$

$$Q_i^* = \frac{Q_{\max} K_L \theta_i}{1 + K_L \theta_i} \quad (5.c)$$

At $i = 1$ and $\eta = 0$ Equation 4.a takes the form described in Equation 5.d:

$$\frac{d\theta_1}{d\tau} = -\frac{\theta_1 - \theta_0}{\Delta\eta} + \frac{1}{Pe} \frac{\theta_2 - 2\theta_1 + \theta_0}{\Delta\eta^2} - \frac{1}{\varepsilon_L} \frac{dQ_1}{d\tau} \quad (5.d)$$

The boundary condition at the bed entrance described by Equation 4.f was used to determine θ_0 , using the central difference on $i = 1$, the arrangement as shown by Equation 5.

$$-\frac{\theta_1 - \theta_0}{2\Delta\eta} = Pe(1 - \theta_0) \therefore \theta_0 = \frac{\theta_1 + 2\Delta\eta Pe}{1 + 2\Delta\eta Pe} \quad (5.e)$$

To determine θ_i at PDE in $i = N_i$ (Equation 5.f), the backward finite difference was applied to the boundary condition of Equation 4.g, which assumed the form shown in Equation 5.g.

$$\frac{d\theta_{N_i-1}}{d\tau} = -\frac{\theta_{N_i-1} - \theta_{N_i-2}}{\Delta\eta} + \frac{1}{Pe} \frac{\theta_{N_i} - 2\theta_{N_i-1} + \theta_{N_i-2}}{\Delta\eta^2} - \frac{1}{\varepsilon_L} \frac{dQ_{N_i-1}}{d\tau} \quad (5.f)$$

$$\left. \frac{\partial\theta}{\partial\eta} \right|_{\eta=1} \Rightarrow 0 \frac{\theta_N - \theta_{N_i-1}}{\Delta\eta} = 0 \therefore \theta_N = \theta_{N_i-1} \quad (5.g)$$

It is important to emphasize that the Method Of Lines is a methodology to obtain an approximate solution of the PDE given by the Equations (4.a-g). Therefore, the limitation of the method tends to be in the amount of precision needed to approximate the exact solution.

This accuracy is related to the number of grid points and available computing power. In this way, a convergence analysis becomes necessary to provide the computational power necessary to reach adequate precision to approximate the solution.

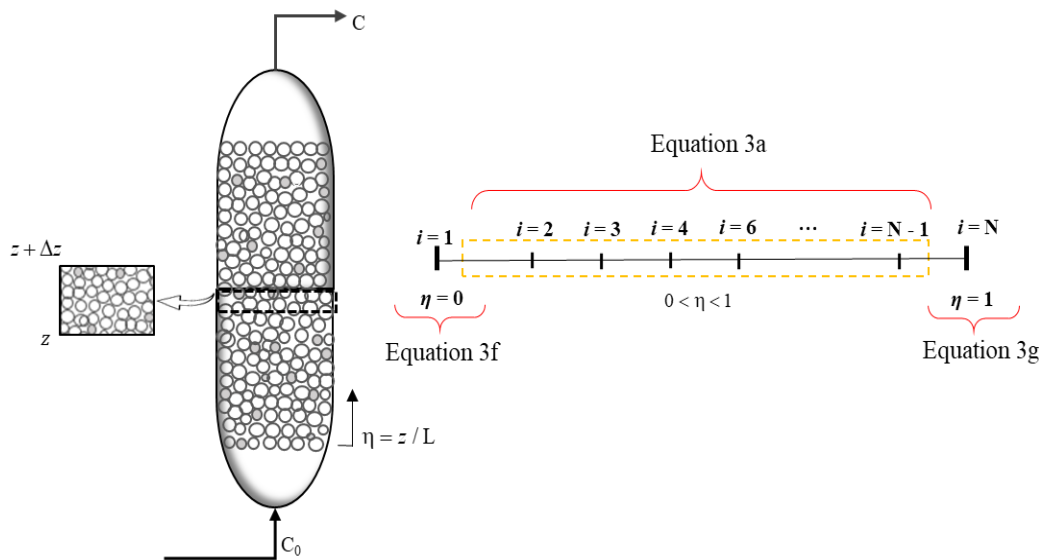


Figure 1. Model of an adsorption column and schematic representation of the domain discretized in the interval $\eta = [0, 1]$

In this work, the algorithm used for convergence analysis is shown below:

1. Obtain θ_1 solving the direct problem using N nodes
2. Obtain θ_2 solving the direct problem using $N + \Delta N$ nodes
3. Calculate the tolerance, $tol = \max(|\theta_1 - \theta_2|)$. If $tol < tol_{sc}$ stop, otherwise do $\theta_1 = \theta_2$ and return to step 2.

where is the value of the dependent variable obtained for N nodes, θ_2 the value of the dependent variable obtained for $N + \Delta N$ nodes, N is the number of nodes in the mesh, tol is the tolerance and tol_{sc} is the initial defined tolerance.

3.2. Inverse Problem – Markov Chain Monte Carlo

In many cases, different prior probability densities can be assumed for the parameters and thus, it is impossible to obtain an analytical treatment for a posterior probability distribution. In this scenario, the Markov Chain Monte Carlo method, an iterative version of traditional Monte Carlo methods, is used to extract samples of all possible parameters so that posterior probability inference turns into sample inference [41-45].

The MCMC combines the properties of Monte Carlo and the Markov chain. The first is estimating the properties of distribution by examining random samples from the distribution. On the other hand, the second aims at the idea that a given sequential process generates random samples, where each random

selection is used as a step to develop the next one. A particular property is that, although each new choice depends on the previous one, new samples do not rely on any instance before the last one.

In the present work, the Metropolis-Hastings algorithm is used to estimate the parameters of the mathematical model of the breakthrough curve[41;46-50], which following the following steps:

1. Initially, set an initial parameter value for the first iteration of the chain, P^1 . Then, draw a candidate value P^* from an auxiliary distribution $q(P^* | P^i)$. In the present work, the auxiliary distribution adopted is a Gaussian distribution in the following form:

$$P^* = P^i (1 + w \xi) \tag{6}$$

where ξ is a random variable $N(0,1)$ and w is the search step.

2. Compute the probability of acceptance $\alpha(P^{(i)} | P^*)$ of the candidate value given by:

$$\alpha(P^{(i)} | P^*) = \min \left[1, \frac{\pi(P^* | Y) q(P^{(i)} | P^*)}{\pi(P^{(i)} | Y) q(P^* | P^{(i)})} \right] \tag{7}$$

3. Generate a random number u from a uniform distribution $U(0,1)$;
4. If $u \leq \alpha(P^i | P^*)$, accept the new $P^{(i+1)} = P^*$ value. Otherwise, $P^{(i+1)} = P^{(i)}$.
5. Return to step 1.

A flowchart of the Metropolis-Hastings algorithm is illustrated in Figure 2 below.

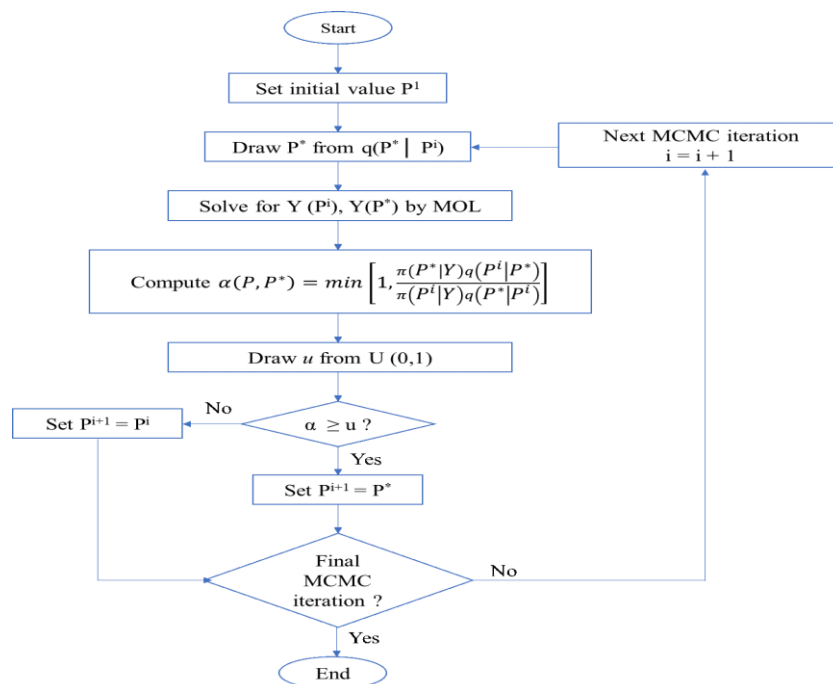


Figure 2. Sequential flowchart of the MCMC method using Metroplis-Hastings

In this work, simulated measures are used to carry out parameter estimates. Such measures are generated by adding noise, \mathbf{v} , so the measures by Equation (8):

$$\boldsymbol{\theta}^{meas} (1, \tau) = \boldsymbol{\theta}^{exact} (1, \tau) + \mathbf{v} \quad (8)$$

where $\boldsymbol{\theta}^{exact} (1, \tau)$ is the solution of the direct problems with knowing reference parameters and $\mathbf{v} = N(\mathbf{0}, \boldsymbol{\sigma}_{meas})$.

4. Results

The numerical tests carried out concerned the direct model's evaluation (presented in section 2) using the technique shown in section 3 to solve the inverse problem of parameter estimation involved in the adsorption phenomenon in a fixed bed column

The system of ordinary differential equations originated from the discretization of the partial differential equation and was solved by the *ode15s* function of the Matlab R2021a software. The same software programmed code for the Metropolis-Hastings algorithm.

The mesh convergence analysis is performed to verify the number of nodes (N_i) sufficient for model discretization when applying the method of lines and reaching a satisfactory convergence.

The number of nodes in the discretized domain varied, and how this variation influenced the computational time was observed. The relevance of this analysis for this work aim at the need that the MCMC method must solve the direct model several

times (10.000 states of Markov Chain), therefore defining the number of nodes and the desirable computational cost to obtain precision in the solution becomes desirable.

Simulated measurements were used to apply the estimates of the parameters of the analyzed model. The prior probability distribution of the parameters was adopted as Gaussian, and its influence and the influence of the acquisition frequency of measurements are evaluated. The simulations were performed using as a reference for the parameters the following values: $Pe = 10.00$, $K_s = 1.00$, $Q_{max} = 7.00$, $K_L = 1.00$ and $\epsilon = 0.40$. The choice of these parameters was to simulate a breakthrough without numerical instabilities, since the Peclet number (Pe) can be important to characterize the transport of solutes by advective or diffusive means, the numerical stability depends on the number of Pe . If they reach some critical limits the numerical solution begins oscillating in space and time.

The parameters Q_{max} , K_s can be calculated, and the porosity ϵ can be obtained experimentally. In this sense, the parameters estimated here were Pe because they included operational and diffusivity information, and K_L referring to the Langmuir isotherm.

4.1. Convergence Analysis

Figure 3 presents the results of the convergence analysis performed. It has been found that increasing the number of nodes increases the computational cost

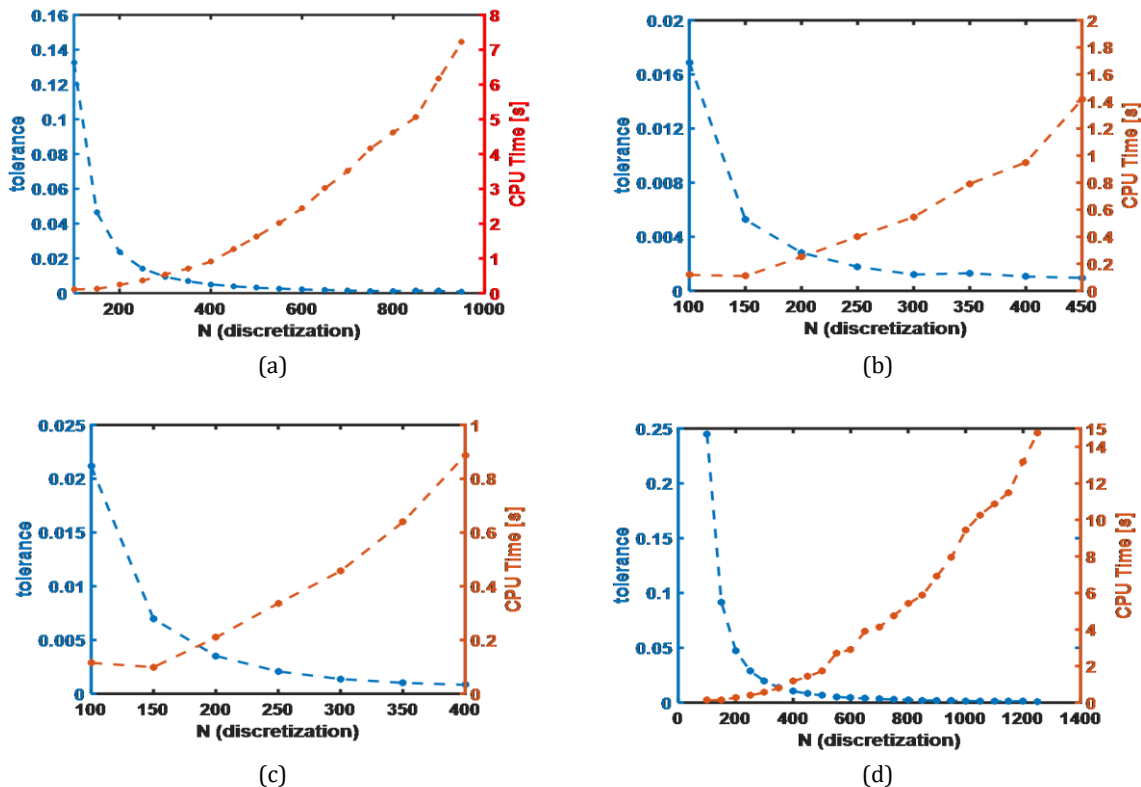


Figure 3. Convergence analysis regarding Q_{max} and ϵ were kept constant in 7.00 and 0.40, respectively. (a) $Pe = 10.00$; $K_L = 1.00$, (b) $Pe = 10.00$; $K_L = 3.00$, (c) $Pe = 2.00$; $K_L = 1.00$ e (d) $Pe = 20.00$; $K_L = 1.00$.

4.2. Prior Mean Analysis

The prior probability distribution of the parameters contains the information previously known. In this sense, variations in the mean of the prior probability distribution of the parameters, shown in Table 1, were performed to evaluate whether the estimated values would approach the exact value when the mean value of this distribution is changed.

The graph of the prior probability distribution function for these case studies is shown in Figure 4. It is possible to notice the displacement of the mean of the probability density distributions of the parameters Pe and K_L for each case concerning the value adopted as reference (green line).

Figure 5 shows the estimation result for case studies 1 and 5 (see Table 2). It is observed that the prior

distribution mean is far from the exact value. After the estimation process, the result shown by the posterior probability distribution converges to a determined region close to the reference, suggesting that despite the displacement carried out in the prior mean, adequate information regions to select candidate parameters could be reached, demonstrating the robustness of the MCMC method.

Table 2 shows the results of the estimates in all cases in which the influence of the displacement of the mean on the prior probability distribution is evaluated. It was possible to observe that there was precision for all cases since the estimated parameters are within the 95% credibility interval and accuracy since the estimates are close to the exact value of the parameters. It is also found that the deviations from the parameters' estimates were low and had a low level of uncertainty.

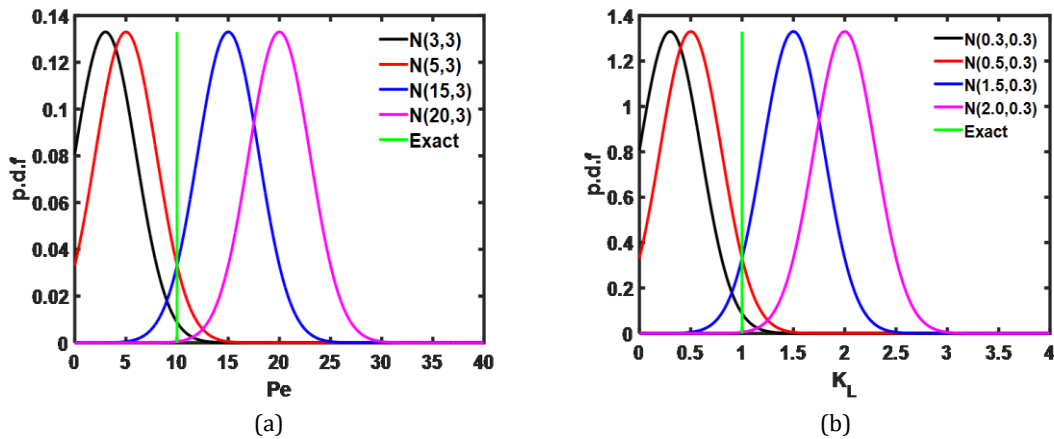


Figure 4. Prior probability distribution function (pdf) evaluating the influence of the mean for the parameters: (a) Pe (b) K_L .

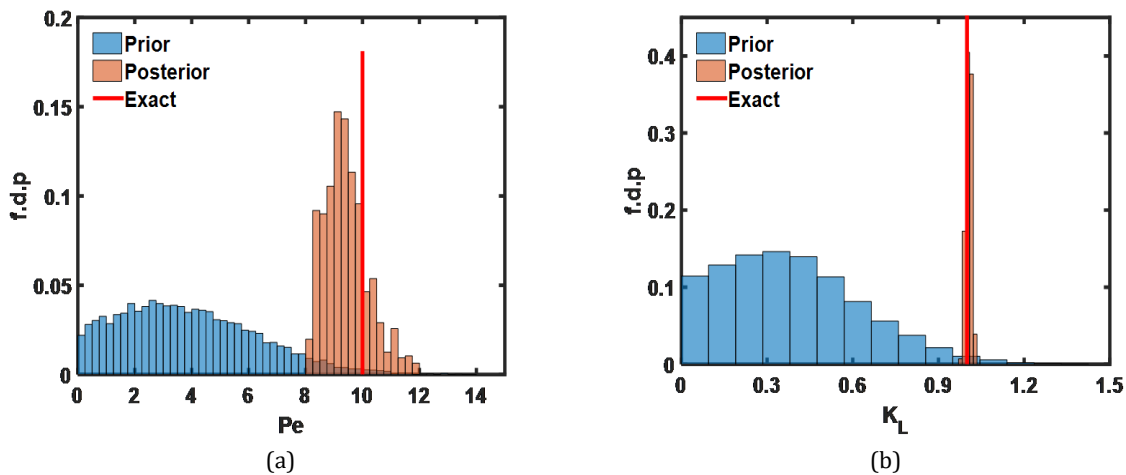


Figure 5. Prior and posterior probability distribution function evaluating the influence of the mean displacement on the parameters' prior: (a) Pe (b) K_L .

Table 2. Influence of the mean on the prior probability distribution.

Caso	Parameter	Exact	$\pi_{prior}(\mathbf{P})$	$\pi_{posterior}(\mathbf{P})$
1	Pe	10.00	N(3, 3)	9.84 (9.39;10.38)
2		10.00	N(5, 3)	9.79 (9.37;10.18)
3		10.00	N(15, 3)	10.02 (9.31;10.66)
4		10.00	N(20, 3)	9.39 (8.96;9.74)
5	K _L	1.00	N(0.3, 0.3)	1.00 (0.99;1.01)
6		1.00	N(0.5, 0.3)	1.00 (0.99;1.02)
7		1.00	N(1.5, 0.3)	1.00 (0.99;1.02)
8		1.00	N(2.0, 0.3)	1.01 (0.99;1.02)

4.3. Prior Standard Deviation Analysis

In addition to analyzing the influence of the mean, another critical assessment is to observe the effect that the variation in the standard deviation can have on the estimates since high standard deviation values can lead to uninformative priors. Even though they lead to own posteriors, poorly informative priors can generate a certain instability when posterior is obtained numerically [51].

Figure 6 shows the influence of different standard deviation values on the prior probability distribution

function of the parameters. It is possible to observe that the search for candidate parameters falls within a reduced range of values, whereas for more significant deviations, this range is extended.

Table 3 shows the results (mean and credibility interval 99%) obtained for the estimates by varying the standard deviation of the prior probability distribution of the parameters. It is observed that the increase in deviation decreases the accuracy of the estimates since the estimated values are far from the exact value.

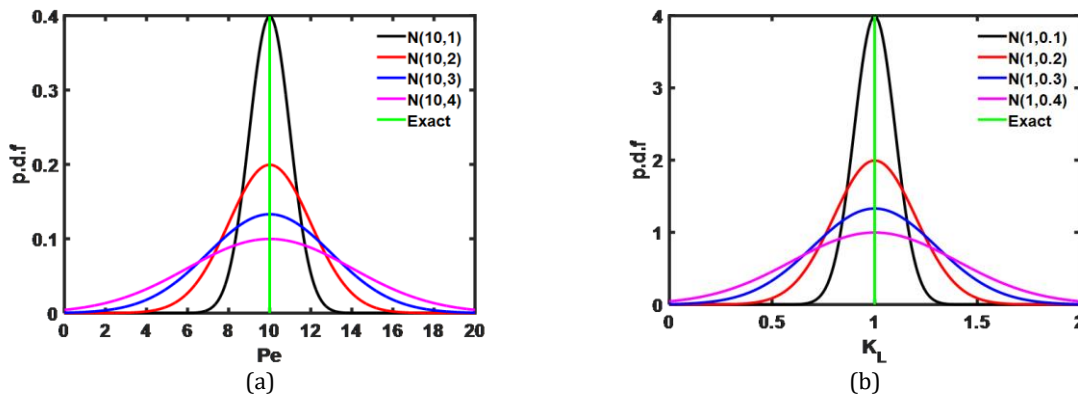


Figure 6. Prior probability distribution function evaluating the influence of standard deviation on the prior for parameters: (a) Pe e (b) K_L.

Table 3. Influence of the standard deviation on the prior probability distribution.

Parameter	Exact	$\pi_{prior}(\mathbf{P})$	$\pi_{posterior}(\mathbf{P})$
Pe	10.00	N (10,1)	10.05 (9.47; 10.68)
	10.00	N (10,2)	9.34 (8.87; 10.10)
	10.00	N (10,3)	9.37 (8.65; 9.94)
	10.00	N (10,4)	9.33 (8.95; 9.70)
K _L	1.00	N(1,0.1)	1.00 (0.99; 1.01)
	1.00	N(1,0.2)	1.01 (0.99; 1.02)
	1.00	N(1,0.3)	1.01 (0.99; 1.02)
	1.00	N(1,0.4)	1.01 (1.00; 1.03)

4.4. Acquisition Frequency Of Measurements

Figure 7 seeks to represent the acquisition frequency of measurements, $d\tau$, and how uncertainties associated, σ_{meas} , influence the data dispersion. As shown in Figure 7a-d, it is possible to observe that as $d\tau$ increases, the number of measurements obtained

decrease. On the other hand, measurements are placed close to the breakthrough curve at low values attributed to uncertainty, such as 1%. Higher values of σ_{meas} were used to represent more realistic scenarios and interfered in the increase of dispersion around the reference curve, as observed in Figure 7e-g.

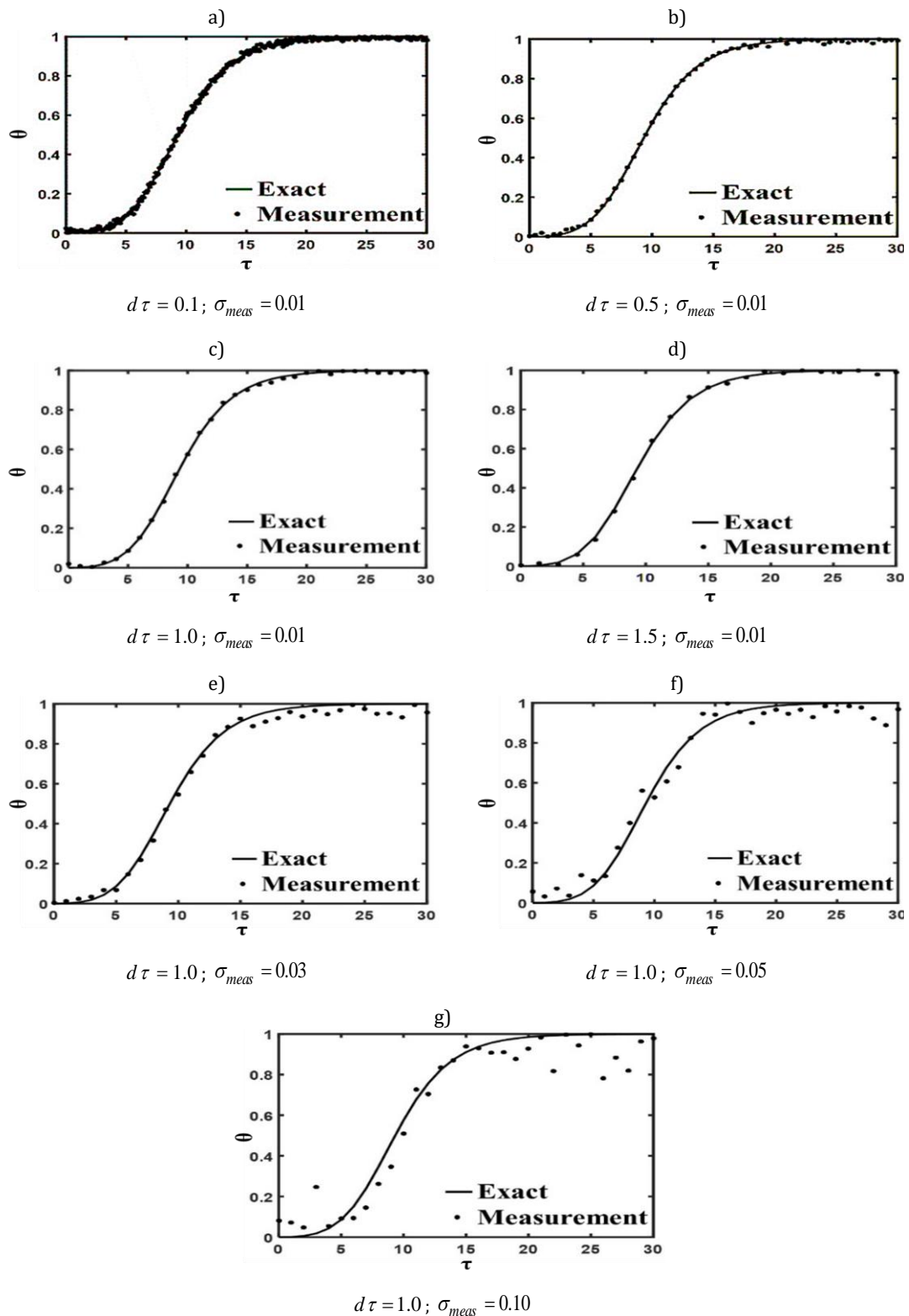


Figure 7. Acquisition frequency of measurements and influence of the increase in uncertainty.

4.5. Breakthrough Curve Estimation

The parameters estimated from the use of the MCMC Bayesian method allowed that measurements obtained in the output current could offer the possibility of predicting curves that form at different points along the column. In this work, the analyzed points were close to the inlet $\theta = 0.25$, in the middle $\theta = 0.5$ and at the exit of the column $\theta = 1$. The results presented in Figure 8 showed the dynamics of the advance of the adsorptive phenomenon.

Figure 8a), c) and e) show the comparison between the exact solution of the model (black line) and the one obtained from the prior probability distribution of the parameters (solid blue line).

Figure 8b), d) and f) show the results for the exact solution of the model (black line) and the one obtained from the a posteriori probability distribution of the estimates made with the MCMC method (solid blue line). You can see that the exact and estimated curves overlap and remain within a 95% confidence interval (dashed blue line). It is evident that an excellent agreement was achieved between the estimated and exact measurements.

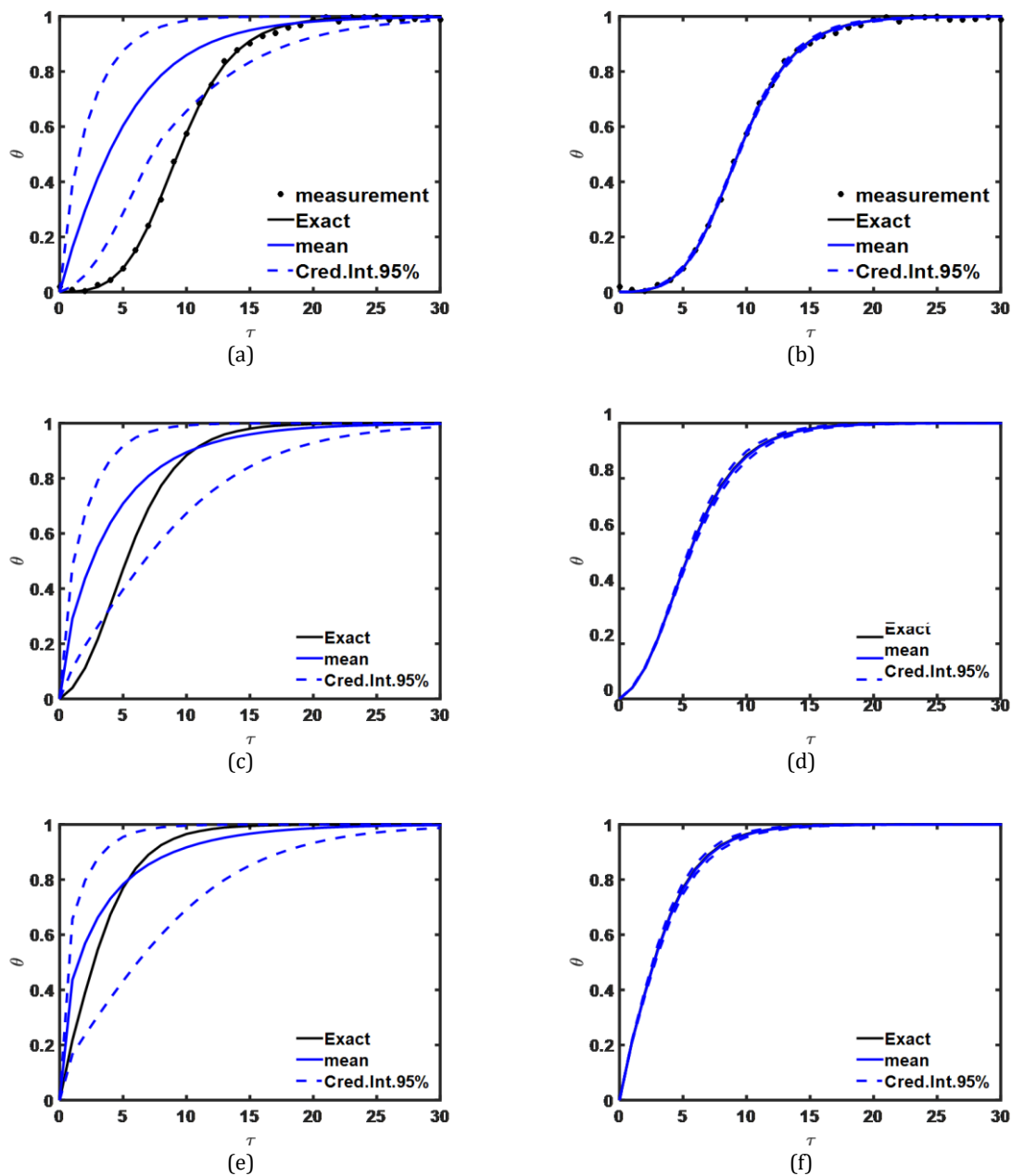


Figure 8. Estimation of the breakthrough curve at different points in the fixed bed column. a) $\theta(1.00, \tau)$ from $\pi_{prior}(\mathbf{P})$, b) $\theta(1.00, \tau)$ from $\pi_{posterior}(\mathbf{P})$, c) $\theta(0.50, \tau)$ from $\pi_{prior}(\mathbf{P})$, d) $\theta(0.50, \tau)$ from $\pi_{posterior}(\mathbf{P})$, e) $\theta(0.25, \tau)$ from $\pi_{prior}(\mathbf{P})$ f) $\theta(0.25, \tau)$ from $\pi_{posterior}(\mathbf{P})$

Conclusion

The parameters estimation of the mathematical model of the adsorption of a chemical species in a fixed bed column was performed using the Markov Chain Monte Carlo method. In addition, simulated measurements generated from Gaussian noises were used to verify the developed algorithm.

The obtained model is solved by the Method of Lines, and a mesh convergence study was carried out to determine a sufficient value of discretization. A high tolerance value demands many discretization, which is not desirable since this increases the computational cost and causes numerical and approximation errors to occur. However, in the present work, the increase in computational cost was not significant.

The estimate analysis explored two scenarios: the influence of the mean and standard deviation on the prior probability distribution of the Peclet number, Pe , and the Langmuir isotherm constant, K_L . In these scenarios, we observed that even changing the prior distribution of the parameters, the posterior distribution samples converge to values close to exact. Thus, the estimated results were satisfactory, and there was both precision and accuracy in the inferences.

From the Bayesian inference, it was possible to use the information at a certain point in the column and thus obtain estimates with considerable precision in other places of interest where measurements were not available. The simulated scenario also allowed the observation of the influence of experimental uncertainties in obtaining measurements, showing that they tend to present greater dispersion the greater the uncertainties associated with their acquisition.

Thus, from the results presented, it is shown that the application of the Bayesian technique of MCMC is robust and presents itself as an excellent tool to understand the dynamics of the fixed bed adsorption process and other mass transfer processes.

Nomenclature

C	Adsorbate concentration at bed outlet, (mg.L ⁻¹)
q	Adsorbate concentration at solid phase, (mg.g ⁻¹)
u_0	Interstitial velocity, (cm.min ⁻¹)
D_{ax}	Axial dispersion coefficient, (cm ² .min ⁻¹)
k_L	Langmuir constant, (L.mg ⁻¹)
q_{max}	Maximum adsorption capacity, (mg.g ⁻¹)
k_s	Global mass transfer coefficient, (min ⁻¹)
q^*	Equilibrium concentration in the solid phase, (mg.g ⁻¹)
ε_L	Porosity

t	Time, (min)
ρ_L	Bed density, (g.L ⁻¹)
θ	Dimensionless concentration of adsorbate at bed outlet
Q	Dimensionless concentration of adsorbate in the solid phase
Pe	Peclet number
K_L	Dimensionless Langmuir Constant
Q_{max}	Dimensionless maximum adsorption capacity
K_s	Dimensionless global mass transfer coefficient
η	Dimensionless length
Q^*	Dimensionless equilibrium concentration in the solid phase
τ	Dimensionless time

Conflicts of Interest

The authors declare that have no conflict of interest regarding the publication of this article.

References

- [1] PEREIRA, A. M., SILVA, L. J., LARANJEIRO, C. S., MEISEL, L. M., LINO, C. M., PENA, A. Human pharmaceuticals in Portuguese rivers: The impact of water scarcity in the environmental risk. *Science of the Total Environment*, v. 609, p. 1182-1191, 2017.
- [2] SOUZA, F. S., SILVA, V. V., JANK, L., ROSIN, C. K., HAINZENREDER, L., ARENZON, A., PIZZOLATO, T., FERIS, L.A., Determination of pharmaceutical compounds in hospital wastewater and their elimination by advanced oxidation processes. *Journal of environmental science and health part a-toxic/hazardous substances & environmental Engineering*, p. 1-9, 2017.
- [3] SOUZA, F.S., SILVA, V.V., ROSIN, C. K., HAINZENREDER, L., ARENZON, A. FÉRIS, L.A., Comparison of different advanced oxidation processes for the removal of amoxicillin in aqueous solution. *Environmental Technology*, 39:5, 549-557, 2018.
- [4] ZOUMPOULI, G. A., SIQUEIRA SOUZA, F., PETRIE, B., FÉRIS, L. A., KASPRZYK-HORDERN, B., WENK, J., Simultaneous ozonation of 90 organic micropollutants including illicit drugs and their metabolites in different water matrices. *Environmental Science: Water Research and Technology*, 6(9), 2020.
- [5] DÁVILA, I. V. J., HÜBNER, J. V. M., NUNES, K. G. P., & FÉRIS, L. A., Caffeine Removal by Adsorption: Kinetics, Equilibrium Thermodynamic and Regeneration Studies. *The Journal of Solid Waste*

- Technology and Management*, 47(1), 95-103, 2021. <https://doi.org/10.5276/ISWTM/2021.95>.
- [6] ROSSET, M., SFREDDO, L. W., PEREZ-LOPEZ, O. W., & FÉRIS, L. A., Effect of concentration in the equilibrium and kinetics of adsorption of acetylsalicylic acid on ZnAl layered double hydroxide. *Journal of Environmental Chemical Engineering*, 8(4), 103991, 2020. <https://doi.org/10.1016/j.jece.2020.103991>.
- [7] COSTA, L. R. D. C., FÉRIS, L. A., Use of functionalized adsorbents for tetracycline removal in wastewater: adsorption mechanism and comparison with activated carbon. *Journal of Environmental Science and Health, Part A*, 55(14), 1604-1614, 2020.
- [8] HARO, N. K., DÁVILA, I. V. J., NUNES, K. G. P., DE FRANCO, M. A. E., MARCILIO, N. R., & FÉRIS, L. A., Kinetic, equilibrium and thermodynamic studies of the adsorption of paracetamol in activated carbon in batch model and fixed-bed column. *Applied Water Science*, 11(2), 2021. <https://doi.org/10.1007/s13201-020-01346-5>.
- [9] SANTOS, T. C.S., ALMEIDA, A. C. M., do Rosario Pinheiro, D., COSTA, C. M. L., ESTUMANO, D. C., & da Paixao Ribeiro, N. F. (2020). Synthesis and characterization of colourful aluminates based on nickel and zinc. *Journal of Alloys and Compounds*, 815, 152477.
- [10] BARROCAS, B., NEVES, M. C., OLIVEIRA, M. C., MONTEIRO, O. C. Enhanced photocatalytic degradation of psychoactive substances using amine-modified elongated titanate nanostructures. *Environmental Science: Nano*, v. 5, n. 2, p. 350-361, 2018. <https://doi.org/10.1039/C7EN00882A>.
- [11] KIM, S., CHU, K. H., AL-HAMADANI, Y. A., PARK, C. M., JANG, M., KIM, D. H., YOON, Y. Removal of contaminants of emerging concern by membranes in water and wastewater: a review. *Chemical Engineering Journal*, v. 335, p. 896-914, 2018. <https://doi.org/10.1016/j.cej.2017.11.044>.
- [12] LIU, C., LI, P., TANG, X., KORSHIN, G. V. Ozonation effects on emerging micropollutants and effluent organic matter in wastewater: characterization using changes of three-dimensional HP-SEC and EEM fluorescence data. *Environmental Science and Pollution Research*, v. 23, n. 20, p. 20567-20579, 2016. <https://doi.org/10.1007/s11356-016-7287-8>.
- [13] OLLER, I.; MALATO, S. Photo-Fenton applied to the removal of pharmaceutical and other pollutants of emerging concern. *Current Opinion in Green and Sustainable Chemistry*, p. 100458, 2021. <https://doi.org/10.1016/j.cogsc.2021.100458>.
- [14] HU, Y.; BOYER, T. H. Removal of multiple drinking water contaminants by combined ion exchange resin in a completely mixed flow reactor. *Journal of Water Supply: Research and Technology-Aqua*, v. 67, n. 7, p. 659-672, 2018. <https://doi.org/10.2166/aqua.2018.101>.
- [15] LV, Y., LIANG, Z., LI, Y., CHEN, Y., LIU, K., YANG, G., LIU, M. Efficient adsorption of diclofenac sodium in water by a novel functionalized cellulose aerogel. *Environmental Research*, v. 194, p. 110652, 2021.
- [16] TATARCHUK, T., MYSLIN, M., LAPCHUK, I., SHYICHUK, A., MURTHY, A. P., GARGULA, R., PĘDZIWIATR, A. T. Magnesium-zinc ferrites as magnetic adsorbents for Cr (VI) and Ni (II) ions removal: cation distribution and antistructure modeling. *Chemosphere*, v. 270, p. 129414, 2021. <https://doi.org/10.1016/j.chemosphere.2020.12.9414>.
- [17] SHARAFEE, M. S., AZHA, S. F., BADAWI, M., BONILLA-PETRICIOLET, A. Performance and interactions of diclofenac adsorption using Alginate/Carbon-based Films: Experimental investigation and statistical physics modelling. *Chemical Engineering Journal*, p. 131929, 2021. <https://doi.org/10.1016/j.cej.2021.131929>.
- [18] RUTHVEN, D. M. *Principles of adsorption and adsorption processes*. John Wiley & Sons, 1984.
- [19] TIEN, C. *Introduction to adsorption: Basics, analysis, and applications*. Elsevier, 2018. <https://doi.org/10.1016/C2018-0-00297-2>.
- [20] DOTTO, G.L., MCKAY, G. Current scenario and challenges in adsorption for water treatment. *Journal of Environmental Chemical Engineering*, 8(4), 103988, 2020. <https://doi.org/10.1016/j.jece.2020.103988>.
- [21] AKSU, Z., GÖNEN, F., Binary biosorption of phenol and chromium (VI) onto immobilized activated sludge in a packed bed: prediction of kinetic parameters and breakthrough curves, *Separation and Purification Technology*, 49(3), 205-216, 2006.
- [22] PATEL, H., Fixed-bed column adsorption study: a comprehensive review, *Applied Water Science*, 9(3), 1-17, 2019. <https://doi.org/10.1007/s13201-019-0927-7>
- [23] XU, Z., CAI, J. G., PAN, B.C., Mathematically modeling fixed-bed adsorption in aqueous systems, *Journal of Zhejiang University SCIENCE A*, 14(3), 155-176, 2013.
- [24] VERA, M., JUELA, D. M., CRUZAT, C., & VANEGAS, E., Modeling and computational fluid dynamic simulation of acetaminophen adsorption using sugarcane bagasse, *Journal of Environmental Chemical Engineering*, 9(2), 105056, 2021.
- [25] THOMAS, H. C. The kinetics of fixed-bed ion exchange. *Ion Exchange, FC Nachod, ed*, 29, 1949.
- [26] YOON, Y. H., NELSON, J. H., Application of gas adsorption kinetics I. A theoretical model for respirator cartridge service life, *American Industrial Hygiene Association Journal*, 45(8), 509-516, 1984.

- [27] CLARK, R. M., Evaluating the cost and performance of field-scale granular activated carbon systems. *Environmental science & technology*, 21(6), 573-580, 1987.
- [28] WOLBORSKA, A., Adsorption on activated carbon of p-nitrophenol from aqueous solution. *Water research*, 23(1), 85-91, 1989.
- [29] DANISH, M., ANSARI, K. B., DANISH, M., KHATOON, A., RAO, R. A. K., ZAIDI, S., & AFTAB, R. A. , 2022. A comprehensive investigation of external mass transfer and intraparticle diffusion for batch and continuous adsorption of heavy metals using pore volume and surface diffusion model. *Separation and Purification Technology*, 292, 120996.
- [30] DORADO, A. D., GAMISANS, X., VALDERRAMA, C., SOLÉ, M., LAO, C., Cr (III) removal from aqueous solutions: a straightforward model approaching of the adsorption in a fixed-bed column. *Journal of Environmental Science and Health, Part A*, 49(2), 179-186, 2014.
- [31] SCHEUFELE, F.B., A.N. MÓDENES, C.E. BORBA, RIBEIRO, C. ESPINOZA-QUIÑONES, F.R. BERGAMASCO, R. N. PEREIRA, C. Monolayer-multilayer adsorption phenomenological model: kinetics, equilibrium and thermodynamics, *Chem. Eng. J.*, 284, 1328-1341, 2016.
- [32] JARIA, G., CALISTO, V., SILVA, C.P., GIL, M.V., OTERO, M., ESTEVES, V.I., Fixed-bed performance of a waste-derived granular activated carbon for the removal of micropollutants from municipal wastewater, *Sci. Total Environ*, 683, 699-708., 2019. <https://doi.org/10.1016/j.scitotenv.2019.05.198>.
- [33] LI, H., HE, J., CHEN, K., SHI, Z., LI, M., GUO, P., WU, L., Dynamic adsorption of sulfamethoxazole from aqueous solution by lignite activated coke, *Materials* 13, 1785, 2020. <https://doi.org/10.3390/ma13071785>.
- [34] JUELA, D., VERA, M., CRUZAT, C., ALVAREZ, X., VANEGAS, E., Mathematical modeling and numerical simulation of sulfamethoxazole adsorption onto sugarcane bagasse in a fixed-bed column. *Chemosphere*, 280, 130687, 2021. <https://doi.org/10.1016/j.chemosphere.2021.130687>.
- [35] YAMAMOTO, Y., YAJIMA, T., & KAWAJIRI, Y., Uncertainty Quantification for Chromatography Model Parameters by Bayesian Inference using Sequential Monte Carlo Method, *Chemical Engineering Research and Design*, 2021.
- [36] DAS, L., SENGUPTA, S., DAS, P., BHOWAL, A., BHATTACHARJEE, C. Experimental and Numerical modeling on dye adsorption using pyrolyzed mesoporous biochar in Batch and fixed-bed column reactor: Isotherm, Thermodynamics, Mass transfer, Kinetic analysis. *Surfaces and Interfaces*, v. 23, p. 100985.
- [37] IHEANACHO, O. C., NWABANNE, J. T., OBI, C. C., ONU, C. E. Packed bed column adsorption of phenol onto corn cob activated carbon: linear and nonlinear kinetics modeling. *South African Journal of Chemical Engineering*, v. 36, p. 80-93, 2021.
- [38] MÓDENES, A. N., BAZARIN, G., BORBA, C. E., LOCATELLI, P. P. P., BORSATO, F. P., PAGNO, V., SCHEUFELE, F. B. Tetracycline adsorption by tilapia fish bone-based biochar: Mass transfer assessment and fixed-bed data prediction by hybrid statistical-phenomenological modeling. *Journal of Cleaner Production*, v. 279, p. 123775, 2021. <https://doi.org/10.1016/j.jclepro.2020.123775>.
- [39] FEIZI, F., SARMAH, A. K., RANGSIVEK, R. Adsorption of pharmaceuticals in a fixed-bed column using tyre-based activated carbon: Experimental investigations and numerical modelling. *Journal of Hazardous Materials*, v. 417, p. 126010, 2021.
- [40] ÖZİŞİK, M. N., ORLANDE, H. R., COLACO, M. J., Cotta, R. M. *Finite difference methods in heat transfer*. CRC press, 2017. <https://doi.org/10.1201/9781315121475>.
- [41] KAIPIO, J., SOMERSALO, E., *Statistical and Computational Inverse Problems*, Springer, New York, NY, 2004. <https://doi.org/10.1007/b138659>.
- [42] MOURA, C. H.R., VIEGAS, B. M., TAVARES, M., MACEDO, E., & ESTUMANO, D. C., (2022). Estimation Of Parameters And Selection Of Models Applied To Population Balance Dynamics Via Approximate Bayesian Computational. *Journal of Heat and Mass Transfer Research*. 10.22075/JHMTR.2022.25186.1361.
- [43] PASQUALETTE, M.A., ESTUMANO, D.C., HAMILTON, F.C. . Bayesian estimate of pre-mixed and diffusive rate of heat release phases in marine diesel engines. *J Braz. Soc. Mech. Sci. Eng.* 39, 1835-1844, 2017. <http://dx.doi.org/10.1007/s40430-016-0649-9>.
- [44] VIEGAS, B. M., MAGALHÃES, E. M., ORLANDE, H. R. B., ESTUMANO, D. C., & MACÊDO, E. N. (2022). Experimental study and mathematical modelling of red mud leaching: application of Bayesian techniques. *International Journal of Environmental Science and Technology*, 1-14. <https://doi.org/10.1007/s13762-022-04346-x>
- [45] AMADOR, I.C.B., NUNES, K.G.P., DE FRANCO, M.A.E., VIEGAS, B.M., MACÊDO, E.N., FÉRIS, L.A., ESTUMANO, D.C., Application of Approximate Bayesian Computational Technique To Characterize The Breakthrough Of Paracetamol Adsorption in Fixed Bed Column, *International Communication in Heat and Mass Transfer*, 132 (2022) 105917, <https://doi.org/10.1016/j.icheatmasstransfer.2022.105917>.
- [46] ESTUMANO, D.C., HAMILTON, F.C., COLAÇO, M.J., LEIROZ, A.J., ORLANDE, H.R., CARVALHO, R.N., & DULIKRAVICH, G.S. (2014). Bayesian estimate of mass fraction of burned fuel in internal combustion engines using pressure

- measurements. *Engineering Optimization IV - Proceedings of the 4th International Conference on Engineering Optimization*, ENGOPT 2014, 2014, pp. 997-1004. <http://dx.doi.org/10.1201/b17488-181>.
- [47] OLIVEIRA, R. F., NUNES, K. G. P., JURADO, I. V., AMADOR, I. C. B., ESTUMANO, D. C., & FÉRIS, L. A., Cr (VI) adsorption in batch and continuous scale: A mathematical and experimental approach for operational parameters prediction, *Environmental Technology & Innovation*, 20, 1092-1105, 2020. <https://doi.org/10.1016/j.eti.2020.101092>.
- [48] MOURA C.H.R., VIEGAS B.M., TAVARES M.R.M., MACÊDO E.N., ESTUMANO D.C., QUARESMA J.N.N. Parameter estimation in population balance through Bayesian technique Markov Chain Monte Carlo, *J. Appl. Comput. Mech.*, 7(2), 2021, 890-901. <https://doi.org/10.22055/JACM.2021.35741.2725>.
- [49] NUNES, K. G. P., DÁVILA, I. V. J., AMADOR, I. C. B., ESTUMANO, D. C., & FÉRIS, L. A. (2021). Evaluation of zinc adsorption through batch and continuous scale applying Bayesian technique for estimate parameters and select model. *Journal of Environmental Science and Health, Part A*, 1-15. <https://doi.org/10.1080/10934529.2021.1977059>.
- [50] NUNES, K. G. P., DAVILA, I. V. J., ARNOLD, D., MOURA, C. H. R., ESTUMANO, D. C., & FÉRIS, L. A. (2022). Kinetics and Thermodynamic Study of Laponite Application in Caffeine Removal by Adsorption. *Environmental Processes*, 9(3), 47.
- [51] GELMAN A, SIMPSON D, BETANCOURT M. The Prior Can Often Only Be Understood in the Context of the Likelihood, *Entropy*, 19(10), 555, 2017. <https://doi.org/10.3390/e19100555>.



Semnan University



Research Article

Monte Carlo Optimization of a Solar Combisystem Using Photovoltaic-Thermal Systems in Hot and Dry Climatic Condition

Maryam Karami ^{*,a}, Kiavash Akbari ^b, Mohammad Jalalizadeh ^b

^aDepartment of Mechanical Engineering, Faculty of Engineering, Kharazmi University, Tehran, Iran

^bDepartment of Architectural Technology, Faculty of Architecture and Urbanism, University of Art, Tehran, Iran

PAPER INFO

Paper history:

Received: 2022-09-19

Revised: 2023-03-10

Accepted: 2023-03-14

Keywords:

Solar combisystem;
Photovoltaic-thermal system;
Dynamic simulation;
Monte Carlo optimization;
TRNSYS.

ABSTRACT

In this study, the performance of a solar combisystem using glazed thermal photovoltaic-thermal systems is investigated and optimized to provide the thermal and electrical demands of a five-story building in Hot/Dry climatic conditions (Tehran, Iran). Dynamic simulation of the system performance is carried out using TRNSYS software. Since there is no type for a glazed thermal photovoltaic-thermal system in TRNSYS, it is modeled in MATLAB software and then the modeling results are coupled with the TRNSYS model. The system optimization using a stochastic economic analysis based on the Monte Carlo method showed the solar combisystem with a photovoltaic-thermal system area of 31.93 m² and a thermal storage tank of 400 l provides the building energy demands optimally. For the optimum system, the probability that the payback time is less than 5 years, the internal rate of return is more than 20% and the life cycle savings is more than the initial cost is 74.2%, 11.5%, and 97%, respectively. The thermoelectric analysis of the optimum solar combisystem indicates that, in August, the maximum electrical, thermal, and total solar fractions of the system are obtained, which are 11%, 87%, and 39%, respectively.

DOI: [10.22075/jhmtr.2023.28432.1394](https://doi.org/10.22075/jhmtr.2023.28432.1394)

© 2022 Published by Semnan University Press. All rights reserved.

1. Introduction

Using renewable energy as an alternative to fossil fuels due to the environmental and economic advantages is one of the ways to reduce energy consumption. Among the types of renewable energy, solar energy is the most widely used source of renewable energy in the world [1,2]. With 300 sunny days a year, Iran is one of the best countries in the world in terms of solar energy potential, and considering the geographical location of Iran and rural distribution in the country, the use of solar energy is one of the most important factors to be considered [3].

In recent years, the application of solar thermal energy in the residential sector has significantly developed. This is because this sector needs a medium

temperature level that can be provided by the solar system [4,5]. Formerly, solar thermal systems were used only to supply domestic hot water (DHW) load; however, with the development of low-temperature heating systems, such as underfloor heating, the use of solar combisystem (SCS) to provide part of the space heating (SH) load of the buildings was also developed. For example, Leckner and Zmeureanu [6] presented a net zero energy house using an SCS. Results showed that the energy payback ratio of the SCS is 3.5–3.8 compared with the conventional heating system and financial payback is never attained because of the high cost of the SCS and the low cost of electricity in Montreal, Canada. Asaee et al. [7] investigated the potential of SCSs in Canadian houses and found that by

*Corresponding Author: Maryam Karami.

Email: karami@khu.ac.ir

increasing collector area, SCS solar fraction is improved. Performance Comparison of an SCS and solar water heater (SWH), done by Sustar et al. [8], shows that the energy savings by an SCS compared to an SWH is as high as 8% for a 6 m² system and 27% for a 9 m² system where relatively high solar radiation is available during the cold season. To provide the heating needs of Tunisian households, Mehdaoui et al. [9] have compared two solar heating technologies: a solar heating system with an integrated active layer on the floor and in the wall. The optimal size of the heating system that provides the maximum solar fraction includes a solar collector with an area of 6 m², a mass flow of 120 kg/h, a 450 l storage tank, and a mass flow within the layer of 300 kg/h. A comparison of the long-term performance of the solar heating systems showed that the use of the floor results in a high solar fraction of about 78%. In another study, Hazami et al. [10] simulated the operation of an SCS to generate electricity and heat using TRNSYS software for Tunisian weather conditions. The results showed that the SCS provides 20% to 40% of the energy required for space heating and 40% to 70% of the energy needed for the DHW. Also, using the SCS, electricity generation between 32 and 225 MJ/m² is obtained. Katsaprakakis and Zidianakis [11] investigated an SCS for heating a school on the Greek island of Crete with biomass fuel. In this study, the building has two desirable features: geographical location with appropriate sunlight and according to school hours (morning shift), all the required thermal energy can be provided by the combisystem, and energy during holidays is stored in a heat storage tank. The two desirable properties mentioned above lead to solar energy supplying more than 50% of the required energy. The effect of weather conditions on the performance of the SCS using the underfloor heating system is investigated by Karami and Javanmardi [12]. They reported that the annual solar fraction in Hot/Dry, Cold/Dry, Moderate/Humid, Hot/semi Humid, and Hot/Humid climates are 74%, 61%, 47.8%, 87.9%, and 92%, respectively. Using a TRNSYS-MATLAB co-simulator, Karami and Nasiri Gahrzaz [13] simulated the thermal performance of an SCS in a Hot/Dry climate using two solar collectors including the flat plate solar collector (FPSC) and a nanofluid-based direct absorption solar collector (DASC) [14, 15]. The results indicate that using FPSC, the annual energy consumption for providing DHW and SH loads using the proposed SCS reduces 94.3% and 17%, respectively. In the case of using a DASC, the solar fraction for DHW and SH in comparison with nanofluid-based DASC increases by 3.7% and 1.7%, respectively. They also considered the thermoelectric and economic performance of the SCS using photovoltaic-thermal (PVT) systems as the energy source [13]. They found that the annual solar fraction of DHW and SH increased 11.3% and 15.6%,

respectively, because of using the electrical energy generated by the system. Based on the results of the economic analysis, the fuel saving cost of 29479 \$ is obtained during the life cycle of the SCS, and the payback period is 3.75 years [16]. Kannan et al. [17] designed and evaluated an off-grid solar combisystem using phase change materials. Their results show that the average energy saving ratio for space heating is about 93%, respectively. Also, the air temperature in the phase change material (PCM) integrated space unit is 4 to 6 °C cooler than that without PCM integrated space unit.

There are several studies on the optimization of SCSs. Bornatico et al. [18] proposed a method for finding the optimal size of the main components of an SCS using the particle swarm optimization (PSO) algorithm and compared the results with the genetic algorithm-based optimization framework. They concluded that the PSO method is a slightly better choice. The optimal size of the main components is the solar collector with an area of 14.5 m², a tank volume of 498.98 l, and an auxiliary power unit of 8.5 kW. The optimized system has a solar fraction of 21.8%, a total energy consumption equivalent to 15806 kWh and an installation cost of 8,983 €. Hin et al. [19] optimized a residential SCS for a house in Montreal, using a hybrid PSO and Hook-Jeeves generalized pattern search algorithm (PSO/HJ) to minimize the life cycle cost (LCC), life cycle energy (LCE) consumption, and life cycle destroyed exergy (LCX) of the system. The optimized system reduces the LCC by 19% and the LCE consumption by 34% compared to the base SCS. The exergy payback time of all system configurations is between 4.2 and 6.3 years. Rey and Zmeureanu [20] used two objective functions, LCC and LCE, to optimize the SCS in Montreal, Canada. Two different approaches including a weight sum method using a PSO/HJ and multi-objective PSO are presented and compared to solve such problems. Finally, the multi-purpose PSO was selected because it was up to six times faster than the PSO/HJ. By different design options of the multi-objective PSO/HJ, LCC and LCE were reduced to 88.6% and 63.9%, respectively, in comparison with the base case SCS. In the next study, they used micro-time variant multi-objective PSO (micro-TVMOPSO) to optimize the performance of an SCS and reported that the number of solar collectors has the most effect on both LCC and LCE [21]. They also selected the SCSs with different configuration capabilities and then investigated the LCC, LCE consumption, and LCX were investigated using the method of micro-TVMOPSO. To minimize LCC, only one FPSC with one storage tank is required, while seven evacuated tube solar collectors (ETSC) and two storage tanks are used for minimum LCE consumption. However, such an improvement requires an additional cost that is not worth much for such economic conditions [22]. Using taguchi method, Li and Kao [23] optimized solar thermal and heat

pump combisystems under five distinct climatic conditions including Tropical monsoon (Tainan), Continental (Madrid), Humid subtropical (Osaka), Humid subtropical (Hong Kong), and Mediterranean (Lisbon). They reported that Tainan and Lisbon have the longest and shortest payback period because of lower and higher electricity price, respectively. Thapa et al. [24] designed, modeled, and optimized an SCS for single-family houses in Nepal. Optimization variables include collector area, DHW, and SH storage tank size. The dynamic simulation using TRNSYS software and PSO method is used for optimization. This system is simulated in two regions including Terai and Hilli with different climates in Nepal. In Tray, has a system with an area of 6 m² of solar collector, DHW, and storage tank with a volume of about 130 l, and in Hilli, a collector with an area of 14 m² and tanks with a volume between 150 l and 170 l are optimum. The LCC of the SCS is reduced by 66% in Terai and 77% in Hilli. A summary of the SCS optimization studies are listed in Table 1.

As the review shows, earlier studies use deterministic economic analysis to optimize the SCSs and ignore the uncertainties in model inputs, which undoubtedly result in uncertainties in model outputs. Therefore, in this study, the SCS is optimized using a stochastic economic analysis based on the Monte Carlo method, in which the uncertainty is considered by designating inputs as probability distributions. Furthermore, the thermoelectric performance of the optimum SCS in Hot and Dry climatic conditions (Tehran, Iran) is investigated using dynamic simulation by TRNSYS-MATLAB cosimulator.

2. Case study building and SCS description

In this study, a five-story building located in Hot/Dry climatic conditions (Tehran, Iran) is selected as the case study building. Figure 1 shows the hourly variation of the ambient temperature and solar radiation of Tehran. Each floor of the building consists of two residential units with a 143 m² area and 4 occupants. The characteristics of the building are shown in Table 2. The daily DHW consumption for each person is considered 50 l.

To determine the electrical, DHW, and SH loads of the building, it is first necessary to simulate the building in Design-Builder software. The annual DHW, SH, and electrical loads of the building are obtained 32.57 MWh, 89.57 MWh, and 60.18 kW, respectively. It should be noted that the building has no central HVAC equipment and instead uses an evaporative cooler for cooling and a packaged gas fired heater for heating. Also, the electrical load and operation schedule of electrical equipment are introduced to the software based on Iranian National Building Code-No.19.

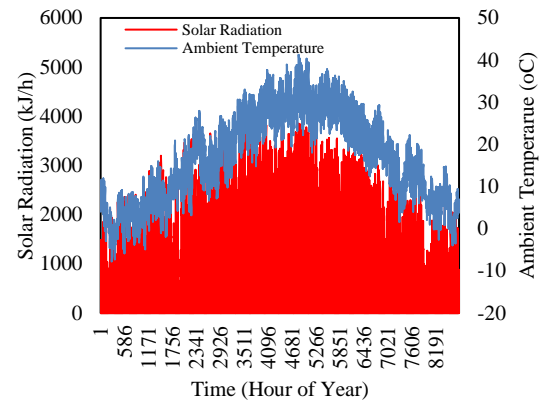


Figure 1. Hourly variation of ambient temperature and solar radiation in Tehran

In this study, the proposed system to supply DHW, SH, and electricity for a building in Tehran (35.7219° N, 51.3347° E) is a PVT-based SCS. Figure 2 shows the schematic of the proposed system. In this system, the heated working fluid in the PVT systems divides between the DHW and SH tanks, exchanges heat with water in the tanks, and then, the cooled working fluid returns from the tanks and enters the PVT system to continue this cycle. The hot water in the SH tank enters the boiler to reach the appropriate temperature for providing the SH load. If the water in the DHW tank is not at the desired temperature, the auxiliary heater inside the tank turns on and heats the water to the set-point temperature.

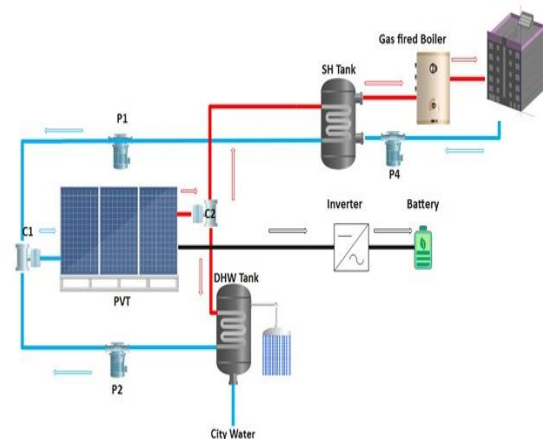


Figure 2. Schematic of the proposed PVT-based SCS

3. Methodology

The flowchart in Figure 3 indicates the process of the simulation and optimization study of the SCS. As shown, the simulation process is divided into two parts: thermoelectric and economic simulations. First, using basic information and TRNSYS software, the thermoelectric simulation is carried out, and then the results are entered the Crystal ball software so that the economic calculations for the considered SCS is carried out using Monte Carlo method.

Table 1. Summary of SCS optimization studies

Ref.	Optimization method	Optimization objectives	Climatic conditions	Findings
Bornatico et al. [18]	PSO algorithm and GA	<ul style="list-style-type: none"> • Collector area • Tank volume • Auxiliary power unit 	Zurich, Switzerland	<ul style="list-style-type: none"> • Collector size is the most important parameter. • Solar fraction of 21.8% for a mid-sized single-family house (150 m²) using collector area of 14.5 m², tank volume of 498.98 l, and an auxiliary power unit of 8.5 kW.
Hin et al. [19]	Hybrid PSO/HJ	<ul style="list-style-type: none"> • LCC • LCE consumption • LCX 	Montreal, Quebec, Canada	<ul style="list-style-type: none"> • Reduction of the LCC by 19% and the LCE consumption by 34%. • The exergy payback time is between 4.2 and 6.3 years.
Rey and Zmeureanu [20]	<ul style="list-style-type: none"> • Hybrid PSO/HJ • MOPSO • Hybrid MOPSO/HJ 	<ul style="list-style-type: none"> • LCC • LCE use 	Montreal, Quebec, Canada	<ul style="list-style-type: none"> • PSO/HJ method is time-consuming, while MOPSO/HJ was more than six times faster. • Collector size and mass flow rate has high and small influence on thermal energy savings, respectively.
Rey and Zmeureanu [21]	<ul style="list-style-type: none"> • Micro-MOPSO • Micro-TVMOPSO 	<ul style="list-style-type: none"> • LCC • LCE use 	Montreal, Quebec, Canada	<ul style="list-style-type: none"> • Micro-TVMOPSO algorithm performed better than other optimization algorithms. • Optimum tilt angle for solar collector is 45° for Montreal.
Rey and Zmeureanu [22]	Micro-TVMOPSO	<ul style="list-style-type: none"> • LCC • LCE consumption • LCX 	Montreal, Quebec, Canada	<ul style="list-style-type: none"> • To minimize LCC, only one FPSC with one storage tank is required, while seven evacuated tube solar collectors (ETSC) and two storage tanks are used for minimum LCE consumption.
Li and Kao [23]	Taguchi	<ul style="list-style-type: none"> • COP of heat pump • Solar fraction of SCS 	<ul style="list-style-type: none"> • Tropical monsoon (Tainan) • Continental (Madrid) • Humid subtropical (Osaka) • Humid subtropical (Hong Kong) • Mediterranean (Lisbon) 	<ul style="list-style-type: none"> • For single tank SCS, the flow rate of heat pump has the high impact, while for dual tank SCS, the flow rate of the collector is most influential. • Tainan and Lisbon have the longest and shortest payback period because of lower and higher electricity price, respectively
Thapa et al. [24]	Hybrid PSO/HJ	<ul style="list-style-type: none"> • Collector area • DHW storage tank size • SH storage tank size 	<ul style="list-style-type: none"> • Terai, Nepal • Hilli, Nepal 	<ul style="list-style-type: none"> • The LCC of the SCS is reduced by 66% in Terai and 77% in Hilli, respectively. • The building envelope insulation plays a key role in the wide use of SCS in Nepal.

Table 2. Characteristics of the case study building

Characteristics	Value
Orientionation	South
External wall U value (W/m ² .K)	1.28
Internal wall U value (W/m ² .L)	1.85
Floor U value (W/m ² .K)	2.23
Roof U value (W/m ² .K)	2.23
Window glazing U value (W/m ² .K)	3.09
The ratio of Windows-to-Wall ratio (%)	20
Infiltration rate (Ach)	0.7

3.1. Thermoelectric analysis

Figure 4 indicates the TRNSYS model of the PVT-based SCS. In Table 3, the TRNSYS types used in the simulation and their characteristics are listed. It should be noted that Type 109 was used to read weather data from the Typical Meteorological Year (TMY) files and

calculates the solar radiation in different directions. System controllers (Type 2b) were used to control the flow rate of the collectors and the storage tanks. For example, if the difference between the outlet and inlet temperature of the collector is less than 5°C, the collector loop pump will be turned off. Also, if the difference exceeds 10°C, the pump will turn on. Type 14b is used to simulate the daily DHW demand, of which profile is obtained in Ref. [12]. As mentioned, the cooling and heating loads of the case study building are obtained using Design Builder modeling and the results are coupled with TRNSYS using Type 9e, which calls the calculated thermal and electrical loads by linking to an external excel file.

Since there is no type for the glazed PVT systems, a model is developed in MATLAB software and then, connected to the TRNSYS model using Type 155. The details of the modeling of the glazed PVT systems can be obtained in Ref. [25].

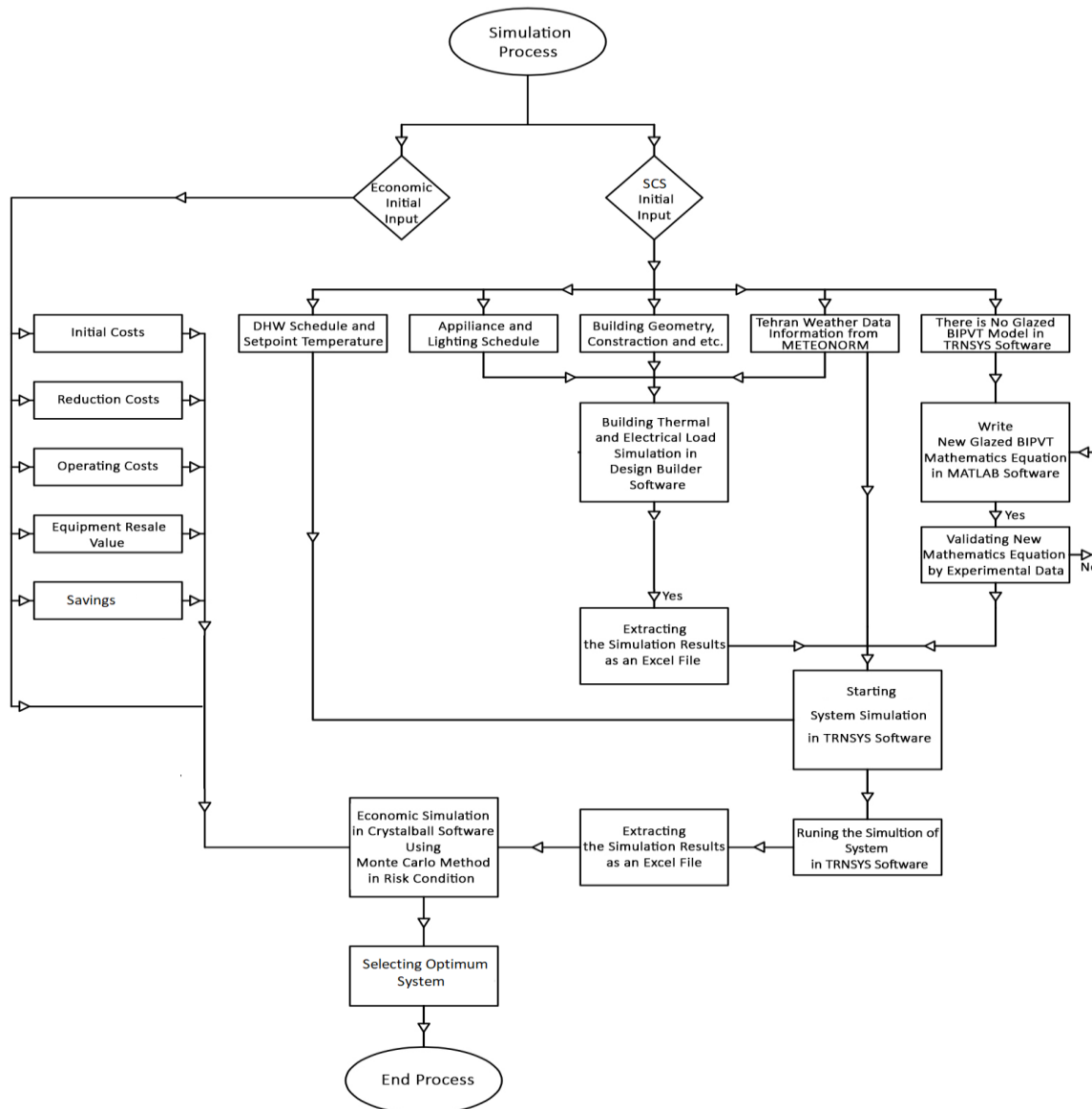


Figure 3. Flow chart diagram of the SCS simulation

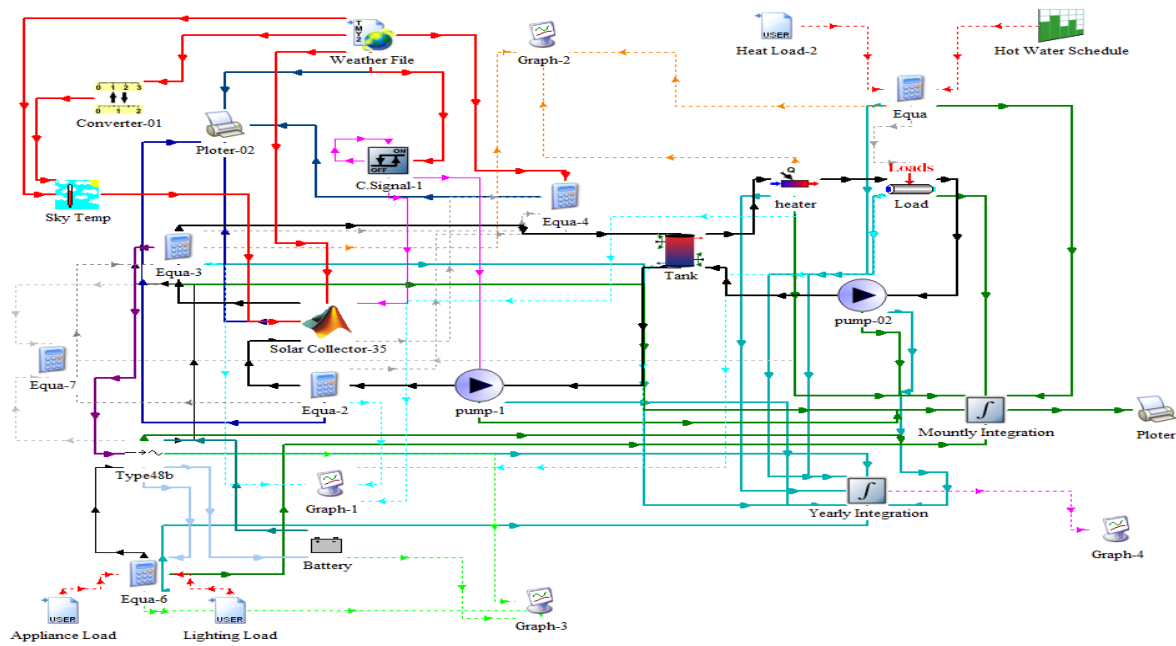


Figure 4. TRNSYS model of the SCS

Table 3. TRNSYS types for modeling the SCS components

Component	Features	TRNSYS type
Case study building	See Section 2	56
Weather information	Tehran, Iran (35.7219° N, 51.3347° E)	109
Sky temperature	---	69
Psychrometric properties	Such as dew point, relative humidity, etc.	33
Glazed PVT systems	BIPVT collector mass flow rate: 50 kg/h Fluid Type: Water	155
Electrical inverter	Inverter output power capacity: 42 kW Regulator efficiency: 0.8 Inverter efficiency: 0.96	48a
Battery	Cell efficiency capacity: 200 Wh Number of cells in parallel: 24 Number of cells in series: 12 Charging efficiency: 0.9	47a
Circulation Pumps	Power coefficient: 0.5 Maximum power: 1 kw Maximum flowrate: 1590 kg/h	3b
Storage tanks	Six thermal nodes level with the same constant flow rate are defined for the thermal storage tank Thermal storage tank loss coefficient: 0.83 W/m ² . K	4
Auxiliary heater	Maximum hear rate: 100 kW Set point temperature: 80°C Efficiency: 0.9	6
DHW	Set point temperature: 60°C	14b
Controllers	Controller type: Feedback controller	2b
Flow diverter and mixing valve	---	11 and 11 h
Cooling and heating load	Calling Excel	9e
Plotter, Printer, and Integrator	---	65d, 25a, and 24

3.2. Economic analysis using Monte Carlo approach

In this study, the Monte Carlo method is used for the economic analysis of the proposed SCS. In general, the Monte Carlo method refers to a computational mathematical technique that provides approximate answers to quantitative problems through statistical sampling. It is mostly used to describe propagating uncertainties in model input and to analyze uncertainties in model output. The Monte Carlo method, then, is a kind of simulation that explicitly and quantitatively shows uncertainty by designating inputs as probability distributions. If the inputs describing a system are uncertain, then the prediction of the performance is essentially uncertain. This means that the result of any analysis based on inputs with probability distribution is itself a probability distribution [26,27].

To show the effect of the price inflation rate during the life of the proposed system, normal distribution was used in the simulation in the stochastic approach of the Monte Carlo method. The electricity and natural gas prices can also change over the life of the system. For this reason, in the calculations, the normal distribution is also used for the price growth of these energy sources. The inflation rate of the discount rate is considered by a triangle distribution with a maximum value of 0.16, a minimum value of 0.10, and a mean value of 0.13. A triangle distribution is used to distribute variables when the minimum and maximum values are constant and the highest probability is different from the other probabilities. As the discount rate is variable, the maintenance cost is also variable, and since the discount is considered a triangle, a triangle distribution has been used to express the inflation rate of the maintenance cost, the range of which is between 1% and 5% with the highest probability of 3% in the first 5 years of operation. However, from the 5th year of operation, it is between 5% and 15% with the highest probability of 10%.

Table 4 shows the variables and value ranges used for the optimization of the proposed SCS for the case study building. It should be noted that the collector slope is assumed constant and equal to the latitude of Tehran (about 35°).

Table 4. Variables used in this study and their value ranges

Variables	Value ranges
PVT area (m ²)	10.6-138.9
Storage tank volume	300-3000 lit
Collector mass flow rate	512- 13300 kg/h
Auxiliary boiler capacity	25-40 kW
Inverter number	1-5

Table 5 shows the cost of the SCS main components. The initial costs include the initial investment cost (PVT systems and related equipment), the cost reduction of the primary heating systems (the cost of purchasing a boiler with a lower capacity), and installation costs. The operating costs of the system are considered equal to 10% of the initial cost.

Table 5. SCS main component cost

Component	Cost
Total PVT systems (\$)	2280-29640
Inverter (\$)	459-2295
Installation cost (\$)	2128-27785
Total initial cost (\$)	4867-58148
Auxiliary boiler (\$)	2428-4000

3.3. Economic indicators

In this study, four economic indicators including payback time (PBT), net present value (NPV), internal rate of return (IRR), and life cycle savings (LCS) are used which determine the decision criteria for the implementation of the proposed systems. The PBT indicates the time required to return the initial costs, which is calculated using the following relation [28]:

$$\sum_{i=0}^{N_{\min}=\text{DPBP}} \frac{F_t}{(1+d)^i} \geq 0 \quad (1)$$

where d is the discount rate. If F_0 is the life cycle cost (LCC) and F_i is the net profit, which is the difference between savings and LCC, then the payback period (N_{\min}) will be the lowest. One of the disadvantages of this indicator is the investment conditions after the payback period in such a way that the amount and duration of profitability are not known, so it is necessary to consider other indicators.

The NPV of investment represents the total present value of all expenses and savings of the project. If the NPV is positive, the system is affordable and the project earnings exceed the anticipated costs. If NPV is zero, the earnings are equal to the costs and if it is negative, the system is not affordable [29]. The main disadvantage of this indicator is that it does not provide any information about the initial costs. The NPV can be calculated through Eq. (2):

$$\text{NPV} = \sum_{i=0}^N \frac{F_i}{(1+d)^i} \quad (2)$$

The IRR is the interest rate that results in the present value of the expenses equal to the present value of the savings. In fact, the IRR is the interest rate at which the NPV is zero:

$$\text{NPV} = \sum_{i=0}^N \frac{F_i}{(1+\text{IRR})^i} = 0 \quad (3)$$

The LCS is the difference between the LCC of a conventional fuel-only system and the LCC of the solar plus auxiliary system [30], which by discounting is calculated as follows:

$$LCS = \sum_{i=0}^N \frac{F_i}{(1+d)^i} \tag{4}$$

4. Results and discussion

4.1. Optimization analysis using Monte Carlo algorithm

The incomes of the lifetime include the electricity generated and the natural gas saved which is given in Figure 5. The equipment resale value, which is equal to 25% of the initial cost of the system, is also an income. It is a recovery value, which is returned during the life of the system or at the end of it when the components are sold as scrap metal for recycling [30]. It should be mentioned that the variable price of gas and electricity are included in the Monte Carlo method.

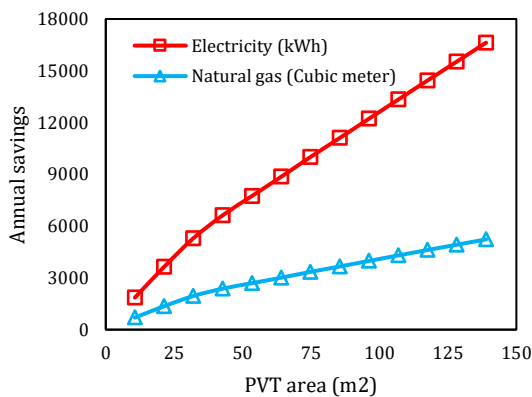


Figure 5. Annual electricity and natural gas savings for different SCSs

By determining the distribution of the variables using the Monte Carlo method, the LCS, PBT, and IRR indicators are calculated. To analyze the LCS in risky conditions, a suitable criterion is needed. The best criterion for showing the optimality of this indicator is the probability that it is higher than the initial costs of the system (Table 5).

Figure 6 shows the PBT, IRR, and LCS indicators, taking into account the probability of the PBT, the IRR, and the LCS are less than 5 years, less than 20%, and more than system’s initial cost, respectively. As can be seen, the optimum indicators are obtained using the SCS with a PVT area of about 31.9 m². Table 6 shows the various economic indicators for the optimum SCS.

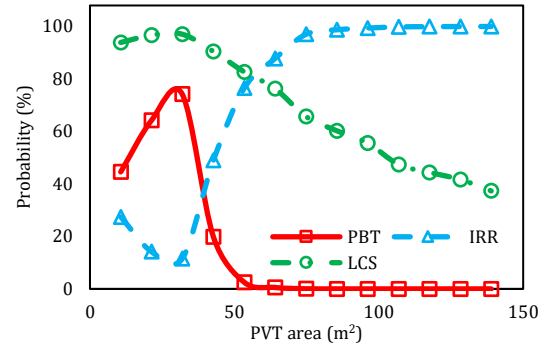


Figure 6. Probability of the PBT (less than 5 years), IRR (less than 20%) and LCS (more than initial cost)

Table 6. Features of the optimum SCS

Feature	Value
PVT area	31.9 m ²
Collector mass flow rate	1536 kg/h
Thermal Storage Tank Volum	400 l
Inverter No.	1
Auxiliary Boiler Capacity	35 kW
Probability of PBT less than 5 years	74.2%
Probability of IRR less than 20%	11.5%
Probability of LCS more than initial cost	97%

4.2. Optimization analysis using Monte Carlo algorithm

Figure 7 shows the monthly variation of incident solar radiation and electrical energy generation (EEG), electrical energy consumption (EEC), and electrical energy received from the grid (EER_Grid). It is observed that by increasing the solar radiation, the EEG also increases; so that more EEG is obtained in warm months and as a result, EER_Grid is reduced. As can be seen, the highest incident radiation and EEG are 207.83 kWh and 566.5 kWh, respectively. As expected, the lowest EEG (276.1 kWh) is obtained in December because of low incident radiation (110.8 kWh). On average, the PVT panels generate 4% of the EEC in the cold months and 7% in the warm months.

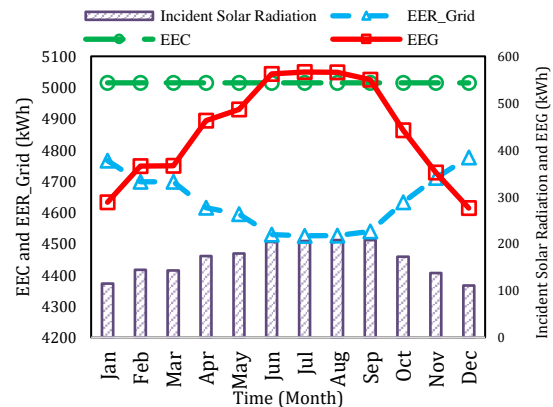


Figure 7. Monthly variation of incident solar radiation, EEG, EEC, and EER_Grid

Table 7 shows the annual electrical performance of the SCS. As can be seen, the annual EEC of the building is more than 60 MWh, of which about 54% is related to appliances (AEC) and the rest is related to lighting (LEC). The ratio of electrical energy received from the inverter (EER_Inv) to EEC is about 7.6%; however, the ratio of electrical energy received from the grid (EER_Grid) to EEC is 92.4%. It should be noted that the difference between the EEG and EER_Inv is because of the power loss in the system.

Table 7. Annual electrical performance of SCS

Parameter	Value (MWh)
Total electrical energy consumption (EEC)	60.18
Appliance electrical energy consumption (AEC)	32.60
Lighting electrical energy consumption (LEC)	27.58
Total electrical energy generation (EEG)	5.29
Electrical energy received from the grid (EER_Grid)	55.61
Electrical energy received from the inverter (EER_Inv)	4.57

Figure 8 shows the monthly variation of incident solar radiation, thermal energy generation (TEG), and consumption (TEC) including thermal energy consumption for providing DHW (DTEC) and SH (STEC). As observed, in warm months, almost all DHW load is provided by the SCS, because there is no need for SH. In the cold months, the STEC and thus, TEC have higher values, while TEG has lower values because of low incident radiation; so, the lowest TEG is obtained in December, which is 787 kWh. As can be seen, the ratio of STEC to TEG decreases from April and reaches zero from May to September, due to the lack of need for space heating. Nonetheless, it increases from October, so it is about 26 times larger in December compared to October. It is also found that the maximum ratio of TEC to TEG is 20.46 in January and the minimum one is 1.06 in August.

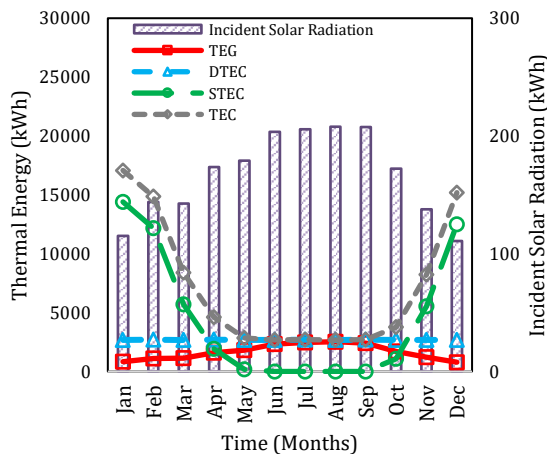


Figure 8. Monthly variation of incident solar radiation, TEG and, TEC

The annual thermal performance of the SCS is shown in Table 8. Based on the results, the annual TEC of the building is 89.57 MWh, of which about 60% is related to space heating (TEC_SH) and the rest is related to domestic hot water consumption (TEC_DHW). The ratio of TEG by the SCS to the TEC of the building is 22.5%.

Table 8. Annual thermal performance of SCS

Parameter	Value (MWh)
Total thermal energy consumption (TEC)	89.57
Thermal energy consumption for DHW (TEC_DHW)	32.57
Thermal energy consumption for SH (TEC_SH)	54.05
Total thermal energy generation (TEG)	20.13

The monthly variations of thermal, electrical, and total solar fractions of the SCS are shown in Figure 9. As the results show, in the warm months, due to the increase of incident solar radiation and the lack of need for SH, the thermal and total fractions have significantly grown. Due to the constant need for electricity, the monthly electrical fraction does not change much, but in the warmer months of the year, due to more radiation, a slight increase in the electrical fraction is observed.

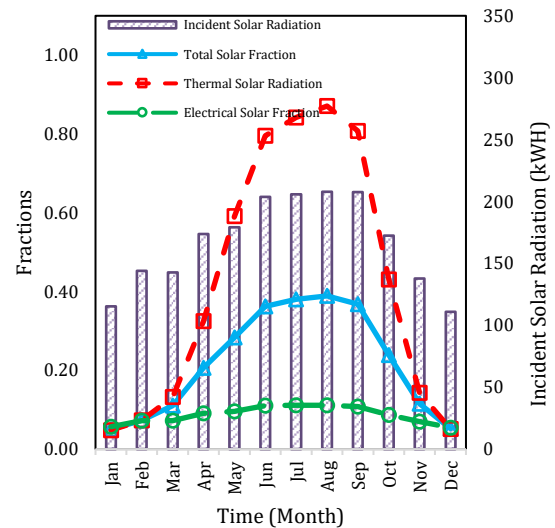


Figure 9. Monthly variation of different solar fractions

Conclusion

In this study, the performance of the SCS using PVT systems for supplying electricity, DHW, and SH demands of a case study building have been investigated and optimized using the Monte Carlo method. In the Monte Carlo method, by considering the risk conditions and calculating the probability of the

LCS, PBT, and IRR indicators, the optimum SCS system for the case study building is determined. The probability that the PBT is less than 5 years, the IRR is more than 20% and the LCS are more than the initial cost is 74.2%, 11.5%, and 97%, respectively. The analysis of the electrical performance of the optimum SCS indicates that a minimum of 5% and a maximum of 11% of the building's electrical load is provided by the system. The maximum electrical solar fraction is obtained from June to September. The annual electrical solar fraction of the SCS is 8.7%. In terms of thermal performance, it is found that the optimum SCS provided about 5%-87% of the building's thermal load. In the warm months (from April to October), about 66.6% of the building thermal demand is provided by the SCS; while, in the cold months (from November to March), on average 72% of the building thermal demand should be provided by fossil fuels. Finally, the maximum savings in electrical, thermal, and total energy consumption of the building using the optimum SCS are 11%, 87%, and 39%, respectively, which are related to the month of August. It is concluded that the optimization of the SCSs for providing the energy demands of the buildings leads to an efficient reduction of energy consumption.

It should be noted that a limitation of the research is the economic conditions of Iran and low price of the primary energies, which forced us to use the economic conditions and energy costs of the United States. It is recommended that the optimization of the SCS is performed for other climatic conditions and using other types of SCSs including different collector types and configurations of the storage tanks.

Nomenclature

d	Discount rate
F	Cash flow
N	Number
t	Time

Acronyms

AEC	Appliance Energy Consumption
DASC	Direct Absorption Solar Collector
DHW	Domestic Hot Water
DTEC	Domestic Thermal Energy Consumption
EEC	Electrical Energy Consumption

EEG	Electrical Energy Generation
EER	Electrical Energy Received
ETSC	Evacuated Tube Solar Collector
FPSC	Flat Plate Solar Collector
IRR	Internal Rate of Return
LCC	Life Cycle Cost
LCE	Life Cycle Energy
LCS	Life Cycle Savings
LEC	Lighting Energy Consumption
NPV	Net Positive Value
PBT	Payback Time
PVT	Photovoltaic-Thermal
PSO	Particle Swarm Optimization
SCS	Solar Combisystem
SH	Space Heating
TEC	Thermal Energy Consumption
STEC	Space Thermal Energy Consumption
TEG	Thermal Energy Generation
WWR	Windows-to-Wall Ratio

References

- [1] Karami, M., Raisee, M., and Delfani, S., 2014. Numerical investigation of nanofluid-based solar collectors. *IOP Conf. Ser.: Mater. Sci. Eng.*, 64 (1), 012044.
- [2] Amin, Z., Nematollahi, O., and Alemrajabi, A.A., 2021. Disinfection process with solar drying system. *Journal of Heat and Mass Transfer Research*, 8 (1), pp. 23-28.
- [3] Alamdari, P., Salihoglu, N.K., and Amin, Z., 2013. Solar energy potentials in Iran: A review. *Renewable and Sustainable Energy Reviews*, 21, pp. 778-788.
- [4] Hormozi Moghaddam, M. and Karami, M., 2022. Heat transfer and pressure drop through mono and hybrid nanofluid-based photovoltaic-thermal systems. *Energy Science & Engineering*, 10 (3), pp. 918-931.
- [5] Karami, M., Delfani, S., and Noroozi, A., 2020. Performance characteristics of a solar desiccant/M-cycle air-conditioning system

- for the buildings in hot and humid areas. *Asian Journal of Civil Engineering*, 21, pp. 189-199.
- [6] Leckner, M., Zmeureanu, R., 2011. Life cycle cost and energy analysis of a Net Zero Energy House with solar combisystem. *Applied Energy*, 88 (1), pp. 232-241.
- [7] Rasoul Asaee, S., Ismet Ugursal, V., Beausoleil-Morrison, I., Ben-Abdallah, N., 2014. Preliminary study for solar combisystem potential in Canadian houses. *Applied Energy*, 130, pp. 510-518.
- [8] Sustar, J. L., Burch, J., Krarti, M., 2015. Performance Modeling Comparison of a Solar Combisystem and Solar Water Heater. *J. Sol. Energy Eng.*, 137 (6), 061001.
- [9] Mehdaoui, F., Hazami, M., Messaouda, A., and Guizani, A.A., 2020. Performance analysis of two types of Solar Heating Systems used in buildings under typical North African climate (Tunisia). *Applied Thermal Engineering*, 165, 114203.
- [10] Hazami, M., Mehdaoui, F., Naili, N., Noro, M., Lazzarin, R., and Guizani, A. A., 2017. Energetic, exergetic and economic analysis of an innovative Solar CombiSystem (SCS) producing thermal and electric energies: Application in residential and tertiary households. *Energy Convers. Manag.*, 140, pp. 36-50.
- [11] Katsaprakakis, D. A. and Zidianakis, G., 2019. Optimized Dimensioning and Operation Automation for a Solar-Combi System for Indoor Space Heating: A Case Study for a School Building in Crete. *Energies*, 12 (1).
- [12] Karami, M. and Javanmardi, F., 2020. Performance assessment of a solar thermal combisystem in different climate zones. *Asian Journal of Civil Engineering*, 21, pp.751-762.
- [13] Karami, M. and Nasiri Gahraz, S.S., 2022. Improving thermal performance of a solar thermal/desalination combisystem using nanofluid-based direct absorption solar collector. *Sientia Iranica*, 29 (3), *Transactions on Mechanical Engineering (B)*, pp. 1288-1300.
- [14] Esmaeili, M., Karami, M. and Delfani, S., 2020. Performance enhancement of a direct absorption solar collector using copper oxide porous foam and nanofluid. *International Journal of Energy Research*, 44 (7), pp. 5527-5544.
- [15] Delfani, S., Karami, M., Akhavan-Behabadi, M.A., 2016. Experimental investigation on performance comparison of nanofluidbased direct absorption and flat plate solar collectors. *International Journal of Nano Dimension (IJND)*, 7 (1), pp. 85-96.
- [16] Karami, M. and Nasiri Gahraz, S.S., 2021. Transient simulation and life cycle cost analysis of a solar polygeneration system using photovoltaic-thermal collectors and hybrid desalination unit. *Journal of Heat and Mass Transfer Research*, 8 (2), pp. 243-256.
- [17] Kannan, A., Prakash, J., Roan, D., 2021. Design and performance of an off-grid solar combisystem using phase change materials. *International Journal of Heat and Mass Transfer*, 164, 120574.
- [18] Bornatico, R., Pfeiffer, M., Witzig, A. and Guzzella, L., 2012. Optimal sizing of a solar thermal building installation using particle swarm optimization. *Energy*, 41(1), pp. 31-37.
- [19] Hin, J.N.C. and Zmeureane, R., 2014. Optimization of a residential solar combisystem for minimum life cycle cost, energy use and exergy destroyed. *Solar Energy*, 100, pp. 102-113.
- [20] Rey, A. and Zmeureanu, R., 2016. Multi-objective optimization of a residential solar thermal combisystem. *Solar Energy*, 139, pp. 622-632.
- [21] Rey, A. and Zmeureanu, R., 2017. Micro-time variant multi-objective particle swarm optimization (micro-TVMOPSO) of a solar thermal combisystem. *Swarm and Evolutionary Computation*, 36, pp. 76-90.
- [22] Rey, A. and Zmeureanu, R., 2018. Multi-objective optimization framework for the selection of configuration and equipment sizing of solar thermal combisystems. *Energy*, 145, pp. 182-194.
- [23] Li, Y.H., Kao, W.C., 2018. Taguchi optimization of solar thermal and heat pump combisystems under five distinct climatic conditions. *Applied Thermal Engineering*, 133, pp. 283-297.
- [24] Thapa, B. and Wang, W., Williams, W., 2021. Life-cycle cost optimization of a solar combisystem for residential buildings in Nepal. *Journal of Asian Architecture and Building Engineering*, 21 (3), pp. 1137-1148.
- [25] Jalalizadeh, M., Fayaz, Rima, Delfani, S., Jafari Mosleh, H. and Karami, M., 2021. Dynamic simulation of a trigeneration system using an absorption cooling system and building integrated photovoltaic thermal solar collectors. *Journal of Building Engineering*, 43, 102482.
- [26] Goldsim. 2022. Monte Carlo Simulation. *Monte Carlo Simulation and Methods Introduction - GoldSim*.
- [27] Mun, J., 2006. Modeling risk: Applying Monte Carlo simulation, real options analysis, forecasting, and optimization techniques 347. John Wiley & Sons.
- [28] Fuller, S., 2010. Life-cycle cost analysis (LCCA). National Institute of Building Sciences, An Authoritative Source of

- Innovative Solutions for the Built Environment 1090.
- [29] Gu, Y., Zhang, X., Myhren, J. A., Han, M., Chen, X. and Yuan, Y., 2018. Techno-economic analysis of a solar photovoltaic/thermal (PV/T) concentrator for building application in Sweden using Monte Carlo method. *Energy Convers. Manag.* 165, pp. 8-24.
- [30] Kalogirou, S., 2014. *Solar Energy Engineering: Processes and Systems*, Academic Press, second edition.



Semnan University



Research Article

Monte Carlo Optimization of a Solar Combisystem Using Photovoltaic-Thermal Systems in Hot and Dry Climatic Condition

Maryam Karami ^{*,a}, Kiavash Akbari ^b, Mohammad Jalalizadeh ^b

^aDepartment of Mechanical Engineering, Faculty of Engineering, Kharazmi University, Tehran, Iran

^bDepartment of Architectural Technology, Faculty of Architecture and Urbanism, University of Art, Tehran, Iran

PAPER INFO

Paper history:

Received: 2022-09-19

Revised: 2023-03-10

Accepted: 2023-03-14

Keywords:

Solar combisystem;
Photovoltaic-thermal system;
Dynamic simulation;
Monte Carlo optimization;
TRNSYS.

ABSTRACT

In this study, the performance of a solar combisystem using glazed thermal photovoltaic-thermal systems is investigated and optimized to provide the thermal and electrical demands of a five-story building in Hot/Dry climatic conditions (Tehran, Iran). Dynamic simulation of the system performance is carried out using TRNSYS software. Since there is no type for a glazed thermal photovoltaic-thermal system in TRNSYS, it is modeled in MATLAB software and then the modeling results are coupled with the TRNSYS model. The system optimization using a stochastic economic analysis based on the Monte Carlo method showed the solar combisystem with a photovoltaic-thermal system area of 31.93 m² and a thermal storage tank of 400 l provides the building energy demands optimally. For the optimum system, the probability that the payback time is less than 5 years, the internal rate of return is more than 20% and the life cycle savings is more than the initial cost is 74.2%, 11.5%, and 97%, respectively. The thermoelectric analysis of the optimum solar combisystem indicates that, in August, the maximum electrical, thermal, and total solar fractions of the system are obtained, which are 11%, 87%, and 39%, respectively.

DOI: [10.22075/jhmtr.2023.28432.1394](https://doi.org/10.22075/jhmtr.2023.28432.1394)

© 2022 Published by Semnan University Press. All rights reserved.

1. Introduction

Using renewable energy as an alternative to fossil fuels due to the environmental and economic advantages is one of the ways to reduce energy consumption. Among the types of renewable energy, solar energy is the most widely used source of renewable energy in the world [1,2]. With 300 sunny days a year, Iran is one of the best countries in the world in terms of solar energy potential, and considering the geographical location of Iran and rural distribution in the country, the use of solar energy is one of the most important factors to be considered [3].

In recent years, the application of solar thermal energy in the residential sector has significantly developed. This is because this sector needs a medium

temperature level that can be provided by the solar system [4,5]. Formerly, solar thermal systems were used only to supply domestic hot water (DHW) load; however, with the development of low-temperature heating systems, such as underfloor heating, the use of solar combisystem (SCS) to provide part of the space heating (SH) load of the buildings was also developed. For example, Leckner and Zmeureanu [6] presented a net zero energy house using an SCS. Results showed that the energy payback ratio of the SCS is 3.5–3.8 compared with the conventional heating system and financial payback is never attained because of the high cost of the SCS and the low cost of electricity in Montreal, Canada. Asaee et al. [7] investigated the potential of SCSs in Canadian houses and found that by

*Corresponding Author: Maryam Karami.

Email: karami@khu.ac.ir

increasing collector area, SCS solar fraction is improved. Performance Comparison of an SCS and solar water heater (SWH), done by Sustar et al. [8], shows that the energy savings by an SCS compared to an SWH is as high as 8% for a 6 m² system and 27% for a 9 m² system where relatively high solar radiation is available during the cold season. To provide the heating needs of Tunisian households, Mehdaoui et al. [9] have compared two solar heating technologies: a solar heating system with an integrated active layer on the floor and in the wall. The optimal size of the heating system that provides the maximum solar fraction includes a solar collector with an area of 6 m², a mass flow of 120 kg/h, a 450 l storage tank, and a mass flow within the layer of 300 kg/h. A comparison of the long-term performance of the solar heating systems showed that the use of the floor results in a high solar fraction of about 78%. In another study, Hazami et al. [10] simulated the operation of an SCS to generate electricity and heat using TRNSYS software for Tunisian weather conditions. The results showed that the SCS provides 20% to 40% of the energy required for space heating and 40% to 70% of the energy needed for the DHW. Also, using the SCS, electricity generation between 32 and 225 MJ/m² is obtained. Katsaprakakis and Zidianakis [11] investigated an SCS for heating a school on the Greek island of Crete with biomass fuel. In this study, the building has two desirable features: geographical location with appropriate sunlight and according to school hours (morning shift), all the required thermal energy can be provided by the combisystem, and energy during holidays is stored in a heat storage tank. The two desirable properties mentioned above lead to solar energy supplying more than 50% of the required energy. The effect of weather conditions on the performance of the SCS using the underfloor heating system is investigated by Karami and Javanmardi [12]. They reported that the annual solar fraction in Hot/Dry, Cold/Dry, Moderate/Humid, Hot/semi Humid, and Hot/Humid climates are 74%, 61%, 47.8%, 87.9%, and 92%, respectively. Using a TRNSYS-MATLAB co-simulator, Karami and Nasiri Gahrzaz [13] simulated the thermal performance of an SCS in a Hot/Dry climate using two solar collectors including the flat plate solar collector (FPSC) and a nanofluid-based direct absorption solar collector (DASC) [14, 15]. The results indicate that using FPSC, the annual energy consumption for providing DHW and SH loads using the proposed SCS reduces 94.3% and 17%, respectively. In the case of using a DASC, the solar fraction for DHW and SH in comparison with nanofluid-based DASC increases by 3.7% and 1.7%, respectively. They also considered the thermoelectric and economic performance of the SCS using photovoltaic-thermal (PVT) systems as the energy source [13]. They found that the annual solar fraction of DHW and SH increased 11.3% and 15.6%,

respectively, because of using the electrical energy generated by the system. Based on the results of the economic analysis, the fuel saving cost of 29479 \$ is obtained during the life cycle of the SCS, and the payback period is 3.75 years [16]. Kannan et al. [17] designed and evaluated an off-grid solar combisystem using phase change materials. Their results show that the average energy saving ratio for space heating is about 93%, respectively. Also, the air temperature in the phase change material (PCM) integrated space unit is 4 to 6 °C cooler than that without PCM integrated space unit.

There are several studies on the optimization of SCSs. Bornatico et al. [18] proposed a method for finding the optimal size of the main components of an SCS using the particle swarm optimization (PSO) algorithm and compared the results with the genetic algorithm-based optimization framework. They concluded that the PSO method is a slightly better choice. The optimal size of the main components is the solar collector with an area of 14.5 m², a tank volume of 498.98 l, and an auxiliary power unit of 8.5 kW. The optimized system has a solar fraction of 21.8%, a total energy consumption equivalent to 15806 kWh and an installation cost of 8,983 €. Hin et al. [19] optimized a residential SCS for a house in Montreal, using a hybrid PSO and Hook-Jeeves generalized pattern search algorithm (PSO/HJ) to minimize the life cycle cost (LCC), life cycle energy (LCE) consumption, and life cycle destroyed exergy (LCX) of the system. The optimized system reduces the LCC by 19% and the LCE consumption by 34% compared to the base SCS. The exergy payback time of all system configurations is between 4.2 and 6.3 years. Rey and Zmeureanu [20] used two objective functions, LCC and LCE, to optimize the SCS in Montreal, Canada. Two different approaches including a weight sum method using a PSO/HJ and multi-objective PSO are presented and compared to solve such problems. Finally, the multi-purpose PSO was selected because it was up to six times faster than the PSO/HJ. By different design options of the multi-objective PSO/HJ, LCC and LCE were reduced to 88.6% and 63.9%, respectively, in comparison with the base case SCS. In the next study, they used micro-time variant multi-objective PSO (micro-TVMOPSO) to optimize the performance of an SCS and reported that the number of solar collectors has the most effect on both LCC and LCE [21]. They also selected the SCSs with different configuration capabilities and then investigated the LCC, LCE consumption, and LCX were investigated using the method of micro-TVMOPSO. To minimize LCC, only one FPSC with one storage tank is required, while seven evacuated tube solar collectors (ETSC) and two storage tanks are used for minimum LCE consumption. However, such an improvement requires an additional cost that is not worth much for such economic conditions [22]. Using taguchi method, Li and Kao [23] optimized solar thermal and heat

pump combisystems under five distinct climatic conditions including Tropical monsoon (Tainan), Continental (Madrid), Humid subtropical (Osaka), Humid subtropical (Hong Kong), and Mediterranean (Lisbon). They reported that Tainan and Lisbon have the longest and shortest payback period because of lower and higher electricity price, respectively. Thapa et al. [24] designed, modeled, and optimized an SCS for single-family houses in Nepal. Optimization variables include collector area, DHW, and SH storage tank size. The dynamic simulation using TRNSYS software and PSO method is used for optimization. This system is simulated in two regions including Terai and Hilli with different climates in Nepal. In Tray, has a system with an area of 6 m² of solar collector, DHW, and storage tank with a volume of about 130 l, and in Hilli, a collector with an area of 14 m² and tanks with a volume between 150 l and 170 l are optimum. The LCC of the SCS is reduced by 66% in Terai and 77% in Hilli. A summary of the SCS optimization studies are listed in Table 1.

As the review shows, earlier studies use deterministic economic analysis to optimize the SCSs and ignore the uncertainties in model inputs, which undoubtedly result in uncertainties in model outputs. Therefore, in this study, the SCS is optimized using a stochastic economic analysis based on the Monte Carlo method, in which the uncertainty is considered by designating inputs as probability distributions. Furthermore, the thermoelectric performance of the optimum SCS in Hot and Dry climatic conditions (Tehran, Iran) is investigated using dynamic simulation by TRNSYS-MATLAB cosimulator.

2. Case study building and SCS description

In this study, a five-story building located in Hot/Dry climatic conditions (Tehran, Iran) is selected as the case study building. Figure 1 shows the hourly variation of the ambient temperature and solar radiation of Tehran. Each floor of the building consists of two residential units with a 143 m² area and 4 occupants. The characteristics of the building are shown in Table 2. The daily DHW consumption for each person is considered 50 l.

To determine the electrical, DHW, and SH loads of the building, it is first necessary to simulate the building in Design-Builder software. The annual DHW, SH, and electrical loads of the building are obtained 32.57 MWh, 89.57 MWh, and 60.18 kW, respectively. It should be noted that the building has no central HVAC equipment and instead uses an evaporative cooler for cooling and a packaged gas fired heater for heating. Also, the electrical load and operation schedule of electrical equipment are introduced to the software based on Iranian National Building Code-No.19.

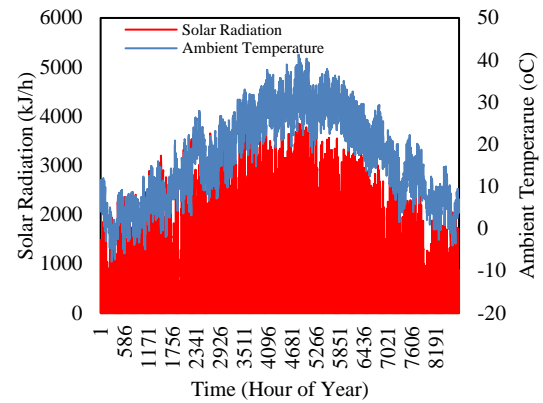


Figure 1. Hourly variation of ambient temperature and solar radiation in Tehran

In this study, the proposed system to supply DHW, SH, and electricity for a building in Tehran (35.7219° N, 51.3347° E) is a PVT-based SCS. Figure 2 shows the schematic of the proposed system. In this system, the heated working fluid in the PVT systems divides between the DHW and SH tanks, exchanges heat with water in the tanks, and then, the cooled working fluid returns from the tanks and enters the PVT system to continue this cycle. The hot water in the SH tank enters the boiler to reach the appropriate temperature for providing the SH load. If the water in the DHW tank is not at the desired temperature, the auxiliary heater inside the tank turns on and heats the water to the set-point temperature.

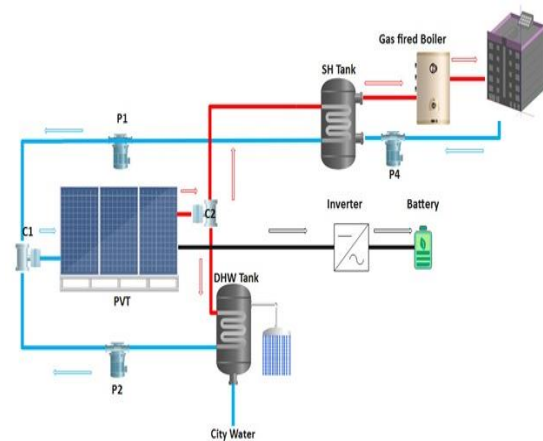


Figure 2. Schematic of the proposed PVT-based SCS

3. Methodology

The flowchart in Figure 3 indicates the process of the simulation and optimization study of the SCS. As shown, the simulation process is divided into two parts: thermoelectric and economic simulations. First, using basic information and TRNSYS software, the thermoelectric simulation is carried out, and then the results are entered the Crystal ball software so that the economic calculations for the considered SCS is carried out using Monte Carlo method.

Table 1. Summary of SCS optimization studies

Ref.	Optimization method	Optimization objectives	Climatic conditions	Findings
Bornatico et al. [18]	PSO algorithm and GA	<ul style="list-style-type: none"> • Collector area • Tank volume • Auxiliary power unit 	Zurich, Switzerland	<ul style="list-style-type: none"> • Collector size is the most important parameter. • Solar fraction of 21.8% for a mid-sized single-family house (150 m²) using collector area of 14.5 m², tank volume of 498.98 l, and an auxiliary power unit of 8.5 kW.
Hin et al. [19]	Hybrid PSO/HJ	<ul style="list-style-type: none"> • LCC • LCE consumption • LCX 	Montreal, Quebec, Canada	<ul style="list-style-type: none"> • Reduction of the LCC by 19% and the LCE consumption by 34%. • The exergy payback time is between 4.2 and 6.3 years.
Rey and Zmeureanu [20]	<ul style="list-style-type: none"> • Hybrid PSO/HJ • MOPSO • Hybrid MOPSO/HJ 	<ul style="list-style-type: none"> • LCC • LCE use 	Montreal, Quebec, Canada	<ul style="list-style-type: none"> • PSO/HJ method is time-consuming, while MOPSO/HJ was more than six times faster. • Collector size and mass flow rate has high and small influence on thermal energy savings, respectively.
Rey and Zmeureanu [21]	<ul style="list-style-type: none"> • Micro-MOPSO • Micro-TVMOPSO 	<ul style="list-style-type: none"> • LCC • LCE use 	Montreal, Quebec, Canada	<ul style="list-style-type: none"> • Micro-TVMOPSO algorithm performed better than other optimization algorithms. • Optimum tilt angle for solar collector is 45° for Montreal.
Rey and Zmeureanu [22]	Micro-TVMOPSO	<ul style="list-style-type: none"> • LCC • LCE consumption • LCX 	Montreal, Quebec, Canada	<ul style="list-style-type: none"> • To minimize LCC, only one FPSC with one storage tank is required, while seven evacuated tube solar collectors (ETSC) and two storage tanks are used for minimum LCE consumption.
Li and Kao [23]	Taguchi	<ul style="list-style-type: none"> • COP of heat pump • Solar fraction of SCS 	<ul style="list-style-type: none"> • Tropical monsoon (Tainan) • Continental (Madrid) • Humid subtropical (Osaka) • Humid subtropical (Hong Kong) • Mediterranean (Lisbon) 	<ul style="list-style-type: none"> • For single tank SCS, the flow rate of heat pump has the high impact, while for dual tank SCS, the flow rate of the collector is most influential. • Tainan and Lisbon have the longest and shortest payback period because of lower and higher electricity price, respectively
Thapa et al. [24]	Hybrid PSO/HJ	<ul style="list-style-type: none"> • Collector area • DHW storage tank size • SH storage tank size 	<ul style="list-style-type: none"> • Terai, Nepal • Hilli, Nepal 	<ul style="list-style-type: none"> • The LCC of the SCS is reduced by 66% in Terai and 77% in Hilli, respectively. • The building envelope insulation plays a key role in the wide use of SCS in Nepal.

Table 2. Characteristics of the case study building

Characteristics	Value
Orientionation	South
External wall U value (W/m ² .K)	1.28
Internal wall U value (W/m ² .L)	1.85
Floor U value (W/m ² .K)	2.23
Roof U value (W/m ² .K)	2.23
Window glazing U value (W/m ² .K)	3.09
The ratio of Windows-to-Wall ratio (%)	20
Infiltration rate (Ach)	0.7

3.1. Thermoelectric analysis

Figure 4 indicates the TRNSYS model of the PVT-based SCS. In Table 3, the TRNSYS types used in the simulation and their characteristics are listed. It should be noted that Type 109 was used to read weather data from the Typical Meteorological Year (TMY) files and

calculates the solar radiation in different directions. System controllers (Type 2b) were used to control the flow rate of the collectors and the storage tanks. For example, if the difference between the outlet and inlet temperature of the collector is less than 5°C, the collector loop pump will be turned off. Also, if the difference exceeds 10°C, the pump will turn on. Type 14b is used to simulate the daily DHW demand, of which profile is obtained in Ref. [12]. As mentioned, the cooling and heating loads of the case study building are obtained using Design Builder modeling and the results are coupled with TRNSYS using Type 9e, which calls the calculated thermal and electrical loads by linking to an external excel file.

Since there is no type for the glazed PVT systems, a model is developed in MATLAB software and then, connected to the TRNSYS model using Type 155. The details of the modeling of the glazed PVT systems can be obtained in Ref. [25].

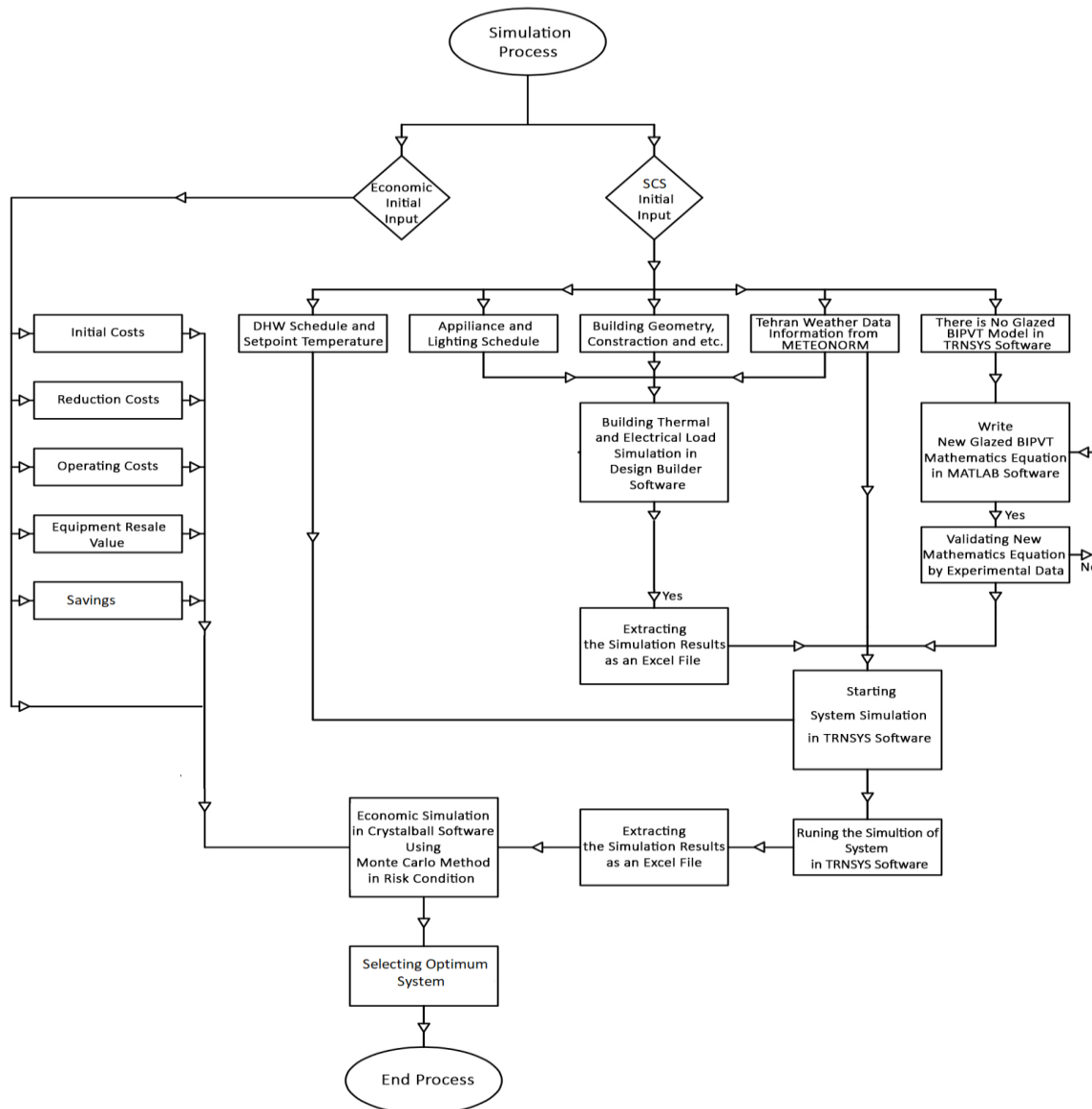


Figure 3. Flow chart diagram of the SCS simulation

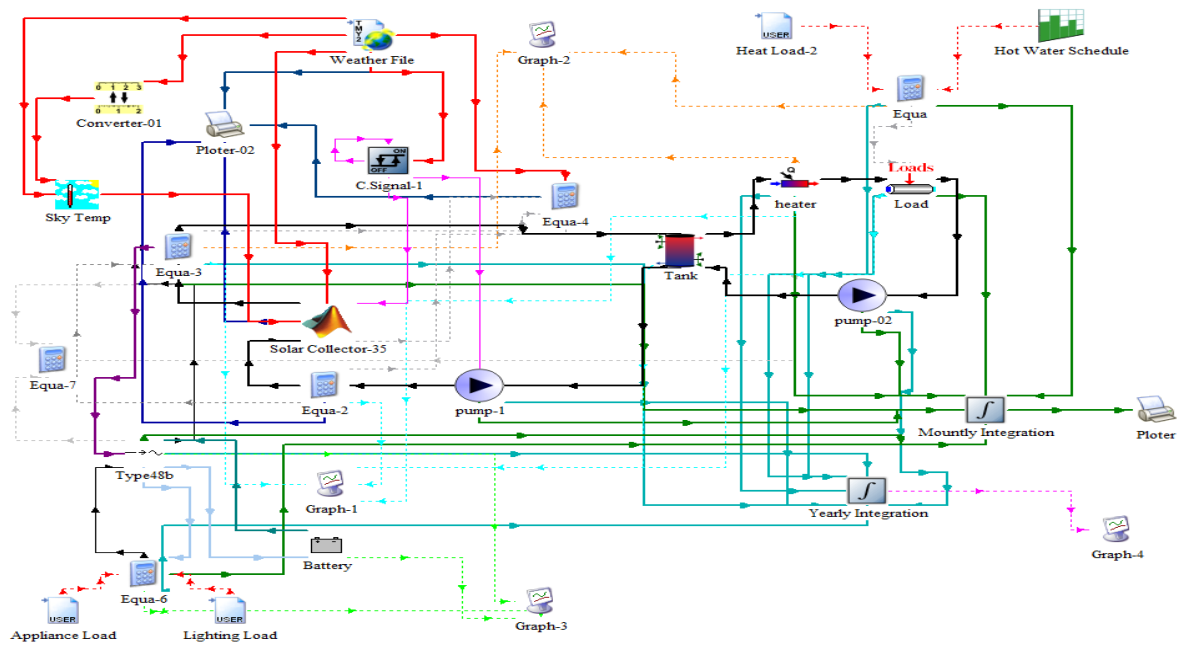


Figure 4. TRNSYS model of the SCS

Table 3. TRNSYS types for modeling the SCS components

Component	Features	TRNSYS type
Case study building	See Section 2	56
Weather information	Tehran, Iran (35.7219° N, 51.3347° E)	109
Sky temperature	---	69
Psychrometric properties	Such as dew point, relative humidity, etc.	33
Glazed PVT systems	BIPVT collector mass flow rate: 50 kg/h Fluid Type: Water	155
Electrical inverter	Inverter output power capacity: 42 kW Regulator efficiency: 0.8 Inverter efficiency: 0.96	48a
Battery	Cell efficiency capacity: 200 Wh Number of cells in parallel: 24 Number of cells in series: 12 Charging efficiency: 0.9	47a
Circulation Pumps	Power coefficient: 0.5 Maximum power: 1 kw Maximum flowrate: 1590 kg/h	3b
Storage tanks	Six thermal nodes level with the same constant flow rate are defined for the thermal storage tank Thermal storage tank loss coefficient: 0.83 W/m ² . K	4
Auxiliary heater	Maximum hear rate: 100 kW Set point temperature: 80°C Efficiency: 0.9	6
DHW	Set point temperature: 60°C	14b
Controllers	Controller type: Feedback controller	2b
Flow diverter and mixing valve	---	11 and 11 h
Cooling and heating load	Calling Excel	9e
Plotter, Printer, and Integrator	---	65d, 25a, and 24

3.2. Economic analysis using Monte Carlo approach

In this study, the Monte Carlo method is used for the economic analysis of the proposed SCS. In general, the Monte Carlo method refers to a computational mathematical technique that provides approximate answers to quantitative problems through statistical sampling. It is mostly used to describe propagating uncertainties in model input and to analyze uncertainties in model output. The Monte Carlo method, then, is a kind of simulation that explicitly and quantitatively shows uncertainty by designating inputs as probability distributions. If the inputs describing a system are uncertain, then the prediction of the performance is essentially uncertain. This means that the result of any analysis based on inputs with probability distribution is itself a probability distribution [26,27].

To show the effect of the price inflation rate during the life of the proposed system, normal distribution was used in the simulation in the stochastic approach of the Monte Carlo method. The electricity and natural gas prices can also change over the life of the system. For this reason, in the calculations, the normal distribution is also used for the price growth of these energy sources. The inflation rate of the discount rate is considered by a triangle distribution with a maximum value of 0.16, a minimum value of 0.10, and a mean value of 0.13. A triangle distribution is used to distribute variables when the minimum and maximum values are constant and the highest probability is different from the other probabilities. As the discount rate is variable, the maintenance cost is also variable, and since the discount is considered a triangle, a triangle distribution has been used to express the inflation rate of the maintenance cost, the range of which is between 1% and 5% with the highest probability of 3% in the first 5 years of operation. However, from the 5th year of operation, it is between 5% and 15% with the highest probability of 10%.

Table 4 shows the variables and value ranges used for the optimization of the proposed SCS for the case study building. It should be noted that the collector slope is assumed constant and equal to the latitude of Tehran (about 35°).

Table 4. Variables used in this study and their value ranges

Variables	Value ranges
PVT area (m ²)	10.6-138.9
Storage tank volume	300-3000 lit
Collector mass flow rate	512- 13300 kg/h
Auxiliary boiler capacity	25-40 kW
Inverter number	1-5

Table 5 shows the cost of the SCS main components. The initial costs include the initial investment cost (PVT systems and related equipment), the cost reduction of the primary heating systems (the cost of purchasing a boiler with a lower capacity), and installation costs. The operating costs of the system are considered equal to 10% of the initial cost.

Table 5. SCS main component cost

Component	Cost
Total PVT systems (\$)	2280-29640
Inverter (\$)	459-2295
Installation cost (\$)	2128-27785
Total initial cost (\$)	4867-58148
Auxiliary boiler (\$)	2428-4000

3.3. Economic indicators

In this study, four economic indicators including payback time (PBT), net present value (NPV), internal rate of return (IRR), and life cycle savings (LCS) are used which determine the decision criteria for the implementation of the proposed systems. The PBT indicates the time required to return the initial costs, which is calculated using the following relation [28]:

$$\sum_{i=0}^{N_{\min}=\text{DPBP}} \frac{F_t}{(1+d)^i} \geq 0 \quad (1)$$

where d is the discount rate. If F_0 is the life cycle cost (LCC) and F_i is the net profit, which is the difference between savings and LCC, then the payback period (N_{\min}) will be the lowest. One of the disadvantages of this indicator is the investment conditions after the payback period in such a way that the amount and duration of profitability are not known, so it is necessary to consider other indicators.

The NPV of investment represents the total present value of all expenses and savings of the project. If the NPV is positive, the system is affordable and the project earnings exceed the anticipated costs. If NPV is zero, the earnings are equal to the costs and if it is negative, the system is not affordable [29]. The main disadvantage of this indicator is that it does not provide any information about the initial costs. The NPV can be calculated through Eq. (2):

$$\text{NPV} = \sum_{i=0}^N \frac{F_i}{(1+d)^i} \quad (2)$$

The IRR is the interest rate that results in the present value of the expenses equal to the present value of the savings. In fact, the IRR is the interest rate at which the NPV is zero:

$$\text{NPV} = \sum_{i=0}^N \frac{F_i}{(1+\text{IRR})^i} = 0 \quad (3)$$

The LCS is the difference between the LCC of a conventional fuel-only system and the LCC of the solar plus auxiliary system [30], which by discounting is calculated as follows:

$$LCS = \sum_{i=0}^N \frac{F_i}{(1+d)^i} \tag{4}$$

4. Results and discussion

4.1. Optimization analysis using Monte Carlo algorithm

The incomes of the lifetime include the electricity generated and the natural gas saved which is given in Figure 5. The equipment resale value, which is equal to 25% of the initial cost of the system, is also an income. It is a recovery value, which is returned during the life of the system or at the end of it when the components are sold as scrap metal for recycling [30]. It should be mentioned that the variable price of gas and electricity are included in the Monte Carlo method.

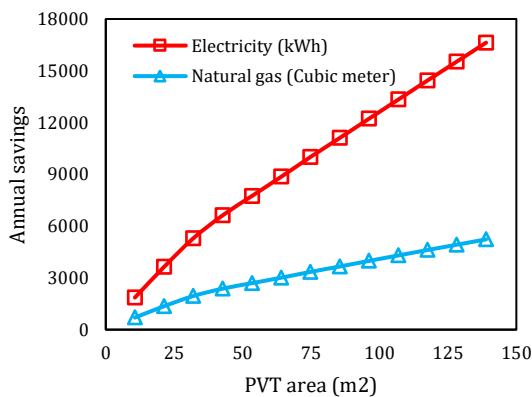


Figure 5. Annual electricity and natural gas savings for different SCSs

By determining the distribution of the variables using the Monte Carlo method, the LCS, PBT, and IRR indicators are calculated. To analyze the LCS in risky conditions, a suitable criterion is needed. The best criterion for showing the optimality of this indicator is the probability that it is higher than the initial costs of the system (Table 5).

Figure 6 shows the PBT, IRR, and LCS indicators, taking into account the probability of the PBT, the IRR, and the LCS are less than 5 years, less than 20%, and more than system’s initial cost, respectively. As can be seen, the optimum indicators are obtained using the SCS with a PVT area of about 31.9 m². Table 6 shows the various economic indicators for the optimum SCS.

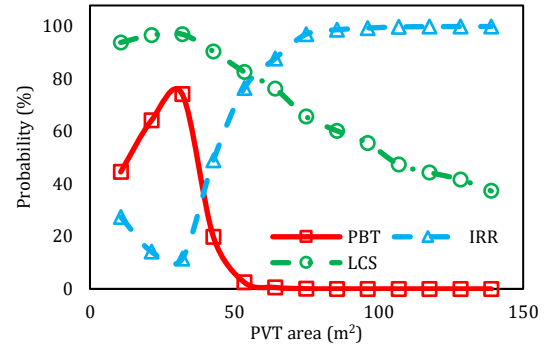


Figure 6. Probability of the PBT (less than 5 years), IRR (less than 20%) and LCS (more than initial cost)

Table 6. Features of the optimum SCS

Feature	Value
PVT area	31.9 m ²
Collector mass flow rate	1536 kg/h
Thermal Storage Tank Volum	400 l
Inverter No.	1
Auxiliary Boiler Capacity	35 kW
Probability of PBT less than 5 years	74.2%
Probability of IRR less than 20%	11.5%
Probability of LCS more than initial cost	97%

4.2. Optimization analysis using Monte Carlo algorithm

Figure 7 shows the monthly variation of incident solar radiation and electrical energy generation (EEG), electrical energy consumption (EEC), and electrical energy received from the grid (EER_Grid). It is observed that by increasing the solar radiation, the EEG also increases; so that more EEG is obtained in warm months and as a result, EER_Grid is reduced. As can be seen, the highest incident radiation and EEG are 207.83 kWh and 566.5 kWh, respectively. As expected, the lowest EEG (276.1 kWh) is obtained in December because of low incident radiation (110.8 kWh). On average, the PVT panels generate 4% of the EEC in the cold months and 7% in the warm months.

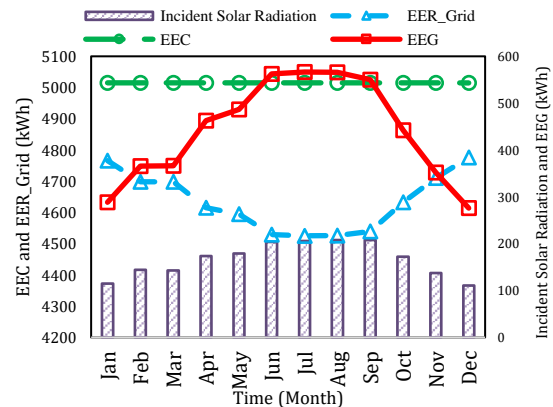


Figure 7. Monthly variation of incident solar radiation, EEG, EEC, and EER_Grid

Table 7 shows the annual electrical performance of the SCS. As can be seen, the annual EEC of the building is more than 60 MWh, of which about 54% is related to appliances (AEC) and the rest is related to lighting (LEC). The ratio of electrical energy received from the inverter (EER_Inv) to EEC is about 7.6%; however, the ratio of electrical energy received from the grid (EER_Grid) to EEC is 92.4%. It should be noted that the difference between the EEG and EER_Inv is because of the power loss in the system.

Table 7. Annual electrical performance of SCS

Parameter	Value (MWh)
Total electrical energy consumption (EEC)	60.18
Appliance electrical energy consumption (AEC)	32.60
Lighting electrical energy consumption (LEC)	27.58
Total electrical energy generation (EEG)	5.29
Electrical energy received from the grid (EER_Grid)	55.61
Electrical energy received from the inverter (EER_Inv)	4.57

Figure 8 shows the monthly variation of incident solar radiation, thermal energy generation (TEG), and consumption (TEC) including thermal energy consumption for providing DHW (DTEC) and SH (STEC). As observed, in warm months, almost all DHW load is provided by the SCS, because there is no need for SH. In the cold months, the STEC and thus, TEC have higher values, while TEG has lower values because of low incident radiation; so, the lowest TEG is obtained in December, which is 787 kWh. As can be seen, the ratio of STEC to TEG decreases from April and reaches zero from May to September, due to the lack of need for space heating. Nonetheless, it increases from October, so it is about 26 times larger in December compared to October. It is also found that the maximum ratio of TEC to TEG is 20.46 in January and the minimum one is 1.06 in August.

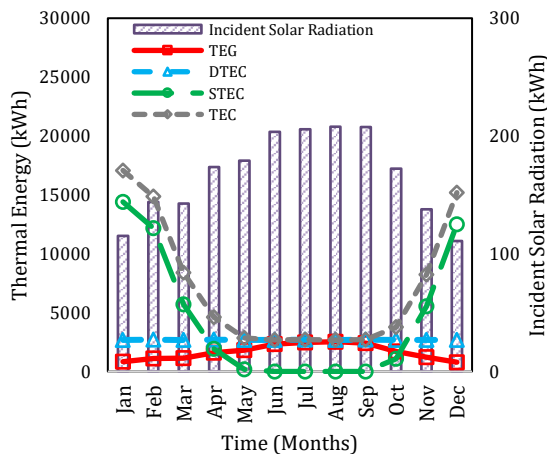


Figure 8. Monthly variation of incident solar radiation, TEG and, TEC

The annual thermal performance of the SCS is shown in Table 8. Based on the results, the annual TEC of the building is 89.57 MWh, of which about 60% is related to space heating (TEC_SH) and the rest is related to domestic hot water consumption (TEC_DHW). The ratio of TEG by the SCS to the TEC of the building is 22.5%.

Table 8. Annual thermal performance of SCS

Parameter	Value (MWh)
Total thermal energy consumption (TEC)	89.57
Thermal energy consumption for DHW (TEC_DHW)	32.57
Thermal energy consumption for SH (TEC_SH)	54.05
Total thermal energy generation (TEG)	20.13

The monthly variations of thermal, electrical, and total solar fractions of the SCS are shown in Figure 9. As the results show, in the warm months, due to the increase of incident solar radiation and the lack of need for SH, the thermal and total fractions have significantly grown. Due to the constant need for electricity, the monthly electrical fraction does not change much, but in the warmer months of the year, due to more radiation, a slight increase in the electrical fraction is observed.

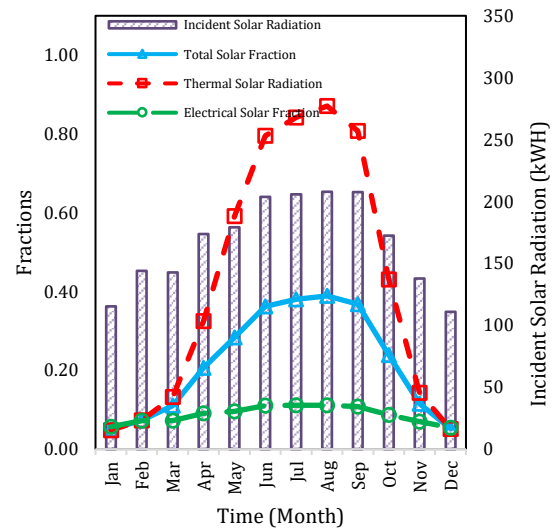


Figure 9. Monthly variation of different solar fractions

Conclusion

In this study, the performance of the SCS using PVT systems for supplying electricity, DHW, and SH demands of a case study building have been investigated and optimized using the Monte Carlo method. In the Monte Carlo method, by considering the risk conditions and calculating the probability of the

LCS, PBT, and IRR indicators, the optimum SCS system for the case study building is determined. The probability that the PBT is less than 5 years, the IRR is more than 20% and the LCS are more than the initial cost is 74.2%, 11.5%, and 97%, respectively. The analysis of the electrical performance of the optimum SCS indicates that a minimum of 5% and a maximum of 11% of the building's electrical load is provided by the system. The maximum electrical solar fraction is obtained from June to September. The annual electrical solar fraction of the SCS is 8.7%. In terms of thermal performance, it is found that the optimum SCS provided about 5%-87% of the building's thermal load. In the warm months (from April to October), about 66.6% of the building thermal demand is provided by the SCS; while, in the cold months (from November to March), on average 72% of the building thermal demand should be provided by fossil fuels. Finally, the maximum savings in electrical, thermal, and total energy consumption of the building using the optimum SCS are 11%, 87%, and 39%, respectively, which are related to the month of August. It is concluded that the optimization of the SCSs for providing the energy demands of the buildings leads to an efficient reduction of energy consumption.

It should be noted that a limitation of the research is the economic conditions of Iran and low price of the primary energies, which forced us to use the economic conditions and energy costs of the United States. It is recommended that the optimization of the SCS is performed for other climatic conditions and using other types of SCSs including different collector types and configurations of the storage tanks.

Nomenclature

d	Discount rate
F	Cash flow
N	Number
t	Time

Acronyms

AEC	Appliance Energy Consumption
DASC	Direct Absorption Solar Collector
DHW	Domestic Hot Water
DTEC	Domestic Thermal Energy Consumption
EEC	Electrical Energy Consumption

EEG	Electrical Energy Generation
EER	Electrical Energy Received
ETSC	Evacuated Tube Solar Collector
FPSC	Flat Plate Solar Collector
IRR	Internal Rate of Return
LCC	Life Cycle Cost
LCE	Life Cycle Energy
LCS	Life Cycle Savings
LEC	Lighting Energy Consumption
NPV	Net Positive Value
PBT	Payback Time
PVT	Photovoltaic-Thermal
PSO	Particle Swarm Optimization
SCS	Solar Combisystem
SH	Space Heating
TEC	Thermal Energy Consumption
STEC	Space Thermal Energy Consumption
TEG	Thermal Energy Generation
WWR	Windows-to-Wall Ratio

References

- [1] Karami, M., Raisee, M., and Delfani, S., 2014. Numerical investigation of nanofluid-based solar collectors. *IOP Conf. Ser.: Mater. Sci. Eng.*, 64 (1), 012044.
- [2] Amin, Z., Nematollahi, O., and Alemrajabi, A.A., 2021. Disinfection process with solar drying system. *Journal of Heat and Mass Transfer Research*, 8 (1), pp. 23-28.
- [3] Alamdari, P., Salihoglu, N.K., and Amin, Z., 2013. Solar energy potentials in Iran: A review. *Renewable and Sustainable Energy Reviews*, 21, pp. 778-788.
- [4] Hormozi Moghaddam, M. and Karami, M., 2022. Heat transfer and pressure drop through mono and hybrid nanofluid-based photovoltaic-thermal systems. *Energy Science & Engineering*, 10 (3), pp. 918-931.
- [5] Karami, M., Delfani, S., and Noroozi, A., 2020. Performance characteristics of a solar desiccant/M-cycle air-conditioning system

- for the buildings in hot and humid areas. *Asian Journal of Civil Engineering*, 21, pp. 189-199.
- [6] Leckner, M., Zmeureanu, R., 2011. Life cycle cost and energy analysis of a Net Zero Energy House with solar combisystem. *Applied Energy*, 88 (1), pp. 232-241.
- [7] Rasoul Asaee, S., Ismet Ugursal, V., Beausoleil-Morrison, I., Ben-Abdallah, N., 2014. Preliminary study for solar combisystem potential in Canadian houses. *Applied Energy*, 130, pp. 510-518.
- [8] Sustar, J. L., Burch, J., Krarti, M., 2015. Performance Modeling Comparison of a Solar Combisystem and Solar Water Heater. *J. Sol. Energy Eng.*, 137 (6), 061001.
- [9] Mehdaoui, F., Hazami, M., Messaouda, A., and Guizani, A.A., 2020. Performance analysis of two types of Solar Heating Systems used in buildings under typical North African climate (Tunisia). *Applied Thermal Engineering*, 165, 114203.
- [10] Hazami, M., Mehdaoui, F., Naili, N., Noro, M., Lazzarin, R., and Guizani, A. A., 2017. Energetic, exergetic and economic analysis of an innovative Solar CombiSystem (SCS) producing thermal and electric energies: Application in residential and tertiary households. *Energy Convers. Manag.*, 140, pp. 36-50.
- [11] Katsaprakakis, D. A. and Zidianakis, G., 2019. Optimized Dimensioning and Operation Automation for a Solar-Combi System for Indoor Space Heating: A Case Study for a School Building in Crete. *Energies*, 12 (1).
- [12] Karami, M. and Javanmardi, F., 2020. Performance assessment of a solar thermal combisystem in different climate zones. *Asian Journal of Civil Engineering*, 21, pp.751-762.
- [13] Karami, M. and Nasiri Gahraz, S.S., 2022. Improving thermal performance of a solar thermal/desalination combisystem using nanofluid-based direct absorption solar collector. *Sientia Iranica*, 29 (3), *Transactions on Mechanical Engineering (B)*, pp. 1288-1300.
- [14] Esmaeili, M., Karami, M. and Delfani, S., 2020. Performance enhancement of a direct absorption solar collector using copper oxide porous foam and nanofluid. *International Journal of Energy Research*, 44 (7), pp. 5527-5544.
- [15] Delfani, S., Karami, M., Akhavan-Behabadi, M.A., 2016. Experimental investigation on performance comparison of nanofluidbased direct absorption and flat plate solar collectors. *International Journal of Nano Dimension (IJND)*, 7 (1), pp. 85-96.
- [16] Karami, M. and Nasiri Gahraz, S.S., 2021. Transient simulation and life cycle cost analysis of a solar polygeneration system using photovoltaic-thermal collectors and hybrid desalination unit. *Journal of Heat and Mass Transfer Research*, 8 (2), pp. 243-256.
- [17] Kannan, A., Prakash, J., Roan, D., 2021. Design and performance of an off-grid solar combisystem using phase change materials. *International Journal of Heat and Mass Transfer*, 164, 120574.
- [18] Bornatico, R., Pfeiffer, M., Witzig, A. and Guzzella, L., 2012. Optimal sizing of a solar thermal building installation using particle swarm optimization. *Energy*, 41(1), pp. 31-37.
- [19] Hin, J.N.C. and Zmeureane, R., 2014. Optimization of a residential solar combisystem for minimum life cycle cost, energy use and exergy destroyed. *Solar Energy*, 100, pp. 102-113.
- [20] Rey, A. and Zmeureanu, R., 2016. Multi-objective optimization of a residential solar thermal combisystem. *Solar Energy*, 139, pp. 622-632.
- [21] Rey, A. and Zmeureanu, R., 2017. Micro-time variant multi-objective particle swarm optimization (micro-TVMOPSO) of a solar thermal combisystem. *Swarm and Evolutionary Computation*, 36, pp. 76-90.
- [22] Rey, A. and Zmeureanu, R., 2018. Multi-objective optimization framework for the selection of configuration and equipment sizing of solar thermal combisystems. *Energy*, 145, pp. 182-194.
- [23] Li, Y.H., Kao, W.C., 2018. Taguchi optimization of solar thermal and heat pump combisystems under five distinct climatic conditions. *Applied Thermal Engineering*, 133, pp. 283-297.
- [24] Thapa, B. and Wang, W., Williams, W., 2021. Life-cycle cost optimization of a solar combisystem for residential buildings in Nepal. *Journal of Asian Architecture and Building Engineering*, 21 (3), pp. 1137-1148.
- [25] Jalalizadeh, M., Fayaz, Rima, Delfani, S., Jafari Mosleh, H. and Karami, M., 2021. Dynamic simulation of a trigeneration system using an absorption cooling system and building integrated photovoltaic thermal solar collectors. *Journal of Building Engineering*, 43, 102482.
- [26] Goldsim. 2022. Monte Carlo Simulation. *Monte Carlo Simulation and Methods Introduction - GoldSim*.
- [27] Mun, J., 2006. Modeling risk: Applying Monte Carlo simulation, real options analysis, forecasting, and optimization techniques 347. John Wiley & Sons.
- [28] Fuller, S., 2010. Life-cycle cost analysis (LCCA). National Institute of Building Sciences, An Authoritative Source of

- Innovative Solutions for the Built Environment 1090.
- [29] Gu, Y., Zhang, X., Myhren, J. A., Han, M., Chen, X. and Yuan, Y., 2018. Techno-economic analysis of a solar photovoltaic/thermal (PV/T) concentrator for building application in Sweden using Monte Carlo method. *Energy Convers. Manag.* 165, pp. 8-24.
- [30] Kalogirou, S., 2014. *Solar Energy Engineering: Processes and Systems*, Academic Press, second edition.



Semnan University



Research Article

Fabrication of Solar Desalination System and Experimental Investigation of its Performance of it, Located in Ahvaz City

Reza Bahoosh ^{*,a}, Ashkan Nazari ^b, Maziyar Changizian ^a, Mojtaba Moravej ^c

^a Faculty member of Mechanical Engineering Group, Shahid Chamran University of Ahvaz, Iran.

^b MSc student, Mechanical Engineering Group, Shahid Chamran University of Ahvaz, Iran.

^c Faculty member of Mechanical Engineering Group, Payame Noor University, Iran.

PAPER INFO

Paper history:

Received: 2021-05-28

Revised: 2023-04-02

Accepted: 2023-04-08

Keywords:

Desalination;
Distilled solar;
Solar radiation;
Heat transfer;
Ceramic.

ABSTRACT

With the increasing population and heightening quality levels of life in the world, the use of freshwater resources has increased to such an extent that their shortage is considered a serious crisis. Today, manufacturing and untiring solar stills, which produce freshwater without polluting the environment, besides, at a low cost, have been considered a suitable solution to eliminate the shortage of fresh water. In recent years, water desalination has been at the center of interest more than ever in Iran because of the drought and water shortage crisis. For this reason, the design and manufacture of distilled solar still suitable for the geographical conditions of Ahvaz were accomplished. And a device with two inclined planes was selected after studying different types of distilled solar stills. In the first step, a thermal model of different heat transfer phenomena including radiation, conductivity, evaporation, and condensation was employed so that it was utilized to predict the performance of the device in various conditions and the heat analysis of the system. The governing equations in MATLAB software were then implemented and solved. According to the results of the software, which estimates the amount of the produced water using meteorological data consisting of radiation intensity and ambient air temperature, as well as the material features of different parts of the device, the dimensions of the device were designed and the device was manufactured. This device was tested on one of the winter days in January and the production amount of freshwater, as well as temperatures of glass coatings, water, and absorbent surface, were recorded. The production amount of freshwater on the 4th of January in a practical test was 0.98 L/m².

DOI: [10.22075/jhmr.2023.23508.1344](https://doi.org/10.22075/jhmr.2023.23508.1344)

© 2022 Published by Semnan University Press. All rights reserved.

1. Introduction

Besides helping to provide drinking water in the cities facing water shortage, solar stills are the best way to make available freshwater in faraway and unreachable villages. Today, due to the sequential droughts in Iran in recent years, lots of areas of the country are facing serious problems to supply water in cities and villages so the problem of water shortage has become one of the crises in the country. It seems that the only solution to this problem is the desalination of

the saline water sources in the north and south of the country. Employing solar energy to produce fresh water is a priority as a result of the advantages of using clean energy. With about 300 sunny days per year, Iran has a superior capability to utilize solar energy so handling the crisis of water shortage will be possible if a mechanism is provided to benefit from it [1]. Noghreabadi et al. [2] studied experimentally two types of flat plate collectors, namely square and rhombic collectors. The results show the rhombic collector has better performance in the morning and

*Corresponding Author: corresponding author's name.

Email: reza.bahoosh@gmail.com

afternoon, consequently, both collectors have the same performance at noon. Yaoxin Zhang et al. [3] studied FW as highly porous carbon-based photothermal materials for low-cost solar desalination and thermoelectric (TE) generation. Rashidi et al. [4] performed a review of the literature on the implementation of nanofluid technology in active and passive solar distillation systems. Rafiei et al. [5] studied a hybrid solar desalination system. The humidification-dehumidification desalination unit comprises a closed-air open-water flow configuration, and the solar dish concentrators are utilized for water heating. Examination of three different shapes of cavity receivers including cylindrical, cubical, and hemispherical, as the solar dish absorbers, was performed.

One of the most important factors to design solar energy systems in any location is to have precise statistics and information on solar radiation in the desired location. Since there is no exact information about the amount of solar radiation in most areas of Iran, the amount of radiation that reached the surface of the device was obtained by theoretical procedures and supposing a clear sky. Designing was performed established upon the theoretical calculations. Another important parameter during the designing process is to acquire the temperatures of water, absorbent surface, and glass coatings based on the considered dimensions and the radiation amount of solar energy [6-12].

Abdul Jabbar and Hussein [13] experimentally investigated the effect of internal and external reflectors in a solar still device having an absorbent surface tilted at angles 0°, 10°, 20°, and 30° on the production of freshwater in summer, autumn and winter. They realized that, except in summer, the influence amount is close to zero. Installing internal reflectors only, and internal reflectors and inclined external reflectors tilted at angles of 0°, 10°, 20°, and 30° led to increasing the production rate up to 19.9%, 34.5%, 34.8%, and 24.7%, respectively. They were tested in a location with a latitude of 33.3°, also, the test device inclined 20° for coatings.

To obtain more freshwater production by decreasing heat losses from the floor and walls of the device and to make certain heat is stored inside the device, Abdul Jabbar and Ahmad [14] studied the amount of adequate isolation for desalination solar devices. They tested the devices with an insulation thickness of 30, 60, and 100 mm and compared the results with those having no isolation. They found that the insulation thickness of up to 60 mm can remarkably affect freshwater production. Moreover, they tried to present a relation between the producing amount of freshwater and the insulation of the device given the importance of the insulation effect on the optimal performance of the distilled solar still device.

Murugavel and Srithar [15] theoretically and experimentally performed an investigation on a distilled solar device with two inclined planes and tried to scrutinize the effect of various factors on the device's performance and production rate. To realize the influence of adding wick materials having the capillary ability, they added light and black cotton cloth, sponge sheet, coir mate, and waste cotton pieces to the floor (basin) and recorded the acquired results. By analyzing and comparing the results of experimental and theoretical trials; they reached a satisfactory agreement between the two trials and found that the best performance is for a device with a floor covered by light and black cotton cloth.

In a practical experiment, Kalbasi and Esfahani [16] examined the influence of water salinity entering distilled solar devices on the production rate of the outlet freshwater. Throughout several phases of the experiment, they increased the salt concentration in the inlet water by dissolving certain amounts of salt in the power supply of the water entering the device. They realized that the daily amount of water production decreases by increasing the salt concentration in the inlet salinity water so that it reduces by 20% by an increase of 0-3.5% in the salt concentration.

To increase the production rate of distilled solar desalination devices, also, to enhance their efficiency through further use of solar radiation, and for easy evaporation of salty water and condensation of fresh water on the glass; Sakthivel et al. [17] utilized jute cloth, which is affordable and available, in the device 8% increase in the efficiency was recorded.

To increase the production rate in a distilled solar desalination device having two inclined planes, Bechki et al. [18] placed a canopy over the northern cover in their experiments to keep the plane cool. This happened by decreasing the temperature of one of the glass planes on which less radiation occurs; consequently; it leads to an increasing temperature difference between water and glass as well as more condensation. They tested the device and the performance of the canopy in several stages and realized that locating a canopy on the northern plane of the device having two inclined planes, which receives the least radiation in the northern hemisphere in comparison with the southern plane, can improve 12% the daily production rate of freshwater.

In a practical experiment, Husham and Khalid [19] investigated the influence of using water sprinklers and fans outside of the device on the production rate of freshwater in a distilled solar still device. To decrease the glass cover temperature and make more temperature difference between the roof cover and water, they designed two experiments; one of them utilized a fan outside of the device and another one is using a water sprinkler that sprays water on the glass cover at different intervals. Experiments showed that

using a fan and increasing wind speed from 1.2 to 3 and 4.5 m/s heightens the freshwater production rate up to 8% and 15.5%, respectively. Moreover, using a water sprinkler at two intervals of 20 and 10 min leads to 15.7% and 31.8% increase in the production rate of freshwater in that order.

In this research, a distilled solar desalination device with two inclined planes suitable for the climatic conditions of Ahvaz was designed and examined. For this purpose, the solution of the heat transfer equations in different parts of the device and obtaining the receivable solar energy in Ahvaz in addition to the optimal design of different parts of the device were investigated. Utilizing the results acquired from the heat transfer equations and the technical performance of the device in the environmental conditions of Ahvaz were studied.

2. Materials and Methods

2.1. Theoretical study

2.1.1. Solar radiation measurement

The amount of solar radiation that is placed on a surface depends on the weather conditions, and as the conditions change, the amount of radiation will also change. For this reason, the clear sky standard is used to calculate the amount of radiation on the horizon. In this standard, the intensity of direct radiation on the horizontal surface of Equation (1) and the intensity of scattered radiation at any moment of Equation (2) are utilized.

$$G_{cb} = G_{on} \times \tau_b \times \cos \theta_Z \tag{1}$$

$$G_{cd} = G_{on} \times \tau_d \times \cos \theta_Z \tag{2}$$

where the peak angle is displayed with θ_Z and G_{on} ; the amount of sunlight outside the atmosphere is obtained using Equation (3).

$$G_{on} = G_{sc} \times \left(1 + 0.033 \times \cos \frac{360n}{365} \right) \tag{3}$$

where G_{sc} is called solar constant and is equal to 1367 W/m². Also τ_b and τ_d can be found in Equations (4,5).

$$\tau_b = \alpha_0 + \alpha_1 \times \exp \left(\frac{-\kappa}{\cos \theta_Z} \right) \tag{4}$$

$$\tau_d = 0.271 - 0.294 \times \tau_b \tag{5}$$

The τ_b and τ_d are transmittance coefficients of direct radiation and scattered rays of the sun are from the atmosphere, respectively.

The values α_0 are obtained using the hotel method and the relations (6-11) are utilized; for the calculation, and conditions of table 1 are used.

$$r_0 = \frac{\alpha_0}{\alpha_0^*} \tag{6}$$

$$r_1 = \frac{\alpha_1}{\alpha_1^*} \tag{7}$$

$$r_\kappa = \frac{\kappa}{\kappa^*} \tag{8}$$

$$\alpha_0^* = 0.4237 - 0.00821 \times (6 - A)^2 \tag{9}$$

$$\alpha_1^* = 0.5055 + 0.00595 \times (6.5 - A)^2 \tag{10}$$

$$\kappa^* = 0.2711 + 0.01858(2.5 - A)^2 \tag{11}$$

where A is the altitude of an observer in kilometers.

Table 1 Recommended Hotel coefficients for different weather types

Climate Type	r_0	r_1	r_κ
1 Tropical	0.95	0.98	1.02
2 Midlatitude Summer	0.97	0.99	1.02
3 Subarctic Summer	0.99	0.99	1.01
4 Midlatitude winter	1.03	1.01	1.00

The amount of radiation intensity on a sloping surface which is obtained by the amount of direct radiation intensity scattered radiation intensity, and also the reflection from the ground surface is obtained using Equation (12).

$$G_{T1} = G_{cb}R_b + G_{cd} \left(\frac{1 + \cos \beta}{2} \right) + G_s \rho_g \left(\frac{1 - \cos \beta}{2} \right) \tag{12}$$

where ρ_g is the ground reflect coefficient and assumed 0.6. G and R_b also introduced by Equations (13,14) respectively.

$$G_s = G_{cb} + G_{cd} \tag{13}$$

$$R_b = \frac{\cos \theta}{\cos \theta_Z} \tag{14}$$

$\cos \theta$ is the orientation of the ramp depends on the south, and since we have two ramps, we will have two $\cos \theta$ and two R_b , from which the intensity of radiation is calculated for each ramp separately. Therefore, $G_T = G_{T1} + G_{T2}$, they are related to slope level 1 and slope level 2.

2.1.2. Heat transfer equations

To determine the temperature of different parts, the heat transfer coefficient between these parts must be obtained; assuming that at the time of starting the

device, the device is in thermal equilibrium with the environment and the temperature of different parts is equal to the air temperature. The Sub-sections b, w, and g are related to the adsorbent surface, water, and glass, respectively; and since there are two sloping surfaces in the device; the parameters related to each of them are distinguished from each other by sub-sections 1 and 2. The equations of this section are taken from [20]. The effective absorption coefficients of glass, water, and adsorbent surface are obtained from Equations (15-17).

$$AB_g = (1 - \rho_g)\alpha_g \tag{15}$$

$$AB_w = (1 - \rho_g - AB_g)\alpha_w \tag{16}$$

$$AB_b = (1 - \rho_g - AB_g - AB_w)\alpha_b \tag{17}$$

which ρ α are reflection and absorption coefficients respectively.

Due to the recording of meteorological data in one-hour intervals by the Meteorological Department; the application of these values causes a temperature shock at the moment of temperature change; because the temperature and wind speed functions are gradual in relation to the time interval. One hour has a constant value, in view of the fact that the temperature and wind speed change gradually; so to get closer to reality the amount of air temperature and speed at each time step is based on linear interpolation between the beginning and the end of an hour is calculated.

Given that the assumed time step is one minute, changes in temperature and wind speed are applied gradually over one hour in sixty steps. The result is smooth temperature-time graphs. Air temperature and wind speed per minute are calculated using equations (18 and 19), respectively.

$$T_a = T_{a,i} + \left(\frac{T_{a,i+1}}{60} \times j\right) \tag{18}$$

$$V = V_i + \left(\frac{V_{i+1}}{60} \times j\right) \tag{19}$$

2.1.3. Absorption

To obtain the temperature of the adsorbent surface, the heat transfer equation must be written for this surface. The heat transferred with the adsorbent surface is shown in Figure 2.

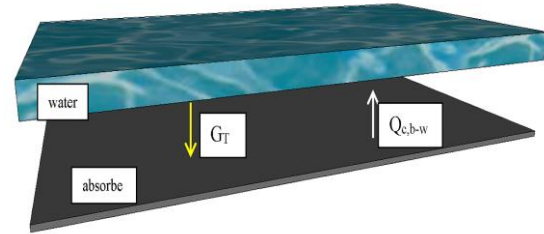


Fig. 1. Heat transfer modeling of the absorber

The heat transfer equation for the absorber is according to Equation (20).

$$m_b \times C_{p,b} \times \left[\frac{dT_b}{dt}\right] = A_b \times AB_b \times G_T - Q_{c,b-w} \tag{20}$$

where m_b , $C_{p,b}$, AB_b , A_b , T_b and G_T are mass, special heat coefficient, area, absorber, temperature, and effective coefficient of absorption surface respectively. Besides, effective absorption coefficient conduction heat transfer between water and absorber can be found as follows.

$$G_T = G_{T1} + G_{T2} \tag{21}$$

$$Q_{c,b-w} = h_{c,b-w} \times A_w \times (T_b - T_w) \tag{22}$$

where $h_{c,b-w}$ is the coefficient heat transfer between water and absorber and calculated by equation (23).

$$h_{c,b-w} = \frac{K_w}{X_w} \tag{23}$$

where K_w is the heat transfer coefficient and X_w is water thickness.

To obtain the water temperature, the heat transfer equation must be written for this level. The heat exchanged with water is shown in Figure 3.

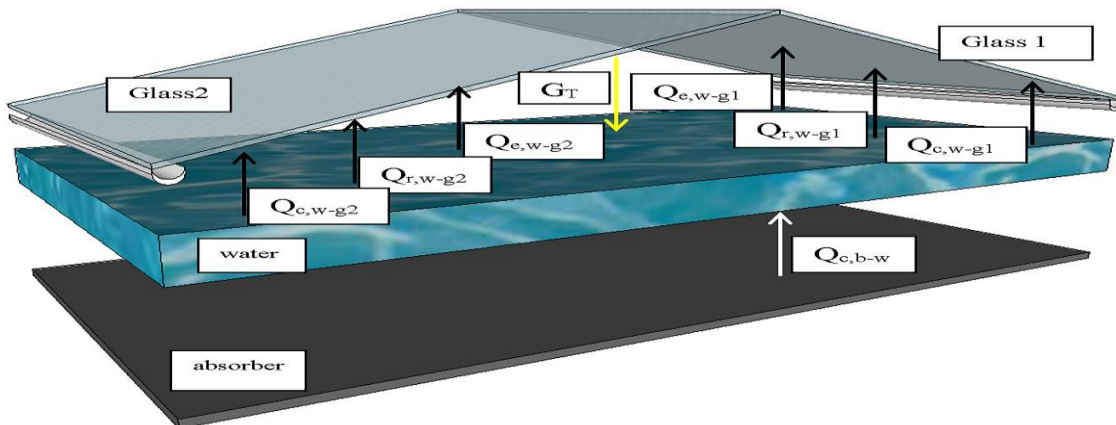


Fig. 2. Heat transfer modeling of water

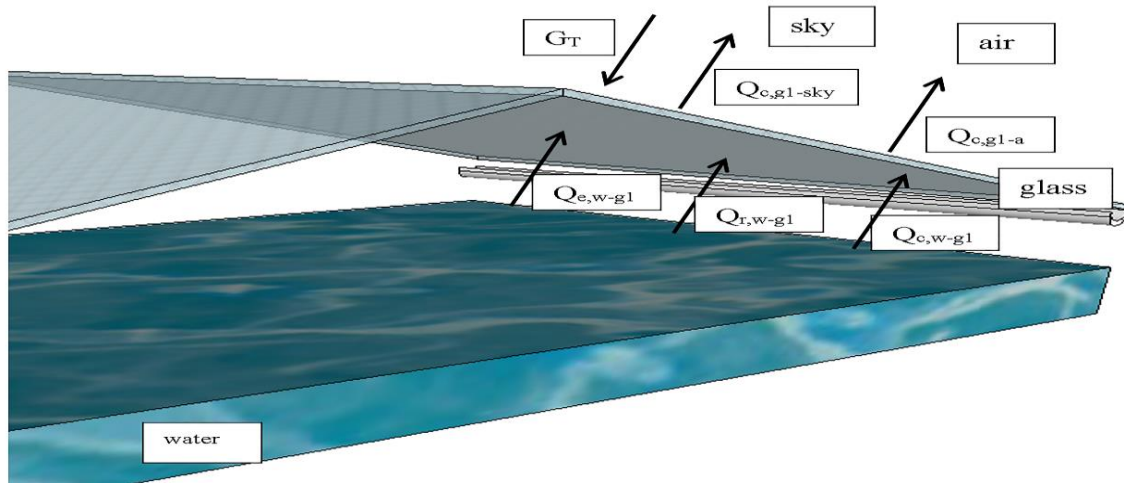


Fig. 3. Heat transfer modeling of the glass cover.

The water heat transfer equation is formed according to Equation (24).

$$m_w \times C_{p,w} \times \left[\frac{dT_w}{dt} \right] = (A_w \times AB_w \times G_T) + Q_{c,b-w} - (Q_{c,w-g1} + Q_{c,w-g2} + Q_{r,w-g1} + Q_{r,w-g2} + Q_{e,w-g1} + Q_{e,w-g2}) \quad (24)$$

where m_w , A_w , AB_w , $C_{p,w}$, T_w are mass, area, absorption coefficient, heat capacity, and temperature of water respectively.

The rate of heat transfer between water and glass, the rate of radiant heat transfer between water and glass, and the rate of heat transfer of vapor between water and glass, are $Q_{r,w-g}$, $Q_{r,w-g}$ and $Q_{e,w-g}$ respectively that are obtained from the relations (25-31).

$$Q_{c,w-g} = h_{c,w-g} \times A_w \times (T_w - T_g) \quad (25)$$

$$h_{c,w-g} = 0.884 \times$$

$$\left[(T_w - T_g) + \frac{(P_w - P_g) \times (T_w + 273.15)}{268900 - P_w} \right]^{\frac{1}{3}} \quad (26)$$

P is the partial pressure of each part depending on its temperature.

$$P = \exp \left[25.317 - \left(\frac{5144}{T + 273.15} \right) \right] \quad (27)$$

$$Q_{r,w-g} = h_{r,w-g} \times A_w \times (T_w - T_g) \quad (28)$$

where $h_{r,w-g}$ is introduced as follows:

$$h_{r,w-g} = \epsilon_{eff} \times \sigma \times \left[\frac{(T_w + 273.15)^4 - (T_g + 273.15)^4}{(T_w - T_g)} \right] \quad (29)$$

where σ is the Stephen-Boltzmann coefficient.

$$\epsilon_{eff} = \left(\frac{1}{\epsilon_w} + \frac{1}{\epsilon_g} - 1 \right)^{-1} \quad (30)$$

emission coefficient ϵ_g

It should be noted that the emission coefficient derives from a handbook for every material which are 0.96 and 0.88 for glass and water respectively.

$$Q_{e,w-g} = h_{e,w-g} \times A_w \times (T_w - T_g) \quad (31)$$

where $h_{e,w-g}$ is introduced as:

$$h_{e,w-g} = 0.016273 \times \left[h_{c,w-g} \times \frac{(P_w - P_g)}{(T_w - T_g)} \right] \quad (32)$$

the above equations $h_{e,w-g}$ is the Steam heat transfer coefficient and ϵ_w is water export coefficient and ϵ_g is glass export coefficient.

To obtain the temperature of the glass cover 1, the heat transfer equation must be written for this coating. The heat exchanged with glass cover 1 is shown in Figure 3.

$$m_{g1} \times C_{p,g1} \times \left[\frac{dT_{g1}}{dt} \right] = (A_{g1} \times AB_{g1} \times G_{T1}) + Q_{c,w-g1} + Q_{r,w-g1} + Q_{e,w-g1} - (Q_{c,g1-a} + Q_{r,g1-sky}) \quad (33)$$

where m_{g1} , $C_{p,g1}$, A_{g1} , T_{g1} and AB_{g1} are mass, heat capacity, area, and the temperature of glass respectively.

Absorption coefficient 1, G_{T1} is the radiation intensity on glass 1. $Q_{c,g1-a}$ is the heat transfer transferred between glass 1 and air; also $Q_{r,g1-sky}$ is the radiant heat transferred between glass 1 and the sky and these parameters are obtained from the relations (34-38).

$$Q_{c,g1-a} = h_{c,g1-a} \times A_{g1} \times (T_{g1} - T_a) \quad (34)$$

$$h_{c,g1-a} = 2.8 + (3 \times V) \quad (35)$$

$$Q_{r,g1-sky} = h_{r,g1-sky} \times A_{g1} \times (T_{g1} - T_{sky}) \quad (36)$$

$$h_{r,g1-sky} = \varepsilon_{g1} \times \sigma \times \left[\frac{(T_{g1} + 273.15)^4 - (T_{sky} + 273.15)^4}{(T_{g1} - T_{sky})} \right] \quad (37)$$

$$T_{sky} = T_a - 6 \quad (38)$$

where T_a is the air temperature, $h_{c,g1-a}$ is the heat transfer coefficient of transfer between glass and air, V is the wind speed, $h_{r,g1-sky}$ is the radiation heat transfer coefficient between glass and sky, and T_{sky} is the estimated temperature of the sky in the above equations. It should be mentioned that all of the equations which are used for heat transfer modeling in glass 1 have the same form as in glass 2.

2.1.4. Estimate production

In this section, according to the physical coordinates of the device, the amount of solar radiation, heat transfer equations, and the amount of output of the device are obtained. The total output of the device is obtained from Equation (39).

$$m_e = m_{e1} + m_{e2} \quad (39)$$

where m_{e1} is the amount of condensate on the glass surface 1 and m_{e2} is the amount of condensate on the glass surface 2 is obtained from the equations (40-42), respectively.

$$m_{e1} = \frac{(Q_{e,w-g1}) \times \Delta t}{h_{fg}} \quad (40)$$

$$m_{e2} = \frac{(Q_{e,w-g2}) \times \Delta t}{h_{fg}} \quad (41)$$

Which h_{fg} is obtained from the following relation.

$$h_{fg} = (2503 - 2.398T_w) \times 1000 \quad (42)$$

2.2. Experimental study

According to Fig. 1, the solar desalination device with two inclined planes was formed of a black absorbent surface to further absorb energy and two glass covers to pass the sun's rays; the glasses also act as the cold surface required for the condensation. The overall features of the device are presented in Table 2. Two gutters at two ends of the glass cover directly distilled freshwater, which has flowed into the gutters outside the device; a container to hold freshwater coming out of the gutters. Two inlet saline water channels are fed from a tanker at a height above the level of the channels (the channels are installed a little above the saline water level of the device). It should be mentioned that the insulator covers around the device, which is responsible to diminish heat losses, is an outline to preserve the glasses and sidewalls of the device.

The experiment location and the solar radiation are measured with Solar Meter TES 132 and illustrated in Table 3. Besides, the device is placed in the east-west direction so that one inclined plane will be facing south (glass 1) and the other will be facing north (glass 2). The slope value of the glass planes for the horizon is one of the very influential factors in the amount of radiation received. In both planes of the device, a 15° slope was considered. The complete state of these details is illustrated in Fig. 5.

Table 2. Characteristics of the manufactured solar desalination.

Material	Characteristics
Angular iron 6cm wide	Maintenance Framework
0.5 mm thick galvanized sheet Dimensions: 92×182 cm 9 cm south and north edges and 4 cm east and west edges	Absorbent maintenance plane
Rectangular black building ceramic tiles Dimensions: 90×60 cm	Absorbent plane
Two 3 mm thick regular glasses Area: 92×46 cm	Glass coating
15° concerning the horizon from both sides	Glass coating slope
Two 3 cm diameter hemispheres made of galvanized material and a 2% locating slope	Freshwater collecting gutters
2 cm thick Polystyrene	Insulator
Waterproof silicone sealant adhesive	Sealing

Table 3. Geographical characteristics of the trial location.

Maximum average of solar radiation (MJm ⁻² day ⁻¹)	Minimum average of solar radiation (MJm ⁻² day ⁻¹)	Latitude and Longitude	Altitude (m)	Name of trial location
24.78	13.6	31 ^o , 30' N, 48 ^o , 65'E	16	Ahvaz-Iran



Fig. 4. Picture of manufactured device.

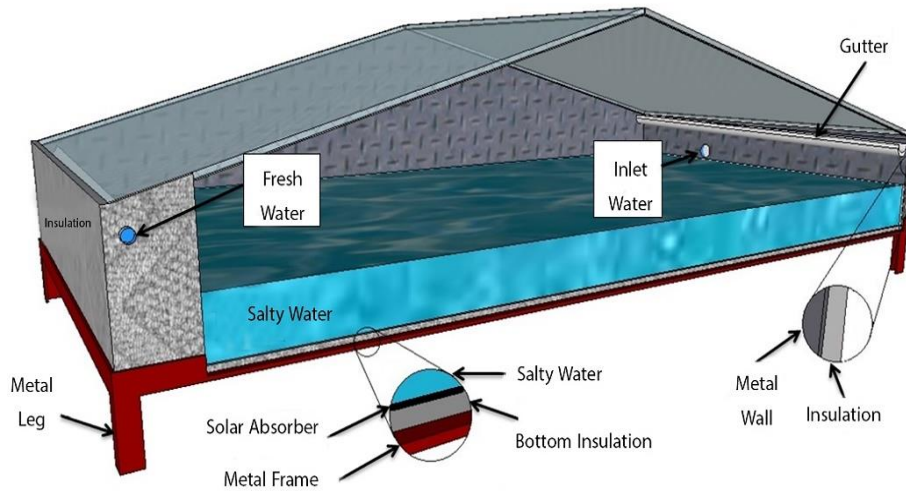


Fig. 5. The schematic picture of the device.

2.3. Uncertainty analysis

Doing experiments in real space and the laboratory is always associated with some errors [21]. Determining the amount of error can help the researcher in terms of the accuracy of quantities and reporting. In the present study, to measure the amount of water produced in the desalination plant, temperature solar radiation, mass and time quantities were directly involved in the analysis, which was used to calculate the total error of the RSSM method to evaluate the uncertainty. If u_1, u_2, \dots, u_n are the measuring parameters of a study, the uncertainty calculated by Equation (43).

$$S = \sqrt{\left(\frac{\Delta u_1}{u_1}\right)^2 + \left(\frac{\Delta u_2}{u_2}\right)^2 + \left(\frac{\Delta u_3}{u_3}\right)^2 + \dots} \quad (43)$$

Therefore, in the present study, the uncertainty analysis will be done according to the mentioned parameters in the form of the following relationship:

$$S = \sqrt{\left(\frac{\Delta T}{T}\right)^2 + \left(\frac{\Delta G}{G}\right)^2 + \left(\frac{\Delta m}{m}\right)^2 + \left(\frac{\Delta t}{t}\right)^2} \quad (44)$$

According to the measurement of the parameter, the temperature, solar radiation, mass and time uncertainty was about 0.5%, 4.1 %, 3.2% and 1.6% respectively. Due to equation (44) the total uncertainty is about 5.46%.

3. Results

By use of the geographical conditions of Ahvaz, the physical coordination of the device, and based on the radiation equations, a computer program separately calculates the amount of solar radiation at sunny

hours; the energy received from every single glass coating surface of the device, and the sum of the two are obtained. Fig. 6 shows the graph of received solar radiation of the glass coating surfaces and the sum of radiation of the two surfaces.

In real weather conditions until two hours after sunrise, the radiation amount was considered zero because of cloudy weather. Two hours after sunrise and clearing the air, solar radiation starts on the surface of the device and upsurges over time; the highest received radiation on both glass surfaces occurs at noon. Solar radiation decreases over time and it reaches zero in the final hour due to cloudy weather. According to the location of Ahvaz in the northern hemisphere and the path of the sun in the sky, solar radiation on the southern surface of the device is higher than on the northern one. For this reason, the graph of the solar radiation on the northern surface (H_{s1}) is underneath that of the solar radiation on the

southern surface (H_{s2}). H_s is the total solar radiation on two surfaces. The radiation intensity and its highest amount are not different from each other in ideal and real weather conditions because it is not dependent on weather conditions. The difference between ideal and real conditions is in the number of sunny hours.

3.1. Temperature of the main components of the device

Based on the amount of solar radiation received during sunny hours and by solving heat transfer equations for the main components of the device, the temperature differences of the absorbent surface, water, and glass coatings are obtained for every minute, hence, the secondary temperatures can be acquired. The graph of temperature variations of the absorbent surface, water, and glass coating during day and night is illustrated in Fig. 7.

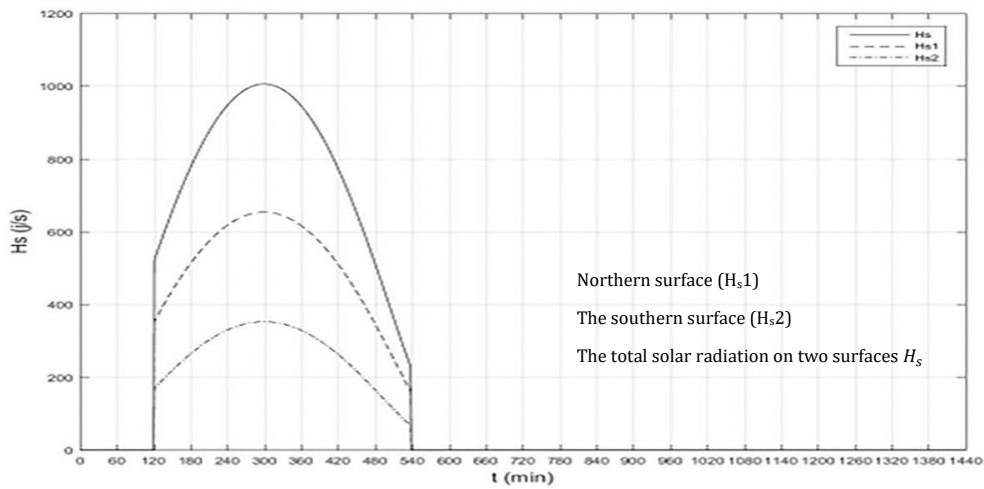


Fig. 6. Solar radiation graph in terms of time in real weather conditions.

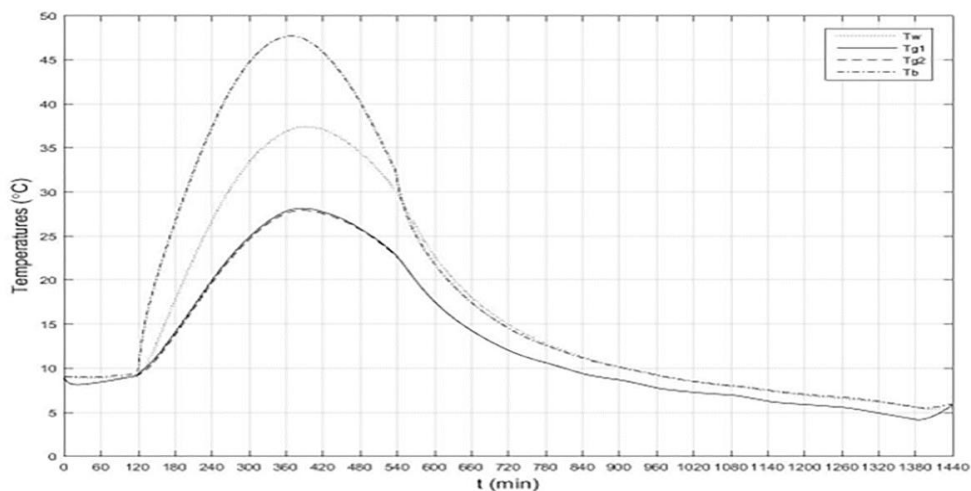


Fig. 7. Graph of the temperature of the absorbent surface, water, and glass coating in terms of temperature in real weather conditions.

At sunrise, owing to the cloudy air and lack of solar radiation on the surface of the device, the temperature of the absorbent surface and water is constant until the beginning of radiation. However, the glass's temperature heightens thanks to its vicinity to the air temperature increases. By starting solar radiation, the temperature of each of the three components increases. The absorbent surface temperature increases faster given its higher absorption coefficient and leads to enhance the temperature of the water because of its proximity to it. The temperature of the glass coatings also increases by increasing solar radiation as well as heat inside the device. It should be mentioned that the little difference between the temperature of the glass coatings 1 and 2 is due to their orientation and the difference in solar radiation received. The littleness of this difference is a result of the low absorption coefficient of the glass. The highest temperature of the absorbent surface is at noon and that of the water and glass is a little later. This delay can be attributed to the heat gradual transfer from the absorbent surface to the other components. Decreasing solar radiation over time leads to diminishing the temperature of all components.

The reduction intensity of temperature of the absorbent surface, water, and glass coatings increases owing to cloudy weather in the last hour of the day. After sunset, the temperature graph of the absorbent surface and water converge because of their proximity to each other. The temperature of the glasses reaches equilibrium with the air around the device as well. It is worth noting that the difference between the temperature of the glasses and the absorbent surface and water after sunset is related to the isolation of the device around the absorbent surface. The temperature graph level of the main components of the device in real weather conditions is a little lower than that in ideal ones. The low difference is because of that although the sunny hours are more in the ideal conditions, the radiation intensity at the beginning, as well as the end of the day, is at a low level. Another difference in temperature graphs is that the main

components reach their highest temperature a few minutes later in real conditions compared to the ideal ones. This is because of the posterior start for receiving solar radiation.

3.2. Amount of freshwater production

Using solar radiation received during sunny hours and by solving heat transfer equations for the main components of the device in addition to considering the temperatures of the main components of the device, the production amount of freshwater for the glass coating surfaces is obtained for each minute. The production graph of the device during the day and night is illustrated in Figure 8.

The production amount of freshwater in the two starting hours of the day is zero due to the lack of solar radiation. By starting solar radiation and increasing water temperature, the production is also started and increased over time, and by heightening solar radiation; it reaches the highest amount in the one-hour afternoon. The little difference between the freshwater produced by glasses 1 and 2 becomes more because of the higher temperature concerning glass 1 (getting more solar radiation). This difference reaches the highest value in the middle of the day. By moving away from noon and decreasing solar radiation, the production amount on both glasses reduces. The production amount reaches zero after a few hours of cloudy weather. The production amount in the real conditions is lower compared to the ideal ones whose reason is more radiation in the ideal conditions in comparison with the real ones.

3.3. Study of solar radiation effect on freshwater production

In a distilled solar still device, solar radiation is the main provision to produce freshwater; it has effects on the increase or the decrease of the production, directly. Figure 9 simultaneously shows the graphs of solar radiation and freshwater production in terms of time.

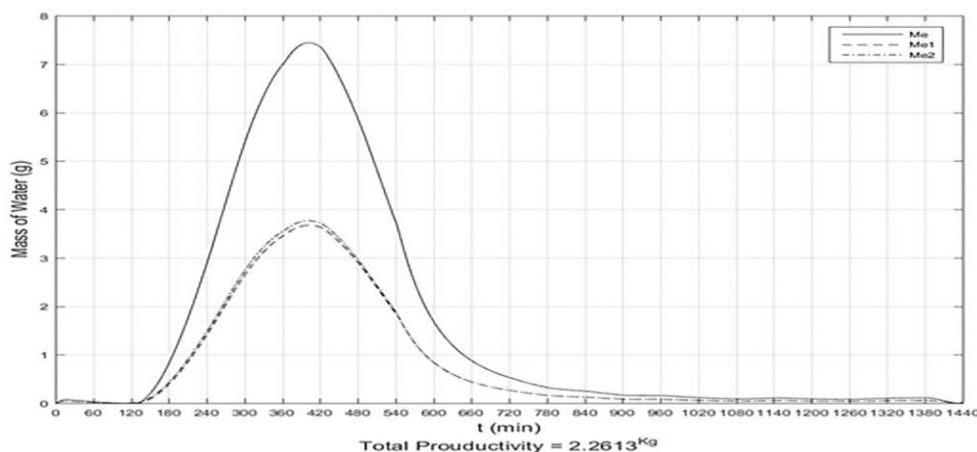


Fig. 8. Production graph of the device in terms of time in real weather conditions.

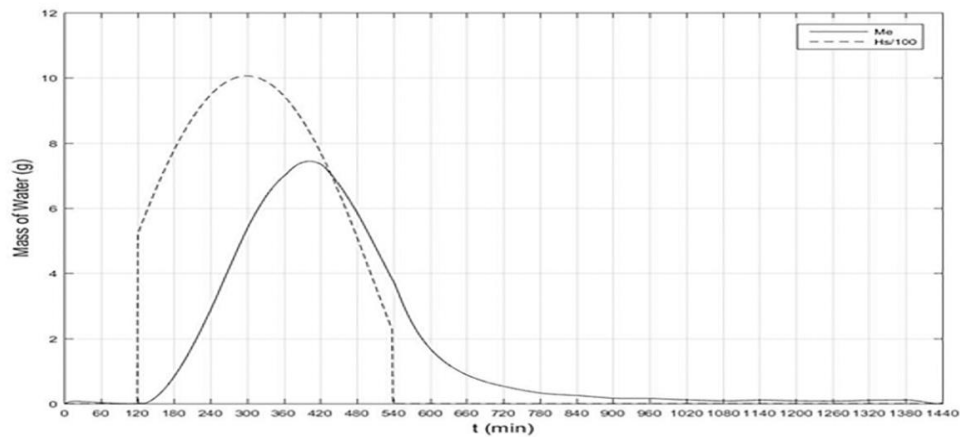


Fig 9. Graphs of solar radiation and freshwater production in terms of time in real weather conditions.

By starting radiation, the production of the device also starts and increases over time. The highest production amount of freshwater is obtained in one and a half hours of the afternoon. This is owing to a delay in increasing the temperature of water thanks to its high thermal capacity. The production amount is also lessened by approaching the end of the day, consequently, decreasing solar radiation. After the weather is cloudy at the end of the day, the production of the device continues due to the absorbent surface and water hot as well as reducing the temperature of the glass coatings, consequently, continuing evaporation. It should be noted that the production closes to zero some hours after sunrise.

3.4. Study of the effect of water temperature variations on freshwater production

By increasing the temperature of water under the influence of solar radiation on its surface and the heat transferred from the absorbent surface, the amounts of evaporation and freshwater production increase. Fig. 10 simultaneously indicates the graphs of the water temperature and freshwater production in terms of time.

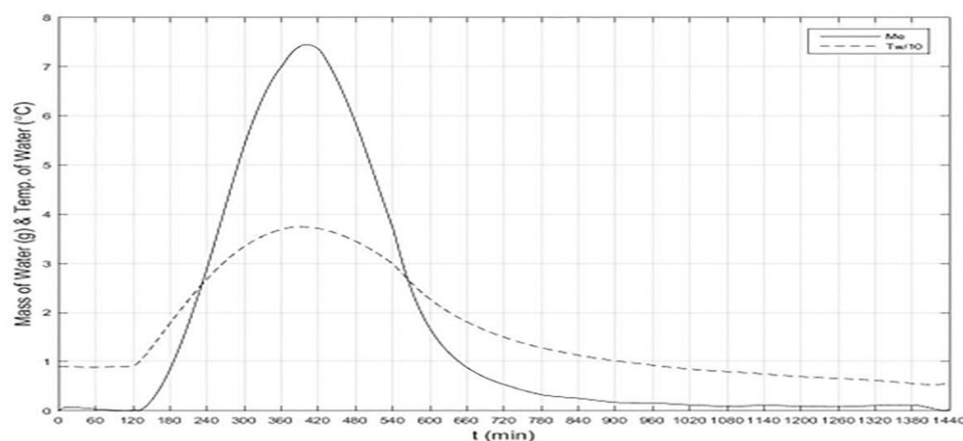


Fig. 10. Graphs of water temperature and freshwater production in terms of time in real weather conditions.

By starting radiation and increasing the water temperature, the production amount also increases and reaches its highest value around noon.

3.5. Results obtained from the practical experiment of the device

The practical experiment was done on 4th January. At the beginning of the day, the weather was cloudy for 2 hours. Furthermore, because of the same reason, i.e. cloudy weather, no solar radiation reaches the device at the end of the day. In the following, the method, recorded data, and their measurement precision, as well as graphs, are presented and analyzed.

3.6. Recorded data

To record the data, the considered time step was 15 min. In this way, the data recording operation starts from the beginning of the sunrise and continues until sunset. The values of the water temperature, absorbent surface, and glasses, also, as the freshwater amount produced by each glass were measured every 15 min. The temperatures of water and absorbent surface and glasses were measured by a regular laser thermometer (accuracy: 0.1 and 0.01°C) in that order.

To exactly measure the amount of water produced, has to be done quickly. For this reason, two glass beakers were provided. When it came time to record the data, the water collected from the gutters of every single glass was drained into a separate beaker, and the water in each beaker was carefully measured after recording the temperatures. In this regard, it should be mentioned that the lowest value to evaluate the volume of water produced is 5 ml (equivalent to 5 gr) which is equal to the smallest volume of the beaker used. Therefore, the measurement precision in the production amount of freshwater is equal to 5 gr. Besides, in the cases in which the volume of the produced water is lower than the measurable amount, that volume is added to the water produced in the next stage. In the following, the recorded temperature data and the amount of production are presented in Tables 4 and 5, respectively. It is worth noting that the presented values are related to the time in which the air was clear and solar radiation reached the device.

Table 4. Temperatures of water, absorbent surface, and glass surfaces from the practical experiment.

T _{g2}	T _{g1}	T _b	T _w	min.
8.87	8.91	9.61	8.70	120
9.55	9.85	15.87	10.10	135
10.61	10.92	19.51	12.30	150
11.90	12.20	22.67	14.70	165
13.26	13.55	25.65	17.10	180
14.67	14.96	28.49	19.40	195
16.11	16.41	31.18	21.70	210
17.56	17.85	33.71	23.80	225
18.99	19.28	36.04	25.80	240
20.33	20.61	38.16	27.70	255
21.56	21.84	40.05	29.30	270
22.69	22.96	41.68	30.80	285
23.70	23.96	43.05	32.10	300
24.61	24.86	44.15	33.20	315
25.40	25.64	44.99	34.20	330
26.05	26.28	45.56	34.90	345
26.56	26.79	45.86	35.50	360
26.81	27.03	45.87	35.90	375
26.86	27.07	45.56	36.00	390
26.74	26.95	44.97	35.90	405
26.47	26.66	44.11	35.70	420
26.16	26.35	43.02	35.20	435
25.87	25.95	41.73	34.70	450
25.29	25.46	40.27	34.00	465
24.72	24.87	38.64	33.20	480
24.09	24.22	36.84	32.20	495
23.38	23.50	34.89	31.20	510
22.60	22.71	32.84	30.00	525
21.72	21.76	29.99	28.70	540
20.49	20.49	26.33	26.90	555
19.15	19.15	24.14	25.00	570
17.95	17.95	22.44	23.30	585

Table 5. Amount of freshwater produced on each of the glass surfaces and their sum

M _e	M _{e2}	M _{e1}	min.
0	0	0	120
0	0	0	135
5	0	0	150
10	5	5	165
15	5	5	180
20	10	10	195
25	15	10	210
30	15	15	225
40	20	20	240
50	25	25	255
55	30	25	270
60	30	30	285
70	35	35	300
75	40	35	315
80	40	40	330
80	40	40	345
90	45	45	360
90	45	45	375
90	45	45	390
90	45	45	405
90	45	45	420
85	45	40	435
80	40	40	450
75	40	35	465
70	35	35	480
60	30	30	495
60	30	30	510
50	25	25	525
40	20	20	540
30	15	15	555
30	15	15	570
20	10	10	585

3.7. Temperature variations of water, absorbent surface, and glasses

The graph of temperature variations of the device components in terms of time is drawn based on the data presented in Table 4. It should be mentioned that this graph was drawn in a period in which there was direct solar radiation. The result is illustrated in Figure. 11.

In this graph, the temperature variations start when the sky is clear and there is direct solar radiation; moreover, by comparing the temperature of the device components with each other, it is observable that the temperature difference of various components is similar to the results acquired from the computer program (Fig. 11).

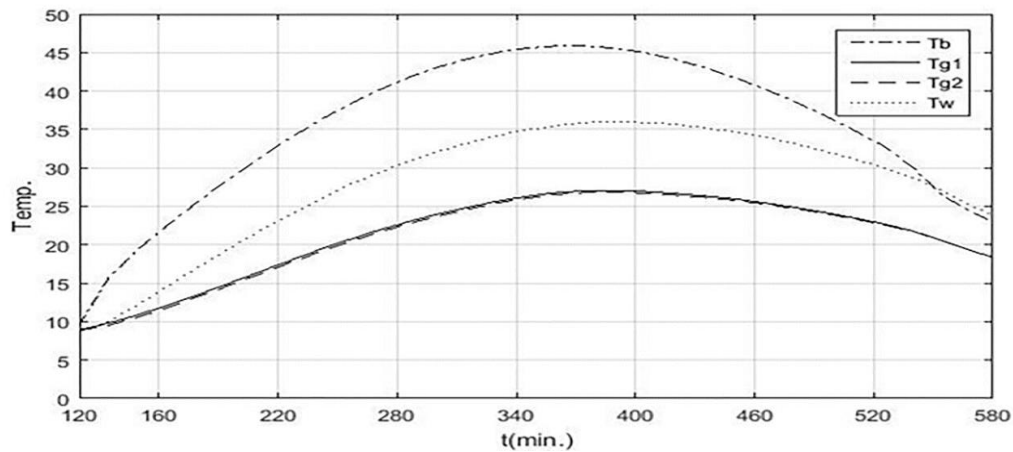


Fig. 11. Temperature graph of water, absorbent surface, and glasses in terms of time in the practical experiment.

The temperature of the absorbent surface is more than that of the other components in view of the fact that its high absorption coefficient.

The temperature of the water is in the next rank; on the other hand, the temperatures of the glass surfaces are close to each other. This can be attributable to their absorption coefficient.

Furthermore, it is observed that the maximum temperatures of the absorbent surface and water and glasses occur at noon and a little thereafter, respectively; because heat transfer from the absorbent surface to the other components of the device exists.

3.8. Amount of freshwater produced

The freshwater production graph in terms of time is drawn for each glass surface and their sum in Fig. 12 based on the data presented in Table 5. This graph was drawn in a period in which there was direct solar radiation. This graph was a broken line due to the measurement accuracy of the values, which was unavoidable as a result of the measurement tools available to the researcher. The maximum value of the production occurs a little afternoon whose reason is a

delay in the heat transfer from the absorbent surface to the water, increasing the water temperature and then evaporating it. As can be seen, at the same time, the production of glass surface 2 is equal to or a little more than that of glass surface 1. This is due to the little difference in the temperature of the two glass surfaces. The orientation of glass surface 1 (toward the south) compared to that of glass surface 2 (toward the north) leads to receiving more solar radiation. For this reason, the temperature of glass surface 2 is less than the other glass, so, more condensation on glass surface 2 is expected. Additionally, the small difference between the productions of each glass surface is owing to the small difference between their temperatures. Another important point is that the production of glass surface 2 is always more than glass surface 1 because the temperature of glass surface 2 is lower than that of glass surface 1 at all times. It should be mentioned that these two values are equal in several cases because the measurement accuracy is not capable of showing a low difference between them. This difference is exposed only in cases where the difference between the production amounts of the two glass surfaces is greater than the measurement accuracy.

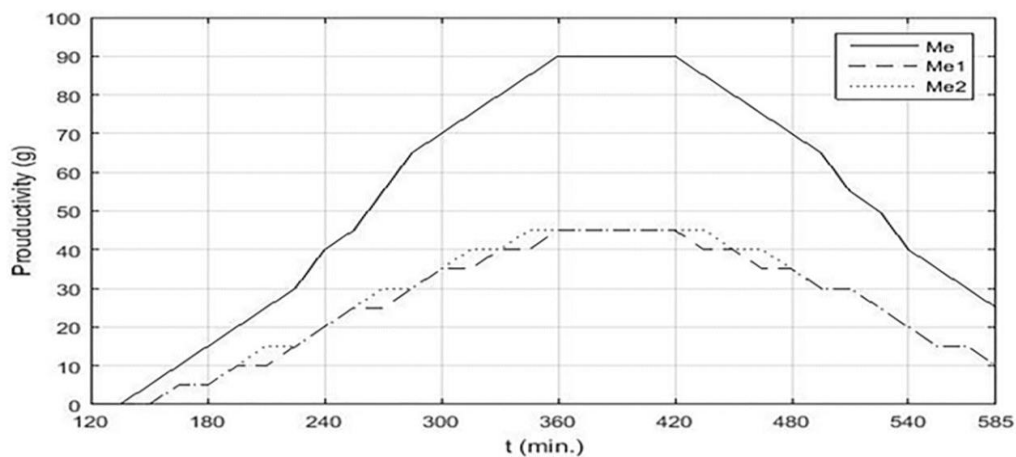


Fig. 12. Graph of production amount of each glass and their sum in terms of time in the practical experiment.

Finally, the total production amount was measured at 1.68 L; this measure was performed on a cloudy winter day (4th January). Most of the difference between this value and the value obtained from the computer program is due to the computer program calculating the production amount in the whole day and night, but the amount reported in this research was merely measured during sunny hours. Furthermore, the presence of vapor leakage from the holes in the body of the device, especially at the joints of the body components of the device is another factor creating this difference.

Conclusion

A solar desalination system is designed and manufactured on the scale of domestic use. All of the device materials are made from building construction materials and there are not expensive. The ceramics of building construction was found as appropriate materials to utilize as an absorbent surface. Temperature variations of the ceramic absorbent surface are highly dependent on the solar radiation amount. The temperature of glass surfaces has a little dependency on their orientation at the beginning of winter. A maximum water temperature occurs a little after the middle of the day. Freshwater production of each glass surface has a little dependency on its orientation at the beginning of winter. The total production amount at the beginning of winter was 1.68 L with a machine area of 1.62 m² on a partly cloudy day in winter; the TDS of the production freshwater was 30; moreover, the result is obtained on a fully cloudy and cold day; this is the worst condition for the device.

Nomenclature

A	Area (m ²)
AB	Effective absorption coefficient
C_p	Heat capacity (J/m ² K)
G_{on}	The amount of sunlight outside the atmosphere (W/m ²)
G_{sc}	Solar constant (W/m ²)
G_{cb}	The intensity of direct radiation on a horizontal surface (W/m ²)
G_{cd}	Scattered radiation intensity (W/m ²)
G_r	Radiation intensity on a sloping surface (W/m ²)
h	Heat transfer coefficient
K	Conduction heat transfer coefficient
m_e	Freshwater production rate (kg)
N	Number of hours of the day
Q	the heat (J)

R_b	The ratio of radiation intensity on a sloping surface to the horizon
P	Partial pressure (Pa)
T	Temperature (°C)
X	Thickness (m)
v	Speed (m/s)
Greek	
δ	The angular position of the sun (degrees)
ϕ	Latitude (degrees)
θ	The angle of impact (degrees)
θ_z	Apex angle (degrees)
β	The angle of the surface with the horizon (degrees)
γ	The angle between the normal surface image on the horizon and the south side (degrees)
ω	Hourly angle (degrees)
τ_b	Direct radiation transmission coefficient
τ_d	Scattered radiation transmission coefficient
ρ	Reflection coefficient
α	Absorption coefficient
σ	Stephen-Boltzmann coefficient (J/m ² sk ⁴)
ε	Issuance coefficient

Acknowledgements

The authors thank the reviewers and editor for the constructive comments. The authors would like to thank the Vice-chancellor for research, Shahid Chamran University of Ahvaz (Grant number: SCU.EM1400.376). The author tank specially to Soraya Banoo water emrchiment compony.

Conflicts of Interest

The author declares that there is no conflict of interest regarding the publication of this manuscript.

References

- [1] Duffie, J.A. and Beckman, W.A., 2013. Solar engineering of thermal processes. John Wiley & Sons.
- [2] Noghrehabadi, A., Hajidavaloo, E., Moravej, M. and Esmailinasab, A., 2018. An experimental study of the thermal performance of the square and rhombic solar collectors. Thermal Science, 22 (1 Part B), pp.487-494.
- [3] Zhang, Y., Ravi, S.K. and Tan, S.C., 2019. Food-derived carbonaceous materials for solar desalination and thermo-electric power generation. Nano Energy, 65, p.104006.

- [4] Rashidi, S., Karimi, N., Mahian, O. and Abolfazli Esfahani, J., 2019. A concise review on the role of nanoparticles upon the productivity of solar desalination systems. *Journal of Thermal Analysis and Calorimetry*, 135, pp.1145-1159.
- [5] Rafiei, A., Alsagri, A. S., Mahadzir, S., Loni, R., Najafi, G., & Kasaeian, A. 2019, Thermal analysis of a hybrid solar desalination system using various shapes of cavity receiver: Cubical, cylindrical, and hemispherical. *Energy Conversion and Management* 198 p. 111861.
- [6] Hassan, H., & Yousef, M. S., 2021. An assessment of energy, exergy and CO₂ emissions of a solar desalination system under hot climate conditions. *Process Safety and Environmental Protection*, 145, pp. 157-171.
- [7] Abd Elbar, Ayman Refat, and Hamdy Hassan, 2020. An experimental work on the performance of new integration of photovoltaic panel with solar still in semi-arid climate conditions. *Renewable Energy* 146, pp. 1429-1443.
- [8] Manokar, A. Muthu, M. Vimala, Ravishankar Sathyamurthy, A. E. Kabeel, D. Prince Winston, and Ali J. Chamkha, 2020. Enhancement of potable water production from an inclined photovoltaic panel absorber solar still by integrating with flat-plate collector *Environment, Development and Sustainability* 22, pp. 4145-4167.
- [9] Salarabadi, Amir, and Masoud Rahimi, 2020. Experimental investigation of using an evaporation inhibitor layer in a solar still. *Solar Energy* 206, pp. 962-973.
- [10] Nazari, Saeed, Habibollah Safarzadeh, and Mehdi Bahiraei, 2019. Performance improvement of a single slope solar still by employing thermoelectric cooling channel and copper oxide nanofluid: an experimental study. *Journal of Cleaner Production* 208. pp. 1041-1052.
- [11] Sharshir, S.W., Ellakany, Y.M., Algazzar, A.M., Elsheikh, A.H., Elkadeem, M.R., Edreis, E.M., Waly, A.S., Sathyamurthy, R., Panchal, H. and Elashry, M.S., 2019. A mini review of techniques used to improve the tubular solar still performance for solar water desalination. *Process Safety and Environmental Protection*, 124, pp.204-212.
- [12] Manokar, A.M., Vimala, M., Winston, D.P., Ramesh, R., Sathyamurthy, R., Nagarajan, P.K. and Bharathwaaj, R., 2019. Different parameters affecting the condensation rate on an active solar still—a review. *Environmental Progress & Sustainable Energy*, 38(1), pp.286-296.
- [13] Khalifa, A.J.N. and Ibrahim, H.A., 2009. Effect of inclination of the external reflector on the performance of a basin type solar still at various seasons. *Energy for Sustainable Development*, 13(4), pp.244-249.
- [14] Khalifa, Abdul Jabbar N., and Ahmad M. Hamood, 2009. Effect of insulation thickness on the productivity of basin type solar stills: an experimental verification under local climate." *Energy Conversion and Management* 50(9), pp. 2457-2461
- [15] Murugavel, K. Kalidasa, and K. Srithar, 2011. Performance study on basin type double slope solar still with different wick materials and minimum mass of water. *Renewable Energy* 36(2), pp. 612-620.
- [16] Kalbasi, Rasool, and M. Nasr Esfahani, 2010. Multi-effect passive desalination system, an experimental approach." *World Applied Sciences Journal* 10(10), pp. 1264-1271.
- [17] Sakthivel, M., S. Shanmugasundaram, and T. Alwarsamy, 2010. An experimental study on a regenerative solar still with energy storage medium—Jute cloth. *Desalination* 264, no. 1(2), pp. 24-31.
- [18] Bechki, D., H. Bouguettaia, J. Blanco-Galvez, S. Babay, B. Bouchekima, S. Boughali, and H. Mahcene, 2010. Effect of partial intermittent shading on the performance of a simple basin solar still in south Algeria. *Desalination* 260(1-3), pp. 65-69.
- [19] Al-Garni, A.Z., 2012. Productivity enhancement of solar still using water heater and cooling fan. *Journal of solar energy engineering*, 134(3).
- [20] Rajaseenivasan, T. and Murugavel, K.K., 2013. Theoretical and experimental investigation on double basin double slope solar still. *Desalination*, 319, pp.25-32.
- [21] Moravej, M., Bozorg, M.V., Guan, Y., Li, L.K., Doranehgard, M.H., Hong, K. and Xiong, Q., 2020. Enhancing the efficiency of a symmetric flat-plate solar collector via the use of rutile TiO₂-water nanofluids. *Sustainable Energy Technologies and Assessments*, 40, p.100783.



Semnan University



Research Article

Spectral Quasi-Linearization Approach for Unsteady MHD Boundary Layer Flow of Casson Fluid Due to an Impulsively Stretching Surface

Adeyemi Isaiah Fagbade *

^aDepartment of Mathematical Sciences, Federal University of Technology, P.M.B 704, Akure Ondo State, Nigeria.

PAPER INFO

Paper history:

Received: 2015-05-03

Revised: 2015-09-20

Accepted: 2016-06-20

Keywords:

Casson fluid;
 Magnetohydrodynamic flow;
 Magnetic field;
 Boundary layer;
 Spectra quasi-linearization method;
 Impulsively stretching sheet;
 Separated by semicolons.

ABSTRACT

The present paper seeks to examine a numerical method of solution called spectra quasi-linearization method (SQLM) to the problem of unsteady MHD boundary layer flow of Casson fluid due to an impulsively stretching surface under the influence of a transverse magnetic field, which is an important physical phenomena in engineering applications. The study extends the previous models to account for a classical non-newtonian fluid called Casson fluid under the influence of a transverse magnetic field. The flow model is described in terms of a highly nonlinear partial differential equations. The method of solution Spectral quasi-linearization methods (SQLM) seeks to linearised the original system of PDEs using the Newton-Raphson based quasilinearization method (QLM). The numerical results for the surface shear stress are compared with those of the analytical approach results, and they are found to be in good agreement. The flow controlling parameters are found to have a profound effect on the resulting flow profiles. It is observed that there is a smooth transition from the small time solution to the large time solution. The magnetic field significantly affects the flow field and skin friction coefficient. Indeed, skin friction coefficient is found to decrease rapidly, initially, in small time interval before attaining a steady state for large time.

DOI: [10.22075/jhmtr.2016.422](https://doi.org/10.22075/jhmtr.2016.422)

© 2022 Published by Semnan University Press. All rights reserved.

1. Introduction

The problem of unsteady convective mass and heat transfer has long been a major subject in the heat transfer theory because of its great importance from both a theoretical and practical viewpoint. In fact there is no actual flow situation, natural or artificial, which does not involve some unsteadiness and examples of unsteady convective flows are very numerous (see [1]). These flows are frequently encountered in technological and environmental situations, such as, energy conservation processes, buildings and structures, the processing of materials, geophysical and biological flows, and the spread of pollutants and fires as well as many others. In the broad class of fluid

and heat transfer problems there are two main categories of truly unsteady problems, namely linear and nonlinear problems. However, most viscous flow problems fall into the second class, which are, of course, more difficult to analyze and model. On the other hand, since most of the fundamental concepts which can be described by linear theory are now fairly well understood, the greatest challenges today are in nonlinear situations. Hence, our attention in this paper is focused on unsteady nonlinear MHD convective boundary layer flow problem of Casson fluid over an impulsively stretching surface. The flow and heat transfer problem in the boundary-layer induced by a continuously moving or stretching surface is important in many manufacturing processes. In industry for

*Corresponding Author: Adeyemi Isaiah Fagbade.

Email: yemi2favours@yahoo.co.uk

instance, polymer sheets and filaments are manufactured by continuous extrusion of the polymer from a die to a wind up roller which is located at finite distant way Chiam [2]. During many mechanical forming processes, such as extrusion, melt-spinning, etc., the extruded material issues through a slot or die. The ambient fluid condition is stagnant but a fluid flow is induced close to the material being extruded, due to the moving surface. In regions away from the slot or die the fluid flow may be considered to be of a boundary-layer type, although this is not true in the vicinity of the slot or die. Similar situations prevail during the manufacture of plastic and rubber sheets where it is often necessary to blow a gaseous medium through the material which is not, as yet, solid, and where the stretching force may be varying with time (see [3]).

Another typical example of industrial application that belongs to the class of boundary-layer flow problems due to moving surfaces is the cooling of a large metallic plate in a bath, which may be an electrolyte. In this case the fluid flow is induced due to the shrinking of the plate [4]. Glass blowing, continuous casting and the spinning of fibres also involve the flow due to a stretching surface. The first study on the boundary-layer adjacent to a continuous moving surface was conducted by Sakiadis [5] and since then it has been much generalized and refined. The fluid flow problem due to a continuously moving surface in an ambient fluid differs from that of the fluid flow past a fixed surface. Unlike the flow past a fixed surface, the continuous moving surface sucks the ambient fluid and pumps it again in the downstream direction. However, in all the earlier studies on boundary-layer flows due to a moving surface, the effects of the transverse magnetic field was neglected. Liao [6] investigated an analytical solution of unsteady boundary-layer flows caused by an impulsively stretching plate. Roslindar et al. [7] studies unsteady boundary layer flow due to an impulsively stretching surface. In their paper, the stretching velocity is assumed to vary linearly with the distance along the sheet and solved numerically using keller-box method. They observed a smooth transition from the small time solution to the large- time solution. Takhar et al. [8] also studied unsteady three-dimensional MHD-boundary layer flow due to the impulsive motion of a stretching surface. Hayat et al. [9] investigated the influence of soret and dufour effect on magnetohydrodynamics MHD flow of casson fluid. In the above mentioned literatures, the fluid viscosity and thermal conductivity were assumed to be constant value within the boundary layer. Prasad and Vajravelu [10] investigated the effect of variable thermal conductivity in a non-isothermal sheet stretching through power law fluids. Abel et al. [11] examined the combined effects of thermal buoyancy and variable thermal conductivity on a magnetohydrodynamic flow and the associated heat transfer in a power-law fluid

past a vertical stretching sheet in the presence of a nonuniform heat source and observed that variable thermal conductivity parameter increases the wall shear stress in the boundary layer region. Bhattacharyya and Pop [12] reported the influence of external magnetic field on the Casson flow over an exponentially shrinking sheet. Recently, Bhattacharyya studied boundary layer stagnation point of Casson fluid and heat transfer towards a shrinking/stretching sheet. It is established that the thermo-physical properties of fluid play a significant role in the engineering applications as seen in aerodynamics, geothermal systems, crude oil extraction, ground water pollution, thermal insulation, heat exchanger, storage of nuclear waste etc.

It is well known that most fluids which are encountered in chemical and allied processing applications do not adhere to the classical Newtonian viscosity postulate and are accordingly known as non-Newtonian fluids Astarita and Marrucci [14]. One particular class of materials which are of considerable practical importance is that in which the viscosity depends on the shear stress or on the flow rate. Most slurries, suspensions and dispersions, polymer solutions, melts and solutions of naturally occurring high-molecular-weight, synthetic polymers, pharmaceutical formulations, cosmetics and toiletries, paints, biological fluids, synthetic lubricants and foodstuffs, exhibit complex rheological behaviour which is not experienced when handling ordinary low-molecular-weight Newtonian fluids such as air, water, silicon oils, etc. Due to the importance of the applications of non-Newtonian fluids for the design of equipment and in industrial processing, considerable efforts have been directed towards the analysis and understanding of such fluids. Further, a fairly large body of fundamental research on non-Newtonian fluid flow can also be found in a number of excellent review articles [15],[16]. A classical example of non-newtonian fluid is Casson fluid. Casson fluid is one of the types of such non-Newtonian fluids, which behaves like an elastic solid such that a yield shear stress exists in the constitutive equation. Some materials e.g. muds, condensed milk, emulsions, paints, printing ink, sugar solutions, exhibit almost all the properties of non-Newtonian fluid. This rheological model was introduced originally by Casson [17] in his research on a flow equation for pigment oil-suspensions of printing ink. Casson model constitutes a plastic fluid model which exhibits shear thinning characteristics, yield stress, and high shear viscosity. According to a research reported by Rao et al. [18], it is stated that Casson fluid model is reduced to a Newtonian fluid at a very high wall shear stress, i.e., when the wall stress is much greater than yield stress. This fluid model also approximates reasonably well the rheological behavior of other liquids including physiological suspensions, foams, cosmetics, syrups, etc. Although different

models are proposed to explain the behavior of non-Newtonian fluids, the most important non-Newtonian fluid possessing a yield value is the Casson fluid. Bird et al. [19] investigated the rheology and flow of viscoplastic materials and reported that the Casson model constitutes a plastic fluid model which exhibits shear thinning characteristics, yield stress, and high shear viscosity. The fundamental analysis of the flow field of non-Newtonian fluids in a boundary layer adjacent to a stretching sheet or an extended surface is very important and is an essential part in the study of fluid dynamics and heat transfer in Mukhopadhyay [20]. The unsteady boundary layer flow and heat transfer of a Casson fluid over a moving flat plate with a parallel free stream were studied by Mustafa et al. [21] and they solved the problem analytically using the Homotopy analysis method (HAM).

The effects of transverse magnetic field on a boundary layer control and on the performance of many systems using electrically conducting fluid such as MHD power generators, cooling of nuclear reactors, plasma studies, etc. has been widely investigated and reported in literatures. Magneto-hydrodynamics (MHD) as a branch of fluid mechanics deals with the study of electrically conducting fluids and electromagnetic forces Srinivasa and Eswara [22]. The idea of MHD is that magnetic fields induce currents in a moving conductive fluid, which create forces on the fluids, and also change the magnetic field itself. MHD problems arise in a wide variety of situations ranging from the explanation of the origin of Earth's magnetic field and the prediction of space weather to the damping of turbulent fluctuations in semiconductor melts during crystal growth and, even in the measurement of the flow rates of beverages in food industry. An interesting application of MHD to metallurgy lies in the purification of molten metals from non-metallic inclusions by the application of a transverse magnetic field. In recent years, MHD flow problems have become more important industrially. Indeed, MHD laminar boundary layer behavior over a stretching surface is a significant type of flow having considerable practical applications in chemical engineering, electrochemistry and polymer processing. The laminar boundary layer on a moving continuous flat surface in the presence of suction and magnetic field was studied by Shrivastava [23]. They observed the effect of magnetic field on boundary layer thickness and skin friction at the surface. Boundary layer flow along a flat plate is considered when a magnetic field acts perpendicular to the plate. Recently, Noghrehabadi et al. [24] considered the effect of magnetic field on the boundary layer flow, heat and mass transfer of nanofluids over a stretching cylinder. Ishak et al. [25] studied the effect of a uniform transverse magnetic field on the stagnation point flow over a stretching and vertical sheet. While, Isa et al. [26] studied the effect of magnetic field on mixed

convection boundary layer flow over an exponentially shrinking vertical sheet with suction.

The aim of the present paper is to investigate the unsteady MHD boundary layer flow of a Casson fluid development caused by an impulsively stretching surface using numerical approach called spectral quasi-linearization method. Finding an optimal numerical solution to the problem of unsteady boundary layer flow due to stretching sheeting that valid for all time, has been a subject of investigations over time by many researchers. In recent years, there has been an increasing amount of literatures that have adopted Liao's analytic approach in solving unsteady boundary layer flows. However, there are limits to how far analytic approaches can be utilised in nonlinear systems of PDEs involving many equations. Nonlinear systems involving many coupled equations are very difficult to solve analytically. In this work, the spectral quasi-linearization method (SQLM) is apply to solve nonlinear PDEs describing unsteady boundary layer flow of Casson fluid due to an impulsively stretching surface. In the SQLM, the governing nonlinear equations are linearized using the Newton-Raphson based quasi-linearization method (QLM), developed by Bellman and Kalaba [27], and are then integrated using Chebyshev spectral collocation method. Spectral method based quasi-linearisation schemes have also been successfully applied to a range of fluid mechanics based ODE model problems (see [28]-[30]).

In this review, investigation is focus on the unsteady boundary layer flow due to an impulsively stretching surface that was previously discussed by Liao [6] using the homotopy analysis method and recently reported in Ishak [3] and Srinivasa [22] using the Keller-box method. Our purpose is to investigate effects of transverse magnetic field, Casson fluid parameter and the applicability of the new SQLM approach to systems of nonlinear PDE-based unsteady boundary layer flows of varying levels of complexity. Numerical simulations are conducted on the sample problems using SQLM. The method is compared in terms of accuracy, with the reported results in literatures.

The rest of the paper is organized as follows: Section 2 discusses the mathematical formulation of an unsteady MHD boundary-layer flow of Casson fluid caused by an impulsively stretching plate. Section 3 presents the implementation of SQLM on an unsteady MHD boundary layer flow of Casson fluid. Section 4 contains the results and discussion, and the conclusions are given in Section 5.

2. Governing Equations

Following Nadeem et al. [4], Liao [6] and Srinivasa and Eswara [17], an unsteady two-dimensional flow of an incompressible Casson fluid over a stretching surface is examined. The fluid is an electrically conducting fluid in the presence of a fixed applied

magnetic field B_o . A magnetic field B_o of uniform strength is applied transversely to the direction of the flow. Since the fluid pressure is constant throughout the boundary, it is assumed that induced magnetic field is small in comparison to the applied magnetic field; hence it is neglected. It is also assume that the

Rheological equation of Casson fluid, following Mustafa et al. [21], is given as :

$$\tau_{ij} = \left[\mu_c + \left(\frac{P_y}{\sqrt{2\pi}} \right)^{1/n} \right]^n 2e_{ij} \tag{1}$$

where μ_c is plastic dynamic viscosity of the non-Newtonian fluid, P_y is the yield stress of fluid, π is the product of the component of deformation rate with itself, namely, $\pi = e_{ij}e_{ij}$, e_{ij} is the (i, j) th component of the deformation rate. Where $n > 1$ is an arbitrary constant. However, in many application this value is $n \gg 1$. With this in mind and aforementioned assumptions, The boundary-layer equations based on conservation of mass and momentum, governing the unsteady two-dimensional flow on the impulsively stretching surface is:

$$\frac{\partial u}{\partial x} + \frac{\partial v}{\partial y} = 0, \tag{2}$$

$$\frac{\partial u}{\partial t} + u \frac{\partial u}{\partial x} + v \frac{\partial u}{\partial y} = \vartheta \left(1 + \frac{1}{\beta} \right) \frac{\partial^2 u}{\partial y^2} - \sigma \frac{\beta_0^2}{\rho} u. \tag{3}$$

here x and y are the longitudinal and the normal directions respectively. u and v are the velocity components in the x and y -directions respectively, B_o is the magnetic field applied in the y - direction, ρ is the fluid density, ϑ is the kinematic viscosity, σ is the electrical conductivity and β is the Casson fluid parameter. The corresponding boundary conditions are:

$$\begin{aligned} t < 0: & \quad u(x, y, t) = v(x, y, t) = 0, \quad y = 0 \\ t \geq 0: & \quad u(x, 0, t) = ax, \\ & \quad v(x, 0, t) = 0, \quad u(x, \infty, t) = 0 \end{aligned} \tag{4}$$

where constant a is positive number. Now the time scale ξ is chosen such as given above so that the region of the time integration can be finite.

One such transformations is given by Williams and Rhyne [33]. The transformations are expressed as;

$$\xi = 1 - e^{-\tau}, \quad \tau = bt,$$

where b is a positive constant and t is the time variable.

The Williams and Rhyne [33] transformation are used to convert from the infinite (original) time scale $0 \leq \tau \leq 1$ to the finite scale $0 \leq \xi \leq 1$ so that the interval of integration is collapsed from an infinite domain to a finite domain.

The similarity variables given in [22] are utilized and are defined as;

$$u = \frac{\partial \psi}{\partial y}, \quad v = -\frac{\partial \psi}{\partial x}, \tag{5}$$

$$\psi = \sqrt{b\vartheta\xi}xf(\xi, \eta), \quad \eta = \sqrt{\frac{b}{\vartheta\xi}}y.$$

Equation (2) is satisfied identically and equation (3) becomes:

$$\begin{aligned} \left(1 + \frac{1}{\beta} \right) f'''' + \frac{\eta}{2}(1 - \xi)f'' + \xi[ff'' - f'^2] \\ - \xi M f' = \xi(1 - \xi) \frac{\partial f'}{\partial \xi}. \end{aligned} \tag{6}$$

Subject to the boundary condition:

$$f(0, \xi) = 0, \quad f'(0, \xi) = 1, \quad f'(\infty, \xi) = 0 \tag{7}$$

In the above equations, the prime denotes the derivative with respect to η , ($c = \frac{b}{a}$) which indicate that the stretching sheet parameter is a positive constant. The local Hartman number M (Magnetic parameter) and the non-newtonian Casson fluid parameter β are defined as;

$$M = \frac{\sigma B_o^2}{b\rho} \quad B = \frac{\mu_c \sqrt{2\pi}}{P_y}.$$

In the analysis of boundary layer flow problems, a quantity of physical interest is the skin friction which is given

$$C_f = \frac{\tau_\omega}{\mu_c^b}$$

where

$$\tau_\omega = \left(\mu_c + \frac{P_y}{\sqrt{2\pi}} \right)$$

Now adopting the expressions in equation 5, the dimensionless form of the skin-friction coefficient is

$$C_f \sqrt{\xi} = \left(1 + \frac{1}{\beta} \right) \sqrt{Re_x} f''(0, \xi)$$

where Re_x is the local reynold number defined as $\frac{bx^2}{\vartheta}$.

The unsteady case can be divided into two cases:

1. Initial unsteady state flow ($t = 0$). When $\tau = 0$ corresponding to $\xi = 0$ and $\beta = \infty$, equation (6) becomes Rayleigh ordinary differential equation viz.,

$$f'''' + \frac{\eta}{2} f'' = 0 \tag{8}$$

Subject to the boundary condition:

$$f(0, 0) = 0, \quad f'(0, 0) = 1, \quad f'(\infty, 0) = 0 \tag{9}$$

Equations (8) together with the boundary conditions (9) admit the closed form analytical solution for the initial unsteady state when $\xi = 0$ given by Srinivasa [22] as:

$$\begin{aligned} f(\eta, 0) = \eta \operatorname{erfc} \left(\frac{\eta}{2} \right) \\ + \left(\frac{2}{\sqrt{\pi}} \right) \left[1 - \exp \left(\frac{-\eta^2}{4} \right) \right] \end{aligned} \tag{10}$$

with

$$erfc(\eta) = \left(\frac{2}{\sqrt{\pi}}\right) \int_0^\eta e^{-t^2} dt \tag{11}$$

defined as the complementary error function

- Final steady state flow ($\xi = 1$) When ($\xi = 1$), corresponding to $\tau = \infty$ and $\beta = \infty$, equation(6) becomes Crane type ordinary differential equation viz.,

$$f''' + ff'' - f'^2 - Mf' = 0 \tag{12}$$

Subject to the boundary condition:

$$f(0,1) = 0, f'(0,1) = 1, f'(\infty, 1) = 0 \tag{13}$$

The exact solution of (12) is given by

$$f(\eta, 1) = \gamma^{-1}[1 - \exp(-\gamma\eta)]$$

where

$$\gamma = (1 + M)^{1/2}$$

3. Method of solution

The nonlinear partial differential equation (6) subject to boundary conditions (7) is solved numerically using spectral quasi-linearization method (SQLM). In applying spectral quasi-linearization method to the above governing equation, equation (6) is separate into linear and non-linear part and called them linear operator F and non-linear operator H respectively. This is expressed as :

$$F(f, f', f'', f''') = \left(1 + \frac{1}{\beta}\right) f''' + \frac{\eta}{2}(1 - \xi)f'' - \xi Mf' - \xi(1 - \xi) \frac{\partial f'}{\partial \xi}, \tag{14}$$

$$H(f, f', f'', f''') = \xi [ff'' - f'^2].$$

Then by linearized the non-linear operator H by using the equation

$$H \approx H(f_r, f'_r, f''_r, f'''_r) + \sum_{k=0}^3 \phi_{k,r} f_{r+1}^{(k)} - \sum_{k=0}^3 \phi_{k,r} f_r^{(k)}. \tag{15}$$

The coefficients $\phi_{k,r}$ in the above equation are given as

$$\phi_{0,r} = \frac{\partial H}{\partial f} [f_r, f'_r, f''_r, f'''_r] = \xi f''_r, \tag{16}$$

$$\phi_{1,r} = \frac{\partial H}{\partial f'} [f_r, f'_r, f''_r, f'''_r] = -2\xi f'_r,$$

$$\phi_{2,r} = \frac{\partial H}{\partial f''} [f_r, f'_r, f''_r, f'''_r] = \xi f_r, \tag{17}$$

$$\phi_{3,r} = \frac{\partial H}{\partial f'''} [f_r, f'_r, f''_r, f'''_r] = 0.$$

And

$$R_r = \sum_{k=0}^3 \phi_{k,r} f_r^{(k)} - \sum_{k=0}^3 \phi_{k,r} f_r^{(k)} - H(f_r, f'_r, f''_r, f'''_r) = \xi f_r f''_r - \xi (f'_r)^2 \tag{18}$$

Such that the linearized form of the governing equation (6) is

$$F[f_{r+1}, f'_{r+1}, f''_{r+1}, f'''_{r+1}] + \sum_{k=0}^n \phi_{k,r} f_{r+1}^{(k)} - f_{r+1} = R_r[f_r, f'_r, f''_r, f'''_r] \tag{19}$$

simplified further as

$$a_{0,r}(\eta, \xi) f'''_{r+1} + a_{1,r}(\eta, \xi) f''_{r+1} + a_{2,r}(\eta, \xi) f'_{r+1} + a_{3,r}(\eta, \xi) f_{r+1} - \xi(1 - \xi) \frac{\partial f'_{r+1}}{\partial \xi} = a_{4,r}(\eta, \xi). \tag{20}$$

Subject to

$$f_{r+1}(0, \xi) = f'_{r+1}(\infty, \xi) = 0, f'_{r+1}(0, \xi) = 1 \tag{21}$$

where

$$a_{0,r}(\eta, \xi) = \left(1 + \frac{1}{\beta}\right), \quad a_{1,r}(\eta, \xi) = \frac{\eta}{2}(1 - \xi) + \xi f_r, \\ a_{2,r}(\eta, \xi) = -2\xi f'_r - \xi M, \quad a_{3,r}(\eta, \xi) = \xi f''_r, \\ a_{4,r}(\eta, \xi) = \xi f_r f''_r - \xi (f'_r)^2.$$

The initial approximation for solving (20)-(21) is obtained as the solutions at $\xi = 0$. Hence $f_0(\eta, \xi)$ as

$$f_0(\eta, 0) = \eta erfc\left(\frac{\eta}{2}\right) + \left(\frac{2}{\sqrt{\pi}}\right) \left[1 - \exp\left(-\frac{\eta^2}{4}\right)\right] \tag{22}$$

The solution for the linearized PDE (20) is obtained by approximating the exact solution of $f(\eta, \xi)$ by the initial approximations given in (22) and a Lagrange form of polynomial $F(\eta, \xi)$ which interpolates $f(\eta, \xi)$ at the selected points (called collocation points):

$$0 = \xi_0 < \xi_1 < \xi_2 < \dots < \xi_{N_\xi} = 1$$

Therefore the approximation for $f(\eta, \xi)$ has the form

$$f(\eta, \xi) \approx \sum_{l=0}^{N_\xi} F(\eta, \xi_l) L_l(\xi) = \sum_{l=0}^{N_\xi} F_l(\eta) L_l(\xi), \tag{23}$$

Which interpolates $f(\eta, \xi)$ at the collocation points defined above. It is remark that, for ease of notation, the subscripts $r+1$ is dropped. The function $L_j(\xi)$ is the well-known characteristic Lagrange cardinal polynomials:

$$L_j(\xi) = \prod_{\substack{j=0 \\ j \neq k}}^M \frac{\xi - \xi_k}{\xi_j - \xi_k}, \quad L_j(\xi_k) = \delta_{jk} = \begin{cases} 0 & \text{if } j \neq k \\ 1 & \text{if } j = k \end{cases} \tag{24}$$

The equations for the solution of $F_j(\eta)$ are obtained by substituting (23) in (20) and compelling the equation to be satisfied exactly at the points $\xi_i, i=0,1,2,\dots,N_\xi$. This process is called collocation. To enable the derivatives of the Lagrange polynomial with respect to ξ to be computable analytically, it is convenient to transform the interval $\xi \in [0, 1]$ to $\zeta \in [-1, 1]$ then choose Chebyshev-Gauss-Lobatto points

$$\zeta_i = \cos\left(\frac{i\pi}{N_\xi}\right),$$

as the collocation points. After using linear transformation to transform ξ to the new variable ζ , the derivative of f with respect to ξ at the collocation points ζ_j is computed as

$$\frac{\partial f'}{\partial \xi} \Big|_{(\xi = \xi_i)} = 2 \sum_{j=0}^{N_\xi} F_j'(\eta) \frac{dL_j}{d\zeta}(\zeta_i) = 2 \sum_{j=0}^{N_\xi} F_j'(\eta) d_{i,j},$$

$$i = 0, 1, 2, 3, \dots, N_\xi \tag{25}$$

where $d_{i,j} = \frac{dL_j}{d\zeta}(\xi_i)$, $i = 0, 1, 2, 3, \dots, N_\xi$ are entries of the standard Chebyshev differentiation matrix. Applying the collocation at ξ_i in (20) gives

$$a_{0,r}^{(i)} f_{r+1}'''(\eta) + a_{1,r}^{(i)} f_{r+1}''(\eta) + a_{2,r}^{(i)} f_{r+1}'(\eta) + a_{3,r}^{(i)} f_{r+1}(\eta)$$

$$- 2\xi_i(1 - \xi_i) \sum_{j=0}^{N_\xi} F_j'(\eta) d_{i,j} = a_{4,r}^{(i)} \tag{26}$$

where $a_{k,r}^{(i)} = a_{k,r}(\eta, \xi)$, $k = 0, 1, 2, 3, 4$. Since the solution at $\xi=0$ and $\xi=N_\xi$ is known, Then equation (29) is only evaluate for $i=0, 1, 2, \dots, N_\xi - 1$. The resulting systems becomes

$$a_{0,r}^{(i)} f_{r+1}'''(\eta) + a_{1,r}^{(i)} f_{r+1}''(\eta) + a_{2,r}^{(i)} f_{r+1}'(\eta) + a_{3,r}^{(i)} f_{r+1}(\eta)$$

$$- 2\xi_i(1 - \xi_i) \sum_{j=0}^{N_\xi} F_j'(\eta) d_{i,j} \tag{27}$$

$$= a_{4,r}^{(i)} + 2\xi_i(1 - \xi_i) d_{i,N_\xi} F_{r+1,N_\xi}'(\eta).$$

It is worth note that for each ξ_i , equation (27) forms a linear ordinary equation with variable coefficients. To solve equation (27) Chebyshev spectral collocation is apply independently in the η direction by choosing $N_\eta+1$ Chebyshev- Gauss-Lobatto points $0=\eta_0 < \eta_1 < \eta_2 < \dots < \eta_{N_\eta} = \eta_e$, where η_e is a finite value that is chosen to be sufficiently large to approximate the conditions at ∞ . Again, before implementing the collocation, the interval $\eta \in [0, \eta_e]$ is transformed into $\iota \in [-1, 1]$ using a linear transformation. Thus, the collocation points are chosen as

$$\iota_j = \cos\left(\frac{j\pi}{N_\eta}\right),$$

The derivatives with respect to η are defined in terms of the Chebyshev differentiation matrix as

$$\frac{d^p F_{r+1,i}}{d\eta^p} \Big|_{(\eta = \eta_e)} = \left(\frac{2}{\eta_e}\right)^p \sum_{k=0}^{N_\eta} D_{j,k}^p F_{r+1,i}(\iota_k)$$

$$= D^p F_{r+1,i} \tag{28}$$

where p is the order of the derivative, $D = \left(\frac{2}{\eta_e}\right) [D_{j,k}] (j, k = 0, 1, 2, \dots, N_\eta)$ with $[D_{j,k}]$ being an $(N_\eta+1) \times (N_\eta+1)$.

Chebyshev derivative matrix, and the vector $F_{r+1,i}$ is defined as $F_{r+1,i} = [F_{r+1,i}(\iota_0), F_{r+1,i}(\iota_1), F_{r+1,i}(\iota_2), \dots, F_{r+1,i}(\iota_{N_\eta})]^T$
By substituting equation (28) into (27), yields:

$$A^{(i)} F_{r+1,i} - 2\xi_i(1 - \xi_i) \sum_{j=0}^{N_\xi-1} D F_{r+1,j} = R^{(i)} \tag{29}$$

where

$$A^{(i)} = a_{0,r}^{(i)} D^3 + a_{1,r}^{(i)} D^2 + a_{2,r}^{(i)} D + a_{3,r}^{(i)}$$

$$R^{(i)} = a_{3,r}^{(i)} + 2\xi_i(1 - \xi_i) \sum_{j=0}^{N_\xi-1} d_{i,N_\xi} D F_{r+1,N_\xi}$$

where $a_{k,r}^{(i)}$ ($k = 0, 1, 2, 3$) is a diagonal matrix with the vector $[a_{k,r}^{(i)}(\iota_0), a_{k,r}^{(i)}(\iota_1), \dots, a_{k,r}^{(i)}(\iota_{N_\eta})]^T$ placed on the main diagonal. After substituting the boundary conditions, for each $i=0, 1, \dots, N_\xi-1$, equation (29) can be written in matrix form as

$$\begin{bmatrix} A_{0,0} & A_{0,1} & \dots & A_{0,N_\xi-1} \\ A_{1,0} & A_{1,1} & \dots & A_{1,N_\xi-1} \\ \vdots & \vdots & \ddots & \vdots \\ A_{N_\xi-1,0} & A_{N_\xi-1,1} & \dots & A_{N_\xi-1,N_\xi-1} \end{bmatrix} \begin{bmatrix} F_{r+1,0} \\ F_{r+1,1} \\ \vdots \\ F_{r+1,N_\xi-1} \end{bmatrix} = \begin{bmatrix} R_1^0 \\ R_1^1 \\ \vdots \\ R_1^{N_\xi-1} \end{bmatrix} \tag{30}$$

where

$$A_{i,i} = A^{(i)} - 2\xi_i(1 - \xi_i) d_{i,i} D, \quad i = 0, 1, 2, \dots, N_\xi - 1$$

$$A_{i,i} = -2\xi_i(1 - \xi_i) d_{i,j} D, \quad \text{where } i \neq j$$

Hence, starting from the initial approximations $f_0(\eta, \xi)$; given by equations (10), equations (29) can be solved iteratively to give approximate solutions for $f_{r+1}(\eta, \xi)$ $r=0, 1, 2, \dots$ until a solution that converges to a given accuracy is obtained.

Table 1. Computed values of wall shear stress $f'(\xi, 0)$ using QSLM as compared with other results in literatures for different values of ξ , when $\beta = \infty$ and $M = 0.0$

ξ	Ref. [6]	Ref. [31]	Ref. [32]	Ref. [22]	Present result
0.1	-0.6106105684	-0.6150155043	-0.6106968740	-0.6106120	-0.6104674607
0.3	-0.7015602589	-0.7116696045	-0.7014912575	-0.7115610	-0.7012666313
0.5	-0.7904118776	-0.8018198801	-0.7900472367	-0.8004117	-0.7898281748
0.7	-0.8773153545	-0.8856581275	-0.8764799121	-0.8873160	-0.8762663192
0.8	-0.9200563754	-0.9252701770	-0.9198114759	-0.9200550	-0.9187007163
0.9	-0.9623399700	-0.9633761429	-0.9607448540	-0.9623398	-0.9605377533
1.0	-	-	-1.0000000000	-1.0000000	-0.9951954343

Table 2. Computed values of wall shear stress $f'(\xi, 0)$ for various values of Magnetic parameter M when $\beta = 100, \xi = 0.5$

M	$f'(\xi, 0)$
0.0	-0.7878602743
0.5	-0.9121941670
0.7	-0.9591901558
1.0	-1.0270440776

Table 3. Computed values of wall shear stress $f'(\xi, 0)$ for various values of Casson fluid parameter β when $M = 0.5, \xi = 0.5$

β	$f'(\xi, 0)$
1.0	-0.7465920225
10	-0.8924220729
100	-0.9121941670
∞	-0.9144728990

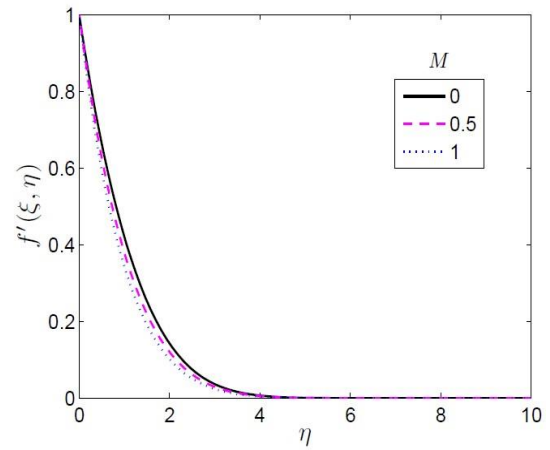


Figure 3. Effect of magnetic parameter (M) on velocity profile of the Casson fluid.

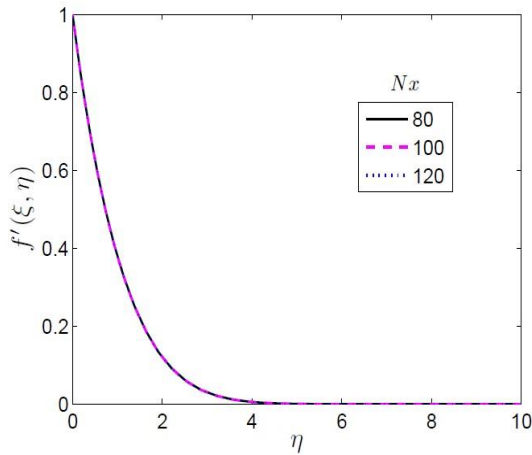


Figure 1. Velocity profile of the Casson fluid at different collocation point along η domain to check grid independent test.

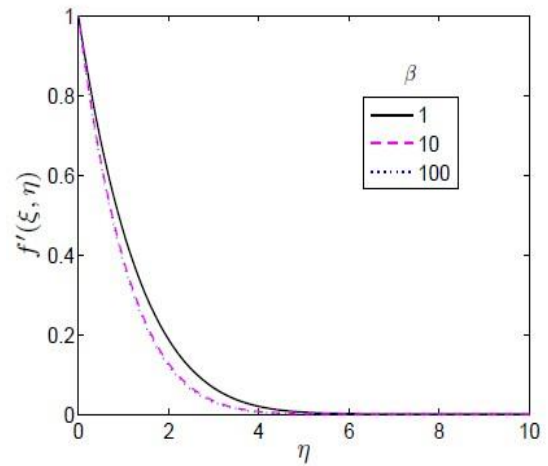


Figure 4. Effect of Casson fluid parameter (β) on velocity profile of the fluid.

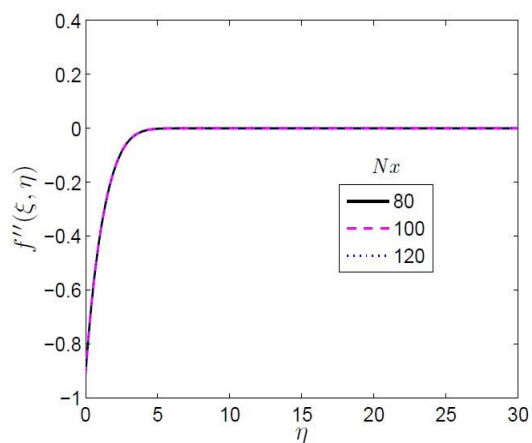


Figure 2. Skin-friction coefficient profile of the Casson fluid at different collocation point along η domain to check grid independent test.

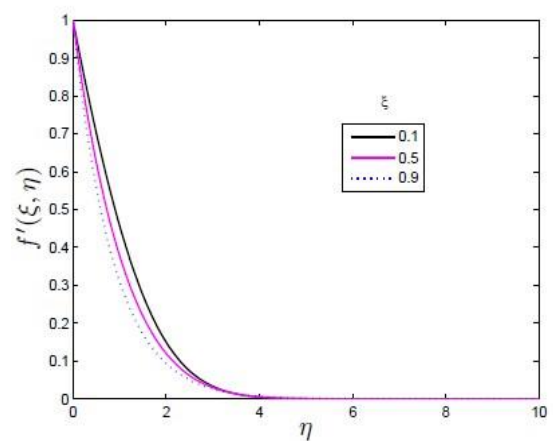


Figure 5. Velocity profile of the Casson fluid for various values of ξ

4. Results and Discussion

In this section, the numerical results obtained using spectral quasi-linearization method (SQRM) on the governing nonlinear partial differential equation (6) is presented. Numerical computation were carried out using the proposed method as discussed in the previous sections for the velocity and the local skin friction for different values of the significant physical parameters in this study. Results are displayed in tabular and graphical formats. The SQRM was used to generate results from the initial approximate at $\xi=0$ up to results close to the steady state values at $\xi=1$. The accuracy of the computed SQRM results was validated against numerical results obtained using the Keller-box method as reported in literatures. The results presented in this work were generated using $L=30$, which was found to give accurate results through numerical experimentation. In computing the numerical results presented in this paper, unless otherwise stated, the following values of physical parameters were used: $M=0.5$, $\beta=10$, $\xi=0.5$ and $Nt=50$. Grid independence tests as illustrated in Figures 1 and 2 revealed that $N_x = 120$ and $N_t = 50$ collocation points in the η and ξ domain, respectively, were sufficient to give accurate and consistent results. A further increase in the number of collocation points did not result in a change in the computed results. Furthermore, the minimum number of iterations required to give results that are consistent to within a tolerance level of 10^{-7} were used. In all the results presented below, it was found that 50 iterations were sufficient to give consistent results. The value of η_∞ was set to be 10. All graphs and tables therefore corresponds to these values except otherwise indicated. The values of all other physical parameters governing the fluid flow are chosen based on values earlier used in literatures.

In order to test the method of solution, the special case of the problem is solved and compared with Liao [6], Srinivasa [22], Awang [31] and Fadzilah [32] in Table 1. Table 1 is drawn for a special case when pertinent parameters $M=\xi=0$ and $\beta=\infty$. The available results obtained in literatures above and SQRM are compared and are in very good agreement. The comparison shows that the present results obtained using SQRM has an excellent agreement with the solution obtained using other method of solution such as implicit finite difference scheme called Keller-box method and homotopy analysis method (HAM).

Table 2 gives account on the effect of the Magnetic parameter M , on local wall shear stress of the flow. From the Table 2, It is noticed that an increase in the values of magnetic parameter M results in narrowing of horizontal velocity of the fluid. The transverse contraction of the velocity boundary layer is due to the applied magnetic field which invokes the Lorentz force producing noticeable opposition to the fluid flow. Hence, the magnetic parameter M influences the

control of surface shear stress. Further, it is found that absolute value of $f'(0, \xi)$ increases with the increase of magnetic field M . This is because when M increases, the Lorentz force produces more resistance to the transport phenomena which leads to the deceleration of the flow, enhancing the surface shear stress. These results are in good agreement with those obtained by Srinivasa and Eswara [22].

Similarly Table 3 gives the skin friction coefficient for selected Casson fluid parameter β values. Here It is observed that as the Casson fluid parameter increase, the absolute values of skin friction coefficient increases.

In Fig. 3, the effect of increasing the magnetic field strength on the momentum boundary layer thickness is illustrated. It is established fact that the magnetic field presents a damping effect on the velocity field by creating drag force that opposes the fluid motion, causing the velocity to decrease. That is the boundary layer thickens and the magnitude of the velocity decreases with an increase in Hartmann number, M . This clearly indicates that the transverse magnetic field opposes the transport phenomena. This is because the variation of M leads to the variation of Lorentz force due to the magnetic field, and the Lorentz force produces more resistance to the transport phenomena. Therefore, the momentum boundary layer thickness becomes larger, and the separation of the boundary layer occurs earlier.

Figure 4 shows the graphical influence of fluid Casson parameter β on the velocity profile of the flow. It shows that the magnitude of velocity and boundary layer thickness decreases with an increase in Casson fluid parameter, β . It is noticed that when the fluid parameter approaches infinity, the problem in the given case reduces to a Newtonian case.

Figure 5 exhibits velocity profiles for different values of ξ . It is obvious from this figure that increase in ξ results in the reduction of momentum boundary layer thickness and thereby enhancing the velocity gradient at the surface. Further, the velocity profiles decrease monotonically with the distance from the surface and finally become zero for away from it, satisfying the boundary conditions asymptotically, and thus supporting the numerical results obtained.

5. Conclusions

The study investigated the application of the spectral quasi-linearization technique coupled with the Chebyshev pseudo-spectral collocation method to obtain a numerical solution of unsteady MHD boundary layer flow of Casson fluid due to an impulsively stretching surface. Approximate numerical results were generated using spectral quasi-linearization for the solution of the skin friction coefficient as well as velocity profile of the fluid at different flow parameter values. The accuracy of the

SQLM was demonstrated by comparing with results generated using the implicit finite difference method (keller box) and homotopy analysis method (HAM) and a good agreement was achieved between the two set of results up to a fixed level of accuracy. Other parameters which appear to have a marginal influence on the velocity distribution also have strong influence on the surface shear stress.

The study showed that the SQLM can be used as an alternative method to obtain numerical solutions of partial differential equations (PDEs). The SQLM approach presented in this study also adds to a growing body of literature on numerical methods for solving complex nonlinear fluid flow problems in fluid mechanics. The results reveal that:

- An increase in the Casson fluid parameter β of Casson fluid corresponds to an increase in the velocity profiles.
- The magnetic field exerts significant influence on skin friction coefficient and reduces the momentum boundary layer thickness

Conflicts of Interest

The author declares that there is no conflict of interest regarding the publication of this manuscript. In addition, the authors have entirely observed the ethical issues, including plagiarism, informed consent, misconduct, data fabrication and/or falsification, double publication and/or submission, and redundancy.

References

- [1] Bird, R.B., Stewart, W.E. and Lightfoot, E.N, 2007. Transport Phenomena (Revised Second Edition ed.) John Wiley and Sons. ISBN 978-0-470-11539-8.
- [2] Chiam, T.C., 1993. Magnetohydrodynamic boundary layer flow due to a continuously moving flat plate. *Computers & Mathematics with Applications*, 26(4), pp.1-7.
- [3] Ishak, A., Nazar, R. and Pop, I., 2009. Heat transfer over an unsteady stretching permeable surface with prescribed wall temperature. *Nonlinear Analysis: Real World Applications*, 10(5), pp.2909-2913.
- [4] Nadeem, S., Haq, R.U. and Lee, C., 2012. MHD flow of a Casson fluid over an exponentially shrinking sheet. *Scientia Iranica*, 19(6), pp.1550-1553.
- [5] Sakiadis, B.C., 1961. Boundary-layer behavior on continuous solid surfaces: II. The boundary layer on a continuous flat surface. *AiChE Journal*, 7(2), pp.221-225.
- [6] Liao, S., 2006. An analytic solution of unsteady boundary-layer flows caused by an impulsively stretching plate. *Communications in Nonlinear Science and Numerical Simulation*, 11(3), pp.326-339.
- [7] Nazar, R., Ishak, A. and Pop, I., 2008. Unsteady boundary layer flow over a stretching sheet in a micropolar fluid. *International Journal of Mathematical, Physical and Engineering Sciences*, 2(3), pp.161-165.
- [8] Takhar, H.S., Chamkha, A.J. and Nath, G., 2001. Unsteady three-dimensional MHD-boundary-layer flow due to the impulsive motion of a stretching surface. *Acta Mechanica*, 146(1-2), pp.59-71.
- [9] Hayat, T., Shehzad, S.A. and Alsaedi, A., 2012. Soret and Dufour effects on magnetohydrodynamic (MHD) flow of Casson fluid. *Applied Mathematics and Mechanics*, 33, pp.1301-1312.
- [10] Prasad, K.V. and Vajravelu, K., 2009. Heat transfer in the MHD flow of a power law fluid over a non-isothermal stretching sheet. *International Journal of Heat and Mass Transfer*, 52(21-22), pp.4956-4965.
- [11] Abel, M.S., Siddheshwar, P.G. and Mahesha, N., 2009. Effects of thermal buoyancy and variable thermal conductivity on the MHD flow and heat transfer in a power-law fluid past a vertical stretching sheet in the presence of a non-uniform heat source. *International journal of non-linear mechanics*, 44(1), pp.1-12.
- [12] Bhattacharyya, K. and Pop, I., 2011. MHD boundary layer flow due to an exponentially shrinking sheet. *Magnetohydrodynamics*, 47(4), pp.337-344.
- [13] Bhattacharyya, K., 2013. Boundary layer stagnation-point flow of Casson fluid and heat transfer towards a shrinking/stretching sheet. *Frontiers in Heat and Mass Transfer (FHMT)*, 4(2).
- [14] Astarita, G. and Marrucci, G., 1974. Principles of non-Newtonian fluid mechanics.
- [15] Shenoy, A.V. and Mashelkar, R.A., 1982. Thermal convection in non-Newtonian fluids. In *Advances in heat transfer* (Vol. 15, pp. 143-225). Elsevier.
- [16] Crochet, M.J. and Walters, K., 1983. Numerical methods in non-Newtonian fluid mechanics. *Annual Review of Fluid Mechanics*, 15(1), pp.241-260.
- [17] Casson, N., 1959. Flow equation for pigment-oil suspensions of the printing ink-type. *Rheology of disperse systems*, pp.84-104.
- [18] Subba Rao, A., Ramachandra Prasad, V., Bhaskar Reddy, N. and Anwar Bég, O., 2015. Heat transfer in a Casson rheological fluid from a semi-infinite vertical plate with partial slip. *Heat Transfer—Asian Research*, 44(3), pp.272-291.
- [19] Bird, R.B., Dai, G.C. and Yarusso, B.J., 1983. The rheology and flow of viscoplastic materials. *Reviews in chemical engineering*, 1(1), pp.1-70.
- [20] Mukhopadhyay, S., 2013. Casson fluid flow and heat transfer over a nonlinearly stretching surface. *Chinese Physics B*, 22(7), p.074701.
- [21] Mustafa, M., Hayat, T., Pop, I. and Aziz, A., 2011. Unsteady boundary layer flow of a Casson fluid due to an impulsively started

- moving flat plate. *Heat Transfer—Asian Research*, 40(6), pp.563-576.
- [22] Srinivasa, A.H. and Eswara, A.T., 2014. Unsteady MHD Laminar Boundary Layer Flow and Heat Transfer due to an Impulsively Stretching Surface. *International Journal of Modern Sciences and Engineering Technology (IJMSET)*. V1, (7), pp.32-40.
- [23] Shrivastava, U.N. and Usha, S., 1987. Magneto-fluid dynamic boundary layer on a moving continuous flat surface. *Indian J. pure appl. Math*, 18, pp.741-751.
- [24] A. Noghrehabadi, M. Ghalambaz, E. Izadpanahi and R. Pourrajab. Effect of Magnetic Filed on the Boundary Layer Flow, Heat and Mass Transfer of Nanofluids over a Stretching Cylinder. *Journal of Heat and Mass Transfer Research*, 2014;1: 9-16.
- [25] Ishak, A., Nazar, R. and Pop, I., 2008. Hydromagnetic flow and heat transfer adjacent to a stretching vertical sheet. *Heat and Mass Transfer*, 44(8), pp.921-927.
- [26] Isa, S.S.P.M., Arifin, N.M., Nazar, R., Bachok, N., Ali, F.M. and Pop, I., 2014. Effect of magnetic field on mixed convection boundary layer flow over an exponentially shrinking vertical sheet with suction. *International Journal of Mechanical, Aerospace, Industrial and Mechatronics Engineering*, 8, p.1519.
- [27] Bellman, R.E., 1965. *Quasilinearization and nonlinear boundary-value problems* (Vol. 3). American Elsevier Publishing Company.
- [28] Motsa, S.S., Hayat, T. and Aldossary, O.M., 2012. MHD flow of upper-convected Maxwell fluid over porous stretching sheet using successive Taylor series linearization method. *Applied Mathematics and Mechanics*, 33, pp.975-990.
- [29] Motsa, S.S. and Shateyi, S., 2012. Successive linearization analysis of the effects of partial slip, thermal diffusion, and diffusion-thermo on steady MHD convective flow due to a rotating disk. *Mathematical Problems in Engineering*, 2012.
- [30] Awad, F.G., Sibanda, P., Motsa, S.S. and Makinde, O.D., 2011. Convection from an inverted cone in a porous medium with cross-diffusion effects. *Computers & Mathematics with Applications*, 61(5), pp.1431-1441.
- [31] Kechil, S.A. and Hashim, I., 2007. Series solution for unsteady boundary-layer flows due to impulsively stretching plate. *Chinese Physics Letters*, 24(1), p.139.
- [32] Md, A.F., Roslinda, N.A.Z.A.R. and Md, A.N., 2010. Numerical solutions of unsteady boundary layer flow due to an impulsively stretching surface. *Journal of Applied Computer Science & Mathematics*, 4(2), pp.25-30.
- [33] Williams, III, J.C. and Rhyne, T.B., 1980. Boundary layer development on a wedge impulsively set into motion. *SIAM Journal on Applied Mathematics*, 38(2), pp.215-224.



Semnan University



Research Article

The Synthesis of Lanthanum Oxide/Ni Catalyst on the CMK-3 for the CO₂ reforming of CH₄

Abbas Kakoo, Mardali Yousefpour ^{*},

Faculty of Materials and Metallurgical Engineering, Semnan University, Semnan, Iran.

PAPER INFO

Paper history:

Received: 2021-11-28

Revised: 2023-01-17

Accepted: 2023-03-03

Keywords:

Dioxide carbon gas;
Methane;
Lanthanum oxide;
Promoter;
Nickel catalyst.

ABSTRACT

The catalysts with valve metals had been modified to use in the reforming process. Furthermore, there is a trend to the cheaper materials due to the deactivation and high price of the mentioned catalysts. In this case, at the present research work, the Nickel/CMK-3 catalysts with La₂O₃ as the promoter were synthesized by an impregnation method with 3 wt. % of La₂O₃. Also, the Nickel catalysts/CMK-3 and Nickel catalysts-La₂O₃/CMK-3 were characterized by N₂ adsorption-desorption, X-ray diffraction (XRD), Transmission electron microscopy (TEM), Field emission scanning electron microscopy (FE-SEM), Temperature programmed reduction (TPR), and the performance of the catalysts for CO₂ reforming of CH₄. In addition, the temperature programmed reduction (TPR) technique was selected to evaluate the catalyst properties for the CO₂ reforming of CH₄. In final, the obtained results demonstrated that the formation of amorphous mesoporous Carbon with NiO nanoparticles inside the channels of the supported base and also the Lantana oxide addition induced better Nickel oxide dispersion and increased the interaction of the catalyst particles with support. As a result, the Nickel catalysts supported on the Carbon mesoporous has shown enough activity for the CO₂ reforming of CH₄ at 650 °C. However, the mentioned samples were deactivated due to Carbon oxidation according to the TGA results. Therefore, the addition of La₂O₃ with 3 wt. % as a promoter improved the catalytic activity up to 57% and enhanced the catalytic stability at a duration time of 2 hr.

DOI: [10.22075/jhmtr.2023.25371.1367](https://doi.org/10.22075/jhmtr.2023.25371.1367)

© 2022 Published by Semnan University Press. All rights reserved.

1. Introduction

In recent years, the Carbon dioxide reforming of methane has been paid more attention to Syngas production than the other reforming methods [1,2]. According to reaction (1), the CH₄ and CO₂ (Dry reforming reaction feed and greenhouse gases) convert to Syngas [3].



The Syngas can be used to prepare a raw material for Fischer–Tropsch Synthesis to produce the Alkanes and Oxygenates materials [4,5]. The main disadvantage of Carbon dioxide reforming of CH₄ in industrial application is the deactivation of the

catalysts due to the coke deposition on the surface catalysts. The catalyst modified with noble metal has been enough reviewed for reforming process [6]. In addition, metals ions loading, such as Ru, Ce, La, Y. etc. into the pores framework, is one of the excellent routes to provide the active sites [7-11]. So, having the fundamental knowledge of the metal ions effects as the promoter and their interactions with barriers is very noticeable. Yttrium and Yttria with high redox properties and chemical durability are also a proper candidate for the promotion of catalytic properties [12-15]. Costa et al. [16], examined the partial oxidation of methane by Pd/CeO₂ and Pd/Y₂O₃. They concluded that the selectivity to CO in Pd/Y₂O₃ catalyst

*Corresponding Author: Mardali Yousefpour

Email: myousefpour@semnan.ac.ir

is higher than that of Pd/CeO₂. Because, Pd/Y₂O₃ catalyst facilitates the transformation of ethoxy species to the reforming reaction, however, Pd/CeO₂ catalyst leads to the high-speed oxidization of Carbon monoxide to Carbon dioxide. Wu et al. [17] reported an impregnated to synthesis the different Rh-supported catalysts in the reforming of methane. They found the order of catalytic activity as follow: Rh/Y₂O₃ > Rh/CeO₂ > Rh/La₂O₃ > Rh/Al₂O₃. The activity of Rh/Y₂O₃ in the reforming route was modified due to the formation of the surface oxygen vacancies by Y₂O₃ [18]. Furthermore, Chen et al. studied the Cu effect on Ni-Cu bimetallic catalysts on YSZ base and reported the Cu addition induced the Ni-Cu alloy formation and the inhibition of coke formation in the reforming process [19]. Besides, Niazi et al. investigated the Cu, Mg, and Co effects on Ni/CeO₂ base in reforming reaction. They showed that the addition of the mentioned elements caused to improve the stability and selectivity of the catalyst [20]. However, the expensive cost and the deactivation of the catalysts with a noble element can be led a trend toward cheaper metals.

The deactivation of the catalyst is the Carbon deposition on the surface catalyst. As a result, it decreases the specific surface area, the active sites, and selective properties. Therefore, Nickel catalysts are preferred to other noble metal catalysts as they are cheaper, more active, and resistant to Carbon depositions in CO₂ reforming reaction [21]. Furthermore, the Carbon materials have been applied as catalysts or catalyst supports in the different processes due to having porosity or Oxygen surface groups, which can affect the selectivity and activity of the catalysts [22]. Therefore, a large number of Carbonaceous materials (Carbon black, activated Carbon, and the Carbon materials created from biomass remains) are investigated as the catalyst in the decomposition of methane gas [23]. Carbon-based catalysts are more beneficial than metal catalysts and Carbon-based catalysts due to having available, durable, and resistant to sulfur or other impurities [24-26]. In this case, Fidalgo et al. [27] studied the Carbon catalysts and microwave receptors in the CO₂ reforming of methane. They found that the oxidized Carbon observed on the surface of the catalysts happens under microwave heating, especially. Moreover, an important activity of CO₂ on the Carbon materials was reported. Jun et al. [28] applied La and Ce/CMK-3 as the catalysts for the CO₂ reforming of the CH₄ reaction. As a result, they reported that the ordered mesoporous Carbon materials, which were made of SBA-15 and KIT-6 hard Silica templates, could be used as the catalyst. The activity and stability of the catalyst doped with Ce and La on the CMK-3 base were higher as compared to the similar catalyst on the SBA-15 and KIT-6. Despite all of those, the research in the field of Carbon and Carbon catalysts in the CO₂

reforming of CH₄, the Nickel/CMK-3 catalysts have not been studied. Therefore, this research work was focused on the Nickel catalysts/CMK-3, and Nickel catalysts-La₂O₃/CMK-3 in the CO₂ reforming of CH₄, and the mentioned catalysts were synthesized and characterized.

2. Research Method and Materials

2.1. Preparation of precursors

The salt of Ni(NO₃)₂·6H₂O and La(NO₃)₃·6H₂O, Sucrose, and TEOS (Merck, 99%) were considered as the Nickel and Lanthanum, Carbon, and Silicon precursor. Furthermore, (Poly(ethylene glycol)-block-poly(propylene glycol)-block-poly(ethylene glycol), M=5800, Aldrich) and hydrochloride acid were used as the matrix and the pH stabilizer.

2.2. Synthesis of SBA-15

In the present work, Silica mesoporous is made as a hard template by using the hydrothermal route [29]. In the further step, the surfactant wax (8.0 g) is dissolved in the solution of deionized water (60 ml) and HCl (2M, 240 ml). Then, the TEOS (17 g) is added drop by drop to the mentioned solution at 40 °C and then is stirred vigorously for 24 hr. Subsequently, the obtained solution is transferred to a sealed Teflon vessel and dried at 100 °C for 24 hr. In the final step, the white powder is centrifuged, washed with deionized water, and heated at 90 °C until dehydrating. Then, the calcination treatment is carried out at 550 °C under the atmosphere conditions for 6 hr.

2.3. Synthesis of CMK-3

The replication method was used to form the combination of ordered mesoporous Carbon (CMK-3) and SBA-15. Furthermore, Sucrose was applied as a hard template and Carbon source according to method used by Gharahshiran et al. [25]. In this case, Silica (2.0 g) template was dispersed in the solution of Sucrose (2.5 g), H₂SO₄ (0.28 g, 98%), and deionized water (10 g). The mixture was heated at 100 °C for 6 hr in a heater and then the temperature was increased to 160 °C for 6 hr. The Silica template with partial polymerized and carbonized sucrose was heated again at 100 °C and then at 160 °C by a heater. In follow, the mixed solution of Sucrose (1.6 g), H₂SO₄ (0.18 g, 98%), and H₂O (10 g) was prepared. To complete the carbonization, the Sucrose-Silica composite was heated at 900 °C for 6 hr under the Argon atmosphere with a stream rate of 170 ml/min. Furthermore, hydrofluoric acid (5 wt. %) was used to remove the hard template of Silica at room temperature. In follow, mesoporous Carbon was filtered, washed with ethanol, and heated at 110 °C for 12 hr. To loading of Nickel (10 wt. %) into the mesoporous matrix, the impregnation method was used [30-31]. Subsequently, the heated Nickel catalyst was impregnated with La(NO₃)₃·6H₂O (3 wt. %) in the

same way as the addition of La_2O_3 , and two metal catalysts were heated at 90°C similar to Ni catalysts as well. The schematic of synthesis of mesoporous Carbon and catalysts was shown in Figure 1.

2.4. Catalyst evaluation

The catalyst and promoter crystalline phase were studied using the X-ray diffraction analysis by a Bruker D8 diffractometer. The source of XRD analysis was carried out using the $\text{Cu-K}\alpha$ radiation with $\lambda=0.15418$ nm and operated at 40 kV and 30 mA. Field emission electron scanning microscopy (MIRA3 TESCAN-XMU, FE-SEM) with an EDS detector was used for the observation of the morphology of the materials. A surface area analyzer (BEL, Sorp mini-II) was carried out to evaluate the N_2 adsorption/desorption isotherms of catalysts at 196°C . The specific surface area calculation was determined using the Brunauer-Emmett-Teller (BET) technique. Furthermore, the pore diameter (DBJH) and pore volume were determined from the adsorption branch of isotherm curves by the conventional Barrett-Joyner-Halenda (BJH) method [32-33]. Before each test, the catalysts were heated to dry at 150°C for 3 hr. The X-ray fluorescence examination was considered to evaluate the chemical compositions of the samples (ED, 2000 model, Oxford Co.). To take the TEM images, the samples were dispersed in an alcohol solution under ultrasonic conditions and thus a drop of the obtained solution was placed over the Carbon film grid to remove the water [34]. The reduction properties of the catalysts were studied using the temperature-programmed reduction analysis with a micrometric chemisorb2750. Subsequently, 50 mg of the sample was placed into the fixed-bath reactor and heated from

100°C to 700°C with a heat rate of $10^\circ\text{C}/\text{min}$ in the mixture of Hydrogen: Argon (10:90) atmosphere with a stream rate of 30ml/min. Before each test, the specimens were degassed in the Argon atmosphere at 250°C for 1 hr. The thermogravimetric (L70/2171, Germany) analysis was applied to confirm the existence of Carbon element over the fresh catalyst. The H_2 depletion during the reduction process was evaluated using the gas chromatograph equipped with the thermal conductivity detector.

2.5. Activity study of catalysts

The catalytic activity was determined using a quartz tubular fixed bath continuous stream micro reactor (i.e. 8 mm) at different temperatures under atmospheric pressure. Then, the specimens with 10Nickel/CMK-3 and $3\text{La}_2\text{O}_3/10\text{Ni}/\text{CMK-3}$ were pressed, crushed, and separated from 40 to 60 mesh. Furthermore, a micro reactor was filled with the granules of catalyst in the constant weight (0.2g). In addition, before doing the catalytic reaction, the specimens were reduced in an atmosphere of pure H_2 with a stream rate of 30 ml/min at 700°C for 3 hr. Then, the reactor was cooled to temperature of 500°C [34]. In a final step, a mixture of reactants (CH_4 and CO_2 with: $\text{GHSV}=12000\text{ml}/(\text{h.g}_{\text{cat}})$, $\text{CO}_2/\text{CH}_4=1:1$, $P=1\text{atm}$) were transferred into micro reactor. The activity evaluation was carried out at different temperatures in the range of 500 to 700°C with a rate of $50^\circ\text{C}/\text{min}$. To remove the water from the specimens, they were sent to a water-trap chamber [34]. Subsequently, the chemical composition of the gas was evaluated using a gas chromatograph (HID YL-6100, with a carboxen 1010 column).

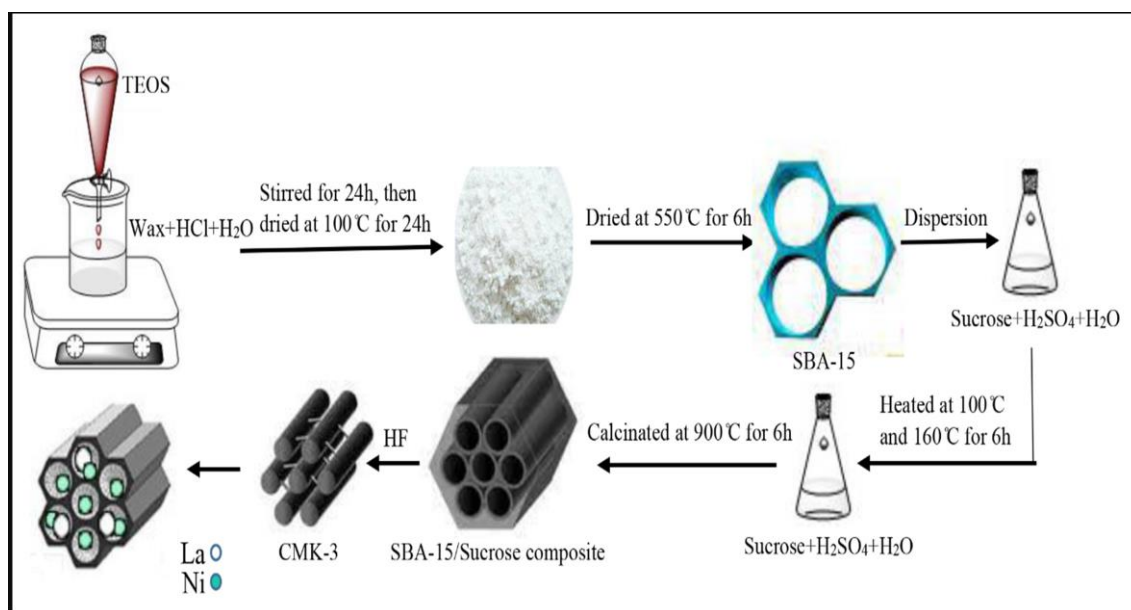


Figure 1. The schematic figure of the synthesis of mesoporous Carbons and catalysts.

3. Results and Discussions

3.1. Structural evaluation

The high-angle X-ray diffraction spectra from 10 to 70 degree for the Nickel catalysts/CMK-3 and Nickel catalysts-La₂O₃/CMK-3 is observed in Figure 2. As shown in Figure 2, the intensity of the peaks of specimens is in the range of 10 to 30 degree and is related to the amorphous mesoporous Carbon [33-35]. The XRD spectra of Ni-CMK-3 shows the three diffraction peaks at 2θ of 37.18, 43.31, and 62.77 degree; which are confirmed the NiO nanoparticles formation inside the support channels according to JCPDS 04-0835 standard. Furthermore, in the La₂O₃/Nickel-CMK-3 catalyst, similar to the Ni/CMK-3 catalyst, there are the main peaks of Nickel oxide. Additionally, any diffraction peak of La₂O₃ is not observed due to the low or well-dispersed non-crystalline phase of lanthanum oxide or the small crystallite size of oxides, which are out of the detection limit of the XRD analyzer [34].

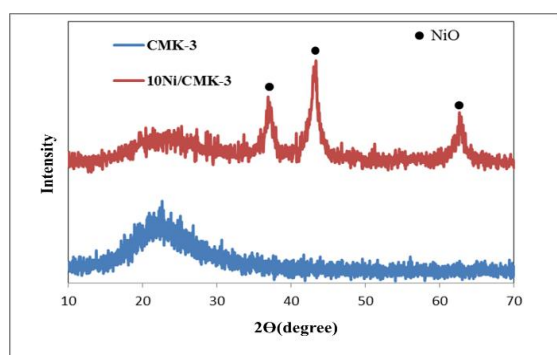


Figure 2. Intensity (a.u.) via 2Teta (degree) of CMK-3, 10Ni/CMK-3, 3La₂O₃/10Ni/CMK-3.

Besides, the textural details of fresh catalysts are observed in Table 1. The average size of Nickel oxides crystalline is determined using the following Scherrer equation:

$$D = (K\lambda) / (\beta \cos\theta) \quad (2)$$

In the Scherrer relation, D is the average size of the crystalline grains, which is smaller or equal to the grain size; K is a dimensionless shape factor and can be assumed to be 1. λ is the wavelength of X-ray; β is the width of line broadening at the half of peak with maximum intensity and θ is the diffraction angle. The

XRD results indicated that the addition of La₂O₃ (3 wt%) decreased the Ni crystallite size and increased the dispersion of Ni particles (Table 1). The XRF examination data of the Ni/SBA-15/La₂O₃ catalysts are summarized in Table 1 (the weight percent of Ni less than 10% and the weight percent of La less than 3%). The results in Table 1 show some of the Nickel and La particles that are not wholly incorporated in the channels of the synthesized specimens. Also, the weight loss phenomena has happened in the duration of the washing treatment in the impregnation duration process. Furthermore, the oxide materials of Al₂O₃, P₂O₅, MgO, and Fe₂O₃ are in XRF data due to the existence of impurities in raw materials that are used to produce the samples.

Figure 3, shows the N₂ adsorption-desorption isotherms and pore size distribution spectra of the CMK-3 support, Nickel/CMK-3, and La₂O₃/Nickel-CMK-3 catalysts. The curves in Figure 3a and 3b display the classic type-IV of the N₂ adsorption-desorption isotherms with a perfect hysteresis loop, which indicate the formation and presence of the mesoporous materials.

In all samples, after loading the Ni and La₂O₃ inside the Silica template, the hysteresis loop is observed that has altered from H1 to H4 type. In the Nickel catalyst supported on Carbon mesoporous, the type of hysteresis loop is similar to the CMK-3 hysteresis loop, which is indicated by the CMK-3 mesoporous channels after loading of the Nickel (10 wt. %). However, in the La₂O₃/10Nickel-CMK-3 catalyst, the loop hysteresis is very weak. As a result, the adsorption branch over the desorption branch and the width of the loop hysteresis are very wide, which is expected a very border pore size distribution compared to the data reported in Table 2. Furthermore, Table 2 displays the results of the textural parameters of the S_{BET}, the volume of the total pore (V), average pore diameter (d), Nickel oxide crystallite size (d_{NiO}), and Nickel oxide dispersion (D_{NiO}). Thus, the results show the specific surface area, and the average pore volume of the CMK-3 support, which is reduced after the Nickel loading from 781 to 240 m²/g and from 0.78 to 0.58 cm³/g, respectively. However, the average pore diameter increases from 4 to 9 nm due to the filling of mesoporous of the CMK-3 matrix with Nickel oxide nanoparticles, which leads to the closure of the Carbon micro pores. Therefore, the larger average pore diameter is obtained due to the simultaneous reduction in the surface and pores volume, which is expected that most Nickel oxide nanoparticles are incorporated within the mesopores.

In comparison to the structural properties of the Nickel catalysts with and without a promoter, it can be concluded that the specific surface area of the modified catalyst with lanthana has decreased.

Table 1. The composition of with and without promoter catalysts

NiO (%wt)	La ₂ O ₃ (%wt)	Al ₂ O ₃ (%wt)	P ₂ O ₅ (%wt)	MgO (%wt)	Fe ₂ O ₃ (%wt)	Sample
9.02	-	0.92	0.17	0.31	0.3	10Nickel/CMK-3
8.79	2.96	0.8	0.07	0.27	0.2	3La ₂ O ₃ /10Ni/CMK-3

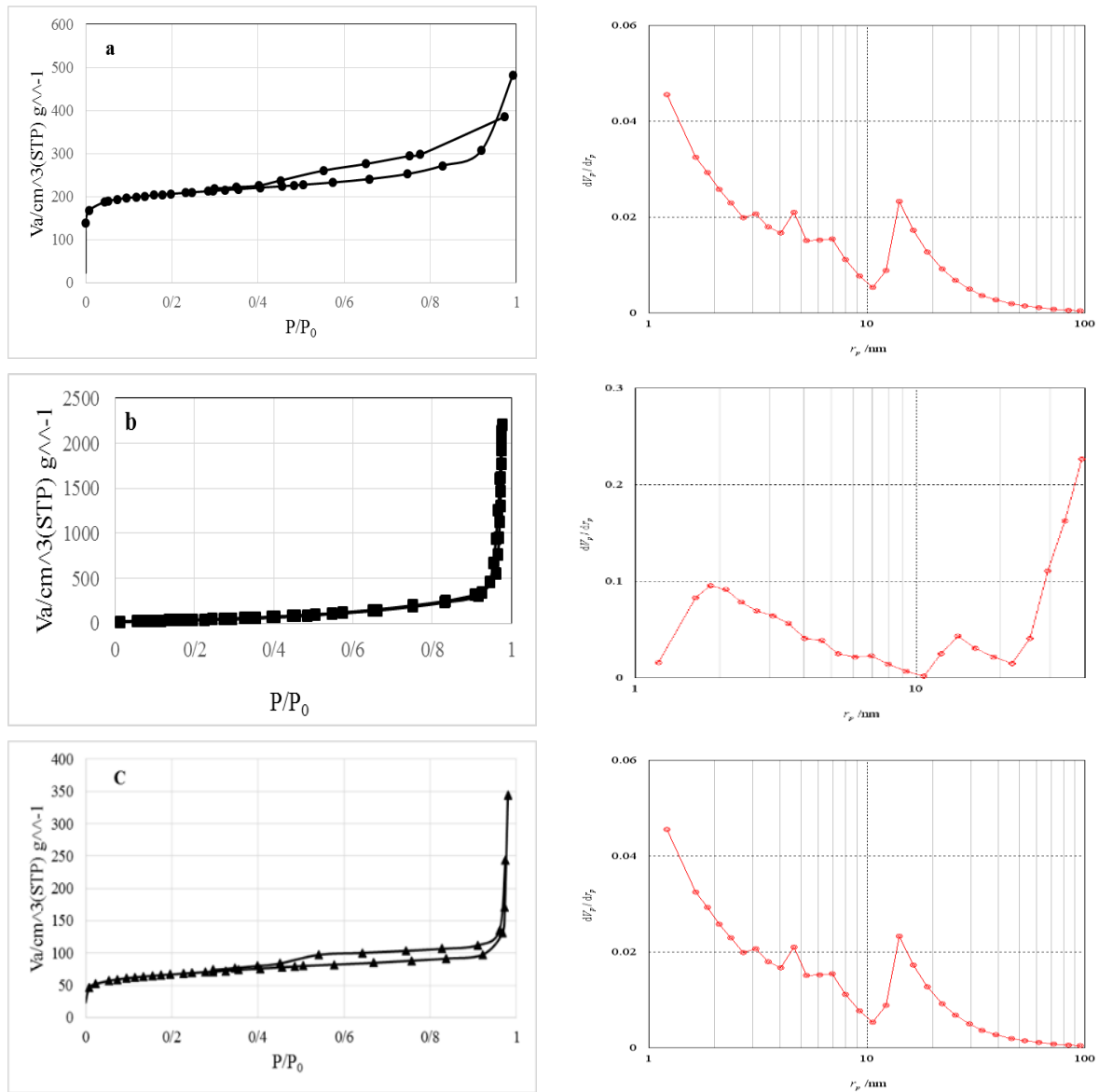


Figure 3. a: Adsorption-Desorption Isotherms, BJH Adsorption pore size distribution in supported catalyst b: CMK-3, 10Nickel/CMK-3, and c: 3La₂O₃/10Ni/CMK-3.

Table 2. The structural properties of the matrix with and without promoter catalyst

Surface area (m ² /g)	Average pore volume (cm ³ /g)	Average pore diameter (nm)	NiO crystallite size (nm)	%Dispersion	Sample
781	0.73	3.8	-	-	CMK-3
239.7	0.53	8.86			10Nickel/CMK-3
175	49.3	9.77	6.7	5.13	3La ₂ O ₃ /10Ni/CMK-3

However, the amount of average diameter and the amount of volume of pores have increased. Furthermore, the size of the NiO nanoparticles at the catalyst decreases after the addition of Lanthanum oxide. In particular, the Lantana addition leads to better Nickel oxide dispersion and increases the interaction of the catalyst particles with the support.

Moreover, the loading of the Lanthanum oxide as a promoter can induce a further decrease in the amount of specific surface area, which is indicated by the addition of Lanthanum oxide and is induced the filling of more mesoporous channels. Therefore, the average pore volume is decreased. To know more details about Ni distribution over the 10Ni/CMK-3 and

3La₂O₃/10Ni/CMK-3 catalysts, TEM analysis is carried out to evaluate the primary sample of the catalysts. Then, TEM micro images of the catalyst specimens are presented in Figure 4.

In the CMK-3 support and unmodified Ni catalyst, a long uniform channel of the mesoporous can be observed at the highly ordered materials [29], which are known as the self-assembly of the mesostructured nanoparticles and a like-hierarchical structure [25]. These results are in agreement with the obtained results of the N₂ adsorption-desorption curves. Moreover, the semispherical Nickel oxide particles are well-dispersed on the surface of the mesoporous channels and inside the mesoporous channels [29].

Furthermore, Figure 4 shows the mesoporous Carbon materials, which are modified by La₂O₃. The main mechanism of the Lanthanum promoter is related to the roughness formation on the surface of the Nickel catalyst by providing the defects and disorders of network and then has an important role to control the activity and selectivity of the catalyst. As a result, the catalyst with La (3 % wt.) has the highest resistance to Carbon deposition due to the reduction in the size of the Nickel oxide particles, which prevents the creation and growth of the graphite. Therefore, it can be found that the main role of Lanthanum was the high nitrogen storage capacity of La₂O₃, which gasified the deposit of Carbon from methane decomposition reaction (Figures 4 and 5). Thus, less formation of Carbon and the best stability are obtained in the catalyst with the addition of La₂O₃ (3 % wt.). Furthermore, scanning electron microscopy images indicate the presence of the agglomerated nanometer particles in the matrix of metal particles (Figure 5).

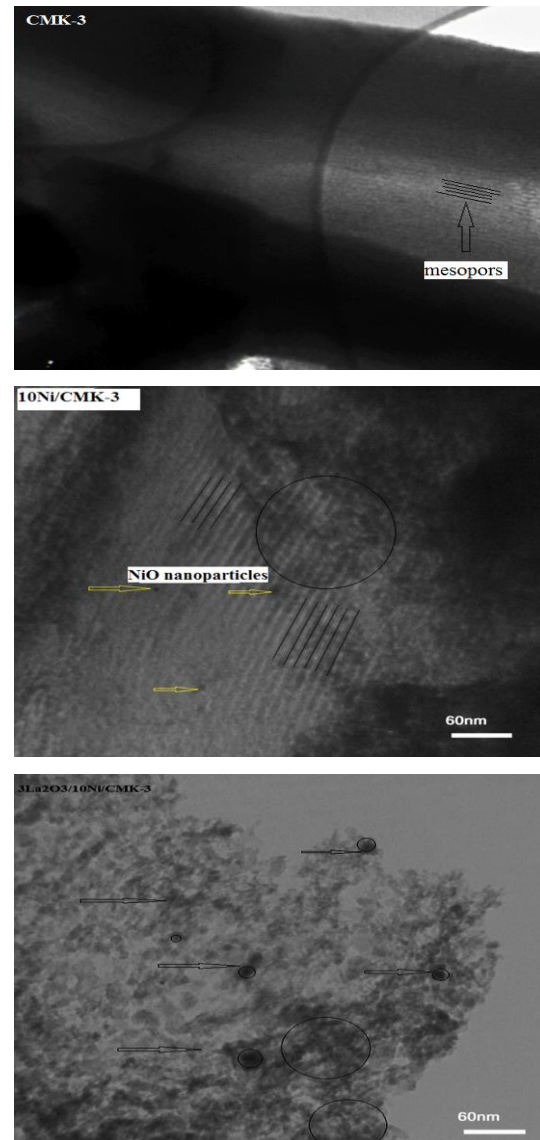


Figure 4. TEM micrographs of a: CMK-3, b: 10Nickel/CMK-3, and c: 3La₂O₃/10Ni/CMK-3.

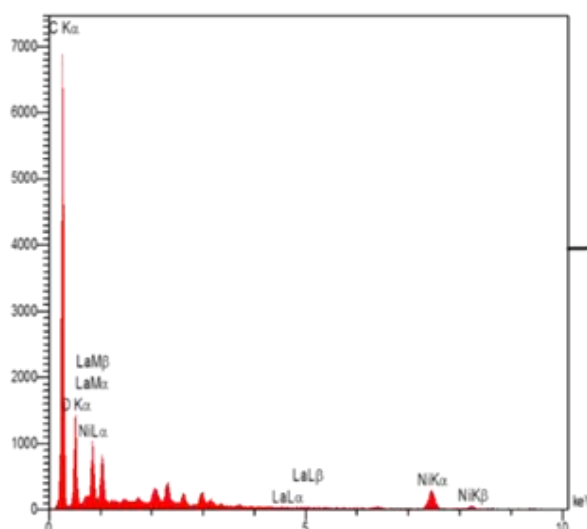


Figure 5. Image of Scanning electron microscope of 3La/10Nickel/CMK-3 sample

A semi-quantitative chemical analysis obtained with X-ray diffraction spectroscopy indicates the presence of elements (Table 3). A study on the reduction behavior of the catalysts and the TPR profiles for the Nickel catalysts with and without La₂O₃ (3 % wt.) is carried out and the results are presented in Figure 6. As shown in this figure, a reduction peak appears at the 400 °C in the Nickel/CMK-3. The Nickel oxide reduction point is appeared in the range of 300 to 400 °C as well [33]. Hence, the reduction point is observable at 400 °C, which is related to the NiO nanoparticles with relatively well-interacted in the support. In other words, the reduction of Nickel oxide into metallic Nickel has completely happened. In the TPR profile of 3La₂O₃/10Ni/SBA-15, three peaks are appeared. In comparison to the Nickel catalyst, the first peak appeared at a lower temperature of 300 °C. Furthermore, the second peak at the average temperature from 400 °C to 500 °C and the third peak at 700 °C are observed.

Table 3. The percentage of weight elements specified with EDS analysis.

EL.	C	O	Ni	La
W%	71.19	22.95	5.74	0.11

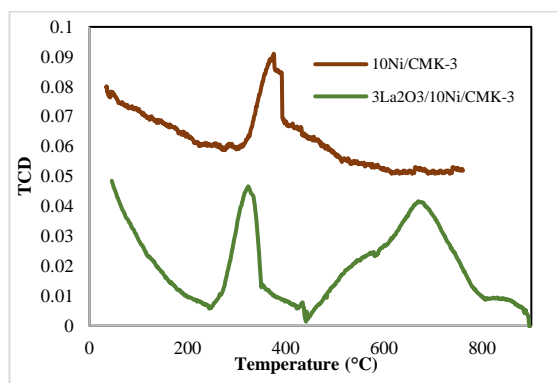


Figure 6. H₂-TPR profiles of 10Nickel/CMK-3, 3La₂O₃/10Ni/CMK-3.

As a final result, the first point had related to a reduction of the Nickel oxide with the weaker reaction with the support. Furthermore, the second point had attributed to the methane formation on the CMK-3 support according to the following reaction:



In addition, the third point had related to the stronger interaction between the lanthanum and the Nickel oxide. This means that the presence of the lanthanum oxide as a promoter facilitates the reduction of the Nickel oxide and thus the lanthanum oxide leads to the formation of the Ni-La solid solution phase with a stronger interaction with support, and then improves the thermal stability of the catalys [36].

3.2. CO₂ reforming of CH₄

To evaluate the dry reforming of CH₄, the catalysts are heated to 700 °C for 3hr, and then the temperature is decreased to 500 °C. Furthermore, the Hydrogen gas is injected during the evolution of Methane and Carbon dioxide conversion, and the temperature is increased in the range of 500 to 700 °C. Besides, the reactor tests are carried out in the same conditions for the Nickel catalysts/CMK-3 and Nickel catalysts-La₂O₃/CMK-3. Thus, the results have demonstrated the activation of the Nickel catalysts with and without the Lanthanum oxide on CMK-3, which is started at 600 °C and below 600 °C. Therefore, Methane conversion and catalytic activity have not appeared in the mentioned conditions.

Moreover, the initial activity of both catalysts achieved at 600°C and reached near the maximum activity at 650 °C. Then, they were immediately deactivated after about one hour of reaction. In the previous research [25], the same results have been obtained for the La/CMK-3 and Ce-CMK-3 catalysts as well. The reason for the rapid deactivation of these catalysts can be attributed to various factors. The reactor tests shown that the thermal stability of the mesoporous Carbon support is weaker than the thermal stability of the mesoporous Silica supports at 700 °C. Thus, at the experimental evaluation, the problem of evaporation and burning of the Carbon support are observed at temperature up to 650 °C.

The results of the catalytic activity of the Nickel catalysts/CMK-3 and Nickel catalysts-La₂O₃/CMK-3 at 650 °C are reported in Table 4. Furthermore, the reverse water-gas shift reaction (RWGS) causes an increase to CO₂ conversion than CH₄ conversion for both catalysts. The molar ratio of H₂/CO in the CO₂/methane reforming of CH₄ must be equal to 1, which in this study is less than 1 for both catalysts. This molar ratio can be affected by the different reactions of RWGS for example; Boudwouard reaction and CH₄ decomposition. Therefore, in this work, the RWGS reaction can be induced the lower formation of the H₂/CO ratio. These results indicated that the addition of La₂O₃ as a promoter has a positive effect on promoting the catalyst performance than the unprompted Ni catalyst. The higher catalytic activity of La₂O₃ is incorporated into the Nickel/CMK-3 catalyst, and related to well-dispersed and excellent metal-support interaction [35].

Table 4. Methane and Carbon dioxide via temperature with: GHSV=12000ml/(h.g_{cat}), CO₂/CH₄=1:1, P=1atm.

Samples	%CH ₄ Conversion	%CO ₂ Conversion
10Nickel/CMK-3	15.08	21.02
3La ₂ O ₃ /10Ni/CMK-3	35.1	40.14

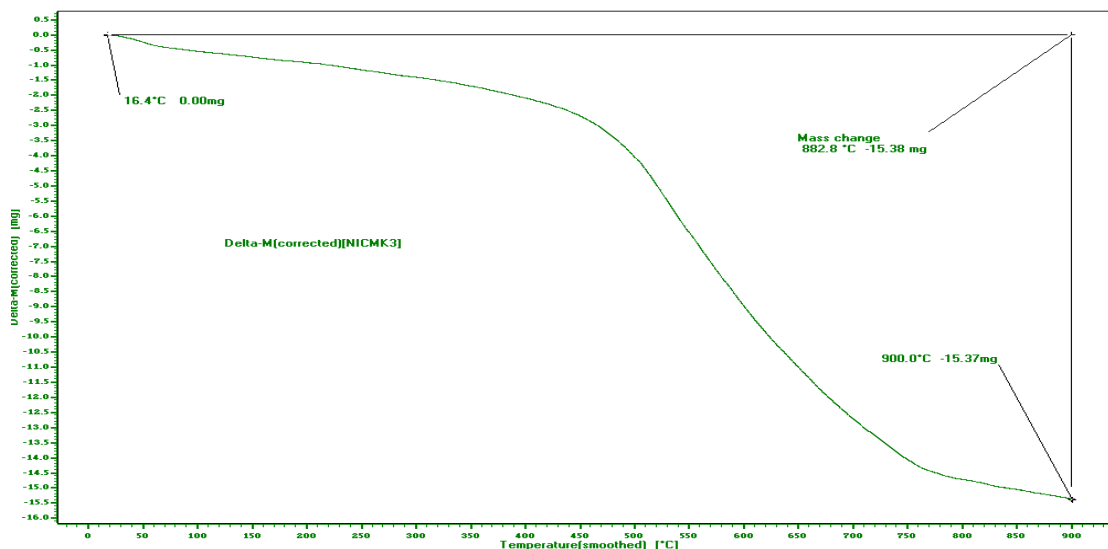


Figure 7. TGA analysis of 10Nickel/CMK-3.

Figure 7 shows TGA graph of the Nickel catalyst. As shown in this figure, the weight loss via temperature is observed, which it has a low rate from room temperature up to 450 °C. However, weight loss is observed with a high slope above 450 °C. The evaluations show that a cation-free Nickel catalyst on the mesoporous Carbon without Lanthanum addition will be about 70% from room temperature to 900 °C. It is most likely due to the burning of Carbon in the vicinity of Oxygen under the TGA reaction conditions.

3.3. Catalytic stability

In the evaluation of the Ni catalysts supported on the Carbon mesoporous performance, it is observed that the Carbon mesoporous as support is not stable at temperatures above 650 °C and is evaporated and deactivated by rapid oxidation as shown in Figure 7.

Previously, there has not been published any result in the field of Methane dry reforming by the Nickel catalysts supported on the Carbon mesoporous. Similar results reported that the stability of the La and Ce catalysts supported on the Carbon mesoporous is about one hour at 650 °C [25]. In the present work, the stability examination is indicated by the Nickel/CMK-3 catalysts, which is not shown good stability. However, after adding Lanthanum oxide to the Nickel/CMK-3 catalyst, the catalyst stability is increased to two hours and then is suddenly deactivated.

Probably, the formation of an intermetallic phase of the Nickel-Lanthanum with a strong interaction with the support is formed with a higher thermal stability of the barrier. In addition, other factors such as the particles sintering of the catalyst, the Carbon deposition, and catalyst oxidation at the high temperature of the reaction can be caused a rapid

deactivation of the catalysts supported on the Carbon mesoporous materials.

4. Conclusions

The Nickel catalysts/CMK-3 and the Nickel catalysts-La₂O₃/CMK-3 were synthesized by an impregnation route to use in the CO₂ reforming of CH₄. In comparison to the Nickel/CMK-3 and 3La₂O₃/10Ni/CMK-3, according to the XRD spectra and Scherer equation, the most dispersion of the Nickel oxide and the minimum size of particle were related to the 3La₂O₃/10Ni/CMK-3. Furthermore, the BET data was shown the addition of Lanthanum oxide, which reduced the surface area of the Nickel/CMK-3 catalyst. The TPR data revealed the addition of a promoter (3 % wt.) into the Nickel/CMK-3 catalyst, which changed the temperature reduction of the NiO to Ni⁰ and enhanced the second temperature peak due to a well-interaction of the La₂O₃ with the support. According to the CO₂ reforming examination, the greatest catalytic activity and stability are related to the La₂O₃-promoted Nickel/CMK-3.

Acknowledgements

The authors acknowledge from Semnan University and Nanonafez Company in Semnan University Science and Technology Park.

Conflicts of Interest

The author declares that there is no conflict of interest regarding the publication of this manuscript. In addition, the authors have entirely observed the ethical issues, including plagiarism, informed consent, misconduct, data fabrication and/or falsification, double publication and/or submission, and redundancy.

References

- [1] Hu, Y.H. and Ruckenstein, E., 2004. Catalytic conversion of methane to synthesis gas by partial oxidation and CO₂ reforming. *Advances in catalysis*, 48(1), pp.297-345.
- [2] Pakhare, D. and Spivey, J., 2014. A review of dry (CO₂) reforming of methane over noble metal catalysts. *Chemical Society Reviews*, 43(22), pp.7813-7837.
- [3] York, A.P., Xiao, T.C., Green, M.L. and Claridge, J.B., 2007. Methane oxyforming for synthesis gas production. *Catalysis Reviews*, 49(4), pp.511-560.
- [4] Fan, M.S., Abdullah, A.Z. and Bhatia, S., 2009. Catalytic technology for carbon dioxide reforming of methane to synthesis gas. *ChemCatChem*, 1(2), pp.192-208.
- [5] Huang, J., Ma, R., Huang, T., Zhang, A. and Huang, W., 2011. Carbon dioxide reforming of methane over Ni/Mo/SBA-15-La₂O₃ catalyst: Its characterization and catalytic performance. *Journal of Natural Gas Chemistry*, 20(5), pp.465-470.
- [6] García-Diéguez, M., Finocchio, E., Larrubia, M.Á., Alemany, L.J. and Busca, G., 2010. Characterization of alumina-supported Pt, Ni and PtNi alloy catalysts for the dry reforming of methane. *Journal of Catalysis*, 274(1), pp.11-20.
- [7] Alvarez-Galvan, C., Melian, M., Ruiz-Matas, L., Eslava, J.L., Navarro, R.M., Ahmadi, M., Roldan Cuenya, B. and Fierro, J.L.G., 2019. Partial oxidation of methane to syngas over nickel-based catalysts: influence of support type, addition of rhodium, and preparation method. *Frontiers in Chemistry*, 7, p.104.
- [8] De Souza, T.L., da SILVA, V.S.T. and Cardozo Filho, L., 2015. Thermodynamic Analysis of synthesis gas production from autothermal reforming of methane. *Blucher Chemical Engineering Proceedings*, 1(2), pp.15460-15468.
- [9] Nikolla, E., Holewinski, A., Schwank, J. and Linic, S., 2006. Controlling carbon surface chemistry by alloying: carbon tolerant reforming catalyst. *Journal of the American Chemical Society*, 128(35), pp.11354-11355.
- [10] Wang, Z., Xu, H., Zhang, Z., Wang, S., Ding, L., Zeng, Q., Yang, L., Pei, T., Liang, X., Gao, M. and Peng, L.M., 2010. Growth and performance of yttrium oxide as an ideal high-κ gate dielectric for carbon-based electronics. *Nano letters*, 10(6), pp.2024-2030.
- [11] Yan, Z., Xu, Z., Yu, J. and Jaroniec, M., 2015. Highly active mesoporous ferrihydrite supported Pt catalyst for formaldehyde removal at room temperature. *Environmental Science & Technology*, 49(11), pp.6637-6644.
- [12] Ballarini, A., Benito, P., Fornasari, G., Scelza, O. and Vaccari, A., 2013. Role of the composition and preparation method in the activity of hydrothermalite-derived Ru catalysts in the catalytic partial oxidation of methane. *International journal of hydrogen energy*, 38(35), pp.15128-15139.
- [13] Kodo, M., Soga, K., Yoshida, H. and Yamamoto, T., 2010. Doping effect of divalent cations on sintering of polycrystalline yttria. *Journal of the European Ceramic Society*, 30(13), pp.2741-2747.
- [14] Liu, H.M. and He, D.H., 2010. Physicochemical properties of Ni/γ-Al₂O₃-Aln and effects of aln on catalytic performance of Ni/γ-Al₂O₃-Aln in partial oxidation of methane. *The Journal of Physical Chemistry C*, 114(32), pp.13716-13721.
- [15] Zhu, Q., Zhao, X. and Deng, Y., 2004. Advances in the partial oxidation of methane to synthesis gas. *Journal of Natural Gas Chemistry*, 13(4), p.191.
- [16] Costa, L.O.O., Silva, A.M., Borges, L.E.P., Mattos, L.V. and Noronha, F.B., 2008. Partial oxidation of ethanol over Pd/CeO₂ and Pd/Y₂O₃ catalysts. *Catalysis Today*, 138(3-4), pp.147-151.
- [17] Wu, X. and Kawi, S., 2010. Steam reforming of ethanol to H₂ over Rh/Y₂O₃: crucial roles of Y₂O₃ oxidizing ability, space velocity, and H₂/C. *Energy & Environmental Science*, 3(3), pp.334-342.
- [18] Liu, H. and He, D., 2011. Properties of Ni/Y₂O₃ and its catalytic performance in methane conversion to syngas. *International journal of hydrogen energy*, 36(22), pp.14447-14454.
- [19] Chen, F., Tao, Y., Ling, H., Zhou, C., Liu, Z., Huang, J. and Yu, A., 2020. Ni-Cu bimetallic catalysts on Yttria-stabilized zirconia for hydrogen production from ethanol steam reforming. *Fuel*, 280, p.118612.
- [20] Niazi, Z., Irankhah, A., Wang, Y. and Arandiyan, H., 2020. Cu, Mg and Co effect on nickel-ceria supported catalysts for ethanol steam reforming reaction. *International Journal of Hydrogen Energy*, 45(41), pp.21512-21522.
- [21] Jabbour, K., El Hassan, N., Casale, S., Estephane, J. and El Zakhem, H., 2014. Promotional effect of Ru on the activity and stability of Co/SBA-15 catalysts in dry reforming of methane. *International journal of hydrogen energy*, 39(15), pp.7780-7787.
- [22] Fidalgo, B. and Menendez, J.Á., 2011. Carbon materials as catalysts for decomposition and CO₂ reforming of methane: a review. *Chinese journal of catalysis*, 32(1-2), pp.207-216.
- [23] Yousefpor, M., Tajally, M., Taherian, Z. and Khoshandam, B., 2021. A comparison of catalyst behavior of Samaria Modified Ni Catalyst Supported on Mesoporous Silica and Carbon for Methane CO₂ Reforming. *Journal of Heat and Mass Transfer Research*, 8(1), pp.105-113.
- [24] Zhao, D., Feng, J., Huo, Q., Melosh, N., Fredrickson, G.H., Chmelka, B.F. and Stucky, G.D., 1998. Triblock copolymer syntheses of mesoporous

- silica with periodic 50 to 300 angstrom pores. *science*, 279(5350), pp.548-552.
- [25] Gharahshiran, V.S., Yousefpour, M. and Amini, V., 2020. A comparative study of zirconia and yttria promoted mesoporous carbon-nickel-cobalt catalysts in steam reforming of ethanol for hydrogen production. *Molecular Catalysis*, 484, p.110767.
- [26] Goscianska, J., Pietrzak, R. and Matos, J., 2018. Catalytic performance of ordered mesoporous carbons modified with lanthanides in dry methane reforming. *Catalysis Today*, 301, pp.204-216.
- [27] Fidalgo, B., Arenillas, A. and Menéndez, J.A., 2010. Influence of porosity and surface groups on the catalytic activity of carbon materials for the microwave-assisted CO₂ reforming of CH₄. *Fuel*, 89, 4002-7.
- [28] Jun, S., Joo, S.H., Ryoo, R., Kruk, M., Jaroniec, M., Liu, Z., Ohsuna, T. and Terasaki, O., 2000. Synthesis of new, nanoporous carbon with hexagonally ordered mesostructure. *Journal of the American chemical society*, 122(43), pp.10712-10713.
- [29] Imperor-Clerc, M., Bazin, D., Appay, M.D., Beunier, P. and Davidson, A., 2004. Crystallization of β-MnO₂ nanowires in the pores of SBA-15 silicas: in situ investigation using synchrotron radiation. *Chemistry of materials*, 16(9), pp.1813-1821.
- [30] Taherian, Z., Yousefpour, M., Tajally, M. and Khoshandam, B., 2017. Promotional effect of samarium on the activity and stability of Ni-SBA-15 catalysts in dry reforming of methane. *Microporous and Mesoporous Materials*, 251, pp.9-18.
- [31] Taherian, Z., Yousefpour, M., Tajally, M. and Khoshandam, B., 2017. A comparative study of ZrO₂, Y₂O₃ and Sm₂O₃ promoted Ni/SBA-15 catalysts for evaluation of CO₂/methane reforming performance. *International Journal of Hydrogen Energy*, 42(26), pp.16408-16420.
- [32] Rouquerol, J., Rouquerol, F., Llewellyn, P., Maurin, G. and Sing, K.S., 2013. *Adsorption by powders and porous solids: principles, methodology and applications*. Academic press.
- [33] Cohen, E.R., Mills, I.M., Cvitas, T., Frey, J.G., Quack, M., Holström, B. and Kuchitsu, K. eds., 2007. *Quantities, units and symbols in physical chemistry*. Royal Society of Chemistry.
- [34] Taherian, Z., Yousefpour, M., Tajally, M. and Khoshandam, B., 2017. Catalytic performance of Samaria-promoted Ni and Co/SBA-15 catalysts for dry reforming of methane. *International Journal of Hydrogen Energy*, 42(39), pp.24811-24822.
- [35] Li, J.F., Xia, C., Au, C.T. and Liu, B.S., 2014. Y₂O₃-promoted NiO/SBA-15 catalysts highly active for CO₂/CH₄ reforming. *International journal of hydrogen energy*, 39(21), pp.10927-10940.
- [36] Juan-Juan, J., Román-Martínez, M.C. and Illán-Gómez, M.J., 2009. Nickel catalyst activation in the carbon dioxide reforming of methane: effect of pretreatments. *Applied Catalysis A: General*, 355(1-2), pp.27-32.
- [37] Nabgan, W., Abdullah, T.A.T., Mat, R., Nabgan, B., Jalil, A.A., Firmansyah, L. and Triwahyono, S., 2017. Production of hydrogen via steam reforming of acetic acid over Ni and Co supported on La₂O₃ catalyst. *international journal of hydrogen energy*, 42(14), pp.8975-8985.